

Topics in Fluorescence Spectroscopy

Volume 5 Nonlinear and Two-Photon- Induced Fluorescence

Edited by
JOSEPH R. LAKOWICZ

Topics in Fluorescence Spectroscopy

Volume 5
Nonlinear and
Two-Photon-Induced Fluorescence

Topics in Fluorescence Spectroscopy

Edited by JOSEPH R. LAKOWICZ

Volume 1: Techniques

Volume 2: Principles

Volume 3: Biochemical Applications

Volume 4: Probe Design and Chemical Sensing

Volume 5: Nonlinear and Two-Photon-Induced Fluorescence

Topics in Fluorescence Spectroscopy

Volume 5
Nonlinear and
Two-Photon-Induced Fluorescence

Edited by

JOSEPH R. LAKOWICZ

*Center for Fluorescence Spectroscopy and
Department of Biochemistry and Molecular Biology
University of Maryland School of Medicine
Baltimore, Maryland*

KLUWER ACADEMIC PUBLISHERS
NEW YORK, BOSTON, DORDRECHT, LONDON, MOSCOW

eBook ISBN: 0-306-47070-5
Print ISBN: 0-306-45553-6

©2002 Kluwer Academic Publishers
New York, Boston, Dordrecht, London, Moscow

All rights reserved

No part of this eBook may be reproduced or transmitted in any form or by any means, electronic, mechanical, recording, or otherwise, without written consent from the Publisher

Created in the United States of America

Visit Kluwer Online at: <http://www.kluweronline.com>
and Kluwer's eBookstore at: <http://www.ebooks.kluweronline.com>

Contributors

Valery L. Bogdanov • Vavilov State Optical Institute, 199034 St. Petersburg, Russia; *present address*: Molecular Tool Inc., Hopkins Bayview Research Campus, Baltimore, Maryland 21224

K. M. Berland • Laboratory for Fluorescence Dynamics, Department of Physics, University of Illinois at Urbana-Champaign, Urbana, Illinois 61801

G. J. Blanchard • Department of Chemistry, Michigan State University, East Lansing, Michigan 48824

Patrik R. Callis • Department of Chemistry and Biochemistry, Montana State University, Bozeman, Montana 59717

S.-Y. Simon Chen • Department of Physics and Astronomy, Western Kentucky University, Bowling Green, Kentucky 42101; *present address*: MPAUDIO, Inc., East Brunswick, New Jersey 08816

C. Y. Dong • Laboratory for Fluorescence Dynamics, Department of Physics, University of Illinois at Urbana-Champaign, Urbana, Illinois 61801

T. French • Laboratory for Fluorescence Dynamics, Department of Physics, University of Illinois at Urbana-Champaign, Urbana, Illinois 61801

E. Gratton • Laboratory for Fluorescence Dynamics, Department of Physics, University of Illinois at Urbana-Champaign, Urbana, Illinois 61801

Ignacy Gryczynski • Center for Fluorescence Spectroscopy, Department of Biochemistry and Molecular Biology and Medical Biotechnology Center, University of Maryland at Baltimore School of Medicine, Baltimore, Maryland 21201

Stefan W. Hell • High Resolution Optical Microscopy Group, Max-Planck-Institute for Biophysical Chemistry, D-37070 Göttingen, Germany

Carey K. Johnson • Department of Chemistry, The University of Kansas, Lawrence, Kansas 66045

Borys Kierdaszuk • Department of Biophysics, University of Warsaw, PL-02089 Warsaw, Poland

Joseph R. Lakowicz • Center for Fluorescence Spectroscopy, Department of Biochemistry and Molecular Biology and Medical Biotechnology Center, University of Maryland at Baltimore School of Medicine, Baltimore, Maryland 21201

P. T. C. So • Laboratory for Fluorescence Dynamics, Department of Physics, University of Illinois at Urbana-Champaign, Urbana, Illinois 61801

B. Wieb Van der Meer • Department of Physics and Astronomy, Western Kentucky University, Bowling Green, Kentucky 42101

Chaozhi Wan • Department of Chemistry, The University of Kansas, Lawrence, Kansas 66045; *present address*: Department of Chemistry, California Institute of Technology, Pasadena, California 91125

Watt W. Webb • School of Applied Physics, Cornell University, Ithaca, New York 14853

Chris Xu • School of Applied Physics, Cornell University, Ithaca, New York 14853

Preface

Fluorescence spectroscopy continues its advance to more sophisticated methods and applications. As one looks over the previous decades, it appears that the first practical instruments for time-resolved measurements appeared in the 1970's. The instrumentation and analysis methods for time-resolved fluorescence advanced rapidly throughout the 1980's. Since 1990 we have witnessed a rapid migration of the principles of time-resolved fluorescence to cell biology and clinical applications. Most recently, we have seen the introduction of multi-photon excitation, pump-probe and stimulated emission methods for studies of biological macromolecules and for cellular imaging. These advanced topics are the subject of the present volume.

Two-photon excitation was first predicted by Maria Goppert-Mayer in 1931, but was not experimentally observed until 1961. Observation of two-photon excitation required the introduction of lasers which provided adequate photon density for multi-photon absorption. Since the early observations of two-photon excitation in the 1960s, multi-photon spectroscopy has been limited to somewhat exotic applications of chemical physics, where it is used to study the electronic symmetry of small molecules. Placing one's self back in 1980, it would be hard to imagine the use of multi-photon excitation in biophysics or cellular imaging. Fortunately, rapid advances in laser technology make such applications not only possible, but increasingly routine throughout the biological sciences. The availability of picosecond and femtosecond lasers has allowed multi-photon excitation and time-resolved fluorescence on dilute solutions. The use of multi-photon excitation allows molecules typically absorbing in the ultraviolet and visible regions of the spectrum to be excited with long wavelength red or near-infrared pulses. These longer wavelengths are not absorbed by blood and most biological molecules. Also skin is translucent at longer wavelengths, suggesting the possibility of non-invasive methods for subdermal measurements and imaging. In fluorescence microscopy, the use of multi-photon excitation allows selective excitation of chosen volumes in a three-dimensional sample, without photobleaching or absorption in regions outside of the focal plane. This possibility of three-dimensional imaging, with suppression of out-of-focus fluorescence comparable to confocal detection, has stimulated much of the current interest in

multi-photon spectroscopy. Because of the long wavelengths employed, work is already in progress to do three-dimensional imaging of skin with multi-photon excitation.

And finally, it seems valuable to mention a change in the paradigm of time-resolved fluorescence. Until recently, almost all such measurements were performed with a single excitation pulse to create the excited state population, followed by measurement of the resulting emission. The availability of sophisticated pulsed lasers is now allowing multi-pulse experiments to be performed in solution and in microscopy. Such experiments include stimulated emission microscopy and fluorescence quenching by stimulated emission. The latter technique allows the excited state population to be controlled based on decay time, wavelength, or orientation. In summary, we are now in the midst of the transfer of sophisticated multi-photon and stimulated emission concepts to problems in biophysics and cell biology.

Joseph R. Lakowicz
Baltimore

Contents

1. The Theory of Two-Photon-Induced Fluorescence Anisotropy

Patrick R. Callis

1.1. Introduction	1
1.2. Two-Photon Absorption	2
1.2.1. Qualitative Aspects.	2
1.2.2. A Brief History	7
1.2.3. Quantitative Description	9
1.3. Anisotropy Theory	11
1.3.1. Introduction and Scope	11
1.3.2. Excitation with Linearly Polarized Light	13
1.3.3. Excitation with Circularly Polarized Light	14
1.3.4. The Two-Dimensional Limit with Linear Polarization.	15
1.3.5. Three-Dimensional Tensors	20
1.4. Comparison with Experiment	25
1.4.1. Introduction	25
1.4.2. Polyenes.	25
1.4.3. Benzene Derivatives	26
1.4.4. Indoles.	31
1.5. Some Predictions	35
1.5.1. Phenylalanine	35
1.5.2. Tyrosine	36
1.5.3. Indole in Nonpolar Solvent	37
1.5.4. 5-Methoxyindole	37
1.5.5. Nucleotides.	37
1.6. Concluding Remarks	38
References	39

2. Anisotropy Decays Induced by Two-Photon Excitation

Carey K. Johnson and Chaozhi Wan

2.1. Introduction	43
-----------------------------	----

2.1.1.	Theoretical Background	45
2.1.2.	Time-Resolved Two-Photon Excitation	48
2.2.	Orientational Distributions Induced by Two-Photon Excitation	50
2.2.1.	Orientational Averages and Spherical Tensors.	50
2.2.2.	Spherical Tensors: A Primer	51
2.2.3.	Two-Photon Photoselection	55
2.2.4.	Two-Photon Anisotropies	59
2.2.5.	Two-Photon Anisotropic Distributions.	64
2.2.6.	The Special Case of a 2×2 Tensor	69
2.3.	Two-Photon Anisotropy Decay	71
2.3.1.	Rotational Diffusion.	71
2.3.2.	Two-Photon-Induced Reorientational Decay	73
2.3.3.	Time Dependence of the Two-Photon Anisotropies	75
2.3.4.	Example: Perylene.	77
2.4.	Conclusion	82
	References.	83

3. Multiphoton Excitation of Biochemical Fluorophores

Joseph R. Lakowicz and Ignacy Gryczynski

3.1.	Introduction.	87
3.2.	Two-Photon Excitation of DPH.	89
3.2.1.	Emission Spectra and DPH Intensity Decays for 1PE and 2PE	89
3.2.2.	Anisotropy Spectra with 2PE.	92
3.2.3.	Theory of Photoselection with MPE.	93
3.2.4.	Anisotropy Decays of DPH with 2PE	97
3.2.5.	Two-Photon Excitation of DPH in Membranes	98
3.3.	Two-Photon Excitation of Fluorophore-Stained DNA	99
3.3.1.	Emission Spectra of Hoechst 33342	101
3.3.2.	Fluorescence Intensity Decays of Hoechst 33342	102
3.3.3.	Anisotropy Excitation Spectra of Hoechst 33342 in Glycerol at -20°C	104
3.3.4.	Anisotropy Excitation Spectra of Hoechst 33342-DNA Complex	105
3.4.	Two-Photon Excitation of Indole, Tryptophan, and Proteins.	106
3.4.1.	Emission Spectra.	107
3.4.2.	Anisotropy Spectra	108
3.4.3.	Two-Photon Excitation of HSA	110
3.5.	Two-Photon-Induced Fluorescence of Alkanes.	112
3.6.	Standards for 2PE.	116
3.6.1.	A ps Two-Photon Standard	119

3.7.	Three-Photon Excitation of Fluorescence	123
3.7.1.	Three-Photon Excitation of 2,5-Diphenyloxazole	123
3.7.2.	Three-Photon Excitation of DPH in Membranes	125
3.7.3.	Three-Photon Excitation of the Calcium Probe Indo-1 . .	126
3.7.4.	Three-Photon Excitation of Tryptophan and Proteins . .	131
3.7.5.	Perspectives on 3PE	132
3.8.	Two-Color Two-Photon Excitation	134
3.9.	Future Applications of MPE	138
	References	139

4. Two-Photon Excitation and Anisotropy Decays in Membranes and Oriented Systems

B. Wieb Van der Meer and S.-Y. Simon Chen

4.1.	Introduction	145
4.2.	Two-Photon Anisotropy Theory in Isotropic Suspensions	146
4.3.	Two-Photon Anisotropy Theory in Oriented Membranes	150
4.4.	Conclusions	154
4.5.	Appendix A	155
	Appendix A.1	159
	Appendix A.2	160
4.6.	Appendix B	161
	Appendix B.1	166
	Appendix B.2	168
	Appendix B.3	170
4.7.	Appendix C	173
4.8.	Appendix D	175
4.9.	Appendix E	176
4.10.	Appendix F	178
4.11.	Appendix G	179
4.12.	Appendix H	181
	References	184

5. Two-Photon Induced Fluorescence of Proteins

Borys Kierdaszuk, Ignacy Gryczynski, and Joseph R. Lakowicz

5.1.	Introduction	187
5.2.	Excitation and Emission Spectra of Aromatic Amino Acids for One- and Two-Photon Excitation	189
5.2.1.	Studies of Tryptophan, Tyrosine, and Phenylalanine in Solution	189
5.2.2.	Tryptophan and Tyrosine in Proteins	195

5.3. Fluorescence Anisotropy of One- and Two-Photon Excitation of Tryptophan and Tyrosine	196
5.3.1. Limiting-Anisotropy Spectra	196
5.3.2. Anisotropy of Tryptophan- and/or Tyrosine-Containing Proteins.	200
5.4. Two-Photon Induced Fluorescence of Protein-Bound Chromophores	202
5.5. Experimental Methods.	205
References	206

6. Fluorescence and Multiwave Mixing Induced by Photon Absorption of Excited Molecules

Valery L. Bogdanov

6.1. Introduction	211
6.2. Emission of Highly Excited Molecules.	212
6.2.1. Methods of Excitation	212
6.2.2. Radiationless Decay of Highly Excited States	214
6.2.3. Emission Spectra and Relaxations of Short-Lived Highly Excited States	217
6.2.4. Quantum Yield of Fluorescence from Highly Excited States	222
6.2.5. Anisotropy of Fluorescence from Highly Excited States. .	224
6.2.6. Vibrational Relaxation and Fluorescence Spectra of Highly Excited Molecules.	226
6.2.7. Energy Transfer from Highly Excited States	228
6.2.8. Stepped Excitation of Biflurophore.	230
6.3. Transient Third-Order Nonlinearity and Relaxation of Excited Molecules.	233
6.3.1. Preliminary Remarks	233
6.3.2. Dispersion of Transient Susceptibility and Ultrafast Relaxation of Highly Excited Molecules	234
6.3.3. Transient Nonlinear Susceptibility and Orientational Anisotropy of Excited Molecules.	238
6.3.4. Time-Resolved Dispersion of Transient Susceptibility and Spectral Dynamics of Excited Molecules.	242
6.4. Summary	245
References.	247

7. Ultrafast Stimulated-Emission Spectroscopy

G. J. Blanchard

7.1. Stimulated-Emission Pumping Spectroscopies	255
7.2. Experimental Implementation of Ultrafast Stimulated-Emission Pump-Probe Spectroscopy	256
7.3. Applications of Stimulated-Emission Spectroscopy to Rotational Diffusion Dynamics Measurements	260
7.4. Measuring Vibrational Population Relaxation Using Stimulated Emission.	268
7.4.1. Chemical Information Content of Ultrafast Stimulated-Emission T_1 Measurements: Perylene and 1-Methylperylene in <i>n</i> -Alkanes	274
7.4.2. T_1 Relaxation in Different Electronic States	274
7.4.3. Solvent-Dependent T_1 Relaxation Dynamics of S_0 Perylene.	278
7.4.4. Understanding the Length Scales over Which Intermolecular Vibrational Energy Transfer Operates	287
7.4.5. 1-Methylperylene Vibrational Population Relaxation	288
7.4.6. Reorientation Dynamics of 1-Methylperylene in the Alkanes.	293
7.4.7. Comparison of T_1 and τ_{OR} Data for 1-Methylperylene	294
7.5. Summary and Overview.	296
References	297

8. Fluorescence Quenching by Stimulated Emission

Joseph R. Lakowicz and Ignacy Gryczynski

8.1. Introduction	305
8.2. One-Pulse and Two-Pulse Light Quenching	309
8.2.1. One-Pulse Time-Coincident Light Quenching	310
8.2.2. Two-Pulse Time-Delayed Light Quenching.	312
8.3. Effects of Light Quenching on Time-Resolved Intensity and Anisotropy Decays	315
8.4. Lifetime-Resolved Experiments by Two-Beam Light Quenching .	318
8.5. Experimental Results on One-Pulse Light Quenching	321
8.5.1. One-Pulse Light Quenching of DCM	321
8.5.2. One-Pulse Light Quenching with Two-Photon Excitation..	326
8.6. Experimental Results on Two-Pulse Light Quenching	330
8.6.1. Steady-State Measurements with Two-Beam Light Quenching	331

8.6.2. Time-Domain and Frequency-Domain Studies of Light Quenching	333
8.6.3. Wavelength-Selective Light Quenching with Time-Dependent Spectral Relaxation	335
8.7. Applications of Light Quenching	341
8.7.1. Wavelength- or Lifetime-Selective Light Quenching	341
8.7.2. Light Quenching with Total Internal Reflectance	347
8.8. Discussion	352
8.8.1. Comparison of Light Quenching and Induced Stimulated Emission	352
8.8.2. Biophysical Applications of Light Quenching	352
8.8.3. Pulse-Width-Dependent Light Quenching	354
8.8.4. Perspectives on Light Quenching	355
References	355

9. Increasing the Resolution of Far-Field Fluorescence Light Microscopy by Point-Spread-Function Engineering

Stefan W. Hell

9.1. Introduction	361
9.1.1. Why Far-Field Light Microscopy?	363
9.1.2. Imaging with a Lens: The Point-Spread Function	364
9.1.3. Scanning Fluorescence Microscopy	367
9.2. PSF Engineering through Fluorescence Inhibition	369
9.2.1. STED Fluorescence Microscopy	372
9.2.2. Ground-State-Depletion Fluorescence Microscopy	387
9.3. PSF Engineering through Aperture Increase: 4Pi Confocal Microscopy	392
9.3.1. 4Pi Illumination and Detection PSF	393
9.3.2. The 4Pi Confocal Microscope and Its Imaging Modes	396
9.3.3. Two-Photon Excitation 4Pi Microscopy	401
9.3.4. Confocal Two-Photon Excitation 4Pi Microscopy	405
9.3.5. Limitations and Further Potentials of 4Pi Confocal Microscopy	410
9.4. Other Examples of PSF Engineering	412
9.4.1. Offset-Beam Overlap Microscopy	412
9.4.2. Theta-4Pi Confocal Microscopy	414
9.5. Recent Developments	417
9.5.1. STED 4Pi Confocal Microscopy	417
9.5.2. 4Pi Confocal Microscopy Combined with Image Restoration Provides 3D-Resolution in the 100 nm Range	418

9.6. Conclusion	421
References	422
10. Time-Resolved Stimulated-Emission and Transient-Absorption Microscopy and Spectroscopy	
P. T. C. So, C. Y. Dong, K. M. Berland, T. French, and E. Gratton	
10.1. Introduction	427
10.1.1. Pump-Probe Spectroscopy	427
10.1.2. Time-Resolved Fluorescence Microscopy	430
10.1.3. Overview	431
10.2. Theory	431
10.2.1. Pump-Probe Spectroscopy	431
10.2.2. Pump-Probe Microscopy	437
10.3. Instrumentation and Methods	446
10.3.1. Pump-Probe Light Sources	446
10.3.2. Optics for Absorption-Mode Measurement	447
10.3.3. Optics for Stimulated-Emission Mode	449
10.3.4. Scanner Optics for Microscopy	452
10.3.5. Signal Detection and Processing	452
10.4. Spectroscopy Applications and Performance	453
10.4.1. Pump-Probe Absorption Spectroscopy	453
10.4.2. Stimulated-Emission Pump-Probe Spectroscopy	456
10.5. Applications and Performances of Pump-Probe Fluorescence Microscope	458
10.5.1. Linearity of Pump-Probe Signal Response on Laser Power Level	459
10.5.2. Experimental Verification of Pump-Probe Microscopy Resolution	461
10.5.3. Time-Resolution of Pump-Probe Microscopy	461
10.5.4. Comparison between Conventional Microscopy and Pump-Probe Fluorescence Microscopy in Human Erythrocytes and Mouse Fibroblasts	462
10.5.5. Multiple-Dye-Labeling Application	464
10.6. Conclusion	466
References	466
11. Multiphoton Excitation of Molecular Fluorophores and Nonlinear Laser Microscopy	
Chris Xu and Watt W. Webb	
11.1. Introduction	471

11.2.	Multiphoton Spectroscopy	472
11.2.1.	Estimations of Multiphoton Cross Section	473
11.2.2.	Theoretical Analysis of MPE	475
11.2.3.	Two- and Three-Photon Excitation Spectra.	485
11.2.4.	Power Dependence of Two- and Three-Photon-Excited Fluorescence	493
11.2.5.	Dependence of Two-Photon-Excited Fluorescence on Pulse Width	497
11.2.6.	One-, Two-, and Three-Photon-Excited Fluorescence Emission Spectra Compared	499
11.2.7.	Two-Photon Spectra Excited by CW and Femtosecond Pulsed Laser Compared	499
11.3.	Multiphoton Microscopy	501
11.3.1.	Instrument of Nonlinear Microscopy.	502
11.3.2.	Multiphoton Excitation Volume	506
11.3.3.	Multiphoton Uncaging	509
11.3.4.	Imaging of Intrinsic Fluorophores with Multiphoton Excitation.	509
11.3.5.	Deep Imaging	510
11.4.	Considerations in MPE Spectroscopy and Microscopy	516
11.4.1.	Fluorophore Ground-State Depletion.	516
11.4.2.	Intersystem Crossing and Photobleaching.	521
11.4.3.	Laser-Matter Interaction at High Intensity	529
Appendix:	Absolute Measurement of Two-Photon Absorption Cross Sections and Two-Photon-Excited Fluorescence Emission Quantum Efficiencies Using Saturation	535
	References	537
Index		541

The Theory of Two-Photon-Induced Fluorescence Anisotropy

Patrik R. Callis

1.1. Introduction

Fluorescence anisotropy (photoselection) techniques have played an important role in elucidating the nature of excited electronic states in polyatomic molecules and their rotational dynamics for many years.^(1–3) In the classic experiments single photons of linearly polarized light are absorbed by a randomly oriented sample, creating a partially oriented (photoselected) ensemble of excited molecules. In the usual electric dipole mechanism the probability of absorption goes as the square of the projection of the molecule's transition dipole vector onto the polarization direction of the light. The average orientation is revealed by the polarization (anisotropy) of the subsequently emitted photons, provided there is little molecular rotation prior to emission of the second photon. The rate of loss of the anisotropy is directly related to the rotational diffusion rate during the excited-state lifetime.

The widespread availability of high rep-rate picosecond pulsed lasers has made two-photon excitation (TPE) more accessible in recent years, and with it a desire to exploit the fluorescence anisotropy created from TPE.^(4–17) However, it is fair to say that most spectroscopists today are not very familiar with the two-photon absorption process. It is the purpose of this chapter to present a formal theory of *steady-state* anisotropy of fluorescence produced by TPE and to review some of the major differences between one- and two-photon spectroscopy and how they translate into differences in the anisotropy of the fluorescence.

The scope of this chapter is limited to a subspace of the elegant treatment of general three-photon processes by McClain,^(18,19) wherein only the case of two identical photons absorbed (one-color case) followed by fluorescence (at

Patrik R. Callis • Department of Chemistry and Biochemistry, Montana State University, Bozeman, Montana 59717.

Topics in Fluorescence Spectroscopy; Volume 5: Nonlinear and Two-Photon-Induced Fluorescence, edited by J. Lakowicz. Plenum Press, New York, 1997.

much later times) will be considered. Only the off-resonance case will be considered, wherein the photons cannot be absorbed individually by separate one-photon events. In general it will be assumed that no molecular rotation occurs prior to emission. The focus will be on exploring this space thoroughly, especially with respect to all possible “shapes” of the two-photon tensor and how they relate to possible observable anisotropies. In addition, considerable effort is made to connect Ω , the ratio of two-photon absorptivity using circularly and linearly polarized excitation light, to the possible range of allowed anisotropies. This is motivated by the fact that many measurements of Ω were made in the past without measuring the anisotropy, whereas most recent measurements of anisotropy are not accompanied by measurement of Ω . Chapters 2 and 4 in this volume relax the restriction of fixed molecules, being concerned primarily with time-resolved anisotropy. However, both chapters introduce some formalism equivalent to that in this chapter. Van der Meer’s equations are virtually the same as those given here, but he also considers systems of partially oriented chromophores. Johnson’s development uses the spherical tensor basis and is also more general, including the cases of nonidentical photons and one-photon resonance cases.

Section 1.2 is devoted to introducing the subject of two-photon absorption spectroscopy, qualitatively at first, with special attention to tensors and the contrast between one- and two-photon spectroscopy of aromatic systems. Section 1.3 is the theory section, a more general version of what was recently published by this author⁽²⁰⁾ with connections to closely related works by Chen and Van der Meer⁽²¹⁾ and Wan and Johnson.^(22,23) Section 1.4 is devoted to interpreting several cases of experimentally observed two-photon anisotropy. Section 1.5 is devoted to making some predictions based on past measurements of Ω and semiempirical excited electronic wavefunctions.

1.2. Two-Photon Absorption

1.2.1. Qualitative Aspects

The manner in which visible light can be absorbed by a “colorless” solution—two photons at a time—strikes most as mysterious. Some of the mystery may be removed by recognizing the close relation of two-photon absorption to light scattering, particularly Raman scattering. In the scattering process a photon of light is transiently “absorbed” by the molecule, even though not in resonance (ΔE not equal to $h\nu$), thereby reaching a virtual state. The virtual state is very short lived because it does not correspond to one of the energy levels of the molecule, and the photon is reemitted within about 1 fs. Provided the light is not very intense, the photon is emitted spontaneously in a new

direction. When the light is sufficiently intense, two new processes become important: stimulated light scattering and two-photon absorption. Both evolve from the same virtual state as the spontaneous event and differ only by the relative phase of the stimulating photon. A modified Planck' law governs these two-photon processes:

$$\begin{array}{ll} \text{For scattering} & \Delta E = h\nu_1 - h\nu_2 \\ \text{For two-photon absorption} & \Delta E = h\nu_1 + h\nu_2 \end{array}$$

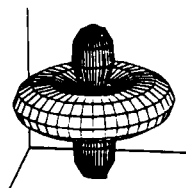
Because two photons are involved, two electric field vectors are needed to describe the interaction with the molecule. The amplitude for the process, instead of being governed by the projection of a single field vector onto the molecular transition dipole moment vector, is given by the double projection of two field vectors onto a molecular tensor, represented by a 3×3 matrix.⁽²⁴⁾ The two-photon absorptivity tensor is the focus of this chapter.

Whereas the electric dipole transition moment may be likened unto a molecular antenna, in reasonable analogy to the common receiving and transmission of radio waves, the two-photon process is less tangible. For one-photon absorption, the rate of absorption is proportional to the square of the cosine of the angle between the light's electric vector and the transition moment vector (a rank 1 tensor). The significance of the two-photon tensor (a rank 2 tensor) is as follows. First let us describe each of the nine elements with the usual Cartesian indices in the molecular frame, xx , xy , xz , for the first row, yx , yy , yz for the second row, and zx , zy , zz for the third row. The relative sizes and signs of the numbers in this matrix, S , will determine the rate and polarization dependence of two-photon absorption of two identical linearly polarized photons by the relation

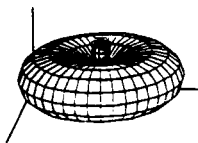
$$\begin{aligned} \text{Rate} = \text{const} \times & |S_{xx}x^2 + S_{xy}xy + S_{xz}xz \\ & + S_{yx}yx + S_{yy}y^2 + S_{yz}yz \\ & + S_{zx}zx + S_{zy}zy + S_{zz}z^2|^2 \end{aligned}$$

where x , y , z are the Cartesian components of the polarization direction of the light.

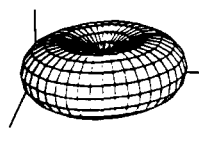
Figure 1.1 portrays representative two-photon tensor types as spherical polar surface plots, wherein the length of a radius vector drawn from the origin to the surface gives the *amplitude* for the absorption of two identical linearly polarized photons with electric field pointing in the direction of the vector. The relative rate of absorption is then given by the square of that length. For example, a particularly simple case would be if the xx element were the



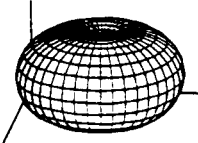
$(1, 1, -1)$
 $\Omega = \frac{8}{7}, Q_y = \frac{1}{3}$
 $r_+ = 0.082, r_- = -0.163$



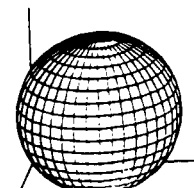
$(1, 1, -\frac{1}{2})$
 $\Omega = \frac{2}{3}, Q_y = 1$
 $r_+ = 0.159, r_- = -0.317$



$(1, 1, 0)$
 $\Omega = 0.25, Q_y = 2$
 $r_+ = \frac{1}{7}, r_- = -\frac{2}{7}$



$(1, 1, \frac{1}{2})$
 $\Omega = 0.047, Q_y = 2.78$
 $r_+ = 0.073, r_- = -0.146$



$(1, 1, 1)$
 $\Omega = 0, Q_y = 3$
 $r_+ = 0, r_- = 0$

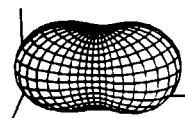
$[+, -]$



$(1, \frac{1}{2}, -\frac{1}{2})$
 $\Omega = \frac{7}{8}, Q_y = \frac{2}{3}$
 $r_+ = 0.357, r_- = -\frac{2}{7}$



$(1, \frac{1}{2}, 0)$
 $\Omega = 0.316, Q_y = 1.8$
 $r_+ = 0.346, r_- = -\frac{2}{7}$



$(1, \frac{1}{2}, \frac{1}{2})$
 $\Omega = 0.071, Q_y = 2.67$
 $r_+ = 0.204, r_- = -0.102$

$[+, +]$



$(1, 0, 0)$

$\Omega = \frac{2}{3}, Q_y = 1$
 $r_+ = 0.571, r_- = -\frac{2}{7}$

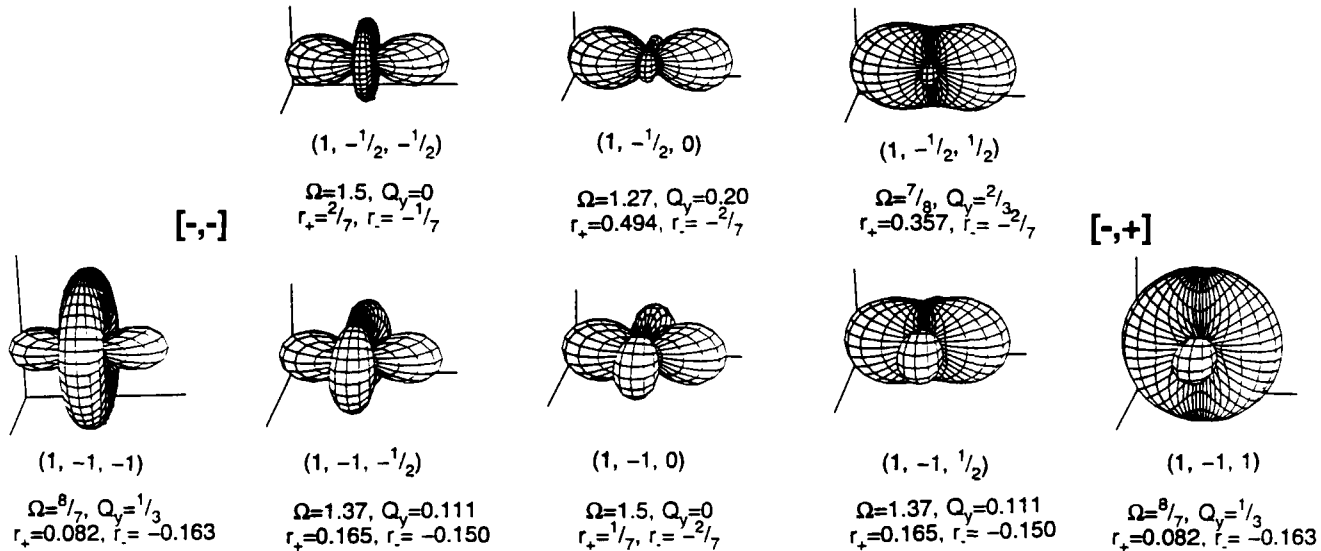


Figure 1.1. Polar spherical surface plots of the possible tensor shapes for two-photon absorption of identical linearly polarized photons. The distance to the surface from the origin gives the *amplitude* for absorption and should be squared to obtain the relative rate. Adjacent lobes have opposite sign and are separated by nodal surfaces. Relative principal tensor values, normalized trace squared (Q_y), Ω value, and anisotropy range are given under each tensor. For these diagonal tensors, $|S_{xx}| \geq |S_{yy}| \geq |S_{zz}|$. S_{zz} increases from left to right. S_{yy} increases from bottom to top. x is the horizontal axis, z the vertical axis, and y points out of the page.

only nonzero element, which is the central tensor in Figure 1.1. The rate of absorption will be proportional to the square of the product of the x polarization components of the two photons multiplied by the tensor element. For a linearly polarized beam, there would be maximal absorption when the light is polarized parallel to the molecular x direction and zero absorption when perpendicular to x . In between, the rate will depend on the fourth power of the cosine of the angle between the x direction and the polarization. For this simplest case, the degree of photoselection is greater than for one-photon excitation because of the higher power of angle dependence. Thus, r will have the limits 4/7 to -2/7 instead of the one-photon range, 2/5 to -1/5.^(9,25,26)

Although this case is nearly realized for certain transitions in certain molecules, it is generally not the case for most aromatic molecules. A particularly common situation for a two-photon allowed transition of a substituted benzene is a tensor with nonzero xy and yx elements only. In this case, maximal absorbance of linearly polarized light will occur when the polarization direction is at 45° to the x and y axes. Absorption vanishes when the light is polarized parallel to either x , y , or z . Such a tensor would have the same shape as the tensor at the bottom center of Figure 1.1, but is rotated 45° in the xy plane. Because tensors of this type are common for the lowest $\pi\pi^*$ transition of substituted aromatics, such molecules typically will show *lower* anisotropy with two-photon excitation than for one-photon excitation.

Circularly polarized light has played an important role in TPE studies. With the latter tensor, circularly polarized light directed normal to the xy plane is absorbed maximally, regardless of the molecular orientation about the z axis.

As a final illustration in this section, it is useful to relate two-photon absorption to the simplest of electronic systems, the hydrogen atom. The one-photon selection rules are $\Delta l = \pm 1$. The transition dipole for the $1s \rightarrow 2p_z$ transition points in the z direction. The two-photon selection rules are $\Delta l = 0, \pm 2$. For the $1s \rightarrow 2s$ transition the two-photon tensor is isotropic (spherical) and is shown in the upper right corner of Figure 1.1; the xx , yy , and zz elements are equal and the other elements are zero. Physically this means that two photons polarized in the same direction are required. The absorptivity for circularly polarized light is zero. This can also be understood from conservation of angular momentum. Neither the $1s$ nor $2s$ states have angular momentum, but circularly polarized photons do. To reach the $3d_{x^2-y^2}$ state, the tensor would have equal and opposite xx and yy elements, with the rest zero. It is the tensor shown at bottom center of Figure 1.1. This transition requires two linearly polarized photons, one x and the other y polarized and phase-shifted by π , or one right and one left circularly polarized photon. To reach the $3d_{xy}$ state, the tensor would have only nonzero xy and yx elements of the same magnitude and sign.

1.2.2. A Brief History

1.2.2.1. Use of Symmetry

Dating from Maria Goeppert-Mayer's theoretical treatise⁽²⁷⁾ on two-photon absorption, including the era of early experiments following the development of lasers,^(28,29) the most obvious aspect of two-photon spectroscopy compared to one-photon was the parity rule for dipole absorption: $g \leftrightarrow u$ for one- and $g \leftrightarrow g$ or $u \leftrightarrow u$ for two-photon spectroscopy. Thus, for systems with inversion symmetry the two spectroscopies are complementary. This fact tends to be misleading, suggesting that transitions which are strong in one-photon absorption will necessarily be weak in two-photon, and *vice versa*. An important theme of this chapter is to raise awareness of how untrue this often is, and how vibrationally induced intensity can overwhelm other considerations.

The early 1970s saw a major advance in the science of molecular two-photon spectroscopy. McClain⁽³⁰⁾ used point group theory to show how the symmetry of molecular excited states dictated the absorptivity tensor pattern, which, in turn, could be determined by measuring the dependence of the two-photon absorptivity upon the relative polarization of the simultaneously absorbed photons. In this new kind of photoselection, both photons are absorbed within $\sim 10^{-16}$ s, so that it is useful for gas or fluid solutions, where the molecules undergo randomizing rotational motion prior to emission. This technique has been often applied in the convenient limit of a single laser beam, where the nature of the two-photon tensor is revealed through the ratio, Ω , of absorptivities using circular and linear polarization:

$$\Omega = \delta_{\text{circular}} / \delta_{\text{linear}}$$

Subsequently, McClain⁽¹⁸⁾ presented the general case of three-photon photo-selection, covering at once many phenomena involving various permutations of absorption and emission of three photons. Included are the coherent simultaneous absorption of three different photons, hyper-Raman scattering, and the case of interest in this chapter, when two identical photons are absorbed simultaneously (coherently) and the third is emitted much later by ordinary (incoherent) fluorescence. Friedrich and McClain reviewed the field at this point.⁽³¹⁾

1.2.2.2. Beyond the Use of Symmetry: Electronic Effects

Although symmetry-related techniques are powerful, they should not be placed on a pedestal. There is a tendency to forget that symmetry-based selection rules tell only when a result must be zero. They have nothing to say about

how intense a symmetry-allowed process will be, and for most molecules all transitions are two-photon-allowed. A second surge of progress came about in the early 1980s when experiments and theory converged to answer the question of absolute and relative two-photon absorption strengths for allowed transitions, particularly for aromatic hydrocarbons and their derivatives. Dick, Gonska, and Hohlneicher made an extensive experimental survey of the TPE spectra and Ω values of several aromatic hydrocarbons in solution, exposing the basic patterns.⁽³²⁾ During this time Rava and Goodman^(33–37) made an exhaustive study of the effect of inductive and mesomeric substituent effects on the two-photon absorption of benzene, discovering the empirical rules and supporting them with perturbation calculations. Also at this time Callis, Scott, and Albrecht,^(38,39) by studying first-order transition density patterns, were able to generalize existing empirical and theoretical pseudoparity rules for one-photon absorption to multiphoton absorption of any order (in principle) for a large class of neutral aromatic hydrocarbons. One of the major findings for aromatic systems is that the vibrationally induced part of the two-photon absorption to the 1L_b state, which is S_1 for most substituted benzenes and naphthalenes, dominates the intensity from substituents, opposite the case in one-photon absorption.

Semiempirical quantum mechanical methods have been useful in understanding and predicting two-photon absorption intensities induced by substituents and by vibrations. Early use of the Pariser–Parr–Pople⁽⁴⁰⁾ and INDO–PCISD⁽⁴¹⁾ methods were applied to linear polyenes. Hohlneicher and Dick applied CNDO/S-Cl^(42,43) to the two-photon absorption and Ω for a number of aromatic hydrocarbons, demonstrating the effectiveness of this tool for interpretation of their experiments. Callis extended CNDO/S-Cl⁽⁴⁴⁾ and INDO/S-Cl^(45,46) studies to substituted and vibrationally distorted aromatics, showing that the method is quite effective in that area as well.

1.2.2.3. *Vibrationally Induced Two-Photon Absorption*

As noted, for aromatic systems there is a *complete reversal* between one- and two-photon absorption spectra regarding the effect of inductive and vibrational perturbations on the intensity. In one-photon absorption we are accustomed to ignoring vibronic coupling effects in S_1 for substituted benzenes because the inductive effect of most substituents overwhelms the relatively weak vibronic coupling part. In two-photon absorption, just the *opposite* is the case. For example, two-photon absorption by azabenzenes and fluorobenzenes is almost entirely due to the vibrationally induced part. This behavior is *highly state dependent*. Specifically, it is the 1L_b transition which has the properties just mentioned; 1L_a , which is usually S_2 for substituted benzenes, has the opposite

behavior. That is, in one-photon absorption 1L_a is almost unaffected by inductive perturbations and has a very strong absorption due to vibronic coupling. Just the reverse is true in two-photon absorption.^(38,39)

Thus, an understanding of the fluorescence anisotropy for the lowest transition for most aromatics requires at least a qualitative understanding of the consequences of having a large vibrational component. The main effect is that the anisotropy and/or Ω may vary wildly through-out the absorption band, if the vibronic and allowed parts are of comparable magnitude and resolved. If the vibronic part dominates, the behavior will usually be quite different from that deduced from the electronic state symmetry alone, and will be *blue-shifted* by the frequency of the inducing vibration (see Section 1.4.3.3).

1.2.3. Quantitative Description

1.2.3.1. General

For identical photons the two-photon absorption rate is given by the Kramers–Heisenberg–Dirac second-order perturbation expression⁽²⁴⁾

$$\text{Rate} = 128\pi^3\alpha^2\omega^2g_M(2\omega)|\boldsymbol{\mu} \cdot \mathbf{S} \cdot \boldsymbol{\mu}|^2\phi^2$$

where $\boldsymbol{\mu}$ is the unit polarization vector of the exciting light, \mathbf{S} is the two-photon tensor, ϕ is the flux of the excitation light, α is the fine-structure constant, and $g_M(2\omega)$ is the line-shape function. For one-color excitation from the ground state, g , to a final state, f , \mathbf{S} is given by⁽²⁴⁾

$$\mathbf{S} = \sum_i \frac{r_{fi}r_{ig}}{\nu_{ig} - \nu_{\text{laser}}} \quad (1.1)$$

A given Cartesian component of the 3×3 matrix S_{ab} is⁽²⁴⁾

$$S_{ab} = \sum_i \frac{a_f b_{ig}}{\nu_{ig} - \nu_{\text{laser}}} \quad (1.2)$$

where $a, b = x, y, z$. The summation is over *all* states of the molecule, including the ground and final states (see next section). Note that each term in the sum is the product of the transition dipole between the initial state and *any* of the states of the molecule, i , times the transition dipole from state i to the final state. Thus, it is evident that the two-photon absorption event often will have no direct relation to the transition dipole for direct one-photon absorption to the

final state. In such cases it is necessary that there be one or more other states, i , of the molecule for which there exists strong one-photon absorption from both the ground state *and* from the final state. Such states are commonly called “intermediate states.” They are the states for which there *could* be consecutive one-photon events: absorption $g \rightarrow i$, followed by emission $i \rightarrow f$.

It is important to realize that such transitions occur only in a virtual sense, because the only photons available have frequency $\nu_{fg}/2$. McClain⁽⁴⁷⁾ notes that each photon with frequency $\nu_{fg}/2$ individually sets up small electrical oscillations at that frequency, and that these can sum to ν_{fg} and therefore become large when both are present because of the resonance. It is the very short time scale of the two-photon event which allows these photons to be effectively in resonance with all the states of the molecule because of the time-energy form of the uncertainty principle, $\Delta E \approx \hbar/\Delta t$. Another way to translate Eq. (1.2) is that absorption of the first photon puts the molecule in a virtual (polarized) state which—in the sense of a Fourier analysis—may be described as a linear combination of all the states of the molecule, i . The weighting factor in the sum is the transition dipole to that state from the ground state divided by the energy difference between the photon and the energy of state i . Time-dependent quantum mechanics says that each term in the sum will oscillate at frequency ν_{ig} , so the various terms will dephase on the order of a femtosecond or less. However—and this is where the uncertainty principle comes in—at very short times there is coherence between the different terms; if there is a nonzero transition dipole between this superposition state and the final state, there will be two-photon absorption. Note, however, that the terms in the sum must be added *before* squaring, allowing for the possibility of either constructive or destructive interference in the expression for the transition dipole to the final state. In this way a transition may be two-photon-forbidden, even though several intermediate states contribute large terms (in magnitude) to the sum.

1.2.3.2. Involvement of the Direct Transition Dipole

The sum over i includes all states of the molecule, including g and f (initial and final). The direct transition dipole \mathbf{r}_{fg} can contribute to the two-photon tensor only if there is also a change in permanent dipole, i.e., when both \mathbf{r}_{fg} and $|\mathbf{r}_{ff} - \mathbf{r}_{gg}|$ are nonzero. It is easily shown⁽⁴⁸⁻⁵⁰⁾ that this charge transfer contribution from $i = g, f$ in Eq. (1.1) is

$$\mathbf{S}_{CT} = 2 \frac{(\mathbf{r}_{ff} - \mathbf{r}_{gg})\mathbf{r}_{fg}}{\nu_{fg}} \quad (1.3)$$

Then, if the change in dipole (charge transfer direction) is parallel to \mathbf{r}_{fg} , and if f is the emitting state, there will be a dominant diagonal tensor element parallel

to the emitting dipole. This appears to be the case for several molecules studied recently (see Section 1.4).

1.2.3.3. *Pseudo-Involvement of the Direct Transition Dipole*

If the lowest absorption band is actually a composite of a strong one-photon transition ($S_0 \rightarrow {}^1A_g$) and a dipole-forbidden, two-photon-allowed transition ($S_0 \rightarrow {}^1B_u$), as happens for many linear polyenes, it will *appear* that the direct one-photon transition dipole plays a dominant role in the two-photon tensor. In such a case the tensor may be dominated by a single term, i in Eq. (1.1). It is required that \mathbf{r}_{fi} be nearly parallel to \mathbf{r}_{ig} , often true for long polyenes. Fluorescence will also be due to \mathbf{r}_{fg} , either because the 1B_u state is the fluorescing state or because the 1A_g state is lowest and derives dipole strength by vibronic coupling to the nearby 1B_u state. However, even in hydrocarbon solutions, local solvent fields will mix such close-lying states with a large transition electric dipole between them,⁽⁵¹⁾ sending us back to case 1.2.3.2.

1.2.3.4. *Aromatic 1L_b Transitions*

The conditions described in the previous two sections are rarely, if ever, met by aromatic-derived molecules because, unlike linear polyenes, their strongest dipole-allowed transitions lie much higher than the fluorescing transition and the molecules are not linear. The sum in Eq. (1.1) usually has many terms involving transition moments spanning the full plane of the molecule.^(20,42,43)

1.3. Anisotropy Theory

1.3.1. Introduction and Scope

Treated here is the case for two identical photons, far from one-photon resonance, being absorbed coherently followed by a fluorescence photon emitted incoherently (no phase relation to the two absorbed photons). Prompted by recent interest in two-photon fluorescence anisotropy, Callis⁽²⁰⁾ has shown how the previously more commonly measured quantity Ω is related to the anisotropy in the limit of two-dimensional tensors. During the same time Chen and Van Der Meer⁽²¹⁾ and Wan and Johnson⁽²²⁾ presented works for the purpose of describing time-resolved fluorescence anisotropy from TPE which independently derive McClain's^(18,19) results for the case of fluorescence. There is some overlap in their works with what is presented here. In this chapter we are concerned only with steady-state polarization, with the molecules either completely motionless or

completely randomized following absorption. With these restrictions, the fluorescence intensity is given by⁽¹⁸⁾

$$I = \sum_{i,j=1}^4 P_i M_{ij} Q_j \quad (1.4)$$

The P_i are geometric factors depending on the polarization vectors of the excitation and emission photons, μ and λ , respectively, whereas the Q_i depend on the symmetrized^{(52)†} molecular two-photon absorption tensor S and the fluorescence transition dipole F . The averaging matrix, M , connecting the geometric and molecular factors for the limit considered here is⁽¹⁸⁾

$$M = \frac{1}{210} \begin{pmatrix} 22 & -24 & -10 & 16 \\ -24 & 72 & 16 & -48 \\ -10 & 16 & 16 & -20 \\ 16 & -48 & -20 & 60 \end{pmatrix} \quad (1.5)$$

Following McClain's original treatment,⁽¹⁸⁾ but normalizing the Q_i by dividing by $|S|^2|F|^2$, the P_i and Q_i are conveniently defined in terms of a three-dimensional "experiment space" X , Y , and Z (not to be confused with the laboratory Cartesian space) where

$$P_1 = 1, \quad Q_1 = 1 \quad (1.6a)$$

$$P_2 \equiv X = \frac{1}{2}(|\lambda \cdot \mu|^2 + |\lambda \cdot \mu^*|^2), \quad Q_2 = Q_X = \frac{|\mathbf{F} \cdot \mathbf{S}|^2}{|\mathbf{F}|^2 \delta_G} \quad (1.6b)$$

$$P_3 \equiv Y = |\mu \cdot \mu^*|^2, \quad Q_3 = Q_Y = \frac{\delta_F}{\delta_G} \quad (1.6c)$$

$$P_4 \equiv Z = \text{Re}(\lambda \cdot \mu)(\lambda^* \cdot \mu)(\mu^* \cdot \mu^*), \quad Q_4 = Q_Z = \frac{(\mathbf{F} \cdot \mathbf{S} \cdot \mathbf{F}) \text{Tr } S}{|\mathbf{F}|^2 \delta_G} \quad (1.6d)$$

and where

$$\delta_G = \sum_{a,b} S_{ab} S_{ab}^* = |\mathbf{S}|^2 \quad \text{and} \quad \delta_F = \sum_{a,b} S_{aa} S_{bb} = |\text{Tr } \mathbf{S}|^2$$

[†] When the general form of the tensor involving two photons of different frequency is collapsed to the one-color case by setting $\nu_1 = \nu_2$, a sum tensor is obtained, related to Eq. (1.2) by $S_{ab} = (S_{ab} + S_{ba})/2$.⁽¹⁸⁾ It is argued in Ref. 52 that this is formally incorrect and that the tensor is unsymmetrical. In practice, there is no consequence from using the symmetrized form because S_{ab} and S_{ba} become added when the absorption rate is evaluated in Eq. (1.1).

The important ratio δ_F/δ_G has often been measured in experiments when the emission is isotropic via the so-called two-photon polarization, Ω , where

$$\Omega = \left(\frac{\delta_{\text{circular}}}{\delta_{\text{linear}}} \right)_{\text{isotropic}} = \frac{3 - \delta_F/\delta_G}{2 + \delta_F/\delta_G} \quad (1.7)$$

or

$$\frac{\delta_F}{\delta_G} = \frac{3 - 2\Omega}{1 + \Omega} \quad (1.8)$$

The definitions of δ_F and δ_G show that Ω can vary only from 0 to 3/2 for isotropic emission.

The coordinates X , Y , Z have the following meanings: X gives the mutual projection of the absorption and fluorescence polarization vectors of the light; Y gives the degree of linearity of the excitation polarization, vanishing for circular polarizations; and Z is a measure of the projection of excitation and fluorescence polarizations and also the degree of linearity.

The corresponding molecular properties Q_X , Q_Y , and Q_Z give the projection of the fluorescence transition moment onto the two-photon tensor, the square of the normalized two-photon tensor, and the projection of the fluorescence transition moment onto $S \cdot F$ times the trace of S , respectively.

1.3.2. Excitation with Linearly Polarized Light

For this chapter we consider a laboratory frame wherein the excitation light is vertically polarized and the fluorescence signal is viewed in the horizontal plane and 90° to the excitation beam propagation direction, giving two intensities, I_{VV} and I_{VH} , when viewed through polarizers oriented to pass vertically and horizontally polarized light respectively. Under these conditions Y is always = 1, and X and Z are 1 or 0 when the viewing polarizer is vertical or horizontal respectively. Application of Eqs. (1.4)-(1.6) gives the ratio A :

$$A = \frac{I_{VV}}{I_{VH}} = \frac{I_{VV}}{I_{HV}} = \frac{2 + 8Q_X + Q_Y + 4Q_Z}{6 - 4Q_X + 3Q_Y - 2Q_Z} \quad (1.9)$$

The corresponding anisotropy, r , is

$$r = \frac{I_{VV} - I_{VH}}{I_{VV} + 2I_{VH}} = \frac{A - 1}{A + 2} = \frac{-4 + 12Q_X - 2Q_Y + 6Q_Z}{14 + 7Q_Y} \quad (1.10)$$

This equation is precisely equivalent to Eqs. (8) and (9) of Chen and Van Der Meer,⁽²¹⁾ which have the added advantage of being expressed in terms of the

second Legendre polynomial for the direction of the fluorescing moment. Wan and Johnson's⁽²²⁾ equations clearly give the same results, but are expressed in terms of spherical tensors. Although they were able to define δ_G and δ_F in terms of their parameters, they did not do so for Q_x and Q_z .

1.3.3. Excitation with Circularly Polarized Light

The three variables Q_x , ([^]and Q_z may be recovered if two more independent ratios are established by measuring I_{CV} and I_{CH} . These are analogous to I_{VV} and I_{VH} defined earlier, except that the excitation light is circularly instead of vertically polarized. In this case the excitation polarization is complex; e.g., $\mu = (1/\sqrt{2})(1 \ i \ 0)$ for light propagating in the Cartesian z direction. Thus, $\mu \cdot \mu = 0$, making Y and $Z=0$ and $X=1/2$ and 0 for the V and H viewing polarizer orientations respectively.

The most compact choice of ratios seems to be (again from Eqs. (1.4)–(1.6)

$$B = \frac{I_{CV}}{I_{VH}} = \frac{5 + 6Q_X - Q_Y - 4Q_Z}{6 - 4Q_X + 3Q_Y - 2Q_Z} \quad (1.11)$$

$$C = \frac{I_{CH}}{I_{VH}} = \frac{11 - 12Q_X - 5Q_Y + 8Q_Z}{6 - 4Q_X + 3Q_Y - 2Q_Z} \quad (1.12)$$

Three linear combinations of Eqs. (1.9), (1.11), and (1.12) isolate the individual variables so that each is expressible by a combination of the three ratios A , B , and C , after rearranging:

$$\frac{I_{CV} + I_{VV}}{2I_{CV} + I_{CH} + I_{VV} + 2I_{VH}} = \frac{1}{5} + \frac{2}{5}Q_X \quad (1.13a)$$

$$Q_X = \frac{-2 + 4A + 3B - C}{4 + 2A + 4B + 2C} \quad (1.13b)$$

$$\frac{2I_{CV} + I_{CH}}{I_{VV} + 2I_{VH}} = \frac{3 - Q_Y}{2 + Q_Y} = \Omega \quad (1.14a)$$

$$Q_Y = \frac{12 + 6A - 8B - 4C}{4 + 2A + 4B + 2C} \quad (1.14b)$$

$$\frac{3(I_{VV} + I_{VH}) + 2(I_{CV} + I_{CH})}{2I_{CV} + I_{CH} + I_{VV} + 2I_{VH}} = \frac{8}{5} + \frac{2}{5}Q_Z \quad (1.15a)$$

$$Q_Z = \frac{-1 + 7A - 6B + 2C}{4 + 2A + 4B + 2C} \quad (1.15b)$$

Thus, from three experimental intensity ratios come the three molecular properties Q_X , Q_Y , and Q_Z . Wan and Johnson⁽²²⁾ speak of four independent parameters. However, the fourth is the integrated absorptivity (Q_1 here), which does not affect the anisotropy.

1.3.3.1. Other Ratios

It is of interest to define other ratios, which can be used as checks, or which might be forced because of adverse measuring conditions. One such ratio is the circular anisotropy defined as

$$r_C = \frac{I_{CV} - I_{CH}}{I_{CH} + 2I_{CV}} = \frac{B - C}{C + 2B} = \frac{-6 + 18Q_X + 4Q_Y - 12Q_Z}{21 - 7Q_Y} \quad (1.16)$$

An alternative to Ω comes about naturally when measuring $\delta_{\text{circular}}/\delta_{\text{linear}}$ when there is virtually no rotation of the molecules before emission. This is defined here as Ω° :

$$\Omega^\circ = \frac{I_{CV} + I_{CH}}{I_{VV} + I_{VH}} = \frac{B + C}{A + 1} = \frac{16 - 6Q_X - 6Q_Y + 4Q_Z}{8 + 4Q_X + 4Q_Y + 2Q_Z} \quad (1.17)$$

1.3.4. The Two-Dimensional Limit with Linear Polarization

Because recent experiments have been focused on in-plane (x , y) polarized transitions of planar molecules using linearly polarized light, and because there is evidence that S_{zz} is often small compared to S_{xx} and S_{yy} for such systems in condensed phase,⁽⁵³⁾ it is instructive to consider the two-dimensional limit, wherein F_z , S_{xz} , S_{yz} , and S_{zz} are all zero.

1.3.4.1. Determination of Q_X from r and Ω

Although r in general is determined by three molecular parameters, we show now that in the 2D case r depends only on Q_X and Q_Y , i.e., only on the “shape” of the tensor (Q_Y) and how the emission dipole projects onto the tensor (Q_X). For

compactness the normalized forms of \mathbf{F} and \mathbf{S} (symmetrized),⁽⁵²⁾ \mathbf{f} and \mathbf{s} , are introduced:

$$\mathbf{f} = \frac{\mathbf{F}}{|\mathbf{F}^2|^{1/2}} \quad \text{and} \quad \mathbf{s} = \frac{\mathbf{S}}{\delta_G^{1/2}}$$

$$\begin{aligned} Q_X &= \left| (f_x \ f_y) \cdot \begin{pmatrix} s_{xx} & s_{xy} \\ s_{xy} & s_{yy} \end{pmatrix} \right|^2 \\ &= (f_x s_{xx} + f_y s_{xy})^2 + (f_x s_{xy} + f_y s_{yy})^2 \\ &= f_x^2 s_{xx}^2 + 2f_x s_{xx} f_y s_{xy} + f_y^2 s_{xy}^2 + f_x^2 s_{xy}^2 + 2f_x s_{xy} f_y s_{yy} + f_y^2 s_{yy}^2 \end{aligned}$$

Likewise,

$$\begin{aligned} Q_Z &= (f_x \ f_y) \cdot \begin{pmatrix} s_{xx} & s_{xy} \\ s_{xy} & s_{yy} \end{pmatrix} \cdot \begin{pmatrix} f_x \\ f_y \end{pmatrix} \cdot (s_{xx} + s_{yy}) \\ &= (f_x^2 s_{xx} + 2f_x f_y s_{xy} + f_y^2 s_{yy})(s_{xx} + s_{yy}) \\ &= f_x^2 s_{xx}^2 + 2f_x f_y s_{xx} s_{xy} + f_y^2 s_{xx} s_{yy} \\ &\quad + f_x^2 s_{xx} s_{yy} + 2f_x f_y s_{xy} s_{yy} + f_y^2 s_{yy}^2 \end{aligned}$$

Because $f_x^2 + f_y^2 = 1$, we have $Q_Z - Q_X = s_{xx}s_{yy} - s_{xy}^2$. But since $\delta_F/\delta_G = Q_Y = (s_{xx} + s_{yy})^2$ and $s_{xx}^2 + s_{yy}^2 + 2s_{xy}^2 = 1$,

$$Q_Z = Q_X + \frac{1}{2}(Q_Y - 1) \tag{1.18}$$

Substituting this relation into Eq. (1.10) gives

$$r = \frac{18Q_X + Q_Y - 7}{7Q_Y + 14} \tag{1.19}$$

When r and Q_Y are known, one can find Q_X from

$$Q_X = \frac{7r(Q_Y + 2) + 7 - Q_Y}{18} \tag{1.20}$$

1.3.4.2. Allowed Space of Q_X

The space of Q_X , the normalized squared projection of the fluorescence dipole vector onto the two-photon tensor, is further restricted by the nature of the tensor; the limits are dictated solely by Q_Y . To establish this relation we imagine a rotation of the coordinate system which diagonalizes s such that $s_{x'y} = 0$ and $s_{x'x'} \geq s_{y'y'}$.

The maximum projection squared of any unit vector in the (x, y) plane, Q_X^{\max} , will then be $s_{x'x'}^2$. Further, since $\delta_F/\delta_G = (s_{x'x'} + s_{y'y'})^2 = 1 + 2s_{x'x'}s_{y'y'}$ one obtains, after rearranging and squaring,

$$s_{x'x'}^2 s_{y'y'}^2 = \frac{1}{4}(\delta_F/\delta_G - 1)^2$$

or

$$Q_X^{\max}(1 - Q_X^{\max}) = \frac{1}{4}(Q_Y - 1)^2$$

Solving the resulting quadratic equation for Q_X^{\max} yields

$$Q_X^{\max} = \frac{1}{2} + \frac{1}{2}(Q_Y(2 - Q_Y))^{1/2} \quad (1.21a)$$

$$Q_X^{\min} = \frac{1}{2} - \frac{1}{2}(Q_Y(2 - Q_Y))^{1/2} \quad (1.21b)$$

Substituting Eq. (1.21) for Q_X into Eq. (1.19) gives the maximum and minimum r values:

$$r_{\pm} = \frac{2 \pm 9[Q_Y(2 - Q_Y)]^{1/2} + Q_Y}{14 + 7Q_Y} \quad (1.22)$$

In this way a knowledge of Q_Y through a measurement of Ω prescribes the possible range of r , i.e., between r_- (r_{\min}) and r_+ (r_{\max}). Only measured r values falling outside this range should be considered anomalous. Figure 1.2 shows the r_{\max} and r_{\min} values as a function of Ω obtained from Eqs. (1.8) and (1.22).

1.3.4.3. Tensor Shapes

We have seen how Ω is uniquely determined in the 2D limit by δ_F/δ_G , which, in turn, determines the tensor “shape.” We now define the tensor shape

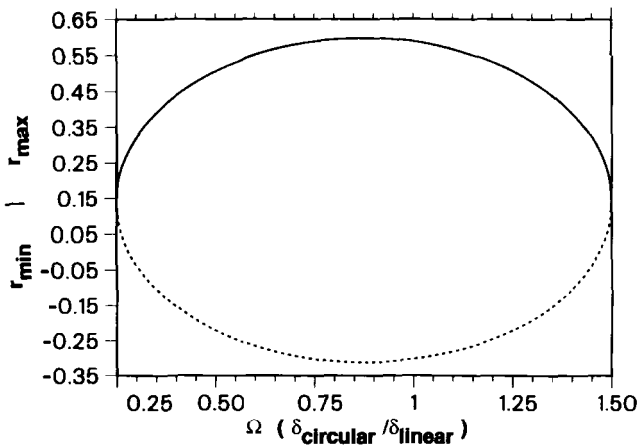


Figure 1.2. Maximum (solid line) and minimum (dashed line) fluorescence anisotropies from two-photon excitation with linearly polarized light as a function of $\Omega = \delta_{\text{circular}}/\delta_{\text{linear}}$ for $S_{zz} = 0$ (2D case).

to be the two-photon absorption *amplitude*, $A^{(2)}$ as a function of the incident-light polarization angle using linear polarized light. That is,

$$A^{(2)} = \boldsymbol{\mu} \cdot \mathbf{S} \cdot \boldsymbol{\mu} \quad (1.23)$$

The amplitude is used here because the small features which lead to anisotropies greater than $4/7$ are more easily seen. The *rate* of two-photon absorption is given by the absolute square of the absorption amplitude.

Figure 1.1 surveys the possible variety of shapes within the scope of interest here. The range of shapes was generated by considering all possible diagonal tensors such that $|S_{xx}| \geq |S_{yy}| \geq |S_{zz}|$ and arbitrarily choosing S_{xx} as positive. Only diagonal tensors need be considered because the symmetric real tensors under consideration here may always be diagonalized by a simple coordinate transformation (rotation of axes). In Figure 1.1 the individual plots have x to the right, z toward the top, and y toward the reader. The tensors are arranged such that the yy term grows from -1 to $+1$, going from the bottom of the figure to the top. The zz term grows from -1 to $+1$, going from left to right in the figure. The entire range of shapes is displayed at representative points, with redundancy of shape appearing only along the line of tensors connecting the upper left and lower right corners of the figure. The values of S_{xx} , S_{yy} , and S_{zz} are displayed beneath each drawing, along with the corresponding Ω , Q_y , r_{\max} and r_{\min} values.

The 2D limit can be seen to lie entirely on the center vertical axis. The δ_F/δ_G (and Ω) values depend only on the shape of the tensor, so any orientation of the tensor axes will give the same Ω . The absolute orientation of the tensor

cannot be obtained from experiments on a randomly oriented sample unless the absolute direction of the fluorescing moment is known.

1.3.4.4. The Tensor–Transition Moment Angle

It is convenient to describe Q_X in terms of an angle, θ_{FS} , which the fluorescing transition moment makes with the long principal axis of the two-photon tensor. This is easily done in terms of Q_X^{\max} and Q_X^{\min} described earlier:

$$\begin{aligned} Q_X &= Q_X^{\max} \cos^2 \theta_{FS} + Q_X^{\min} \sin^2 \theta_{FS} \\ Q_X &= (Q_X^{\max} - Q_X^{\min}) \cos^2 \theta_{FS} + Q_X^{\min} \\ \theta_{FS} &= \pm \cos^{-1} \left[\left(\frac{Q_X - Q_X^{\min}}{Q_X^{\max} - Q_X^{\min}} \right)^{1/2} \right] \end{aligned} \quad (1.24)$$

As in most spectroscopic experiments of this type only the absolute value of the angle is measurable.

1.3.4.5. Some Special 2D Cases

1.3.4.5a. Two-Dimensional Isotropic Case ($\Omega = 1/4$, $Q_Y = 2$). This natural limit occurs when $\delta_F/\delta_G = 2$, its maximum value in the 2D case. This occurs when $\mathbf{S}_{xx} = \mathbf{S}_{yy}$, i.e., the top middle tensor of Figure 1.1. Thus, $Q_X = 1/2$, $Q_Y = 2$, $Q_Z = 1$ independent of F so that r is always $1/7$ if the fluorescing moment lies in the (xy) plane.

1.3.4.5b. Single-Diagonal Case ($\Omega = 2/3$, $Q_Y = 1$). If $Q_Y = \delta_F/\delta_G = 1$, corresponding to a single diagonal \mathbf{S} , then $\Omega = 2/3$ and Q_X and Q_Z can vary from 0 to 1. If $Q_X = Q_Z = 1$, then $r = 4/7$. But, if $\mathbf{F} \cdot \mathbf{S} = 0$, Q_X and $Q_Z = 0$, giving $r = 2/7$. This is the tensor in the center of Figure 1.1.

1.3.4.5c. Maximum Anisotropy Case ($\Omega = 7/8$, $Q_Y = 2/3$). Somewhat surprisingly, the maximum 2D anisotropy possible is not the $4/7$ value derived by many for the single-diagonal case, but occurs when $Q_Y = 2/3$ ($\Omega = 7/8$), a situation which can arise, for example, if $S_{xx}/S_{yy} = \sqrt{8} - 3 = -0.1716$ and \mathbf{F} is parallel to x . From Eq. (1.21) one finds that $Q_Y = 2/3$ leads to

$$r_{\max} = \frac{4 + 9\sqrt{2}}{28} = 0.5974 \quad \text{and} \quad r_{\min} = -0.3117$$

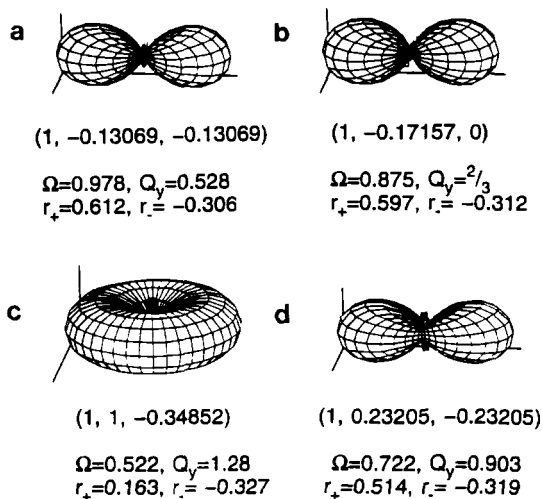


Figure 1.3. Polar spherical surface plots as in Figure 1.1 of tensors giving extreme anisotropy values beyond the range $4/7$ to $-2/7$. Relative principal tensor values, normalized trace squared (Q_y), Ω value, and anisotropy range are given under each tensor.

a slightly larger range than $4/7$ (0.5714) to $-2/7$ (-0.2857). This tensor is displayed in Figure 1.3b, along with other exceptional tensors to be considered in Section 1.3.5.

1.3.4.5d. $\Omega = 13/12, Q_Y = 2/5$. From Eq. (1.21) it is seen that $r_{\max} = 4/7$ for this tensor shape also. The r_{\max} values fall symmetrically about $\Omega = 7/8$, with $r_{\max} = 4/7$ occurring at $\Omega = 7/8 \pm 5/12$.

1.3.4.5e. Zero-Trace Case ($\Omega = 1.5, Q_Y = 0$). $Q_X = 1/2, Q_Z = Q_Y = 0$. This is common and is always the case when the excited state is of different symmetry than the ground state⁽³⁰⁾ In this limit $\Omega = 1.5$ and $r = 1/7$, independent of how S and F are oriented in the molecular plane. Two-dimensional zero-trace tensors always have the shape of the cloverleaf tensor at the bottom center of Figure 1.1.

1.3.5. Three-Dimensional Tensors

Now we consider the general case, i.e., with no restriction on the tensor and fluorescing moment. As expressed in Figure 1.1, all possible tensor shapes are contained in the set of all diagonal tensors with principle axes a, b, c , with $-1 \leq a/b \leq 1$ and $-1 \leq b/c \leq 1$. Each will have a minimum and maximum possible r value depending on the direction of the fluorescing moment relative to the minor axis of the tensor. Interferences which could lead to a maximum or a minimum at intermediate angles are not possible when detection is by fluorescence, because only the square of the transition moment is involved.

Figure 1.1 shows one way of organizing the shapes in the space of possible principal axes, and was introduced in Sections 1.2.1 and 1.3.4.3. The minor tensor axis, z , increases from -1 to $+1$ in the horizontal direction across the figure, and the intermediate axis varies from -1 to $+1$, going from bottom to top in the figure. The individual tensors have been rescaled. There are four natural sectors of Figure 1.1, reflecting the four possible combinations of signs of the minor and intermediate tensor magnitudes relative to the major axis. The areas omitted in the figure are redundant; they give the same shapes in a different orientation.

Each sector may be thought of as starting from the simplest tensor in the center, the one with only a single diagonal element, and growing either positive or negative lobes in one or both of the other directions. Two lobes of opposite sign destructively interfere, creating a nodal surface between them. Light linearly polarized in a nodal surface cannot be absorbed in a two-photon process. The possibility of absorptivity nodes is one of the major differences between one- and two-photon absorption. We shall see that small negative lobes can lead to greater-than-expected photoselection and are responsible for the maximum and minimum two-photon anisotropies given by the tensors in Figure 1.3. In one-photon absorption there is only a node perpendicular to the transition dipole, and then only if the absorption is governed by a single transition dipole. Within each sector the tensor shapes are unique. There is some duplication at the interfaces because of symmetry.

The possible range of anisotropy values for each of the four groups is given in Figures 1.4–1.7 as a function of Q_Y . In each figure, r values corresponding to the fluorescing moment parallel to the major, intermediate, and minor tensor axes are given by a horizontal bar, a solid circle, and a vertical bar, respectively.

1.3.5.1. The $[+, +]$ Sector

The $[+, +]$ sector has all lobes positive, and therefore no nodes are possible, and the normalized trace squared, Q_Y , can range only from 1 to 3 (Ω from $2/3$ to 0). As seen in Figures 1.4–1.7, Q_Y values above 2 are unique to this sector. The extreme point is the completely isotropic case, the sphere. It uniquely has $\Omega=0$ and can only exhibit $r=0$, independent of the fluorescing moment direction. Because there are no nodes, the maximum and minimum r values are $+4/7$ and $-2/7$, and it is the only sector for which this is true. The $+4/7$ value occurs uniquely for the single-diagonal tensor case. However, $-2/7$ is possible for the family of tensors having a vanishing minor axis when fluorescence is polarized along the minor axis, i.e., for the two-dimensional tensors. As the shape becomes more spherical, the range of possible r values

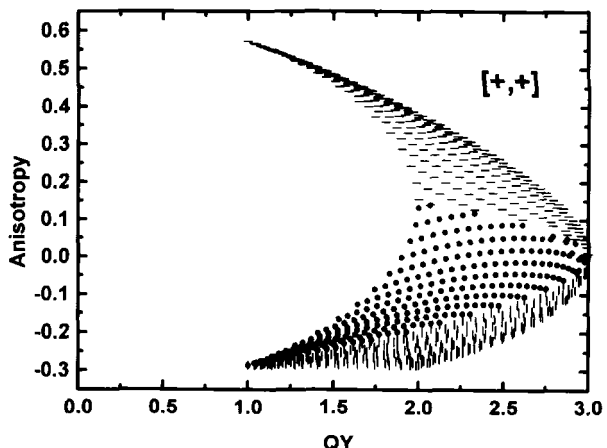


Figure 1.4. Plots of two-photon-induced anisotropy as a function of Q_Y for selected diagonal tensors with principal values $a \geq b \geq c$ where all elements are positive. The emission dipole direction is indicated by the type of symbol: —, along a; ·, along b; |, along c.

decreases monotonically. Vapor-phase benzene offers an example. It was found that the zz component was nearly equal to the in-plane elements.⁽⁵⁴⁾ This element apparently arises from the large number of $\sigma\pi^*$ and $\pi\sigma^*$ intermediate Rydberg states possible for planar molecules. However, when in liquid solutions the zz component was found to be only about 10% of the in-plane elements.⁽⁵³⁾

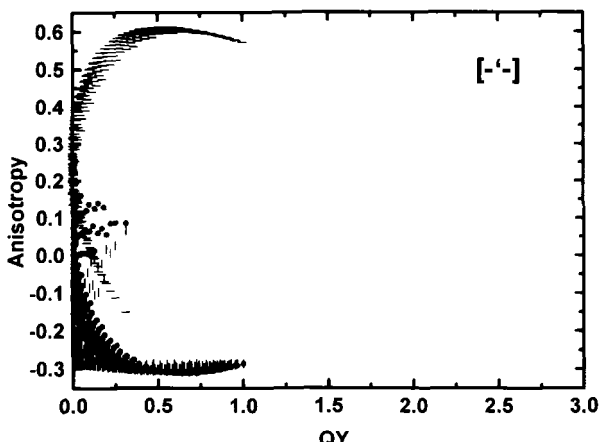


Figure 1.5. Plots of two-photon-induced anisotropy against Q_Y for selected diagonal tensors as in Figure 1.4 but with a/b and a/c negative.

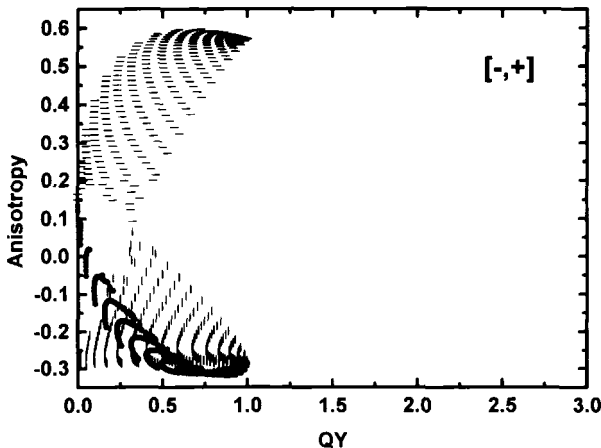


Figure 1.6. Plots of two-photon-induced anisotropy against Q_Y for selected diagonal tensors as in Figure 1.4 but with a/b positive and a/c negative.

1.3.5.2. The $[-, -]$ Sector

Here only the major axis is positive, causing this sector to be dominated by tensors with small traces, including the important zero-trace cases. The Q_Y ranges from 0 to 1. Something of a curiosity is the occurrence of the maximum anisotropy case for a tensor differing from the single-lobe tensor by having a small

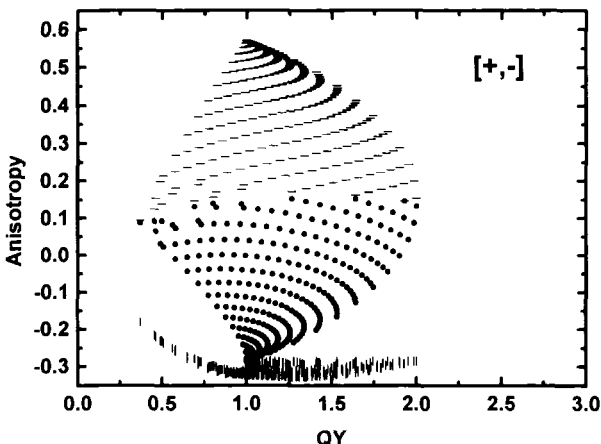


Figure 1.7. Plots of two-photon-induced anisotropy against Q_Y for selected diagonal tensors as in Figure 1.4 but with a/b negative and a/c positive.

negative “doughnut” lobe. Such a tensor has two conical nodal surfaces lying just off the yz plane. This tensor is shown in Figure 1.3a along with other exceptional tensor shapes. The effect is to create a somewhat more vertically oriented photo-selected population than in the absence of the negative lobe. The maximum anisotropy is $r = 0.6123\ 3362\ 0718\ 714$ when the ratio of principal tensor values is $S_{\text{major}}/S_{\text{minor}} = -0.1306936$ (cylindrical symmetry). Thus, an observed value of $r = 4/7$ does not necessarily imply a pure single-diagonal tensor. The r_{min} for this tensor is $-0.3061\ 6681$, a value considerably more negative than $-2/7$, but not the most negative possible value.

The zero-trace tensors are special because they are common when a molecule has some degree of symmetry and the excited state is not totally symmetric.⁽³⁰⁾ Such tensors have $\Omega = 1.50$. As noted, in two dimensions $r = 1/7$, regardless of the emission moment. In three dimensions, $r_{\text{max}} = +2/7$ for $S_{\text{major}} = -2S_{\text{minor}}$. However, as can be seen in Figure 1.5, r increases rapidly with increasing trace so that if $Q_Y = 0.1$ ($\Omega = 1.38$), $r_{\text{max}} = 0.5$ for tensors approaching this one.

1.3.5.3. The [−, +] Sector

In this sector the intermediate principal value is negative so that the possible range for Q_Y is also 0–1. The maximum r in this sector comes from the same two-dimensional tensor which gave the minimum value in the [−, −]sector, shown in Figure 1.3b with $r_{\text{max}} = 0.5974$. The minimum r comes from the tensor shown in Figure 1.3d having $r_{\text{min}} = -0.3188$ and $Q_Y = 0.904$.

1.3.5.4. The [+ , −] Sector

In this sector the minor value is negative and the intermediate value is positive, with the result that Q_Y ranges from $1/3$ to 2 , thereby overlapping all the other sectors. As the minor negative lobe grows from the disk, moving left from the top center in Figure 1.1, the interference causes decreased orientation of the minor axis, thereby causing a minimum in the anisotropy when the emission moment is along the minor axis. The tensor shown in Figure 1.3c appears to give the global minimum, with $r_{\text{min}} = -0.3266\ 1933\ 5004\ 43$.[†] In this sector the anisotropy when emission is along the minor axis is confined to the “boat” in Figure 1.7, a narrow region near $-2/7$, rising only to 0.16 at $Q_Y = 1/3$. The maximum anisotropy is the ordinary $4/7$ at the $Q_Y = 1$ point.

[†]The value of -0.3277 in Ref. 20 is a misprint.

1.3.5.5. Exclusive Domains

Figures 1.4–1.7 have points corresponding only to emission moments pointing along one of the two-photon tensor principal axes. Providing that a molecule has sufficient symmetry that this restriction obtains, each of the aforementioned sectors has exclusive domains in the space of r and Q_Y , allowing for the possibility of narrowly identifying the tensor shape. When such symmetry constraints are relaxed, the points are only the extrema, with all possibilities lying between.

1.4. Comparison with Experiment

1.4.1. Introduction

The number of molecules for which two-photon anisotropy has been measured is very few. Probably the earliest measurement was by Peticolas *et al.*⁽⁵⁵⁾ for anthracene in the very dawn of two-photon spectroscopy. Application of McClain's theory was made by Scott, Haber, and Albrecht⁽⁵³⁾ to the case of two-photon fluorescence excitation of the $^1B_{2u}$ state of benzene in glassy solvent. Since then there seem to be no reports of two-photon anisotropy until the work of Lakowicz *et al.*, who have recently measured time-resolved and steady-state two-photon-induced fluorescence for several compounds, and the two-photon-induced transient absorption by Wan *et al.* on bacteriorhodopsin. Following are summaries of the experimental anisotropies known to the author along with brief interpretations in the context of the theoretical framework presented.

1.4.2. Polyenes

The linear polyenes offer the simplest theoretical case because almost all of the low-lying one-photon absorption bands are polarized along the long axis. For this reason the two-photon tensor must be dominated by a single-diagonal element, i.e., $Q_Y = 1$ and $\Omega = 2/3$. Also, the emission must be polarized along the same axis so that Q_X and $Q_Z = 1$, giving $r = 4/7$. This result is expected independent of various complicating details involving mixing of the two-photon-allowed and -forbidden states and vibronic coupling, a consequence of all the pertinent dipole intensity being along the long axis.

Experimentally this is borne out for the three linear polyene-related molecules studied: diphenylhexatriene (DPH), $r = 0.52$,⁽⁵⁾ diphenyloxyzole (POP), $r = 0.0.54$,⁽⁹⁾ and bacteriorhodopsin (BR), $r = 0.55$,⁽¹²⁾ each approaching the ideal limit of 4/7 (0.5714). Given the many possibilities for error in such experi-

ments, it might be reasonable to suspect that the measured values deviate from the ideal values by unknown experimental errors. On the other hand, there is no reason to believe that the tensors are rigorously single element and that Q_X is precisely 1.

Formally, DPH has the classic separation of states into u and g categories because of its formal center of symmetry. Thus, it is possible that much of the two-photon absorption is directly due to the two-photon-allowed A_g state with the nearby strongly one-photon-allowed B_u state acting as the intermediate state. However, because the lowest two states are often superimposed, much of the absorption may be due to vibronic and solvent field mixtures of these two states. If the local solvent configuration creates an electric field at the solute, the 1B_u and 1A_g states will be strongly mixed. This can happen even in hydrocarbon matrices.⁽⁵¹⁾ When this happens, the 1B_u state can gain two-photon allowedness through the charge transfer mechanism pointed out in Section 1.2. The latter mechanism is almost certainly the main mechanism of the very strong two-photon absorption by BR,⁽⁴⁹⁾ so strong that measurable ground-state depletion is obtained.⁽¹²⁾ This is also likely to be the main mechanism in POP.⁽⁵⁶⁾

1.4.3. Benzene Derivatives

In contrast to the linear polyenes, planar aromatic systems, being more circular, typically have their $\pi\pi^*$ one-photon intensity related to two strong transitions polarized perpendicular to each other and lying well above the lowest two excited states, 1L_b and 1L_a . As a result, the two-photon tensors tend to be of the type lying at the top and bottom center of Figure 1.1, and therefore are prone to having low two-photon fluorescence anisotropy. In addition, S_1 is the 1L_b state for most substituted benzenes and naphthalenes. As noted in Section 1.2, the spectroscopic behavior of 1L_b and 1L_a regarding substituents and vibronic coupling is reversed in two-photon relative to one-photon spectra, with the result being that vibrationally induced intensity often dominates the S_1 two-photon absorption of these molecules, whereas it is in the background in one-photon absorption.

1.4.3.1. Benzene: The Pure Vibrational Baseline

Because of the importance of vibrations in the S_1 two-photon spectra of substituted benzenes, benzene itself provides an important base line: because of its hexagonal symmetry, almost all of its S_1 one- and two-photon intensity is vibrationally induced when in *vapor*. In solution there is a significant solvent-induced component as well. It is therefore fitting that benzene was the subject of

the first application of McClain's⁽⁴⁸⁾ formalism in the elegant study of Scott, Haber, and Albrecht⁽⁵³⁾ carried out on benzene dissolved in an isopentane-3-methylpentane glass at liquid nitrogen temperature. Although the anisotropy, as such, was not reported, three ratios were reported from which the anisotropy could be recovered.

1.4.3.1a. Vibrational versus Allowed Intensity. The hexagonal symmetry dictates that the 0–0 electronic transition (the origin) to S_1 (B_{2u} or 1L_b) is forbidden in both one- and two-photon excitation. The same is true for any benzene vibronic transition originating in the ground vibrational state of the ground electronic state and terminating in a totally symmetric vibrational state of S_1 . However, benzene does have substantial UV and two-photon absorptivity to S_1 due to vibrationally induced transitions, often referred to as Herzberg–Teller vibronic coupling, intensity borrowing, or intensity stealing.⁽⁵⁷⁾ This vibrationally induced intensity is not very strong in one-photon absorption, having an oscillator strength of about 0.001, and giving a maximum molar decadic extinction coefficient of about $200 \text{ L}^{-1} \text{ mol cm}^{-1}$. Virtually all of the vibrationally induced intensity is due to v_6 , a 520 cm^{-1} in-plane bending mode of e_{2g} symmetry. This means that the absorption envelope has its origin (a so-called false origin) at 520 cm^{-1} above the true origin (0–0). A progression of lines consisting of successive numbers of quanta of the 900 cm^{-1} totally symmetric ring breathing mode make up the main features of the absorption band. The relative height of the lines depends only on the Franck–Condon factors for the change in size of the ring, so the shape of the absorption envelope is the same in one- and two-photon excitation; as will be noted, only the position of the false origin(s) will be different in the two spectroscopies. When the symmetry is broken by a substituent, the 0–0 band is no longer forbidden, and in general two (or more) overlapping vibronic progressions, one based on the true origin and the other(s) based on their respective false origins, will coexist. The relative intensity of each envelope depends on the ability of the substituent to induce intensity and the ability of each active vibration to induce intensity. The vibrationally induced parts play a vital role in the TPE of 1L_b of aromatics because the vibrations are very effective and because substituents tend to act weakly at bringing in two-photon intensity, in contrast to the patterns in one-photon spectra. It is much more important, then, to carefully learn about benzene's two-photon spectrum and anisotropy if one is to understand, say, phenol, because the hydroxyl does not increase the two-photon absorptivity much over what is already present from the vibrations in benzene itself.

1.4.3.1b. Benzene Vibrational Components. In the D_{6h} point group a vibronic two-photon transition must belong to either the A_{1g} , E_{2g} , or E_{1g} irreducible representation.⁽³⁰⁾ For S_1 , the electronic wave function is B_{2u} , so b_{2u} , e_{1u} , and e_{2u} vibrations are allowed to be Herzberg–Teller active. The b_{2u}

mode v_{14} is extremely effective at inducing two-photon intensity.^(53,54) This CC stretching mode is particularly simple to describe in that it simply alternates the bond lengths about the ring; i.e., it moves the ring toward one of its two Kekulé resonance structures. It is therefore identifiable in the TPE of a great many aromatic hydrocarbons as a very strong false origin beginning about 1500 cm^{-1} to the blue of the true origin.⁽³²⁾ So effective is this mode that it dominates the two-photon intensity of molecules like fluorobenzene, phenol, pyrimidine, quinolines, and other such systems.^(36,48,58)

In addition, two lower-frequency modes—an in-plane bend (e_{1u} , v_{18}) and an out-of-plane (oop) bend (e_{2u} , v_{17}) with frequencies at 900 and 700 cm^{-1} respectively—are effective in the benzene two-photon absorption to 1L_b , but are an order of magnitude weaker than v_{14} .^(53,54)

If we take the molecular plane as x , y , v_{14} induces a diagonal two-photon tensor with equal xx and yy elements.⁽³⁰⁾ Also, S_{zz} may be nonzero, but it is almost negligible in solution.⁽⁵³⁾ Thus, this tensor lies somewhere along the top row of Figure 1.1. If one assumes $S_{zz}=0$, it is the toroid shape at the top center; the predicted r is 0.14, because the emission moment lies in plane. The experiment gave 0.077.⁽⁵³⁾

The two degenerate components of the v_{18} tensor (e_{2g}) have xy and $x^2 - y^2$ symmetry. They are cloverleaves, one rotated 45° from the other. Again, $r=0.14$ is predicted and 0.064 is observed.⁽⁵³⁾

The third vibration to consider is v_{17} , the oop bend at 700 cm^{-1} . It is also doubly degenerate, having the symmetry of xz and yz , and the corresponding tensors are cloverleaves lying in the xz and yz planes, respectively, with the lobes 45° to the axes. This time not all of the emission is polarized in the plane of the tensor. Because of the symmetry of the benzene ring, the emission dipole may be thought of as x -polarized half the time and y -polarized half the time. Thus, the emission polarization is 50% in the plane and 50% perpendicular to the plane of each tensor, giving a predicted $r=(0.14 - 0.28)/2 = -0.07$. The observed value was -0.045 .⁽⁵³⁾

Thus, there is qualitative agreement between theory and experiment. Systematic deviations from the ideal are common in steady-state photoselection studies.⁽¹⁾

1.4.3.1c. Solvent-Induced Component. A number of studies have been concerned with the solvent-induced 0–0 transition seen for benzene in solution. Although completely absent in vapor—as it must be by symmetry—it is quite strong in TPE of solutions of benzene,^(53,59,60) being about 10% as strong as the v_{14} vibrational contribution and about equal to the v_{17} contribution. It therefore must be considered for any benzene derivative having a weak 0–0 transition, such as tyrosine, which will be discussed.

The anisotropy of the solvent-induced component does not seem to have been measured. However, several measurements of Ω give $\Omega=0.6-0.7$ for a

variety of cases in various nonpolar solvents at room temperature,^(53,59,60) where it dominates the 700 and 900 cm^{-1} vibrational contributions. Also, $\Omega = 1.2$ (whereas 1.5 is expected) for the 0–0 of neat toluene⁽⁶⁰⁾ and toluene in ethanol solution⁽³²⁾ and for phenylalanine in *aqueous* solution,⁽⁴⁵⁾ suggesting that much of the origin intensity is solvent induced and that it is not very sensitive to solvent polarity.

1.4.3.2. Phenol

Lakowicz *et al.*⁽¹⁷⁾ have recently reported two-photon fluorescence anisotropy of phenol, tyrosine, and N-acetyl-L-tyrosinamide (NATyrA) with excitation on the extreme low-energy edge of the S_1 transition, 566 to 578 nm. Based on the previous section, the important issue is the ratio of intensity in the true origin to that in the false origins. It is assumed that the vibrationally induced part is substantially the same as for benzene. For gas-phase phenol, it is known that the hydroxyl induces two-photon intensity only about half that induced by $v_{14,\text{in}}$ in contrast to the one-photon case, where the hydroxyl provides an order of magnitude more intensity than the vibrations^(34–37). The two-photon-allowed origin for S_1 of singly substituted benzenes will have only xy and yx elements;⁽³⁰⁾ i.e., it will have the cloverleaf shape. The predicted anisotropy, r , is therefore $r = 0.1428$, independent of the direction of the fluorescence transition dipole, as seen in Section 1.3.4.5e. The experimental values reported in the present paper for phenol range from 0.07 to 0.10, not far from the ideal value just mentioned. Agreement is better if one recognizes that experimental anisotropies are almost always smaller in magnitude than theoretical expectations, even when every effort is made to eliminate experimental artifacts. Even more pertinent is the two-photon-induced fluorescence anisotropy of benzene under these conditions⁽⁵³⁾ where e_{2g} vibronic states yield $r = 0.08$ compared to the expected 0.14, and e_{1g} states yield -0.045 when -0.07 is expected. It is likely that the solvent-induced intensity mentioned previously could also contribute to these deviations if it has an anisotropy near zero.

1.4.3.3. Tyrosine

The anisotropy for excitation near the origin for tyrosine and NATyrA is significantly lower than for phenol, reaching about -0.04 . This surprising result appears to be the consequence of special circumstances involving the interference of para-substituted groups, which is opposite the effect found in one-photon absorption.^(33–39)

In one-photon absorption, the hydroxyl group induces about 10 times more intensity than the weak vibronic part present in benzene, thereby all but over-

whelming the vibronic component, which manifests itself only by the small-wavelength dependence of the anisotropy. A methyl group, on the other hand, induces absorptivity only weakly, contributing at the same level as the vibronic part. A methyl added to phenol therefore has only a small effect, and phenol and tyrosine are very similar in one-photon spectroscopy.

The story is almost completely reversed in two-photon spectroscopy for this transition. The vibrationally induced intensity overwhelms the substituent contributions by an order of magnitude.^(36,38,39,44,48,60) The methyl group is about equal to hydroxyl in its ability to induce two-photon absorbance.^(34,36) And, of particular contrast to the one-photon case, when methyl and hydroxyl are para to each other their perturbations nearly cancel,^(34,36,38,44) leaving only the vibrational and solvent-induced contributions as in benzene. This pattern can also be seen in the two-photon properties computed from semiempirical molecular orbital theory using INDO/S-SCI.^(44,45) Data from Goodman and Rava⁽³⁶⁾ suggest that the origin (0–0) band for *p*-methylphenol will be nearly 200 times weaker than that of phenol. This is largely confirmed by the appearance of the TPE for NATyrA in room-temperature aqueous solution,⁽⁴⁵⁾ which has the same band shape as in one-photon absorption (OPA) but the entire spectrum is blue-shifted 1500–2000 cm^{−1}. This is because the origin is very weak and most of the TPE intensity arises from the strongly TPE-inducing 1570 cm^{−1} *b*_{2u} vibration.⁽⁵⁴⁾

Thus, it is seen that intuition based on UV spectroscopy is completely misleading. *A much better working model for the two-photon anisotropy of tyrosine is benzene itself.*

Comparing tyrosine in aqueous solution to benzene in a nonpolar glass is complicated by three unknown factors. (1) The methyl- and hydroxyl-induced intensities probably do not exactly cancel. Unfortunately, the vapor TPE for *p*-methylphenol does not seem to be known, but there is probably a weak intrinsic 0–0 intensity. (2) The anisotropy of the considerable solvent-induced 0–0 intensity is unknown. (3) The polar nature of the solute and solvent means the origin and vibrationally induced transitions about 700 and 900 cm^{−1} to the blue are probably overlapped.

One can rule out dominance by the intrinsic 0–0 absorption and the strong ν_{14} component 1600 cm^{−1} to the blue because these should give $r = 0.14$. It appears that the ν_{17} component, which gives $r = -0.05$ in benzene, could be a major source of the anisotropy, but much of the intensity must be solvent induced. The former will definitely give the slightly negative r values seen, but by itself would give $\Omega = 1.5$, a much larger value than the observed 0.9.⁽⁴⁵⁾ The solvent-induced origin is probably a significant component, and if present at the 30% level would provide the observed Ω . If its r is about 0 ± 0.01 , the resulting r would still be consistent with that observed. The emission moment direction, which is short-axis polarized, does not enter the discussion because of the shape of the tensors involved.

1.4.3.4. RNAase A Behavior

A possible reason for the red-shifted tyrosyl emission seen for TPE of RNAase A⁽¹⁷⁾ could be the presence of one or more tyrosinate forms in the native protein. The reason this is plausible is that, unlike tyrosine itself where the OH and alkyl moieties cancel, the $-O^-$ group overwhelms the alkyl and the resultant TPE intensity is strong. This may be inferred from experiments on aniline.^(35,36) In addition, an INDO/S computation⁽⁵⁶⁾ predicts that tyrosinate will have about 100 times stronger two-photon absorptivity than tyrosine. Furthermore, the absorption curve is known to be shifted to longer wavelengths, so that even one tyrosinate with an abnormal pK_a could dominate the two-photon-induced fluorescence. It is expected that tyrosinate emission would be red-shifted, as observed. In addition, the higher anisotropy seen is consistent with the expectation noted for phenol.

1.4.4. Indoles

Lakowicz *et al.* have measured the two-photon-induced fluorescence anisotropy for a number of indoles, including indole,⁽⁸⁾ *N*-acetyltryptophanamide (NATA),⁽⁸⁾ tryptophan in water and in proteins,⁽⁷⁾ and others. It was found that, unlike DPH and POP, the anisotropies were about the same or less than the one-photon anisotropies. This finding was at first puzzling, partly because of the historical accident of having first observed the anisotropy for DPH and POP, for which there were very high anisotropies due to special nature of these molecules.

Indoles have two low-lying singlet $\pi\pi^*$ states, 1L_a and 1L_b , each with a distinctive transition dipole direction and two-photon tensor shape and orientation. No symmetry restrictions require the transition dipoles to be related to the direction of the two-photon tensor principal axes. The two transitions are next considered separately, since the state properties seem to be somewhat independent of substitution pattern.

1.4.4.1. 1L_a Excitation

The TPE of fluorescence from 3-methylindole (3MI), 2,3-dimethylindole, and tryptophan (3-alanylindole) in fluid hydroxylic solvents invariably gives Ω values near 0.50,^(45,61) when exciting at the extreme long-wavelength edge, where it is believed excitation is solely to 1L_a .^(62,63) This corresponds to $\delta_F/\delta_G = 1.33$. From Eq. (1.22), the possible range of anisotropies is $r = -0.22$ to $+0.51$. The same range is seen from Figures 1.4–1.7, assuming the emitting moment to be in-plane. The two-photon-induced anisotropies observed by Lakowicz *et al.*^(7,8)

exciting pure 1L_a at the red edge of several indole absorption bands range from 0.2 to 0.3, well within the possible range.

For $\delta_F/\delta_G = 1.33$, one obtains from Eq. (1.20) that $Q_X = 0.704$ when $r = 0.31$, and $Q_X = 0.57$ when $r = 0.21$, using the highest values reported for indole and NATA, respectively.⁽⁸⁾ From Eq. (1.24) the Q_X values correspond to $\theta_{FS} = \pm 31^\circ$ when $r = 0.31$ and $\theta_{FS} = \pm 40^\circ$ when $r = 0.21$. These angles represent the new information regarding the 1L_a tensor and fluorescing transition dipole when exciting on the red edge.

Since the direction of the fluorescing moment is known with reasonable certainty, it was possible to make a statement about the direction of the tensor major axis.⁽²⁰⁾ The convention used here to denote transition dipole directions and tensor orientations relative to the indole molecular frame is shown in Figure 1.8. The angle between the dipole or tensor principal axis and a line from C₂ bisecting the 5–6 bond is measured such that a line between C₈ and C₃ is about $+45^\circ$. Since light absorption and emission depend upon the square of a transition dipole, there is no physical distinction between a given angle θ and $\theta \pm \pi$.

For indole, if the value of -46° ⁽⁶⁴⁾ is used for the transition dipole direction, the two-photon tensor direction is located at $-46 \pm 31^\circ$, i.e., either at -15° or -77° . For NATA/3MI the value is $-44 \pm 40^\circ$, i.e., either -4° or -84° . INDO/S computations were strongly in accord with the values which lie near the long molecular axis, -15° and -4° .⁽²⁰⁾ Figures 1.8–1.9 display the experimental and calculated tensor and transition dipole directions for the 1L_a and 1L_b transitions for indole and NATA (3MI).

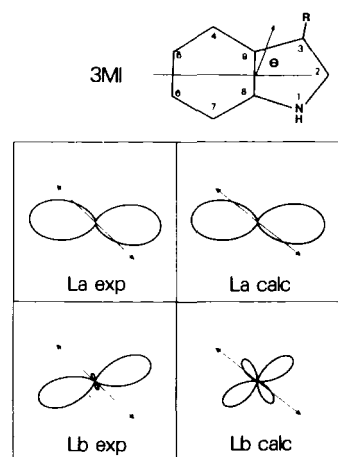


Figure 1.8. Experimental (from Ref. 8 for NATA) and calculated (Ref. 20) 2D two-photon tensor shapes for the 1L_b and 1L_a transitions of 3-methylindole. The vectors give the experimental (from Ref. 64) transition dipole direction for the emitting state 1L_a . The indicated angle on the indole ring at the top is used in the text to give directions of dipoles and tensor axes.

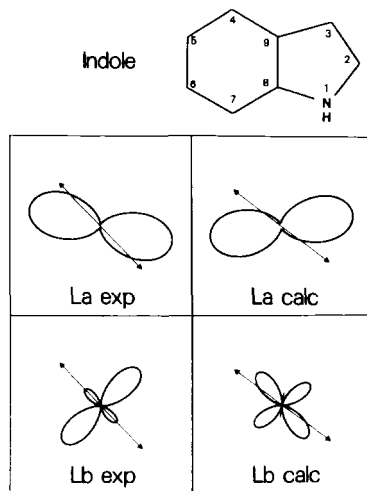


Figure 1.9. The same as for Figure 1.8, except for indole.

1.4.4.2. 1L_b Excitation

In the two-photon fluorescence anisotropy experiments of Lakowicz *et al.*,⁽⁸⁾ excitation in the region of the 1L_b origin results in a sharp decrease in anisotropy, similar to what is found for one-photon excitation.^(62,63) The dip in the one-photon anisotropy suggests that the absorption is about 50% due to 1L_b at the minimum in r . It is found from linear excitation that the ratio of 1L_a and 1L_b bands in TPE is similar to that for one-photon excitation.^(45,61) In fact, using the Ω value observed for indole in butanol ($\Omega = 0.95$) also gives 50% 1L_b absorption, assuming that pure 1L_b and 1L_a have $\Omega = 1.4$ and 0.5, respectively. Using 50% 1L_b leads to $r_b = -0.1$. Using $\Omega = 1.40$ in Eq. (1.8) gives $Q_Y = 0.0833$, and Eq. (1.20) gives $Q_X = 0.30$.

Again we can ask if this is a possible result. According to Eq. (1.21), $Q_X^{\max} = 0.70$ and $Q_X^{\min} = 0.30$. Fortunately, the observed Q_X is close to Q_X^{\min} , meaning that θ_{FS} is near 90° ; i.e., the fluorescing dipole is nearly perpendicular to the major axis of the 1L_b two-photon tensor. Thus, a rather definite prediction for the orientation of the 1L_b tensor for indole comes from the assumptions made here if the 1L_a transition dipole is known. The value -46° ⁽⁶⁴⁾ for the fluorescing transition dipole direction for indole predicts the major tensor direction to be $+44 \pm 5^\circ$. This happens to be nearly parallel to the 1L_b transition dipole direction. Accordingly, if a TPE experiment were performed in a nonpolar solvent where 1L_b is the fluorescing state, the initial anisotropy is predicted to be 0.39 when exciting 1L_b .

For NATA, where r at the minimum is 0.08, it is somewhat less clear what the intrinsic $^1L_b \Omega$ is. Recent measurements in vapor,⁽⁶⁵⁾ jet-cooled beams,⁽⁶⁶⁾ and in perfluorohexane solution⁽⁶⁷⁾ all point to a value near 1.15 for Ω for the 1L_b origin of 3 MI, considerably lower than that for indole, which maintains a value near 1.40 for those conditions. Using $\Omega = 1.15$ for 1L_b for tryptophan, we deduce 42% 1L_b absorption at the 1L_b origin for tryptophan in water, where $\Omega = 0.80$ and $\Omega = 0.55$ for excitation at the red edge.⁽⁴⁵⁾ This value is in accord with that deduced by Valeur and Weber⁽⁶²⁾ from one-photon anisotropy. One then deduces that $r_b = -0.1 \pm 0.02$ for NATA.

To obtain $r = -0.1$ when $\Omega = 1.15$ (characteristic of a more directed tensor than if $\Omega = 1.4$), θ_{FS} need only be 63° (instead of $\approx 90^\circ$). This still predicts the major lobe is in the positive xy quadrant, but it is ambiguous as to whether directed to $+19$ or $+73^\circ$.

1.4.4.3. Out-of-Plane Contributions

The 2D limit was used in the foregoing analysis. If S_{zz} is assumed to be $\pm 10\%$ of the largest in-plane tensor element, the conclusions regarding the orientation of the 1L_a tensor are affected by no more than 1° in the 1L_a cases.⁽²⁰⁾ The shape of the deduced tensor is only slightly different, depending on whether S_{zz} is positive or negative. For 1L_b the general conclusions are also unaffected by including zz components up to 10% of the other elements.

1.4.4.4. INDO/S Predictions

One reason for doing two-photon spectroscopy is to test spectroscopically calibrated semiempirical molecular orbital computations, e.g., INDO/S.^(68,69) Callis *et al.* have reported previously that such computations predict qualitatively correct Ω values for 1L_b and 1L_a simultaneously with a reasonable fit to transition dipoles and permanent dipoles.^(20,45,46,61,70) This means that the *shape* of the two-photon tensors is predicted reasonably well. The *directions* of the tensor principle axes were recently compared to the above experimental values, including more recent computations on 3 MI, as a representation of NATA, in vacuum and simulated aqueous solvent environment.⁽⁷⁰⁾

1.4.4.4a. 3-Methylindole. The INDO/S results were in fair agreement with the experimental picture. The 1L_a two-photon tensor was uniformly predicted to have $\Omega = 0.5\text{--}0.7$ and a major direction close to the long molecular axis (x) no matter which geometry or environment was used. The predicted anisotropies for 1L_a absorption and emission range from 0.21 to 0.30, not far from the observed value of 0.21 seen when exciting NATA at the red edge. The high predictions are seen when using the 1L_a geometry, primarily because the calculated transition moment direction is in worse agreement.

Agreement for exciting 1L_b is not quite as good, although it is also harder to assess. The predicted Ω values, ranging from 1.35 to 1.50, are consistently higher than observed. Nevertheless, in most cases the 1L_b tensor is directed in roughly the direction required to cause a substantial decrease in anisotropy at the 1L_b origin. The average r value in H_2O using ground-state geometry was predicted to be 0.04, much below the value when exciting 1L_a , but considerably higher than the estimated experimental value of ~ -0.1 . The calculated value varied by ± 0.08 in different simulated water environments.⁽²⁰⁾

1.4.4.4b. Indole. The 1L_a predictions for indole did not agree with experiment as well as for 3MI. The higher anisotropy seen experimentally for indole suggests that the tensor is aligned more closely to the 1L_a transition dipole direction than for NATA. However, the INDO/S results predicted that there is a bigger angle, consistently predicting θ_S near $+10^\circ$ while maintaining a prediction near -35° for the transition dipole. Although only an 8° difference, it is in the opposite direction required to produce good agreement with experiment.

Much worse agreement was found for the indole 1L_b case. In vacuum, the two-photon tensor is predicted to be nearly zero trace, giving $\Omega = 1.5$. The symmetrical cloverleaf shape of such a tensor yields an anisotropy near 0.14, independent of the fluorescence moment direction. However, the observed anisotropy for 1L_b in indole must be near -0.1 to produce the pronounced minimum in r . It was noted that this can come about only if the tensor is fairly directed (so as to give $\Omega \approx 1.45$ or less) with the major lobes pointing near the $+45^\circ$ direction. However, for those parameters and geometries for which INDO/S does give Ω values < 1.5 , the tensor major lobes are invariably predicted to be near -45° , resulting in a high predicted anisotropy.

1.5. Some Predictions

The ratio Ω has been measured for considerably more systems and at more wavelengths than has two-photon-induced fluorescence anisotropy. Considering the relationship between Ω and the permitted range of r , it is of interest to make some predictions of r based on known Ω values and emission moment directions. In addition, INDO/S-calculated tensors provide predictions in some cases.⁽⁵⁶⁾

1.5.1. Phenylalanine

The effect of the alanyl group should closely mimic the effect of methyl. The TPE spectrum for phenylalanine (Phe) in H_2O ⁽⁴⁵⁾ is, indeed, quite similar to the TPE of toluene in vapor,⁽³⁶⁾ ethanol solution,⁽³²⁾ and as the neat

liquid.^(71,72) The vibrational structure is more pronounced and modulated in the two-photon spectrum of Phe, relative to one-photon, because the allowed part does not fill in the "valleys" of the vibronic part. The two-photon spectral envelope is generally shifted ca. 1000 cm^{-1} to higher energy, essentially the difference between the v_{14} - and v_6 -inducing mode frequencies.

For Phe Ω shows an extreme swing from 1.2 to 0.4 with considerable modulation across the TPE excitation spectrum, starting with the origin. This is expected on the basis of the two-photon tensor patterns for the allowed and b_{2u} vibronic parts. The 0-0 and 0-1 peaks of the allowed part (535 and 520 nm) should have zero-trace symmetric tensors according to group theory,⁽³⁰⁾ and thus $\Omega=1.5$. It is presumably reduced by the solvent-induced component. The v_{14} vibronic part has a totally symmetric tensor with $\Omega=0.0$ to 0.25, depending on the relative value of the out-of-plane diagonal element.⁽⁵³⁾ The sharp drop in Ω coincides with one quantum of v_{14} , and the modulation is caused by the mismatch in the peaks of the vibronic and allowed parts. It is expected that $r=0.14$ for the 0-0, v_{14} , and v_{18} -induced components. The v_{17} part, and probably the solvent-induced part, will reduce r somewhat.

1.5.2. Tyrosine

1.5.2.1. S_1 Maximum

At shorter wavelengths near the band maximum, it is expected that the b_{2u} vibronic component will dominate and that r values near 0.1 will be found. In more detail, the same arguments just applied to phenylalanine are equally valid for tyrosine, except that no detailed vibronic structure is seen because of the strong inhomogeneous broadening from the solvent interaction with the -OH group, and because of the low-frequency torsional vibrations of the -OH. Note that in TPE we may expect phenylalanine and tyrosine to appear on a more equal footing than for UV excitation.

If the two-photon spectrum were 100% vibrationally induced by v_{14} , the Ω value would be consistently low throughout the band. That it drops from 0.8 in the low-energy toe to 0.45 is attributed to a small amount of allowed component and weaker vibronic coupling by lower- frequency modes related to v_{18} (e_{2u}), 923 cm^{-1} , which is known to be active in the benzene spectrum with $\Omega=1.5$.⁽⁵⁴⁾ Assuming that $\Omega=0.45$ comes from a mixture of v_{14} , v_{18} , and pure 0-0 contributions gives a predicted $r=0.14$. The solvent-induced component may reduce this value slightly.

1.5.2.2. S_2

INDO/S computations predict the tensor for the transition to S_2 of tyrosine to be dominated by a single diagonal element, directed long axis. Because the emission moment is mostly directed short axis, $r = -0.28$ is strongly predicted.

1.5.3. Indole in Nonpolar Solvent

Indole in a hydrocarbon solvent is known to have 1L_b as S_1 at the time of absorption,⁽⁶¹⁾ and is believed to have 1L_b emission. The direction of the two-photon tensor shown in Figure 1.9 is nearly parallel to the 1L_b transition moment,⁽⁶⁴⁾ meaning that fairly high two-photon anisotropy is predicted, around 0.4.

1.5.4. 5-Methoxyindole

Because it is believed that 1L_b is S_1 even in quite polar solvents for this molecule, it is expected that, in analogy with the previous prediction, an anisotropy of about 0.4 will be observed during S_1 TPE, provided the methoxy substituent does not greatly alter the 1L_b tensor and transition moment direction. Excitation into S_2 (1L_a) is expected to give negative r values.

1.5.5. Nucleotides

Williams and Callis⁽⁷³⁾ have measured Ω° (Eq. 1.17) for the four DNA nucleotides in neutral aqueous solution at room temperature. The value of Ω° was measured because the short fluorescence lifetimes of the nucleotides in room-temperature water allow almost no rotation during the excited-state lifetime. INDO/S computations done at the time showed fair agreement. Here we use the results of those calculations to predict the two-photon-induced anisotropy for excitation into S_1 .

1.5.5.1. Thymidine Monophosphate

Thymidine Monophosphate (TMP) represents a case of a nearly-single-diagonal tensor directed parallel to the emission dipole because the charge transfer term dominates. There is good agreement between the INDO/S transition moment and that from single-crystal experiments.^(74,75) INDO/S predicts $r = 0.51 \pm 0.02$, very close to the ideal limit of 4/7. For this system one-

photon *steady-state* anisotropy in *room-temperature aqueous* solution is 0.34 because of the very short lifetime (about 2 ps).⁽⁷⁴⁾

1.5.5.2. Cytidine Monophosphate (CMP)

In CMP there is some discrepancy between the transition moment calculated in vacuum and that from single-crystal measurements.^(74,76) The INDO/S-calculated anisotropy is 0.33. If one uses the crystal transition moment direction, the predicted r is 0.53–0.59. The latter gives better agreement with experimental Ω° .

1.5.5.3. Guanosine Monophosphate (GMP)

Again there was considerable disagreement between the transition dipole calculated in vacuum and that observed in a single crystal.^(74,77) This is attributed to the strong crystal field. The effect of solvation by water is unknown. The calculated tensor major axis is directed approximately along the amino group bond, but has considerable cloverleaf character ($\Omega = 1.33\text{--}1.46$). The INDO/S result alone gives $r = 0.3\text{--}0.4$. The experimental moment makes a larger angle with the main tensor direction, predicting $r = 0.15$.

1.5.5.4. Adenosine Monophosphate (AMP)

AMP has the S_1 and S_2 bands superimposed, much as the case of indole. Indeed, the adenine and indole chromophore are closely related. It is not clear which of the two states is the fluorescing state in aqueous solution. Using the Ohno–Klopman parameters and including doubly excited configurations in an INDO/S calculation lead to greater distinction between the 1L_a - and 1L_b -type states.⁽⁷³⁾ Assuming that the higher-energy state is the emitting state (possible if it is broader as for indole) gives better agreement with the measured Ω° . That assumption predicts $r = 0.59$ for excitation into S_2 and $r = 0.15$ for excitation into S_1 .

1.6. Concluding Remarks

There is general agreement between the three recent works on two-photon fluorescence anisotropy^(20–22) which were produced independently in the same time period, and they are in accord with McClain's original treatments.^(18,19) There appear to be no conflicts between theory and the few experimental determinations to date. The prediction of anisotropies well outside the range 4/7 to

–2/7 is one of the most intriguing aspects of the theory as it stands, and its experimental confirmation poses a demanding challenge.

Acknowledgments

The author expresses appreciation to Ms. Bent Burgess for help in preparing the figures and to Professor Carey Johnson for making his chapter available during the preparation stage.

References

1. A. C. Albrecht, Polarizations and assignments of transitions: The method of photoselection, *J. Mol. Spectrosc.* 6, 84–108 (1961).
2. A. Kawski, Fluorescence anisotropy: theory and application of rotational depolarization, *Crit. Rev. Anal. Chem.* 23, 459–529 (1993).
3. J. Michl and E. W. Thulstrup, *Spectroscopy with Polarized Light* VCH, New York (1986).
4. A. P. Blokhin, V. A. Povedailo, and V. A. Tolkachev, Polarization of two-photon-excited fluorescence of vapors of complex organic molecules, *Opt. Spectrosc. (USSR)* 60, 37–40 (1986).
5. J. R. Lakowicz, I. Gryczynski, J. Kusba, and E. Danielsen, Two photon-induced fluorescence intensity and anisotropy decays of diphenylhexatriene in solvents and lipid bilayers, *J. Fluoresc.* 2, 247–258(1992).
6. J. R. Lakowicz and I. Gryczynski, Fluorescence intensity and anisotropy decay of the 4',6-diamidino-2-phenylindole-DNA complex resulting from one-photon and two-photon excitation, *J. Fluoresc.* 2, 117–122 (1992).
7. J. R. Lakowicz and I. Gryczynski, Tryptophan fluorescence intensity and anisotropy decays of human serum albumin resulting from one-photon and two-photon excitation, *Biophys. Chem.* 45, 1–6 (1992).
8. J. R. Lakowicz, I. Gryczynski, E. Danielsen, and J. Frisoli, Anisotropy spectra of indole and *N*-acetyl-L-tryptophanamide observed for two-photon excitation of fluorescence, *Chem. Phys. Lett.* 194, 282–287 (1992).
9. J. R. Lakowicz, I. Gryczynski, Z. Gryczynski, E. Danielsen, and M. J. Wirth, Time-resolved fluorescence intensity and anisotropy decays of 2,5-diphenyloxazole by two-photon excitation and frequency-domain fluorometry, *J. Phys. Chem.* 96, 3000–3006 (1992).
10. J. R. Lakowicz, I. Gryczynski, J. Kusba, and E. Danielsen, Two-photon-induced fluorescence intensity and anisotropy decays of diphenylhexatriene in solvents and lipid bilayers, *J. Fluoresc.* 2, 247–258 (1992).
11. J. Lakowicz and I. Gryczynski, Characterization of 7-bis(*O*-methylstyryl) benzene as a lifetime and anisotropy decay standard for two-photon induced fluorescence, *Biophys. Chem.* 47, 1–7 (1993).
12. C. Wan, Q. Song, and C. K. Johnson, Two-photon-induced anisotropic transient absorption in bacteriorhodopsin, *Chem. Phys. Lett.* 210, 94–100 (1993).
13. I. Gryczynski and J. R. Lakowicz, Fluorescence intensity and anisotropy decays of the DNA stain Hoechst 33342 resulting from one-photon and two-photon excitation, *J. Fluoresc.* 4, 331–336 (1994).

14. I. Gryczynski and J. R. Lakowicz, Fluorescence intensity and anisotropy decays of the DNA stain Hoechst 33342 resulting from one-photon and two-photon excitation, *Proc. SPIE-Int. Soc. Opt. Eng.* 2137, 302–310 (1994).
15. L. I. Burov, E. S. Voropai, and A. P. Klishchenko, in: *Fluorescence Anisotropy during Two-Photon Excitation 2* (A. A. Bogush, ed.), pp. 18–19, Akad. Nauk Beloruss. SSR, Inst. Fiz., Minsk, USSR (1995).
16. B. Kierdaszuk, I. Gryczynski, A. Modrak-Wojcik, A. Bzowska, D. Shugar, and J. R. Lakowicz, Fluorescence of tyrosine and tryptophan in proteins using one- and two-photon excitation, *Photochem. Photobiol.* 61, 319–323 (1995).
17. J. R. Lakowicz, B. Kierdaszuk, P. R. Callis, H. Malak, and I. Gryczynski, Fluorescence anisotropy of tyrosine using one- and two-photon excitation, *Biophys. Chem.* 56, 263–271 (1995).
18. W. M. McClain, Polarization dependence of three-photon phenomena for randomly oriented molecules, *J. Chem. Phys.* 57, 2264–2272 (1972).
19. W. M. McClain, Polarization of two-photon excited fluorescence, *J. Chem. Phys.* 58, 324–326 (1973).
20. P. R. Callis, On the theory of two-photon induced fluorescence anisotropy with application to indoles, *J. Chem. Phys.* 99, 27–37 (1993).
21. S. Y. Chen and B. W. Van Der Meer, Theory of two-photon induced fluorescence anisotropy decay in membranes, *Biophys. J.* 64, 1567–1575 (1993).
22. C. Wan and C. K. Johnson, Time-resolved anisotropic two-photon spectroscopy, *Chem. Phys.* 179, 513–531 (1994).
23. C. Wan and C. K. Johnson, Time-resolved two-photon induced anisotropy decay: the rotational diffusion regime, *J. Chem. Phys.* 101, 10283–10291 (1994).
24. W. M. McClain and R. A. Harris, Two-photon spectroscopy in liquids and gases, in: *Excited States 3* (E. C. Lim, ed.), pp. 2–77. Academic Press, New York (1977).
25. P. P. Feofilov, Polarization of the luminescence of isotropic media in the case of two-photon excitation, *Opt. Spectrosc. (USSR)* 26, 306–310 (1969).
26. Y. T. Mazyrenko, Polarization of luminescence from complex molecules with two-photon excitation. Dichroism of two-photon light absorption, *Opt. Spectrosc. (USSR)* 31, 413–414 (1971).
27. M. Goeppert-Mayer, Über Elementarakte mit zwei quantensprungen, *Ann. Phys.* 9, 273 (1931).
28. W. L. Peticolas, *Anna. Rev. Phys. Chem.* 18, 233–260 (1967).
29. H. Mahr, Two-photon absorption spectroscopy, in: *Nonlinear Optics, Part A*, pp. 285–361, Academic Press, New York (1975).
30. W. M. McClain, Excited state symmetry assignment through polarized two-photon absorption studies of fluids, *J. Chem. Phys.* 55, 2789–2796 (1971).
31. D. M. Friedrich and W. M. McClain, Two-photon molecular electronic spectroscopy, *Anna. Rev. Phys. Chem.* 31, 559–577 (1980).
32. B. Dick, H. Gonska, and G. Hohlneicher, Two photon spectroscopy of dipole forbidden transitions. III: Experimental determination of two-photon absorption spectra including polarization control, *Ber. Bunsenges. Phys. Chem.* 85, 746–754 (1981).
33. L. Goodman and R. P. Rava, Two-photon spectra of substituted benzenes, *J. Chem. Phys.* 74, 4826–4831 (1981).
34. R. P. Rava, L. Goodman, and J. G. Philis, Regularities in the two-photon spectra of polysubstituted benzenes, *J. Chem. Phys.* 77, 4912–4918 (1982).
35. R. P. Rava and L. Goodman, Probing of chemical bonding through two-photon spectroscopy of substituted benzenes, *J. Am. Chem. Soc.* 104, 3815–3822 (1982).
36. L. Goodman and R. P. Rava, Two-photon spectroscopy of perturbed benzenes, *Adv. Chem. Phys.* 54, 177–230 (1983).

37. L. Goodman and R. P. Rava, Two-photon spectra of aromatic molecules, *Acc. Chem. Res.* **17**, 250–257 (1984).
38. P. R. Callis, T. W. Scott, and A. C. Albrecht, Perturbation selection rules for multiphoton electronic spectroscopy of neutral alternant hydrocarbons, *J. Chem. Phys.* **78**, 16–22 (1983).
39. T. W. Scott, P. R. Callis, and A. C. Albrecht, Alternant hydrocarbon selection rules in the two-photon spectroscopy of perturbed benzenes, *Chem. Phys. Lett.* **93**, 111–114 (1982).
40. R. R. Birge and B. M. Pierce, A theoretical analysis of the two-photon properties of linear polyenes and the visual chromophores, *J. Chem. Phys.* **70**, 165–178 (1979).
41. R. R. Birge, J. A. Bennet, L. M. Hubbard, H. L. Fang, B. M. Pierce, D. S. Kliger, and G. E. Leroi, Two-photon spectroscopy of all-trans-retinal. Nature of the low-lying singlet states, *J. Am. Chem. Soc.* **104**, 2519–2525 (1982).
42. G. Hohlneicher and B. Dick, Two-photon spectroscopy of dipole-forbidden transitions. II: Calculation of two-photon cross sections by the CNDO-CI method, *J. Chem. Phys.* **70**, 5427–5437 (1979).
43. G. Hohlneicher and B. Dick, Two-photon spectroscopy of dipole-forbidden transitions. I: Dipole-forbidden transitions and double excited configurations in the CNDO-CI methods, *Theor. Chim. Acta* **53**, 221–251 (1979).
44. P. R. Callis, Two-photon properties of the L_a and L_b bands of substituted benzenes computed from CNDO/S, *Chem. Phys. Lett.* **107**, 125–130 (1984).
45. P. R. Callis and A. A. Rehms, Two-photon fluorescence excitation spectra of aromatic amino acids, *Chem. Phys. Lett.* **208**, 276–282 (1993).
46. P. R. Callis, Molecular orbital theory of the 1L_a and 1L_b states of indole, *J. Chem. Phys.* **95**, 4230–4240 (1991).
47. W. M. McClain, Two-photon molecular spectroscopy, *Acc. Chem. Res.* **7**, 129–135 (1974).
48. P. R. Callis, T. W. Scott, and A. C. Albrecht, Polarized two-photon fluorescence excitation studies of pyrimidine, *J. Chem. Phys.* **75**, 5640–5646 (1981).
49. B. Dick and G. Hohlneicher, Importance of initial and final states as intermediate states in two-photon spectroscopy of polar molecules, *J. Chem. Phys.* **76**, 5755–5760 (1982).
50. B. E. Scharf and Y. B. Band, Enhanced two-photon transitions in molecules with permanent dipole moments, *Chem. Phys. Lett.* **144**, 165–171 (1988).
51. B. E. Kohler, and J. C. Woehl, Measuring internal electric fields with atomic resolution, *J. Chem. Phys.* **102**, 7773–7781 (1995).
52. D.-H. Lee, A theoretical study on nonlinear optical spectroscopies. Ph.D. thesis, Cornell University (1983).
53. T. W. Scott, K. S. Haber, and A. C. Albrecht, Two-photon photoselection in rigid solutions: a study of the $B_{2u} \leftarrow A_{1g}$ transition in benzene, *J. Chem. Phys.* **78**, 150–157 (1983).
54. D. M. Friedrich and W. M. McClain, Polarization and assignment of the two-photon excitation spectrum of benzene vapor, *Chem. Phys. Lett.* **32**, 541–549 (1975).
55. W. L. Petricolas, R. Norris, and K. E. Rieckhoff, Polarization effects in the two-photon excitation of anthracene fluorescence, *J. Chem. Phys.* **42**, 4164–4169 (1965).
56. P. R. Callis, Unpublished results.
57. G. Fischer, *Vibronic Coupling: The Interaction between the Electronic and Nuclear Motions*, Academic Press, London (1984).
58. R. D. Jones and P. R. Callis, Two-photon spectra of inductively perturbed naphthalenes, *Chem. Phys. Lett.* **144**, 158–164 (1988).
59. H. Faidas and K. Siomos, Two-photon excitation spectroscopy of benzene and toluene in nonpolar liquids, *J. Mol. Spectrosc.* **130**, 288–302 (1988).

60. D. M. Friedrich, J. V. Alsten, and M. A. Walters, Polarization and concentration dependence of two-photon forbidden electronic origins: the B_{2u} of benzene in solution, *Chem. Phys. Lett.* **76**, 504–509 (1980).
61. A. A. Rehms and P. R. Callis, Resolution of L_a and L_b bands in methyl indoles by two-photon spectroscopy, *Chem. Phys. Lett.* **140**, 83–89 (1987).
62. B. Valeur and G. Weber, Resolution of the fluorescence excitation spectrum of indole into the La and Lb excitation bands, *Photochem. Photobiol.* **25**, 441–444 (1977).
63. M. R. Eftink, L. A. Selvidge, P. R. Callis, and A. A. Rehms, Photophysics of indole derivatives: experimental resolution of La and Lb transitions and comparison with theory, *J. Phys. Chem.* **94**, 3469–3479 (1990).
64. B. Albinsson and B. Norden, Excited-state properties of the indole chromophore. Electronic transition moment directions from linear dichroism measurements: effect of methyl and methoxy substituents, *J. Phys. Chem.* **96**, 6204–6212 (1992).
65. J. R. Cable, Polarization resolved two-photon ionization spectroscopy of indole and 3-methylindole, *J. Chem. Phys.* **92**, 1627–1633 (1990).
66. D. M. Sammeth, S. S. Siewert, L. H. Spangler, and P. R. Callis, 1L_a transitions of jet-cooled 3-methylindole, *Chem. Phys. Lett.* **193**, 532–538 (1992).
67. D. M. Sammeth, Polarized two-photon fluorescence excitation studies of jet-cooled indoles, Ph.D. thesis, Montana State University (1992).
68. J. Ridley and M. Zerner, Intermediate neglect of differential overlap (INDO) technique for spectroscopy: pyrrole and the azines, *Theor. Chim. Acta (Berl.)* **32**, 111–134 (1973).
69. M. A. Thompson and M. C. Zerner, A theoretical examination of the electronic structure and spectroscopy of the photosynthetic reaction center from *Rhodopseudomonas viridis*, *J. Am. Chem. Soc.* **113**, 8210–8215 (1991).
70. P. L. Muino and P. R. Callis, Hybrid simulations of solvation effects on electronic spectra: indoles in water, *J. Chem. Phys.* **100**, 4093–4109 (1994).
71. T. K. Razumova and I. O. Starobogatov, Two-photon spectroscopy of liquid benzene and toluene, *Opt. Spectrosc. (USSR)* **49**, 654–655 (1980).
72. J. K. Rice and R. W. Anderson, Two-photon, thermal lensing spectroscopy of monosubstituted benzenes in the $^1B_{2u}(^1L_b) \leftarrow ^1A_{1g}(^1A)$ and $^1B_{1u}(^1L_a) \leftarrow ^1A_{1g}(^1A)$ transition regions, *J. Phys. Chem.* **90**, 6793–6800 (1986).
73. S. A. Williams and P. R. Callis, Two-photon electronic spectra of nucleotides, *Proc. SPIE-Int. Soc. Opt. Eng.* **1204**, 332–343 (1990).
74. P. R. Callis, Electronic states and luminescence of nucleic acid systems, *Annu. Rev. Phys. Chem.* **34**, 329–357 (1983).
75. J. S. Novros and L. B. Clark, On the electronic spectrum of 1-methyluracil, *J. Phys. Chem.* **90**, 5666–5668 (1986).
76. M. P. Fulscher and B. O. Roos, A theoretical study on the electronic spectrum of cytosine, *J. Am. Chem. Soc.* **117**, 2089–2095 (1995).
77. D. Theiste, P. R. Callis, and R. W. Woody, Effects of the crystal field on transition moments in 9-ethylguanine, *J. Am. Chem. Soc.* **113**, 3260–3267 (1991).

Anisotropy Decays Induced by Two-Photon Excitation

Carey K. Johnson and Chaozhi Wan

2.1. Introduction

The dynamics of solute molecules in solution, governed by complex many-body interactions, are central to chemical behavior. A powerful method of probing molecular dynamics in solution is to follow the rotational relaxation of solute molecules after photoselection. These molecular reorientations are controlled by interactions with the surrounding solvent (collisions, for example) and by the shape and size of the rotating molecule. In more complex environments such as membranes or proteins, rotations may be partially or completely restricted by the surrounding medium. Hence, both the rate and the amplitude of molecular reorientation can inform us about the nature of the microscopic environment and the interactions of a probe molecule with it.

Since molecular reorientation occurring between the absorption and emission events alters the polarization of the emitted light, the degree of polarization of fluorescence contains information on molecular reorientation. Consequently the dynamics of molecular rotations can be tracked through spectroscopic studies with polarized light. Steady-state fluorescence depolarization ratios have long been measured to learn about reorientation via the dependence of the degree of depolarization on the rate of molecular reorientation relative to the fluorescence decay rate. With the emergence of pulsed lasers and advanced modulation methods, fluorescence depolarization has more recently been followed either through time-domain or frequency-domain anisotropy decay measurements.⁽¹⁾ These studies have a wide array of applications, from testing theories of molecular friction in liquids to probing biological membranes.

Carey K. Johnson and Chaozhi Wan • Department of Chemistry, The University of Kansas, Lawrence, Kansas 66045; present address for CW: Department of Chemistry, California Institute of Technology, Pasadena, California 91125.

Topics in Fluorescence Spectroscopy; Volume 5: Nonlinear and Two-Photon-Induced Fluorescence, edited by J. Lakowicz. Plenum Press, New York, 1997.

Unfortunately, fluorescence anisotropy decay induced by conventional one-photon excitation is a rather blunt probe of reorientational motions. Only one independent parameter sensitive to molecular reorientation can be measured by one-photon excitation of an isotropic sample. This parameter may be the depolarization ratio $d = I_{\perp}/I_{\parallel}$, or any related property. An additional isotropic parameter (independent of orientation), the fluorescence intensity, can also be measured. A particularly useful property is the anisotropy r , defined as

$$r = \frac{I_{\parallel} - I_{\perp}}{I_{\parallel} + 2I_{\perp}} \quad (2.1)$$

which is the ratio of the anisotropic and isotropic fluorescence parameters. All of the available information about reorientational motion in conventional one-photon-induced time-resolved signals is contained in the time dependence of $r(t)$.

Since reorientational motion may be complex, even for rotational diffusion in liquids, a full description of reorientational dynamics in general requires determination of several parameters, such as the three principal diffusion coefficients. In principle, these could be determined from the multiple-exponential decay of $r(t)$. However, $r(t)$ can rarely be measured with sufficient precision to extract accurately more than one decay time. The rotational decay measured by $r(t)$ is usually fit adequately with a single exponential and represents an average of the desired rotational parameters. Exceptions exist where double exponential decays have been detected, notably for perylene⁽²⁻⁵⁾ and tetracene.⁽⁶⁾ However, accurate determination of even two diffusional time constants by fluorescence anisotropy decay measurements requires time- (or modulation frequency) dependent anisotropy data of high quality, and is necessarily subject to the uncertainties of multiple parameter fits, where a range of parameter sets may give satisfactory fits. In order to determine more than one rotational time constant with high confidence, conventional anisotropy studies, even with exceptional signal-to-noise quality, will probably not suffice, and new time-resolved methods need to be implemented.

In recent work,^(7,8) we have shown that two-photon-induced anisotropy decays carry additional information about rotational motion, and can probe reorientational motions in greater detail than conventional methods. In this chapter, we will lay out the theory of the distribution of molecular orientations that is induced by two-photon excitation, and discuss the decay of two-photon-induced anisotropies. Our goal will be to outline a picture of two-photon orientational distributions and to show how information about rotational dynamics can be extracted from two-photon anisotropy decays.

2.1.1. Theoretical Background

The theory of two-photon absorption (TPA), first formulated by Maria Goepert-Mayer,⁽⁹⁾ is almost as old as the theory of quantum mechanics itself. It was an idea whose time was not to come until some 30 years later, when the development of high-powered lasers provided light of sufficient intensity for the effect to be significant.⁽¹⁰⁾ TPA was the first of the new nonlinear spectroscopies to exploit high peak powers available from pulsed lasers. During the following two decades, researchers applied TPA and two-photon excitation (TPE)[†] methods extensively to determine the symmetries of excited states and to locate one-photon forbidden states.⁽¹¹⁻¹⁴⁾

The two-photon absorptivity of the f th excited state is a function not only of the properties of the molecules but also the laser polarizations and frequencies used to induce simultaneous TPA in the molecule, and is given (in Gaussian cgs units) by⁽¹⁵⁾

$$\delta^{(f,o)} = \frac{(2\pi e)^4}{(ch)^2} v_\alpha v_\beta g(v_\alpha + v_\beta) |\mathbf{S}_{\alpha,\beta}^{(f,o)}|^2 \quad (2.2)$$

where v_α and v_β are the frequencies of two the laser beams and $g(v_\alpha + v_\beta)$ is the normalized line-shape function. The two-photon absorptivity $\delta^{(f,o)}$ has units of $\text{cm}^4 \cdot \text{s} \cdot \text{molecule}^{-1} \cdot \text{photon}^{-1}$ and is typically about 10^{-50} . $\mathbf{S}_{\alpha,\beta}^{(f,o)}$ is the two-photon tensor with element α, β given by

$$\mathbf{S}_{\alpha,\beta}^{(f,o)} = \sum_n \left(\frac{(\boldsymbol{\alpha} \cdot \langle n | \mathbf{r} | o \rangle)(\langle f | \mathbf{r} | n \rangle \cdot \boldsymbol{\beta})}{v_n - v_\alpha + i\Gamma_n} + \frac{(\boldsymbol{\beta} \cdot \langle n | \mathbf{r} | o \rangle)(\langle f | \mathbf{r} | n \rangle \cdot \boldsymbol{\alpha})}{v_n - v_\beta + i\Gamma_n} \right) \quad (2.3)$$

where $\boldsymbol{\alpha}$ and $\boldsymbol{\beta}$ are unit vectors defining the polarizations of the two photons in laboratory-fixed coordinates, and v_n and Γ_n are the transition frequency and the homogeneous linewidth of state n , respectively. The summation is over all electronic states of the molecule including the ground and final states.

Whereas the one-photon transition dipole transforms under x, y , or z symmetry, dipole-allowed two-photon transitions are governed by transition dipole products that transform under x^2, y^2, z^2, xy, yz , or xz symmetry. Two-photon spectroscopy manifests a correspondingly richer polarization dependence than one-photon spectroscopy. (See Table 2.1 for a comparison of one-photon and

[†] We use the term *two-photon absorption* to refer to the process of the coherent absorption of two photons by the molecule or to direct measurements of absorption of two photons (for example, by measuring the attenuation of one of the laser beams or by thermal lensing); the term *two-photon excitation* refers here to experiments where TPA is detected indirectly by a subsequent spectroscopic transition, such as fluorescence or induced transient absorption.

two-photon excitations.) In order to assign the symmetry of an excited state by one-photon absorption, one requires samples with oriented solute molecules. In contrast, the two-photon absorptivity of randomly oriented liquid samples is polarization dependent, and this dependence can be exploited to determine the excited-state symmetry in randomly oriented systems.⁽¹⁶⁾ In a randomly oriented molecular system, the two-photon absorptivity measured directly is related to molecular parameters via the orientational average of $|\mathbf{S}^{(f,o)}|^2$ over all molecular orientations:

$$\delta^{(f,o)} = \langle \mathbf{S}^{(f,o)} \mathbf{S}^{(f,o)} \rangle \quad (2.4)$$

where $\langle \dots \rangle$ represents the orientational average. This average was performed in the elegant work of Monson and McClain⁽¹⁷⁾ and completely describes the polarization dependence of TPA detected by direct methods (including thermal lens or photoacoustic techniques). Monson and McClain carried through the orientational average to obtain the expression

$$\delta = \delta_F F + \delta_G G + \delta_H H \quad (2.5)$$

where δ_F , δ_G , and δ_H are molecular two-photon absorptivity parameters, and F , G , and H depend on the polarization directions.

The formalism of Monson and McClain has been used extensively in studies of TPA detected by direct and indirect methods for more than 20 years. However, this approach considers only the TPA event. In contrast, two-photon experiments typically detect TPE of fluorescence, and the signal therefore depends also on the orientation of the emission transition dipole. Hence, a TPE experiment is a three-photon measurement. In the case where the transition dipole moments $\langle n | \mathbf{r} | o \rangle$ and $\langle f | \mathbf{r} | n \rangle$ of the two-photon tensor in Eq. (2.3) are parallel, for example, TPE may excite a secondary transition dipole μ_e parallel or perpendicular to the transition moments of the two-photon transition. Unless the molecular orientations are rapidly randomized by rotational diffusion (relative to the fluorescence lifetime), the orientation of the secondary transition dipole relative to the two-photon tensor must be considered. What is required is the orientational average of a three-photon process: two photons for the absorption event and one photon for the fluorescence (or transient absorption) by which TPE is detected. Recognizing this, McClain carried out the required three-photon orientational average.^(18,19) However, his treatment did not account for rotation between TPA and subsequent emission.

Table 2.1. Comparison of One-Photon and Two-Photon Excitation

	One-photon excitation	Two-photon excitation
Matrix element	$\mu_x = \alpha \cdot \langle f \mathbf{r} o \rangle$	$\mathbf{S}_{x,\beta}^{(f,o)} = \sum_n \left(\frac{\alpha \cdot \langle f \mathbf{r} n \rangle \langle n \mathbf{r} o \rangle \cdot \beta}{v_n - v_x + i\Gamma_n} + \frac{\beta \cdot \langle f \mathbf{r} n \rangle \langle n \mathbf{r} o \rangle \cdot \alpha}{v_n - v_\beta + i\Gamma_n} \right)$
Signal	$I(t) = \langle \mu_a(0) \mu_a^*(0) \cdot \mu_c(t) \mu_c^*(t) \rangle K(t)$	$\delta(t) = \langle \mathbf{S}^{(f,o)}(0) \mathbf{S}^{(f,o)*}(0) \cdot \mu_c(t) \mu_c^*(t) \rangle K(t)$
Spherical components	$\Gamma(\mu_a^* \mu_a) = \Gamma^{(0)} \oplus \Gamma^{(2)}$	$\Gamma(\mathbf{S}^{(fo)} \mathbf{S}^{(fo)*}) = 3\Gamma^{(0)} \oplus 6\Gamma^{(2)} \oplus \Gamma^{(4)}$
Independent parameters	2 (e.g., I_{\parallel} and I_{\perp})	9 in general; 7 for nonresonant intermediate states ($\mathbf{S}^{(f,o)}$ real); 4 for one-color excitation and nonresonant intermediate states (e.g., $I_{\text{lin},\parallel}$, $I_{\text{lin},\perp}$, $I_{\text{cir},\parallel}$, $I_{\text{cir},\perp}$)
Anisotropy	$r = \frac{I_{\parallel} - I_{\perp}}{I_{\parallel} + 2I_{\perp}}$	$r_1 = \frac{I_{\text{lin},\parallel} - I_{\text{lin},\perp}}{I_{\text{lin},\parallel} + 2I_{\text{lin},\perp}}; \quad r_2 = \frac{I_{\text{cir},\parallel} - I_{\text{cir},\perp}}{2I_{\text{cir},\parallel} + I_{\text{cir},\perp}}$ (two additional anisotropies can be defined for two-color excitation)

2.1.2. Time-Resolved Two-Photon Excitation

The time delay between the TPA and emission (or transient absorption) events adds a new dimension to TPE experiments. With state-of-the-art time-domain or frequency-domain time-resolved fluorescence instrumentation and ultrafast laser techniques, the technology now exists to exploit the dimension of time. Time-resolved two-photon techniques include time-resolved fluorescence and transient absorption induced by TPE. Recently, time-resolved TPE fluorescence decays detected by frequency-domain fluorometry were reported by Lakowicz and co-workers.⁽²⁰⁻²³⁾ In our laboratory, we measured time-resolved transient absorption following TPE of bacteriorhodopsin.⁽²⁴⁾ Two-photon-induced transient absorption monitors absorbance changes induced by TPE, while TPE fluorescence decay follows the fluorescence excited by TPE. Although the majority of two-photon spectra has been observed by the fluorescence technique, TPE of transient absorption is a potentially useful method of observing two-photon spectra for samples with low-fluorescence quantum efficiencies. The secondary electronic transition can originate in the ground state, an excited state, or an intermediate state. In the case of a transition from the ground state, for example, TPE is monitored by observing the bleaching of the ground state. The theoretical formalism developed here describes TPE detected either by fluorescence or by transient absorption.

An anisotropy analogous to $r(t)$, defined in Eq. (2.1) for one-photon fluorescence excitation, can also be measured for TPE. (As we show in Section 2.2.4, more than one independent anisotropy parameter can be defined and measured for anisotropic TPE. The anisotropy given in Eq. 2.1 corresponds to the two-photon anisotropy $r_1(t)$, which we call the linear anisotropy.) Although the initial value of $r(t)$ for one-photon transitions is ≤ 0.4 , a wider range of values of the anisotropy $r_1(t)$ have been found by anisotropic TPE measurements. Initial values of the TPE fluorescence anisotropy as high as 0.53–0.54 were reported for 1,6-diphenylhexatriene and 2,5-diphenyloxazole.^(20,21) A similar value of the anisotropy was measured in our laboratory for the protein bacteriorhodopsin by two-photon-induced transient absorption.⁽²⁴⁾ Figure 2.1 shows the two-photon-induced transient absorption in bacteriorhodopsin measured in our laboratory. The resulting anisotropy in the ground state of bacteriorhodopsin, measured by signal averaging at a fixed time delay of 300 us, is 0.55. However, for other molecules, such as indole, much lower values were found.^(22,23)

What is the reason for the wide range of anisotropies induced by TPE? The framework for understanding two-photon-induced anisotropy values has been given in two recent publications. Callis,⁽²⁵⁾ basing his treatment on the theory of the polarization dependence of three-photon phenomena developed by McClain,^(18,19) showed that a wide range of anisotropies is indeed possible, depending on the form of the two-photon tensor (see Chapter 1). The two-

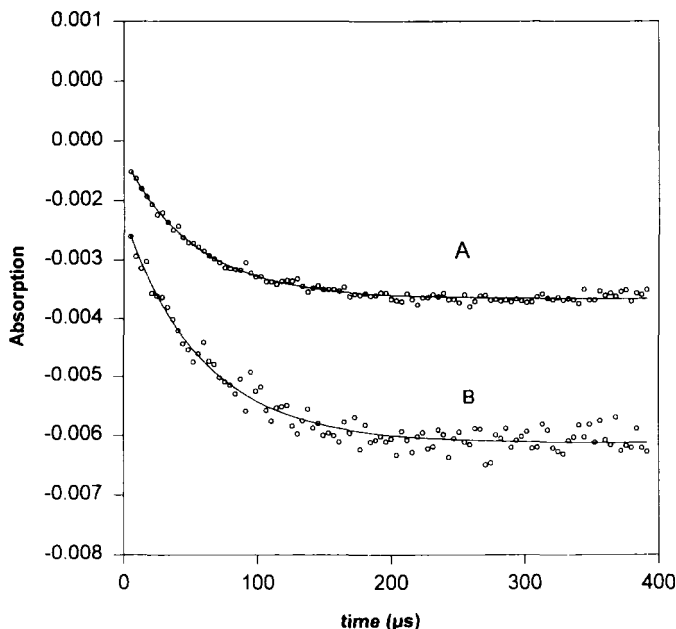


Figure 2.1. Two-photon-induced anisotropic linear dichroism $\Delta A_{\parallel} - \Delta A_{\perp}$ (A) and transient absorption $\Delta A_{\parallel} + 2\Delta A_{\perp}$ (B) in bacteriorhodopsin with photoexcitation at 1064 nm. Absorbance changes probed at 568 nm show bleaching of the ground-state absorption, and decay of the L intermediate of bacteriorhodopsin in 60 μ s. After 300 μ s the signal is due solely to the ground-state bleach, and the ratio of the linear dichroism to the transient absorption gives the anisotropy. Signal averaging at a fixed time delay of 300 μ s yields the value of the linear two-photon anisotropy, $r_1 = 0.55$.

photon fluorescence anisotropy values of indole and 3-methylindole were compared to semiempirical predictions and could be understood in at least a semiquantitative manner. However, the time dependence of the anisotropy was not treated.

Recently, we developed a theoretical formalism to describe the time dependence of fluorescence or transient absorption following TPE.^(7,8) Spherical tensor formalism was employed to distinguish isotropic and anisotropic components of fluorescence or absorption induced by TPE. We have shown that in the most general case three isotropic and six anisotropic two-photon parameters can be measured by time-resolved TPE methods (see Table 2.1). Furthermore, the spherical tensor analysis lends itself to describing anisotropy decays for TPE. The utility of time-resolved anisotropic TPE is found in this additional information on reorientational dynamics. In this chapter, we consider in particular the case of TPE anisotropy decay by rotational diffusion. In the next section, we describe the

orientational distributions induced by TPE. Then in Section 2.3 we treat two-photon-induced anisotropy decay.

2.2. Orientational Distributions Induced by Two-Photon Excitation

2.2.1. Orientational Averages and Spherical Tensors

We consider first the signal expected from a single molecule excited either by one-photon excitation (OPE) or TPE. For OPE the fluorescence probability at time t depends on the orientation of the absorption transition dipole at time $t=0$ relative to the excitation polarization and on the orientation of the emission transition dipole at time t relative to the selected polarization of the detected fluorescence:

$$I_{\alpha\lambda}(t) = |\boldsymbol{\alpha} \cdot \boldsymbol{\mu}_a(0)|^2 |\boldsymbol{\lambda} \cdot \boldsymbol{\mu}_e(t)|^2 \quad (2.6)$$

where $\boldsymbol{\mu}_a$ is the absorption transition dipole, $\boldsymbol{\mu}_e$ is the emission transition dipole, $\boldsymbol{\alpha}$ is the polarization of the excitation light, and $\boldsymbol{\lambda}$ is the polarization of the fluorescence. Similarly, for TPE the fluorescence probability depends on the orientation of the principal axes of the two-photon tensor at $t=0$ and the orientation of the emission transition dipole at time t :

$$\delta_{\alpha\beta,\lambda}(t) = |\boldsymbol{\alpha} \cdot \mathbf{S}^{(f,o)}(0) \cdot \boldsymbol{\beta}|^2 |\boldsymbol{\lambda} \cdot \boldsymbol{\mu}_e(t)|^2 \quad (2.7)$$

for absorption of photons with polarizations $\boldsymbol{\alpha}$ and $\boldsymbol{\beta}$, and fluorescence with polarization $\boldsymbol{\lambda}$.

For OPE or TPE of a collection of randomly oriented molecules, the expressions in Eqs. (2.6) and (2.7) must be averaged over the initial isotropic distribution of orientations of the molecules in the system. (If the system is initially oriented to some degree, as in the case of a fluorescent probe in oriented membrane systems, then the orientational average in these expressions must be taken over the appropriate initial orientational distribution function.⁽²⁶⁾) In the case of OPE for excitation light propagating along Y and polarized along the Z axis, the intensities of light emitted in the X direction with polarizations along Z (I_{\parallel}) and along Y (I_{\perp}) are

$$I_{\parallel} = I_{ZZ} = \langle |\mathbf{Z} \cdot \boldsymbol{\mu}_a|^2 |\mathbf{Z} \cdot \boldsymbol{\mu}_e|^2 \rangle \quad (2.8a)$$

$$I_{\perp} = I_{ZY} = \langle |\mathbf{Z} \cdot \boldsymbol{\mu}_a|^2 |\mathbf{Y} \cdot \boldsymbol{\mu}_e|^2 \rangle \quad (2.8b)$$

where $\langle \dots \rangle$ represents the orientational average over all orientations of μ_a and μ_e . The orientational averages can be carried out in two ways. One approach is to write these expressions in terms of the direction cosines between the molecule-fixed and laboratory-fixed axes. The orientational averages of these direction cosines can then be evaluated. A second approach involves expressing the absorption and emission transition dipoles μ_a and μ_e (or their direct products $\mu_a\mu_a^*$ and $\mu_e\mu_e^*$) as spherical tensors, which transform under rotation in a particularly straightforward manner.⁽²⁷⁾

The same alternative approaches present themselves for evaluation of the orientational average in Eq. (2.7) for TPE. McClain employed the former approach, explicitly averaging the various relevant products of six direction cosines.^(18,19) Our approach has been to carry out the orientational averages in spherical tensor formalism.^(7,24) An advantage of this approach is that it very naturally yields the orientationally averaged TPE intensities as sums of isotropic (independent of orientation) and anisotropic (orientation dependent) contributions, whereas the averages over direction cosines mix these two components. The evolution in time of the isotropic components depends only on the populations of excited states, while the time evolution of the anisotropic components depends also on the reorientational dynamics of the system. Consequently, the results obtained by implementing the spherical-tensor apparatus can be readily applied to the evolution of TPE fluorescence intensities in reorienting systems which, as we show Section 2.3, can provide new information about the reorientational dynamics that is not available in OPE fluorescence depolarization measurements.

2.2.2. Spherical Tensors: A Primer

In this section we review the properties of spherical tensors and illustrate their use to obtain the well-known orientational distribution and anisotropy generated by OPE. The advantages of employing spherical tensors are several. They facilitate calculation of orientational averages, especially for higher-order processes (such as TPE); they afford a natural separation of isotropic and anisotropic components of the signal; and they are readily applied to describe the time evolution of the signal due to rotational diffusion. The use of spherical tensors to carry out orientational averages is not new, and has been applied to obtain orientational averages for OPE of fluorescence,^(28,29) Raman scattering⁽³⁰⁾ coherent Raman spectroscopy (CARS and CSRS)⁽³¹⁾ and time-resolved CARS and Raman spectroscopy.⁽³²⁾

A spherical tensor is expressed as $T_M^{(L)}$, where L labels the rank and M the component, with $-L \leq M \leq L$. The three spherical components of a vector (e.g., the transition moment μ) are given by

$$\mu_{-1}^{(1)} = \frac{\mu_x - i\mu_y}{\sqrt{2}}; \quad \mu_0^{(1)} = \mu_z; \quad \mu_1^{(1)} = -\frac{\mu_x + i\mu_y}{\sqrt{2}} \quad (2.9)$$

Similarly, a second-rank spherical tensor is related to the matrix elements of a 3×3 matrix (e.g., the two-photon tensor $\mathbf{S}^{(f,o)}$) by a unitary transformation

$$S_{ij} = \sum_{L=0}^2 \sum_{P=-L}^L U(ij, LP) S_P^{(L)} \quad (2.10)$$

where S_{ij} is the i,j th matrix element of the two-photon tensor $\mathbf{S}^{(f,o)}$, and $U(ij, LP)$ are the elements of a unitary transformation from Cartesian to spherical-tensor components.⁽³⁰⁾ While the vector μ has only three components, the tensor $\mathbf{S}^{(f,o)}$ has nine components, which reduce in the spherical frame to an $L=0$ (scalar) component, an $L=1$ irreducible tensor, and an $L=2$ irreducible tensor. In most applications, where the intermediate “virtual” state in the two-photon absorption process is nonresonant, the two-photon tensor is symmetric. In this case the $L=1$ component must vanish.

Once the absorption probability, either $|\mu_a|^2$ for OPE or $|\mathbf{S}^{(f,o)}|^2$ for TPE, is expressed in the molecule-fixed spherical frame, the rotation of axes from the molecular coordinate frame to the lab-fixed frame is readily expressed in terms of the Wigner rotation functions $D_{P,M}^{(L)}(\Omega)$:⁽²⁷⁾

$$S_{ij}(\Omega) = \sum_{L=0}^2 \sum_{M=-L}^L \sum_{P=-L}^L U(ij, LP) D_{P,M}^{(L)*}(\Omega) S_M^{(L)} \quad (2.11)$$

where i,j are now in the lab-fixed coordinate system. The molecular orientation relative to space-fixed axes, represented here by the Euler angles $\Omega = (\phi, \theta, \chi)$, conveniently appears here only in the Wigner function. Consequently, the orthogonality properties of the Wigner functions can be used to carry out the orientational averages.

As an illustration of the use of spherical tensors, we next find the orientational distribution and the isotropic and anisotropic components of the fluorescence signal induced by OPE. The anisotropic distribution of excited

states introduced into the sample by excitation with polarized light (OPE or TPE) can be expressed by a distribution function $f(\Omega, t)$ normalized so that

$$\frac{3}{8\pi^2} \int f(\Omega, t) d\Omega = 1 \quad (2.12)$$

The distribution of molecular orientations excited by OPE at $t=0$ can then be written

$$\begin{aligned} f_{\text{OPE}}(\Omega_0) &= \sum_{i,j} \alpha_i \alpha_j \mu_{a,i}(\Omega_0) \mu_{a,j}^*(\Omega_0) \\ &= \sum_{i,j} \alpha_i \alpha_j \sum_{L=0}^2 \sum_{M=-L}^L \sum_{P=-L}^L U(ij, LP) D_{P,M}^{(L)*}(\Omega_0) S_M^{(L)} \end{aligned} \quad (2.13)$$

where $S_M^{(L)}$ is the spherical-tensor form of the absorption probability $\mu_a \mu_a^*$ in molecular axes and $\Omega_0 = (\phi_0, \theta_0, \chi_0)$ specifies the orientation of molecular axes with respect to the lab-fixed axes at time $t=0$. This expression expands the distribution into isotropic ($L=0$) and anisotropic ($L=2$) components. (There is no $L=1$ component since the distribution possesses inversion symmetry.) The orientational average over this distribution will be invariant with respect to the choice of axis system. It is convenient to choose Z as the lab-fixed axis of excitation polarization and the molecular z axis along the absorption dipole. With this choice of axes, $U(ZZ, LP)$ is nonzero only for $P=0$, and $S_M^{(L)}$ is nonzero only for $M=0$. In this case, the isotropic component of the distribution is, from Eq. (2.13),

$$f_{\text{OPE}}^{(0)} = \frac{1}{3} \quad (2.14)$$

and the anisotropic ($L=2$) component is

$$f_{\text{OPE}}^{(2)}(\Omega_0) = \frac{2}{3} P_2(\cos \theta_0) = \cos^2 \theta_0 - \frac{1}{3} \quad (2.15)$$

where $P_2(z) = (3z^2 - 1)/2$ is the second-order Legendre polynomial. Together, Eqs. (2.14) and (2.15) constitute the $\cos^2 \theta_0$ distribution generated by one-photon excitation, where θ_0 is the angle between the lab-fixed Z axis and the absorption dipole at $t=0$.

The fluorescence signal following OPE can now be calculated. The emission matrix element for fluorescence polarized along lab-axis λ is

$$T_{\lambda\lambda}(\Omega_0) = \mu_{e\lambda}(\Omega_0)\mu_{e\lambda}^*(\Omega_0) = \sum_{L=0}^2 \sum_{M'=-L'}^{L'} \sum_{P'=-L'}^{L'} U(\lambda\lambda, L'P') D_{P', M'}^{*(L')}(\Omega_0) T_{M'6'}^{(L')} \quad (2.16)$$

where $T_{M'}^{(L')}$ is the spherical-tensor form of the emission probability. The fluorescence signal with polarization λ is

$$I_{Z\lambda} = \frac{3}{8\pi^2} \int f(\Omega_0) \mu_{e\lambda}(\Omega_0) \mu_{e\lambda}^*(\Omega_0) d\Omega_0 \quad (2.17)$$

By combining Eqs. (2.16) and (2.17), the orientational averages (Eq. 2.8) can now be carried out via the orthogonality properties of the Wigner functions⁽²⁷⁾ to give

$$I_{Z\lambda} = \sum_{L, L'} \sum_{M, M'} \sum_{P, P'} \left(\frac{1}{2L+1} \right) U(ZZ, LP) U(\lambda\lambda, L'P') S_M^{(L)} T_{M'}^{(L')} \delta_{L, L'} \delta_{P, -P'} \delta_{M, -M'} \quad (2.18)$$

This expression is readily evaluated to yield

$$I_{ZZ} = I_{\parallel} = S_0^{(0)} T_0^{(0)} + \frac{2}{5} S_0^{(2)} T_0^{(2)} = \frac{1}{3} + \frac{4}{15} P_2(\cos \theta) \quad (2.19a)$$

$$I_{ZX} = I_{\perp} = S_0^{(0)} T_0^{(0)} - \frac{1}{5} S_0^{(2)} T_0^{(2)} = \frac{1}{3} - \frac{2}{15} P_2(\cos \theta) \quad (2.19b)$$

where θ is the angle between the absorption and emission dipoles. The first term is the isotropic contribution and the second term is the anisotropic contribution to the fluorescence intensity. Equations (2.19) provide the well-known result^(28,33)

$$r = \frac{2}{5} P_2(\cos \theta) \quad (2.20)$$

A similar route can be followed to obtain the orientational averages for TPE.⁽⁷⁾ These orientational averages will be related to the orientational distribution functions generated by TPE.

2.2.3. Two-Photon Photoselection

As for OPE, the probability of TPE depends on the molecular orientation relative to the polarization of the excitation light in lab-fixed coordinates. As in the previous section, we first find the distribution of molecular orientations excited by TPE. Then the fluorescence probability can be averaged over this distribution. In the case of TPE, the initial distribution is proportional to the two-photon absorptivity and can be written in a form analogous to Eq. (2.13) as

$$f(\Omega_0) = \sum_{i,j,k,l} \alpha_i \beta_j \alpha_k^* \beta_l^* S_{ij}(\Omega_0) S_{kl}^*(\Omega_0) \quad (2.21)$$

where $S_{ij}(\Omega_0)$ is the i,j two-photon matrix element for molecules oriented at $\Omega_0 = (\phi_0, \theta_0, \chi_0)$ relative to lab-fixed coordinates, $\boldsymbol{\alpha}$ and $\boldsymbol{\beta}$ are the excitation polarization directions, and i, j, k, l denote the laboratory coordinates. The components $S_{ij}(\Omega_0)$ and $S_{kl}(\Omega_0)$ can be converted to the spherical coordinate system as in Eq. (2.11). Each contains both zero- and second-rank components ($L=0, 2$), and their product will therefore have components with rank $J=L+L, \dots, L-L$, or $J=0, 2$, and 4 . (Since inversion symmetry is preserved in TPE as in OPE, the orientational distribution contains only even J components.) Consequently, the orientational distribution function generated by TPE can be written as a sum of three terms:

$$f(\Omega, t) = f^{(0)}(\Omega, t) + f^{(2)}(\Omega, t) + f^{(4)}(\Omega, t) \quad (2.22)$$

Of these components, only the $J=0$ and $J=2$ portions can be detected by fluorescence, since the emission process is described by a tensor $T_M^{(L)}$ (Eq. 2.16), which has only $L=0$ and $L=2$ components. The zero-rank distribution function $f^{(0)}$ is isotropic. It is the second-rank component, $f^{(2)}(\Omega)$, that is responsible for the reorientational decay in TPE anisotropy decay measurements.

The initial distribution generated by TPE has been derived in Ref. 7 by transforming the two-photon tensors in Eq. (2.21) into spherical-tensor notation. The isotropic ($J=0$) component of the distribution is

$$f^{(0)}(\Omega_0) = \sum_{L=0}^2 a_L \delta^{(L)} \quad (2.23)$$

where

$$a_L = \sum_{i,j,k,l} \alpha_i \beta_j \alpha_k^* \beta_l^* B_{ijkl}^{(L)} \quad (2.24)$$

Table 2.2. Isotropic TPE Coefficients $B_{ijkl}^{(L)}$ and the Anisotropic TPE Coeffecients $B_{ijkl,i}^{(LL')}$

$ijkl, i$	$B_{ijkl}^{(L)}$			$B_{ijkl,i}^{(LL')}$						α	β	i
	0	1	2	2	20	11	12	21	22			
1111,1	$\frac{1}{3}$		$\frac{2}{15}$	$-\frac{2\sqrt{3}}{15}$	$-\frac{2\sqrt{3}}{15}$				$-\frac{4\sqrt{3}}{15\sqrt{7}}$	\uparrow	\uparrow	\uparrow
2222,1	$\frac{1}{3}$		$\frac{2}{15}$	$\frac{\sqrt{3}}{15}$	$\frac{\sqrt{3}}{15}$				$\frac{2\sqrt{3}}{15\sqrt{7}}$	\rightarrow	\rightarrow	\uparrow
1122,1	$\frac{1}{3}$		$-\frac{1}{15}$	$\frac{\sqrt{3}}{15}$	$-\frac{2\sqrt{3}}{15}$				$\frac{2\sqrt{3}}{15\sqrt{7}}$			
2211,1	$\frac{1}{3}$		$-\frac{1}{15}$	$-\frac{2\sqrt{3}}{15}$	$\frac{\sqrt{3}}{15}$				$\frac{2\sqrt{3}}{15\sqrt{7}}$			
2233,1	$\frac{1}{3}$		$-\frac{1}{15}$	$\frac{\sqrt{3}}{15}$	$\frac{\sqrt{3}}{15}$				$-\frac{4\sqrt{3}}{15\sqrt{7}}$			
2323,1		$\frac{1}{6}$	$\frac{1}{10}$			$\frac{1}{5}$			$\frac{\sqrt{3}}{5\sqrt{7}}$	\rightarrow	\odot	\uparrow

1212,1	$\frac{1}{6}$	$\frac{1}{10}$	$-\frac{1}{10}$	$-\frac{\sqrt{3}}{10}$	$-\frac{\sqrt{3}}{10}$	$-\frac{\sqrt{3}}{10\sqrt{7}}$	\uparrow	\rightarrow	\uparrow
2121,1	$\frac{1}{6}$	$\frac{1}{10}$	$-\frac{1}{10}$	$\frac{\sqrt{3}}{10}$	$\frac{\sqrt{3}}{10}$	$-\frac{\sqrt{3}}{10\sqrt{7}}$	\rightarrow	\uparrow	\uparrow
1221,1	$-\frac{1}{6}$	$\frac{1}{10}$	$\frac{1}{10}$	$-\frac{\sqrt{3}}{10}$	$\frac{\sqrt{3}}{10}$	$-\frac{\sqrt{3}}{10\sqrt{7}}$			
2112,1	$-\frac{1}{6}$	$\frac{1}{10}$	$\frac{1}{10}$	$\frac{\sqrt{3}}{10}$	$-\frac{\sqrt{3}}{10}$	$-\frac{\sqrt{3}}{10\sqrt{7}}$			
$\delta_{\text{cir}, \parallel}$		$\frac{1}{5}$				$-\frac{\sqrt{3}}{5\sqrt{7}}$	\circ	\circ	\uparrow
$\delta_{\text{cir}, \perp}$		$\frac{1}{5}$				$\frac{2\sqrt{3}}{5\sqrt{7}}$	\circ	\circ	\odot

and

$$\delta^{(L)} = \sum_{M=-L}^L |S_M^{(L)}|^2 \quad (2.25)$$

The polarization coefficients $B_{ijkl}^{(L)}$, which depend on the polarizations of the two excitation photons, are tabulated in Table 2.2. The isotropic two-photon absorptivities are given by $\delta^{(L)}$, which are defined in terms of the two-photon spherical tensors $S_M^{(L)}$, and can be related to the parameters δ_F , δ_G , and δ_H defined by McClain,⁽⁷⁾ as follows:

$$\begin{aligned} \delta_F &= 3\delta^{(0)} \\ \delta_G &= \delta^{(0)} + \delta^{(1)} + \delta^{(2)} \\ \delta_H &= \delta^{(0)} - \delta^{(1)} + \delta^{(2)} \end{aligned} \quad (2.26)$$

A useful parameter for discerning the symmetry of a two-photon absorbing state is the isotropic polarization ratio Ω , defined as the ratio of circular to linear *isotropic* two-photon parameters.⁽³⁴⁾ This ratio is

$$\Omega = \frac{\delta_{\text{cir}}}{\delta_{\text{lin}}} = \frac{3\delta^{(2)}}{5\delta^{(0)} + 2\delta^{(2)}} \quad (2.27)$$

and has a value $\Omega = 3/2$ for transitions to nontotally symmetric states and values of $\Omega \leq 3/2$ for transitions to totally symmetric states (given a totally symmetric ground state). Note that this ratio contains no anisotropic components. A “magic-angle” method of excluding orientational (anisotropic) contributions to Ω is given in Ref. 7.

The second-rank ($J = 2$) component is

$$f^{(2)}(\Omega_0) = \sum_{L,L'} \sum_{P_J} \sum_{M_J} H_{P_J}^{(LL')} \delta_{M_J}^{(LL')} D_{P_J,M_J}^{(2)}(\Omega_0) \quad (2.28)$$

where

$$H_{P_J}^{(LL')} = \sum_{i,j,k,l} \alpha_i \beta_j \alpha_k^* \beta_l^* h_{P_J}^{(LL')}(i,j,k,l) \quad (2.29)$$

$$h_{P_J}^{(LL')}(i,j,k,l) = \sum_{P=-L}^L \sum_{P'=-L'}^{L'} (-1)^{-P} C(LL'2; -PP'P_J) U(ij, LP) U^*(kl, L'P') \quad (2.30)$$

$$\delta_{M_J}^{(LL')} = \sum_{M,M'} (-1)^M C(LL'2; -MM'M_J) S_M^{(L)} S_{M'}^{(L')}{}^* \quad (2.31)$$

and $C(LL'J; -MM'M_J)$ are the Clebsch–Gordon coefficients. The parameters $\delta_{M_J}^{(LL')}$ are anisotropic two-photon absorptivities. A similar expression can be found for the fourth-rank component of the distribution, $f^{(4)}(\Omega)$.⁽⁸⁾ However, TPE fluorescence anisotropy measurements are insensitive to this component.

The orientational distributions obtained in this way can be used to find the fluorescence anisotropy generated by TPE. Before doing so, however, it is desirable to relate these distributions to experimentally measurable two-photon anisotropy parameters. In the next section, we describe how these parameters can be calculated.

2.2.4. Two-Photon Anisotropies

In order to find expressions for the initial ($t=0$) two-photon anisotropies, analogous to Eq. (2.20) for the one-photon anisotropy, we need an expression for the TPE fluorescence signal at $t=0$. This signal, which we denote by $\langle\delta\rangle$, is given by

$$\langle\delta\rangle = \sum_{i,j,k,l} \alpha_i \beta_j \alpha_k^* \beta_l^* \lambda \lambda \langle\delta\rangle_{ijkl,\lambda} \quad (2.32)$$

where λ labels the polarization of the fluorescence in lab-fixed axes,

$$\langle\delta\rangle_{ijkl,\lambda} = \langle S_{ij} S_{kl}^* \mu_{e\lambda} \mu_{e\lambda}^* \rangle \quad (2.33)$$

and $\langle\cdots\rangle$ represents the average over all orientations Ω_0 at $t=0$. This orientational average can be carried out by averaging the emission probability $\mu_{e\lambda} \mu_{e\lambda}^*$ over the orientational distribution obtained in the previous section; that is,

$$\langle\delta\rangle = \frac{3}{8\pi^2} \int f(\Omega_0) \mu_{e\lambda} \mu_{e\lambda}^* d\Omega_0 \quad (2.34)$$

After substituting for $f(\Omega_0)$ from Eq. (2.21) and $\mu_{e\lambda} \mu_{e\lambda}^*$ from Eq. (2.16), one carries out the orientational average by using the orthogonality properties of the Wigner functions. The result can be written⁽⁷⁾

$$\langle\delta\rangle_{ijkl,\lambda} = I_{ijkl} + A_{ijkl,\lambda} \quad (2.35)$$

where I_{ijkl} and $A_{ijkl,\lambda}$ are the isotropic and anisotropic parts of the signal. The isotropic two-photon absorptivity is

$$I_{ijkl} = \sum_{L=0}^2 B_{ijkl}^{(L)} \delta^{(L)} \quad (2.36)$$

in terms of the isotropic two-photon absorptivities $\delta^{(L)}$ defined in the previous section and the parameters $B_{ijkl}^{(L)}$, given in Table 2.2. The isotropic signal, which is orientation independent, does not depend on the polarization of the fluorescence signal.

The anisotropic TPE signal is

$$A_{ijkl,\lambda} = \sum_{L=0}^2 \sum_{L'=0}^2 B_{ijkl,\lambda}^{(LL')} \delta^{(LL')} \quad (2.37)$$

where

$$B_{ijkl,\lambda}^{(LL')} = \frac{3}{5} \sum_{P_J} h_{P_J}^{(LL')} (ijkl) U(\lambda\lambda, 2P_J) \quad (2.38)$$

where the parameters $h_{P_J}^{(LL')}$ were defined in Eq. (2.30), and

$$\delta^{(LL')} = \sum_{M_J} \delta_{M_J}^{(LL')} T_{M_J}^{(2)} \quad (2.39)$$

Again, the signal depends on the polarization of the incident beams. In addition, in this case they also depend on the polarization of the fluorescence via a polarization parameter $B_{ijkl,\lambda}^{(LL')}$ tabulated in Table 2.2. The second-rank two-photon absorptivity parameters $\delta^{(LL')}$ are given in Table 2.3, where $T_m^{(2)}$ are spherical tensors describing the orientation of the secondary transition dipole in the molecular frame.

The net result of this analysis has been to reduce the two-photon tensor in Eq. (2.3) into nine independent molecular parameters $\delta^{(L)}$ and $\delta^{(LL')}$, of which three are isotropic and six are anisotropic. The existence of nine independent parameters is not surprising, since the 3×3 two-photon tensor contains nine elements. However, if the two-photon intermediate state is not resonant, the number of independent parameters reduces to 7, since $\delta^{(02)} = \delta^{(20)}$ and $\delta^{(12)} = \delta^{(21)}$ because the two-photon tensor is real under these circumstances. If two photons of the same wavelength are absorbed from one laser beam (the usual experimental setup), the number of independent parameters is further reduced to

Table 2.3. Anisotropic Two-Photon Parameters $\delta^{(LL)^\alpha}$

$\delta^{(02)} = T_0^{(2)} S_0^{(0)} S_0^{(2)*} + T_1^{(2)} S_0^{(0)} S_1^{(2)*} + T_{-1}^{(2)} S_0^{(0)} S_{-1}^{(2)*} + T_2^{(2)} S_0^{(0)} S_2^{(2)*} + T_{-2}^{(2)} S_0^{(0)} S_{-2}^{(2)*}$
$\delta^{(20)} = T_0^{(2)} S_0^{(2)} S_0^{(0)*} - T_1^{(2)} S_{-1}^{(2)} S_0^{(0)*} - T_{-1}^{(2)} S_1^{(2)} S_0^{(0)*} + T_2^{(2)} S_{-2}^{(2)} S_0^{(0)*} + T_{-2}^{(2)} S_2^{(2)} S_0^{(0)*}$
$\delta^{(11)} = T_0^{(2)} \frac{1}{\sqrt{6}} (-S_{-1}^{(1)} S_{-1}^{(1)*} + 2S_0^{(1)} S_0^{(1)*} - S_1^{(1)} S_1^{(1)*}) + T_1^{(2)} \frac{1}{\sqrt{2}} (S_0^{(1)} S_1^{(1)*} - S_{-1}^{(1)} S_0^{(1)*}) + T_{-1}^{(2)} \frac{1}{\sqrt{2}} (S_0^{(1)} S_{-1}^{(1)*} - S_1^{(1)} S_0^{(1)*}) - T_2^{(2)} S_{-1}^{(1)} S_1^{(1)*} - T_{-2}^{(2)} S_1^{(1)} S_{-1}^{(1)*}$
$\delta^{(12)} = T_0^{(2)} \frac{1}{\sqrt{2}} (S_1^{(1)} S_1^{(2)*} - S_{-1}^{(1)} S_{-1}^{(2)*}) + T_1^{(2)} \left(-\frac{1}{\sqrt{6}} S_0^{(1)} S_1^{(2)*} - \frac{1}{\sqrt{2}} S_{-1}^{(1)} S_0^{(2)*} + \frac{1}{\sqrt{3}} S_1^{(1)} S_2^{(2)*} \right) + T_{-1}^{(2)} \left(\frac{1}{\sqrt{6}} S_0^{(1)} S_{-1}^{(2)*} + \frac{1}{\sqrt{2}} S_1^{(1)} S_0^{(2)*} - \frac{1}{\sqrt{3}} S_{-1}^{(1)} S_{-2}^{(2)*} \right) - T_2^{(2)} \left(\frac{\sqrt{2}}{\sqrt{3}} S_0^{(1)} S_2^{(2)*} + \frac{1}{\sqrt{3}} S_{-1}^{(1)} S_1^{(2)*} \right) + T_{-2}^{(2)} \left(\frac{\sqrt{2}}{\sqrt{3}} S_0^{(1)} S_{-2}^{(2)*} + \frac{1}{\sqrt{3}} S_1^{(1)} S_{-1}^{(2)*} \right)$
$\delta^{(21)} = T_0^{(2)} \frac{1}{\sqrt{2}} (S_1^{(2)} S_1^{(1)*} - S_{-1}^{(2)} S_{-1}^{(1)*}) + T_1^{(2)} \left(-\frac{1}{\sqrt{2}} S_0^{(2)} S_1^{(1)*} - \frac{1}{\sqrt{6}} S_{-1}^{(2)} S_0^{(1)*} + \frac{1}{\sqrt{3}} S_{-2}^{(2)} S_{-1}^{(1)*} \right) + T_{-1}^{(2)} \left(\frac{1}{\sqrt{2}} S_0^{(2)} S_{-1}^{(1)*} + \frac{1}{\sqrt{6}} S_1^{(2)} S_0^{(1)*} - \frac{1}{\sqrt{3}} S_2^{(2)} S_1^{(1)*} \right) + T_2^{(2)} \left(\frac{\sqrt{2}}{\sqrt{3}} S_{-2}^{(2)} S_0^{(1)*} + \frac{1}{\sqrt{3}} S_{-1}^{(2)} S_1^{(1)*} \right) - T_{-2}^{(2)} \left(\frac{\sqrt{2}}{\sqrt{3}} S_2^{(2)} S_0^{(1)*} + \frac{1}{\sqrt{3}} S_1^{(2)} S_{-1}^{(1)*} \right)$
$\delta^{(22)} = T_0^{(2)} \frac{1}{\sqrt{14}} (2S_2^{(2)} S_2^{(2)*} - S_1^{(2)} S_1^{(2)*}) - 2S_0^{(2)} S_0^{(2)*} - S_{-1}^{(2)} S_{-1}^{(2)*} + 2S_{-2}^{(2)} S_{-2}^{(2)*}) + T_1^{(2)} \frac{1}{\sqrt{14}} (-S_0^{(2)} S_1^{(2)*} + S_{-1}^{(2)} S_0^{(2)*} + \sqrt{6} S_{-2}^{(2)} S_{-1}^{(2)*} - \sqrt{6} S_1^{(2)} S_2^{(2)*}) + T_{-1}^{(2)} \frac{1}{\sqrt{14}} (-S_0^{(2)} S_{-1}^{(2)*} + S_1^{(2)} S_0^{(2)*} + \sqrt{6} S_2^{(2)} S_1^{(2)*} - \sqrt{6} S_{-1}^{(2)} S_{-2}^{(2)*}) + T_2^{(2)} \left(\frac{\sqrt{2}}{\sqrt{7}} S_0^{(2)} S_2^{(2)*} + \frac{\sqrt{2}}{\sqrt{7}} S_{-2}^{(2)} S_0^{(2)*} + \frac{\sqrt{3}}{\sqrt{7}} S_{-1}^{(2)} S_1^{(2)*} \right) + T_{-2}^{(2)} \left(\frac{\sqrt{2}}{\sqrt{7}} S_2^{(2)} S_0^{(2)*} + \frac{\sqrt{2}}{\sqrt{7}} S_0^{(2)} S_{-2}^{(2)*} + \frac{\sqrt{3}}{\sqrt{7}} S_1^{(2)} S_{-1}^{(2)*} \right)$

^a $T_0^{(2)} = (1/\sqrt{6})(3\mu_x^2 - 1)$, $T_{\pm 1}^{(2)} = (\mp\mu_x + i\mu_y)\mu_z$, $T_{\pm 2}^{(2)} = \frac{1}{2}(\mu_x \mp i\mu_y)^2$, where $\mu = (\mu_x, \mu_y, \mu_z)$ is the unit vector of the emission transition dipole. The parameters $S_M^{(r,t)}$ are the spherical-tensor components of the two-photon tensor $\mathbf{S}^{(r,t)}$.

4, corresponding to the fact that the two-photon tensor in this case is symmetric as well as real, and the isotropic parameter $\delta^{(1)}$ and the anisotropic parameters $\delta^{(11)}$, $\delta^{(12)}$, and $\delta^{(21)}$ vanish as a result. Even for the case of TPE in a single-color experiment, more experimental parameters can be determined (four) than in the conventional OPE fluorescence polarization experiment (two).

How can these independent parameters be measured? The experimental signal depends on the choices of polarization configurations in Eq. (2.35). A series of experiments with different polarization configurations will allow these parameters to be determined. As Table 2.2 shows, appropriate sums and differences of coefficients measured with different polarization configurations will yield purely isotropic or purely anisotropic two-photon parameters. These sums and differences can be conveniently expressed as anisotropies. Four such anisotropies can be defined for TPE:

$$r_1 = \frac{\delta_{1111,1} - \delta_{2222,1}}{\delta_{1111,1} + 2\delta_{2222,1}} \quad (2.40)$$

$$r_2 = \frac{\delta_{\text{cir},\parallel} - \delta_{\text{cir},\perp}}{\delta_{\text{cir},\perp} + 2\delta_{\text{cir},\parallel}} \quad (2.41)$$

$$r_3 = \frac{\delta_{1212,1} - \delta_{2121,1}}{\delta_{1212,1} + \delta_{2121,1} + \delta_{2323,1}} \quad (2.42)$$

$$r_4 = \frac{\delta_{1212,1} - \delta_{2323,1}}{\delta_{1212,1} + \delta_{2121,1} + \delta_{2323,1}} \quad (2.43)$$

where $\delta_{\text{cir},\parallel}$ and $\delta_{\text{cir},\perp}$ are the TPE signals generated with circularly polarized excitation for fluorescence polarized parallel and perpendicular, respectively, to the plane of circular polarization. The anisotropy r_1 is the analog of the one-photon anisotropy, while the anisotropies r_3 to r_4 have no one-photon analog. Although an anisotropy analogous to r_2 could be measured by OPE, no additional information would be generated. This is not the case with TPE.

Table 2.4 lists the values of the two-photon anisotropies r_1 and r_2 for some special cases. In many cases, r_1 and r_2 have distinct values, and measurement of both anisotropies can be used to determine symmetry properties of the molecule. For example, if the two-photon tensor is 2×2 (i.e., $S_{xx}, S_{yy}, S_{xy} \gg S_{zz}, S_{xz}$, and S_{yz}), as is typically the case for planar aromatic molecules, then measurement of r_1 and r_2 is sufficient to determine the orientation of the secondary transition dipole relative to the principal axes of the two-photon tensor. This was done for the retinyl chromophore in bacteriorhodopsin, where the transition dipole was calculated to be oriented 13° relative to a principal axis of the two-photon tensor.^(7,24) Thus, in contrast to OPE, additional information can be

Table 2.4. Two-Photon Anisotropies ($t=0$) for Some Special Cases

S	$\begin{pmatrix} 0 & . & . \\ . & 0 & . \\ . & . & s_{zz} \end{pmatrix}$	$\begin{pmatrix} s & . & . \\ . & s & . \\ . & . & 0 \end{pmatrix}$	$\begin{pmatrix} s & . & . \\ . & s & . \\ . & . & 0 \end{pmatrix}$	$\begin{pmatrix} s & . & . \\ . & s & . \\ . & . & s \end{pmatrix}$	$\begin{pmatrix} . & . & s \\ . & . & . \\ s & . & . \end{pmatrix}$	$\begin{pmatrix} . & . & s \\ . & . & . \\ s & . & . \end{pmatrix}$
μ	$\begin{pmatrix} \mu \sin \theta \cos \phi \\ \mu \sin \theta \sin \phi \\ \mu \cos \theta \end{pmatrix}$	$\begin{pmatrix} 0 \\ 0 \\ \mu \end{pmatrix}$	$\begin{pmatrix} \mu \\ 0 \\ 0 \end{pmatrix}$ or $\begin{pmatrix} 0 \\ \mu \\ 0 \end{pmatrix}$	$\begin{pmatrix} \mu_x \\ \mu_y \\ \mu_z \end{pmatrix}$	$\begin{pmatrix} 0 \\ \mu \\ 0 \end{pmatrix}$	$\begin{pmatrix} 0 \\ 0 \\ \mu \end{pmatrix}$ or $\begin{pmatrix} \mu \\ 0 \\ 0 \end{pmatrix}$
r_1	$\frac{2}{\gamma}(3 \cos^2 \theta - 1)$	$-\frac{2}{\gamma}$	$\frac{1}{\gamma}$	0	$-\frac{2}{\gamma}$	$\frac{1}{\gamma}$
r_2	$\frac{1}{\gamma}(3 \cos^2 \theta - 1)$	$\frac{2}{\gamma}$	$-\frac{1}{\gamma}$	0	$-\frac{2}{\gamma}$	$\frac{1}{\gamma}$

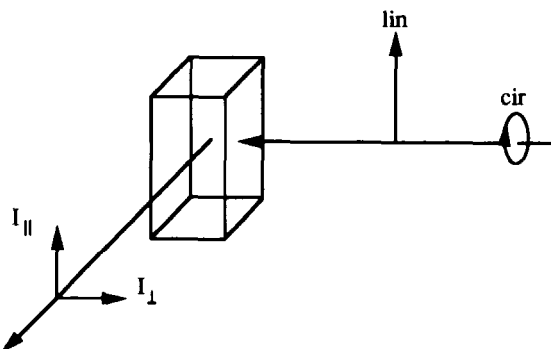


Figure 2.2. Experimental geometry for measurement of anisotropic two-photon-excited fluorescence decays. The linear anisotropy r_1 is measured with linearly polarized excitation and fluorescence polarization parallel (I_{\parallel}) or perpendicular (I_{\perp}) to the excitation. The circular anisotropy r_2 is measured with circularly polarized excitation and fluorescence polarized parallel or perpendicular to the plane of polarization of the excitation.

generated by measuring *both* r_1 and r_2 . Although the measurement of r_3 and r_4 requires two excitation beams with different wavelengths, the anisotropies r_1 and r_2 can be readily measured by TPE with a single pump laser as shown in Figure 2.2.

2.2.5. Two-Photon Anisotropic Distributions

To describe the anisotropy of the fluorescence induced by TPE, we need the distribution of orientations of the secondary transition dipole responsible for the fluorescence. The molecular coordinate system can be chosen such that this transition dipole is along the molecular z axis. Then the distribution of orientations of the secondary transition dipole is given by the distribution functions $f^{(0)}(\Omega_0)$ and $f^{(2)}(\Omega_0)$, which are functions of the three angles $\Omega_0 = (\phi_0, \theta_0, \chi_0)$, where ϕ_0 and θ_0 are the polar angles of the molecular z axis, and χ_0 is the azimuthal orientation about the transition dipole. Since rotation in this direction does not alter the orientation of the molecular transition dipole, the orientational distribution of the secondary transition dipole is obtained by integrating over χ_0 . The result for the $L=2$ distribution is

$$f^{(2)}(\phi, \theta) = \sqrt{\frac{4\pi}{5}} \sum_{L,L'} \sum_{P_J} \delta_0^{(LL')} H_{P_J}^{(LL')} Y_{2,-P_J}(\theta, \phi) \quad (2.44)$$

where $Y_{l,m}(\theta, \phi)$ are the spherical harmonics.

Equation (2.44) now provides a means to calculate the initial orientational distribution of emission transition dipoles generated for any two-photon tensor and for any polarization of the two incident beams. Figures 2.3–2.6 show distribution functions

$$f^{(0)}(\phi, \theta) + f^{(2)}(\phi, \theta) \quad (2.45)$$

generated for several forms of the two-photon tensor by both linear and circular TPE. Each figure represents the distribution of emission dipoles generated in the laboratory axis system by excitation light with either vertical polarization or

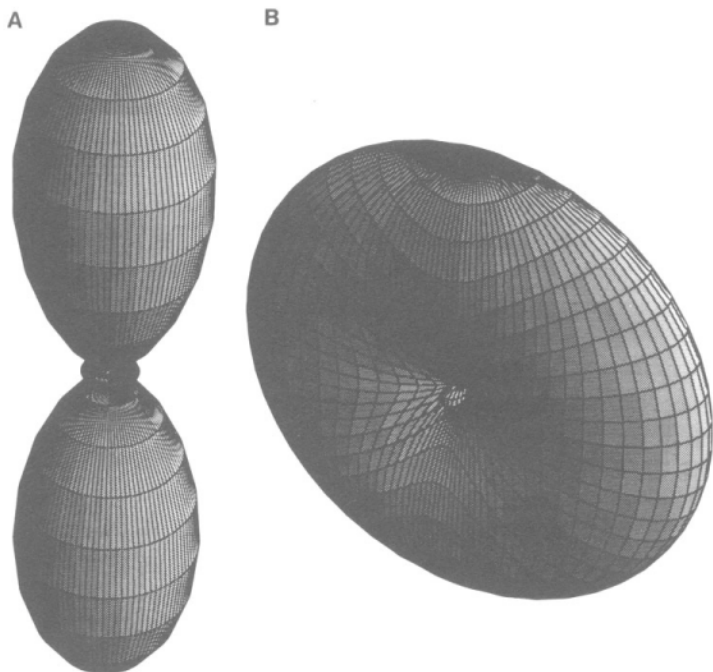


Figure 2.3. Anisotropic distribution (zero- and second-rank components) of emission transition dipoles generated by the two-photon tensor

$$\begin{pmatrix} 0 & & \\ & 0 & \\ & & s_{zz} \end{pmatrix}$$

with emission dipole along the z molecular axis for linearly polarized excitation (A) and circularly polarized excitation (B). The perspective in Figures 2.3–2.6 shows the distributions generated by excitation light propagating from the front left toward the back right.

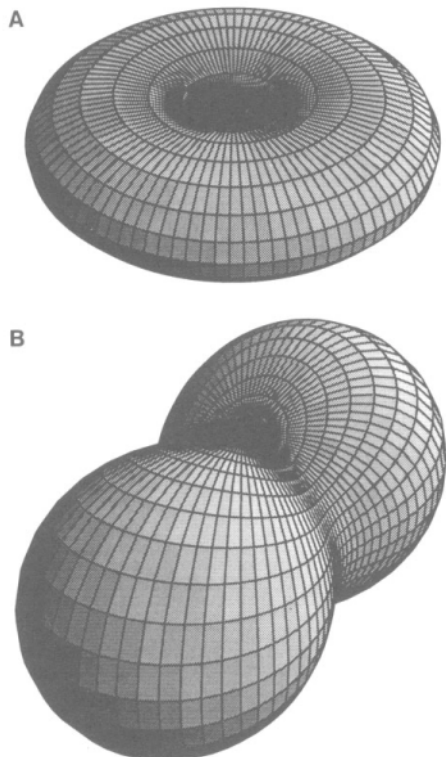


Figure 2.4. Anisotropic distribution (zero- and second-rank components) of emission transition dipoles generated by the two-photon tensor

$$\begin{pmatrix} 0 & & \\ & s_{yy} & \\ & & 0 \end{pmatrix} \quad \text{or} \quad \begin{pmatrix} s_{xx} & 0 & \\ & 0 & \\ & & 0 \end{pmatrix}$$

with emission dipole along the z molecular axis for linearly polarized excitation (A) and circularly polarized excitation (B).

circular polarization. The distribution function for linear TPE determines the linear two-photon anisotropy r_1 , while the distribution function for circular TPE determines the circular two-photon anisotropy r_2 .

Figures 2.3a and b show the two-photon anisotropic distributions for a two-photon tensor containing a single nonzero element, S_{zz} . (The molecular axis system is defined here so that the secondary transition dipole is along the molecular z axis.) Linear TPE in this case generates a $\cos^4 \theta$ distribution. The distribution is predominantly aligned along the laboratory Z axis, the polarization direction of the incident laser beam, giving rise to the large linear anisotropy $r_1 = 4/7$. This two-photon tensor form probably describes linear polyenes to a good approximation and explains the values of the linear anisotropy measured for diphenylhexatriene⁽²¹⁾ and bacteriorhodopsin,⁽²⁴⁾ which are nearly equal to 4/7. Although this distribution is sharper than the $\cos^2 \theta$ distribution generated by OPE, the two-photon anisotropy measurement sees only the projection of the $\cos^4 \theta$ component onto the $L = 2$ and $L = 0$ spherical harmonics. The reason that the TPE distribution in this case generates a higher anisotropy ($r_1 = 4/7$)

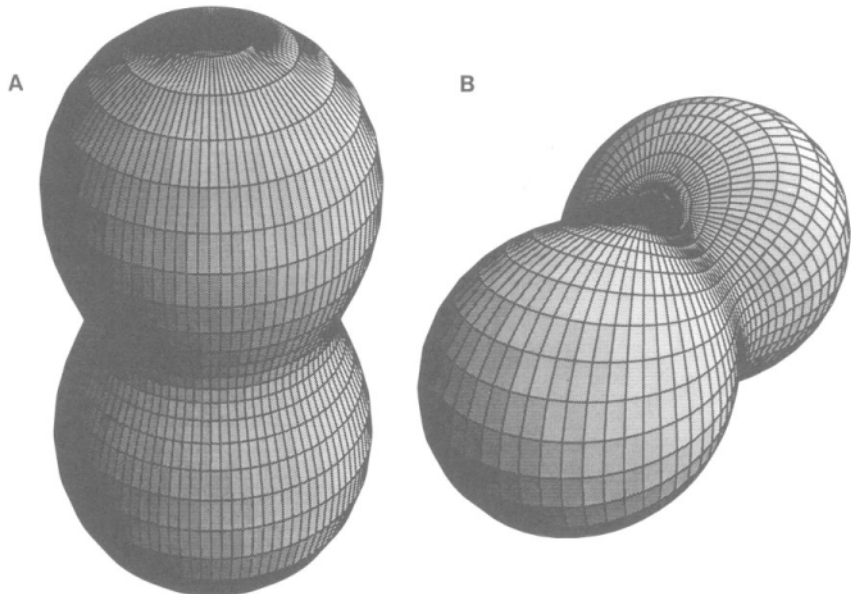


Figure 2.5. Anisotropic distribution (zero- and second-rank components) of emission transition dipoles generated by the two-photon tensor

$$\begin{pmatrix} 1/\sqrt{2} & & \\ & 0 & \\ & & 1/\sqrt{2} \end{pmatrix}$$

with emission dipole along the z molecular axis for linearly polarized excitation (A) and circularly polarized excitation (B).

than the corresponding distribution generated by OPE ($r = 2/5$) is the larger contribution from the $L = 2$ component $Y_{2,0}(\theta, \phi)$ relative to the isotropic component $Y_{0,0}$. Figure 2.3 shows the combined $L = 0$ and $L = 2$ components of that distribution. Excitation with circularly polarized light, on the other hand, generates the distribution in Figure 2.3b. The fluorescence anisotropy in this case is reduced to $r_2 = 2/7$.

Figures 2.4a and b show how the distribution is altered in the case where the two-photon tensor contains a single nonzero element, S_{yy} or S_{xx} , along a molecular axis perpendicular to the secondary transition dipole (z axis). The distribution generated by linear TPE complements the distribution in Figure 2.3a, extending in the X and Y directions rather than along Z , as expected given that the secondary transition dipole orientations are perpendicular to those in Figure 2.3a. The anisotropy in this case is $r_1 = -2/7$. The corresponding

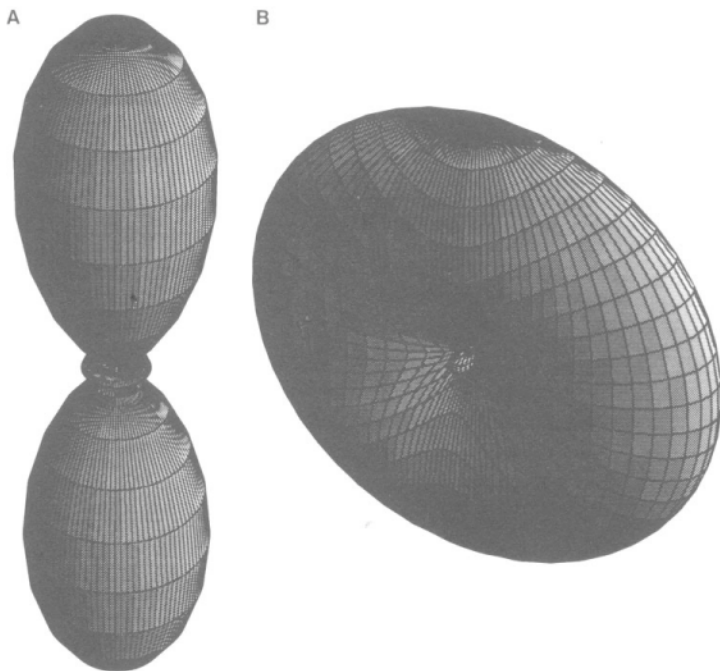


Figure 2.6. Anisotropic distribution (zero- and second-rank components) of emission transition dipoles generated by the two-photon tensor

$$\begin{pmatrix} -0.13 & & \\ & -0.13 & \\ & & 1 \end{pmatrix}$$

with emission dipole along the z molecular axis for linearly polarized excitation (A) and circularly polarized excitation (B).

distribution generated by circularly polarized excitation, shown in Figure 2.4b, consists of secondary transition dipoles perpendicular to those in Figure 2.3b and extended along the Y axis, yielding an anisotropy $r_2 = -1/7$.

For a two-photon tensor with more than one nonzero element, other distributions can be generated. The two-photon tensor

$$\begin{pmatrix} 1/\sqrt{2} & & \\ & 1/\sqrt{2} & \\ & & 0 \end{pmatrix}$$

(with secondary transition dipole again along the molecular z axis) gives rise to the same distribution as that shown in Figure 2.4a ($r_1 = -2/7$) for linear excita-

tion, and the same distribution as that shown in Figure 2.3b ($r_2 = 2/7$) for circular excitation. The two-photon tensor

$$\begin{pmatrix} 1/\sqrt{2} & & \\ & 0 & \\ & & 1/\sqrt{2} \end{pmatrix}$$

produces the distributions in Figure 2.5. Linear TPE generates an anisotropy of 1/7 corresponding to the distribution in Figure 2.5a, which is slightly elongated along the Z axis. Circular TPE generates the same distribution as in Figure 2.5b, elongated along the Y axis.

It is possible to generate anisotropies greater than 4/7.^(25,26) For example, the tensor

$$\begin{pmatrix} -0.13 & & \\ & -0.13 & \\ & & 1 \end{pmatrix}$$

yields anisotropies $r_1 = 30/49$ and $r_2 = 2/7$. The corresponding distributions, shown in Figure 2.6, strongly resemble those in Figure 2.3.

2.2.6. The Special Case of a 2 x 2 Tensor

For many of the molecules that are targets of TPE, the two-photon tensor can be considered to a good approximation to have nonzero elements in only two dimensions. Examples include planar aromatic molecules and many dye molecules, for which it is reasonable to assume that the two-photon tensor is dominated by transitions in the plane of the molecule. In this section, we examine this case in greater detail. We choose an axis system where x and y define the molecular plane. If we further stipulate that the emission dipole is oriented along the molecular x axis, then the initial values (before any reorientation occurs) of r_1 and r_2 and of the two-photon polarization ratio Ω can be expressed as⁽⁷⁾

$$r_1 = \frac{1}{7} \frac{2(S_{xx} + S_{yy})^2 + (S_{xx} - S_{yy})^2 + 4S_{ab}^2 + 9(S_{xx}^2 - S_{yy}^2)^2}{2(S_{xx} + S_{yy})^2 + (S_{xx} - S_{yy})^2 + 4S_{xy}^2} \quad (2.46)$$

$$r_2 = \frac{1}{7} \frac{3(S_{xx} + S_{yy})^2 - (S_{xx} + S_{yy})^2 + 12S_{xy}^2 + 6(S_{xx}^2 - S_{yy}^2)^2}{(S_{xx} + S_{yy})^2 + 3(S_{xx} - S_{yy})^2 + 12S_{xy}^2} \quad (2.47)$$

$$\Omega = \frac{1}{2} \frac{(S_{xx} + S_{yy})^2 + 3(S_{xx} - S_{yy})^2 + 12S_{xy}^2}{2(S_{xx} + S_{yy})^2 + (S_{xx} - S_{yy})^2 + 4S_{xy}^2} \quad (2.48)$$

for a symmetric 2×2 tensor. For highly symmetric molecules, such as perylene, with D_{2h} symmetry, the off-diagonal two-photon tensor elements are zero for transitions to A_g states (assuming a totally symmetric ground state).⁽¹⁶⁾ For these transitions, the element S_{xy} is zero in Eqs. (2.46–2.48).

The dependence of the parameters r_1 , r_2 , and Ω on the ratio of diagonal in-plane tensor elements $s = S_{yy}/S_{xx}$ is plotted in Figure 2.7 with $S_{xy} = 0$. These three parameters represent one set of independent measurements by one-color two-photon excitation. Experimentally determined values of these parameters can be used, for example, to determine the ratio s of two-photon tensor elements and the orientation of the emission dipole axis in the xy plane.⁽²⁴⁾ Examination of Figure 2.7 shows that values of the three parameters are sufficient to overdetermine the parameter s . (A fourth parameter, the overall scaling, could be determined by measurement of the absolute two-photon cross section.)

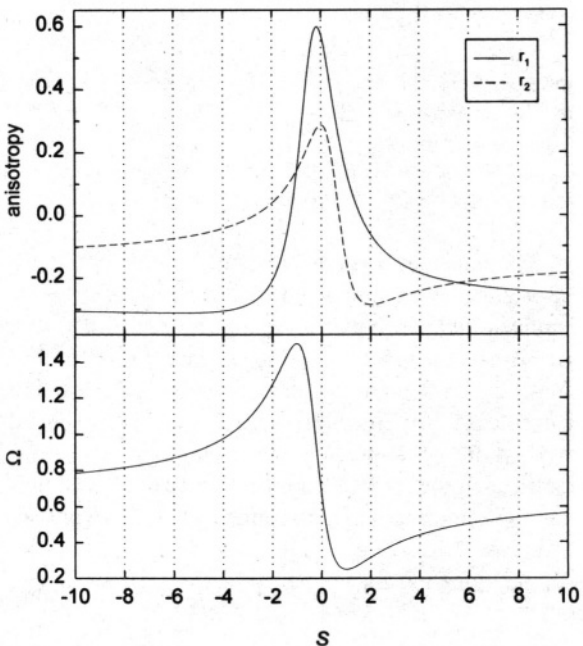


Figure 2.7. The anisotropies r_1 and r_2 and the polarization parameter Ω for the case of a two-dimensional two-photon tensor with nonzero elements S_{xx} and S_{yy} . This is the form of the two-photon tensor for totally symmetric states of planar aromatic molecules, for example. The top panel shows the dependence of the initial ($t = 0$) values of the anisotropies r_1 and r_2 for linearly and circularly polarized TPE, respectively, as a function of the ratio $s = S_{yy}/S_{xx}$ of tensor elements. The bottom panel shows the dependence of the two-photon polarization $\Omega = \delta_{\text{cir}}/\delta_{\text{lin}}$ on s . Measurements of r_1 , r_2 , and Ω uniquely determine the ratio s .

Several additional points are worth noting in Figure 2.7. First, the polarization ratio Ω ranges from a minimum of 0.25 to a maximum of 1.5. The value $\Omega = 1.5$ also results for transitions to nontotally symmetric states, for which the diagonal elements of the two-photon tensor are zero, and only off-diagonal elements contribute. Hence, as noted previously,⁽³⁴⁾ a value of $\Omega < 1.5$ is a signature of a transition to a totally symmetric state. The linear anisotropy r_1 has a value of 4/7 when the S_{xx} diagonal element dominates the two-photon transition (i.e., when $s = 0$). This value corresponds to a $\cos^4 \theta$ orientational distribution of emission dipoles.^(20,21) However, this is not the maximum value of r_1 . The maximum value (for a 2×2 tensor), $r_1 = 0.597$, occurs for $s = -0.172$. The presence of a small negative S_{yy} component in this case, in addition to the dominant S_{xx} element, creates an orientational distribution that is “sharper” than $\cos^4 \theta$, resulting in a higher initial anisotropy. When the S_{yy} diagonal element dominates ($s \rightarrow \infty$), the anisotropy r_1 takes the value $-2/7$. The minimum value of r_1 is -0.312 . The maximum and minimum values of r_2 are $\pm 2/7$, occurring at $s = 0$ and $s = 2$.

Figure 2.7 illustrates the benefit of anisotropic two-photon measurements. The isotropic polarization ratio Ω alone, even for the special case of a 2×2 tensor, is not sufficient to determine the relative values of the tensor elements. However, with measurements of r_1 and r_2 , the relative values of the two-photon tensor elements can be determined for a 2×2 tensor. However, it is important to note that the initial anisotropies, r_1 and r_2 , must be measured under conditions where molecular reorientation between absorption and emission is restricted. This can be done, for example, in a highly viscous solvent or a glass at low temperature. These values can then be used to interpret two-photon anisotropy decay experiments, which are discussed in Section 2.3.

2.3. Two-Photon Anisotropy Decay

2.3.1. Rotational Diffusion

In the previous section, we described the anisotropic orientational distribution and the corresponding TPE fluorescence signal generated by TPE. However, this description does not yet contain the dimension of time. In this section, the time dependence of the TPE signal is added by allowing molecules excited by TPE to reorient between excitation and the subsequent emission. Reorientations affect the anisotropic components of the orientational distribution, which consequently evolves in time. This evolution will be described by a time-dependent orientational distribution function $f(\Omega, t)$. Although a number of models could be considered for molecular rotations,^(35,36) we will treat the simplest realistic model, that of rotational diffusion. This model is valid in the regime where the molecular

collision time is short relative to the time scale probed by the experiment. In this regime, the reorientational dynamics can be described as a series of small stochastic steps, i.e., as diffusive motion.

The evolution of the orientational distribution function due to rotational diffusion is determined by the diffusion equation

$$\frac{\partial f(\Omega, t)}{\partial t} = - \sum_i R_i L_i^2 f(\Omega, t) \quad (2.49)$$

where L_i is the angular-momentum operator, and R_i is the rotational diffusion constant for rotation about molecular axis i in the principal axis system of the rotational diffusion tensor. The operator $-\sum_i R_i L_i^2$ is the rotational diffusion operator, which possesses eigenfunctions and eigenvalues satisfying the eigenvalue equation

$$-\sum_i R_i L_i^2 \Psi_n = E_n \Psi_n \quad (2.50)$$

The functions $\Psi_n(\Omega)$ are the asymmetric rotor eigenfunctions with eigenvalues E_n , where n stands for indices (L, l, m) which label the eigenfunction.

The solutions to Eq. (2.49) have been discussed by a number of authors^(37–43) and can be expanded in terms of the eigenfunctions of the diffusion operator. The result describes the time evolution of the orientational distribution by

$$f(\Omega, t) = \int f(\Omega_0) G(\Omega_0 | \Omega, t) d\Omega_0 \quad (2.51)$$

where $f(\Omega_0)$ is the orientational distribution at the initial time $t=0$. In this equation, the expression

$$G(\Omega_0 | \Omega t) = \sum_n \Psi_n(\Omega_0) \Psi_n(\Omega) e^{-E_n t} \quad (2.52)$$

gives the probability that a molecule with orientation Ω_0 at time $t=0$ will evolve to orientation Ω at time t .^(37–40) The integration in Eq. (2.51) serves to propagate the distribution function from $f(\Omega_0)$ to $f(\Omega)$ at time t .

For higher-order terms ($L > 2$) the asymmetric rotor eigenfunctions $\Psi_n(\Omega)$ cannot be expressed in closed form. However, for terms with $L \leq 2$ the asymmetric rotor eigenfunctions can be expanded in the Wigner functions $D_{m,n}^{(k)}$.⁽²⁷⁾

$$\Psi_{l,m}^{(L)}(\Omega) = \left(\frac{2L+1}{8\pi^2} \right)^{1/2} \sum_k A_{l,k}^{(L)} D_{m,k}^{(L)*}(\Omega) \quad (L \leq 2) \quad (2.53)$$

The coefficients $A_{\tau,M_j}^{(2)}$ have been tabulated in Refs. 38–41 and 43. For an anisotropic distribution of second rank ($L=2$), up to five distinct eigenvalues contribute, labeled by $m = -2, -1, 0, 1, 2$. Hence, decay of the orientational distribution induced by OPE can contain up to five exponential components. The same holds for the second-rank ($L=2$) components of the orientational distribution induced by TPE. The fourth-rank ($L=4$) components of the orientational distribution induced by TPE will exhibit even more complicated rotational diffusion decay. However, as shown in the previous section, these components cannot be detected by fluorescence since the emission process itself is described only by zero- and second-rank irreducible representations. Consequently, we need only concern ourselves with the $L=0$ and $L=2$ components.

2.3.2. Two-Photon-Induced Reorientational Decay

The next step in describing two-photon anisotropy decay is to find the orientational distribution function $f(\Omega, t)$ for two-photon anisotropic distributions. This can be accomplished by substituting the initial distribution (Eq. 2.21) into Eq. (2.51) to yield

$$f(\Omega, t) = \sum_n P_n \Psi_n(\Omega) \exp(-E_n t) \quad (2.54)$$

with

$$P_n = \sum_{i,j,k,l} \alpha_i \beta_j \alpha_k^* \beta_l^* \int S_{ij}(\Omega_0) S_{kl}^*(\Omega_0) \Psi_n^*(\Omega_0) d\Omega_0 \quad (2.55)$$

The coefficients P_n are determined by both the two-photon tensor and the polarizations of the excitation laser beams. The time dependence of the distribution function in the rotational diffusion regime is given by the exponentials $\exp(-E_n t)$.

The orientational average over this distribution function can be carried out following the approach outlined in Section 2.2.3. As expected, the zero-rank component, which is independent of orientation, is unchanged from $f(\Omega_0)$:

$$f^{(0)}(\Omega, t) = \sum_{L=0}^2 a_L \delta^{(L)} \quad (2.56)$$

where the parameters a_L and $\delta^{(L)}$ were defined in Eqs. (2.24) and (2.25). In contrast, the second-rank component evolves in time and is given by

$$f^{(2)}(\Omega, t) = \sum_{\tau=-2}^2 \sum_{L=0}^2 \sum_{L'=0}^2 \sum_{P''=-2}^2 \sum_{T=-2}^2 H_{P''}^{(LL')} \bar{\delta}_{\tau}^{(LL')} A_{\tau,T}^{(2)} D_{P'',T}^{(2)}(\Omega) \exp(-E_{\tau}^{(2)} t) \quad (2.57)$$

where the parameters $H_{P_J}^{(LL')}$ were defined previously (Eq. 2.29) and the anisotropic two-photon parameters $\bar{\delta}_{\tau}^{(LL')}$ are related to the parameters $\delta_{M_J}^{(LL')}$ defined in Eq. (2.31) by

$$\bar{\delta}_{\tau}^{(LL')} = \sum_{M_J} \delta_{M_J}^{(LL')} A_{\tau,M_J}^{(2)} \quad (2.58)$$

The expressions for the parameters $\bar{\delta}_{\tau}^{(LL')}$ are given by the parameters $\delta^{(LL')}$ in Table 2.3 simply by replacing the coefficients $T_{M_J}^{(2)}$ with the expansion coefficients $A_{\tau,M_J}^{(2)}$.

The TPE fluorescence signal as a function of time can now be obtained by averaging the emission probability over this distribution function:

$$\delta(t) = \langle \mathbf{S}_{fo}(0) \mathbf{S}_{fo}^*(0) \cdot \mu(t) \mu^*(t) \rangle K(t) = \frac{3}{8\pi^2} K(t) \int f(\Omega, t) \mu(\Omega) \mu^*(\Omega) d\Omega \quad (2.59)$$

The orientational average in Eq. (2.59) can be carried out in a manner that parallels the description in Section 2.2.4, yielding⁽⁸⁾

$$\delta(t) = K(t) \left(\sum_{L=0}^2 a_L \delta^{(L)} + \sum_{\tau=-2}^2 \sum_{L=0}^2 \sum_{L'=0}^2 b_{LL'} B_{\tau} \bar{\delta}_{\tau}^{(LL')} \exp(-E_{\tau}^{(2)} t) \right) \quad (2.60)$$

In Eq. (2.60), B_τ is a parameter describing the orientation of the secondary transition dipole and is given by

$$B_\tau = \sum_{m=-2}^2 A_{\tau,m}^{(2)} T_m^{(2)} \quad (2.61)$$

where $T_m^{(2)}$ are the spherical components of the emission transition dipole. The parameters a_L have already been defined (Eq. 2.24), and $b_{LL'}$ are given by the analogous expression

$$b_{LL'} = \sum_{i,j,k,l,\lambda} \alpha_i \beta_j \alpha_k^* \beta_l^* \lambda \lambda^* B_{ijkl,\lambda}^{(LL')} \quad (2.62)$$

in terms of the polarization coefficients $B_{ijkl,\lambda}^{(LL')}$ given in Table 2.2 (see Eq. 2.38). The parameters a_L and $b_{LL'}$ in Eq. (2.60) are polarization parameters for the isotropic and anisotropic decay, respectively, and can be varied by selecting the polarizations of the excitation pulses. This allows various superpositions of the anisotropic two-photon parameters $\delta_\tau^{(LL')}$ to be measured.

2.3.3. Time Dependence of the Two-Photon Anisotropies

Equation (2.60) is the key result of the preceding section, and describes the decay of the TPE fluorescence signal in systems undergoing rotational diffusion. The decay of the isotropic component of the signal is governed purely by $K(t)$, which describes the decay of the excited-state population. The anisotropic components, however, experience additional decay due to reorientational motion. In Eq. (2.60) this is described by the rotational diffusion eigenvalues $E_\tau^{(2)}$. Consequently, as in OPE anisotropy decay, up to five exponentials may contribute to TPE anisotropy decay. This number is reduced for certain symmetries. For example, two exponentials ($\tau=0,2$) will contribute if the principal axes of the two-photon tensor coincide with those of the diffusion tensor or if the emission transition dipole is along one of the principal axes of the diffusion tensor.

Since similar considerations hold for rotational diffusion detected by both OPE and TPE, the question might be asked: what then is the advantage of measuring anisotropy decay by TPE rather than OPE? To answer this question, it is necessary to examine the time dependence of the two-photon anisotropies. Here, we consider only the linear and circular two-photon anisotropies, r_1 and r_2 , which are relevant in the case of degenerate (one-color) TPE. By substitution of the time-dependent two-photon signal (Eq. 2.60) into the two-photon anisotropies

defined in the previous section (Eqs. 2.40 and 2.41), the following expressions are obtained:⁽⁸⁾

$$r_1(t) = \sum_{\tau=-2}^2 \frac{-\sqrt{3}B_\tau(\bar{\delta}_\tau^{(02)} + \bar{\delta}_\tau^{(20)} + 2\bar{\delta}_\tau^{(22)}/\sqrt{7})}{5\bar{\delta}_\tau^{(0)} + 2\bar{\delta}_\tau^{(2)}} e^{-E_\tau^{(2)}t} \quad (2.63)$$

$$r_2(t) = -\frac{\sqrt{3}}{\sqrt{7}} \sum_{\tau=-2}^2 \frac{B_\tau \bar{\delta}_\tau^{(22)}}{\bar{\delta}_\tau^{(2)}} e^{-E_\tau^{(2)}t} \quad (2.64)$$

(Similar expressions for the two-photon anisotropies r_3 and r_4 are given in Ref. 8. However, these anisotropies require two distinct excitation beams and are more difficult to measure.)

An important feature of Eqs. (2.63) and (2.64) is that the weight given each rotational decay eigenvalue depends on the anisotropic two-photon absorptivities $\bar{\delta}_\tau^{(02)}$, $\bar{\delta}_\tau^{(20)}$, and $\bar{\delta}_\tau^{(22)}$. The relative weights (or preexponential factors) of the rotational components for $\tau = 2, 1, 0, -1, -2$ will differ for r_1 and r_2 if $\bar{\delta}_\tau^{(02)} + \bar{\delta}_\tau^{(20)} \neq 0$. On the other hand, if $\bar{\delta}_\tau^{(02)} + \bar{\delta}_\tau^{(20)} = 0$, the weights of each component τ will be the same in r_1 and r_2 (to within a constant factor). If this is the case, the time dependence of the decays of $r_1(t)$ and $r_2(t)$ will be identical except for an overall difference in amplitude. Under such circumstances $r_1(t)$ and $r_2(t)$ contain the same information about rotational decays, and there is no advantage to measuring both anisotropies.

However, if $\bar{\delta}_\tau^{(02)} + \bar{\delta}_\tau^{(20)} \neq 0$, then the time dependence of $r_1(t)$ and $r_2(t)$ is different, and it should be possible to extract additional information about the rotational rates $E_\tau^{(2)}$ by independent measurement of $r_1(t)$ and $r_2(t)$. When can we expect to find $\bar{\delta}_\tau^{(02)} + \bar{\delta}_\tau^{(20)} \neq 0$? If we examine the coefficients $A_{\tau,M_J}^{(L)}$ and the anisotropic two-photon absorptivities $\bar{\delta}_\tau^{(02)}$, $\bar{\delta}_\tau^{(20)}$, and $\bar{\delta}_\tau^{(22)}$, the following rules can be formulated (for a real, symmetric two-photon tensor):

1. If $\text{Tr}(\mathbf{S}^{(\text{fo})}) = 0$ then $\bar{\delta}_\tau^{(20)} + \bar{\delta}_\tau^{(20)} = 0$,
2. If $\mathbf{S}^{(\text{fo})}$ is diagonal ($S_{ij}(i \neq j) = 0$), then $\bar{\delta}_\tau^{(02)} + \bar{\delta}_\tau^{(20)} = 0$ if $S_{xx} = S_{yy} = S_{zz}$,
3. If $\mathbf{S}^{(\text{fo})}$ is diagonal and the diagonal components S_{xx} , S_{yy} , S_{zz} , are not all equal, then $\bar{\delta}_\tau^{(02)} + \bar{\delta}_\tau^{(20)} \neq 0$ for $\tau = 0, 2$,
4. If $\mathbf{S}^{(\text{fo})}$ has nonzero elements in only two dimensions (e.g., S_{xx} , S_{yy} , and S_{xy}), then $\bar{\delta}_\tau^{(02)} + \bar{\delta}_\tau^{(20)} \neq 0$ for $\tau = 0, \pm 2$.

The consequence of these rules is that the decays of $r_1(t)$ and $r_2(t)$ will have different time dependencies if (1) the trace of the two-photon tensor is not zero and (2) the diagonal elements of the two-photon tensor are not all equal for a tensor containing no off-diagonal elements. The first requirement is met only for

the totally symmetric representation of the molecular point group.⁽¹⁶⁾ The second requirement is satisfied for the totally symmetric representations of all point groups except T , T_d , T_h , O , and O_h . Thus, in order to exploit the time dependencies of $r_1(t)$ and $r_2(t)$ to obtain additional information about rotations, we require a two-photon transition to a state that is totally symmetric overall (assuming the typical situation where the ground state is totally symmetric). This could be a totally symmetric electronic excited state or a totally symmetric vibronic state built on a non-totally-symmetric electronic state.

2.3.4. Example: Perylene

Perylene provides a useful test case for the concepts discussed. Since many studies of TPE over the past 25 years have focused on planar aromatic molecules, their two-photon spectroscopy is probably better understood than that of any other class of systems. Many investigations of rotational diffusion have also used planar aromatic probe molecules. Perylene is a particularly interesting example, since its rotational dynamics have been studied by a number of workers,^(2-5,44) and in several cases⁽²⁻⁵⁾ two exponentials were discerned in the rotational decay.

The TPE spectrum of perylene was measured by Yu *et al.*⁽⁴⁵⁾ The lowest excited electronic state is a B_{3u} state (1L_a) reached by a dipole-allowed one-photon transition polarized along the long axis (x axis) in the plane (xy) of the molecule. This state is dipole forbidden by TPE and appears only weakly with a false origin at $26,350\text{ cm}^{-1}$ in the TPE spectrum. A two-photon-allowed state (B_{1g}) appears at $28,950\text{ cm}^{-1}$, and a strong A_g state appears at $33,450\text{ cm}^{-1}$. The latter state fills the requirement of a totally symmetric state needed to observe distinct r_1 and r_2 anisotropy decays. The isotropic polarization ratio at 570 nm is $\Omega \approx 0.9$,⁽⁴⁵⁾ consistent with a totally symmetric state.

We have measured two-photon-polarized fluorescence decays for perylene in a series of n -alcohols excited with linearly and circularly polarized pulses at 570 nm.⁽⁴⁶⁾ Figures 2.8 and 2.9 show the TPE fluorescence decays of perylene in two alcohols, hexanol and undecanol. The decays of fluorescence polarized parallel and perpendicular to the excitation polarization (or, for circularly polarized excitation, the plane of polarization) were fit simultaneously with a single rotational time constant and a single fluorescence lifetime.⁽⁴⁷⁾ The results of this analysis are shown in Table 2.5. As the data in Table 2.5 show, for each solvent the rotational time constants are different with linear and circular excitation. This demonstrates that the rotational time constant determined by a single exponential fit must be an average of at least two fundamental rotational correlation times, and that *these rotational decay times are weighted differently in anisotropy decays generated by linear or circular TPE*, as predicted by the

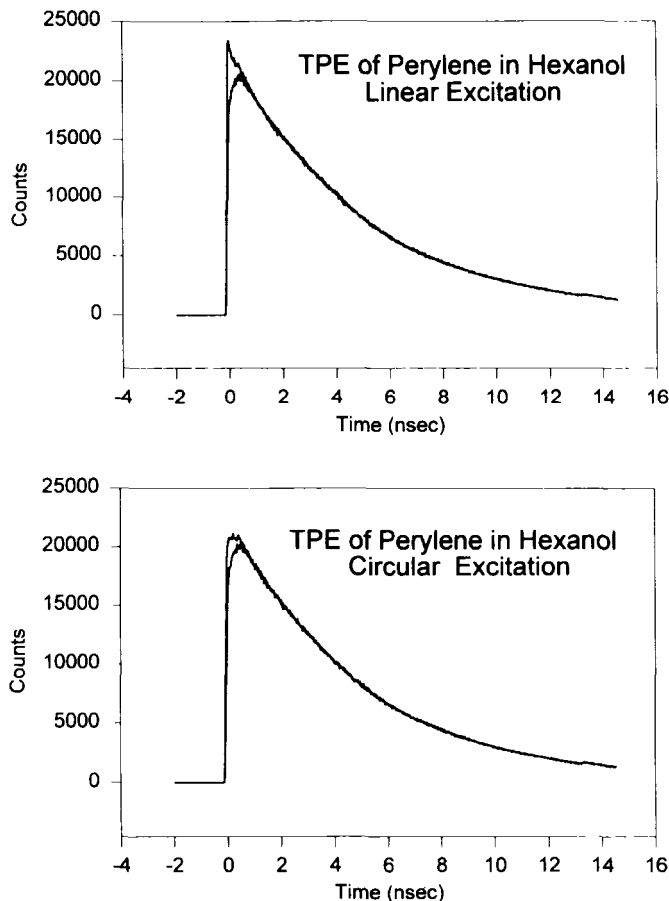


Figure 2.8. Two-photon-excited fluorescence decay of perylene in hexanol measured by time-correlated single-photon counting. The upper panel shows the decay excited with linearly polarized light (570 nm), and the lower panel shows the decay excited with circularly polarized light. In each panel, the upper curve is I_{\parallel} and the lower curve is I_{\perp} .

theory described in the preceding sections. Thus, even though the data are fit to a single rotational component, the difference between TPE anisotropy decays for linear and circular excitation indicates a more complex rotational relaxation. Note that a fit to OPE fluorescence data with a single rotational correlation time would not uncover the underlying contributions of more than one rotational component. Since in most applications, a single rotational component is all that is warranted by the data, one-photon measurements must inevitably gloss over the contributions from more than one rotational correlation time and rather

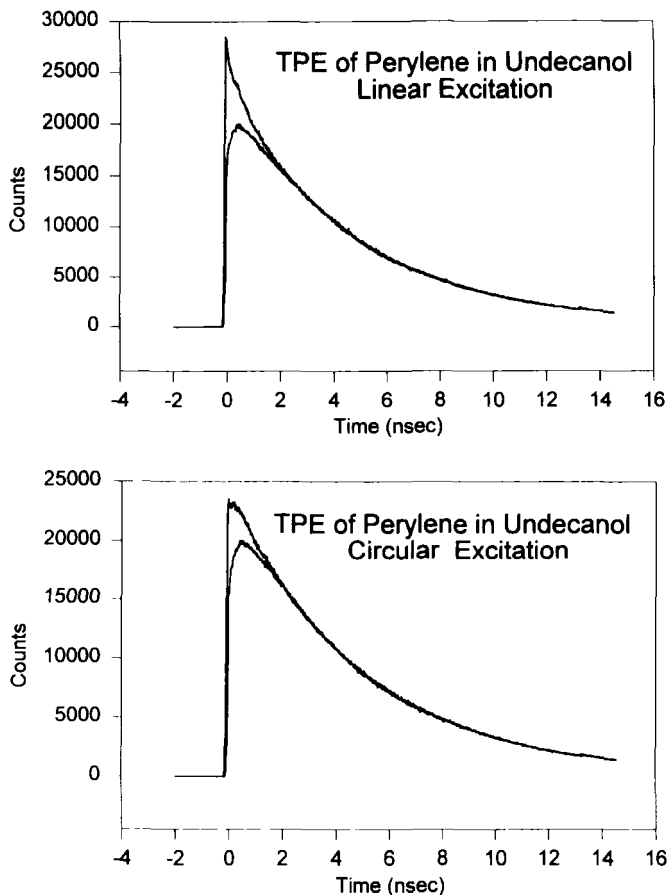


Figure 2.9. Two-photon-excited fluorescence decay of perylene in undecanol measured by time-correlated single-photon counting. The upper panel shows the decay excited with linearly polarized light (570 nm), and the lower panel shows the decay excited with circularly polarized light. In each panel, the upper curve is I_{\parallel} and the lower curve is I_{\perp} .

measure an average rotational time constant. The rotational time constants determined with linearly and circularly polarized pulses are plotted as a function of viscosity in Figure 2.10. The dependence on viscosity is linear in both cases but with different slopes, reflecting the different weights of the underlying rotational eigenvalues.

Further analysis based on the two-photon anisotropy decays $r_1(t)$ and $r_2(t)$ provides additional insight into the rotational decay of perylene. The linear and circular TPE decays for each solvent (i.e., the data sets $I_{\text{lin},\parallel}$, $I_{\text{lin},\perp}$, $I_{\text{cir},\parallel}$, $I_{\text{cir},\perp}$)

Table 2.5. Fitting Parameters for Two-Photon Anisotropy Decays of Perylene Excited at 570 nm

Solvent	Linear		Circular		Global	
	τ_{r1} (ps)	$r_1(0)$	τ_{r2} (ps)	$r_2(0)$	τ_1 (ps)	τ_2 (ps)
Hexanol	93	0.20	130	0.095	26	295
Octanol	202	0.20	285	0.095	43	304
Decanol	289	0.20	526	0.095	70	660
Undecanol	351	0.20	610	0.095	70	756

were fit simultaneously with two rotational correlation times, τ_1 and τ_2 . The resulting rotational correlation times, also shown in Table 2.5, differ by about a factor of 10 in each case. For the present we treat perylene as a symmetric rotor with diffusion constants $R_x = R_y = R_{\perp}$ and $R_z = R_{\parallel}$. The rotational eigenvalues are

$$E_0^{(2)} = 6R_{\perp}, \quad E_2^{(2)} = 4R_{\parallel} + 2R_{\perp} \quad (2.65)$$

Thus, if $R_{\parallel} > R_{\perp}$, the $\tau = 2$ rotational component is faster than the $\tau = 0$ decay since $E_2^{(2)} > E_0^{(2)}$. This model has been applied with $R_{\parallel} > R_{\perp}$ in several studies of OPE anisotropy decay in viscous solvents.⁽²⁻⁵⁾ Values of the ratio R_{\parallel}/R_{\perp} ranging

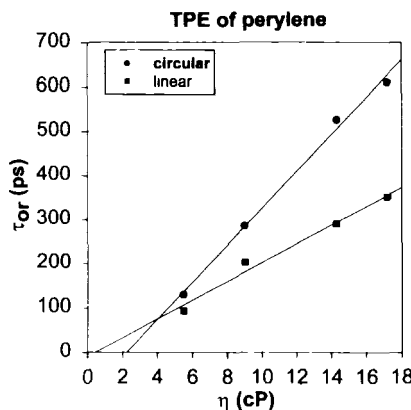


Figure 2.10. Plot of the rotational correlation times determined by TPE anisotropy decays of perylene in *n*-alcohols with linearly and circularly polarized excitation light at 570 nm, as a function of the solvent viscosity. For each solvent, the rotational correlation time was found to be longer with circularly polarized excitation than with linearly polarized excitation.

from 6.25 to 22 for different solvents were derived from the observed biexponential decays. These values correspond to ratios of rotational correlation times $E_2^{(2)}/E_0^{(2)}$ ranging from 5 to 15. Hence, the ratio of about 10 determined from the TPE data is consistent with previous results.

In addition to the measurements in Table 2.5, the anisotropy values $r_1(0)$ and $r_2(0)$ were also measured for perylene in propylene glycol at -5°C . The results were $r_1(0)=0.31$ and $r_2(0)=0.17$. These values can be compared with the values of $r_1(0)$ and $r_2(0)$ obtained from the fits in Table 2.5. The initial anisotropy values determined from the fits are somewhat lower than the values measured in propylene glycol. Similar discrepancies often arise with one-photon excitation as well, where the initial anisotropies determined from fits are frequently lower than the values measured in highly viscous or glassy matrices. This is true of OPE of perylene, for example, even with excitation in the visible, where the absorption and emission dipoles are expected to be parallel.^(4,5) This phenomenon is not presently adequately understood. There are several possible explanations. First, there may be fast components of anisotropy decay due, for example, to librational motion, which would result in an anisotropy decay that is unresolved in the present measurements. A second possibility is solvent-induced state mixing, which could alter the predicted principal axes of the two-photon tensor or the direction of the emission dipole. Both static and dynamic solvent effects could affect the anisotropy. Third, more than one two-photon transition may contribute to the TPE signal. For example, a two-photon transition to a vibronic level of a lower-lying excited state or a vibronic coupling contribution to the two-photon intensity could lead to a superposition of anisotropic distributions generated by transitions with different tensor patterns. The resulting signal would mix emission from more than one anisotropic distribution, resulting in a measured anisotropy averaged over the contributing distributions. The measured value of the polarization parameter Ω would also be an average over more than one two-photon transition, with the result that the initial anisotropies predicted for a pure transition would not be accurate. These considerations suggest that quantitative agreement of zero-time anisotropies with predicted values may not occur except under special circumstances (e.g., when the molecular transition moments and tensor elements are essentially one dimensional as in linear polyenes). Quantum chemical calculations of the two-photon tensor would be tremendously helpful in interpreting the observed anisotropies.

We consider further here the possibility of overlapping two-photon transitions. The TPE spectrum⁽⁴⁵⁾ displays several B_{1g} transitions, including one around $32,000\text{ cm}^{-1}$. Consequently, it might be expected that the measured two-photon parameters, $r_1(0)$, $r_2(0)$, and Ω , are averages of values from overlapping A_g and B_{1g} transitions. The two-photon tensor for planar aromatic molecules can be considered to a good approximation to be two dimensional

and dominated by $\pi\pi^*$ transitions. The two-photon tensors associated with the A_g and B_{1g} transitions have the form⁽¹⁶⁾

$$S_{A_g} = \begin{bmatrix} S_{xx} & 0 & 0 \\ 0 & S_{yy} & 0 \\ 0 & 0 & 0 \end{bmatrix}, \quad S_{B_{1g}} = \begin{bmatrix} 0 & S_{xy} & 0 \\ S_{yx} & 0 & 0 \\ 0 & 0 & 0 \end{bmatrix} \quad (2.66)$$

The B_{1g} component contributes $\Omega = 1.5$ and $r_1 = r_2 = 1/7$.⁽⁷⁾ For a 2×2 tensor, the contributions of the A_g transition to $r_1(0)$, $r_2(0)$, and Ω are all determined by a single parameter, the ratio S_{xx}/S_{yy} .⁽¹⁷⁾ Hence, if we assume that A_g and B_{1g} transitions overlap, the parameters $r_1(0)$, $r_2(0)$, and Ω can be used to determine two other parameters: the fractional contribution f of the B_{1g} transition and the ratio S_{xx}/S_{yy} for the A_g transition. The result is $f = 0.43$ and $S_{xx}/S_{yy} = 2.9$ ($s = 0.34$ in Figure 2.7).⁽⁴⁶⁾ The fact that these two parameters consistently predict the measured values $r_1(0)$, $r_2(0)$, and Ω lends support to the validity of this analysis. From the ratio S_{xx}/S_{yy} , the contributions of the A_g transition are found to be

$$r_{1(A_g)}(0) = 0.42, \quad r_{2(A_g)}(0) = 0.22, \quad \Omega_{A_g} = 0.38$$

In summary, the model treating perylene as a symmetric top is consistent with our results. Different anisotropy decays following linearly and circularly polarized TPE reflect the underlying decay components, which differ by a factor of 10. The results illustrate the added information contained in the two-photon anisotropy decays $r_1(t)$ and $r_2(t)$. The experimental anisotropy decay times can also be compared with predictions for the weights of the decay components $E_2^{(2)}$ and $E_0^{(2)}$ with linearly and circularly polarized TPE. Because these weights depend on the diffusion coefficients for different molecular axes, they provide information about the actual nature of the molecular rotational motions.⁽⁴⁶⁾

2.4. Conclusion

Subsequent to the report of experimentally measured two-photon anisotropies,⁽²⁰⁻²⁴⁾ several theoretical descriptions appeared^(7,8,25,26) that were built on the work of McClain.^(18,19) These descriptions have provided a basis for understanding two-photon photoselection. The approach taken in our work^(7,8) allows the expressions describing the TPE fluorescence signal to be separated into isotropic and anisotropic components. This in turn has permitted a description of the time dependence of the anisotropic signal due to rotational diffusion.

Anisotropy decays measured for perylene with linearly and circularly polarized TPE confirm that the time dependence of the anisotropy decays is different, as predicted for transitions to a totally symmetric final state. Because the fundamental rotational diffusion times (the inverses of the rotational diffusion eigenvalues $E_2^{(2)}$ and $E_0^{(2)}$) are independent of the mode of excitation, the differences in time dependence of the anisotropy decays is a consequence of the different weights of the underlying decay components. Global fits to the linear and circular anisotropy decays can then be used to determine the decay components. We expect that future TPE experiments will use this approach to add greater precision and depth to our understanding of the rotational relaxation of molecules in solution.

Acknowledgments

The authors wish to acknowledge helpful discussions with Professors J. R. Lakowicz and Pat Callis. We are grateful to Professors Graham Fleming and Jake Petrich for sharing their computer programs for fitting fluorescence decays. The measurements of TPE fluorescence depolarization were carried out by Professor J. Hedstrom and Steve Pauls. We thank David Skinner and Steve Pauls for their assistance in plotting orientational distributions. This work was supported by NSF under EPSCoR Grant No. OSR-9255223 and by the University of Kansas General Research Fund.

References

1. R. F. Steiner, Fluorescence anisotropy: Theory and applications, in: *Topics in Fluorescence Spectroscopy*, Vol. 2 (J. R. Lakowicz, ed.), pp. 1–52, Plenum, New York (1991).
2. D. W. Piston, T. Bilash, and E. Gratton, Compartmental analysis approach to fluorescence anisotropy: perylene in viscous solvents, *J. Phys. Chem.* 93, 3963–3967 (1989).
3. R. L. Christensen, R. C. Drake, and D. Phillips, Time-resolved fluorescence anisotropy of perylene, *J. Phys. Chem.* 90, 5960–5967 (1986).
4. B. Brocklehurst and R. N. Young, Rotation of perylene in alkanes: nonhydrodynamic behavior, *J. Phys. Chem.* 99, 40–43 (1995).
5. J. R. Lakowicz, H. Cherek, B. P. Maliwal, and E. Gratton, Time-resolved fluorescence anisotropies of diphenylhexatriene and perylene in solvents and lipid bilayers obtained from multifrequency phase-modulation fluorometry, *Biochemistry* 24, 376–383 (1985).
6. M. J. Wirth and S.-H. Chou, Behavior of the rotational diffusion tensor of tetracene under subslip conditions, *J. Phys. Chem.* 95, 1786–1789 (1991).
7. C. Z. Wan and C. K. Johnson, Time-resolved anisotropic two-photon spectroscopy, *Chem. Phys.* 179, 513–531 (1994).
8. C. Z. Wan and C. K. Johnson, Time-resolved two-photon induced anisotropy decay: the rotational diffusion regime, *J. Chem. Phys.* 101, 10283–10291 (1994).

9. M. Goeppert-Mayer, Über Elementarakte mit zwei Quantensprüngen, *Ann. Phys.* **9**, 273–294 (1931).
10. W. Kaiser and C. Garrett, Two-photon excitation in $\text{CaF}_2:\text{Eu}^{2+}$, *Phys. Rev. Lett.* **7**, 229–231 (1961).
11. W. L. Peticolas, Multiphoton spectroscopy, *Annu. Rev. Phys. Chem.* **18**, 233–260 (1967).
12. W. M. McClain, Two-photon molecular spectroscopy, *Acc. Chem. Res.* **7**, 129–135 (1974).
13. R. R. Birge, J. A. Bennett, L. M. Hubbard, H. L. Fang, B. M. Pierce, D. S. Klier, and G. E. Leroi, Two-photon spectroscopy of *all-trans*-retinal. Nature of the low-lying singlet states, *J. Am. Chem. Soc.* **104**, 2519–2525 (1982).
14. A. A. Rehms and P. R. Callis, Resolution of L_a and L_b bands in methyl indoles by two-photon spectroscopy, *Chem. Phys. Lett.* **140**, 83–89 (1987).
15. R. R. Birge and C.-F. Zhang, Two-photon double resonance spectroscopy of bacteriorhodopsin. Assignment of the electronic and dipolar properties of the low-lying ${}^1A_g^{*-}$ -like and ${}^1B_u^{*+}$ -like π , π^* states, *J. Chem. Phys.* **92**, 7178–7195 (1990).
16. W. M. McClain, Excited state symmetry assignment through polarized two-photon absorption studies of fluids, *J. Chem. Phys.* **55**, 2789–2796 (1971).
17. P. R. Monson and W. M. McClain, Polarization dependence of the two-photon absorption of tumbling molecules with application to liquid 1-chloronaphthalene and benzene, *J. Chem. Phys.* **53**, 29–37 (1970).
18. W. M. McClain, Polarization dependence of three-photon phenomena for randomly oriented molecules, *J. Chem. Phys.* **57**, 2264–2272 (1972).
19. W. M. McClain, Polarization of two-photon excited fluorescence, *J. Chem. Phys.* **58**, 324–326 (1973).
20. J. R. Lakowicz, I. Gryczynski, Z. Gryczynski, E. Danielsen, and M. J. Wirth, Time-resolved fluorescence intensity and anisotropy decays of 2,5-diphenyloxazole by two-photon excitation and frequency-domain fluorometry, *J. Phys. Chem.* **96**, 3000–3006 (1992).
21. J. R. Lakowicz, I. Gryczynski, and E. Danielsen, Anomalous differential polarized phase angles for two-photon excitation with isotropic depolarizing rotations, *Chem. Phys. Lett.* **191**, 47–53 (1992).
22. J. R. Lakowicz, I. Gryczynski, E. Danielsen, and J. Firsoli, Anisotropy spectra of indole and *N*-acetyl-L-tryptophanamide observed for two-photon excitation of fluorescence, *Chem. Phys. Lett.* **194**, 282–287 (1992).
23. J. R. Lakowicz and I. Gryczynski, Tryptophan fluorescence intensity and anisotropy decays of human serum albumin resulting from one-photon and two-photon excitation, *Biophys. Chem.* **47**, 1–6 (1993).
24. C. Z. Wan, Q. Song, and C. K. Johnson, Two-photon-induced anisotropic transient absorption in bacteriorhodopsin, *Chem. Phys. Lett.* **210**, 94–100 (1993).
25. P. R. Callis, On the theory of two-photon induced fluorescence anisotropy with application to indoles, *J. Chem. Phys.* **99**, 27–37 (1993).
26. S.-Y. Chen and B. W. Van Der Meer, Theory of two-photon induced fluorescence anisotropy decay in membranes, *Biophys. J.* **64**, 1567–1575 (1993).
27. R. N. Zare, *Angular Momentum. Understanding Spatial Aspects in Chemistry and Physics*, Wiley, New York (1988).
28. D. Wallach, Effect of internal rotation on angular correlation functions, *J. Chem. Phys.* **47**, 5258–5268 (1967).
29. A. Szabo, Theory of polarized fluorescent emission in uniaxial liquid crystals, *J. Chem. Phys.* **72**, 4620–4626 (1980).

30. S. Mortensen and S. Hassing, Polarization and interference phenomena in resonance Raman scattering, in: *Advances in Infrared and Raman Spectroscopy, Vol. 4*, (R. J. H. Clark and R. E. Hester, eds.), pp. 1–60, Heyden, London (1988).
31. B. Dick, Response function theory of time-resolved CARS and CSRS of rotating molecules in liquids under general polarization conditions, *Chem. Phys.* 113, 131–147 (1987).
32. C. Z. Wan and C. K. Johnson, Time-resolved anisotropic coherent anti-Stokes Raman scattering: a new probe of reorientational dynamics, *J. Chem. Phys.* 99, 7602–7613 (1993); C. Z. Wan, Time-resolved resonance Raman anisotropy. Rotational motion studied by Raman spectroscopy, *Chem. Phys. Lett.* 208, 119–124 (1993).
33. R. G. Gordon, Molecular collisions and the depolarization of fluorescence in gases, *J. Chem. Phys.* 45, 1643–1655 (1966).
34. R. P. Drucker and W. M. McClain, Polarized two-photon studies of biphenyl and several derivatives, *J. Chem. Phys.* 61, 2609–2619 (1974).
35. B. J. Berne and R. Pecora, *Dynamic Light Scattering*, Wiley, New York (1976), Chapter 7.
36. J. L. Dote, D. Kivelson, and R. N. Schwartz, A molecular quasi-hydrodynamic free-space model for molecular rotational relaxation in liquids, *J. Phys. Chem.* 85, 2169–2180 (1981).
37. L. D. Favro, Theory of the rotational Brownian motion of a free rigid body, *Phys. Rev.* 119, 53–62 (1960).
38. W. T. Huntress, Effects of anisotropic molecular rotational diffusion on nuclear magnetic relaxation in liquids, *J. Chem. Phys.* 48, 3524–3533 (1968).
39. T. Tao, Time-dependent fluorescence depolarization and Brownian rotational diffusion coefficients of macromolecules, *Biopolymers* 8, 609–632 (1969).
40. T. J. Chuang and K. B. Eisenthal, Theory of fluorescence depolarization by anisotropic rotational diffusion, *J. Chem. Phys.* 57, 5094–5097 (1972).
41. M. Ehrenberg and R. Rigler, Polarized fluorescence and rotational Brownian motion, *Chem. Phys. Lett.* 14, 539–544 (1972).
42. G. G. Belford, R. L. Belford, and G. Weber, Dynamics of fluorescence polarization in macromolecules, *Proc. Natl. Acad. Sci. U.S.A.* 69, 1392–1393 (1972).
43. A. J. Cross, D. H. Waldeck, and G. R. Fleming, Time resolved polarization spectroscopy: level kinetics and rotational diffusion, *J. Chem. Phys.* 78, 6455–6467 (1983).
44. Y. Jiang and G. J. Blanchard, Rotational diffusion dynamics of perylene in *n*-alkanes. Observation of a solvent length-dependent change of boundary condition, *J. Phys. Chem.* 98, 6436–6440 (1994).
45. J.-A. Yu, D. G. Nocera, and G. E. Leroi, Two-photon excitation spectrum of perylene in solution, *Chem. Phys. Lett.* 167, 85–89 (1990).
46. S. W. Pauls, J. F. Hedstrom, and C. K. Johnson, unpublished data.
47. A. J. Cross and G. R. Fleming, Analysis of time-resolved fluorescence anisotropy decays, *Bioophys. J.* 46, 45–56 (1984).

This page intentionally left blank.

Multiphoton Excitation of Biochemical Fluorophores

Joseph R. Lakowicz and Ignacy Gryczynski

3.1. Introduction

Pulsed lasers are used in many laboratories as an excitation source for time-resolved fluorescence spectroscopy. Although these laser sources are most often used for one-photon excitation (1PE), the high peak power of picosecond and femtosecond laser pulses can result in two-photon excitation (2PE), wherein the fluorophore simultaneously absorbs two long-wavelength photons to yield the first excited singlet state. Two-photon absorbance or excitation requires high peak powers to increase the probability that two photons are simultaneously available for absorption. Because of the interaction of two photons with the fluorophore, the selection rules for light absorption are, in principle, different from those for one-photon spectroscopy. Hence, two-photon spectroscopy was initially used as a tool to study the excited-state symmetry of organic chromophores or to identify additional energy levels.⁽¹⁻³⁾ Two-photon spectroscopy has been applied to a wide range of chromophores, including the study of excited states of aromatic hydrocarbons,^(4,5) porphyrins,⁽⁶⁾ and polyenes.^(7,8) Two-photon excitation has also become a tool of the biophysical scientists, as evidenced by two-photon studies of protein-bound chromophores⁽⁹⁾ and indole derivatives.^(10,11)

While polarized excitation is often used in two-photon spectroscopy, the experimental conditions and interpretation of the data are distinct from its use in time-resolved fluorescence. In classical two-photon spectroscopy one obtains information about the symmetry of the excited state from the differential absorption of linearly and circularly polarized light of molecules in fluid solution.^(12,13)

Joseph R. Lakowicz and Ignacy Gryczynski • Center for Fluorescence Spectroscopy, Department of Biochemistry and Molecular Biology and Medical Biotechnology Center, University of Maryland at Baltimore School of Medicine, Baltimore, Maryland 21201.

Topics in Fluorescence Spectroscopy; Volume 5: Nonlinear and Two-Photon-Induced Fluorescence, edited by J. Lakowicz. Plenum Press, New York, 1997.

In contrast, in time-resolved fluorescence one measures the anisotropy of the emission with excitation with linearly polarized light, which provides information about the rotational dynamics of the fluorophore.

The interest in 2PE has increased dramatically during the past four years as the result of its applications to fluorescence microscopy and time-resolved fluorescence. In 2PE the intensity of the emission depends on the square of the local optical power. This property is valuable in fluorescence microscopy because the excitation is localized to the focal point, and out-of-focus fluorophores are not excited. Consequently, one obtains the equivalent of confocal microscopy, without the complexity and light losses associated with confocal conditions.^(14,15) Additionally, since the out-of-focus fluorophores do not absorb, they are not photobleached, and thus remain available for three-dimensional image reconstruction. The use of 2PE has been suggested to result in less interference due to sample autofluorescence,⁽¹⁵⁾ but to the best of our knowledge selective excitation of the desired probes without excitation of autofluorescence has not been demonstrated. The potential advantages in microscopy has resulted in expanding applications, including localized release of caged neurotransmitters⁽¹⁶⁾ and to determine the effects of the intense illumination used for optical tweezers.⁽¹⁷⁻¹⁸⁾

Two-photon excitation is also of interest in time-resolved fluorescence. Two-photon-induced fluorescence has been observed for a wide variety of biochemical fluorophores, including membranes labeled with 1,6-diphenyl-3,4,5- hexatriene (DPH),⁽¹⁹⁾ labeled DNA,⁽²⁰⁻²¹⁾ and proteins.⁽²²⁾ In all cases examined to date, the emission spectra and intensity decays have been identical for 1PE and 2PE. However, the anisotropies are often distinct. In some cases the anisotropy is predictable based on the higher order of excitation photoselection expected for 2PE ($\cos^4 \theta$) versus 1PE ($\cos^2 \theta$). In other cases the anisotropies for 1PE and 2PE are distinct. For example, the excitation anisotropy spectra of indole and its derivative are quite different and cannot be explained by simple photoselection arguments.⁽²³⁾ Explanation of the anisotropy spectra requires consideration of the tensor properties of the transitions.⁽²⁴⁾ Knowledge of the spectral properties of fluorophores with 2PE is of interest for its application to biophysics, time-resolved fluorescence, and for interpretation of the results with fluorescence microscopy where the anisotropy can be used to determine the mode of excitation.

The interest in 2PE has resulted in several new opportunities not anticipated a few years ago. While not widely known, saturated hydrocarbons or alkanes are fluorescent when excited in the vacuum ultraviolet and the alkanes fluoresce near 220 nm. We now know that alkanes can be excited by two photons near 300 nm and that alkane fluorescence is sensitive to quenching by alcohols, water, and oxygen.⁽²⁵⁾ Finally, the introduction of fs Ti:sapphire lasers has allowed observation of three-photon excitation (3PE) of a calcium probe⁽²⁶⁾ and of a tryptophan derivative.⁽²⁷⁾ The possibility of 3PE allows the excitation of even UV-absorbing

proteins (below 300 nm) using wavelengths readily available from the fundamental output of a Ti:sapphire laser (700–900 nm).

In this chapter we provide an overview of 2PE and 3PE with an emphasis on the results of time-resolved fluorescence spectroscopy. Other chapters describe the theory of two-photon-induced fluorescence and its applications to cellular imaging.

3.2. Two-Photon Excitation of DPH

An intuitive description of 2PE is given in Figure 3.1. The fluorophore interacts simultaneously with two long-wavelength photons to arrive at the first excited state (left). Hence, the wavelength of the individual photon is typically longer than the emission maximum of the fluorophore (right). As our first example of this phenomena, we describe results obtained with the widely used membrane probe DPH. In this case the 1PE was at 358 nm and the 2PE wavelength was at 716 nm, twice the original wavelength. While it is standard practice to perform 2PE at twice the one-photon wavelength, we must remember that the two-photon absorption spectra are usually not equivalent to the one-photon spectra.

3.2.1. Emission Spectra and DPH Intensity Decays for 1PE and 2PE

Emission spectra of DPH in the solvent triacetin are shown in Figure 3.2. The emission spectra resulting from 1PE and 2PE are superimposable, demonstrating that emission occurs from the same excited state independent of the mode of the excitation. The fact that the emission is due to a biphotonic process is demonstrated in the insert, which shows a quadratic dependence of the DPH emission intensity on the excitation at 716 nm but a linear dependence on the intensity at 358 nm. During measurement of such dependencies on excitation intensity, it is important not to change the pulse width or shape of the 2PE. The observation of identical emission spectra with 1PE and 2PE was not an

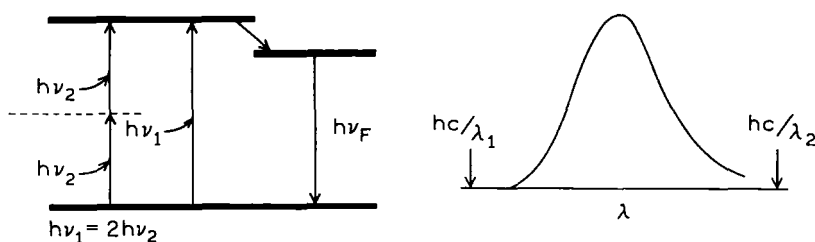


Figure 3.1. Jablonski diagram for two-photon-induced fluorescence.

obvious result. It is known that there are lower-energy states of polyenes, such as DPH and diphenyloctatetraene, which can be reached by 2PE.^(28,29) Additionally, a recent report suggested the presence of emission from *cis* conformers of DPH.⁽³⁰⁾ Two-photon excitation could have resulted in selective excitation of such conformers, resulting in an increased contribution of these conformers to the observed emission. Future studies of 2PE may reveal such selective excitation.

We also examined the emission spectra of DPH-labeled dipalmitoy 1-L- α -phosphatidylglycerol (DPPG) bilayers with 1PE and 2PE (Figure 3.2, lower panel). Within our experimental error the emission spectra were identical. This

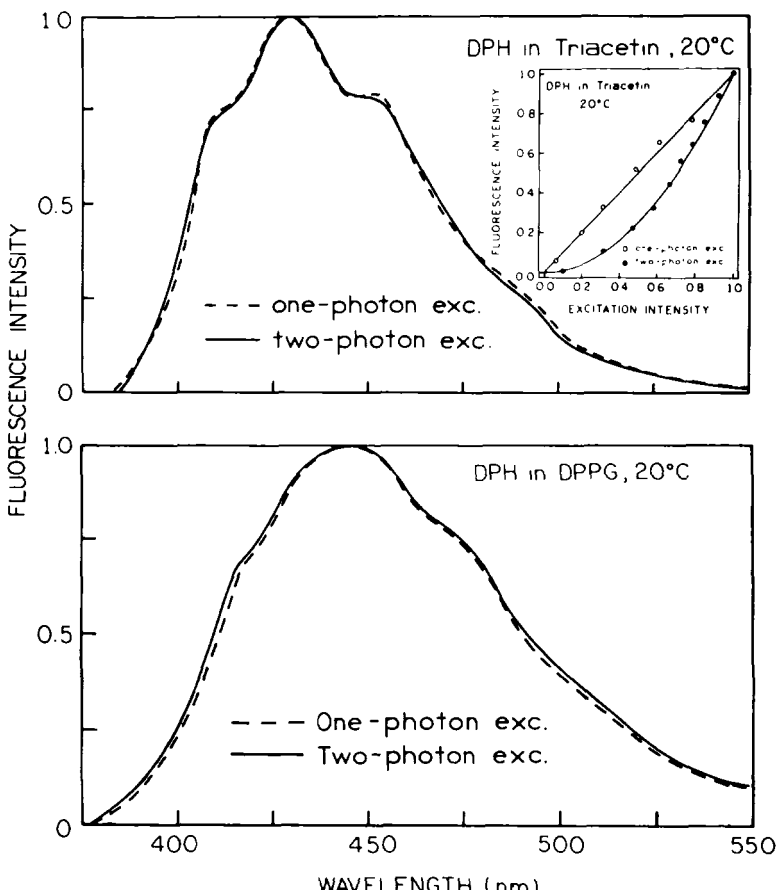


Figure 3.2. Fluorescence emission spectra of DPH in triacetin (top) and in DPPG bilayers (bottom) for excitation at 358 nm (---) and 716 nm (—). Insert shows the linear and quadratic dependence of the DPH intensity on excitation at 358 and 716 nm, respectively.

suggested that the membranes were not being perturbed by the intense focused illumination needed for 2PE. However, DPH is not a very environmentally sensitive fluorophore, and thus may not reveal modest amounts of heating. Such effects could be better studied with fluorophores which display different emission spectra above and below the membrane phase transition temperature.

We next examined the intensity decays of DPH in the triacetin solvent (Figure 3.3), and in the DMPG bilayers (Figure 3.4). Frequency-domain intensity decays of DPH in triacetin were analyzed in terms of the single or multi-exponential decay model according to previous descriptions.⁽³¹⁾ The intensity decays for 1PE and 2PE are both single exponentials and display the same decay time independent of the mode of excitation. Similarly single-exponential decays for 1PE and 2PE were observed from 10° to 40°. The intensity decays of DPH in lipids were found to be multiexponential (Figure 3.4), as observed with other time- or frequency-domain measurements using 1PE.⁽³²⁾ In the case of membrane-bound DPH, several authors have proposed that the minor components in the intensity decay are due to a subpopulation of DPH which is in unusual conformations and/or environments.^(33,34) If these populations are selectively excited to a different extent for 1PE and 2PE, then the amplitudes (α_i) of the intensity decay are expected to depend on the mode of excitation. However, the α_i and τ_i values are practically unchanged for 1PE and 2PE. The similarity of the DPH intensity decays for 1PE and 2PE is illustrated in Figure 3.4 for DPH in DMPG at 10°C. Additional multiexponential intensity

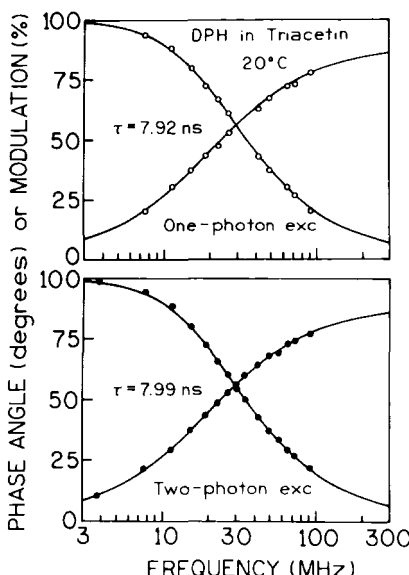


Figure 3.3. Frequency-domain intensity decay of DPH in triacetin observed for 1PE at 358 nm (top) and 2PE at 716 nm (bottom). (From Ref. 19.)

decays are given elsewhere⁽¹⁹⁾ for DPPG, DMPG, and DMPG/cholesterol, at 10 to 55°C. While the precise α_i and τ_i values are not identical in every case, the frequency responses for 1PE and 2PE are similar (not shown). We do not feel that these indicate a significantly different decay law for DPH for 1PE and 2PE, and overall the intensity decays are similar for 1PE and 2PE.

3.2.2. Anisotropy Spectra with 2PE

When measured in frozen solution, where rotational diffusion does not occur during the excited-state lifetime, the excitation anisotropy spectrum of a fluorophore is a measure of the angle (β) between the absorption and emission moments. For 1PE it is well known that the maximum possible value of the anisotropy (r_0) is 0.4, which is a consequence of $\cos^2 \theta$ photoselection, where θ is the angle between the polarized excitation and the absorption transition moments (Figure 3.5) of the randomly distributed fluorophores. The value of r_0 depends on the angle (β) between the absorption and emission transitions:

$$r_0 = 0.4 \left(\frac{3 \cos^2 \beta - 1}{2} \right) \quad (3.1)$$

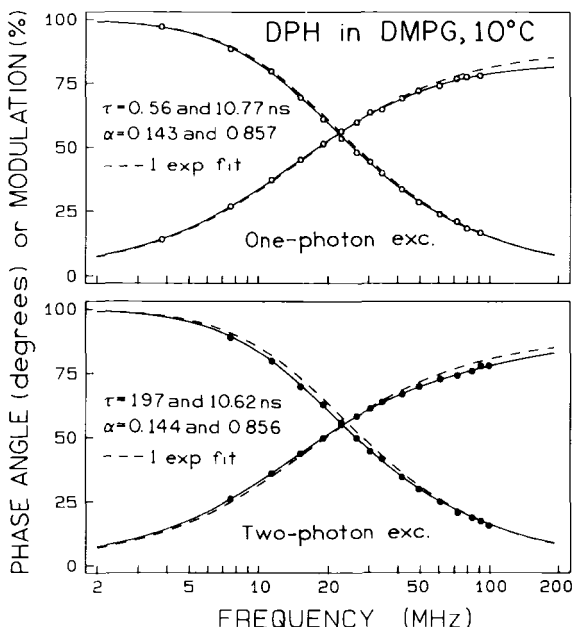


Figure 3.4. Frequency-domain intensity decay for DPH in DMPG vesicles, 10°C, for 1PE at 358 nm (top) and 2PE at 716 nm (bottom). (From Ref. 19.)

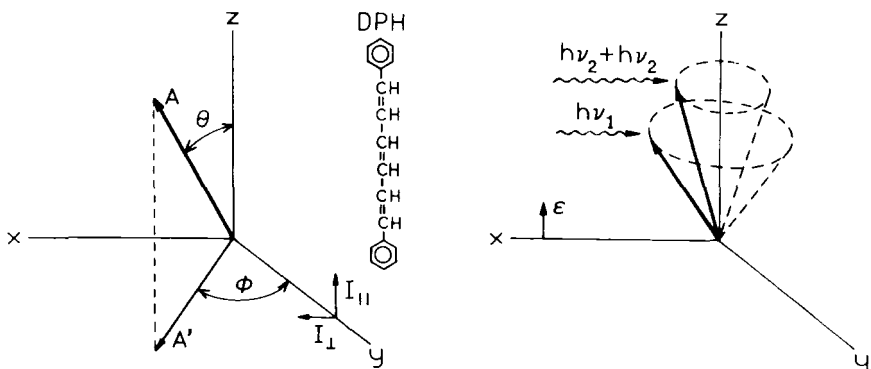


Figure 3.5. (Left) Emission dipole in our coordinate system. (Right) Schematic for one- and two-photon photoselection. The excitation light is polarized along the z axis. Reprinted from Ref. 42 with kind permission from Elsevier Science-NL, Sara Burgerhartstraat 25, 1055 KV Amsterdam, The Netherlands.

For collinear absorption and emission transitions $\beta = 0$ and $r_0 = 0.4$.

Excitation anisotropy spectra of DPH in frozen triacetin are shown in Figure 3.6. For 1PE (●) the maximum anisotropy is near 0.4, which indicates that the absorption and emission transitions are nearly collinear. Remarkably, for 2PE the anisotropy exceeds 0.4 and is as large as 0.52. Initially we were very surprised by this observation of an anisotropy in excess of the theoretical maximum of 0.4. However, we quickly realized that such large values can be explained by a new type of photoselection, which depends on $\cos^4 \theta$ for 2PE, as compared with $\cos^2 \theta$ for 1PE. The simultaneous interactions with more than one photon can result in higher values of the fundamental anisotropy (r_0) or a more highly oriented excited-state population (Figure 3.5).

3.2.3. Theory of Photoselection with MPE

The theory of fluorescence anisotropy for 1PE has been described elsewhere.⁽³⁵⁻³⁶⁾ We now consider the effect of multiphoton excitation (MPE), initially in the absence of rotational motions. The fluorescence anisotropy is a measure of the displacement of the emission transition moment from the direction of the polarized excitation. For vertically polarized (z axis) excitation (Figure 3.5) with one or more photons, the anisotropy is given by

$$r_0(\theta, \beta) = (\frac{3}{2} \langle \cos^2 \theta \rangle - \frac{1}{2})(\frac{3}{2} \cos^2 \beta - \frac{1}{2}) \quad (3.2)$$

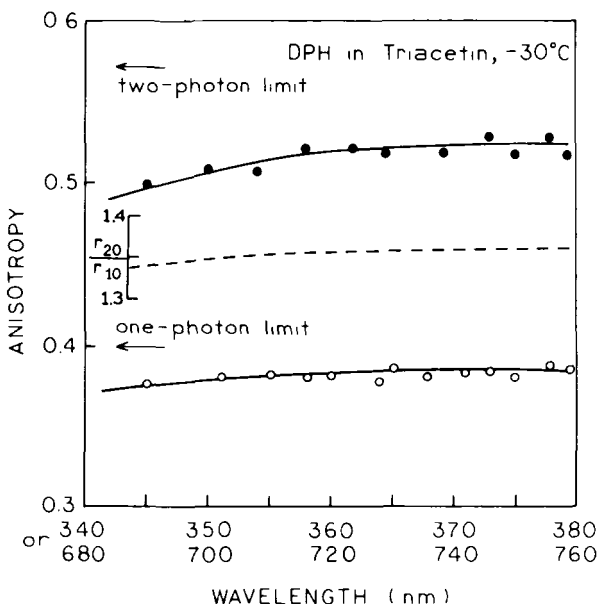


Figure 3.6. Steady-state anisotropies of DPH in triacetin at -30°C measured with 1PE or 2PE. (From Ref. 19.)

where θ is the angle from the z axis, and β is the angle between the absorption and emission transition moments. The subscript 0 indicates the absence of rotational diffusion during the excited-state lifetime or the time = zero anisotropy.

The average value of $\cos^2 \theta$ depends on the type of photoselection. It is

$$\langle \cos^2 \theta \rangle = \frac{\int_0^{\pi/2} \cos^2 \theta f_i(\theta) d\theta}{\int_0^{\pi/2} f_i(\theta) d\theta} \quad (3.3)$$

when $f_i(\theta)$ is the directional distribution of the excited state.⁽³⁷⁾ For 1PE this distribution is

$$f_1(\theta) = \cos^2 \theta \sin \theta d\theta \quad (3.4)$$

For 1PE Eq. (3.2) becomes

$$r_{01}(\beta) = \frac{2}{5} \left(\frac{3}{2} \cos^2 \beta - \frac{1}{2} \right) \quad (3.5)$$

The factor of 2/5 originates with $\cos^2 \theta$ photoselection (Eq. 3.4). For collinear transitions ($\beta=0$) the fundamental anisotropy (r_{01}) without rotational diffusion is

0.40. For many fluorophores the direction of the emission moment can be displaced from the absorption transition, and this angle β can range from 0° to 90° . For such molecules or excitation wavelengths displaying nonzero values of β the anisotropy ranges from 0.40 to -0.20.

The anisotropy expected for 2PE (r_{02}) or 3PE (r_{03}) can be calculated from the relations

$$f_2(\theta) = \cos^4 \theta \sin \theta \quad (3.6)$$

$$f_3(\theta) = \cos^6 \theta \sin \theta \quad (3.7)$$

where the subscript (2 or 3) refers to 2PE or 3PE. Substitution into Eq. (3.2) yields

$$r_{02}(\beta) = \frac{4}{7} \left(\frac{3}{2} \cos^2 \beta - \frac{1}{2} \right) \quad (3.8)$$

$$r_{03}(\beta) = \frac{2}{3} \left(\frac{3}{2} \cos^2 \beta - \frac{1}{2} \right) \quad (3.9)$$

For 2PE and 3PE the maximal anisotropies for $\beta = 0$ are 0.571 and 0.667, respectively (Table 3.1). Hence, for collinear transitions, 2PE or 3PE is expected to result in a more highly oriented excited-state population (Figure 3.5). For molecules which display $\cos^2 \theta$, $\cos^4 \theta$, and $\cos^6 \theta$ photoselection for 1PE, 2PE, and 3PE, respectively, one can expect the anisotropies to have relative values of 1.0, 10/7, and 5/3. Observation of a larger anisotropy for 2PE or 3PE, as compared to 1PE, provides strong evidence for 3PE. However, molecules can display lower anisotropies with 3PE than with 1PE.

In the theory described we assumed that the two-photon transition could be described by a vector. In reality, the multiphoton transitions are more correctly described as tensors.⁽³⁸⁻⁴¹⁾ Under special conditions the anisotropy for 2PE can be as high as 0.61.⁽⁴⁰⁾ For the present data the simple theory described in Eqs. (3.2-3.9) is adequate for interpreting the results.

Table 3.1. Relationship between Angular Displacement of the Absorption and Emission Dipoles (β) and r_0 for Δ_{0i} for Various Kinds of Excitation

β (deg)	One-photon excitation		Two-photon excitation		Three-photon excitation	
	r_0	Δ_{01}	r_0	Δ_{02}	r_0	Δ_{03}
0	0.40	30°	0.57	41.8°	0.67	48.6°
45	0.10	8.2°	0.14	11.3°	0.17	13.6°
54.7	0.00	0°	0.00	0°	0.00	0°
90	-0.20	-19.5°	-0.29	30.6°	-0.33	-36.4°

For many fluorophores the absorption and emission transitions are not collinear, and for many fluorophores the value of β depends on the excitation wavelength. It is this property which leads to r_0 values less than 0.4. The simple theory described by Eqs. (3.2)–(3.9) can be extended to include nonzero values of β . The range of β is from 0° to 90° , and the possible values of r_0 are summarized in Table 3.1. One notices that the r_0 values can range from 0.67 to –0.33 for 3PE, a significantly greater range than for 2PE (0.57 to –0.29) or 1PE (0.40 to –0.20).

Fluorophores or fluorescent macromolecules are often observed under conditions where rotational motions can occur during the excited-state lifetime. In these cases it is of interest to examine the anisotropy decays, which reveal the rates and amplitudes of fluorophore motions. Anisotropy decays are most often analyzed by using the multiexponential model

$$r(l) = \sum_j r_{0j} e^{-t/\theta_j} \quad . \quad (3.10)$$

where r_{0j} are the amplitudes associated with the correlation time θ_j . For simplicity assume that the anisotropy decay is a single exponential

$$r(t) = r_{0i} e^{-t/\theta_k} \quad (3.11)$$

In this case the subscript i indicates the mode of excitation (one, two, or three photons). For such a fluorophore displaying a single correlation time, we expect the value of r_{0k} to depend on the excitation mode. The values of r_{0k} are the anisotropies at $t = 0$ and should thus be equivalent to the r_{0i} values for 1PE, 2PE, or 3PE. However, for spherical molecules one expects the same correlation time independent of the excitation mode. Detection of a shorter correlation time for MPE could be evidence for local heating of the sample due to the locally intense excitation.

Anisotropy decays are often measured in the frequency domain, where the measured quantities are the phase-angle difference (Δ) between the polarized components and the modulation ratio (A) of the polarized components, as summarized elsewhere in detail.⁽⁴²⁾ The differential phase angles can provide a proof of MPE. It can be shown^(42a) that the maximum observable value of Δ is

$$\tan \Delta_{0i} = \frac{3r_{0i}}{2[(1 + 2r_{0i})(1 - r_{0i})]^{1/2}} \quad (3.12)$$

Here the subscript 0 refers to a limiting value, analogous to the definition of r_0 and the subscript i refers to the mode of excitation, respectively.

For 1PE collinear absorption, and emission dipoles, $r_0 = 0.4$ and the maximal value of Δ is $\Delta_{01} = 30^\circ$ (Table 3.1). For 2PE, r_0 can be as high as

0.57, resulting in a maximal value of $\Delta_{02} = 41.8^\circ$. Additional values are listed in Table 3.1 for β values of 45° , 54.7° , and 90° . Observation of Δ values larger than 30° or less than -19.5° can be regarded as a unique consequence of MPE. To avoid confusion we note that these predictions are independent of τ , R, or ω and the maximum value of Δ_{0i} occurs for high values of the product $\omega\tau$.

The theory described can be strictly applied only to spherical molecules or molecules which display a single rotational correlation time. It is well known that nonspherical molecules can display up to five correlation times,⁽⁴³⁾ with three expected to be experimentally observable. For such molecules the anisotropy decay may be different for 1PE or 2PE.⁽³⁸⁾

3.2.4. Anisotropy Decays of DPH with 2PE

We used the considerations of Δ_{0i} described in Eq. (3.12) to determine if 2PE of DPH could be demonstrated by values of Δ_0 above the 1PE limit. We examined the frequency-domain data for DPH in triacetin (Figure 3.7). We varied the temperature and viscosity of triacetin to obtain different phase angles close to the maximum values. As temperature increases from 10 to 40°C the maximum differential phase angles increase, resulting in a maximum value of 28° for 40°C and 300 MHz for 1PE. The measurements were limited to 300 MHz because of the low modulation of the emission (0.07) resulting from the 7.27-ns decay times

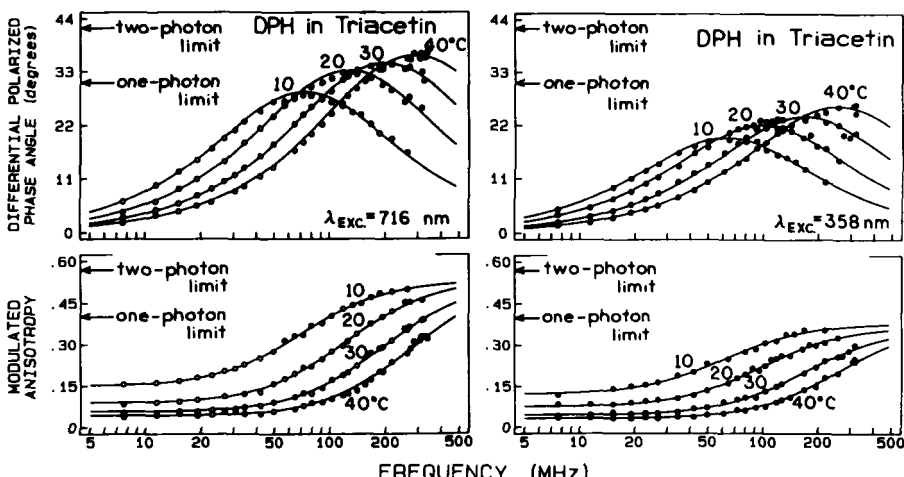


Figure 3.7. Frequency-domain fluorescence anisotropy data obtained with 1PE ($\lambda_{\text{exc}} = 358 \text{ nm}$, right) and for 2PE ($\lambda_{\text{exc}} = 716 \text{ nm}$, left) for DPH in triacetin at various temperatures. The absolute limits of differential phases are 30° for 1PE (●) and 41.8° for 2PE (○). The absolute limits of modulated anisotropies are $2/5$ for 1PE and $4/7$ for 2PE.

of DPH, and higher temperatures will shift the frequency of the $\tan \Delta_{\max}$ above 300 MHz. The value of 28° is close to the predicted maximum of 30° .

The anisotropy data resulting from 716-nm 2PE are also shown in Figure 3.7. These results clearly demonstrate Δ values well in excess of 30° , with a maximum observed value of about 37° . Another measure of the time-dependent anisotropy decay is provided by the modulated anisotropy (r_ω), shown in the lower panels of Figure 3.7. This parameter displays properties similar to the steady-state (r) or fundamental anisotropy (r_0). The value of r_ω is calculated from the ratio of the polarized and amplitude-modulated components of the emission

$$r = \frac{\Lambda - 1}{\Lambda + 2} \quad (3.13)$$

where Λ is the ratio of AC_{\parallel} to AC_{\perp} .⁽⁴²⁾ At low modulation frequencies (ω) r_ω is equal to the steady-state anisotropy. At high modulation frequencies $r_{0\omega}$ approaches the value of r_0 . Examination of the modulated anisotropies also demonstrated 2PE. The modulated anisotropies exceed the single-photon limit of 0.4. Such data must have their origin in 2PE, and confirm our prediction that 2PE should result in a more strongly oriented photoselected population, or, equivalently, values of r_0 in excess of 0.4. The elevated values of r_0 are also evident from least-squares analysis of the frequency-domain anisotropy data. The average values of r_0 recovered from the frequency-domain anisotropy data were 0.373 and 0.523 for 1PE and 2PE, respectively.

3.2.5. Two-Photon Excitation of DPH in Membranes

Two-photon excitation requires locally intense excitation. While it is generally accepted that the low power levels used for 1PE do not cover sample heating, it seemed important to determine if 2PE was accompanied by thermal effects. Hence, we examined the steady-state anisotropy, intensity decay, and anisotropy decays of DPH-labeled bilayers. We reasoned that heating of the sample would result in decreased rotational correlation times or steady-state anisotropies. The steady-state anisotropies of DPH-labeled bilayers are shown in Figure 3.8. While the anisotropies are higher for 2PE than for 1PE, the temperature-dependent changes are similar. That is, the bilayer phase transition temperatures are the same for 1PE and 2PE. This result suggests that local heating of the bilayers is not significant for 2PE of DPH.

To further evaluate the possible heating effects during 2PE, we examined the DPH intensity decays and anisotropy decays of DPH in model membranes.⁽¹⁹⁾ Essentially the same intensity decays and mean decay times were found for 1PE and 2PE (Figure 3.4). Representative anisotropy decays are shown in Figure 3.9

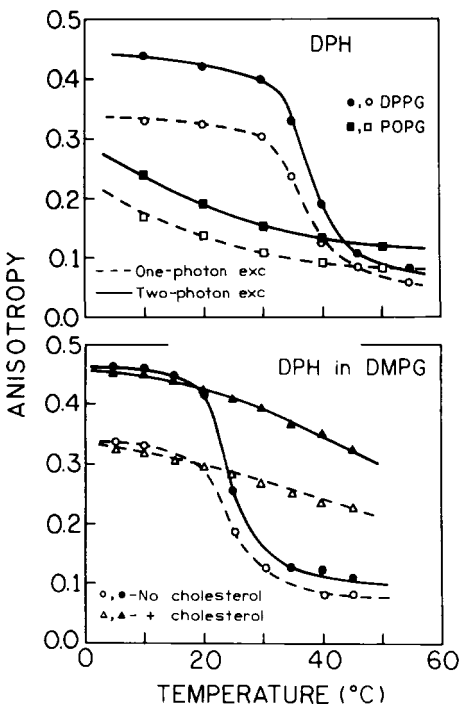


Figure 3.8. Temperature dependence of steady-state anisotropies of DPH in lipids. (Top) DPH in DPPG or 1-Palmitoyl-2-olcoyl-sn-glycero-3-phospho-tac-glycerol (POPG). (Bottom) DPH in DMPG in the absence and presence of cholesterol. The open symbols and dashed lines refer to 1PE, and filled symbols and solid lines to 2PE. (From Ref. 19.)

for time-domain measurements and in Figure 3.10 for frequency-domain measurements. The anisotropies are uniformly higher for 2PE than for 1PE. The time-domain DPH anisotropy decays (Figure 3.9) show the well-known nonzero anisotropy at long times for DPH whether excited by one or two photons, as do the frequency-domain data (Figure 3.10). These results suggest there are no significant heating effects for labeled membranes with 2PE. DPH displayed one of the weaker signals we observed for 2PE, suggesting a low two-photon cross section. Hence, this is a worst-case example, and the heating effects are expected to be less for fluorophores with higher two-photon cross sections.

3.3. Two-Photon Excitation of Fluorophore-Stained DNA

A wide variety of fluorophores are known to bind to DNA and display enhanced fluorescence. Such dye-DNA complexes are widely used in fluorescence microscopy to image DNA in cells. Hence, it was of interest to examine the fluorescence spectral properties of labeled DNA. We examined DNA stained with

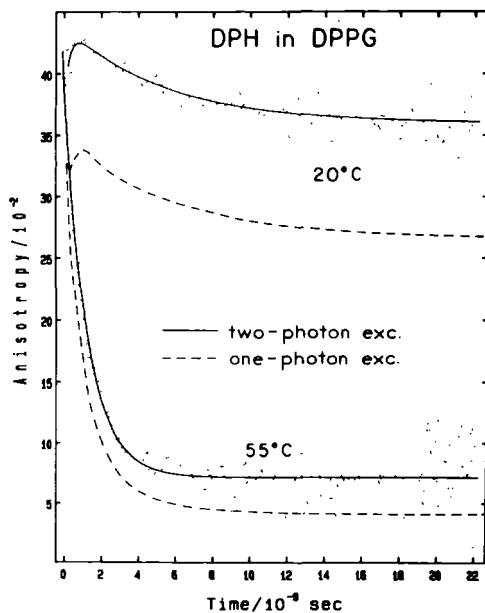


Figure 3.9. Time-domain anisotropy decay of DPH in DPPG bilayers for IPE and 2PE.

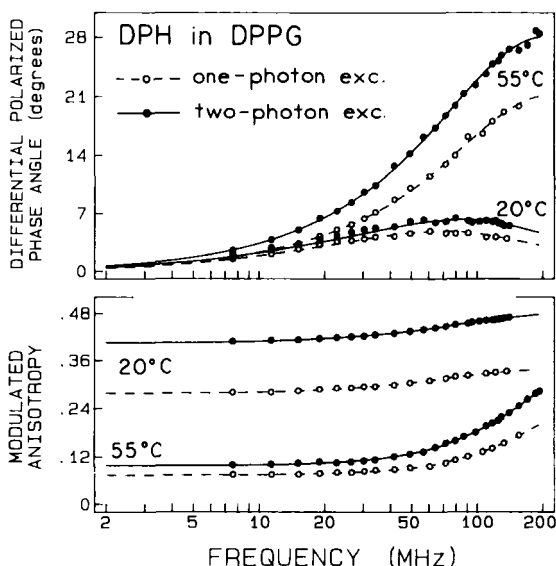


Figure 3.10. Frequency-domain anisotropy decay data for DPH in DPPG obtained with IPE (—○—) and 2PE (—●—). (From Ref. 19.)

4,6-diamidino-2-phenylindole (DAPI)⁽²⁰⁾ and with Hoechst 33342,⁽²¹⁾ two of the more widely used DNA stains. In both cases we found that these probes displayed the $\cos^2 \theta$ and $\cos^4 \theta$ photoselection described for DPH. That is, the anisotropy for 2PE is 10/7 larger than for 1PE. For Hoechst 33342 we also found that at comparable wavelengths there is less evidence of energy transfer from the DNA bases to Hoechst for 2PE, compared to 1PE. That is, the extent of excitation of the DNA appeared to be smaller for 2PE.

3.3.1. Emission Spectra of Hoechst 33342

Emission spectra of Hoechst 33342 (HOE) in ethanol are shown in Figure 3.11. The same emission spectra were observed for 1PE (----) and 2PE (—) at 380 and 760 nm, respectively. The emission was quadratically dependent on the incident intensity at 760 nm (●), but linearly dependent on intensity at 380 nm (○) (Figure 3.11, insert). This quadratic intensity dependence is strong evidence that the observed emission was due to simultaneous absorption of two photons at 760 nm. That the emission spectra are identical for 1PE and 2PE indicates that emission occurs from the same state, irrespective of the excitation mode. Similar results were obtained for HOE bound to DNA (not shown), which also showed a quadratic dependence on intensity for 2PE, and identical emission spectra for 1PE and 2PE.

The use of Hoechst 33342 as a two-photon probe in fluorescence microscopy requires a usefully high cross section for two-photon absorption. It is difficult to directly measure the cross sections for two-photon absorption, and even more difficult to measure a two-photon absorption spectrum. Such measurements are difficult because of the small amounts of absorption and because the extent of absorption will depend on the focusing properties of the optics and the mode intensity profile of the laser beam. For these reasons most two-photon cross sections are determined by comparison with fluorophores which display known

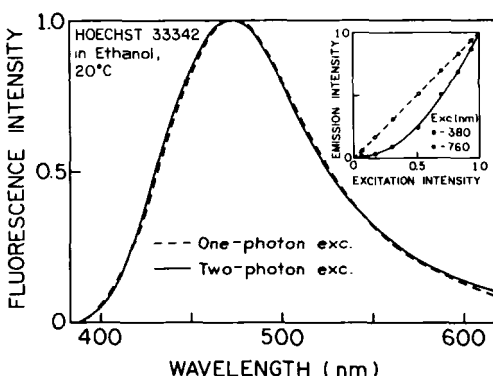


Figure 3.11. Fluorescence emission spectra for 1PE (---; 380 nm) and 2PE (—; 760 nm) of Hoechst 33342 in ethanol. The inset shows the dependence of the intensity on the incident light level, normalized to that observed for the highest incident light level. (From Ref. 21.)

two-photon cross sections. We estimated the relative two-photon cross sections for HOE, DAPI, and other biofluorophores by comparison with *p*-bis(*o*-methylstyryl)benzene (bis-MSB), which has a known two-photon cross section and the largest cross section known at this time.⁽⁴⁴⁾ Based on this comparison, using excitation wavelengths of 580 nm, 694 nm, and 720 nm, we estimated the relative two-photon cross sections ($\sigma_{\text{HOE}}/\sigma_{\text{MSB}}$) of HOE to be about 0.3, 0.5, and 0.8, respectively (Table 3.2), which compares very favorably with bis-MSB. Hence, Hoechst 33342 and DAPI can be expected to be useful two-photon probes in fluorescence spectroscopy and microscopy. Recently, two leading microscopy groups published absolute two-photon cross sections of number of fluorophores excitable by femtosecond Ti:sapphire laser.^(45,46)

3.3.2. Fluorescence Intensity Decays of Hoechst 33342

We questioned whether HOE would display the same decay time(s) for 1PE and 2PE. In ethanol the decay of HOE is a single exponential, 3.3 ns, independent of 1PE or 2PE. When bound to DNA, the intensity decay of HOE is weakly multiexponential (not shown). While slightly different α_i and τ_i values were found for 1PE and 2PE, we believe the minor difference between the 1PE and 2PE decay is due to experimental uncertainties. In total, the data suggest that the intensity decay of HOE is not dependent on the mode of excitation.

The frequency-domain anisotropy data are distinct for 1PE and 2PE of Hoechst 33342 in ethanol (Figure 3.12) and in Hoechst DNA complex (Figure 3.13). The differential phase and modulated anisotropy values are higher for 2PE (●) than for 1PE (○). This effect is reminiscent of our previous results for DPH (Figures 3.7, 3.9, and 3.10), 2,5-diphenyloxazole (PPO), and DAPI.^(20,47) For DPH and PPO, we found that the anisotropy values for 1PE and 2PE were related by a factor of 10/7, indicating that all of the diagonal elements in the two-photon transition matrix are zero. The larger 2PE anisotropy values are consistent with $\cos^4 \theta$ photoselected for 2PE. Importantly, the correlation time(s) are identical for 1PE and 2PE. This suggests that there are no adverse affects and/or local heating due to the intense illumination at 760 nm.

The similarity of the anisotropy decays for 1PE and 2PE were also examined by global analysis. The principles of global analysis have been described elsewhere.^(48,49) We performed global analysis of the 1PE and 2PE anisotropy decays in which the correlation times were restricted to be equal, but the amplitude factors (r_0 values in Eq. 3.10) were allowed to be distinct. For this analysis we recovered an acceptable fit with the same correlation time for 1PE and 2PE, and the recovered r_0 values were related by a factor of 10/7. This result strongly supports our assertion that the nature of the anisotropy decay is not affected by the excitation mode.

Table 3.2. Relative Two-Photon Cross Sections of Biochemical Fluorophores

TPIF standards ^a	Solvent	Exc. (nm)	Em (nm)	Rel. δ ^b	τ (ns)	r(0)	θ (ns)
MSB	CH	580	420	1.0	1.63	0.51	0.120
	EtOH	580	420	1.0	1.63	0.52	0.125
	PG	580	420	1.0	1.46	0.52	4.40
PPO	MeOH	580	360	0.05	1.440	0.50	0.038
	PG	580	360	0.05	1.450	0.51	2.60
PPD	EtOH	580	340	0.15	1.23	0.50	0.077
TPB	Hexadecane	580	450	0.22	1.94	0.36	0.242
	Mineral Oil	580	450	0.26	2.03	0.36	6.65
DMSS	MeOH	720	440	0.8	0.034	0.53	0.106
		694	440	0.5	—	—	—
DDPS	n-Butanol	720	430	0.7	0.032	0.54	0.390
		694	430	0.4	—	—	—
HOE	EtOH	720	450	0.8	3.39	0.54	0.622
		694	450	0.5	—	—	—
		580	450	0.3	—	—	—
DAPI	EtOH	720	450	0.9	—	—	—
		694	450	0.6	—	—	—
		580	450	0.4	—	—	—

^a TPIF = two-photon-induced fluorescence; MSB = p-bis(*o*-methylstyryl)benzene; PPO = 2,5-diphenyloxazole; PPD = 2,5-diphenyl-1,3,4-oxadiazole; TPB = 1,1,4,4-tetraphenylbutadiene; DMMS = 4-dimethylamino-*ω*-methylsulfonyl-*trans*-styrene; DDPS = 4-dimethylamino-*ω*-diphenylphosphenyl-*trans*-styrene; HOE = HOECHST-33342-bis-benzimidazole,2,5-1*H*-benzimidazole,2'-(4-ethoxy-phenyl)-5-(4-methyl-1-piperazinyl); DAPI = 4',6-diamidino-2-phenylindole.

^b Two-photon cross sections are relative to bis-MSB.^(44,45)

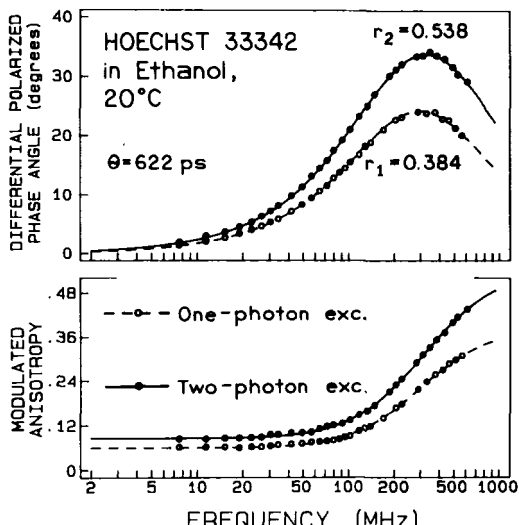


Figure 3.12. Differential polarized phase angles for Hoechst 33342 in ethanol at 20°C, obtained for 1PE (○) and 2PE (●). (From Ref. 21.)

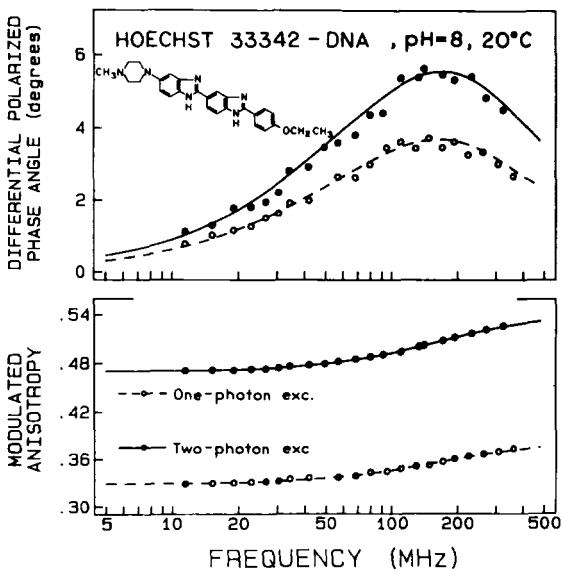


Figure 3.13. Frequency-domain anisotropy data for 1PE (○) and 2PE (●) of Hoechst 33342-DNA. (From Ref. 21.)

3.3.3. Anisotropy Excitation Spectra of Hoechst 33342 in Glycerol at -20°C

In fluid solution (ethanol) and when bound to DNA, the HOE anisotropy values are decreased by rotational diffusion. A more accurate comparison of the anisotropy values for 1PE and 2PE can be obtained by measuring the anisotropy values with no diffusion. This was done by measuring the excitation anisotropy spectra of HOE in glycerol at -20°C (Figure 3.14). For excitation with the lowest singlet state (1PE, 345–380 nm and 2PE, 690–760 nm), the anisotropy values are almost exactly related by the factor 10/7. In the shorter-wavelength range (1PE, 285–310 nm and 2PE, 560–620 nm), where some excitation to the S_2 state probably occurs, the 1PE anisotropy values decrease with wavelength (Figure 3.14, ○○○), whereas the 2PE values remain high and constant (· · ·). This result suggests that 1PE results in some excitation to a different (higher) electronic state, where the absorption and emission oscillators are less collinear. For 2PE these oscillators remain collinear, which suggests that the S_0-S_2 transition has a lower two-photon cross section or that excitation is occurring in a different electronic state for 2PE.

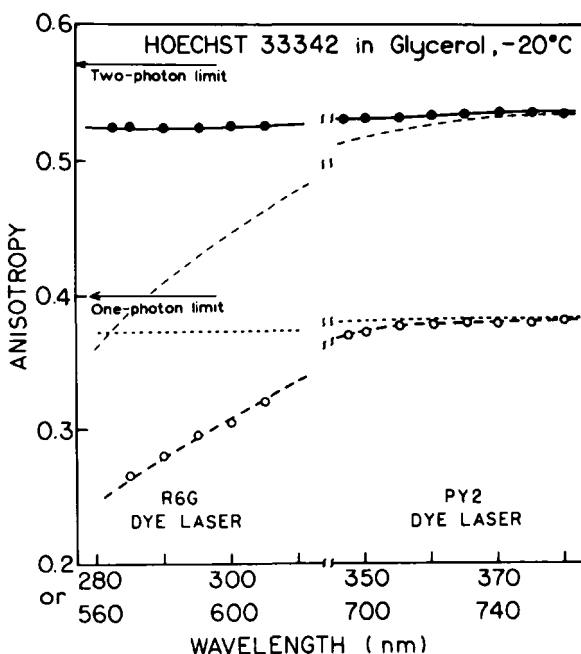


Figure 3.14. Excitation anisotropy spectra of Hoechst 33342 in glycerol, -20°C . The upper dashed line shows the anisotropy values expected for an increased 2PE photoselection factor of 10/7. (From Ref. 21.)

3.3.4. Anisotropy Excitation Spectra of Hoechst 33342–DNA Complex

We also examined the anisotropy spectra of HOE when bound to DNA (Figure 3.15). In this case, the steady-state anisotropy values decreased rapidly for 1PE below 300 nm. This wavelength coincides with the onset of the DNA absorption, so it seems likely that the decrease in anisotropy is due to single-photon absorption by the DNA bases followed by energy transfer from the DNA bases to HOE. Surprisingly, the 2PE anisotropy values do not decrease in this range of wavelength, which suggests that the relative cross section for two-photon absorption of DNA is smaller for 2PE than for 1PE. This result suggests that 2PE of HOE-stained DNA can be accomplished without undesired excitation of the DNA itself.

Hoechst 33342 displays a high cross section for two-photon absorption in the wavelength range from 560 to 760 nm ($\sim 10^{-48} \text{ cm}^4 \text{ s/photon molecule}$). The anisotropy remains high over this range, suggesting there is a dominant two-photon cross transition with collinear absorption and emission oscillators. Hoechst 33342 displays essentially the same lifetimes and correlation times for

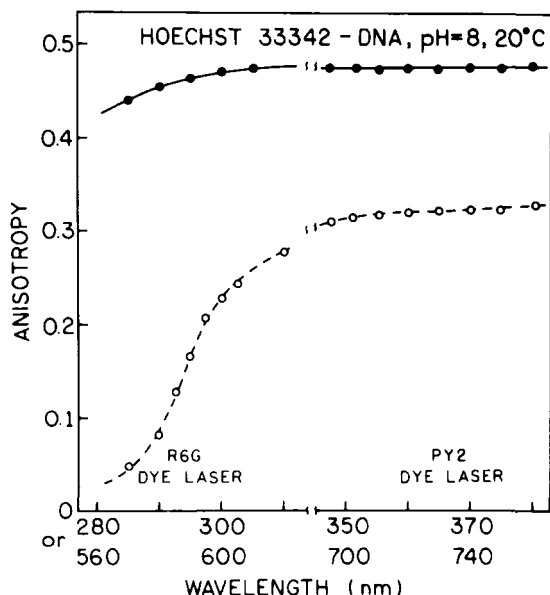


Figure 3.15. Excitation anisotropy spectra of the Hoechst 33342-DNA complex. (From Ref. 21.)

1PE and 2PE, which will allow direct comparison of the one-photon and two-photon experimentation data. And finally, the 2PE of Hoechst 33342 appears to be possible without two-photon absorption of DNA. These results suggest that Hoechst 33342 is a useful probe for two-photon spectroscopy and microscopy, and that one can directly compare the one- and two-photon experiments.

It can be valuable to know the anisotropy expected for 2PE or 3PE. For instance, there have been a number of recent reports on 2PE in fluorescence microscopy, some with the use of continuous-wave (CW) excitation.^(17,18) There have also been suggestions of 3PE with CW excitation. In our opinion it is essential to rule out other possible origins of the signal. For instance, perhaps optical elements in the microscope or elsewhere result in a low level of frequency-doubled or -tripled excitation, which in turn excites the UV-absorbing fluorophores. If this occurred, then the anisotropy of the signal would be the value expected for 1PE and not the higher values found for 2PE. Hence, the steady-state anisotropy of probes like DPH and Hoechst 33342 can be used to test whether 1PE, 2PE, or 3PE (below) excitation is occurring.

3.4. Two-Photon Excitation of Indole, Tryptophan, and Proteins

It is well known that the electronic spectra of indole and tryptophan are complex and that the fundamental anisotropy (r_0) is strongly dependent on

excitation wavelength.⁽⁵⁰⁾ At present the accepted model for the complex anisotropy spectrum is the presence of two overlapping electronic transitions, 1L_a and 1L_b , with emission occurring only from the 1L_a state.^(51,52) The electronic transition moments are thought to be oriented 90° relative to each other within the indole plane. The 1L_b absorption is thought to be structured and insensitive to solvent, and 1L_a displays an unstructured solvent-sensitive absorption spectrum. Hence, the fundamental anisotropy of indole is high for excitation into the 1L_a state. When excited into the 1L_b state, emission occurs from the perpendicular 1L_a transition, and hence the anisotropy is low. Because of the complexity of indole and tryptophan and its use as an intrinsic probe for proteins, we examined the spectral properties for 1PE and 2PE.

3.4.1. Emission Spectra

Emission spectra of indole are shown in Figure 3.16. Essentially the same emission spectra were observed for 1PE and 2PE. Similarly results were obtained for human serum albumin (HSA, not shown). Observations of the same emission spectra was not an obvious result. Given the complexity of the indole spectra, it was possible that the absorption was due to a unknown state, or that excitation occurred to the 1L_b state with emission from this same state. Emission from the

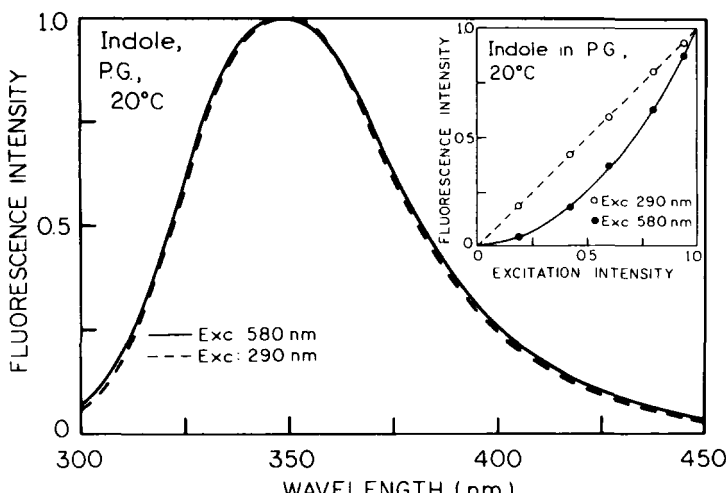


Figure 3.16. Emission spectra of indole propylene glycol at 20°C, resulting from 1PE (---) and 2PE (—) at 290 and 580 nm, respectively. The insert shows the dependence of the emission intensity on the excitation intensity at 290 (○) and 580 nm (●).

1L_b state with 2PE seemed possible given the observation of 1L_b emission from 5-methyl indole.⁽⁵³⁾ However, for the moment it seems that 1L_a emission of tryptophan occurs for both 1PE and 2PE.

3.4.2. Anisotropy Spectra

Based on the foregoing considerations we examined the excitation anisotropy spectra of indole and L-tryptophan (Figure 3.17). At first glance the anisotropy spectra of indole (Figure 3.17, left) appear similar for 1PE and 2PE. However, the 2PE spectrum is 1.429-fold larger than for the 1PE spectrum due to increased photoselection. Hence, one should compare the one-photon data with the two-photon data following correction for this effect—that is, division of the two-photon anisotropies by 1.429. This corrected spectrum is shown as the dashed line, which indicates that the excitation polarization spectra of indole for 1PE and 2PE are distinct.

Still more dramatic differences between the one- and two-photon anisotropy spectra were observed for L-tryptophan (Figure 3.17, right). In this case the 2PE

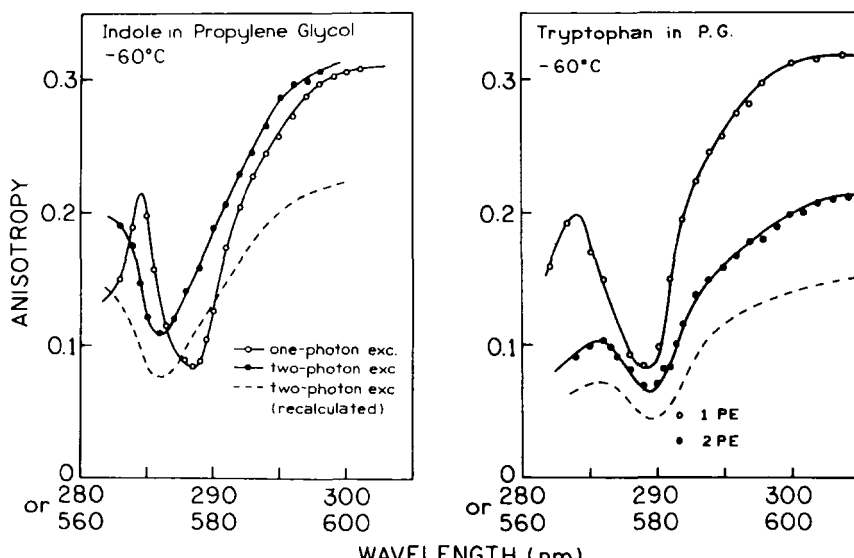


Figure 3.17. Excitation anisotropy spectrum of indole in propylene glycol at -60°C (left) and for L-tryptophan in propylene glycol (right), at -60°C . $[\text{Indole}] = [\text{Trp}] = 2 \times 10^{-3} \text{ M}$ for both (\bigcirc) 1PE and (\bullet) 2PE. The dashed line shows the two-photon anisotropy spectrum corrected for the more highly oriented photoselected population resulting from 2PE; that is, the 2PE values were divided by 1.429.

spectrum is nearly 30% lower than the 1PE spectrum at most excitation wavelengths. Correction of the 2PE spectrum for the photoselection factor further enhances the difference between the one- and two-photon anisotropy spectra. Control experiments have indicated that the unusual anisotropy spectra for 2PE is not the result of energy transfer or other experimental artifacts. The r_0 values were also recovered from the frequency-domain anisotropy decays (not shown).

What is the origin of the unusual two-photon anisotropy spectrum of indole and tryptophan? The complex one-photon anisotropy spectrum of indole has been explained by the presence of two electronic states, 1L_a and 1L_b . The transition moments of the 1L_a and 1L_b states are thought to be oriented 90° relative to each other. The 1L_a state is preferentially excited at long wavelengths above 295 nm. One explanation of the anisotropy spectra in Figure 3.17 is an increase in the relative absorption of the 1L_b state in indole and tryptophan. It is known that the two-photon absorption cross sections are different for various molecules,⁽¹¹⁾ so it seems probable that the relative cross section for the 1L_a and 1L_b states could be different for 1PE and 2PE. To explain the two-photon anisotropy spectra, we must invoke a redshift of the 1L_b absorption spectrum for 2PE and emission from the 1L_a state.

We questioned whether the 1PE and 2PE values of other indole derivatives were linked by the photoselection factor of 10/7. Hence, we examined the 1PE and 2PE steady-state anisotropies (r_{01} and r_{02}) of indole derivatives in frozen solution (Table 3.3). In all cases, the value of r_{02} was not 10/7 larger than r_{01} . In some cases, r_{02} was less than r_{01} . Additionally, the values of r_{02} were sensitive to ring substitutions on the indole. These data strongly suggest that either the rela-

Table 3.3. Comparison of the Initial Anisotropies (r_0) to HSA^a and Indole Derivatives^b for One- and Two-Photon Excitation^c

Compound	1PE at 298 nm	2PE at 596 nm ^d	Expected ^e
Indole	0.29	0.31	0.41
NATA	0.30	0.17	0.43
Trp	0.30	0.18	0.43
2,3-Dimethyl indole	0.32	0.28	0.46
5-Methoxy indole	0.28	0.10	0.40
HSA	0.25	0.28	0.36

^a 70% (v/v) propylene glycol–water, –60°C.

^b Propylene glycol, –60°C.

^c The 1PE and 2PE measurements of each compound were performed on the same solution. The fluorophore concentrations were 5×10^{-4} to $2 \times 10^{-3} M$.

^d Observed value for 2PE.

^e Expected value assuming $r_{02} = (10/7)r_{01}$.

tive absorbance of the 1L_a and 1L_b transitions are different for 1PE and 2PE or that additional states are probed by the 2PE experiment.

3.4.3. Two-Photon Excitation of HSA

We next questioned whether two-photon-induced fluorescence could be observed for proteins. For the initial studies⁽²²⁾ we chose the single tryptophan protein HSA. Essentially the same emission spectra were observed for 1PE and 2PE. The HSA emission showed a quadratic dependence on the incident intensity at 590 nm but a linear dependence on intensity at 295 nm. This quadratic dependence on intensity demonstrates that the observed emission was due to a biphotonic process at 590 nm. For more details on steady-state anisotropies of proteins see Chapter 5.

Most proteins, even those with a single tryptophan residue, display multi-exponential intensity decays,⁽⁵⁴⁾ and the intensity decays are typically sensitive to the conformation and/or structural heterogeneity of the protein. Hence, it was of interest to determine if 2PE probed the same population of conformers as seen with 1PE. The frequency response of the HSA emission is shown in Figure 3.18 for 1PE (top) and 2PE (bottom). The frequency responses for 1PE and 2PE were essentially identical, or that can be seen from the mean decay time ($\langle \tau \rangle$) and the α_i and τ_i values determined from the double-exponential fit. We do not feel the small decrease in $\langle \tau \rangle$ is significant. Hence, in this case, the intensity decay analysis did not reveal additional information. However, we expect that in some proteins the excited-state population with 2PE may be distinct from that observed for 1PE.

In contrast to the frequency-domain (FD) intensity decays, the FD anisotropy data for HSA are markedly different for 1PE and 2PE (Figure 3.19). The differential phase angles are comparable in magnitude (top), but the modulated anisotropies are distinct (bottom). When analyzed individually, the 1PE and 2PE data yield nearly identical anisotropy decays. As is typical for tryptophan residues in proteins, the anisotropy decay contains a short correlation time, due to segmental motions of the tryptophan residue, and a longer correlation time, reflecting overall rotational diffusion of the protein. However, the initial anisotropies, whether obtained from the FD data ($r_0 = \sum r_{0j}$) or from measurement in vitrified solutions, are not related by the expected factor of 10/7. This suggests that the values of β are different for 1PE and 2PE, that the anisotropy must be described in terms of tensors,⁽²⁴⁾ or that the relative $^1L_a - ^1L_b$ cross sections are different for 1PE and 2PE. We note that the anisotropy data for 1PE and 2PE were obtained using the same HSA sample and same HSA concentration. Also, the size of the HSA molecule precludes close contact between the tryptophan residues. For this reason energy transfer between the single tryptophan residue in each HSA molecule is unlikely.

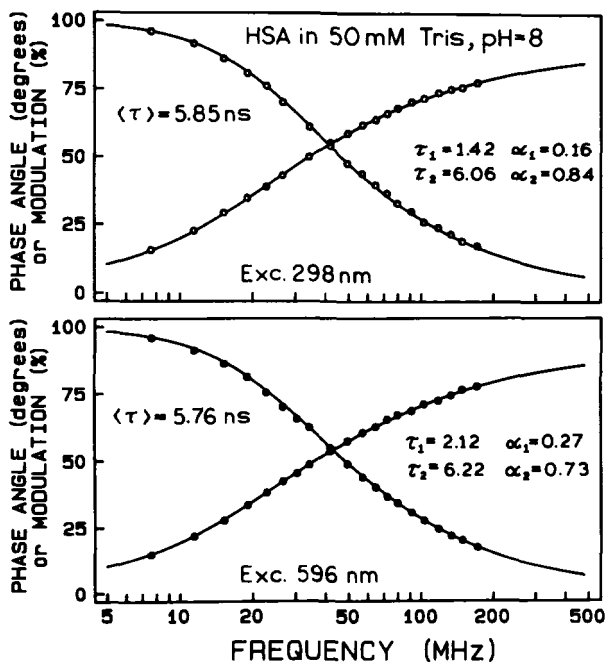


Figure 3.18. Frequency response of the intrinsic tryptophan emission of HSA for 1PE (top, ○) and 2PE (●). The solid lines represent the best two-exponential fit to the data.

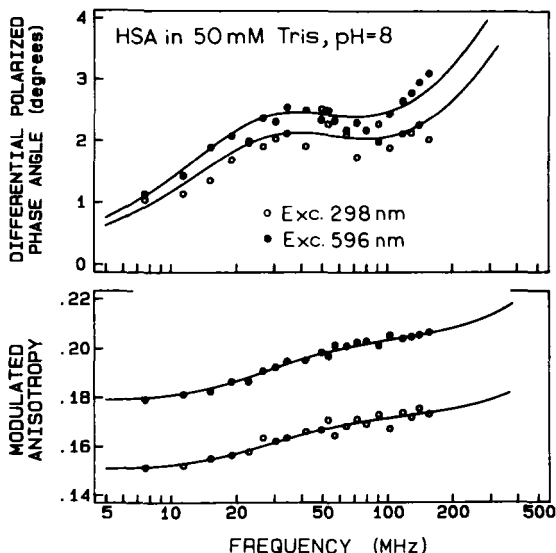


Figure 3.19. Frequency-domain anisotropy data for the tryptophan emission from HSA for excitation at 298 (○) and 596 nm (●). The solid lines represent the best two-correlation-time fits to the data, assuming independent values of r_0 at each excitation wavelength.

3.5. Two-Photon-Induced Fluorescence of Alkanes

While not widely known, saturated hydrocarbons, including linear, branched, and cyclic alkanes, are known to be fluorescent when excited in the vacuum ultraviolet (VUV) near 140 to 160 nm.⁽⁵⁵⁻⁵⁷⁾ These saturated hydrocarbons display emission from 200 to 240 nm, which is readily transmitted by the usual quartz optic. However, VUV excitation conditions are not compatible with biochemical experiments because it is necessary to exclude oxygen, which absorbs below 250 nm, and to use special optics which transmit the VUVexcitation.

In recent reports we demonstrated that alkanes can be excited with 2PE near 300 nm. Emission was observed for the cyclic alkanes cyclohexane (CH) and methylcyclohexane (MCH)^(58,59) and for the linear alkane tetradecane.⁽⁶⁰⁾ Emission spectra of the three alkanes are shown in Figure 3.20. Excitation at 300 nm results in deep UV emission below 250 nm. The emission depends quadratically on the peak intensity of the laser pulse train (inserts), which strongly suggests that excitation is due to a biphotonic process. We believe that this process is the simultaneous absorption of two 300-nm photons, as there is no reason to expect interaction of CH or MCH with a single photon whose energy is below that needed for absorption by CH or MCH. Two-photon excitation of cyclohexane was reported at 337 nm with a nitrogen laser,⁽⁶¹⁾ which suggests that wavelengths from 300 to 350 nm will be effective for 2PE. The intensity of MCH is seen to be about threefold higher than CH. These emission spectra are in agreement with the result obtained using 1PE at 147 nm,⁽⁵⁵⁻⁵⁷⁾ where MCH was reported to display an approximate twofold higher quantum yield than CH.

During these experiments on 2PE of alkanes we attempted to examine more dilute solutions. It was difficult to select a solvent for dilution because other alkanes would also be fluorescent and thus unsuitable as a solvent. Hence, we dissolved the alkanes in alcohols. To our surprise, the alkanes were quenched by alcohols. This is shown in Figure 3.20 (bottom), where the emission of tetradecane is quenched more than twofold by 33 mM *n*-propanol. The decrease in tetradecane intensity follows Stern–Volmer kinetics, as seen by the linear intensity Stern–Volmer plot (Figure 3.21, ●). Quenching of tetradecane by *n*-propanol is most likely collisional in that the Stern–Volmer quenching constant of 37 M^{-1} and the unquenched lifetime of 4.4 ns (below) result in a bimolecular quenching constant of $8.4 \times 10^9\text{ M}^{-1}\text{ s}^{-1}$. This value is near that expected for 100% efficient collisional quenching in a solvent of the viscosity of tetradecane (2.18 cP). Tetradecane and *n*-propanol do not appear to form observable exciplexes since the emission spectrum is unchanged in the presence of *n*-propanol, but future studies could alter the initial conclusion. Quenching by inner filter effects or fluorescence resonance energy transfer seems unlikely since *n*-propanol does

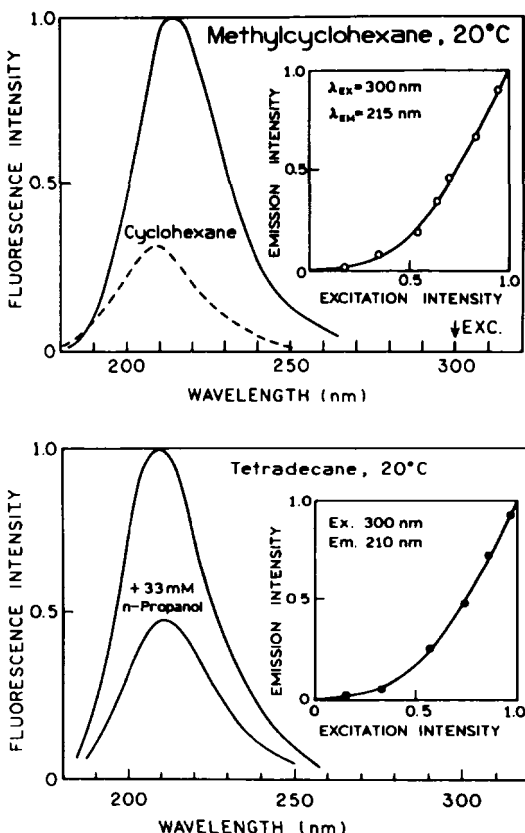


Figure 3.20. Emission spectra of cyclohexane and methycyclohexane (top) and tetradecane (bottom) with 2PE at 300 nm. Spectra for tetradecane are shown for neat tetradecane (—) and in the presence of 33 mM *n*-propanol. The inserts show the quadratic dependence on the emission, with 300-nm excitation.

not absorb significantly at the excitation (300 nm) or emission (210 nm) wavelengths.

The nature of *n*-propanol quenching can be determined by measurement of the fluorescence lifetime. Frequency-domain intensity decays of tetradecane are shown in Figure 3.22. In the absence of *n*-propanol the intensity decay is dominantly a single exponential of 4.36 ns, which accounts for 97% of the total intensity. With present instrumentation a 4.4-ns decay time can be regarded as comfortably long to allow detailed studies of factors affecting the emission of tetradecane. The presence of *n*-propanol in tetradecane results in a shift in the frequency response to higher frequencies (Figure 3.22, middle and bottom panels), which indicates a decrease in the decay time of tetradecane. The mean decay time of tetradecane decreases from 4.4 to 0.70 ns as the concentration of *n*-propanol is increased to 134 mM. The decrease in lifetime is comparable to the decrease in intensity (Figure 3.21), demonstrating that *n*-propanol quenching of

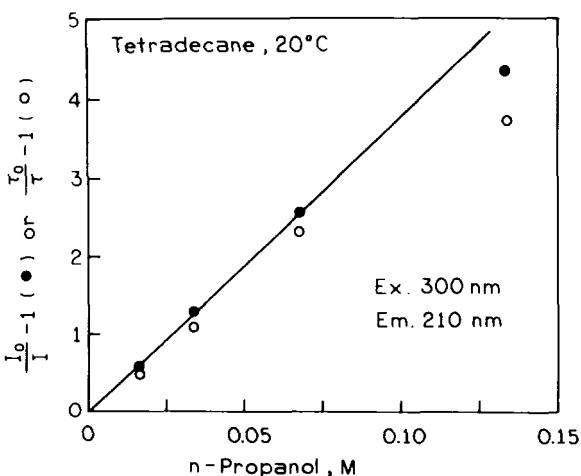


Figure 3.21. Stern–Volmer plot for quenching of tetradecane fluorescence by methanol, as observed by fluorescence intensity (I) or lifetime (τ). Reprinted from Ref. 60 with kind permission from Elsevier Science–NL, Sara Burgerhartstraat 25, 1055 KV Amsterdam, The Netherlands.

tetradecane is dynamic. Another indication of the dynamic nature of *n*-propanol quenching is the modest multi- or nonexponential decay in the presence of *n*-propanol. Such effects are known to occur due to transit effects in diffusional quenching.⁽⁶²⁾

Tetradecane fluorescence is readily quenched by dissolved oxygen.⁽⁶⁰⁾ Equilibration with air, rather than nitrogen, decreases its decay time from 4.4 to 3.0 ns (Figure 3.23). Using the known solubility of oxygen in liquid alkanes like dodecane (about 0.009 M/atm O₂)⁽⁶³⁾, the bimolecular quenching constant is $4.8 \times 10^{10} M^{-1} s^{-1}$, slightly above the diffusion-controlled limit. In previous studies⁽⁶⁴⁾ we observed oxygen bimolecular quenching constants near $2.2 \times 10^{10} M^{-1} s^{-1}$ in dodecane. The present values of $4.8 \times 10^{10} M^{-1} s^{-1}$ could be the result of absorption of oxygen at 200 nm, which could in effect increase the interaction distance for quenching due to energy transfer. Irrespective of these details, the sensitivity of alkane fluorescence to dissolved oxygen suggests that alkane fluorescence can provide an intrinsic probe of oxygen transport in membranes.

Tetradecane also appears to be collisionally quenched by water, as seen by a decrease in the decay time (not shown). The cyclic alkanes were also shown to be collisionally quenched by water and alcohols.⁽⁵⁹⁾ In recent experiments we observed two-photon-induced fluorescence of the saturated cholesterol analog cholestan,⁽⁶⁵⁾ which was also quenched by water and alcohols. Hence, it appears that alkyl groups can be regarded as intrinsic fluorophores present in all macro-

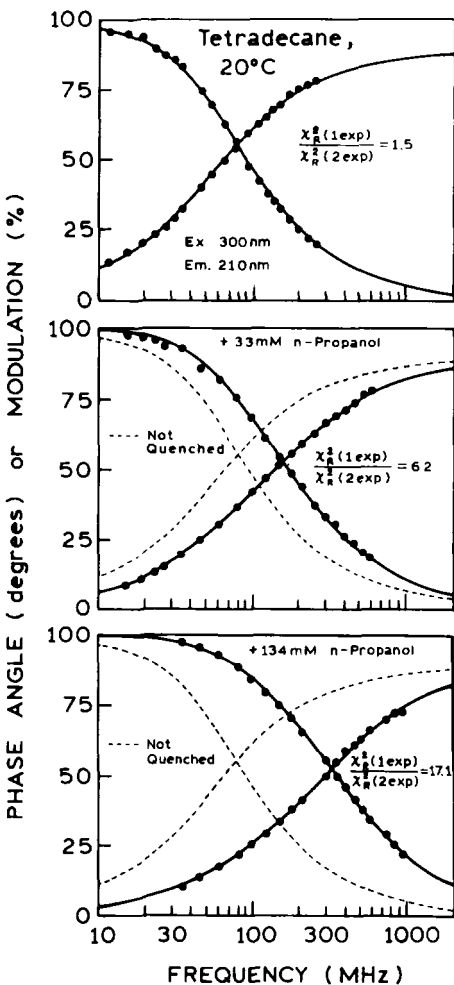


Figure 3.22. Frequency-domain intensity decays of tetradecane in the absence and presence of *n*-propanol. The solid (—) lines are the best two-exponential fits to the data. The thinner dashed line is the unquenched frequency response of MCH in the absence of *n*-propanol. Reprinted from Ref. 60 with kind permission from Elsevier Science-NL, Sara Burgerhartstraat 25, 1055 KV Amsterdam, The Netherlands.

molecules. Based on present limited knowledge, emission from alkyl groups can be expected whenever they are shielded from contact with a polar environment. It seems probable that clusters of hydrophobic amino acid side chains in proteins will be fluorescent, as will the acyl side-chain regions of membranes. Absence of alkane fluorescence would suggest the presence of polar groups or energy transfer to nearly acceptors such as carbonyl groups. Further research is needed to determine whether useful alkane fluorescence is observable from biological macromolecules.

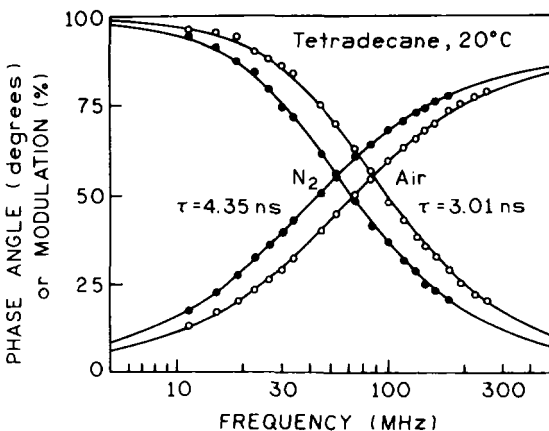


Figure 3.23. Frequency-domain intensity decay of tetradecane in the absence (●) and presence (○) of dissolved oxygen from the equilibration with air. Reprinted from Ref. 60 with kind permission from Elsevier Science-NL, Sara Burgerhartstraat 25, 1055 KV Amsterdam, The Netherlands.

3.6. Standards for 2PE

Time-resolved measurements with 2PE, particularly when combined with microscopy, are difficult and prone to error due to the need for intense excitation and the possibility of reflections and stray light. To evaluate the performance of the optical and detection system, we felt it would be valuable to have standard fluorophores which display known lifetimes and correlation times for 1PE and 2PE. We characterize the one- and two-photon-induced intensity and anisotropy decay of bis-MSB in several solvents.⁽⁶⁶⁾ Bis-MSB was described previously as a standard for two-photon absorption by Kennedy and Lytle⁽⁴⁴⁾ and was chosen for its high two-photon cross section. Fortunately, the two- (540–780 nm) and one-photon absorption spectra (270–350 nm) span the wavelengths of interest for a wide variety of intrinsic and extrinsic probes.

The emission spectra of bis-MSB were the same for 1PE and 2PE. The emission intensity was stable with continuous illumination, and bis-MSB did not appear to display significant photodecomposition or bleaching in cyclohexane, ethanol, or propylene glycol (PG). Frequency-domain intensity decay data for bis-MSB in cyclohexane are shown in Figure 3.24. The frequency responses for 1PE and 2PE are essentially identical. The intensity decay was found to be a single exponential in CH (Figure 3.24), ethanol, and PG (Table 3.4). Essentially identical lifetimes were observed for 1PE and 2PE (Table 3.4). Examination of Table 3.4 reveals that the lifetimes for 2PE are smaller to a small extent (about 50 ps) than for 1PE. At present we are uncertain

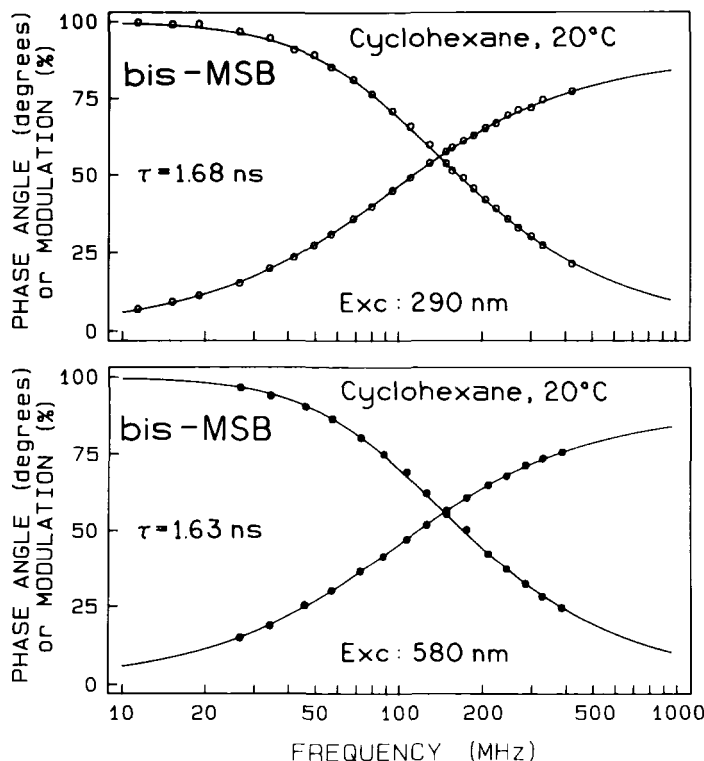


Figure 3.24. Frequency-domain intensity data for bis-MSB in cyclohexane at 20°C, obtained using 1PE (top) or 2PE (bottom). The solid lines show the best single-exponential fits to the data. Reprinted from Ref. 66 with kind permission from Elsevier Science-NL, Sara Burgerhartstraat 25, 1055 KV Amsterdam, The Netherlands.

Table 3.4. Fluorescence Intensity Decay Analysis of bis-MSB

Solvent 20°C	One-photon excitation		Two-photon excitation	
	λ_{ex} (nm)	τ (ns)	λ_{ex} (nm)	τ (ns)
Cyclohexane	290	1.68	580	1.63
Ethanol	290	1.63	580	1.63
	365	1.58	730	1.56
Propylene glycerol	290	1.51	580	1.46
	283	1.51	566	1.46
	305	1.50	610	1.45

as to the origin of this minor effect, which could be due to the well-known color effects in photomultiplier tubes (PMTs).

The steady-state and time-resolved anisotropy behavior of bis-MSB make it a suitable standard for one- and two-photon experiments. Bis-MSB displays a single rotational correlation time in CH, PG, and ethanol, and the same correlation time for one- and two-photon-induced fluorescence (Table 3.5). This allows direct comparison of the measured correlation times for a variety of experimental configurations. For instance, the one-photon correlation time measured in a standard cuvette can serve as the reference for 2PE in a time-resolved fluorescence microscope. The fact that the elongated bis-MSB molecule displays a single correlation time, and the same correlation time for 1PE and 2PE, implies that the one- and two-photon transitions are parallel and probably aligned along the long axis of the molecule. Only rotational motions which displace this axis contribute to the anisotropy decay.

The amplitudes of the bis-MSB anisotropy decays provide opportunities for comparing one- and two-photon experiments. The amplitudes for 1PE and 2PE (r_0^1 and r_0^2 , respectively) were recovered from the FD data (Figure 3.25). In all cases the differential phase angles and modulated anisotropies were larger for 2PE than for 1PE (Figure 3.25), but the shapes of the frequency responses were similar, as were the frequencies at which the differential phase angles displayed the maximal values. For collinear absorption and emission transition measurements for 1PE and 2PE, one expects $r_0^2/r_0^1 = 10/7 = 1.43$. Ratios larger than 1.43 were found for bis-MSB in CH, PG, and ethanol (Table 3.5). However, this effect was found to depend on the excitation wavelength, with the expected ratio of 1.43 being observed for excitation above 310 (620) nm. Hence, for excitation at these wavelengths, bis-MSB can be expected to display a known ratio of the amplitudes of the steady-state or time-resolved anisotropy decays. We also investigated the steady-state anisotropy spectra of bis-MSB in the absence of rotational diffusion (Figure 3.26). At wavelengths above 310 nm, the steady-state anisotropies display a ratio near 1.43 (Figure 3.26). At shorter wavelengths below 310 nm, the anisotropy of bis-MSB decreases for 1PE but

Table 3.5. Anisotropy Decay Analyses of bis-MSB Fluorescence

Solvent 20°C	One-photon excitation			Two-photon excitation			
	λ_{ex} (nm)	r_0	θ (ns)	λ_{ex} (nm)	r_0	θ (ns)	r_0^2/r_0^1
Cyclohexane	290	0.304	0.130	580	0.509	0.121	1.67
Ethanol	290	0.301	0.129	580	0.517	0.125	1.72
	365	0.373	0.117	730	0.537	0.114	1.44
Propylene glycol	290	0.299	4.41	580	0.516	4.40	1.73
	283	0.262	4.45	566	0.508	4.49	1.94
	305	0.342	4.39	610	0.522	4.45	1.53

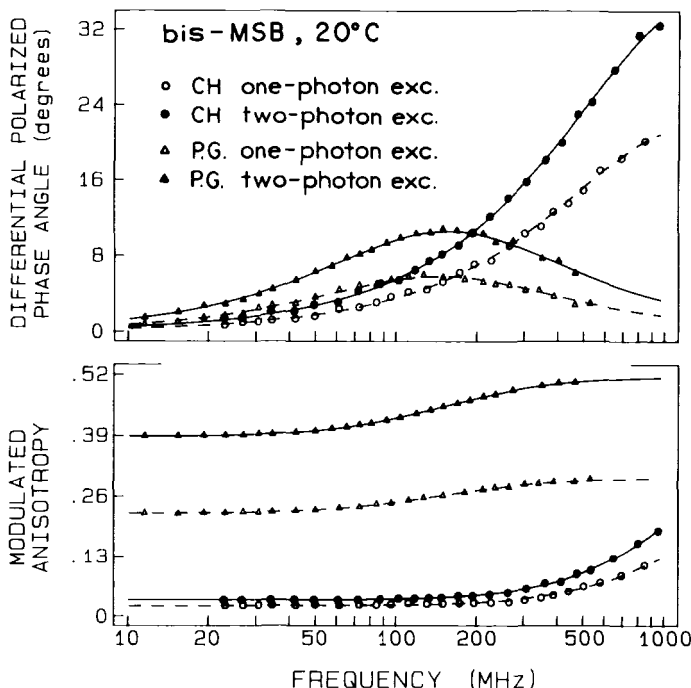


Figure 3.25. Frequency-domain anisotropy decays data for bis-MSB in cyclohexane (\circ , \bullet) and propylene glycol (Δ , \blacktriangle) at 20°C , resulting from 1PE (\circ , Δ) and 2PE (\bullet , \blacktriangle). Reprinted from Ref. 66 with kind permission from Elsevier Science-NL, Sara Burgerhartstraat 25, 1055 KV Amsterdam, The Netherlands.

remains high for 2PE. Apparently, a second transition contributes to the one-photon absorbance at 300 nm, but the two-photon absorbance from 280 (560) to 370 (740) is due to a single transition. This result seems to be consistent with the one- and two-photon absorption spectra of bis-MSB, reproduced from Ref. 44 as the insert in Figure 3.26. This spectrum shows that the two-photon absorption spectrum is distinct from the wavelength-shifted one-photon spectrum. Concurrently, bis-MSB displays a constant anisotropy for 2PE from 570 to 750 nm.

3.6.1. A ps Two-Photon Standard

While bis-MSB is a useful two-photon standard, it is occasionally useful to have a standard with a shorter decay time. Kawski and co-workers⁽⁶⁷⁾ identified the highly favorable properties of 4-dimethylamino- ω -diphenylphosphenyl-

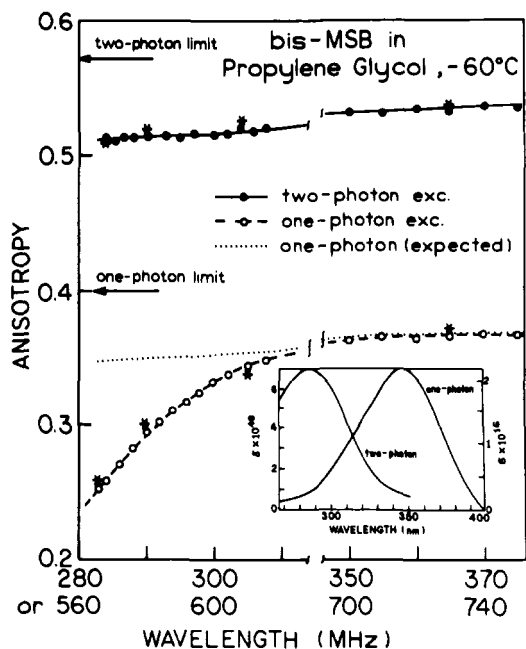


Figure 3.26. Steady-state anisotropy spectrum of bis-MSB in propylene glycol at -60°C measured with 1PE (\circ) and 2PE (\bullet). The dotted line (···) is the 1PE anisotropy spectrum predicted for collinear transition moments from the one-photon anisotropy spectrum. The asterisks (*) are anisotropies at $t=0$, obtained from time-resolved measurements. Reprinted from Ref. 66 with kind permission from Elsevier Science-NL, Sara Burgerhartstraat 25, 1055 KV Amsterdam, The Netherlands. The insert shows the one- and two-photon absorption spectra reproduced from Ref. 44 with kind permission from American Chemical Society.

trans-styrene (DPPS). Emission spectra (Figure 3.27) are the same for 1PE and 2PE. A favorable property of DPPS is its nearly constant anisotropy with 2PE from 685 to 760 nm (Figure 3.28). Additionally, the anisotropy in butanol is high and near the limiting anisotropy independent of temperature from 20 to 80°C (Figure 3.29). The high anisotropy in this fluid solvent is because of the short decay time (Table 3.6). The decay time decreases with increasing temperature in a manner which results in an anisotropy which is essentially independent of temperature (Figure 3.29 and Table 3.7).

The availability of a two-photon lifetime and anisotropy standards should be useful in future two-photon experiments. For instance, most phototubes have decreased or no sensitivity above 600 nm. Consequently, it is difficult to perform time- or frequency-domain measurements with 2PE because of the inability to measure a light-scattering reference. This problem of detecting the reference scattered light may become more troublesome with the larger excitation wavelengths from Ti:sapphire lasers and/or for 3PE. Bis-MSB or DPPS can be used to convert the red-wavelength excitation to visible emission with known decay-time characteristics. Lifetime measurements may then be carried out by using the reference corrections described for the time⁽⁶⁸⁾ and frequency domains.⁽⁶⁹⁾ Additionally, the one- and two-photon anisotropy values observed for DPPS can be used to determine and/or correct for the effect of

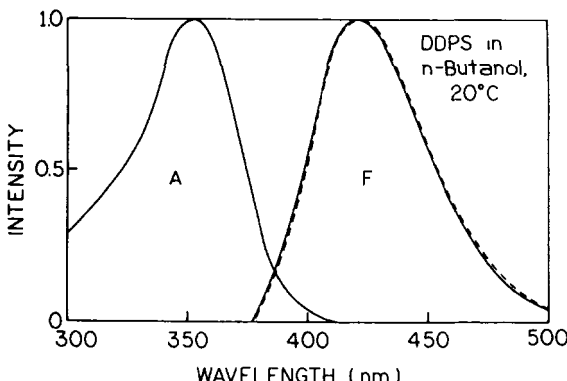


Figure 3.27. Normalized absorption and fluorescence of DDPS in *n*-butanol at 20°C with 1PE (—), $\lambda_{\text{exc}} = 365$ nm, and 2PE (---), $\lambda_{\text{exc}} = 730$ nm. Reprinted from Ref. 67 with kind permission from Verlag der Zeitschrift für Naturforschung.

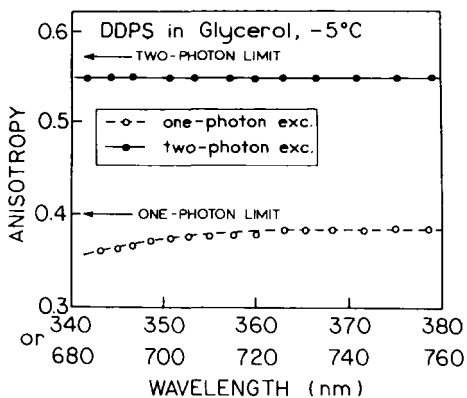


Figure 3.28. Steady-state fluorescence anisotropy spectrum of DDPS in glycerol at -5°C. The arrows indicate maximal values of 2/5 for 1PE and 4/7 for 2PE. Reprinted from Ref. 67 with kind permission from Verlag der Zeitschrift für Naturforschung.

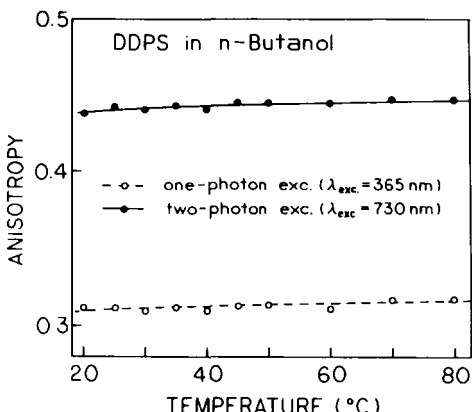


Figure 3.29. Steady-state fluorescence anisotropy of DDPS in *n*-butanol vs. temperature, measured with 1PE and 2PE. Reprinted from Ref. 67 with kind permission from Verlag der Zeitschrift für Naturforschung.

Table 3.6. Phase, Modulation, and Lifetimes of DDPS in *n*-Butanol at Different Temperatures

T (°C)	Frequency (MHz)	Phase (degree)	τ_p (ps) ^a	Modulation	τ_m (ps) ^a
20	4087.2	39.6	32	0.775	32
25	4254.2	39.1	30	0.780	30
30	4975.3	40.1	27	0.768	26
35	5400.3	38.9	24	0.777	24
40	5908.8	39.7	23	0.771	22
45	6493.3	39.2	20	0.780	19
50	7677.3	38.8	17	0.789	16
60	8466.6	37.1	14	0.802	14
70	9438.2	37.9	13	0.800	13
80	9438.2	35.3	12	0.822	12

^a Decay time calculated from the phase (p) or modulation (m) values assuming a single exponential decay.

Table 3.7. Steady-State Anisotropy of the DPPS Fluorescence in *n*-Butanol at Different Temperatures for One- and Two-Photon Excitation⁹

T (°C)	η^a (10 ⁻³ Pa•s)	Emission anisotropy		
		r_1 1PE $\lambda_{exc} = 365$ nm	r_2 2PE $\lambda_{exc} = 730$ nm	r_2/r_1
20	2.948	0.311	0.438	1.408
25		0.312	0.443	1.420
30	2.300	0.308	0.441	1.432
35		0.312	0.444	1.423
40	1.782	0.309	0.442	1.430
45		0.311	0.447	1.437
50	1.411	0.313	0.446	1.425
60		0.309	0.445	1.440
70	0.930	0.318	0.449	1.412
80		0.318	0.452	1.421

^a From *Handbook of Chemistry and Physics*, CRC Press, Boca Raton, FL, 1967.

wide-aperture microscope objectives on the measured anisotropy values.⁽⁷⁰⁾ And finally, we note that other fluorescent molecules may display unusual anisotropy spectra for 2PE, as observed for indole. Hence, it will be valuable to have a two-photon reference molecule to exclude instrumental effects or other artifacts in the two-photon measurements.

3.7. Three-Photon Excitation of Fluorescence

The 2PE experiments described above were performed using cavity-dumped dye lasers with pulse widths near 5 ps. Observation of two-photon-induced fluorescence with such lasers is surprising, as conventional wisdom suggested that fs lasers were needed for 2PE. We recently received a fs Ti:sapphire laser which provides pulse widths near 80 fs from 700 to 950 nm. Using this laser, we made the surprising observation of 3PE for a variety of fluorophores and biochemical probes. Remarkably, the intensity is not orders of magnitude weaker than for 2PE and is typically 50- to 100-fold less intense. An advantage of 3PE is that it can be accomplished with the fundamental output of a Ti: sapphire laser near the peak of its tuning range. To date, 3PE has been observed for scintillator-type fluorophores,⁽⁷¹⁻⁷³⁾ for DPH in membranes,⁽⁷⁴⁾ for the calcium probe Indo-1,^(79,80) and for the tryptophan derivative NATA.⁽⁷⁷⁾ Three-photon excitation has also been used for imaging of stained beads in fluorescence microscopy.⁽⁷⁸⁾ Hence, it appears that the phenomena of MPE can become a general tool in biochemical spectroscopy.

3.7.1. Three-Photon Excitation of 2,5-Diphenyloxazole

Emission spectra of 2,5-diphenyloxazole (PPO) are shown in Figure 3.30 for 1PE at 290 nm and for 3PE at 870 nm. These emission spectra were obtained from the same solution of PPO, using the same instrument, the only difference

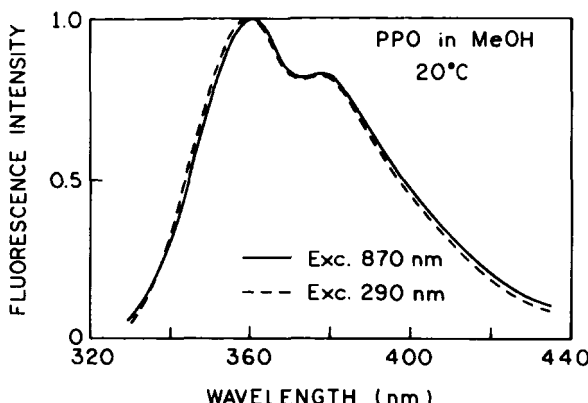


Figure 3.30. Emission spectra of PPO in methanol at 20°C for 1PE and 3PE. $[PPO] = 5 \times 10^{-4} M$. Reprinted from Ref. 71 with kind permission from Elsevier Science-NL, Sara Burgerhartstraat 25, 1055 KV Amsterdam, The Netherlands.

being the excitation wavelength. The emission spectra are essentially identical for both modes of excitation. Since the absorption of PPO is essentially zero above 350 nm, it seems unlikely that this emission could result from 2PE, which would require excitation wavelengths below 700 nm.

Observation of three-photon-induced fluorescence is unusual, and one must be careful to exclude alternative explanations. To clarify the nature of the excitation process, we examined the effect of laser power on the observed intensity of PPO. We found that the emission intensity of PPO depended on the third power of the incident power (Figure 3.31). In this experiment the emission intensity closely followed P^3 , where P is the laser power (Figure 3.31). The observed dependence could not even be closely approximated by P^2 , which is the expected and observed⁽⁷⁻¹⁰⁾ dependence for 2PE.

As shown for 2PE, the time-zero anisotropy is characteristic of the nature of the excitation photoselection. We examined the anisotropy of PPO in the absence of rotational diffusion, in glycerol at -5°C, where rotation does not occur during the excited-state lifetime. The measured anisotropy for 3PE is higher than for 1PE or 2PE (Figure 3.32), and higher than the limit of 0.57 for two-photon-induced

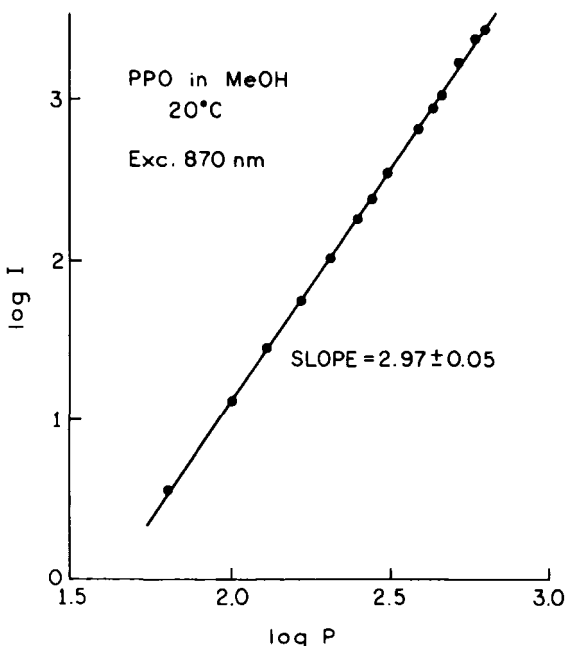


Figure 3.31. Dependence of the emission intensity of PPO on laser power (in mW). The maximum power at 870 nm was 600 mW.

fluorescence with collinear transitions. The wavelength-dependent steady-state anisotropies appear to be independent of excitation wavelength from 850 to 885 nm (Figure 3.32). While a modest change with wavelength is seen for 1PE and 2PE, the anisotropy is independent of wavelength for 3PE.

The extent to which the excitation follows $\cos^2 \theta$, $\cos^4 \theta$, or $\cos^6 \theta$ photoselection can be estimated from the ratio of the anisotropies for 1PE, 2PE, or 3PE. For collinear transitions the expected ratios are $r_{02}/r_{01} = 1.429$ and $r_{03}/r_{01} = 1.667$. With r_{0i} values for PPO (Figure 3.32) the ratios are 1.442 and 1.752, respectively. These results suggest that the anisotropy values of PPO are closely approximated by $\cos^4 \theta$ and $\cos^6 \theta$ photoselection for 2PE and 3PE, respectively, as shown schematically in Figure 3.33.

Although not shown, the same single exponential lifetime and anisotropy decay time were observed for 1PE, 2PE, and 3PE.⁽⁷¹⁾ Similar results were obtained for *p*-quarterphenyl⁽⁷²⁾ and 2,5-bis(4-biphenyl)oxazole.⁽⁷³⁾ Hence, it appears that 3PE can be accomplished without undesired photochemical or photothermal effects on the fluorophores.

3.7.2. Three-Photon Excitation of DPH in Membranes

It was of interest to examine DPH in membranes for the possibility of 3PE. Given the dependence of the apparent phase transition temperature on local

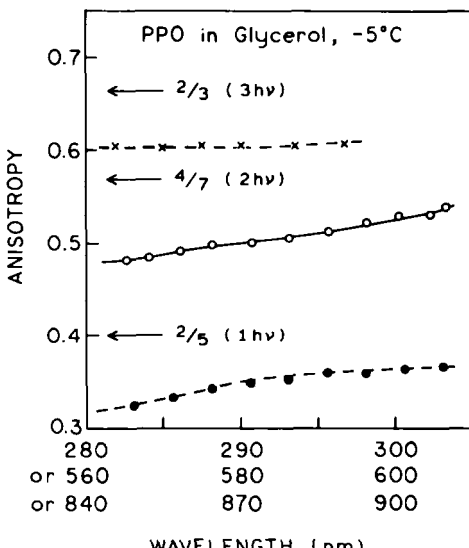


Figure 3.32. Excitation anisotropy spectrum of PPO in glycerol at -5°C , for 1PE, 2PE, and 3PE. Reprinted from Ref. 71 with kind permission from Elsevier Science-NL, Sara Burgerhartstraat 25, 1055 KV Amsterdam, The Netherlands.

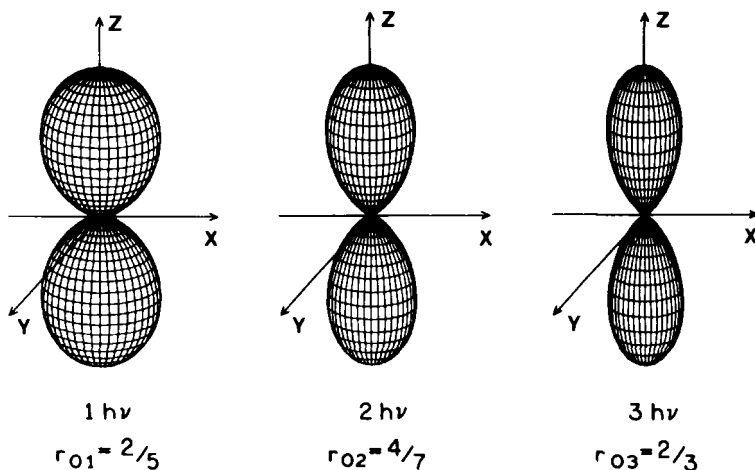


Figure 3.33. Orientation distribution of the excited-state population for 1PE, 2PE, and 3PE. The values in the figure (r_0) are the maximum values for collinear transitions. Reprinted from Ref. 71 with kind permission from Elsevier Science-NL, Sara Burgerhartstraat 25, 1055 KV Amsterdam, The Netherlands.

heating, this system could indicate whether 3PE could be useful with biochemical samples. We found that DPH displayed $\cos^2 \theta$, $\cos^4 \theta$, and $\cos^6 \theta$ photoselection for 1PE, 2PE, and 3PE, respectively.⁽⁷⁴⁾ Additionally, the DPH-labeled membranes displayed the same intensity decay time, anisotropy decay, and phase transition temperature for all modes of excitation, and DPH displayed one of the weaker three-photon signals we have observed. These results suggest that 3PE can be observed in biochemical systems without adverse effects due to the locally intense illumination. However, we have found it necessary to stir most samples being used for 3PE, as the signals decreased with continued illumination. At present we do not understand the nature of these effects of illumination.

3.7.3. Three-Photon Excitation of the Calcium Probe Indo-1

In recognition of the importance of calcium imaging in cell physiology and the growing availability of laser scanning microscope for 2PE, we examined the possibility of 3PE of Indo-1.^(79,80) Emission spectra of Ca^{2+} -free Indo-1 are shown in Figure 3.34 for excitation at 820 and 885 nm. The emission spectra are identical for both excitation wavelengths and are identical to that observed for 1PE with 351-nm excitation. We examined the nature of the long-wavelength excitation by attenuating the peak laser power using neutral density filters. A

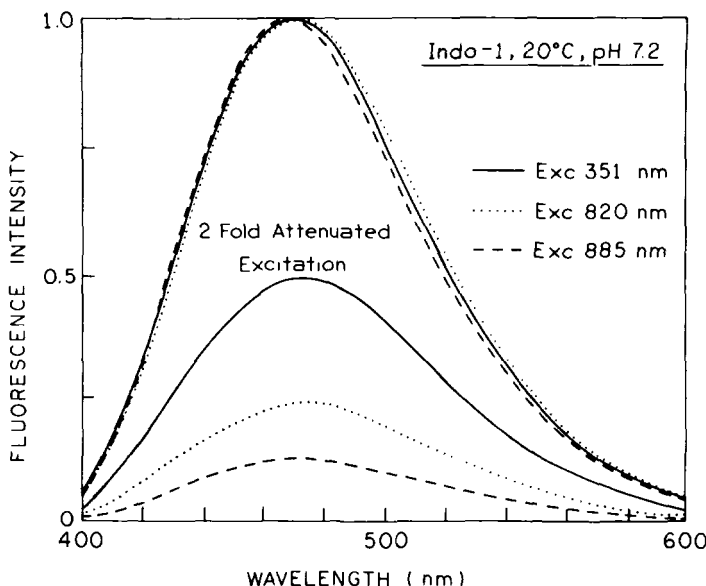


Figure 3.34. Emission spectra of Indo-1 for excitation at 351, 820, and 885 nm. Also shown are the emission spectra for each excitation wavelength with a twofold attenuation of the incident light using a neutral density filter. Reprinted from Ref. 79 with kind permission from the American Society for Photobiology.

twofold attenuation of the incident light for 351-nm excitation results in a twofold attenuation of the emission (Figure 3.34). For 820-nm excitation a twofold attenuation results in a fourfold decrease in the emission of Indo-1, suggesting 2PE. At 885-nm excitation a twofold decrease in the incident intensity results in an eightfold decrease in the signal from Indo-1. This dependence on the square and cube of the laser power suggests that the emission is due to 3PE at 885 nm.

We examined the dependence of Indo-1 emission on laser power (Figure 3.35). The emission intensity at 885-nm excitation was found to be almost exactly dependent on the cube of the peak laser power, strongly suggesting that the emission is due to simultaneous absorption of three 885-nm photons. When using 885-nm excitation, we could not observe any signal from the sample or the buffer blank at the third harmonic of 295 nm, indicating that Indo-1 is not being excited by any third harmonic which might have been generated by the sample or the cuvette. In addition, a harmonic generation in the sample also appears unlikely in that 410- or 443-nm light was not apparent in the emission spectra of Indo-1 (Figure 3.34), and second-harmonic generation is unlikely in isotropic media.

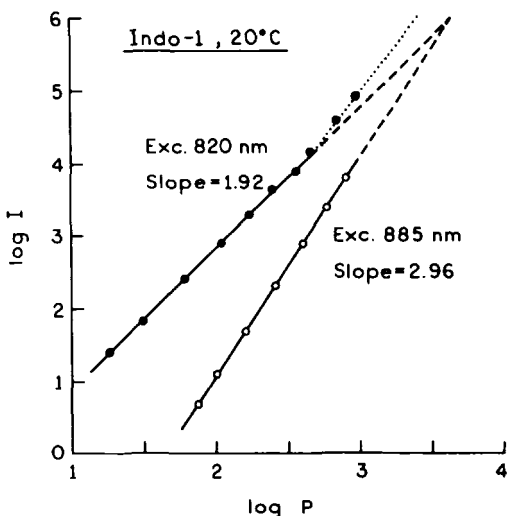


Figure 3.35. Dependence of the emission intensity of Indo-1 on laser power at 820 and 885 nm. The dotted line at 820 nm shows the slope at higher laser power. The laser power is in mW. Reprinted from Ref. 79 with kind permission from the American Society for Photobiology.

For excitation at 820 nm the emission of Indo-1 depends on the square of the laser power (Figure 3.35), suggesting that 2PE is dominant at this wavelength. However, at the highest laser power at 820 nm the slope of the line changes to larger than 2 (Figure 3.35), indicating a mixture of 2PE and 3PE.

To further demonstrate the presence of 3PE, we examined the steady-state anisotropy of the Indo-1 emission. The steady-state anisotropies of Indo-1 are shown in Figure 3.36. The anisotropy was found to be independent of laser power at 820- and 885-nm excitation and at 351 nm (not shown). This result suggests that the sample is not being heated by the focused excitation. Importantly, the anisotropy is significantly higher for 3PE at 885 nm than for 2PE at 820 nm. This result is consistent with the more highly oriented photoselective population expected for simultaneous interaction with 3PE when the absorption and emission oscillators are collinear (Figure 3.33).

We made a surprising observation for the anisotropy of Indo-1 for excitation at 840 nm. At this wavelength the anisotropy of Indo-1 is seen to depend on the laser power (Figure 3.36). A similar dependence can be expected for 820-nm excitation at higher laser power. These results imply that the mode of excitation, two- or three-photon absorption, can depend on the particular experimental arrangement, peak power, and extent of focusing. Additionally, the power-dependent anisotropies observed at 840 nm (Figure 3.36) indicate that the anisotropy with MPE is not an absolute molecular quantity, but depends on the laser peak power. The dependence of the anisotropy on the experimental conditions must be considered in anisotropy measurements with MPE.

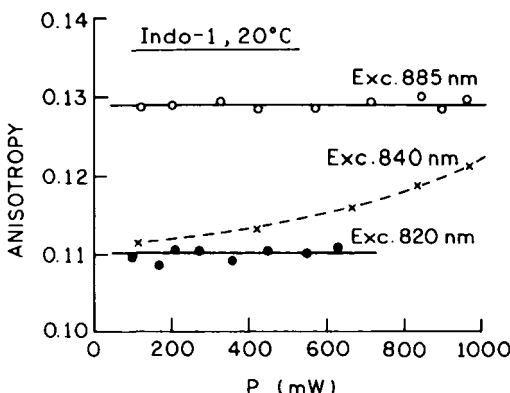


Figure 3.36. Dependence of the emission anisotropy of Indo-1 on laser power at 820, 840, and 885 nm. Reprinted from Ref. 79 with kind permission from the American Society for Photobiology.

Calcium-dependent emission spectra of Indo-1 are shown in Figure 3.37 for 1PE, 2PE, and 3PE at 295, 590, and 885 nm, respectively. These wavelengths were selected to be consistent with 1PE, 2PE, and 3PE of Indo-1 when the one-photon wavelength is 295 nm. The poorer quality of the spectra for 590-nm excitation is due to our use of a ps dye laser as the excitation source, whereas the fs Ti:sapphire was used for 885-nm excitation. Since the signal intensity depends on the square or cube of the peak laser power, one expects significantly smaller signals using ps rather than fs pulses.

For 295-nm excitation the emission is dominated by the Ca^{2+} -bound form of Indo-1 (Figure 3.37). For 885-nm excitation, there is much less emission from the Ca^{2+} -bound form for comparable concentrations of Ca^{2+} . To obtain emission from only the Ca^{2+} -bound form of Indo-1 for 885-nm excitation, we used a higher Ca^{2+} concentration of $250 \mu\text{M}$. These results suggests that the relative cross section for 3PE of Indo-1 is less for the Ca^{2+} -bound form, as compared to the selective cross sections for 1PE. Of course, the three-photon cross sections are likely to depend on excitation wavelength, so that one expects the wavelength-ratiometric calibration to be different for different modes of excitation. This point is illustrated by the emission spectra observed for 590-nm excitation, which are intermediate between the one- and three-photon-induced emission spectra. Importantly, the emission spectra for 885-nm excitation rules out excitation of Indo-1 by the third harmonic at 295 nm. If this occurred, the spectra would be identical to those observed at 295-nm excitation. The observation of different relative intensities for a mixture of fluorescent species for 1PE and 3PE can be regarded as evidence against third-harmonic generation in the sample and 1PE by this harmonic.⁽⁸¹⁾

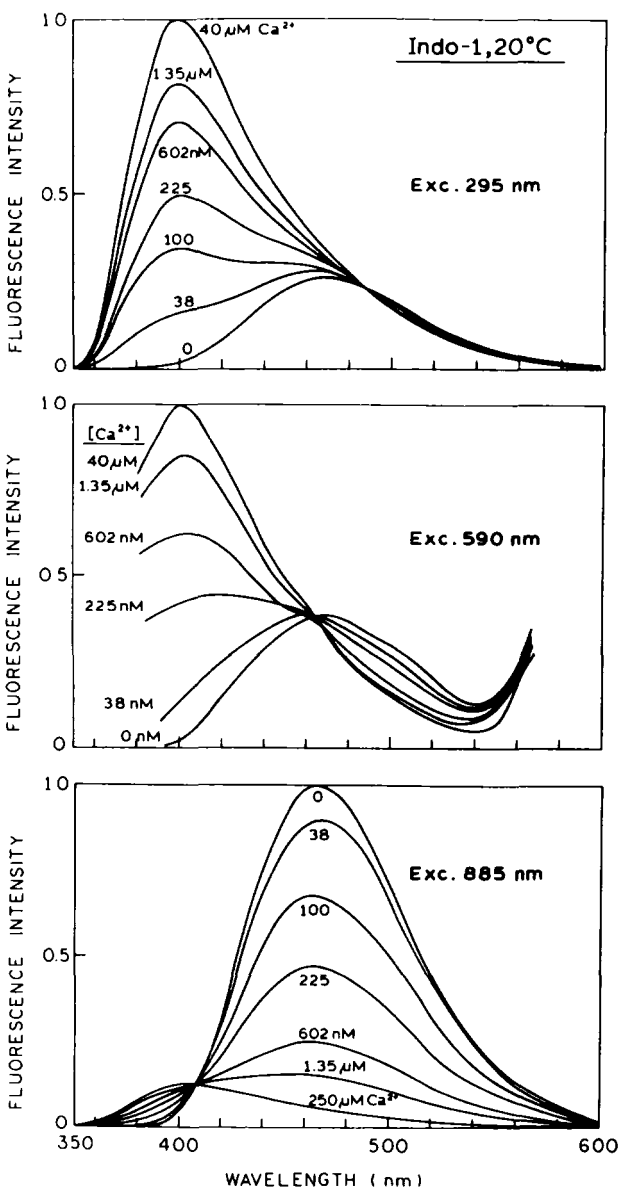


Figure 3.37. Calcium-dependent emission spectra of Indo-1 for 1PE, 2PE, and 3PE at 295, 590, and 885 nm, respectively. Reprinted from Ref. 80 with kind permission from the Biophysical Society.

3.7.4. Three-Photon Excitation of Tryptophan and Proteins

At present Ti:sapphire lasers are the lasers of choice for 2PE in fluorescence microscopy. However, the lower wavelength limit of the Ti:sapphire tuning range near 700 nm precludes 2PE of proteins. However, we recognized that 3PE of tryptophan could allow observations of protein fluorescence with a Ti:sapphire excitation source.⁽⁷⁷⁾ For the initial studies we chose *N*-acetyl- L-tryptophanamide (NATA). Emission spectra are shown in Figure 3.38 for 1PE (280) and 3PE (840 nm).

We were surprised by the ability to observe NATA emission with 840-nm excitation. In previous studies we observed excitation of tryptophan and proteins with excitation near 600 nm, which was found to be due to 2PE.^(22,23) However, 2PE is not expected to occur for wavelengths longer than twice the single-photon wavelength, above which there is insufficient energy in 2PE to elevate NATA to the first singlet state. In the case of tryptophan, 2PE is improbable above 620 nm.

We examined the dependence of the emission intensity of NATA on laser power at 840 nm (Figure 3.39). The emission intensity was found to depend on the cube of the laser power both in water and in glycerol–water (30:70). We considered the possibility that NATA was being excited by the third harmonic of the 840-nm light generated by the solution or the optical components. Under the experimental conditions in Figures 3.38 and 3.39, we could detect no light at 280 nm. These results suggest that NATA is being excited by the 840-nm light by a three-photon process.

To further characterize the emission of NATA with long-wavelength excitation, we examined the intensity decays using the frequency-domain method. Precisely the same decay time for NATA was observed for excitation at 280 and 840 nm (not shown). Heating of the sample by the intense 840-nm excitation is expected to reduce the decay time of NATA. Hence, the similarity of the decay times suggest that the sample is not being significantly heated.

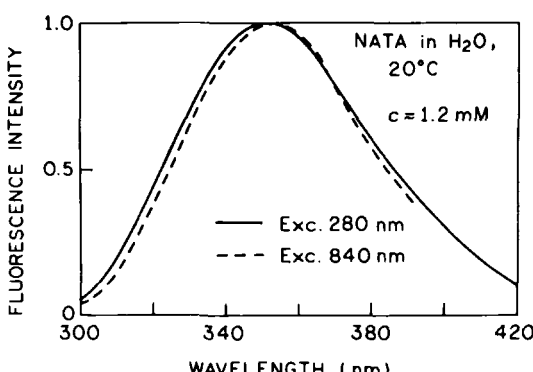


Figure 3.38. Emission spectra of NATA in water for excitation at 280 and 840 nm. Reprinted from Ref. 77 with kind permission from John Wiley & Sons.

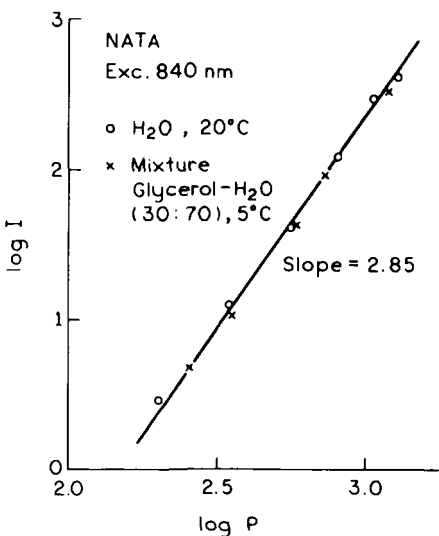


Figure 3.39. Effect of laser power at 840 nm in the emission intensity of NATA in water and glycerol–water (30:70, v/v). Reprinted from Ref. 77 with kind permission from John Wiley & Sons.

Time-domain anisotropy decay data for NATA in glycerol–water are shown in Figure 3.40. One notices that the anisotropies are positive for 280-nm excitation and negative for 840-nm excitation (Figure 3.40). The data were used to calculate the rotational correlation time (θ_R) and time-zero anisotropy (r_{01} and r_{03}) for 1PE and 3PE, respectively. The correlation times were identical, again indicating the absence of significant heating. However, the time-zero anisotropy is positive for 280-nm excitation ($r_{01} \approx 0.13$) and negative for 840-nm excitation ($r_{03} \approx -0.07$), which indicates a different direction for the electronic transition(s) for 1PE and 3PE.

3.7.5. Perspectives on 3PE

Three-photon excitation has a number of potential advantages in time-resolved fluorescence and fluorescence microscopy. The fundamental output of Ti:sapphire lasers is most intense from 800 to 900 nm, which is suitable for 3PE of UV-absorbing fluorophores potentially including the intrinsic fluorescence of proteins. The Ti:sapphire fundamental wavelengths are above the absorption bands of most biological chromophores, suggesting that the amounts of auto-fluorescence will be minimal for 3PE. Furthermore, these wavelengths are below the absorption bands of water, suggesting that the biological samples will not be excessively heated by 800–900 nm illumination. An additional advantage of these excitation wavelengths is that they are poorly detected by most PMTs,

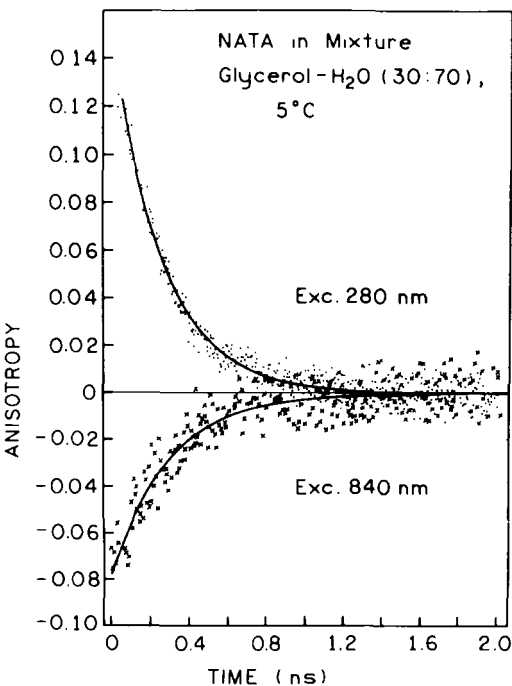


Figure 3.40. Time-domain anisotropy decay of NATA in glycerol-water (30:70, v/v) for excitation at 280 nm and 840 nm. Reprinted from Ref. 77 with kind permission from John Wiley & Sons.

and PMTs without significant sensitivity above 600 nm are readily available. Hence, experimental problems due to stray or scattered excitation should be easily minimized with 3PE.

A further advantage of 3PE is the smaller excited volumes. In 2PE the absence of signal from outside the focal region has been used to avoid out-of-focus signal.⁽⁸²⁻⁸⁶⁾ By visual comparison of the emission from cuvettes containing fluorophores which display 2PE or 3PE, we have observed that the emission is seen from a smaller area for 3PE. This indicates that higher spatial resolution in laser scanning microscopy can be obtained by 3PE. One can also predict improved contrast in pattern photobleaching with evanescent-wave illumination, as calculated for 2PE.⁽⁷⁵⁾

In recent publications we have shown that under conditions of 2PE the emission can be simultaneously quenched by the excitation pulse.^(76,87,88) Light quenching depends on overlaps of the emission spectrum of the fluorophore with the excitation wavelength, which is a common occurrence with 2PE. However, with 3PE the wavelengths are generally longer than those of the emission spectra, so the intense pulses are not likely to cause light quenching. The use of 3PE may prevent light quenching in laser scanning confocal microscopy with 2PE where

the intensely focused excitation can overlap with the emission spectra of the fluorophores.

3.8. Two-Color Two-Photon Excitation

In all the experiments described, the fluorophores absorbed two or three photons from the same laser beam. Hence, the photons had the same wavelength and polarization. A different type of 2PE is also possible, in which the fluorophore absorbs two photons of different wavelengths and/or polarizations. Such measurements are technically more demanding because one must adjust the location and timing of two laser beams so that the pulses overlap at the focal point of the optic within the sample. Until recently, only two-color two-photon (2C2P) absorption has been observed, and these experiments were done with ruby lasers and arc lamp illumination.⁽⁸⁹⁻⁹³⁾

We recently examined the possibility of 2C2P excitation using a ps dye laser. For these experiments we used the fundamental (760 nm) and frequency-doubled (380 nm) output of a pyridine 2 dye laser. For 2,5-diphenyl-1,3,4-oxadiazole (PPD) we observed⁽⁹⁴⁾ emission when both wavelengths were present (Figure 3.41) and much less emission for only 380- or 760-nm illumination (Figure 3.42). The emission spectrum revealed that the signal was due to PPD (Figure 3.42). This spectrum was identical to that observed for 250-nm illumination, which provides energy approximately equivalent to 360 and 760 nm. Upon simultaneous illumination with both wavelengths no signal could be observed at 253 nm, suggesting the absence of any unwanted generation of 253-nm excitation within the sample itself.

It was of interest to determine how the 2C2P signal depended on the intensity of each laser beam. If the 380- and 760-nm beams were simultaneously attenuated with neutral density filters, the 2C2P signal depended quadratically on intensity (Figure 3.43). This result indicates that two photons are involved in the excitation process. If each beam is separately attenuated the 2C2P signal depends linearly on the intensity of each beam (Figure 3.43), indicating the involvement of one photon from each beam in the excitation process. Hence, at least for the present fluorophore and wavelengths, the origin of the excitation energy seem clear. In the future one can expect more complex behavior if each beam is capable of MPE of the fluorophore.

For our initial studies of 2C2P excitation both beams were vertically polarized. However, for 2C2P excitation the polarization of each beam can be independently varied. Hence, it was of interest to examine the effects of rotating the electric vector of either beam (Figure 3.44). We found that the 2C2P signal varied approximately as a cosine function, with maximal signal for parallel 380-

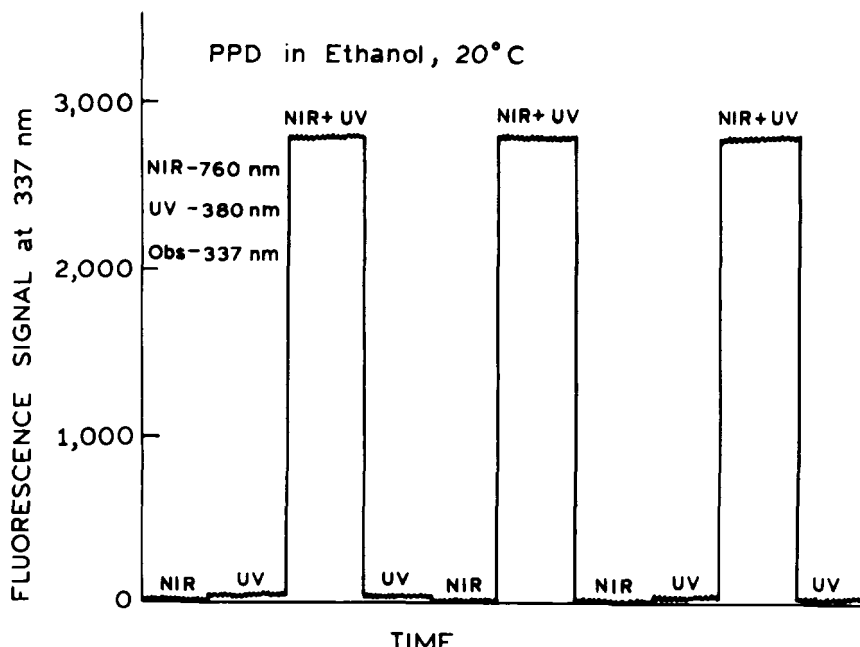


Figure 3.41. Emission intensity of PPD in ethanol with near-infrared (760 nm), UV (380 nm), and temporally overlapped 380- and 760-nm pulses.

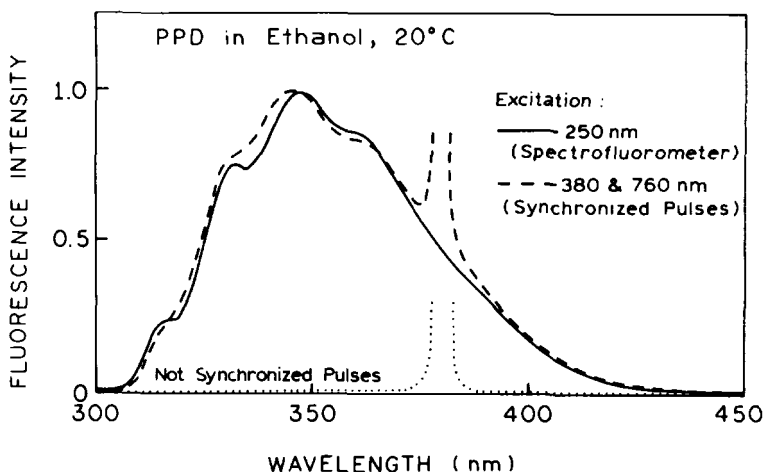


Figure 3.42. Emission spectra of PPD in ethanol with 250-nm excitation (one-photon) and with 2C2P excitation at 380 and 760 nm. The dotted line shows the signal with nonoverlapping pulses at 380 and 760 nm.

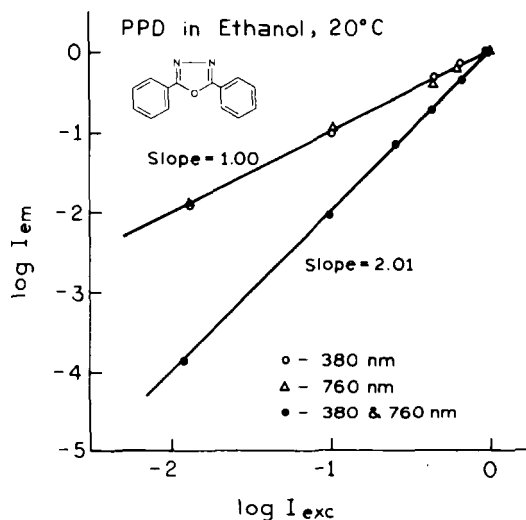


Figure 3.43. Dependence of the normalized emission intensity on the excitation intensity for each wavelength at 380 or 760 nm (\circ , Δ), and for the total intensity at 380 and 760 nm (\bullet).

and 760-nm beams and minimum signal for perpendicular beams. It did not matter which beam was rotated. However, unlike a cosine function the 2C2P signal did not go to zero for perpendicularly polarized beams (Figure 3.44), but the minimal value was about one third of the maximum value. These results seem to be consistent with the virtual electronic transitions at 380 and 760 nm being collinear in the PPD molecule. The value of one third for perpendicular beams can be understood as the projection of a $\cos^2 \theta$ distribution onto a perpendicular axis,⁽⁹⁵⁾ where θ is the angle between the polarized excitation and the electronic transition moment in the fluorophore.

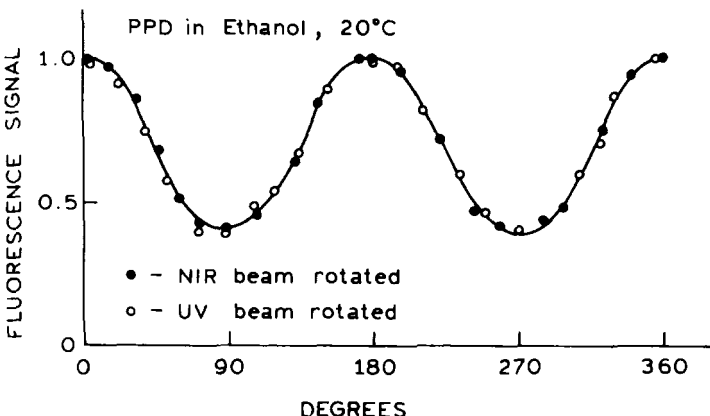


Figure 3.44. Effect of polarization angle of the 380- and 760-nm beams on the 2C2P signal.

Two-color 2PE has considerable potential in chemical and biochemical spectroscopy. It is not limited to PPD, but has also been observed for *p*-terphenyl⁽⁹⁶⁾ and indole.⁽⁹⁷⁾ At the most basic level the use of two excitation beams provides independent control of the wavelength, polarization, intensity, and pulse width of the two excitation beams. Previous reports have indicated that additional information is available about the symmetry of excited states from experiments with different polarization,^(92,93) and that the anisotropy decays may be distinct with 2C2P and 1C2P excitation.^(38,39) Additionally, control of the intensity or wavelength of each beam may provide an ability to decrease unwanted background signals. Control of each wavelength provides an opportunity to measure new types of excitation and excitation anisotropy spectra in which one wavelength is held constant while the other is varied. It is possible that some transitions or anisotropy values will be observed with 2C2P excitation which are not accessible with one-color measurements.^(92,98) For instance, in 2C2P excitation one can independently control the polarization of each photon, which can be expected to result in an excited-state population that is not symmetric about the *z*-axis. At present we do not know what to expect from such experiments, which represent a new class of fluorescence spectral data.

Another opportunity of 2C2P excitation is the ability to localize the excited volume at the desired point by overlap of the excitation beam. This feature of 2C2P excitation can be advantageous in analytical chemistry and fluorescence microscopy. For instance, in capillary electrophoresis the excitation can be localized at the desired position and thereby minimize the background signal from optical elements or the sample volume. In favorable circumstances it may be possible to vary the wavelengths or intensities of the excitation beams to result in minimal background from interfering substances. These potential advantages of 2C2P excitation seem equally valuable in fluorescence microscopy, where the overlapped beams can provide localized excitation in a manner comparable to confocal methods.⁽⁹⁹⁾

In previous reports we described the use of light pulses, with wavelengths overlapping the emission spectra, to modify the excited-state population, orientation, and emission spectra of fluorophores.⁽¹⁰⁰⁻¹⁰²⁾ This phenomenon, which we call light quenching, has been applied to fluorescence microscopy.^(103,104) In Ref. 104 the authors describe the use of a modulated signal when the light-quenching pulses are at a repetition frequency offset from the excitation pulse rate. One can readily imagine the use of 2C2P excitation in an analogous manner, in which the signal arises from the region of beam overlap. An advantage of 2C2P excitation in microscopy, as compared to "a synchronous pump-probe microscopy,"⁽¹⁰⁴⁾ is the appearance of a signal against a dark background. In pump-probe microscopy⁽¹⁰⁴⁾ the modulated signal appears against the bright background of the excited fluorophore.

The study of 2C2P excitation is just beginning. One can expect rapid development of the understanding and applications of this phenomenon.

3.9. Future Applications of MPE

Until the past several years 2PE, 3PE, or MPE were regarded as exotic topics with minimal applications outside of molecular spectroscopy. Hence, in spite of the recent activity in MPE the range of applications is still to be explored. At present we can imagine applications of MPE to biophysics, cell biology, and clinical sensing.

In the application of time-resolved fluorescence one is often hindered by the intrinsic absorbance of interfering species. Such interference occurs in studies of fluorescence quenching when the quenchers absorb at the 1PE wavelength. Interference are also found in fluorescence resonance energy transfer (FRET) when the acceptors are simultaneously excited upon donor excitation. In both cases it is possible that the cross sections for MPE will be relatively smaller for the quenchers or acceptors, thereby avoiding the need for correcting the data.

A favorable opportunity in MPE is the possibility of selective excitation in mixtures of fluorophores. Perhaps certain fluorophores or classes of fluorophores will be found which display high (or low) MPE cross sections and low (or high) 1PE cross sections. In such cases the relative proportions of each excited species could be altered dramatically for the different modes of excitation. One can even imagine selective cellular imaging of multiple probes based on a change from 1PE to MPE. Increased selectivity in excitation can provide numerous new experimental opportunities in both time-resolved fluorescence and cellular imaging.⁽¹⁰⁵⁾

Finally, we mention the potential of MPE for noninvasive sensing or imaging at depths in tissues. It is well known that red light penetrates the skin due to the low absorbance of skin in the red and near-infrared region of the spectrum. Hence, it may be possible to excite suitable sensing probes located under the skin by a two-photon or multiphoton process. If the emission is red, it can escape the tissue and be detected. While it is difficult to quantify fluorescence intensities in such turbid media, we have shown that lifetimes can be readily measured through skin⁽¹⁰⁶⁾ or in turbid suspensions.⁽¹⁰⁷⁾ Additionally, a wide variety of fluorescent probes are now known which display changes in decay time in response to pH, Cl⁻, K⁺, Mg²⁺, and Ca²⁺,⁽¹⁰⁸⁾ due to binding interactions⁽¹⁰⁹⁾ or glucose.⁽¹¹⁰⁾ Hence, we can imagine excitation of such fluorophores through skin to quantify the desired substance.

Acknowledgments

This work was supported by a grant from the NIH National Center for Research Resources (RR-08119).

References

1. D. M. Friedrich and W. M. McClain, Two-photon molecular electronic spectroscopy, *Annu. Rev. Phys. Chem.* 31, 559–577 (1980).
2. M. J. Wirth, A. Koskelo, and M. J. Sanders, Molecular symmetry and two-photon spectroscopy, *Appl. Spectrosc.* 35, 14–21 (1981).
3. R. R. Birge, One-photon and two-photon excitation spectroscopy, in: *Ultrasensitive Laser Spectroscopy* (D. S. Kliger, ed.), pp. 109–174, Academic Press, New York (1983).
4. R. D. Jones and P. R. Callis, Two-photon spectra of inductively perturbed naphthalene, *Chem. Phys. Letts.* 144, 158–164 (1989).
5. M. J. Wirth, A. C. Koskelo, C. E. Mohler, and B. L. Lentz, Identification of methyl derivatives of naphthalene by two-photon symmetry parameters, *Anal. Chem.* 53, 2045–2048 (1981).
6. M. B. Masthay, L. A. Findsen, B. M. Pierce, D. F. Bocian, J. S. Lindsey, and R. R. Birge, A theoretical investigation of the one- and two-photon properties of porphyrins, *J. Chem. Phys.* 84, 3901–3915 (1986).
7. H. L.-B. Fang, R. J. Thrash, and G. E. Leroi, Observation of the low-energy 1A_g state of diphenylhexatriene by two-photon excitation spectroscopy, *Chem. Phys. Letts.* 57, 59–63 (1978).
8. B. Hudson, Linear polyene electronic structure and spectroscopy, *Ann. Rev. Phys. Chem.* 25, 437–460 (1974).
9. R. R. Birge, Two-photon spectroscopy of protein-bound chromophores, *Acc. Chem. Res.* 19, 138–146 (1986).
10. B. E. Anderson, R. D. Jones, A. A. Rehms, P. Illich, and P. R. Callis, Polarized two-photon fluorescence excitation Spectra of indole and benzimidazole, *Chem. Phys. Letts.* 125, 106–112 (1986).
11. A. Rehms and P. R. Callis, Resolution of L_a and L_b bands in methyl indoles by two-photon spectroscopy, *Chem. Phys. Letts.* 140, 83–89 (1987).
12. W. M. McClain, Excited state symmetry assignment through polarized two-photon absorption studies of fluids, *J. Chem. Phys.* 55, 2789–2796 (1971).
13. M. Wirth, A. Koskelo, and M. J. Sanders, Molecular symmetry and two-photon spectroscopy, *Appl. Spectry.* 35, 14–21 (1981).
14. W. Denk, J. H. Strickler, and W. W. Webb, Two-photon laser scanning fluorescence microscopy, *Science* 248, 73–76(1990).
15. D. W. Piston, D. R. Sandison, and W. W. Webb, Time-resolved fluorescence imaging and background rejection by two-photon excitation in laser scanning microscopy, *Proc. SPIE* 1640, 379–389 (1992).
16. W. Denk, K. R. Delaney, A. Gelperin, D. Kleinfeld, B. W. Strowbridge, D. W. Tank, and R. Yuste, Anatomical and functional imaging of neurons using 2-photon laser scanning microscopy, *J. Neurosci. Meth.* 54, 151–152 (1994).
17. Y. Liu, G. J. Sonek, M. W. Berns, K. Konig, and B. J. Tromberg, Two- photon fluorescence excitation in continuous-wave infrared optical tweezers, *Opt. Lett.* 20, 2246–2248 (1995).
18. K. Loenig, T. Krasieva, Y. Liu, M. W. Berns, and B. J. Tromberg, Two-photon excitation in living cells induced by low-power CW laser beams, *SPIE Proc.* 2678, 30–37 (1996).
19. J. R. Lakowicz, I. Gryczynski, J. Kusba, and E. Danielsen, Two-photon induced fluorescence intensity and anisotropy decays of diphenylhexatriene in solvents and lipid bilayers, *J. Fluoresc.* 2, 247–258 (1992).
20. J. R. Lakowicz and I. Gryczynski, Fluorescence intensity and anisotropy decay of the 4',6-diamidino-2-phenylindole-DNA complex resulting from one-photon and two-photon excitation, *J. Fluoresc.* 2, 117–022 (1992).

21. I. Gryczynski and J. R. Lakowicz, Fluorescence intensity and anisotropy decays of the DNA stain HOECHST 33342 resulting from one-photon and two-photon excitation, *J. Fluoresc.* **4**, 331–336 (1994).
22. J. R. Lakowicz and I. Gryczynski, Tryptophan fluorescence intensity and anisotropy decays of human serum albumin resulting from one-photon and two-photon excitation, *Biophys. Chem.* **45**, 1–6 (1993).
23. J. R. Lakowicz, I. Gryczynski, E. Danielsen, and J. Frisoli, Anisotropy spectra of indole and *N*-acetyl-L-tryptophanamide observed for two-photon excitation of fluorescence, *Chem. Phys. Lett.* **194**, 282–287 (1992).
24. P. R. Callis, On the theory of two-photon induced fluorescence anisotropy with applications to indoles, *J. Chem. Phys.* **99**, 27–37 (1993).
25. I. Gryczynski and J. R. Lakowicz, Quenching of methylcyclohexane fluorescence by methanol, *Photochem. Photobiol.* **62**, 426–432 (1995).
26. I. Gryczynski, H. Szmacinski, and J. R. Lakowicz, On the possibility of calcium imaging using Indo-1 with three-photon excitation, *Photochem. Photobiol.* **62**, 804–808 (1995).
27. I. Gryczynski, H. Malak, and J. R. Lakowicz, Three-photon excitation of a tryptophan derivative using a fs Ti:sapphire laser, *Biospectroscopy* **2**, 9–15 (1996).
28. B. S. Hudson and B. E. Kohler, A low-lying weak transition in the polyene α,ω -diphenyloctatetraene, *Chem. Phys. Lett.* **14**, 299–304 (1972).
29. H. L.-B. Fang, R. J. Thrash, and G. E. Leroi, Observation of the low-energy 1A_g state of diphenylhexatriene by two-Photon excitation spectroscopy, *Chem. Phys. Lett.* **57**, 59–63 (1978).
30. J. Saltiel, D. F. Sears, Jr., Y.-P. Sun, and J.-O. Choi, Evidence for ground-state *s-cis* conformers in the fluorescence spectra of *all-trans*-1,6-diphenyl-1,3,5-hexatriene, *J. Am. Chem. Soc.* **114**, 3607–3612 (1992).
31. J. R. Lakowicz and I. Gryczynski, Frequency-domain fluorescence spectroscopy, in: *Topics in Fluorescence Spectroscopy, Vol. 1: Techniques* (J. R. Lakowicz, ed.), Plenum Press, New York, pp. 293–355 (1991).
32. C. D. Stubbs and B. W. Williams, in: *Topics in Fluorescence Spectroscopy, Vol. 3* (J. R. Lakowicz, ed.), Plenum Press, New York, pp. 231–271 (1992).
33. F. Mulders, H. van Langen, G. van Ginkel, and Y. K. Levine, The static and dynamic behaviour of fluorescent probe molecules in lipid bilayers, *Biochim. Biophys. Acta.* **859**, 209–218 (1986).
34. M. Straume and B. J. Litman, Equilibrium and dynamic structure of large, unilamellar, unsaturated acyl chain phosphatidylcholine vesicles. Higher order analysis of 1,6-diphenyl-1,3,5-hexatriene and 1-[4-(trimethylammonio)phenyl]-6-phenyl-1,3,5-hexatriene anisotropy decays, *Biochemistry* **26**, 5113–5120 (1987).
35. G. Weber, Polarization of the fluorescence of solution, in: *Fluorescence and Phosphorescence Analysis: Principles and Applications*, Interscience, New York, pp. 217–240 (1966).
36. A. Kawski, I. Gryczynski, and Z. Gryczynski, Fluorescence anisotropies of 4-dimethylamino- ω -diphenylphosphinyl-rran.s-styrene in isotropic media in the case of one- and two-photon excitation, *Z. Naturforsch.* **48a**, 551–556 (1993).
37. J. R. Lakowicz, I. Gryczynski, Z. Gryczynski, E. Danielsen, and M. J. Wirth, Time-resolved fluorescence intensity and anisotropy decays of 2,5-diphenyloxazole by two-Photon excitation and frequency-domain fluorometry, *J. Phys. Chem.* **96**, 3000–3006 (1992).
38. C. Wan and C. K. Johnson, Time-resolved anisotropic two-photon spectroscopy, *Chem. Phys.* **179**, 513–531 (1994).
39. C. Wan and C. K. Johnson, Time-resolved two-photon induced anisotropy decay: the rotational diffusion regime, *J. Chem. Phys.* **101**, 10283–10291 (1994).
40. P. R. Callis, On the theory of two-photon induced fluorescence anisotropy with application to indole, *J. Chem. Phys.* **99**, 27–37 (1993).

41. S.-Y. Chen and B. W. Van Der Meer, Theory of two-photon induced fluorescence anisotropy decay in membranes, *Biophys. J.* **64**, 1567–1575 (1993).
42. J. R. Lakowicz, H. Cherek, J. Kuśba, I. Gryczynski, and H. Malak, Review of fluorescence anisotropy decay analysis by frequency-domain fluorescence spectroscopy, *J. Fluoresc.* **3**, 103–116(1990).
- 42a. J. R. Lakowicz, I. Gryczynski, and E. Danielsen, Anomalous differential polarized phase angles for two-photon excitation with isotropic depolarizing rotations, *Chem. Phys. Lett.* **191**, 47–53 (1992).
43. G. G. Belford, R. L. Belford, and G. Weber, Dynamics of fluorescence polarization in macromolecules, *Proc. Natl. Acad. Sci.* **69**, 1392–1393 (1972).
44. S. M. Kennedy and F. E. Lytle, *p*-Bis(*o*-methylstyryl)benzene as a power-squared sensor for two-photon absorption measurements between 537 and 694 nm, *Anal. Chem.* **58**, 2643–2647 (1986).
45. C. Xu and W. W. Webb, Measurement of two-photon excitation cross sections of molecular fluorophores with data from 690 to 1050 nm, *J. Opt. Soc. Am. B.* **13**, 481–491 (1996).
46. A. Fischer, C. Cremer, and E. H. K. Stelzer, Fluorescence of coumarins and xanthenes and two-photon absorption with a pulsed titanium-sapphire laser, *Appl. Opt.* **34**, 1989–2003 (1995).
47. J. R. Lakowicz, I. Gryczynski, Z. Gryczynski, E. Danielsen, and M. J. Wirth, Time resolved fluorescence intensity and anisotropy decays of 2,5-diphenyloxazole by two-photon excitation and frequency-domain fluorometry, *J. Phys. Chem.* **96**, 3000–3006 (1992).
48. J. M. Beechem, E. Gratton, M. Ameloot, J. R. Knutson, and L. Brand, The global analysis of fluorescence intensity and anisotropy decay data: second-generation theory and programs, in: *Topics in Fluorescence Spectroscopy, Vol. 2: Principles* (J. Lakowicz, ed.), Plenum Press, New York, pp. 241–305 (1991).
49. M. Straume, S. C. Frasier-Cadoret, and M. L. Johnson, Least-squares analysis of fluorescence data, in: *Topics in Fluorescence Spectroscopy, Vol. 2: Principles* (J. Lakowicz, ed.), Plenum Press, New York, pp. 177–239 (1991).
50. G. Weber, Polarization of the fluorescence of solutions, in: *Fluorescence and Phosphorescence Analysis* (D. M. Hercules, ed.), Interscience, New York, pp. 217–240 (1966).
51. M. R. Eftink, L. A. Selvidge, P. R. Callis, and A. A. Rehms, Photophysics of indole derivatives: experimental resolution of L_a and L_b transitions and comparison with theory, *J. Phys. Chem.* **94**, 3469–3479 (1990).
52. B. Valeur and G. Weber, Resolution of the fluorescence excitation spectrum of indole into the 1L_a and 1L_b excitation bands, *Photochem. Photobiol.* **25**, 441–444 (1977).
53. M. R. Eftink and Z. Chen, Evidence for dual L_a and L_b emission in 5-methylindole, *J. Fluoresc.* **4**, 165–168(1994).
54. J. M. Beechem and L. Brand, Time-resolved fluorescence of proteins, *Annu. Rev. Biochem.* **54**, 43–71 (1985).
55. F. Hirayama and S. Lipsky, Fluorescence of saturated hydrocarbons, *J. Chem. Phys.* **51**, 3616–3617(1969).
56. F. Hirayama, W. Rothman, and S. Lipsky, Fluorescence of saturated hydrocarbons. II: The effect of alkyl substituents, *Chem. Phys. Lett.* **5**, 296–298 (1970).
57. W. Rothman, F. Hirayama, and S. Lipsky, Fluorescence of saturated hydrocarbons. III: The effect of molecular structure, *J. Chem. Phys.* **58**, 1300–1317 (1973).
58. J. R. Lakowicz and I. Gryczynski, Fluorescence intensity decays of cyclohexane and methylcyclohexane with two-photon excitation from a high repetition rate frequency-doubled dye laser, *Biospectroscopy* **1**(3–8), 3–8 (1995).
59. I. Gryczynski and J. R. Lakowicz, Quenching of methylcyclohexane fluorescence by methanol, *Photochem. Photobiol.* **62**, 426–432 (1995).

60. I. Gryczynski, A. Razynska, and J. R. Lakowicz, Two-photon induced fluorescence of linear alkanes; a possible intrinsic lipid probe, *Biophys. Chem.* 57, 291–295 (1996).
61. S. Dellonte, E. Gardini, F. Barigelli, and G. Orlandi, Two-photon excitation of saturated hydrocarbons, *Chem. Phys. Lett.* 49, 596–598 (1977).
62. M. R. Eftink, Fluorescence quenching: theory and applications, in: *Topics in Fluorescence Spectroscopy* (J. R. Lakowicz, ed.), Plenum Press, New York, pp. 53–126 (1991).
63. Landolt-Bornstein, *Physikalische und Chemische Konstanten*, 2. Teil, Bandteil B, p. 267 (1962).
64. J. R. Lakowicz and G. Weber, Quenching of fluorescence by oxygen-A probe for structural fluctuations in macromolecules, *Biochemistry* 12, 4161–4170 (1973).
65. R. A. Agbaria, I. Gryczynski, H. Malak, and J. R. Lakowicz, Two-photon induced fluorescence of cholestan, *Biospectroscopy* 2, 219–224 (1996).
66. J. R. Lakowicz and I. Gryczynski, Characterization of *p*-bis(*O*-methylstyryl) benzene as a lifetime and anisotropy decay standard for two-photon induced fluorescence, *Biophys. Chem.* 47, 1–7 (1993).
67. A. Kawski, I. Gryczynski, and Z. Gryczynski, Fluorescence anisotropies of 4-dimethylamino-*o*-diphenylphosphinyl-trans-styrene in isotropic media in the case of one- and two-photon excitation, *Z. Naturforsch.* 48a, 551–556 (1993).
68. L. J. Libertini and E. W. Small, FF deconvolution of fluorescence decay data, *Anal. Biochem.* 138, 314–318 (1984).
69. J. R. Lakowicz, H. Cherek, and A. Baiter, Correction of timing errors in photomultiplier tubes used for phase-modulation fluorometry, *Biochem. Biophys. Meth.* 5, 131–146 (1981).
70. R. A. White, K. J. Kutz, and J. Wampler, in: *Topics in Fluorescence Spectroscopy, Vol. 1: Techniques* (J. R. Lakowicz, ed.), Plenum Press, New York, pp. 379–407 (1991).
71. I. Gryczynski, H. Malak, and J. R. Lakowicz, Three-photon induced fluorescence of 2,5-diphenyloxazole with a femtosecond Ti: sapphire laser, *Chem. Phys. Lett.* 245, 30–35 (1995).
72. I. Gryczynski, H. Malak, and J. R. Lakowicz, Three-photon excitation of *p*-quaterphenyl with a mode-locked fs Ti:sapphire laser, *J. Fluoresc.* 6, 139–145 (1996).
73. I. Gryczynski, H. Malak, S. W. Hell, and J. R. Lakowicz, Three-photon excitation of 2,5-bis(4-biphenyl)oxazole, *J. Biomed. Opt.* 1, 473–480 (1996).
74. H. Malak, I. Gryczynski, J. Dattelbaum, and J. R. Lakowicz, Three-photon induced fluorescence of diphenylhexatriene in solvents and lipid bilayers, *J. Fluoresc.* 7, 99–106 (1997).
75. Z. Huang and N. L. Thompson, Theory for two-photon excitation in pattern. Photobleaching with evanescent illumination, *Biophys. Chem.* 47, 241–249 (1993).
76. I. Gryczynski, V. Bogdanov, and J. R. Lakowicz, Light quenching of tetraphenylbutadiene fluorescence observed during two-photon excitation, *J. Fluoresc.* 3, 85–92 (1993).
77. I. Gryczynski, H. Malak, and J. R. Lakowicz, Three-photon excitation of a tryptophan derivative using a fs-Ti: sapphire laser, *Biospectroscopy* 2, 9–15 (1996).
78. S. W. Hell, K. Bahlmann, M. Schrader, A. Soini, H. Malak, I. Gryczynski, and J. R. Lakowicz, Three-photon excitation in fluorescence microscopy, *J. Biomed. Opt.* 1, 71–74 (1996).
79. I. Gryczynski, H. Szmacinski, and J. R. Lakowicz, On the possibility of calcium imaging using Indo-1 with three-photon excitation, *Photochem. Photobiol.* 62, 804–808 (1995).
80. H. Szmacinski, I. Gryczynski, and J. R. Lakowicz, Three-photon induced fluorescence of the calcium probe Indo-1, *Biophys. J.* 70, 547–555 (1996).
81. J. R. Cable and A. C. Albrecht, A condensed phase study of the benzene $B_{2u} - A_{1g}$ three-photon transition, *J. Chem. Phys.* 85, 3155–3164 (1986).
82. W. Denk, K. R. Delaney, A. Gelperin, D. Kleinfeld, B. W. Strowbridge, D. W. Tank, and R. Yuste, Anatomical and functional imaging of neurons using 2-photon laser scanning microscopy, *J. Neurosci. Meth.* 54, 151–152 (1994).

83. S. W. Hell, S. Lindek, and E. H. Stelzer, Enhancing the axial resolution in far-field microscopy: two-photon 4Pi confocal fluorescence microscopy, *J. Mod. Opt.* **41**, 675–681 (1994).
84. E. H. K. Stelzer, S. Hell, S. Lindek, R. Stricker, R. Pick, C. Storz, G. Ritter, and N. Salmon, Nonlinear absorption extends confocal fluorescence microscopy into the ultra-violet regime and confines the illumination volume, *Opt. Commun.* **104**, 223–228 (1994).
85. D. W. Piston, D. R. Sandison, and W. W. Webb, Time-resolved fluorescence imaging and background rejection by two-photon excitation in laser scanning microscopy, *Proc. SPIE* **1640**, 379–389 (1992).
86. W. Denk, Two-photon scanning photochemical microscopy: mapping ligand-gated ion channel distributions, *Proc. Natl. Acad. Sci.* **91**, 6629–6633 (1994).
87. I. Gryczynski and J. R. Lakowicz, Fluorescence intensity and anisotropy decays of the DNA stain HOECHST 33342 resulting from one-photon and two-photon excitation, *J. Fluoresc.* **4**, 331–336 (1994).
88. I. Gryczynski, J. Kuśba, and J. R. Lakowicz, Light quenching of fluorescence using time-delayed laser pulses as observed by frequency-domain fluorometry, *J. Phys. Chem.* **98**, 8886–8895 (1994).
89. P. R. Monson and W. M. McClain, Polarization dependence of the two-photon absorption of tumbling molecules with application to liquid 1-chloronaphthalene and benzene, *J. Chem. Phys.* **53**, 29–37 (1970).
90. P. R. Monson and W. M. McClain, Complete polarization study of the two-photon absorption of liquid 1-chloronaphthalene, *J. Chem. Phys.* **56**, 4817–4825 (1972).
91. D. Frolich and H. Mahr, Two-photon spectroscopy of anthracene, *Phys. Rev. Lett.* **16**, 895–898 (1966).
92. W. M. McClain, Excited state symmetry assignment through polarized two-photon absorption studies of fluids, *J. Chem. Phys.* **55**, 2789–2796 (1971).
93. M. W. Dowley, K. B. Eisenthal, and W. L. Peticolas, Two-photon laser excitation of polycyclic aromatic molecules, *J. Chem. Phys.* **47**, 1609–1619 (1967).
94. J. R. Lakowicz, I. Gryczynski, H. Malak, and Z. Gryczynski, Fluorescence spectral properties of 2,5-diphenyl-1,3,4-oxadiazole with two-color two-photon excitation, *J. Phys. Chem.* **100**, 19406–19411 (1996).
95. J. R. Lakowicz (ed.), *Principles of Fluorescence Spectroscopy*, Plenum Press, New York, p. 157 (1983).
96. J. R. Lakowicz, I. Gryczynski, H. Malak, and Z. Gryczynski, Two-color two-photon excitation of fluorescence, *Photochem. Photobiol.* **64**, 632–635 (1996).
97. I. Gryczynski, H. Malak, and J. R. Lakowicz, Two-color two-photon excitation of indole, *Biospectroscopy*, **3**, 97–101 (1996).
98. W. M. McClain, Two-photon molecular spectroscopy, *Acc. Chem. Res.* **7**, 129–135 (1974).
99. J. B. Pawley, (ed.), *Handbook of Biological Confocal Microscopy*, rev. ed., Plenum Press, New York (1990); 2nd ed., p. 632 (1995).
100. J. R. Lakowicz, I. Gryczynski, J. Kuśba, and V. Bogdanov, Light quenching of fluorescence: a new method to control the excited state lifetime and orientation of fluorophores, *Photochem. Photobiol.* **60**, 546–562 (1994).
101. I. Gryczynski, J. Kuśba, Z. Gryczynski, H. Malak, and J. R. Lakowicz, Effect of fluorescence quenching by stimulated emission on the spectral properties of a solvent-sensitive fluorophore, *J. Phys. Chem.* **100**, 10135–10144 (1996).
102. I. Gryczynski, J. Kuśba, and J. R. Lakowicz, Wavelength-selective light quenching of biochemical fluorophores, *J. Biomed. Optics* **2**, 80–87 (1997).

103. S. W. Hell, M. Schrader, K. Bahlmann, F. Meinecke, J. R. Lakowicz, and I. Gryczynski, Stimulated emission on microscopic scale: light quenching of pyridine 2 using a Ti: sapphire laser, *J. Microsc.* **180**, RP1–RP2 (1995).
104. C. Y. Dong, P. T. C. So, T. French, and E. Gratton, Fluorescence lifetime imaging by a synchronous pump–probe microscopy, *Biophys. J.* **69**, 2234–2242 (1995).
105. D. W. Piston, B. R. Masters, and W. W. Webb, Three-dimensionally resolved NAD(P)H cellular metabolic redox imaging of the *in situ* cornea with two-photon excitation laser scanning microscopy, *J. Microsc.* **178**, 20–27 (1995).
106. S. B. Bambot, G. Rao, M. Romauld, G. M. Carter, J. Sipior, E. Terpetschnig, and J. R. Lakowicz, Sensing oxygen through skin using a red diode laser and fluorescence lifetimes, *Biosensors Bioelectron.* **10**, 643–652 (1995).
107. H. Szmacinski and J. R. Lakowicz, Frequency-domain lifetime measurements and sensing in highly scattering media, *Sensors Actuators B* **30**, 207–215 (1996).
108. H. Szmacinski and J. R. Lakowicz, Fluorescence lifetime-based sensing and imaging, *Sensors Actuators B* **29**, 16–24 (1995).
109. A. J. Ozinskas, H. Malak, J. Joshi, H. Szmacinski, J. Britz, R. B. Thompson, P. A. Koen, and J. R. Lakowicz, Homogeneous model immunoassay of thyroxine by phase-modulation fluorescence spectroscopy, *Anal. Biochem.* **213**, 264–270 (1992).
110. J. R. Lakowicz and B. P. Maliwal, Optical sensing of glucose using phase-modulation fluorometry, *Anal. Chim. Acta.* **271**, 155–164 (1993).

Two-Photon Excitation and Anisotropy Decays in Membranes and Oriented Systems

B. Wieb Van der Meer and S.-Y. Simon Chen

4.1. Introduction

Recent developments in laser technology have enabled the use of intense light pulses in fluorescence. A very interesting application of high-intensity excitation is two-photon excitation. Instead of using conventional ultraviolet light, the same excited singlet state of the fluorophore can be populated by using a longer and less damaging excitation wavelength, namely red light, via the two-photon absorption process. In comparison with the one-photon-excitation cross section, the two-photon-excitation cross section for a typical molecule is extremely low at the intensity of conventional light sources. With the help of ultrafast pulsed lasers, a very high local instantaneous intensity can be achieved at the point where the laser beam is focused.

Employing the quadratic intensity dependence of two-photon excitation and using a pulsed laser, Webb *et al.*^(1,2) showed that fluorescence from two-photon excitation enhanced the signal-to-background ratio and spatial resolution of fluorescence imaging in laser scanning microscopy without using confocal spatial filters and UV optics. The two-photon absorption probability depends not only on intensity but also on the polarizations of those two exciting photons. By the use of polarized two-photon absorption studies, the symmetries of all excited molecular states involved in the two-photon process can be elucidated.⁽³⁻⁶⁾ Moreover, the two-photon-induced fluorescence depolarizations of fluorophores in various solvents and at different temperatures have been studied by frequency-domain fluorometry.⁽⁷⁻⁹⁾

B. Wieb Van der Meer and S.-Y. Simon Chen
Western Kentucky University, Bowling Green, Kentucky 42101; present address for S.-Y. Chen:
MPAUDIO, Inc., East Brunswick, New Jersey 08816.

Department of Physics and Astronomy,

Topics in Fluorescence Spectroscopy; Volume 5: Nonlinear and Two-Photon-Induced Fluorescence,
edited by J. Lakowicz. Plenum Press, New York, 1997.

A significantly higher fundamental fluorescence anisotropy was reported by using two-photon excitation than by one-photon excitation in these studies. In other words, $r_{[2]}(0)$, the fluorescence anisotropy at the moment of excitation by a very short polarized pulse using two-photon excitation is higher than that with one-photon excitation, $r_{[1]}(0)$: $r_{[2]}(0) > r_{[1]}(0)$. The observed higher fundamental anisotropy value indicates that a larger oriented population was photoselected by two-photon excitation. Two-photon excitation was therefore suggested to be able to enhance the experimental resolution for time-resolved fluorescence anisotropy measurements.⁽⁷⁻⁹⁾ An interesting question: Is it possible to obtain more information about the reorientational dynamics with two-photon excitation than with one-photon excitation? In this chapter we focus on that question, limiting ourselves to membranes and fluorescence anisotropy using excitation with two identical photons as compared to single-photon excitation.

Chapters 1 and 2 are closely related to our contribution. They both deal with the anisotropy of the fluorescence following two-photon excitation, which is also the subject of this chapter. Callis is more concerned with the relation between molecular properties and the fundamental anisotropy and not with the time dependence of the anisotropy.⁽¹⁰⁾ Johnson discusses the anisotropy decays (discussed here as well) and treats the cases of nonidentical photons and one-photon resonance cases (not discussed here).^(11,12) Our conclusion is that in isotropic membrane suspensions no new information can be obtained by using two-photon excitation, although interesting differences exist between fluorescence anisotropies from two- and one-photon excitation. In oriented membranes, however, two-photon excitation allows us to obtain information on orientational order that is not available with one-photon excitation.

The outline of this chapter is as follows: The introduction is the first section. In the second section we analyze the results of a fluorescence anisotropy experiment in an isotropic membrane suspension comparing two- and one-photon excitation. In Section 4.3 we consider angle-resolved fluorescence depolarization measurements in oriented membrane systems using two- and one-photon excitation. Section 4.4 summarizes the results and gives concluding remarks. Our approach is highly mathematical. To improve the readability of this contribution we have removed almost all details from the text and given the derivations in appendixes.

4.2. Two-Photon Anisotropy Theory in Isotropic Suspensions

Consider the experimental setup in Figure 4.1, in which a sample of membrane suspensions containing fluorescent molecules is located at the center of a laboratory coordinate system with its z_L axis along the vertical. Polarized light is coming in along the x_L axis. The polarization direction of this light is set

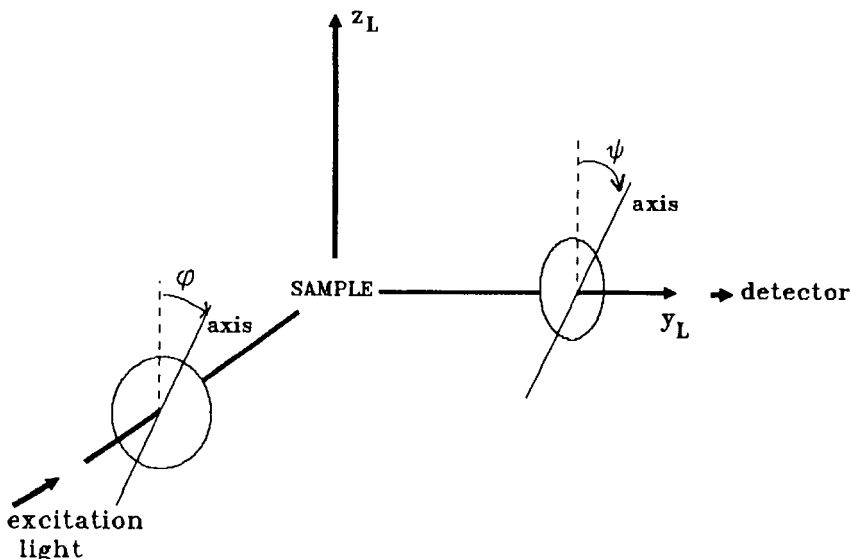


Figure 4.1. Experimental setup for fluorescence depolarization studies in isotropic systems. The excitation light travels along the negative x_L direction toward the origin where the sample is located. Emitted light going in the y_L direction is detected. The angle φ is between the z_L axis and the polarization direction of the exciting light. The angle ψ is between the z_L axis and the polarization of the emitted light that is detected.

with a polarizer perpendicular to the x_L axis and has a variable angle φ with the vertical. The emitted light is detected along the y_L axis. The polarization direction of this fluorescent light is controlled by an emission polarizer perpendicular to the y_L axis and has a variable angle ψ with the vertical. We are interested in the response to a very short excitation pulse at time 0. The intensity of the emitted light depends on the time t elapsed after the excitation and on angles φ and ψ . We call this intensity $I_{[m]}(\varphi, \psi, t)$ in one-photon excitation and $I_{[2]}(\varphi, \psi, t)$ in two-photon excitation. Interestingly, the dependence on the angles is exactly the same for the two cases (see Appendix A for $m = 1$ and B for $m = 2$):

$$I_{[m]}(\varphi, \psi, t) = I_{[m]}(0^\circ, 54.7^\circ, t) \{1 + r_{[m]}(t)[3 \cos^2 \varphi \cos^2 \psi - 1]\} \quad (m = 1, 2) \quad (4.1)$$

where $\psi = 54.7^\circ$ is the magic angle at which $\cos^2 \psi = 1/3$, and the fluorescence anisotropy for one-photon excitation, $r_{[1]}(t)$, and that for two-photon excitation, $r_{[2]}(t)$, is defined as usual:

$$r_{[m]}(t) = \frac{I_{[m]}(0^\circ, 0^\circ, t) - I_{[m]}(0^\circ, 90^\circ, t)}{I_{[m]}(0^\circ, 0^\circ, t) + 2I_{[m]}(0^\circ, 90^\circ, t)} \quad (m = 1, 2) \quad (4.2)$$

The one-photon anisotropy, $r_{[1]}(t)$, is

$$r_{[1]}(t) = \frac{2}{5} \langle P_2(\mathbf{a}_0 \cdot \mathbf{e}_t) \rangle = \frac{1}{5} (3 \langle \cos^2 \theta_{0t} \rangle - 1) \quad (4.3)$$

where $P_2(x) = 3/2x^2 - 1/2$ is the second Legendre polynomial, \mathbf{a}_0 is a unit vector along the absorption transition moment of the fluorophore at time 0, the time of the excitation, and \mathbf{e}_t is a unit vector along the emission moment at time t after the excitation. The dot product $\mathbf{a}_0 \cdot \mathbf{e}_t$ is equal to $\cos \theta_{0t}$, where θ_{0t} is the angle between the unit vectors. The angle brackets in Eq. (4.3) indicate an ensemble average over all fluorophores in the sample. The two-photon anisotropy depends on S_{xx} , $S_{xy} = S_{yx}$, $S_{xz} = S_{zx}$, S_{yy} , $S_{yz} = S_{zy}$, and S_{zz} , which are given by^(3-6,10-12,13)

$$S_{\alpha\beta} = \sum_n \frac{\langle g|\alpha|n\rangle \langle n|\beta|f\rangle + \langle g|\beta|n\rangle \langle n|\alpha|f\rangle}{E_n - h\nu} \quad \alpha, \beta = x, y, z \quad (4.4)$$

where $|g\rangle$ and $|f\rangle$ are the ground state and the final excited state, respectively. These two molecular states are connected via simultaneous two-photon absorption of the incident frequency v ; E_n is the energy of the virtual intermediate state $|n\rangle$, and h is Planck's constant.

It is convenient to employ a molecule-fixed Cartesian coordinate system along the principal axes of the two-photon absorption tensor. In this coordinate system S_{xx} , S_{yy} , and S_{zz} are the only nonzero elements of the tensor. The two-photon fluorescence anisotropy, $r_{[2]}(t)$, depends on σ_1 , σ_2 , M_z , and M_y , which are defined as follows (see Appendix C):

$$\sigma_1 = S_{xx}/S_{zz} \quad \sigma_2 = S_{yy}/S_{zz} \quad (4.5)$$

$$M_z = \frac{(3 + 3\sigma_1 + \sigma_2)(1 - \sigma_1)}{3 + 2\sigma_1 + 2\sigma_2 + 2\sigma_1\sigma_2 + 3\sigma_1^2 + 3\sigma_2^2} \quad (4.6)$$

$$M_y = \frac{(1 + 3\sigma_1 + 3\sigma_2)(\sigma_2 - \sigma_1)}{3 + 2\sigma_1 + 2\sigma_2 + 2\sigma_1\sigma_2 + 3\sigma_1^2 + 3\sigma_2^2} \quad (4.6)$$

$$r_{[2]}(t) = \frac{4}{7} M_z \langle P_2(\mathbf{z}_0 \cdot \mathbf{e}_t) \rangle + \frac{4}{7} M_y \langle P_2(\mathbf{y}_0 \cdot \mathbf{e}_t) \rangle \quad (4.7)$$

It is reasonable to assume that the emission moment is along the long axis (that is, the axis with the smallest moment of inertia) of the fluorophore and that this is the

z axis of the two-photon absorption tensor. With this assumption we rewrite $r_{[1]}(t)$ and $r_{[2]}(t)$ as

$$r_{[1]}(t) = \frac{2}{5} \cos^2 \theta_A \langle P_2(\mathbf{z}_0 \cdot \mathbf{z}_t) \rangle + \frac{2}{5} \sin^2 \theta_A \langle P_2(\mathbf{y}_0 \cdot \mathbf{z}_t) \rangle \quad (4.8a)$$

and

$$r_{[2]}(t) = \frac{4}{7} M_z \langle P_2(\mathbf{z}_0 \cdot \mathbf{z}_t) \rangle + \frac{4}{7} M_y \langle P_2(\mathbf{y}_0 \cdot \mathbf{z}_t) \rangle \quad (4.8b)$$

where θ_A is the angle between the absorption and emission transition moments, and it is assumed that these moments are in the yz plane (see Appendix D for the derivation of Eq. 4.8a). The lowest and highest values for the fundamental one- and two-photon anisotropies are

$$-0.2 \leq r_{[1]}(0) = \frac{2}{5} P_2(\cos \theta_A) \leq 0.4 \quad (4.9)$$

$$-0.3266 \leq r_{[2]}(0) = \frac{4}{7} M_z - \frac{2}{7} M_y \leq 0.6123 \quad (4.10)$$

where the highest value for $r_{[1]}(0)$ corresponds to $\theta_A = 0^\circ$ and the lowest to $\theta_A = 90^\circ$, and the highest value for $r_{[2]}(0)$ corresponds to $\sigma_1 = \sigma_2 = -0.1307$ and the lowest to $\sigma_1 = \sigma_2 = -2.8693$ (see Appendix E).

The generalized strong-collision model⁽¹⁴⁾ allows an evaluation of the time dependence of the one- and two-photon anisotropies. In this approximation the correlation functions $\langle P_2(\mathbf{z}_0 \cdot \mathbf{z}_t) \rangle$ and $\langle P_2(\mathbf{y}_0 \cdot \mathbf{z}_t) \rangle$, which determine this time dependence, are (see Appendix F)

$$\langle P_2(\mathbf{z}_0 \cdot \mathbf{z}_t) \rangle = S^2 + (1 - S^2)e^{-t/\tau_{R1}} \quad (4.11)$$

$$\langle P_2(\mathbf{y}_0 \cdot \mathbf{z}_t) \rangle = FS(1 - e^{-t/\tau_{R2}}) - \frac{1}{2}S^2 - \frac{1}{2}(1 - S^2)e^{-t/\tau_{R2}} \quad (4.12)$$

where S and F are order parameters, τ_{R1} is the rotational correlation time for $\langle P_2(\mathbf{z}_0 \cdot \mathbf{z}_t) \rangle$, and τ_{R2} is that for $\langle P_2(\mathbf{y}_0 \cdot \mathbf{z}_t) \rangle$ (one correlation time is assumed for each correlation function; see Appendix F). The order parameter S is the average of $3/2 \cos^2 \vartheta - 1/2$, where ϑ is the angle between the z axis of the fluorophore and the membrane normal. The order parameter F is the average of $3/4 \sin^2 \vartheta \cos 2\beta$, where β is the angle between the projection of the molecular y axis on the plane of the membrane and the projection of the molecular z axis on this plane. The value for S is between -0.5 (all molecular long axes are in the

plane of the membrane) and 1 (all molecular axes are along the membrane normal). The range of values for F depends on (see Appendix F) S :

$$-\frac{1}{2}(1-S) \leq F \leq \frac{1}{2}(1-S) \quad (4.13)$$

Both $r_{[1]}(t)$ and $r_{[2]}(t)$ decay from an initial value to a plateau value and depend on the same correlation functions (see Eq. 4.8). In general, they are expected to be different. The ratio $r_{[2]}(t)/r_{[1]}(t)$ will be constant in time only if $M_y/M_z = \tan^2 \theta_A$ or $F=0$ and $\tau_{R1} \approx \tau_{R2}$. However, in most cases $r_{[2]}(t)/r_{[1]}(t)$ will not be constant. Examples of time dependence are shown in Figure 4.2.

4.3. Two-Photon Anisotropy Theory in Oriented Membranes

A propagating light wave in a uniaxial medium such as an oriented membrane can have two independent directions of polarizations of the electric field.⁽¹⁵⁾ The first, the ordinary ray, has its electric field polarized perpendicular to the axis of symmetry for all angles of incidence. The second, the extraordinary ray, is polarized in the plane of incidence—that is, the plane through the

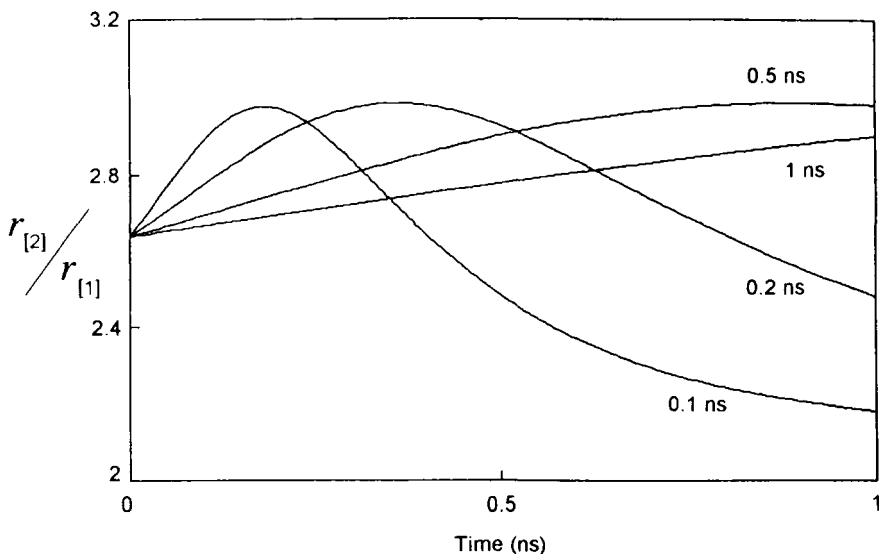


Figure 4.2. The ratio $r_{[2]}(t)/r_{[1]}(t)$ versus the time t after excitation with a very short flash at time 0. The numbers indicated at the curves represent the values for the rotational correlation time τ_{R1} . The values of the other parameters are $\tau_{R2} = 3\tau_{R1}$, $S = 0.5$, $F = 0.25$, $\theta_A = 21.42^\circ$, $\sigma_1 = -0.1$, and $\sigma_2 = 0$.

incoming beam and the normal to the oriented membrane. We will assume that the oriented membrane consists of bilayers parallel to each other and to the cover slides.⁽¹⁶⁾ The preferred orientation of the molecules in such samples coincides with the normal to the cover slides. In fluorescence depolarization experiments in oriented membranes, it is thus possible to measure the intensity for four combinations of polarized directions: I_{oo} , I_{oe} , I_{eo} , and I_{ee} . The subscripts o and e denote the ordinary and extraordinary ray, respectively. The first subscript refers to the exciting light, and the second corresponds to the emitted light.⁽¹⁵⁾

To eliminate the dependence of these intensities on unknown quantities, such as the incident light intensity and illuminated volume, one measures the depolarization ratios $R_o = I_{oe}/I_{oo}$ and $R_e = I_{eo}/I_{ee}$. The experimental arrangements for measuring these ratios are depicted in Figure 4.3. Other geometries are also possible.⁽¹⁷⁾ The intensity ratio R_o is a linear function of the geometrical factor $\sin^2 \Theta$, where Θ is defined in Figure 4.3. This linear relationship holds for $R_{o[1]}$, the ratio for single-photon excitation, and for $R_{o[2]}$, the ratio for two-photon excitation. However, $R_{o[1]}$ contains information about second- and fourth-rank order parameters, while $R_{o[2]}$ depends on second-, fourth-, and sixth-rank order parameters.

To exhibit this difference we examine $R_{o[1]}$ and $R_{o[2]}$ for a rodlike molecule in a perfectly flat membrane at time 0, immediately after excitation by a flash of polarized light. In this case $R_{o[1]}$ and $R_{o[2]}$ are

$$R_{o[m]}(0) = A_m - B_m \sin^2 \Theta \quad (m = 1, 2) \quad (4.14)$$

where A_1 and B_1 (derived in Appendix G) depend on the order parameters $\langle P_2 \rangle$ and $\langle P_4 \rangle$ (defined in Eq. 4.17) according to

$$A_1 = \frac{1}{3} C_1 \quad B_1 = \frac{1}{3}(C_1 - 1) \quad C_1 = \frac{7 + 5\langle P_2 \rangle - 12\langle P_4 \rangle}{7 - 10\langle P_2 \rangle + 3\langle P_4 \rangle} \quad (4.15)$$

and A_2 and B_2 (derived in Appendix H) depend on the order parameters $\langle P_2 \rangle$, $\langle P_4 \rangle$, and $\langle P_6 \rangle$ (defined in Eq. 4.17) according to

$$A_2 = \frac{1}{5} C_2 \quad B_2 = \frac{1}{5}(C_2 - 1) \quad C_2 = \frac{33 - 63\langle P_4 \rangle + 30\langle P_6 \rangle}{33 - 55\langle P_2 \rangle + 27\langle P_4 \rangle - 5\langle P_6 \rangle} \quad (4.16)$$

The order parameters $\langle P_n \rangle$ of rank $n = 2, 4, 6$ are polynomials of the ensemble average of $\cos \vartheta$, where ϑ is the angle between the long axis of the rodlike

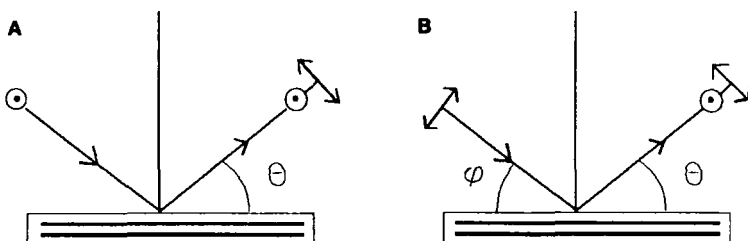


Figure 4.3. (A) Experimental arrangement for measuring the “ordinary ratio,” $R_o = I_{oe}/I_{oo}$, I_{oe} is the intensity of the fluorescence at excitation with polarized light in the ordinary direction (the X axis, perpendicular to the page) viewed through a polarizer in the extraordinary direction (along the arrow: \leftrightarrow , perpendicular to the fluorescent beam), and I_{oo} is the fluorescence intensity for which both excitation and emission polarizers are along the X axis. The sample consists of a stack of parallel membranes (represented by the heavy parallel lines) between two cover slides. The angle Θ between the fluorescent beam and the plane of the membrane can be varied. (B) Experimental arrangement for measuring the “extraordinary ratio,” $R_e = I_{eo}/I_{ee}$, I_{eo} is the intensity of the fluorescence at excitation with polarized light in the extraordinary direction (along the arrow: \leftrightarrow , perpendicular to the incident beam) viewed through a polarizer along the X direction, I_{ee} is the intensity for which both excitation and emission polarizers are along the extraordinary direction. In the incident beam the polarization is along the arrow: \leftrightarrow , perpendicular to the incident beam, the polarizer on the emission side is along the arrow: \leftrightarrow , perpendicular to the fluorescence beam. The angle ϕ (between the incident beam and the plane of the membrane) and the angle Θ (between the fluorescent beam and the plane of membrane) can be varied. The preferred direction of the molecules is along the Z axis, the normal to the stack of membranes. The system will have some disorder, however, allowing the molecules to undergo wobbling of their long axes and other motions.

molecule and the membrane normal. These order parameters are defined as

$$\langle P_2 \rangle = \left\langle \frac{3}{2} \cos^2 \vartheta - \frac{1}{2} \right\rangle \quad (4.17a)$$

$$\langle P_4 \rangle = \left\langle \frac{35}{8} \cos^4 \vartheta - \frac{30}{8} \cos^2 \vartheta + \frac{3}{8} \right\rangle \quad (4.17b)$$

$$\langle P_6 \rangle = \left\langle \frac{231}{16} \cos^6 \vartheta - \frac{315}{16} \cos^4 \vartheta + \frac{105}{16} \cos^2 \vartheta - \frac{5}{16} \right\rangle \quad (4.17c)$$

The range of possible values of $\langle P_6 \rangle$ for given $\langle P_2 \rangle$ and $\langle P_4 \rangle$ can be obtained from the following inequality, derived in Appendix H:

$$-\frac{5}{16} + \frac{35}{352} (\langle P_2 \rangle + \frac{1}{2}) G \leq \langle P_6 \rangle \leq 1 - \frac{49}{88} (1 - \langle P_2 \rangle) H \quad (4.18)$$

with

$$G = \frac{1}{5} \left[\frac{27}{7} + \frac{264}{35} \left(\frac{\langle P_4 \rangle - \frac{3}{8}}{\langle P_2 \rangle + \frac{1}{2}} \right) \right]^2 - 1 \quad (4.19)$$

and

$$H = \frac{1}{7} \left[-\frac{25}{7} + \frac{132}{35} \left(\frac{1 - \langle P_4 \rangle}{1 - \langle P_2 \rangle} \right) \right]^2 + 1 \quad (4.20)$$

For instance, if $\langle P_2 \rangle = 0.6$ and $\langle P_4 \rangle = 0.5$, the possible $\langle P_6 \rangle$ values are 0.064 to 0.736. Figure 4.4 shows the values of $R_{0[1]}(0)$ and $R_{0[2]}(0)$ as a function of $\sin^2 \Theta$ (Θ is the angle between the fluorescent beam and the plane of the membrane) for an oriented membrane system with $\langle P_2 \rangle = 0.6$ and $\langle P_4 \rangle = 0.5$. A wide range of $R_{0[2]}(0)$ is possible for this pair of order parameters. The lower and upper limits of $R_{0[2]}(0)$ are shown in Figure 4.3, and they correspond to a $\langle P_6 \rangle$ value of 0.064 and 0.736, respectively.

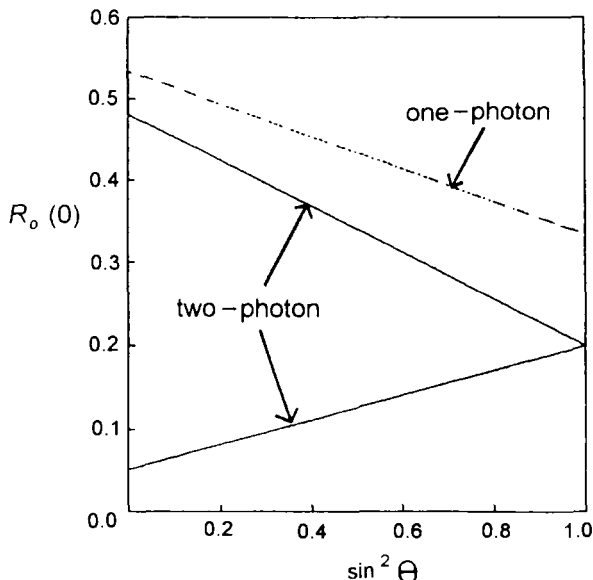


Figure 4.4. A plot of the limiting depolarization ratio $R_o(0)$ with the ordinary ray incident as a function of $\sin^2 \Theta$ (Θ is the angle between the fluorescent beam and the plane of the membrane) by one-photon excitation $R_{o[1]}(0)$ (dotted line) and two-photon excitation $R_{o[2]}(0)$ (solid lines). The dotted line is drawn for a system with $\langle P_2 \rangle = 0.6$ and $\langle P_4 \rangle = 0.5$. The upper solid line is drawn for a system with $\langle P_2 \rangle = 0.6$, $\langle P_4 \rangle = 0.5$, and $\langle P_6 \rangle = 0.736$ (the maximum value for $\langle P_6 \rangle$ in this case). The lower solid line is for a system with $\langle P_2 \rangle = 0.6$, $\langle P_4 \rangle = 0.5$, and $\langle P_6 \rangle = 0.064$ (the minimum value for $\langle P_6 \rangle$ in this case). (Reproduced from the *Biophysical Journal*, 1993, vol. 64, p. 1572 (Ref. 13) by copyright permission of the Biophysical Society.)

4.4. Conclusions

We have compared the emission anisotropy after two-photon excitation, $r_{[2]}(t)$, with that using single-photon excitation, $r_{[1]}(t)$. The time dependence of the total fluorescence intensity should not depend on the mode of excitation because the same excited state is populated and the decay from this state determines the total intensity. The anisotropies, however, are sensitive to photo-selection probabilities, and the photoselection rules for two-photon excitation differ from the ones for single-photon excitation. In isotropic systems, however, $r_{[2]}(t)$ and $r_{[1]}(t)$ turn out to be surprisingly similar and to depend on the same correlation functions. The coefficients of these correlation functions and, therefore, the preexponential factors of the contributing exponentials may be different, just as the $r_{[1]}(t)$ at one excitation wavelength will in general differ from the $r_{[1]}(t)$ at another excitation wavelength. From frequency-domain fluorescence anisotropy measurements, a constant anisotropy ratio ($r_{[2]}(t)/r_{[1]}(t)$) of 1.44 ± 0.02 ($\approx 10/7$) was observed for 2,5-diphenyloxazole (PPO) in propylene glycol⁽⁷⁾ and 1,6-diphenylhexatriene (DPH) in triacetin⁽⁸⁾ at all frequencies. This corresponds to a constant ratio of $r_{[2]}(t)/r_{[1]}(t)$ at all times. Because of this identical time-dependent decay behavior of one- and two-photon anisotropy, it appears to signify that the two-photon transition tensor of PPO and DPH possesses a dominant element and the corresponding axis is along the one-photon transition moment. However the reported $r_{[2]}(0)$ values of PPO and DPH are 0.54 and 0.52, respectively.^(7,8) These values are significantly smaller than the maximum $r_{[2]}(0)$ of 0.57 predicted by the theory for a rodlike probe.⁽¹³⁾ These lower $r_{[2]}(0)$ values imply that the emission dipole is not along the dominant axis of the two-photon transition tensor for both fluorophores.

Values for the two-photon-induced anisotropies are between $\frac{1}{7} - \frac{3}{7}\sqrt{\frac{6}{5}} = -0.3266$ and $\frac{1}{7} + \frac{3}{7}\sqrt{\frac{6}{5}} = 0.6123$. The anisotropy ratio $r_{[2]}/r_{[1]}$ can be larger or smaller than unity. Note that the general two-photon-induced time-dependent fluorescence anisotropy decay is very complicated and depends not only on the patterns of the two-photon absorption tensor but also on the time-dependent correlations of the emission moment at time t to all three principal axes of the two-photon absorption tensor at time 0 (see Eq. 4.125). Even for a planar molecule like anthracene with D_{2h} symmetry, the photon-selection probability for the two-photon $B_{1g} \leftarrow A_{1g}$ transition is proportional to $(\cos \theta' \sin \theta' \cos \beta')^2$.⁽¹⁸⁾ Here θ' is the angle between a chosen molecular axis and the excitation polarization, and β' is the angle between the plane of the molecule and the plane perpendicular to the excitation polarization.⁽¹⁸⁾ In this case the ratio of two-photon fluorescence anisotropy over one-photon fluorescence anisotropy can be proven to be 5/14 (instead of 10/7), which will cause a decrease (instead of an increase) for the resolution of time-resolved fluorescence anisotropy decay measurements.

Ideally, only when the two-photon transition tensor of the probe satisfies the special conditions discussed in Section 4.2, can theoretical dynamic models and their corresponding functional forms of $r_{11}(t)$ in liquids⁽¹⁹⁾ and macroscopically isotropic membrane systems^(15,16, 19–21) still be applied to the two-photon case by simply multiplying by a constant. Note that the two-photon experiments mentioned here used two identical photons. If two photons of mixed polarizations are used to investigate the system, a different time-dependent fluorescence anisotropy decay profile can be expected due to a different photon-selection process (see Chapter 2). The information concerning the two-photon-induced excited-state symmetry and the rotational dynamics of the fluorophore with respect to each of its molecular axes could be resolved with a combination of mixed polarized photons.

In oriented systems fluorescence depolarization after two-photon excitation markedly differs from that using single-photon excitation. The information on orientational order from two-photon depolarization measurements is significantly more extensive than that from single-photon depolarization studies. The limiting value of $R_{o[2]}$ at time 0 obtained from angle-resolved fluorescence anisotropy measurements can be used to extract the value of the sixth-rank order parameter, $\langle P_6 \rangle$, which was considered to be inaccessible by the conventional one-photon-induced fluorescence measurements.^(15–17) In combination with the second- and fourth-rank order parameters ($\langle P_2 \rangle$ and $\langle P_4 \rangle$) obtained from conventional one-photon-induced angle-resolved fluorescence measurements, a more detailed molecular orientational distribution for the membrane system can be reconstructed. Polarized fluorescence microscopy is a very interesting alternative for angle-resolved fluorescence depolarization studies. Order parameters of sixth rank can be obtained from measurements of polarized fluorescence intensity ratios as a function of position for cell membranes or liposomes in a fluorescence microscope using two-photon excitation.

Appendix A

This appendix contains the derivation of Eq. (4.1) for $m = 1$:

$$I_{[1]}(\varphi, \psi, t) = I_{[1]}(0^\circ, 54.7^\circ, t)\{1 + r_{[1]}(t)[3 \cos^2 \varphi \cos^2 \psi - 1]\} \quad (4.21)$$

This derivation starts with an expression for $I_{[1]}(\varphi, \psi, t)$:

$$I_{[1]}(\varphi, \psi, t) = K \langle \cos^2 \theta_{0A\varphi} \cos^2 \theta_{tE\psi} \rangle \quad (4.22)$$

Here $\theta_{0A\varphi}$ is the angle between the axis of the excitation polarizer (see Figure 4.1) and the absorption transition moment at time 0, the time of excitation by a very short flash. The angle $\theta_{tE\psi}$ is the angle between the axis of the emission polarizer and the emission transition moment at time t . The factor K is proportional to fluorophore concentration, absorbance, and quantum yield, which also depends on the lifetime and the time. The angle brackets indicate an ensemble average. The factor $\cos^2 \theta_{0A\varphi}$ is proportional to the probability that an incoming photon is absorbed; it depends on the angle φ in Figure 4.1 as follows:

$$\cos^2 \theta_{0A\varphi} = \{(\mathbf{a}_0 \cdot \mathbf{z}_L) \cos \varphi + (\mathbf{a}_0 \cdot \mathbf{y}_L) \sin \varphi\}^2 \quad (4.23)$$

where \mathbf{a}_0 is a unit vector along the absorption transition dipole moment at time 0, and, \mathbf{z}_L and \mathbf{y}_L are unit vectors along the laboratory z and y axis, respectively. The factors $\mathbf{a}_0 \cdot \mathbf{z}_L$ and $\mathbf{a}_0 \cdot \mathbf{y}_L$ are dot products. Similarly,

$$\cos^2 \theta_{tE\psi} = \{(\mathbf{e}_t \cdot \mathbf{z}_L) \cos \psi + (\mathbf{e}_t \cdot \mathbf{y}_L) \sin \psi\}^2 \quad (4.24)$$

where \mathbf{e}_t is a unit vector along the emission transition dipole at time t , and \mathbf{x}_L is a unit vector along the laboratory x axis. The brackets in Eq. (4.21) refer to two types of averaging processes: (1) the averaging in a distribution of molecular orientations axially symmetric with respect to the membrane normal, and (2) the averaging of local molecular coordinate systems which are randomly distributed with respect to the laboratory coordinate system because of the isotropy of the membrane suspension. As a result of the latter averaging process the following factors vanish:

$$\begin{aligned} \langle (\mathbf{a}_0 \cdot \mathbf{z}_L)(\mathbf{a}_0 \cdot \mathbf{y}_L)(\mathbf{e}_t \cdot \mathbf{z}_L)^2 \rangle &= \langle (\mathbf{a}_0 \cdot \mathbf{z}_L)(\mathbf{a}_0 \cdot \mathbf{y}_L)(\mathbf{e}_t \cdot \mathbf{x}_L)^2 \rangle \\ &= \langle (\mathbf{a}_0 \cdot \mathbf{z}_L)^2 (\mathbf{e}_t \cdot \mathbf{z}_L)(\mathbf{e}_t \cdot \mathbf{x}_L) \rangle \\ &= \langle (\mathbf{a}_0 \cdot \mathbf{y}_L)^2 (\mathbf{e}_t \cdot \mathbf{z}_L)(\mathbf{e}_t \cdot \mathbf{x}_L) \rangle = 0 \end{aligned} \quad (4.25)$$

Substituting Eqs. (4.23) and (4.24) into Eq. (4.21), working out the squares, and employing Eq. (4.25) yields

$$\begin{aligned} I_{[1]}(\varphi, \psi, t) &= K \{ \cos^2 \varphi \cos^2 \psi \langle (\mathbf{z}_L \cdot \mathbf{a}_0)^2 (\mathbf{e}_t \cdot \mathbf{z}_L)^2 \rangle \\ &\quad + \cos^2 \varphi \sin^2 \psi \langle (\mathbf{z}_L \cdot \mathbf{a}_0)^2 (\mathbf{e}_t \cdot \mathbf{x}_L)^2 \rangle \\ &\quad + \sin^2 \varphi \cos^2 \psi \langle (\mathbf{y}_L \cdot \mathbf{a}_0)^2 (\mathbf{e}_t \cdot \mathbf{z}_L)^2 \rangle \\ &\quad + \sin^2 \varphi \sin^2 \psi \langle (\mathbf{y}_L \cdot \mathbf{a}_0)^2 (\mathbf{e}_t \cdot \mathbf{x}_L)^2 \rangle \} \end{aligned} \quad (4.26)$$

To execute the second averaging process, we decompose \mathbf{a}_0 and \mathbf{e}_t in Cartesian components, using a local coordinate system with unit vectors x, y, z along these local x, y, z axes, with one of these axes along the membrane normal:

$$\mathbf{a}_0 = \sum_{\alpha} a_{0\alpha} \boldsymbol{\alpha} \quad \mathbf{e}_t = \sum_{\beta} e_{t\beta} \boldsymbol{\beta} \quad (4.27)$$

where the summations run over x, y , and z . Expanding the unit vectors along the transition moments in Cartesian components as in Eq. (4.27) yields the following expressions for the correlation functions in Eq. (4.26):

$$\langle (\mathbf{z}_L \cdot \mathbf{a}_0)^2 (\mathbf{e}_t \cdot \mathbf{z}_L)^2 \rangle = \sum_{\alpha, \beta, \gamma, \rho} \langle a_{0\alpha} a_{0\beta} e_{t\gamma} e_{t\rho} (\mathbf{z}_L \cdot \boldsymbol{\alpha}) (\mathbf{z}_L \cdot \boldsymbol{\beta}) (\mathbf{z}_L \cdot \boldsymbol{\gamma}) (\mathbf{z}_L \cdot \boldsymbol{\rho}) \rangle \quad (4.28)$$

$$\langle (\mathbf{z}_L \cdot \mathbf{a}_0)^2 (\mathbf{e}_t \cdot \mathbf{x}_L)^2 \rangle = \sum_{\alpha, \beta, \gamma, \rho} \langle a_{0\alpha} a_{0\beta} e_{t\gamma} e_{t\rho} (\mathbf{z}_L \cdot \boldsymbol{\alpha}) (\mathbf{z}_L \cdot \boldsymbol{\beta}) (\mathbf{x}_L \cdot \boldsymbol{\gamma}) (\mathbf{x}_L \cdot \boldsymbol{\rho}) \rangle \quad (4.29)$$

$$\langle (\mathbf{y}_L \cdot \mathbf{a}_0)^2 (\mathbf{e}_t \cdot \mathbf{z}_L)^2 \rangle = \sum_{\alpha, \beta, \gamma, \rho} \langle a_{0\alpha} a_{0\beta} e_{t\gamma} e_{t\rho} (\mathbf{y}_L \cdot \boldsymbol{\alpha}) (\mathbf{y}_L \cdot \boldsymbol{\beta}) (\mathbf{z}_L \cdot \boldsymbol{\gamma}) (\mathbf{z}_L \cdot \boldsymbol{\rho}) \rangle \quad (4.30)$$

$$\langle (\mathbf{y}_L \cdot \mathbf{a}_0)^2 (\mathbf{e}_t \cdot \mathbf{x}_L)^2 \rangle = \sum_{\alpha, \beta, \gamma, \rho} \langle a_{0\alpha} a_{0\beta} e_{t\gamma} e_{t\rho} (\mathbf{y}_L \cdot \boldsymbol{\alpha}) (\mathbf{y}_L \cdot \boldsymbol{\beta}) (\mathbf{x}_L \cdot \boldsymbol{\gamma}) (\mathbf{x}_L \cdot \boldsymbol{\rho}) \rangle \quad (4.31)$$

where all the summations run over x, y , and z of the local coordinate system. Using the Kronecker delta δ_{ij} , defined as $\delta_{ij} = 1$ if $i=j$ and $\delta_{ij} = 0$ if $i \neq j$, for $i, j = \alpha, \beta, \gamma, \rho$, we have

$$\langle (\mathbf{z}_L \cdot \boldsymbol{\alpha}) (\mathbf{z}_L \cdot \boldsymbol{\beta}) (\mathbf{z}_L \cdot \boldsymbol{\gamma}) (\mathbf{z}_L \cdot \boldsymbol{\rho}) \rangle = \frac{1}{15} (\delta_{\alpha\beta} \delta_{\gamma\rho} + \delta_{\alpha\gamma} \delta_{\beta\rho} + \delta_{\alpha\rho} \delta_{\beta\gamma}) \quad (4.32)$$

$$\langle (\mathbf{z}_L \cdot \boldsymbol{\alpha}) (\mathbf{z}_L \cdot \boldsymbol{\beta}) (\mathbf{x}_L \cdot \boldsymbol{\gamma}) (\mathbf{x}_L \cdot \boldsymbol{\rho}) \rangle = \frac{1}{30} (4 \delta_{\alpha\beta} \delta_{\gamma\rho} - \delta_{\alpha\gamma} \delta_{\beta\rho} - \delta_{\alpha\rho} \delta_{\beta\gamma}) \quad (4.33)$$

$$\langle (\mathbf{y}_L \cdot \boldsymbol{\alpha}) (\mathbf{y}_L \cdot \boldsymbol{\beta}) (\mathbf{z}_L \cdot \boldsymbol{\gamma}) (\mathbf{z}_L \cdot \boldsymbol{\rho}) \rangle = \frac{1}{30} (4 \delta_{\alpha\beta} \delta_{\gamma\rho} - \delta_{\alpha\gamma} \delta_{\beta\rho} - \delta_{\alpha\rho} \delta_{\beta\gamma}) \quad (4.34)$$

$$\langle (\mathbf{y}_L \cdot \boldsymbol{\alpha}) (\mathbf{y}_L \cdot \boldsymbol{\beta}) (\mathbf{x}_L \cdot \boldsymbol{\gamma}) (\mathbf{x}_L \cdot \boldsymbol{\rho}) \rangle = \frac{1}{30} (4 \delta_{\alpha\beta} \delta_{\gamma\rho} - \delta_{\alpha\gamma} \delta_{\beta\rho} - \delta_{\alpha\rho} \delta_{\beta\gamma}) \quad (4.35)$$

Equation (4.32) is derived in Appendix A.1, and Eqs. (4.33)–(4.35) are derived in Appendix A.2. Substituting Eq. (4.32) into (4.28) and evaluating the summations yields

$$\langle (\mathbf{z}_L \cdot \mathbf{a}_0)^2 (\mathbf{e}_t \cdot \mathbf{z}_L)^2 \rangle = \frac{1}{15} \sum_{\alpha\gamma} \langle a_{0\alpha}^2 e_{t\gamma}^2 \rangle + \frac{2}{15} \sum_{\alpha\gamma} \langle a_{0\alpha} e_{t\alpha} a_{0\gamma} e_{t\gamma} \rangle = \frac{1}{15} + \frac{2}{15} \langle (\mathbf{a}_0 \cdot \mathbf{e}_t)^2 \rangle \quad (4.36)$$

Similarly, combining Eqs. (4.33) with (4.29), (4.34) with (4.30), and (4.35) with (4.31) results in

$$\begin{aligned} \langle (\mathbf{z}_L \cdot \mathbf{a}_0)^2 (\mathbf{e}_t \cdot \mathbf{x}_L)^2 \rangle &= \langle (\mathbf{y}_L \cdot \mathbf{a}_0)^2 (\mathbf{e}_t \cdot \mathbf{z}_L)^2 \rangle = \langle (\mathbf{y}_L \cdot \mathbf{a}_0)^2 (\mathbf{e}_t \cdot \mathbf{x}_L)^2 \rangle \\ &= \frac{4}{30} \sum_{\alpha\gamma} \langle a_{0\alpha}^2 e_{t\gamma}^2 \rangle - \frac{2}{30} \sum_{\alpha\gamma} \langle a_{0\alpha} e_{t\alpha} a_{0\gamma} e_{t\gamma} \rangle \\ &= \frac{2}{15} - \frac{1}{15} \langle (\mathbf{a}_0 \cdot \mathbf{e}_t)^2 \rangle \end{aligned} \quad (4.37)$$

Substituting Eqs. (4.36) and (4.37) into Eq. (4.26) yields

$$\begin{aligned} I_{[1]}(\varphi, \psi, t) &= K \{ \cos^2 \varphi \cos^2 \psi [\frac{1}{15} + \frac{2}{15} \langle (\mathbf{a}_0 \cdot \mathbf{e}_t)^2 \rangle - (\frac{2}{15} - \frac{1}{15} \langle (\mathbf{a}_0 \cdot \mathbf{e}_t)^2 \rangle)] \\ &\quad + (\frac{2}{15} - \frac{1}{15} \langle (\mathbf{a}_0 \cdot \mathbf{e}_t)^2 \rangle) \} \\ &= K \{ \cos^2 \varphi \cos^2 \psi [\frac{3}{15} \langle (\mathbf{a}_0 \cdot \mathbf{e}_t)^2 \rangle - \frac{1}{15}] + (\frac{2}{15} - \frac{1}{15} \langle (\mathbf{a}_0 \cdot \mathbf{e}_t)^2 \rangle) \} \\ &= \frac{1}{9} K \{ 1 + \frac{2}{5} \langle P_2(\mathbf{a}_0 \cdot \mathbf{e}_t) \rangle (3 \cos^2 \varphi \cos^2 \psi - 1) \} \end{aligned} \quad (4.38)$$

where P_2 is the second Legendre polynomial, defined as $P_2(x) = \frac{3}{2}x^2 - \frac{1}{2}$ for any x between -1 and $+1$. Note that for $\varphi = 0^\circ$, $\cos^2 \varphi = 1$, and for $\psi = 54.7^\circ$, $\cos^2 \psi = \frac{1}{3}$, so $3 \cos^2 \varphi \cos^2 \psi - 1 = 0$, and

$$I_{[1]}(0^\circ, 54.7^\circ, t) = \frac{1}{9} K \quad (4.39)$$

Also note that

$$I_{[1]}(0^\circ, 0^\circ, t) = \frac{1}{9} K \{ 1 + \frac{4}{5} \langle P_2(\mathbf{a}_0 \cdot \mathbf{e}_t) \rangle \} \quad (4.40)$$

and

$$I_{[1]}(0^\circ, 90^\circ, t) = \frac{1}{9} K \{ 1 - \frac{2}{5} \langle P_2(\mathbf{a}_0 \cdot \mathbf{e}_t) \rangle \} \quad (4.41)$$

so

$$I_{[1]}(0^\circ, 0^\circ, t) - I_{[1]}(0^\circ, 90^\circ, t) = \frac{1}{9} K \frac{6}{5} \langle P_2(\mathbf{a}_0 \cdot \mathbf{e}_t) \rangle \quad (4.42)$$

and

$$I_{[1]}(0^\circ, 0^\circ, t) + 2I_{[1]}(0^\circ, 90^\circ, t) = \frac{1}{3} K \quad (4.43)$$

From Eqs. (4.42) and (4.43) it follows that

$$r_{[1]} = \frac{I_{[1]}(0^\circ, 0^\circ, t) - I_{[1]}(0^\circ, 90^\circ, t)}{I_{[1]}(0^\circ, 0^\circ, t) + 2I_{[1]}(0^\circ, 90^\circ, t)} = \frac{2}{5} \langle P_2(\mathbf{a}_0 \cdot \mathbf{e}_t) \rangle \quad (4.44)$$

After K is eliminated from Eq. (4.38) by using Eq. (4.39), and $\langle P_2(\mathbf{a}_0 \cdot \mathbf{e}_t) \rangle$ from Eq. (4.38) by using Eq. (4.44), Eq. (4.38) becomes

$$I_{[1]}(\varphi, \psi, t) = I_{[1]}(0^\circ, 54.7^\circ, t) \{1 + r_{[1]}(3 \cos^2 \varphi \cos^2 \psi - 1)\} \quad (4.45)$$

which is Eq. (4.1) for $m = 1$.

Appendix A.1

In this appendix the derivation of Eq. (4.32) is presented (see also Ref. 13). Because of the isotropy of the distribution of the local Cartesian coordinate system with respect to the laboratory coordinate system, it is clear that $\langle (\mathbf{z}_L \cdot \boldsymbol{\alpha})(\mathbf{z}_L \cdot \boldsymbol{\beta})(\mathbf{z}_L \cdot \boldsymbol{\gamma})(\mathbf{z}_L \cdot \boldsymbol{\rho}) \rangle$ can be nonzero only if each of the elements in the set $\{\alpha, \beta, \gamma, \rho\}$ is equal to at least one other of these elements. Therefore, two types of terms of the form $\langle (\mathbf{z}_L \cdot \boldsymbol{\alpha})(\mathbf{z}_L \cdot \boldsymbol{\beta})(\mathbf{z}_L \cdot \boldsymbol{\gamma})(\mathbf{z}_L \cdot \boldsymbol{\rho}) \rangle$ must be considered, for which we introduce the following names: a (4)-term and a (2,2)-term. A (4)-term is a term in which all elements of $\{\alpha, \beta, \gamma, \rho\}$ are equal to each other, and a (2,2)-term is a term in which each element is equal to one other but not more than two elements are equal to each other. There is only one (4)-term, and this corresponds to $\alpha = \beta = \gamma = \rho$. Its average value is

$$\langle (\mathbf{z}_L \cdot \mathbf{z})^4 \rangle = \frac{1}{2} \int_0^\pi \cos^4 \theta \sin \theta d\theta = \frac{1}{5} \quad (4.46)$$

There are three (2,2)-terms, corresponding to $\alpha = \beta \neq \gamma = \rho$, $\alpha = \gamma \neq \beta = \rho$, and $\alpha = \rho \neq \beta = \gamma$. These three terms have the same average value, which can be calculated as

$$\langle (\mathbf{z}_L \cdot \mathbf{z})^2 (\mathbf{z}_L \cdot \mathbf{x})^2 \rangle = \frac{1}{4\pi} \int_0^{2\pi} \int_0^\pi \cos^2 \theta \sin^2 \theta \cos^2 \phi \sin \theta d\theta d\phi = \frac{1}{15} \quad (4.47)$$

The fact that $\langle (\mathbf{z}_L \cdot \boldsymbol{\alpha})(\mathbf{z}_L \cdot \boldsymbol{\beta})(\mathbf{z}_L \cdot \boldsymbol{\gamma})(\mathbf{z}_L \cdot \boldsymbol{\rho}) \rangle$ is nonzero only if the unit vectors are pairwise equal to each other suggests that this average can be expressed in terms

of products of Kronecker deltas. The following equation summarizes all the possible values of this average:

$$\langle(\mathbf{z}_L \cdot \alpha)(\mathbf{z}_L \cdot \beta)(\mathbf{z}_L \cdot \gamma)(\mathbf{z}_L \cdot \rho)\rangle = \frac{1}{15}(\delta_{\alpha\beta}\delta_{\gamma\rho} + \delta_{\alpha\gamma}\delta_{\beta\rho} + \delta_{\alpha\rho}\delta_{\beta\gamma})$$

This is Eq. (4.32).

Appendix A.2

This appendix contains the derivation of Eqs. (4.33)–(4.35):

$$\begin{aligned} \langle(\mathbf{z}_L \cdot \alpha)(\mathbf{z}_L \cdot \beta)(\mathbf{z}_L \cdot \gamma)(\mathbf{z}_L \cdot \rho)\rangle &= \langle(\mathbf{y}_L \cdot \alpha)(\mathbf{y}_L \cdot \beta)(\mathbf{z}_L \cdot \gamma)(\mathbf{z}_L \cdot \rho)\rangle \\ \langle(\mathbf{y}_L \cdot \alpha)(\mathbf{y}_L \cdot \beta)(\mathbf{x}_L \cdot \gamma)(\mathbf{x}_L \cdot \rho)\rangle &= \frac{1}{30}(4\delta_{\alpha\beta}\delta_{\gamma\rho} - \delta_{\alpha\gamma}\delta_{\beta\rho} - \delta_{\alpha\rho}\delta_{\beta\gamma}) \end{aligned} \quad (4.48)$$

Because the average of $(\mathbf{z}_L \cdot \alpha)(\mathbf{z}_L \cdot \beta)(\mathbf{x}_L \cdot \gamma)(\mathbf{x}_L \cdot \rho)$ should be invariant for a 90° rotation around any of the laboratory coordinate axes, the three averages in Eq. (4.48) must be equal. We will evaluate $\langle(\mathbf{z}_L \cdot \alpha)(\mathbf{z}_L \cdot \beta)(\mathbf{x}_L \cdot \gamma)(\mathbf{x}_L \cdot \rho)\rangle$. As in Appendix A.1, we have one (4)-term (corresponding to $\alpha=\beta=\gamma=\rho$) and three (2,2)-terms (corresponding to $\alpha=\beta\neq\gamma=\rho$, $\alpha=\gamma\neq\beta=\rho$, and $\alpha=\rho\neq\beta=\gamma$). The average of the (4)-term is

$$\langle(\mathbf{z}_L \cdot \mathbf{z})^2(\mathbf{x}_L \cdot \mathbf{z})^2\rangle = \frac{1}{4\pi} \int_0^{2\pi} \int_0^\pi \cos^2 \theta \sin^2 \theta \cos^2 \xi \sin \theta d\theta d\xi = \frac{1}{15} \quad (4.49)$$

The value of the (2,2)-term with $\alpha=\beta\neq\gamma=\rho$ is

$$\begin{aligned} \langle(\mathbf{z}_L \cdot \mathbf{x})^2(\mathbf{x}_L \cdot \mathbf{z})^2\rangle &= \frac{1}{8\pi^2} \int_0^{2\pi} \int_0^\pi \int_0^\pi \sin^2 \theta \cos^2 \phi \sin^2 \theta \cos^2 \xi \sin \theta d\theta d\phi d\xi \\ &= \frac{2}{15} \end{aligned} \quad (4.50)$$

The other two (2,2)-terms with $\alpha=\gamma\neq\beta=\rho$ and $\alpha=\rho\neq\beta=\gamma$ can be written as $\langle(\mathbf{z}_L \cdot \mathbf{z})(\mathbf{x}_L \cdot \mathbf{z})(\mathbf{z}_L \cdot \mathbf{x})(\mathbf{x}_L \cdot \mathbf{x})\rangle$. This average can be calculated from the dot product, $\mathbf{z}_L \cdot \mathbf{x}_L = 0 = (\mathbf{z}_L \cdot \mathbf{x})(\mathbf{x}_L \cdot \mathbf{x}) + (\mathbf{z}_L \cdot \mathbf{y})(\mathbf{x}_L \cdot \mathbf{y}) + (\mathbf{z}_L \cdot \mathbf{z})(\mathbf{x}_L \cdot \mathbf{z})$:

$$\begin{aligned} \langle(\mathbf{z}_L \cdot \mathbf{z})(\mathbf{x}_L \cdot \mathbf{z})(\mathbf{z}_L \cdot \mathbf{x}_L)\rangle &= 0 = \langle(\mathbf{z}_L \cdot \mathbf{z})(\mathbf{x}_L \cdot \mathbf{z})(\mathbf{z}_L \cdot \mathbf{x})(\mathbf{x}_L \cdot \mathbf{x})\rangle \\ &\quad + \langle(\mathbf{z}_L \cdot \mathbf{z})(\mathbf{x}_L \cdot \mathbf{z})(\mathbf{z}_L \cdot \mathbf{y})(\mathbf{x}_L \cdot \mathbf{y})\rangle \\ &\quad + \langle(\mathbf{z}_L \cdot \mathbf{z})(\mathbf{x}_L \cdot \mathbf{z})(\mathbf{z}_L \cdot \mathbf{z})(\mathbf{x}_L \cdot \mathbf{z})\rangle \end{aligned} \quad (4.51)$$

The first two terms on the right-hand side are equal by symmetry. The last term is equal to $\frac{1}{15}$, as calculated in Eq. (4.49). Therefore,

$$\begin{aligned} 0 &= 2\langle(\mathbf{z}_L \cdot \mathbf{z})(\mathbf{x}_L \cdot \mathbf{z})(\mathbf{z}_L \cdot \mathbf{x})(\mathbf{x}_L \cdot \mathbf{x})\rangle + \frac{1}{15} \\ &\Rightarrow \langle(\mathbf{z}_L \cdot \mathbf{z})(\mathbf{x}_L \cdot \mathbf{z})(\mathbf{z}_L \cdot \mathbf{x})(\mathbf{x}_L \cdot \mathbf{x})\rangle = -\frac{1}{30} \end{aligned} \quad (4.52)$$

The following equation, which is Eq. (4.33) and is equivalent to Eq. (4.34) and Eq. (4.35), summarizes all possible values of the average of $(\mathbf{z}_L \cdot \boldsymbol{\alpha})(\mathbf{z}_L \cdot \boldsymbol{\beta})(\mathbf{x}_L \cdot \boldsymbol{\gamma})(\mathbf{x}_L \cdot \{\mathbf{p}\})$:

$$\langle(\mathbf{z}_L \cdot \boldsymbol{\alpha})(\mathbf{z}_L \cdot \boldsymbol{\beta})(\mathbf{x}_L \cdot \boldsymbol{\gamma})(\mathbf{x}_L \cdot \{\mathbf{p}\})\rangle = \frac{1}{30}(\delta_{\alpha\beta}\delta_{\gamma\rho} - \delta_{\alpha\gamma}\delta_{\beta\rho} - \delta_{\alpha\rho}\delta_{\beta\gamma})$$

Appendix B

This appendix contains the derivation of Eq. (4.2) for $m = 2$. In the geometry of Figure 4.1 the probability, $P_{[2]\text{ABS}}$, that two identical photons are absorbed by a fluorophore at time 0, the time of excitation by a very short flash, is proportional to

$$P_{[2]\text{ABS}} \sim (\mathbf{p}_{\text{ex}} \cdot \mathbf{S}_0 \cdot \mathbf{p}_{\text{ex}})^2 \quad (4.53)$$

where \mathbf{S}_0 is the two-photon absorption tensor at time 0, the dots represent dot products, and \mathbf{p}_{ex} is a unit vector along the polarization direction of the exciting light. For the geometry of Figure 4.1, this unit vector can be written as

$$\mathbf{p}_{\text{ex}} = \mathbf{z}_L \cos \varphi + \mathbf{y}_L \sin \varphi \quad (4.54)$$

The unit vector along the polarization direction of the light passing through the polarizer in the emission, \mathbf{p}_{em} , in this case is

$$\mathbf{p}_{\text{em}} = \mathbf{z}_L \cos \psi + \mathbf{y}_L \sin \psi \quad (4.55)$$

In Figure 4.1 the probability, P_{EMI} , that an emitted photon will pass through the emission polarizer at time t is proportional to

$$P_{\text{EMI}} \sim (\mathbf{e}_t \cdot \mathbf{p}_{\text{em}})^2 \quad (4.56)$$

where \mathbf{e}_t is a unit vector along the emission transition dipole moment of the fluorophore. The fluorescence intensity at time t , after two-photon excitation at time 0, for Figure 4.1 is proportional to

$$I_{[2]}(\varphi, \psi, t) \sim \langle P_{[2]\text{ABS}} P_{\text{EMI}} \rangle \quad (4.57)$$

where the angle brackets denote ensemble average. Combining Eqs. (4.53)–(4.57) yields the following expression for this intensity:

$$\begin{aligned} I_{[2]}(\varphi, \psi, t) = & K' \langle \{\cos^2 \varphi (\mathbf{z}_L \cdot \mathbf{S}_0 \cdot \mathbf{z}_L) + \cos \varphi \sin \varphi (\mathbf{z}_L \cdot \mathbf{S}_0 \cdot \mathbf{y}_L + \mathbf{y}_L \cdot \mathbf{S}_0 \cdot \mathbf{z}_L) \\ & + \sin^2 \varphi (\mathbf{y}_L \cdot \mathbf{S}_0 \cdot \mathbf{y}_L)\}^2 \\ & \times \{\cos^2 \psi (\mathbf{e}_t \cdot \mathbf{z}_L)^2 + 2 \cos \psi \sin \psi (\mathbf{e}_t \cdot \mathbf{z}_L)(\mathbf{e}_t \cdot \mathbf{x}_L) \\ & + \sin^2 \psi (\mathbf{e}_t \cdot \mathbf{x}_L)^2\} \rangle \end{aligned} \quad (4.58)$$

where the time-dependent factor K' is proportional to two-photon absorbance and depends on the lifetime of the excited state. After evaluating the products in Eq. (4.58), realizing that the terms proportional to $(\mathbf{z}_L \cdot \mathbf{S}_0 \cdot \mathbf{y}_L + \mathbf{y}_L \cdot \mathbf{S}_0 \cdot \mathbf{z}_L)$ and $(\mathbf{e}_t \cdot \mathbf{z}_L)(\mathbf{e}_t \cdot \mathbf{x}_L)$ vanish because of the isotropic symmetry of the system, we have for Eq. (4.58)

$$\begin{aligned} I_{[1]}(\varphi, \psi, t) = & K' \{A_1 \cos^4 \varphi \cos^2 \psi + A_2 \cos^4 \varphi \sin^2 \psi + A_3 \sin^4 \varphi \cos^2 \psi \\ & + A_4 \sin^4 \varphi \sin^2 \psi + A_5 \cos^2 \varphi \sin^2 \varphi \cos^2 \psi \\ & + A_6 \cos^2 \varphi \sin^2 \varphi \sin^2 \psi\} \end{aligned} \quad (4.59)$$

where the following abbreviations have been used:

$$A_1 = \langle (\mathbf{z}_L \cdot \mathbf{S}_0 \cdot \mathbf{z}_L)^2 (\mathbf{e}_t \cdot \mathbf{z}_L)^2 \rangle \quad (4.60)$$

$$A_2 = \langle (\mathbf{z}_L \cdot \mathbf{S}_0 \cdot \mathbf{z}_L)^2 (\mathbf{e}_t \cdot \mathbf{x}_L)^2 \rangle \quad (4.61)$$

$$A_3 = \langle (\mathbf{y}_L \cdot \mathbf{S}_0 \cdot \mathbf{y}_L)^2 (\mathbf{e}_t \cdot \mathbf{z}_L)^2 \rangle \quad (4.62)$$

$$A_4 = \langle (\mathbf{y}_L \cdot \mathbf{S}_0 \cdot \mathbf{y}_L)^2 (\mathbf{e}_t \cdot \mathbf{x}_L)^2 \rangle \quad (4.63)$$

$$\begin{aligned} A_5 = & \langle \{(\mathbf{z}_L \cdot \mathbf{S}_0 \cdot \mathbf{y}_L)^2 + (\mathbf{y}_L \cdot \mathbf{S}_0 \cdot \mathbf{z}_L)^2 + (\mathbf{z}_L \cdot \mathbf{S}_0 \cdot \mathbf{y}_L)(\mathbf{y}_L \cdot \mathbf{S}_0 \cdot \mathbf{z}_L) \\ & + (\mathbf{y}_L \cdot \mathbf{S}_0 \cdot \mathbf{z}_L)(\mathbf{z}_L \cdot \mathbf{S}_0 \cdot \mathbf{y}_L) + (\mathbf{z}_L \cdot \mathbf{S}_0 \cdot \mathbf{z}_L)(\mathbf{y}_L \cdot \mathbf{S}_0 \cdot \mathbf{y}_L) \\ & + (\mathbf{y}_L \cdot \mathbf{S}_0 \cdot \mathbf{y}_L)(\mathbf{z}_L \cdot \mathbf{S}_0 \cdot \mathbf{z}_L)\} (\mathbf{e}_t \cdot \mathbf{z}_L)^2 \rangle \end{aligned}$$

$$\begin{aligned} A_6 = & \langle \{(\mathbf{z}_L \cdot \mathbf{S}_0 \cdot \mathbf{y}_L)^2 + (\mathbf{y}_L \cdot \mathbf{S}_0 \cdot \mathbf{z}_L)^2 + (\mathbf{z}_L \cdot \mathbf{S}_0 \cdot \mathbf{y}_L)(\mathbf{y}_L \cdot \mathbf{S}_0 \cdot \mathbf{z}_L) \\ & + (\mathbf{y}_L \cdot \mathbf{S}_0 \cdot \mathbf{z}_L)(\mathbf{z}_L \cdot \mathbf{S}_0 \cdot \mathbf{y}_L) + (\mathbf{z}_L \cdot \mathbf{S}_0 \cdot \mathbf{z}_L)(\mathbf{y}_L \cdot \mathbf{S}_0 \cdot \mathbf{y}_L) \\ & + (\mathbf{y}_L \cdot \mathbf{S}_0 \cdot \mathbf{y}_L)(\mathbf{z}_L \cdot \mathbf{S}_0 \cdot \mathbf{z}_L)\} (\mathbf{e}_t \cdot \mathbf{x}_L)^2 \rangle \end{aligned} \quad (4.65)$$

After expanding \mathbf{S}_0 and \mathbf{e}_t in the Cartesian components of a local coordinate system and employing the isotropic symmetry of the system, we can rewrite

Eqs. (4.60)–(4.65) as

$$A_1 = \sum_{\alpha, \beta, \gamma, \rho, \eta, \chi} \langle S_{\alpha\beta}(0) S_{\gamma\rho}(0) e_\eta(t) e_\chi(t) \rangle \langle \mathbf{A} \rangle \quad (4.66)$$

$$A_2 = A_3 = A_4 = \sum_{\alpha, \beta, \gamma, \rho, \eta, \chi} \langle S_{\alpha\beta}(0) S_{\gamma\rho}(0) e_\eta(t) e_\chi(t) \rangle \langle \mathbf{B} \rangle \quad (4.67)$$

$$A_5 = \sum_{\alpha, \beta, \gamma, \rho, \eta, \chi} \langle D_{\alpha\beta\gamma\rho\eta\chi} \rangle \langle \mathbf{B} \rangle \quad (4.68)$$

$$\begin{aligned} D_{\alpha\beta\gamma\rho\eta\chi} = & S_{\gamma\eta}(0) S_{\rho\chi}(0) e_\alpha(t) e_\beta(t) + S_{\chi\rho}(0) S_{\eta\gamma}(0) e_\alpha(t) e_\beta(t) \\ & + S_{\gamma\chi}(0) S_{\eta\rho}(0) e_\alpha(t) e_\beta(t) + S_{\eta\rho}(0) S_{\gamma\chi}(0) e_\alpha(t) e_\beta(t) \\ & + S_{\gamma\rho}(0) S_{\eta\chi}(0) e_\alpha(t) e_\beta(t) + S_{\eta\chi}(0) S_{\gamma\rho}(0) e_\alpha(t) e_\beta(t) \end{aligned} \quad (4.69)$$

$$A_6 = \sum_{\alpha, \beta, \gamma, \rho, \eta, \chi} \langle E_{\alpha\beta\gamma\rho\eta\chi} \rangle \langle \mathbf{C} \rangle \quad (4.70)$$

$$\begin{aligned} E_{\alpha\beta\gamma\rho\eta\chi} = & S_{\alpha\gamma}(0) S_{\beta\rho}(0) e_\eta(t) e_\chi(t) + S_{\rho\beta}(0) S_{\gamma\alpha}(0) e_\eta(t) e_\chi(t) \\ & + S_{\alpha\rho}(0) S_{\gamma\beta}(0) e_\eta(t) e_\chi(t) + S_{\gamma\beta}(0) S_{\alpha\rho}(0) e_\eta(t) e_\chi(t) \\ & + S_{\alpha\beta}(0) S_{\gamma\rho}(0) e_\eta(t) e_\chi(t) + S_{\gamma\rho}(0) S_{\alpha\beta}(0) e_\eta(t) e_\chi(t) \end{aligned} \quad (4.71)$$

where the following abbreviations have been used:

$$\langle \mathbf{A} \rangle = \langle (\boldsymbol{\alpha} \cdot \mathbf{z}_L)(\boldsymbol{\beta} \cdot \mathbf{z}_L)(\boldsymbol{\gamma} \cdot \mathbf{z}_L)(\boldsymbol{\rho} \cdot \mathbf{z}_L)(\boldsymbol{\eta} \cdot \mathbf{z}_L)(\boldsymbol{\chi} \cdot \mathbf{z}_L) \rangle \quad (4.72)$$

$$\langle \mathbf{B} \rangle = \langle (\boldsymbol{\alpha} \cdot \mathbf{z}_L)(\boldsymbol{\beta} \cdot \mathbf{z}_L)(\boldsymbol{\gamma} \cdot \mathbf{z}_L)(\boldsymbol{\rho} \cdot \mathbf{z}_L)(\boldsymbol{\eta} \cdot \mathbf{x}_L)(\boldsymbol{\chi} \cdot \mathbf{x}_L) \rangle \quad (4.73)$$

$$\langle \mathbf{C} \rangle = \langle (\boldsymbol{\alpha} \cdot \mathbf{z}_L)(\boldsymbol{\beta} \cdot \mathbf{z}_L)(\boldsymbol{\gamma} \cdot \mathbf{y}_L)(\{\boldsymbol{\rho} \cdot \mathbf{y}_L\})(\boldsymbol{\eta} \cdot \mathbf{x}_L)(\boldsymbol{\chi} \cdot \mathbf{x}_L) \rangle \quad (4.74)$$

Evaluating these three averages yields

$$\begin{aligned} 105\langle \mathbf{A} \rangle &= \delta_{\alpha\beta}(\delta_{\gamma\rho}\delta_{\eta\chi} + \delta_{\gamma\eta}\delta_{\rho\chi} + \delta_{\gamma\chi}\delta_{\eta\rho}) + \delta_{\alpha\gamma}(\delta_{\beta\rho}\delta_{\eta\chi} + \delta_{\beta\eta}\delta_{\rho\chi} + \delta_{\beta\chi}\delta_{\eta\rho}) \\ &\quad + \delta_{\alpha\rho}(\delta_{\gamma\beta}\delta_{\eta\chi} + \delta_{\gamma\eta}\delta_{\beta\chi} + \delta_{\gamma\chi}\delta_{\eta\beta}) + \delta_{\alpha\eta}(\delta_{\gamma\rho}\delta_{\beta\chi} + \delta_{\gamma\beta}\delta_{\rho\chi} + \delta_{\gamma\chi}\delta_{\beta\rho}) \\ &\quad + \delta_{\alpha\chi}(\delta_{\gamma\rho}\delta_{\eta\beta} + \delta_{\gamma\eta}\delta_{\rho\beta} + \delta_{\gamma\beta}\delta_{\eta\rho}) \end{aligned} \quad (4.75)$$

$$\begin{aligned} 210\langle \mathbf{B} \rangle &= 6\delta_{\eta\chi}(\delta_{\gamma\rho}\delta_{\alpha\beta} + \delta_{\alpha\eta}\delta_{\beta\rho} + \delta_{\alpha\rho}\delta_{\beta\eta}) - \delta_{\chi\rho}(\delta_{\alpha\beta}\delta_{\gamma\eta} + \delta_{\alpha\gamma}\delta_{\beta\eta} + \delta_{\alpha\eta}\delta_{\beta\gamma}) \\ &\quad - \delta_{\chi\gamma}(\delta_{\alpha\beta}\delta_{\rho\eta} + \delta_{\alpha\rho}\delta_{\beta\eta} + \delta_{\alpha\eta}\delta_{\beta\rho}) - \delta_{\chi\beta}(\delta_{\alpha\gamma}\delta_{\rho\eta} + \delta_{\alpha\rho}\delta_{\gamma\eta} + \delta_{\alpha\eta}\delta_{\gamma\rho}) \\ &\quad - \delta_{\alpha\chi}(\delta_{\gamma\rho}\delta_{\eta\beta} + \delta_{\gamma\eta}\delta_{\rho\beta} + \delta_{\gamma\beta}\delta_{\eta\rho}) \end{aligned} \quad (4.76)$$

$$\begin{aligned} 210\langle \mathbf{C} \rangle &= \delta_{\alpha\beta}(16\delta_{\gamma\rho}\delta_{\eta\chi} - 5\delta_{\gamma\eta}\delta_{\rho\chi} - 5\delta_{\gamma\chi}\delta_{\eta\rho}) \\ &\quad + \delta_{\alpha\gamma}(-5\delta_{\beta\rho}\delta_{\eta\chi} + 2\delta_{\beta\eta}\delta_{\rho\chi} + 2\delta_{\beta\chi}\delta_{\eta\rho}) \\ &\quad + \delta_{\alpha\rho}(-5\delta_{\gamma\beta}\delta_{\eta\chi} + 2\delta_{\gamma\eta}\delta_{\beta\chi} + 2\delta_{\gamma\chi}\delta_{\eta\beta}) \\ &\quad + \delta_{\alpha\eta}(-5\delta_{\gamma\rho}\delta_{\beta\chi} + 2\delta_{\gamma\beta}\delta_{\rho\chi} + 2\delta_{\gamma\chi} + 2\delta_{\gamma\chi}\delta_{\beta\rho}) \\ &\quad + \delta_{\alpha\chi}(-5\delta_{\gamma\rho}\delta_{\eta\beta} + 2\delta_{\gamma\eta}\delta_{\rho\beta} + 2\delta_{\gamma\beta}\delta_{\eta\rho}) \end{aligned} \quad (4.77)$$

Equations (4.75)–(4.77) are derived in Appendixes B.1–B.3, respectively. It is convenient to employ the following definitions:⁽¹³⁾

$$\text{tr } \mathbf{S} = \sum_{\alpha} S_{\alpha\alpha} = S_{xx} + S_{yy} + S_{zz} \quad (4.78)$$

$$\mathbf{S} \cdot \mathbf{S} = \sum_{\alpha, \beta} S_{\alpha\beta} S_{\beta\alpha} \quad (4.79)$$

$$\mathbf{e}_t \cdot \mathbf{S}_0 \cdot \mathbf{e}_t = \sum_{\alpha, \beta} e_{\alpha}(t) S_{\alpha\beta}(0) e_{\beta}(t) \quad (4.80)$$

$$\mathbf{e}_t \cdot \mathbf{S}_0 \cdot \mathbf{S}_0 \cdot \mathbf{e}_t = \sum_{\alpha, \beta, \gamma} e_{\alpha}(t) S_{\alpha\beta}(0) S_{\beta\gamma}(0) e_{\gamma}(t) \quad (4.81)$$

$$T = (\text{tr } \mathbf{S})^2 + 2\mathbf{S} \cdot \mathbf{S} \quad (4.82)$$

$$U_{0t} = \langle (\text{tr } \mathbf{S})(\mathbf{e}_t \cdot \mathbf{S}_0 \cdot \mathbf{e}_t) + 2(\mathbf{e}_t \cdot \mathbf{S}_0 \cdot \mathbf{S}_0 \cdot \mathbf{e}_t) \rangle \quad (4.83)$$

After substituting Eqs. (4.75) into (4.66), (4.76) into (4.67), and (4.77) into (4.70), and using the definitions (4.78)–(4.83), employing the symmetry of the

S tensor ,⁽¹³⁾ we find

$$A_1 = \frac{2}{210} \{T + 4U_{0t}\} \quad (4.84)$$

$$A_2 = A_3 = A_4 = \frac{2}{210} \{(3T - 2U_{0t})\} \quad (4.85)$$

$$A_5 = \frac{2}{210} \{4T + 2U_{0t}(\text{tr } \mathbf{S})\} \quad (4.86)$$

$$A_6 = \frac{2}{210} \{6T - 4U_{0t}\} \quad (4.87)$$

Substituting Eqs. (4.84)–(4.87) into Eq. (4.59) yields

$$I_{[2]}(\varphi, \psi, t) = \frac{2}{210} K' \{TF_1(\varphi, \psi) + U_{0t}F_2(\varphi, \psi)\} \quad (4.88)$$

where the following definitions have been used:

$$\begin{aligned} F_1(\varphi, \psi) &= \cos^4 \varphi \cos^2 \psi + 3 \cos^4 \varphi \sin^2 \psi + 3 \sin^4 \varphi \cos^2 \psi + 3 \sin^4 \varphi \sin^2 \psi \\ &\quad + 4 \cos^2 \varphi \sin^2 \varphi \cos^2 \psi + 6 \cos^2 \varphi \sin^2 \varphi \sin^2 \psi \end{aligned} \quad (4.89)$$

$$\begin{aligned} F_2(\varphi, \psi) &= 4 \cos^4 \varphi \cos^2 \psi - 2 \cos^4 \varphi \sin^2 \psi - 2 \sin^4 \varphi \cos^2 \psi - 2 \sin^4 \varphi \sin^2 \psi \\ &\quad + 2 \cos^2 \varphi \sin^2 \varphi \cos^2 \psi - 4 \cos^2 \varphi \sin^2 \varphi \sin^2 \psi \end{aligned} \quad (4.90)$$

Equations (4.89) and (4.90) can be simplified as follows:

$$\begin{aligned} F_1(\varphi, \psi) &= \cos^2 \psi (\cos^4 \varphi + 3 \sin^4 \varphi + 4 \cos^2 \varphi \sin^2 \varphi) \\ &\quad + \sin^2 \psi (3 \cos^4 \varphi + 3 \sin^4 \varphi + 6 \cos^2 \varphi \sin^2 \varphi) \\ &= \cos^2 \psi (\cos^4 \varphi + \cos^2 \varphi \sin^2 \varphi + 3 \sin^4 \varphi + 3 \cos^2 \varphi \sin^2 \varphi) \\ &\quad + 3 \sin^2 \psi (\cos^2 \varphi + \sin^2 \varphi)^2 \\ &= \cos^2 \psi (\cos^2 \varphi + 3 \sin^2 \varphi) + 3 \sin^2 \psi \\ &= 3 - 2 \cos^2 \varphi \cos^2 \psi = \frac{7}{3} - \frac{2}{3}(3 \cos^2 \varphi \cos^2 \psi - 1) \end{aligned} \quad (4.91)$$

$$\begin{aligned} F_2(\varphi, \psi) &= \cos^2 \psi (4 \cos^4 \varphi - 2 \sin^4 \varphi + 2 \cos^2 \varphi \sin^2 \varphi) \\ &\quad + \sin^2 \psi (-2 \cos^4 \varphi - 2 \sin^4 \varphi - 4 \cos^2 \varphi \sin^2 \varphi) \\ &= \cos^2 \psi (4 \cos^4 \varphi + 4 \cos^2 \varphi \sin^2 \varphi - 2 \sin^4 \varphi - 2 \cos^2 \varphi \sin^2 \varphi) \\ &\quad + \sin^2 \psi (-2)(\cos^2 \varphi + \sin^2 \varphi)^2 \\ &= \cos^2 \psi (4 \cos^2 \varphi - 2 \sin^2 \varphi) - 2 \sin^2 \psi \\ &= 6 \cos^2 \varphi \cos^2 \psi - 2 \cos^2 \psi - 2 \cos^2 \varphi = 2(3 \cos^2 \varphi \cos^2 \psi - 1) \end{aligned} \quad (4.92)$$

Substituting Eqs. (4.91) and (4.92) into (4.88) leads to

$$I_{[2]}(\varphi, \psi, t) = \frac{1}{45} K' T \left\{ 1 + \frac{2}{7} \frac{3U_{0t} - T}{T} (3 \cos^2 \varphi \cos^2 \psi - 1) \right\} \quad (4.93)$$

Note that (see Appendix A)

$$K' T = I_{[2]}(0^\circ, 54.7^\circ, t) \quad (4.94)$$

and that

$$\frac{2}{7} \frac{3U_{0t} - T}{T} = r_{[2]}(t) = \frac{I_{[2]}(0^\circ, 0^\circ, t) - I_{[2]}(0^\circ, 90^\circ, t)}{I_{[2]}(0^\circ, 0^\circ, t) + 2I_{[2]}(0^\circ, 90^\circ, t)} \quad (4.95)$$

Substituting Eqs. (4.94) and (4.95) into (4.93) yields

$$I_{[2]}(\varphi, \psi, t) = \frac{1}{45} K' T \left\{ 1 + \frac{2}{7} \frac{3U_{0t} - T}{T} (3 \cos^2 \varphi \cos^2 \psi - 1) \right\} \quad (4.96)$$

which is Eq. (4.1) for $m = 2$.

Appendix B.1

This appendix contains the derivation of Eq. (4.75). The terms **(A)**, **(B)**, and **(C)** can be nonzero only if each element in the set $\{\alpha, \beta, \gamma, \rho, \eta, \chi\}$ is equal to at least one other element. Therefore, three types of terms must be considered, for which we introduce the following names: a (2,2,2)-term, a (4,2)-term, and a (6)-term. A (2,2,2)-term is a term in which each element is equal to one other, but not more than two elements are equal to each other. There are 15 ways of realizing this possibility:

$$\begin{aligned} \alpha &= \beta \neq \gamma = \rho \neq \eta = \chi, & \alpha &= \beta \neq \gamma = \eta \neq \rho = \chi, & \alpha &= \beta \neq \gamma = \chi \neq \eta = \rho \\ \alpha &= \gamma \neq \beta = \rho \neq \eta = \chi, & \alpha &= \gamma \neq \beta = \eta \neq \rho = \chi, & \alpha &= \gamma \neq \beta = \chi \neq \eta = \rho \\ \alpha &= \rho \neq \beta = \gamma \neq \eta = \chi, & \alpha &= \rho \neq \beta = \eta \neq \gamma = \chi, & \alpha &= \rho \neq \beta = \chi \neq \eta = \gamma \\ \alpha &= \eta \neq \beta = \gamma \neq \rho = \chi, & \alpha &= \eta \neq \beta = \rho \neq \gamma = \chi, & \alpha &= \eta \neq \beta = \chi \neq \rho = \gamma \\ \alpha &= \chi \neq \beta = \gamma \neq \rho = \eta, & \alpha &= \chi \neq \beta = \rho \neq \gamma = \eta, & \alpha &= \chi \neq \beta = \eta \neq \rho = \gamma \end{aligned}$$

A (4,2)-term is a term in which four elements are equal to each other and the other two are equal to each other, but not to the other four. There are 15 ways of realizing this possibility:

$$\begin{aligned} \alpha = \beta \neq \gamma = \rho = \eta = \chi, \quad \alpha = \gamma \neq \beta = \rho = \eta = \chi, \quad \alpha = \rho \neq \beta = \gamma = \eta = \chi \\ \alpha = \eta \neq \beta = \gamma = \rho = \chi, \quad \alpha = \chi \neq \beta = \gamma = \rho = \eta, \quad \beta = \gamma \neq \alpha = \chi = \rho = \eta \\ \beta = \rho \neq \alpha = \chi = \gamma = \eta, \quad \beta = \eta \neq \alpha = \chi = \rho = \gamma, \quad \beta = \chi \neq \alpha = \eta = \rho = \gamma \\ \gamma = \rho \neq \alpha = \beta = \eta = \chi, \quad \gamma = \eta \neq \alpha = \beta = \rho = \chi, \quad \gamma = \chi \neq \alpha = \beta = \rho = \eta \\ \rho = \eta \neq \alpha = \chi = \beta = \gamma, \quad \rho = \chi \neq \alpha = \eta = \beta = \gamma, \quad \eta = \chi \neq \alpha = \beta = \gamma = \rho \end{aligned}$$

A (6)-term corresponds to all elements being equal to each other, which can be realized in only one way: $\alpha = \beta = \gamma = \rho = \eta = \chi$.

Evaluating $\langle \mathbf{A} \rangle$, $\langle \mathbf{B} \rangle$, and $\langle \mathbf{C} \rangle$ can be done by considering these terms, $\langle \mathbf{A} \rangle$ has four possible values:

1. There is one (6)-term, corresponding to $\alpha = \beta = \gamma = \rho = \eta = \chi$; $\langle \mathbf{A} \rangle$ is then

$$\langle \mathbf{A} \rangle = \langle (\mathbf{z}_L \cdot \mathbf{z})^6 \rangle = \frac{1}{2} \int_0^\pi \cos^6 \theta \sin \theta d\theta = \frac{1}{7} \quad (4.97)$$

2. All fifteen (4,2)-terms yield the same answer. Consider, for example, the case $\alpha = \beta \neq \gamma = \rho = \eta = \chi$. If we take $\mathbf{x} = \alpha = \mathbf{B}$ and $\mathbf{z} = \gamma = \rho = \eta = \chi$, then $(\alpha \cdot \mathbf{z}_L)(\beta \cdot \mathbf{z}_L) = \sin^2 \theta \cos^2 \phi$ and $(\gamma \cdot \mathbf{z}_L)(\rho \cdot \mathbf{z}_L)(\eta \cdot \mathbf{z}_L)(\chi \cdot \mathbf{z}_L) = \cos^4 \theta$. We find, therefore,

$$\begin{aligned} \langle \mathbf{A} \rangle &= \langle (\mathbf{z}_L \cdot \mathbf{x})^2 (\mathbf{z}_L \cdot \mathbf{z})^4 \rangle \\ &= \frac{1}{4\pi} \int_0^{2\pi} \int_0^\pi \cos^4 \theta \sin^3 \theta \cos^2 \phi d\theta d\phi = \frac{1}{35} \end{aligned} \quad (4.98)$$

3. All fifteen (2,2)-terms yield the same answer. Consider, for example, the case $\alpha = \beta \neq \gamma = \rho \neq \eta = \chi$. If we take $\mathbf{z} = \alpha = \mathbf{B}$, $\mathbf{x} = \gamma = \mathbf{p}$, and $\mathbf{y} = \eta = \chi$, then we can define the angles θ and ϕ such that

$$(\alpha \cdot \mathbf{z}_L)(\beta \cdot \mathbf{z}_L) = \cos^2 \theta, (\gamma \cdot \mathbf{z}_L)(\rho \cdot \mathbf{z}_L) = \sin^2 \theta \cos^2 \phi,$$

and $(\eta \cdot \mathbf{z}_L)(\chi \cdot \mathbf{z}_L) = \sin^2 \theta \sin^2 \phi$. We find, therefore,

$$\begin{aligned} \langle \mathbf{A} \rangle &= \langle (\mathbf{z}_L \cdot \mathbf{x})^2 (\mathbf{z}_L \cdot \mathbf{z})^2 (\mathbf{z}_L \cdot \mathbf{y})^2 \rangle \\ &= \frac{1}{4\pi} \int_0^{2\pi} \int_0^\pi \cos^2 \theta \sin^5 \theta \cos^2 \phi \sin^2 \phi d\theta d\phi = \frac{1}{105} \end{aligned} \quad (4.99)$$

4. $\langle \mathbf{A} \rangle = 0$ for all other cases.

We now realize that the present derivation is a generalization of those in Appendixes A.1 and A.2. Therefore, we expect that $\langle \mathbf{A} \rangle$ can be written as a linear combination of all possible terms consisting of products of three Kronecker deltas depending on $\alpha, \beta, \gamma, \rho, \eta, \chi$. There are 15 of those terms. Consequently, an expression like that in Eq. (4.75) is expected for $\langle \mathbf{A} \rangle$. The four results for $\langle \mathbf{A} \rangle$ can be summarized with the following equation:¹³

$$\begin{aligned} 105\langle \mathbf{A} \rangle = & \delta_{\alpha\beta}(\delta_{\gamma\rho}\delta_{\eta\chi} + \delta_{\gamma\eta}\delta_{\rho\chi} + \delta_{\gamma\chi}\delta_{\eta\rho}) + \delta_{\alpha\gamma}(\delta_{\beta\rho}\delta_{\eta\chi} + \delta_{\beta\eta}\delta_{\rho\chi} + \delta_{\beta\chi}\delta_{\eta\rho}) \\ & + \delta_{\alpha\rho}(\delta_{\gamma\beta}\delta_{\eta\chi} + \delta_{\gamma\eta}\delta_{\beta\chi} + \delta_{\gamma\chi}\delta_{\eta\beta}) + \delta_{\alpha\eta}(\delta_{\gamma\rho}\delta_{\beta\chi} + \delta_{\gamma\beta}\delta_{\rho\chi} + \delta_{\gamma\chi}\delta_{\beta\rho}) \\ & + \delta_{\alpha\chi}(\delta_{\gamma\rho}\delta_{\eta\beta} + \delta_{\gamma\eta}\delta_{\rho\beta} + \delta_{\gamma\beta}\delta_{\eta\rho}) \end{aligned}$$

which is Eq. (4.75).

Appendix B.2

This appendix contains the derivation of Eq. (4.76). $\langle \mathbf{B} \rangle$ has seven possible values:

1. There is one (6)-term: $\alpha = \beta = \gamma = \rho = \eta = \chi$. In this case, it is convenient to choose the z axis along $\alpha = \beta = \gamma = \rho = \eta = \chi$, so $\mathbf{x} \cdot \mathbf{x}_L = \mathbf{\eta} \cdot \mathbf{x}_L = -\sin \theta \sin \xi$ and $\alpha \cdot \mathbf{z}_L = -\beta \cdot \mathbf{z}_L = \gamma \cdot \mathbf{z}_L = \rho \cdot \mathbf{z}_L = \cos \theta$, yielding

$$\begin{aligned} \langle \mathbf{B} \rangle &= \langle (\mathbf{z}_L \cdot \mathbf{z})^4 (\mathbf{x}_L \cdot \mathbf{z})^2 \rangle \\ &= \frac{1}{4\pi} \int_0^{2\pi} \int_0^\pi \cos^4 \theta \sin^3 \theta \sin^2 \xi d\theta d\xi = \frac{1}{35} \end{aligned} \quad (4.100)$$

2. There is one (4,2)-term with $\eta = \chi$ and neither η nor χ belonging to the group of four elements that are equal to each other: $\eta = \chi \neq \alpha = \beta = \gamma = \rho$. With $\mathbf{x} \cdot \mathbf{x}_L = \mathbf{\eta} \cdot \mathbf{x}_L = -\sin \theta \sin \xi$ and $\alpha \cdot \mathbf{z}_L = \beta \cdot \mathbf{z}_L = \gamma \cdot \mathbf{z}_L = \rho \cdot \mathbf{z}_L = \sin \theta \cos \phi$, one calculates

$$\begin{aligned} \langle \mathbf{B} \rangle &= \langle (\mathbf{z}_L \cdot \mathbf{x})^2 (\mathbf{z}_L \cdot \mathbf{z})^4 \rangle \\ &= \frac{1}{8\pi^2} \int_0^{2\pi} \int_0^{2\pi} \int_0^\pi \sin^7 \theta \cos^4 \phi \sin^2 \xi d\theta d\phi d\xi = \frac{3}{35} \end{aligned} \quad (4.101)$$

3. There are six (4,2)-terms with $\eta = \chi$ and both η and χ belonging to the group of four elements that are equal to each other: $\eta = \chi = \alpha = \beta$,

$\eta = \chi = \alpha = \gamma$, $\eta = \chi = \alpha = \rho$, $\eta = \chi = \beta = \gamma$, $\eta = \chi = \beta = \rho$, and $\eta = \chi = \gamma = \rho$. In this case the average can be calculated as

$$\begin{aligned}\langle \mathbf{B} \rangle &= \langle (\mathbf{x}_L \cdot \mathbf{x})^2 (\mathbf{z}_L \cdot \mathbf{z})^2 (\mathbf{z}_L \cdot \mathbf{x})^2 \rangle \\ &= \frac{1}{8\pi^2} \int_0^{2\pi} \int_0^{2\pi} \int_0^\pi \sin^5 \theta \cos^2 \theta \cos^4 \phi \sin^2 \xi d\theta d\phi d\xi \\ &= \frac{2}{105}\end{aligned}\quad (4.102)$$

4. There are eight (4,2)-terms $\eta \neq \chi$ with identical results. This term, which can be expressed in terms of dot products as $\langle (\mathbf{x}_L \cdot \mathbf{x})(\mathbf{x} \cdot \mathbf{z}_L)(\mathbf{z} \cdot \mathbf{x}_L)(\mathbf{z} \cdot \mathbf{z}_L)^3 \rangle$, can be evaluated from the dot product $\mathbf{x}_L \cdot \mathbf{z}_L = 0$:

$$\begin{aligned}\langle (\mathbf{x}_L \cdot \mathbf{z}_L)(\mathbf{z} \cdot \mathbf{x}_L)(\mathbf{z} \cdot \mathbf{z}_L)^3 \rangle &= 0 \\ &- \langle (\mathbf{x}_L \cdot \mathbf{x})(\mathbf{x} \cdot \mathbf{z}_L)(\mathbf{z} \cdot \mathbf{x}_L)(\mathbf{z} \cdot \mathbf{z}_L)^3 \rangle \\ &+ \langle (\mathbf{x}_L \cdot \mathbf{y})(\mathbf{y} \cdot \mathbf{z}_L)(\mathbf{z} \cdot \mathbf{x}_L)(\mathbf{z} \cdot \mathbf{z}_L)^3 \rangle \\ &+ \langle (\mathbf{x}_L \cdot \mathbf{z})(\mathbf{z} \cdot \mathbf{x}_L)(\mathbf{z} \cdot \mathbf{z}_L)^4 \rangle\end{aligned}\quad (4.103)$$

The first two terms on the right side are equal, and the last one is equal to $\frac{1}{35}$ (see Eq. 4.101). Therefore,

$$0 = 2 \langle (\mathbf{x}_L \cdot \mathbf{x})(\mathbf{x} \cdot \mathbf{z}_L)(\mathbf{z} \cdot \mathbf{x}_L)(\mathbf{z} \cdot \mathbf{z}_L)^3 \rangle + \frac{1}{35} \quad (4.104)$$

so

$$\langle \mathbf{B} \rangle = \langle (\mathbf{x}_L \cdot \mathbf{x})(\mathbf{x} \cdot \mathbf{z}_L)(\mathbf{z} \cdot \mathbf{x}_L)(\mathbf{z} \cdot \mathbf{z}_L)^3 \rangle = -\frac{1}{70} \quad (4.105)$$

5. There are three (2,2,2)-terms for which $\eta = \chi$: $\alpha = \beta \neq \gamma = \rho \neq \eta = \chi$, $\alpha = \gamma \neq \beta = \rho \neq \eta = \chi$, and $\alpha = \rho \neq \gamma = \beta \neq \eta = \chi$. These yield the same answer:

$$\begin{aligned}\langle \mathbf{B} \rangle &= \langle (\mathbf{x}_L \cdot \mathbf{z})^2 (\mathbf{z}_L \cdot \mathbf{x})^2 (\mathbf{z}_L \cdot \mathbf{y})^2 \rangle \\ &= \frac{1}{8\pi^2} \int_0^{2\pi} \int_0^{2\pi} \int_0^\pi \sin^7 \theta \cos^2 \xi \cos^2 \phi \sin^2 \phi d\theta d\phi d\xi \\ &= \frac{1}{35}\end{aligned}\quad (4.106)$$

6. The 12 other (2,2,2)-terms have $\eta \neq \chi$ and yield the same answer. In this case it is possible to calculate

$$\langle \mathbf{B} \rangle = \langle (\mathbf{z}_L \cdot \mathbf{z})^2 (\mathbf{z}_L \cdot \mathbf{x})(\mathbf{x}_L \cdot \mathbf{x})(\mathbf{x}_L \cdot \mathbf{y})(\mathbf{z}_L \cdot \mathbf{y}) \rangle$$

in a way similar to the one under point 4:

$$\begin{aligned} & \langle (\mathbf{z} \cdot \mathbf{z}_L)^2 (\mathbf{x} \cdot \mathbf{x}_L)(\mathbf{x} \cdot \mathbf{z}_L)(\mathbf{z}_L \cdot \mathbf{x}_L) \rangle = 0 \\ &= \langle (\mathbf{z} \cdot \mathbf{z}_L)^2 (\mathbf{x} \cdot \mathbf{x}_L)^2 (\mathbf{x}_L \cdot \mathbf{x})^2 \rangle \\ &+ \langle (\mathbf{z} \cdot \mathbf{z}_L)^2 (\mathbf{z}_L \cdot \mathbf{x})(\mathbf{x} \cdot \mathbf{x}_L)(\mathbf{x}_L \cdot \mathbf{y})(\mathbf{y} \cdot \mathbf{z}_L) \rangle \\ &+ \langle (\mathbf{z} \cdot \mathbf{z}_L)^2 (\mathbf{z}_L \cdot \mathbf{x})(\mathbf{x} \cdot \mathbf{x}_L)(\mathbf{x}_L \cdot \mathbf{z})(\mathbf{z} \cdot \mathbf{z}_L) \rangle \end{aligned} \quad (4.107)$$

The first term on the right side is equal to the one calculated in Eq. (4.102), the second is the $\langle \mathbf{B} \rangle$ for this case, and the third is evaluated in Eq. (4.105). Therefore,

$$0 = \frac{2}{105} + \langle \mathbf{B} \rangle - \frac{1}{70} \Rightarrow \langle \mathbf{B} \rangle = -\frac{1}{210} \quad (4.108)$$

7. For all other cases $\langle \mathbf{B} \rangle = 0$.

Again, as for $\langle \mathbf{A} \rangle$, we expect $\langle \mathbf{B} \rangle$ for a linear combination of the 15 triple products of Kronecker deltas depending on $\alpha, \beta, \gamma, \rho, \eta, \chi$. Indeed, the seven results for $\langle \mathbf{B} \rangle$ can be summarized in one equation:

$$\begin{aligned} 210\langle \mathbf{B} \rangle = & 6\delta_{\eta\chi}(\delta_{\gamma\rho}\delta_{\alpha\beta} + \delta_{x\eta}\delta_{\beta\rho} + \delta_{x\rho}\delta_{\beta\gamma}) - \delta_{\chi\rho}(\delta_{\alpha\beta}\delta_{\gamma\eta} + \delta_{\alpha\gamma}\delta_{\beta\eta} + \delta_{\alpha\eta}\delta_{\beta\gamma}) \\ & - \delta_{\chi\gamma}(\delta_{\alpha\beta}\delta_{\rho\eta} + \delta_{x\rho}\delta_{\beta\eta} + \delta_{x\eta}\delta_{\beta\rho}) - \delta_{\chi\beta}(\delta_{\alpha\gamma}\delta_{\rho\eta} + \delta_{\alpha\rho}\delta_{\gamma\eta} + \delta_{\alpha\eta}\delta_{\gamma\rho}) \\ & - \delta_{\alpha\chi}(\delta_{\gamma\rho}\delta_{\eta\beta} + \delta_{\gamma\eta}\delta_{\rho\beta} + \delta_{\gamma\beta}\delta_{\eta\rho}) \end{aligned}$$

which is Eq. (4.76).

Appendix B.3

This appendix contains the derivation of Eq. (4.77). $\langle \mathbf{B} \rangle$ has seven possible values:

1. There is one (6)-term:

$$\begin{aligned}
 \langle \mathbf{C} \rangle &= \langle (\mathbf{z}_L \cdot \mathbf{z})^2 (\mathbf{x}_L \cdot \mathbf{z})^2 (\mathbf{y}_L \cdot \mathbf{z})^2 \rangle \\
 &= \frac{1}{4\pi} \int_0^{2\pi} \int_0^\pi \cos^2 \theta \sin^5 \theta \sin^2 \xi \cos^2 \xi d\theta d\xi \\
 &= \frac{1}{105} \tag{4.109}
 \end{aligned}$$

2. There are three (4,2)-terms leading to the same answer. These correspond to $\alpha = \beta = \gamma = \rho \neq \eta = \chi$, $\alpha = \beta \neq \gamma = \rho = \eta = \chi$, and $\alpha = \beta = \eta = \chi \neq \gamma = \rho$. In this case $\langle \mathbf{C} \rangle = \langle (\mathbf{z}_L \cdot \mathbf{z})^2 (\mathbf{x}_L \cdot \mathbf{x})^2 (\mathbf{y}_L \cdot \mathbf{z})^2 \rangle$ can be calculated as follows:

$$\begin{aligned}
 \langle (\mathbf{z}_L \cdot \mathbf{z})^2 (\mathbf{y}_L \cdot \mathbf{z})^2 \rangle &= \frac{1}{15} = \langle (\mathbf{z}_L \cdot \mathbf{z})^2 (\mathbf{y}_L \cdot \mathbf{z})^2 \{(\mathbf{x} \cdot \mathbf{x}_L)^2 \\
 &\quad + (\mathbf{y} \cdot \mathbf{x}_L)^2 + (\mathbf{z} \cdot \mathbf{x}_L)^2\} \rangle \\
 &= \langle (\mathbf{z}_L \cdot \mathbf{z})^2 (\mathbf{y}_L \cdot \mathbf{z})^2 (\mathbf{x} \cdot \mathbf{x}_L)^2 \rangle \\
 &\quad + \langle (\mathbf{z}_L \cdot \mathbf{z})^2 (\mathbf{y}_L \cdot \mathbf{z})^2 (\mathbf{y} \cdot \mathbf{x}_L)^2 \rangle \\
 &\quad + \langle (\mathbf{z}_L \cdot \mathbf{z})^2 (\mathbf{y}_L \cdot \mathbf{z})^2 (\mathbf{z} \cdot \mathbf{x}_L)^2 \rangle \tag{4.110}
 \end{aligned}$$

The first two terms on the right side are equal, and the last one has been calculated in Eq. (4.109). Therefore,

$$\begin{aligned}
 2 \langle (\mathbf{z}_L \cdot \mathbf{z})^2 (\mathbf{x}_L \cdot \mathbf{x})^2 (\mathbf{y}_L \cdot \mathbf{z})^2 \rangle + \frac{1}{105} &= \frac{1}{15} \\
 \Rightarrow \langle (\mathbf{z}_L \cdot \mathbf{z})^2 (\mathbf{x}_L \cdot \mathbf{x})^2 (\mathbf{y}_L \cdot \mathbf{z})^2 \rangle &= \frac{1}{35} \tag{4.111}
 \end{aligned}$$

3. The 12 other (4,2)-terms yield identical results. In this case it is possible to calculate $\langle \mathbf{C} \rangle = \langle (\mathbf{z} \cdot \mathbf{z}_L)^2 (\mathbf{z} \cdot \mathbf{y}_L) (\mathbf{z} \cdot \mathbf{x}_L) (\mathbf{x} \cdot \mathbf{y}_L) (\mathbf{x} \cdot \mathbf{x}_L) \rangle$ from

$$\begin{aligned}
 0 &= \langle (\mathbf{z} \cdot \mathbf{z}_L)^2 (\mathbf{z} \cdot \mathbf{y}_L) (\mathbf{z} \cdot \mathbf{x}_L) (\mathbf{x}_L \cdot \mathbf{y}_L) \rangle \\
 &= \langle (\mathbf{z} \cdot \mathbf{z}_L)^2 (\mathbf{z} \cdot \mathbf{y}_L) (\mathbf{z} \cdot \mathbf{x}_L) (\mathbf{x}_L \cdot \mathbf{x}) (\mathbf{x} \cdot \mathbf{y}_L) \rangle \\
 &\quad + \langle (\mathbf{z} \cdot \mathbf{z}_L)^2 (\mathbf{z} \cdot \mathbf{y}_L) (\mathbf{z} \cdot \mathbf{x}_L) (\mathbf{x}_L \cdot \mathbf{y}) (\mathbf{y} \cdot \mathbf{y}_L) \rangle \\
 &\quad + \langle (\mathbf{z} \cdot \mathbf{z}_L)^2 (\mathbf{z} \cdot \mathbf{y}_L) (\mathbf{z} \cdot \mathbf{x}_L) (\mathbf{x}_L \cdot \mathbf{z}) (\mathbf{z} \cdot \mathbf{y}_L) \rangle \tag{4.112}
 \end{aligned}$$

The first two terms on the right side are equal, and the last one has been calculated in Eq. (4.109). Therefore,

$$\begin{aligned} 0 &= 2\langle(\mathbf{z} \cdot \mathbf{z}_L)^2(\mathbf{z} \cdot \mathbf{y}_L)(\mathbf{z} \cdot \mathbf{x}_L)(\mathbf{x}_L \cdot \mathbf{x})(\mathbf{x} \cdot \mathbf{y}_L)\rangle + \frac{1}{105} \\ \Rightarrow \langle(\mathbf{z} \cdot \mathbf{z}_L)^2(\mathbf{z} \cdot \mathbf{y}_L)(\mathbf{z} \cdot \mathbf{x}_L)(\mathbf{x}_L \cdot \mathbf{x})(\mathbf{x} \cdot \mathbf{y}_L)\rangle &= -\frac{1}{210} \quad (4.113) \end{aligned}$$

4. There is one special (2,2,2)-term, the one for $\alpha = \beta \neq \gamma = \rho \neq \eta = \chi$. Then $\langle \mathbf{C} \rangle = \langle (\mathbf{y}_L \cdot \mathbf{y})^2(\mathbf{x}_L \cdot \mathbf{z})^2(\mathbf{z}_L \cdot \mathbf{x})^2 \rangle$ follows from

$$\begin{aligned} \langle(\mathbf{x} \cdot \mathbf{z}_L)^2(\mathbf{z} \cdot \mathbf{x}_L)^2\rangle &= \frac{2}{15} = \langle(\mathbf{x} \cdot \mathbf{z}_L)^2 \\ &\quad \times \{(\mathbf{y} \cdot \mathbf{y}_L)^2 + (\mathbf{x} \cdot \mathbf{y}_L)^2 + (\mathbf{z} \cdot \mathbf{y}_L)^2\}(\mathbf{z} \cdot \mathbf{x}_L)^2\rangle \\ &\quad - \langle(\mathbf{x} \cdot \mathbf{z}_L)^2(\mathbf{y} \cdot \mathbf{y}_L)^2(\mathbf{z} \cdot \mathbf{x}_L)^2\rangle \\ &\quad + \langle(\mathbf{x} \cdot \mathbf{z}_L)^2(\mathbf{x} \cdot \mathbf{y}_L)^2(\mathbf{z} \cdot \mathbf{x}_L)^2\rangle \\ &\quad + \langle(\mathbf{x} \cdot \mathbf{z}_L)^2(\mathbf{z} \cdot \mathbf{y}_L)^2(\mathbf{z} \cdot \mathbf{x}_L)^2\rangle \quad (4.114) \end{aligned}$$

The last two terms on the right side are equal and equal to the one calculated in Eq. (4.111). Therefore,

$$\begin{aligned} \langle(\mathbf{x} \cdot \mathbf{z}_L)^2(\mathbf{y} \cdot \mathbf{y}_L)^2(\mathbf{z} \cdot \mathbf{x}_L)^2\rangle + \frac{2}{35} &= \frac{2}{15} \\ \Rightarrow \langle(\mathbf{x} \cdot \mathbf{z}_L)^2(\mathbf{y} \cdot \mathbf{y}_L)^2(\mathbf{z} \cdot \mathbf{x}_L)^2\rangle &= \frac{16}{210} \quad (4.115) \end{aligned}$$

5. There are six (2,2,2)-terms with identical results, corresponding to $\alpha = \gamma \neq \beta = \rho \neq \eta = \chi$, $\alpha = \rho \neq \beta = \gamma \neq \eta = \chi$, $\alpha = \beta \neq \gamma = \eta \neq \rho = \chi$, $\alpha = \beta \neq \gamma = \chi \neq \rho = \eta$, $\gamma = \rho \neq \alpha = \eta \neq \beta = \chi$, and $\gamma = \rho \neq \alpha = \chi \neq \beta = \eta$. In this case it is possible to calculate from $\langle \mathbf{C} \rangle = \langle (\mathbf{z} \cdot \mathbf{z}_L)(\mathbf{z} \cdot \mathbf{y}_L)(\mathbf{x} \cdot \mathbf{z}_L)(\mathbf{y} \cdot \mathbf{x}_L) \rangle$ from

$$\begin{aligned} 0 &= \langle(\mathbf{z}_L \cdot \mathbf{y}_L)(\mathbf{x} \cdot \mathbf{z}_L)(\mathbf{x} \cdot \mathbf{y}_L)(\mathbf{y} \cdot \mathbf{x}_L)^2\rangle \\ &= \langle(\mathbf{z}_L \cdot \mathbf{z})(\mathbf{z} \cdot \mathbf{y}_L)(\mathbf{x} \cdot \mathbf{z}_L)(\mathbf{x} \cdot \mathbf{y}_L)(\mathbf{y} \cdot \mathbf{x}_L)^2\rangle \\ &\quad + \langle(\mathbf{z}_L \cdot \mathbf{x})(\mathbf{x} \cdot \mathbf{y}_L)(\mathbf{x} \cdot \mathbf{z}_L)(\mathbf{x} \cdot \mathbf{y}_L)(\mathbf{y} \cdot \mathbf{x}_L)^2\rangle \\ &\quad + \langle(\mathbf{z}_L \cdot \mathbf{y})(\mathbf{y} \cdot \mathbf{y}_L)(\mathbf{x} \cdot \mathbf{z}_L)(\mathbf{x} \cdot \mathbf{y}_L)(\mathbf{y} \cdot \mathbf{x}_L)^2\rangle \quad (4.116) \end{aligned}$$

The second term on the right side is equal to $\frac{1}{35}$ (calculated in Eq. 4.111), and the last term is equal to $-\frac{1}{210}$ (see Eq. 4.113). Therefore,

$$\begin{aligned} \langle(\mathbf{z} \cdot \mathbf{z}_L)(\mathbf{z} \cdot \mathbf{y}_L)(\mathbf{x} \cdot \mathbf{z}_L)(\mathbf{x} \cdot \mathbf{y}_L)(\mathbf{y} \cdot \mathbf{x}_L)^2\rangle + \frac{1}{35} - \frac{1}{210} &= 0 \\ \Rightarrow \langle(\mathbf{z} \cdot \mathbf{z}_L)(\mathbf{z} \cdot \mathbf{y}_L)(\mathbf{x} \cdot \mathbf{z}_L)(\mathbf{x} \cdot \mathbf{y}_L)(\mathbf{y} \cdot \mathbf{x}_L)^2\rangle &= -\frac{5}{210} \quad (4.117) \end{aligned}$$

6. The eight other (2,2,2)-terms yield the same results: This value of $\langle \mathbf{C} \rangle$, which is equal to $\langle (\mathbf{z} \cdot \mathbf{z}_L)(\mathbf{z} \cdot \mathbf{y}_L)(\mathbf{x} \cdot \mathbf{z}_L)(\mathbf{x} \cdot \mathbf{x}_L)(\mathbf{y} \cdot \mathbf{y}_L)(\mathbf{y} \cdot \mathbf{x}_L) \rangle$, follows from

$$\begin{aligned} 0 &= \langle (\mathbf{z} \cdot \mathbf{z}_L)(\mathbf{x} \cdot \mathbf{y}_L)(\mathbf{x} \cdot \mathbf{z}_L)(\mathbf{x} \cdot \mathbf{x}_L)(\mathbf{y}_L \cdot \mathbf{x}_L) \rangle \\ &= \langle (\mathbf{z} \cdot \mathbf{z}_L)(\mathbf{z} \cdot \mathbf{y}_L)(\mathbf{x} \cdot \mathbf{z}_L)(\mathbf{x} \cdot \mathbf{x}_L)(\mathbf{y} \cdot \mathbf{y}_L)(\mathbf{y} \cdot \mathbf{x}_L) \rangle \\ &\quad + \langle (\mathbf{z} \cdot \mathbf{z}_L)(\mathbf{z} \cdot \mathbf{y}_L)(\mathbf{x} \cdot \mathbf{z}_L)(\mathbf{x} \cdot \mathbf{x}_L)(\mathbf{x} \cdot \mathbf{y}_L)(\mathbf{x} \cdot \mathbf{x}_L) \rangle \\ &\quad + \langle (\mathbf{z} \cdot \mathbf{z}_L)(\mathbf{z} \cdot \mathbf{y}_L)(\mathbf{x} \cdot \mathbf{z}_L)(\mathbf{x} \cdot \mathbf{x}_L)(\mathbf{z} \cdot \mathbf{y}_L)(\mathbf{z} \cdot \mathbf{x}_L) \rangle \end{aligned} \quad (4.118)$$

The last two terms are both equal to $-\frac{1}{210}$ (see Eq. 4.113). Therefore,

$$\langle (\mathbf{z} \cdot \mathbf{z}_L)(\mathbf{z} \cdot \mathbf{y}_L)(\mathbf{x} \cdot \mathbf{z}_L)(\mathbf{x} \cdot \mathbf{x}_L)(\mathbf{y} \cdot \mathbf{y}_L)(\mathbf{y} \cdot \mathbf{x}_L) \rangle = \frac{1}{105} \quad (4.119)$$

7. For all other cases $\langle \mathbf{C} \rangle = 0$.

These seven cases can be summarized by the expression

$$\begin{aligned} 210\langle \mathbf{C} \rangle &= \delta_{\alpha\beta}(16\delta_{\gamma\rho}\delta_{\eta\chi} - 5\delta_{\gamma\eta}\delta_{\rho\chi} - 5\delta_{\gamma\chi}\delta_{\eta\rho}) \\ &\quad + \delta_{\alpha\gamma}(-5\delta_{\beta\rho}\delta_{\eta\chi} + 2\delta_{\beta\eta}\delta_{\rho\chi} + 2\delta_{\beta\chi}\delta_{\eta\rho}) \\ &\quad + \delta_{\alpha\rho}(-5\delta_{\gamma\beta}\delta_{\eta\chi} + 2\delta_{\gamma\eta}\delta_{\beta\chi} + 2\delta_{\gamma\chi}\delta_{\eta\beta}) \\ &\quad + \delta_{\alpha\eta}(-5\delta_{\gamma\rho}\delta_{\beta\chi} + 2\delta_{\gamma\beta}\delta_{\rho\chi} + 2\delta_{\gamma\chi}\delta_{\beta\rho}) \\ &\quad + \delta_{\alpha\chi}(-5\delta_{\gamma\rho}\delta_{\eta\beta} + 2\delta_{\gamma\eta}\delta_{\rho\beta} + 2\delta_{\gamma\beta}\delta_{\eta\rho}) \end{aligned}$$

which is Eq. (4.77).

Appendix C

In Eq. (4.7) a Cartesian coordinate system is used with the axes along the principal axes of the two-photon absorption tensor. In this coordinate system the only nonzero elements of the tensor are S_{xx} , S_{yy} , and S_{zz} . Evaluating Eqs. (4.79)–

4.83) in this coordinate system, we find

$$\mathbf{S} \cdot \mathbf{S} = \sum_{\alpha, \beta} S_{\alpha\beta} S_{\beta\alpha} = S_{xx}^2 + S_{yy}^2 + S_{zz}^2 \quad (4.120)$$

$$\mathbf{e}_t \cdot \mathbf{S}_0 \cdot \mathbf{e}_t = \sum_{\alpha, \beta} e_\alpha(t) S_{\alpha\beta}(0) e_\beta(t) = S_{xx}(\mathbf{x}_0 \cdot \mathbf{e}_t)^2 + S_{yy}(\mathbf{y}_0 \cdot \mathbf{e}_t)^2 + S_{zz}(\mathbf{z}_0 \cdot \mathbf{e}_t)^2 \quad (4.121)$$

$$\begin{aligned} \mathbf{e}_t \cdot \mathbf{S}_0 \cdot \mathbf{S}_0 \cdot \mathbf{e}_t &= \sum_{\alpha, \beta, \gamma} e_\alpha(t) S_{\alpha\beta}(0) S_{\beta\gamma}(0) e_\gamma(t) \\ &= S_{xx}^2(\mathbf{x}_0 \cdot \mathbf{e}_t)^2 + S_{yy}^2(\mathbf{y}_0 \cdot \mathbf{e}_t)^2 + S_{zz}^2(\mathbf{z}_0 \cdot \mathbf{e}_t)^2 \end{aligned} \quad (4.122)$$

$$T = (\text{tr } \mathbf{S})^2 + 2\mathbf{S} \cdot \mathbf{S} = (S_{xx} + S_{yy} + S_{zz})^2 + 2S_{xx}^2 + 2S_{yy}^2 + 2S_{zz}^2 \quad (4.123)$$

$$\begin{aligned} U_{0t} &= \langle (\text{tr } \mathbf{S})(\mathbf{e}_t \cdot \mathbf{S}_0 \cdot \mathbf{e}_t) + 2(\mathbf{e}_t \cdot \mathbf{S}_0 \cdot \mathbf{S}_0 \cdot \mathbf{e}_t) \rangle \\ &= S_{xx}(\text{tr } \mathbf{S} + 2S_{xx})\langle (\mathbf{x}_0 \cdot \mathbf{e}_t)^2 \rangle + S_{yy}(\text{tr } \mathbf{S} + 2S_{yy})\langle (\mathbf{y}_0 \cdot \mathbf{e}_t)^2 \rangle \\ &\quad + S_{zz}(\text{tr } \mathbf{S} + 2S_{zz})\langle (\mathbf{z}_0 \cdot \mathbf{e}_t)^2 \rangle \end{aligned} \quad (4.124)$$

where \mathbf{x}_0 , \mathbf{y}_0 , and \mathbf{z}_0 represent unit vectors along the three principal axes of the \mathbf{S} -tensor at time 0, the time of excitation by a short flash. Substituting Eqs. (4.123) and (4.124) into Eq. (4.95) yields

$$r_{0[2]} = \frac{2}{7} \left[\frac{3U_{0t} - T}{T} \right] = \frac{4}{7} \sum_{\alpha=x,y,z} \frac{\langle P_2(\mathbf{e}_t \cdot \mathbf{e}_t) \rangle S_{\alpha\alpha} (\text{tr } \mathbf{S} + 2S_{\alpha\alpha})}{(S_{xx} + S_{yy} + S_{zz})^2 + 2S_{xx}^2 + 2S_{yy}^2 + 2S_{zz}^2} \quad (4.125)$$

Because $(\mathbf{x}_0 \cdot \mathbf{e}_t)^2 = 1 - (\mathbf{y}_0 \cdot \mathbf{e}_t)^2 - (\mathbf{z}_0 \cdot \mathbf{e}_t)^2$, it follows that

$$\begin{aligned} \langle P_2(\mathbf{x}_0 \cdot \mathbf{e}_t) \rangle &= \langle \frac{3}{2}(\mathbf{x}_0 \cdot \mathbf{e}_t)^2 - \frac{1}{2} \rangle \\ &= \langle \frac{3}{2}\{1 - (\mathbf{y}_0 \cdot \mathbf{e}_t)^2 - (\mathbf{z}_0 \cdot \mathbf{e}_t)^2\} - \frac{1}{2} \rangle \\ &= -\langle P_2(\mathbf{y}_0 \cdot \mathbf{e}_t) \rangle - \langle P_2(\mathbf{z}_0 \cdot \mathbf{e}_t) \rangle \end{aligned} \quad (4.126)$$

Substituting (4.126) into (4.125) yields

$$r_{0[2]} = \frac{4}{7} M_y \langle P_2(\mathbf{y}_0 \cdot \mathbf{e}_t) \rangle + \frac{4}{7} M_z \langle P_2(\mathbf{z}_0 \cdot \mathbf{e}_t) \rangle \quad (4.127)$$

with

$$M_y = \frac{(3S_{xx} + 3S_{yy} + S_{zz})(S_{yy} - S_{xx})}{(S_{xx} + S_{yy} + S_{zz})^2 + 2S_{xx}^2 + 2S_{yy}^2 + 2S_{zz}^2} \quad (4.128)$$

and

$$M_z = \frac{(3S_{xx} + S_{yy} + 3S_{zz})(S_{zz} - S_{xx})}{(S_{xx} + S_{yy} + S_{zz})^2 + 2S_{xx}^2 + 2S_{yy}^2 + 2S_{zz}^2} \quad (4.129)$$

From the definitions $\sigma_1 = S_{xx}/S_{zz}$ and $\sigma_2 = S_{yy}/S_{zz}$, it follows that

$$S_{xx} = \sigma_1 S_{zz} \quad \text{and} \quad S_{yy} = \sigma_2 S_{zz} \quad (4.130)$$

Substituting (4.130) into (4.128) and (4.129) leads to

$$M_y = \frac{(3\sigma_1 + 3\sigma_2 + 1)(\sigma_2 - \sigma_1)}{3 + 2\sigma_1 + 2\sigma_2 + 2\sigma_1\sigma_2 + 3\sigma_1^2 + 3\sigma_2^2} \quad (4.131a)$$

and

$$M_z = \frac{(3 + 3\sigma_1 + \sigma_2)(1 - \sigma_1)}{3 + 2\sigma_1 + 2\sigma_2 + 2\sigma_1\sigma_2 + 3\sigma_1^2 + 3\sigma_2^2} \quad (4.131b)$$

Equation (4.127) is Eq. (4.7) and Eq. (4.131) is Eq. (4.6).

Appendix D

Here the derivation of Eq. (4.8a) is presented. Since it is assumed that the emission transition dipole moment is along the z axis of the molecule, Eq. (4.3) can be written as

$$\mathbf{r}_{[1]}(t) = \frac{2}{5} \langle P_2(\mathbf{a}_0 \cdot \mathbf{z}_t) \rangle = \frac{2}{5} \left\{ \frac{3}{2} (\mathbf{a}_0 \cdot \mathbf{z}_t)^2 - \frac{1}{2} \right\} \quad (4.132)$$

where \mathbf{z}_t is a unit vector along the long axis, the molecular z axis, at time t . Because the unit vector along the absorption emission dipole is assumed to lie in the molecular yz plane, we have

$$\mathbf{a}_0 = \mathbf{z}_0 \cos \theta_A + \mathbf{y}_0 \sin \theta_A \quad (4.133)$$

where θ_A is the angle between the absorption and emission transition moments.

Substituting Eq. (4.133) into (4.132) yields

$$\begin{aligned} r_{[1]}(t) &= \frac{2}{5} \left\{ \frac{3}{2} (\cos \theta_A \mathbf{z}_0 \cdot \mathbf{z}_t + \sin \theta_A \mathbf{y}_0 \cdot \mathbf{z}_t)^2 - \frac{1}{2} \right\} \\ &= \frac{2}{5} \cos^2 \theta_A \left\{ \frac{3}{2} (\mathbf{z}_0 \cdot \mathbf{z}_t)^2 - \frac{1}{2} \right\} + \sin^2 \theta_A \left\{ \frac{3}{2} (\mathbf{y}_0 \cdot \mathbf{z}_t)^2 - \frac{1}{2} \right\} \\ &= \frac{2}{5} \cos^2 \theta_A (P_2(\mathbf{z}_0 \cdot \mathbf{z}_t)) + \sin^2 \theta_A (P_2(\mathbf{y}_0 \cdot \mathbf{z}_t)) \end{aligned} \quad (4.134)$$

where we have used the fact that the average of $(\mathbf{z}_0 \cdot \mathbf{z}_t)(\mathbf{y}_0 \cdot \mathbf{z}_t)$ vanishes because of symmetry. Equation (4.132) contains Eq. (4.8a).

Appendix E

We are looking for the maxima and minima of $r_{0[2]}$, which is

$$\begin{aligned} r_{0[2]} &= \frac{4}{7} M_z P_2(\mathbf{z}_0 \cdot \mathbf{e}_0) + \frac{4}{7} M_y P_2(\mathbf{y}_0 \cdot \mathbf{e}_0) \\ &= \frac{4}{7} M_z \left(\frac{3}{2} \cos^2 \theta_E - \frac{1}{2} \right) + \frac{4}{7} M_y \left(\frac{3}{2} \sin^2 \theta_E \sin^2 \varphi_E - \frac{1}{2} \right) \end{aligned} \quad (4.135)$$

where θ_E and φ_E are the polar and azimuthal angle with respect to the $(\mathbf{x}_0, \mathbf{y}_0, \mathbf{z}_0)$ coordinate system along the principal axes of the \mathbf{S} tensor at the time of excitation. The coefficient M_z can be written as

$$M_z = \frac{S_{zz}(2S_{zz} + \text{tr } \mathbf{S}) - S_{xx}(2S_{xx} + \text{tr } \mathbf{S})}{(\text{tr } \mathbf{S})^2 + 2(S_{xx}^2 + S_{yy}^2 + S_{zz}^2)} = \frac{3 + \sigma_2 - \sigma_1 \sigma_2 - 3\sigma_1^2}{N} \quad (4.136)$$

or as

$$M_z = (\sigma_4 - \sigma_3 + 3\sigma_4^2 - 3\sigma_3^2)/N \quad (4.137)$$

or as

$$M_z = (-3 - \sigma_5 + \sigma_5 \sigma_6 + 3\sigma_6^2)/N \quad (4.138)$$

where

$$\begin{aligned} N &= (1 + \sigma_1 + \sigma_2)^2 + 2(1 + \sigma_1^2 + \sigma_2^2) \\ &= (1 + \sigma_3 + \sigma_4)^2 + 2(1 + \sigma_3^2 + \sigma_4^2) \\ &= (1 + \sigma_5 + \sigma_6)^2 + 2(1 + \sigma_5^2 + \sigma_6^2) \end{aligned} \quad (4.139)$$

and $\sigma_1 = S_{xx}/S_{zz}$, $\sigma_2 = S_{yy}/S_{zz}$, $\sigma_3 = S_{xx}/S_{yy}$, $\sigma_4 = S_{zz}/S_{yy}$, $\sigma_5 = S_{yy}/S_{xx}$, and $\sigma_6 = S_{zz}/S_{xx}$.

Similarly, three expressions for M_y are available:

$$M_y = \frac{S_{yy}2S_{yy} + \text{tr } \mathbf{S}) - S_{xx}(2S_{xx} + \text{tr } \mathbf{S})}{(\text{tr } \mathbf{S})^2 + 2(S_{xx}^2 + S_{yy}^2 + S_{zz}^2)} = \frac{\sigma_2 - \sigma_1 + 3\sigma_2^2 - 3\sigma_1^2}{N} \quad (4.140)$$

or

$$M_y = (3 + \sigma_4 - \sigma_3\sigma_4 - 3\sigma_3^2)/N \quad (4.141)$$

or

$$M_z = (-3 - \sigma_6 + \sigma_5\sigma_6 + 3\sigma_5^2)/N \quad (4.142)$$

Differentiating $r_{0[2]}$ of Eq. (4.135) with respect to θ_E and φ_E yields the following three possibilities for extrema: (1) $\theta_E = 0$, (2) $\theta_F = \varphi_F = 90^\circ$, (3) $\theta_E = 90^\circ$, $\varphi_E = 0$. In the first case it is convenient to work with the variables σ_1 and σ_2 , in the second case σ_2 and σ_4 are preferable, and in the third case working with σ_5 and σ_6 turns out to be better. The results follow.

(1) For $\theta_E = 0$, $r_{0[2]} = \frac{4}{7}M_z - \frac{2}{7}M_v$. Substituting Eqs. (4.137)–(4.139) into this expression for the time-zero anisotropy yields

$$r_{0[2]} = \frac{2}{7} \left\{ \frac{6 + \sigma_1 + \sigma_2 - 2\sigma_1\sigma_2 - 3\sigma_1^2 - 3\sigma_2^2}{(1 + \sigma_1 + \sigma_2)^2 + 2(1 + \sigma_1^2 + \sigma_2^2)} \right\} \quad (4.143)$$

Conditions for maxima and minima of this expression are $\partial r_{0[2]}/\partial\sigma_1 = 0$ and $\partial r_{0[2]}/\partial\sigma_2 = 0$. The first condition is satisfied if

$$N = (3 + \sigma_1 + \sigma_2)(2 + 6\sigma_1 + 2\sigma_2) \quad (4.144)$$

where N is given by the first line of Eq. (4.139). The second condition is satisfied if

$$N = (3 + \sigma_1 + \sigma_2)(2 + 2\sigma_1 + 6\sigma_2) \quad (4.145)$$

Combining Eqs. (4.144) and (4.145) yields

$$(3 + \sigma_1 + \sigma_2)(\sigma_1 - \sigma_2) = 0 \quad (4.146)$$

Note that $3 + \sigma_1 + \sigma_2 \neq 0$, because if $3 + \sigma_1 + \sigma_2$ were zero, then from Eqs. (4.143) and (4.144) we would obtain that N would be zero. However, from Eq.

(4.139) it is obvious that N is larger than zero for all values of σ_1 and σ_2 . Therefore, conditions (4.139) and (4.144) can only be satisfied if $\sigma_1 = \sigma_2$. Substituting $\sigma_1 = \sigma_2$ into Eq. (4.139) yields

$$3 + 24\sigma_1 + 8\sigma_1^2 = 0 \quad (4.147)$$

This quadratic equation has solutions $\sigma_1 = -\frac{3}{2} + \sqrt{\frac{15}{8}}$ and $\sigma_1 = -\frac{3}{2} - \sqrt{\frac{15}{8}}$. Substituting the first solution with $\sigma_1 = \sigma_2$ into Eq. (4.142) yields $r_{0[2]} = \frac{1}{7} + \frac{3}{7}\sqrt{\frac{6}{3}} = 0.6123$. Substituting the second solution with $\sigma_1 = \sigma_2$ into Eq. (4.142) yields $r_{0[2]} = \frac{1}{7} - \frac{3}{7}\sqrt{\frac{6}{5}} = -0.3266$. Therefore, for $\theta_E = 0$, the maximum is $r_{0[2]} = 0.6123$ for $\sigma_1 = \sigma_2 = -\frac{3}{2} + \sqrt{\frac{15}{8}}$, and the minimum is $r_{0[2]} = -0.3266$ for $\sigma_1 = \sigma_2 = -\frac{3}{2} - \sqrt{\frac{15}{8}}$.

(2) For $\theta_E = \varphi_E = 90^\circ$, $r_{0[2]} = -\frac{2}{7}M_z + \frac{4}{7}M_y$, which, by Eqs. (4.139) and (4.141), can be written as

$$r_{0[2]} = \frac{2}{7} \left\{ \frac{6 + \sigma_3 + \sigma_4 - 2\sigma_3\sigma_4 - 3\sigma_3^2 - 3\sigma_4^2}{(1 + \sigma_3 + \sigma_4)^2 + 2(1 + \sigma_3^2 + \sigma_4^2)} \right\} \quad (4.148)$$

Equation (4.148) has the same functional form as Eq. (4.143). Therefore, the same maximum and minimum are found: For $\theta_E = \varphi_E = 90^\circ$, the maximum if $r_{0[2]} = 0.6123$ for $\sigma_3 = \sigma_4 = -\frac{3}{2} + \sqrt{\frac{15}{8}}$, and the minimum is $r_{0[2]} = -0.3266$ for $\sigma_3 = \sigma_4 = -\frac{3}{2} - \sqrt{\frac{15}{8}}$.

(3) For $\theta_E = 90^\circ$ with $\varphi_E = 0$, $r_{0[2]} = -\frac{2}{7}M_z - \frac{2}{7}M_y$, which, by Eqs. (4.138) and (4.142), can be written as

$$r_{0[2]} = \frac{2}{7} \left\{ \frac{6 + \sigma_5 + \sigma_6 - 2\sigma_5\sigma_6 - 3\sigma_5^2 - 3\sigma_6^2}{(1 + \sigma_5 + \sigma_6)^2 + 2(1 + \sigma_5^2 + \sigma_6^2)} \right\} \quad (4.149)$$

Equation (4.149) also has the same functional form as Eq. (4.143). Therefore, the same maximum and minimum are found: For $\theta_E = 90^\circ$ with $\varphi_E = 0$, the maximum is $r_{0[2]} = 0.6123$ for $\sigma_5 = \sigma_6 = -\frac{3}{2} + \sqrt{\frac{15}{8}}$, and the minimum is $r_{0[2]} = -0.3266$ for $\sigma_5 = \sigma_6 = -\frac{3}{2} - \sqrt{\frac{15}{8}}$.

Appendix F

Here Eqs. (4.11)-(4.13) are derived. In the generalized strong-collision model^{*14>} a correlation function $C(t)$ (t =time) has the form

$$C(t) = C(\infty) + \{C(0) - C(\infty)\}e^{-t/\tau_R} \quad (4.150)$$

where τ_R is a rotational correlation time characteristic for this correlation function and $C(\infty)$ is the value of the correlation function at times long compared to τ_R . The initial value and long-time value of $\langle P_2(\mathbf{z}_0 \cdot \mathbf{z}_t) \rangle$ are

$$\langle P_2(\mathbf{z}_0 \cdot \mathbf{z}_0) \rangle = 1 \quad \langle P_2(\mathbf{z}_0 \cdot \mathbf{z}_\infty) \rangle = \langle P_2(\mathbf{z}_0 \cdot \mathbf{z}_M) \rangle \langle P_2(\mathbf{z}_\infty \cdot \mathbf{z}_M) \rangle = S^2 \quad (4.151)$$

where \mathbf{z}_M is a unit vector along the membrane normal. Substituting these values in Eq. (4.150) for $C(t) = \langle P_2(\mathbf{z}_0 \cdot \mathbf{z}_t) \rangle$ yields Eq. (4.11). The initial value and long-time value of $\langle P_2(\mathbf{y}_0 \cdot \mathbf{z}_t) \rangle$ are

$$\langle P_2(\mathbf{y}_0 \cdot \mathbf{z}_0) \rangle = -\frac{1}{2} \quad (4.152a)$$

$$\begin{aligned} \langle P_2(\mathbf{y}_0 \cdot \mathbf{z}_\infty) \rangle &= \langle P_2(\mathbf{y}_0 \cdot \mathbf{z}_M) \rangle \langle P_2(\mathbf{z}_\infty \cdot \mathbf{z}_M) \rangle \\ &= \langle \frac{3}{2} \sin^2 \vartheta \cos^2 \beta - \frac{1}{2} \rangle S \\ &= \langle \frac{3}{4} \sin^2 \vartheta + \cos 2\beta + \frac{1}{4} - \frac{3}{4} \cos^2 \vartheta \rangle S \\ &= (F - \frac{1}{2} S)S \end{aligned} \quad (4.152b)$$

Substituting these values in Eq. (4.150) for $C(t) = \langle P_2(\mathbf{y}_0 \cdot \mathbf{z}_t) \rangle$ yields Eq. (4.12). Equation (4.13) follows from

$$-\langle \frac{3}{4} \sin^2 \vartheta \rangle \leq F = \langle \frac{3}{4} \sin^2 \vartheta \cos 2\beta \rangle \leq \langle \frac{3}{4} \sin^2 \vartheta \rangle \quad (4.153)$$

and

$$\langle \frac{3}{4} \sin^2 \vartheta \rangle = \langle \frac{3}{4} (1 - \cos^2 \vartheta) \rangle = \langle \frac{1}{2} - \frac{1}{2} (\frac{3}{2} \cos^2 \vartheta - \frac{1}{2}) \rangle = \frac{1}{2} (1 - S) \quad (4.154)$$

Substituting Eq. (4.154) into (4.153) produces Eq. (4.13).

Appendix G

The derivation of Eqs. (4.14) and (4.15) for $m=1$ starts with an expression for $R_{o[1]}(0)$ as a ratio of intensities, using for these intensities equations such as Eq. (4.22):

$$R_{o[1]}(0) = \frac{\langle (\mathbf{p} \cdot \mathbf{a}_0)^2 (\mathbf{x} \cdot \mathbf{a}_0)^2 \rangle}{\langle (\mathbf{x} \cdot \mathbf{a}_0)^4 \rangle} \quad (4.155)$$

where \mathbf{p} , \mathbf{x} , and \mathbf{a}_0 are unit vectors; \mathbf{p} is along the extraordinary polarization direction of the emitted light (see Figure 4.3), \mathbf{x} is along the membrane surface

perpendicular to the plane of incidence (perpendicular to the plane of the paper in Figure 4.3), and \mathbf{a}_0 is along the long axis of the rodlike molecule at time 0, the time of excitation by a very short flash. Since the molecule is assumed to behave like a rod, the absorption and emission dipole transition moments are also along \mathbf{a}_0 at time 0. The unit vector \mathbf{p} can be expressed in unit vectors \mathbf{z} and \mathbf{y} , along the membrane normal and along the surface of the membrane in the plane of incidence, respectively:

$$\mathbf{p} = \mathbf{z} \cos \Theta + \mathbf{y} \sin \Theta \quad (4.156)$$

where Θ is the angle between the membrane surface and the emitted light, as indicated in Figure 4.2. Substituting Eq. (4.156) into Eq. (4.155) yields

$$R_{o[1]}(0) = \frac{\cos^2 \Theta (\langle \mathbf{z} \cdot \mathbf{a}_0 \rangle^2 \langle \mathbf{x} \cdot \mathbf{a}_0 \rangle^2) + \sin^2 \Theta (\langle \mathbf{y} \cdot \mathbf{a}_0 \rangle^2 \langle \mathbf{x} \cdot \mathbf{a}_0 \rangle^2)}{\langle (\mathbf{x} \cdot \mathbf{a}_0)^4 \rangle} \quad (4.157)$$

where we have used the fact that, due to symmetry, the average of $(\mathbf{z} \cdot \mathbf{a}_0)(\mathbf{y} \cdot \mathbf{a}_0)(\mathbf{x} \cdot \mathbf{a}_0)^2$ vanishes. Because of azimuthal symmetry around the \mathbf{z} axis, the averages $\langle \mathbf{z} \cdot \mathbf{a}_0 \rangle^2 \langle \mathbf{x} \cdot \mathbf{a}_0 \rangle^2$, $\langle \mathbf{y} \cdot \mathbf{a}_0 \rangle^2 \langle \mathbf{x} \cdot \mathbf{a}_0 \rangle^2$, and $\langle (\mathbf{x} \cdot \mathbf{a}_0)^4 \rangle$ can be reduced to

$$\langle (\mathbf{z} \cdot \mathbf{a}_0)^2 \langle \mathbf{x} \cdot \mathbf{a}_0 \rangle^2 \rangle = \frac{1}{2} \langle \xi^2 (1 - \xi^2) \rangle \quad (4.158)$$

$$\langle (\mathbf{y} \cdot \mathbf{a}_0)^2 \langle \mathbf{x} \cdot \mathbf{a}_0 \rangle^2 \rangle = \frac{1}{8} \langle (1 - \xi^2)^2 \rangle \quad (4.159)$$

$$\langle (\mathbf{x} \cdot \mathbf{a}_0)^4 \rangle = \frac{3}{8} \langle (1 - \xi^2)^2 \rangle \quad (4.160)$$

where $\xi = \mathbf{z} \cdot \mathbf{a}_0 = \cos \vartheta$ (ϑ = angle between \mathbf{a}_0 and membrane normal). Substituting Eqs. (4.158-4.160) and $\cos^2 \Theta = 1 - \sin^2 \Theta$ into Eq. (4.157) yields

$$R_{o[1]}(0) = A_1 - B_1 \sin^2 \Theta \quad (4.161)$$

with

$$A_1 = \frac{1}{3} C_1 \quad B_1 = \frac{1}{3} (C_1 - 1) \quad C_1 = \frac{4 \langle \xi^2 (1 - \xi^2) \rangle}{\langle (1 - \xi^2)^2 \rangle} \quad (4.162)$$

Solving $\langle \xi^2 \rangle = \langle \cos^2 \vartheta \rangle$ and $\langle \xi^4 \rangle = \langle \cos^4 \vartheta \rangle$ from Eqs. (4.17a) and (4.17b) in terms of $\langle P_2 \rangle$ and $\langle P_4 \rangle$ yields

$$\langle \xi^2 \rangle = \frac{1}{3} + \frac{2}{3} \langle P_2 \rangle \quad (4.163)$$

and

$$\langle \xi^4 \rangle = \frac{1}{5} + \frac{4}{7} \langle P_2 \rangle + \frac{8}{35} \langle P_4 \rangle \quad (4.164)$$

Substituting Eqs. (4.163) and (4.164) into the expression for C_1 of (4.162) gives

$$C_1 = \frac{7 + 5\langle P_2 \rangle - 12\langle P_4 \rangle}{7 - 10\langle P_2 \rangle + 3\langle P_4 \rangle} \quad (4.165)$$

Equation (4.165) with (4.162) is Eq. (4.15), and (4.161) is Eq. (4.14) for $m = 1$.

Appendix H

This appendix yields the derivations of Eqs. (4.14), for $m = 2$, (4.16), and (4.18)–(4.20). The depolarization ratio $R_{o[2]}(0)$ for the geometry of Figure 4.3A is

$$R_{o[2]}(0) = \frac{\langle (\mathbf{x} \cdot \mathbf{S}_0 \cdot \mathbf{x})^2 (\mathbf{e}_0 \cdot \mathbf{p})^2 \rangle}{\langle (\mathbf{x} \cdot \mathbf{S}_0 \cdot \mathbf{x})^2 (\mathbf{e}_0 \cdot \mathbf{x})^2 \rangle} \quad (4.166)$$

For the special case of a rodlike molecule considered here the only dominant principal axis of the tensor \mathbf{S}_0 is along \mathbf{a}_0 (defined in Appendix G), so $(\mathbf{x} \cdot \mathbf{S}_0 \cdot \mathbf{x})^2$ is equal to $(\mathbf{x} \cdot \mathbf{a}_0)^4$. The emission transition dipole moment, \mathbf{e}_0 , is also along \mathbf{a}_0 . Substituting (4.156) for \mathbf{p} , $(\mathbf{x} \cdot \mathbf{S}_0 \cdot \mathbf{x})^2 = (\mathbf{x} \cdot \mathbf{a}_0)^4$, into Eq. (4.166), we find

$$R_{o[2]}(0) = \frac{\cos^2 \Theta \langle (\mathbf{z} \cdot \mathbf{a}_0)^2 (\mathbf{x} \cdot \mathbf{a}_0)^4 \rangle + \sin^2 \Theta \langle (\mathbf{y} \cdot \mathbf{a}_0)^2 (\mathbf{x} \cdot \mathbf{a})^4 \rangle}{\langle (\mathbf{x} \cdot \mathbf{a}_0)^6 \rangle} \quad (4.167)$$

where, due to symmetry, the average of $(\mathbf{z} \cdot \mathbf{a}_0)\mathbf{y} \cdot \mathbf{a}_0(\mathbf{x} \cdot \mathbf{a}_0)^4$ vanishes. Because of azimuthal symmetry around the z axis, the averages $\langle (\mathbf{z} \cdot \mathbf{a}_0)^2 (\mathbf{x} \cdot \mathbf{a}_0)^4 \rangle$, $\langle (\mathbf{y} \cdot \mathbf{a}_0)^2 (\mathbf{x} \cdot \mathbf{a}_0)^4 \rangle$, and $\langle (\mathbf{x} \cdot \mathbf{a}_0)^6 \rangle$ can be reduced to

$$\langle (\mathbf{z} \cdot \mathbf{a}_0)^2 (\mathbf{x} \cdot \mathbf{a}_0)^4 \rangle = \frac{3}{8} \langle \xi^2 (1 - \xi^2)^2 \rangle \quad (4.168)$$

$$\langle (\mathbf{y} \cdot \mathbf{a}_0)^2 (\mathbf{x} \cdot \mathbf{a}_0)^2 \rangle = \frac{1}{16} \langle (1 - \xi^2)^3 \rangle \quad (4.169)$$

$$\langle (\mathbf{x} \cdot \mathbf{a}_0)^6 \rangle = \frac{5}{16} \langle (1 - \xi^2)^3 \rangle \quad (4.170)$$

where $\xi = \mathbf{z} \cdot \mathbf{a}_0 = \cos \theta$ (θ = angle between \mathbf{a}_0 and membrane normal). Substituting Eqs. (4.168)–(4.170) and $\cos^2 \Theta = 1 - \sin^2 \Theta$ into Eq. (4.167) yields

$$R_{o[2]}(0) = A_2 - B_2 \sin^2 \Theta \quad (4.171)$$

with

$$A_2 = \frac{1}{5} C_2 \quad B_2 = \frac{1}{5}(C_2 - 1) \quad C_2 = \frac{6(\xi^2(1 - \xi^2)^2)}{\langle(1 - \xi^2)^3\rangle} \quad (4.172)$$

Solving $\langle\xi^6\rangle = \langle\cos^6\vartheta\rangle$ from Eqs. (4.17c) in terms of $\langle P_2 \rangle$, $\langle P_4 \rangle$, and $\langle P_6 \rangle$ with the aid of Eqs. (4.163) and (4.164), we find

$$\langle\xi^6\rangle = \frac{1}{7} + \frac{10}{21}\langle P_2 \rangle + \frac{24}{77}\langle P_4 \rangle + \frac{16}{231}\langle P_6 \rangle \quad (4.173)$$

Substituting Eqs. (4.163), (4.164), and (4.173) into the expression for C_2 of (4.172) gives

$$C_2 = \frac{33 - 63\langle P_4 \rangle + 30\langle P_6 \rangle}{33 - 55\langle P_2 \rangle + 27\langle P_4 \rangle - 5\langle P_6 \rangle} \quad (4.174)$$

Equation (4.174) with (4.172) is Eq. (4.16), and (4.171) is Eq. (4.14) for $m=2$.

Equations (4.18)–(4.20) can be obtained as follows: For a given distribution function the order parameters $\langle P_2 \rangle$, $\langle P_4 \rangle$, and $\langle P_6 \rangle$ are defined as

$$\langle P_n \rangle = \int_{-1}^1 P_n(\xi)f(\xi) d\xi \quad (n = 2, 4, 6) \quad (4.175)$$

where $\xi = \cos\vartheta$ (ϑ = angle between \mathbf{a}_0 and membrane normal), $f(\xi)$ is the orientational distribution function (equilibrium distribution function), and $P_n(\xi)$ ($n = 2, 4, 6$) are the second-, fourth-, and sixth-order Legendre polynomials. A geometrical interpretation of the possible ranges for these order parameters can be derived as follows: Every continuous distribution function can be approximated by a series of delta functions:

$$f(\xi) = \sum_{n=1}^N \alpha_n \delta(\xi - \xi_n) \quad (4.176)$$

where the coefficients α_n are positive or zero, the sum of α_n (from $n=1$ to $n=N$) is equal to 1, and the values ξ_n are between -1 and 1 . This approximation becomes better for larger values of N . The points ξ_n correspond to points $(x_n, y_n, z_n) = (P_2(\xi_n), P_4(\xi_n), P_6(\xi_n))$ in three-dimensional space forming a polyhedron touching the curve $(P_2(\xi), P_4(\xi), P_6(\xi))$. Parametric three-dimensional plots of the curve $(P_2(\xi), P_4(\xi), P_6(\xi))$ with $0 \leq \xi \leq 1$ are shown in Figure 4.5 from two viewpoints. The possible values for $\langle P_2 \rangle$, $\langle P_4 \rangle$, and $\langle P_6 \rangle$ correspond to points $(\langle P_2 \rangle, \langle P_4 \rangle, \langle P_6 \rangle)$ inside or at the surface of such polyhe-

drons. From visual inspection of the $(P_2(\xi), P_4(\xi), P_6(\xi))$ curve, it is clear that these polyhedrons are between the following two surfaces:

$$\text{Upper surface } \begin{pmatrix} x \\ y \\ z \end{pmatrix} = (1 - \lambda) \begin{pmatrix} 1 \\ 1 \\ 1 \end{pmatrix} + \lambda \begin{pmatrix} P_2(\xi) \\ P_4(\xi) \\ P_6(\xi) \end{pmatrix} \quad (4.177)$$

with $0 \leq \lambda < 1$ and $-1 \leq \xi \leq 1$; and

$$\text{Lower surface } \begin{pmatrix} x \\ y \\ z \end{pmatrix} = (1 - \mu) \begin{pmatrix} \frac{-1}{2} \\ \frac{3}{8} \\ -\frac{5}{16} \end{pmatrix} + \mu \begin{pmatrix} P_2(\xi) \\ P_4(\xi) \\ P_6(\xi) \end{pmatrix} \quad (4.178)$$

with $0 \leq \mu \leq 1$ and $-1 \leq \xi \leq 1$. This geometrical relation yields an inequality for $\langle P_6 \rangle$ at $\langle P_2 \rangle$ and $\langle P_4 \rangle$:

$$-\frac{5}{16}(1 - \mu) = \mu P_6(\xi_1) \leq \langle P_6 \rangle \leq 1 - \lambda + \lambda P_6(\xi_2) \quad (4.179)$$

where λ , μ , ξ_1 , and ξ_2 are given by

$$\langle P_2 \rangle = 1 - \lambda + \lambda P_2(\xi_2) = -\frac{1}{2}(1 - \mu) + \mu P_2(\xi_1) \quad (4.180)$$

$$\langle P_4 \rangle = 1 - \lambda + \lambda P_4(\xi_2) = \frac{3}{8}(1 - \mu) + \mu P_4(\xi_1) \quad (4.181)$$

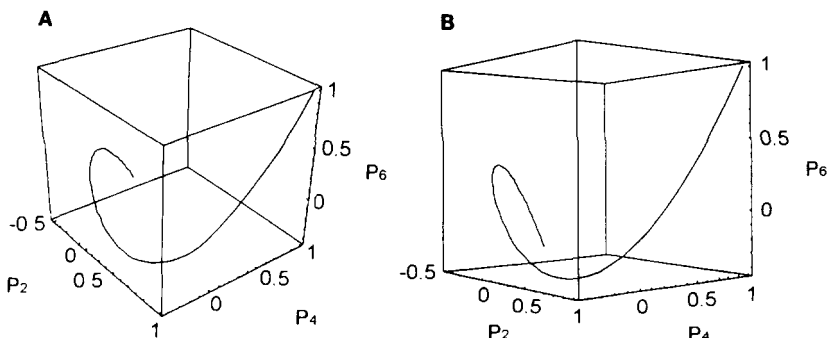


Figure 4.5. The three-dimensional parametric plots of the curve $(P_2(\xi), P_4(\xi), P_6(\xi))$ for $0 \leq \xi \leq 1$ (A) from the viewpoint of $(2.64, -2.11, 2)$ and (B) from the viewpoint of $(2.64, -2.11, 0)$. These plots are made by using the Mathematica program. (Reproduced from the *Biophysical Journal*, 1993, vol. 64, p. 1571 (Ref. 13) by copyright permission of the Biophysical Society.)

Solving for λ , μ , ξ_1 , and ξ_2 , expressing λ , μ , $P_2(\xi_1)$, $P_2(\xi_2)$, $P_4(\xi_1)$, and $P_4(\xi_2)$ in terms of $\langle P_2 \rangle$ and $\langle P_4 \rangle$, and substituting these expressions into (4.179) yields

$$-\frac{5}{16} + \frac{35}{352} (\langle P_2 \rangle + \frac{1}{2}) G \leq \langle P_6 \rangle \leq 1 - \frac{49}{88} (1 - \langle P_2 \rangle) H \quad (4.182)$$

with

$$G = \frac{1}{5} \left\{ \frac{27}{7} + \frac{264}{35} \left(\frac{\langle P_4 \rangle - \frac{3}{8}}{\langle P_2 \rangle + \frac{1}{2}} \right) \right\}^2 - 1 \quad (4.183)$$

and

$$H = \frac{1}{7} \left[-\frac{25}{7} + \frac{132}{35} \left(\frac{1 - \langle P_4 \rangle}{1 - \langle P_2 \rangle} \right) \right]^2 + 1 \quad (4.184)$$

Equation (4.182) is Eq. (4.18), (4.183) is Eq. (4.19), and (4.184) is Eq. (4.20).

Acknowledgment

This work was partly supported by NASA, NCCW-60.

References

1. D. W. Piston, D. R. Sandison, and W. W. Webb, Time-resolved fluorescence imaging and background rejection by two-photon excitation in laser scanning microscopy, *SPIE 1640* (1992).
2. W. Denk, J. H. Strickler, and W. W. Webb, Two-photon excitation in laser scanning microscopy, *Science 248*, 73–76 (1991).
3. W. M. McClain, Excited state symmetry assignment through polarized two-photon absorption studies of fluids, *J. Chem. Phys.* 55, 2789–2796 (1971).
4. W. M. McClain, Polarization dependence of three-photon phenomena for randomly oriented molecules, *J. Chem. Phys.* 57, 2264–2272 (1972).
5. T. W. Scott, K. S. Haber, and A. C. Albrecht, Two-photon photoselection in rigid solutions: a study of the B_{2u} – A_{1g} transition in benzene, *J. Chem. Phys.* 78, 150–157 (1983).
6. J. R. Cable, and A. C. Albrecht, Theory of three-photon photoselection with application to the hexagonal point groups, *J. Chem. Phys.* 85, 3145–3154 (1986).
7. J. R. Lakowicz, I. Gryczynski, E. Danielsen, and M. J. Wirth, Time-resolved fluorescence intensity and anisotropy decays of 2,5-diphenyloxazole by two-photon excitation and frequency-domain fluorometry, *J. Phys. Chem.* 96, 3000–3006 (1992).
8. J. R. Lakowicz, I. Gryczynski, and E. Danielsen, Anomalous differential polarized phase angles for two-photon excitation with isotropic depolarizing rotations, *Chem. Phys. Lett.* 191, 47–53 (1992).

9. J. R. Lakowicz, I. Gryczynski, J. Kusba, and E. Danielsen, Two-photon-induced fluorescence intensity and anisotropy decays of diphenylhexatriene in solvents and lipid bilayers, *J. Fluoresc.* 2, 247–258 (1992).
10. P.R. Callis, On the theory of two-photon induced fluorescence anisotropy with application to indoles, *J. Chem. Phys.* 99, 27–37 (1993).
11. C. Wan and C. K. Johnson, Time-resolved anisotropic two-photon spectroscopy, *Chem. Phys.* 179, 513–531 (1994).
12. C. Wan and C. K. Johnson, Time-resolved two-photon induced anisotropy decay: the rotational diffusion regime, *J. Chem. Phys.* 101, 10283–10291 (1994).
13. S.-Y. Chen and B. W. Van der Meer, Theory of two-photon induced fluorescence anisotropy decay in membranes, *Biophys. J.* 64, 1567–1575 (1993).
14. C. Zannoni, A. Arcioni, and P. Cavatorta, Fluorescence depolarization in liquid crystals and membrane bilayers, *Chem. Phys. Lipids* 32, 179–250 (1983).
15. B. W. Van der Meer, R. P. H. Kooyman, and Y. K. Levine, A theory of fluorescence depolarization in macroscopically ordered membrane systems, *Chem. Phys.* 66, 39–50 (1982).
16. R. P. H. Kooyman, Y. K. Levine, and B. W. Van der Meer, Measurement of 2nd and 4th rank order parameters by fluorescence polarization in a lipid membrane system, *Chem. Phys.* 60, 317–326 (1981).
17. H. Vogel and F. Jähnig, Fast and slow orientational fluctuations in membranes, *Proc. Natl. Acad. Sci. U.S.A.* 82, 2029–2033 (1985).
18. W. L. Petricolas, R. Norris, and K. E. Rieckhoff, Polarization effects in the two-photon excitation of anthracene fluorescence, *J. Chem. Phys.* 42, 4164–4169 (1965).
19. B. W. Van der Meer, H. Pottel, W. Herremans, M. Ameloot, H. Hendrickx, and H. Schroder, Effect of orientational order on the decay of the fluorescence anisotropy in membrane suspensions, *Biophys. J.* 46, 515–523 (1984).
20. A. Szabo, Theory of fluorescence depolarization in macromolecules and membranes, *J. Chem. Phys.* 81, 150–167 (1984).
21. B. W. Van der Meer, K. H. Cheng, and S.-Y. Chen, Effects of lateral diffusion on the fluorescence anisotropy in hexagonal lipid phases, I: Theory, *Biophys. J.* 6, 515–523 (1990).

This page intentionally left blank.

Two-Photon Induced Fluorescence of Proteins

*Borys Kierdaszuk, Ignacy Gryczynski,
and Joseph R. Lakowicz*

5.1. Introduction

By two-photon excitation (TPE) or two-photon induced fluorescence (TPIF) of proteins, we mean the simultaneous absorption of two long-wavelength photons by an aromatic amino acid (tryptophan, tyrosine, phenylalanine) or by an extrinsic fluorophore molecule, which are associated with protein by means of covalent bond or protein–ligand complexes. This process depends on the simultaneous interaction of the single fluorophore with two photons, and thus on the square of the light intensity.⁽¹⁾ We are not considering the sequential absorption of two photons by the fluorophore.

The advantages and rationale for using two-photon absorption spectroscopy are that the selection rules for absorption differ from the one-photon selection rules.^(1–6) For an allowed one-photon transition, the initial and final states must be of opposite inversion symmetry (*gerade (g) → ungerade (u)* or *u → g* transitions). For an allowed two-photon transition, the states must have the same inversion symmetry (*g → g* or *u → u* transitions). Two-photon optical spectroscopy thus provides an opportunity to observe electronic states, which are not accessible to one-photon measurements.

The goal of almost all earlier two-photon spectroscopic studies has been to find electronic transitions and to interpret the data in terms of molecular orbital theory and excited-state symmetry.^(4–7) By the end of 1980, there were only a

Borys Kierdaszuk • Department of Biophysics, University of Warsaw, PL-02089 Warsaw, Poland.

Ignacy Gryczynski and Joseph R. Lakowicz • Center for Fluorescence Spectroscopy
Department of Biochemistry and Molecular Biology, University of Maryland at Baltimore School of Medicine, Baltimore, Maryland 21201.

Topics in Fluorescence Spectroscopy; Volume 5: Nonlinear and Two-Photon-Induced Fluorescence,
edited by J. Lakowicz. Plenum Press, New York, 1997.

few reports on two-photon spectroscopy of proteins related to a steady-state data (Table 5.1).⁽⁸⁻¹¹⁾ They have been summarized in several reviews⁽¹²⁻¹⁴⁾ and therefore, are not included here.

In the beginning of 1990, Lakowicz and co-workers developed the use of two-photon excitation in steady-state and time-resolved fluorescence spectroscopy of biomolecules,⁽¹⁵⁻²⁹⁾ which has resulted in increased interest in TPE in biochemistry.⁽³⁰⁻³³⁾ Two-photon excitation of fluorescence offers the potential advantages of decreased photochemical damage, decreased autofluorescence, intrinsic confocal excitation in microscopy, and, most importantly, excitation to different excited states and the possibility of new information content in steady-state and time-resolved fluorescence. This extensive review is written to systematize the scope and limitations of the steady-state two-photon spectroscopy of proteins, their components and protein-ligand complexes, while time-resolved two-photon data are reviewed by Gryczynski and Lakowicz in the separate chapter.

Table 5.1. Proteins and Aromatic Aminoacids Studied by Two-Photon Spectroscopic Methods

Proteins or amino acids	Fluorescence data	References
Tryptophan	emission spectra	10-11, 14, 18, 25,
	excitation spectra	25, 34
	anisotropy	18
Tyrosine	emission spectra	11, 25-26
	excitation spectra	25, 34
	anisotropy	18
Phenylalanine	emission spectra	n.d.
	excitation spectra	34
Trypsin	emission spectra	11
Thyroglobulin	emission spectra	11
Hemoglobin	emission spectra	10-11
Apohemoglobin	emission spectra	10
Chlorophyll a	emission spectra	48
Rhodopsin	emission spectra	7-8, 12
Bacteriorhodopsin	emission spectra	13, 49-50
11-cis-retinal binding protein	emission spectra	51
Retinal analogues	emission spectra	9-10
Human serum albumin	emission spectra	10-11, 21, 25
	anisotropy	21
	emission spectra	25
Purine nucleoside phosphorylases	emission spectra	26
Ribonuclease A	emission spectra	26
Leu ⁵ -enkephaline	anisotropy	26
Liver alcohol dehydrogenase	emission spectra	28
NADH and NAMH	anisotropy	28
	emission spectra	29
	anisotropy	29

5.2. Excitation and Emission Spectra of Aromatic Amino Acids for One- and Two-Photon Excitation

5.2.1. Studies of Tryptophan, Tyrosine and Phenylalanine in Solution

Two-photon-induced fluorescence of aromatic amino acids (tryptophan, tyrosine, and phenylalanine) was studied using amide or *N*-acetyl derivatives and their fluorescent counterparts such as indole and its derivatives or phenol. Fluorescence emission spectra of *N*-acetyl-L-tryptophanamide (NATA)⁽¹⁸⁾ and *N*-acetyl-L-tyrosinamide (NATyrA)⁽²⁶⁾ in propylene glycol are similar for one photon excitation (OPE) and TPE (Figure 5.1) and indicate that essentially the same electronic states are reached for both modes of excitation. For OPE the emission intensity is linearly proportional to the intensity of the 283-nm incident light (Figure 5.1, inserts), while for TPE the intensity depends quadratically on the intensity at 566 nm (Figure 5.1, inserts); i.e., the observed emission spectra of NATA and NATyrA are due to a biphotonic absorption at 566 nm. Similar results were obtained for fluorescent parts of NATA and NATyrA, i.e., for indole⁽¹⁸⁾ and phenol⁽²⁶⁾ (data not shown). There are no such data for OPE and TPE emission spectra of phenylalanine, although its two-photon excitation spectrum is available.⁽³⁴⁾

The two-photon crosssection for NATA is very low (Table 5.2), for NATyrA it is even lower (Table 5.2), and millimolar concentrations of NATA and NATyrA are needed to get a measurable fluorescence signal. This can limit application of tryptophan or tyrosine as an intrinsic fluorescence probe for proteins, and could be a reason for the discrepancy existing in previously published data,^(10,11) where TPE emission spectra of tryptophan were observed at 382 nm by Xu *et al.*⁽¹¹⁾ and at 340 nm by Jiang *et al.*⁽¹⁰⁾

Furthermore, selective excitation may be possible due to the shifted one- and two-photon absorption spectra of tyrosine and tryptophan.^(25,34) Reruns and Callis⁽³⁴⁾ (Figures 5.2 and 5.3) and Kierdaszuk *et al.*⁽²⁵⁾ (Figure 5.4) have reported that the two-photon absorption spectrum of tyrosine is shifted to shorter wavelengths relative to the one-photon absorption spectrum. Such selective excitation was unequivocally confirmed from studies of tyrosine–tryptophan mixtures (Figure 5.5) and proteins containing tyrosine and tryptophan residues⁽²⁵⁾ (Figure 5.6). For a mixture of NATyrA and NATA, OPE results in a dominant tyrosine emission (Figure 5.5). In TPE the emission from the same mixture is dominantly from tryptophan (NATA).

In indole, tryptophan, and tryptophan-containing proteins, it was not known whether one of the states (1L_a and 1L_b) would dominate the two-photon absorption and if emission would still be observed from the more solvent-sensitive 1L_a state following TPE. Two-photon excitation spectra and semiempirical calculations have been used to locate electronic states in the spectra of indole and its deriva-

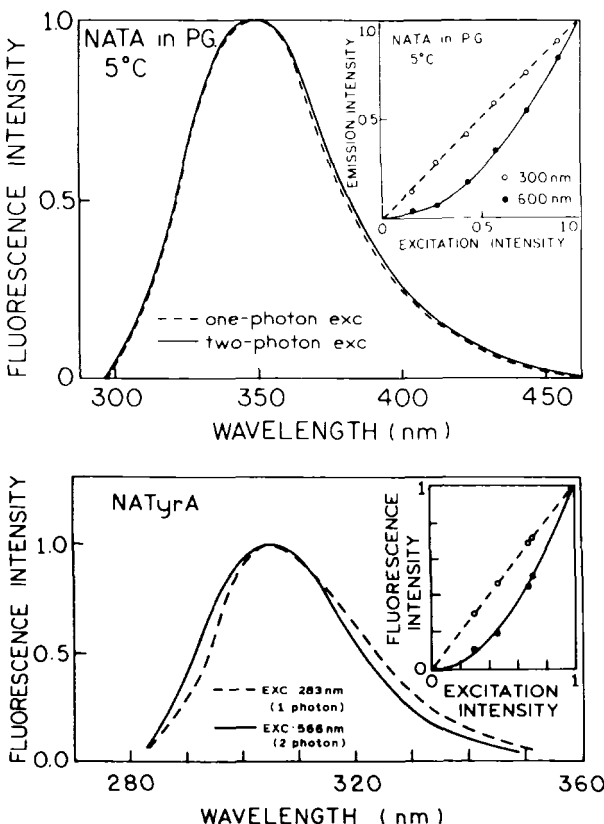


Figure 5.1. Fluorescence emission spectra of NATA (top) and NATyrA (bottom) obtained with one- (— — —) and two-photon excitation (— — —). The inserts show the dependence of the one- (— — ○— —) and two-photon-induced fluorescence intensity (— ●— —) on the intensity of the 283-nm (○) or 566-nm (●) incident light, both normalized to unity at the maximum, as indicated. (Adapted from Refs. 18 (for NATA) and 25 (for NATyrA).)

tives.^(35,36) In tryptophan (or its model analog NATA) the same emission spectra⁽¹⁸⁾ (Figure 5.1, top) and excitation spectra⁽³⁴⁾ (Figure 5.2, left) were observed for OPE and TPE. This observation, when combined with the different relative cross sections of the 1L_a and 1L_b states for OPE and TPE (below), confirm the widely held view of rapid relaxation between these states with emission occurring from the 1L_a state. However, as shown, emission from the 1L_b state can be observed for some indole derivatives with TPE.

Since the 1L_b absorption of NATA appeared to redshifted, it was interesting if one could detect emission from the 1L_b state. Such 1L_b emission is not observed

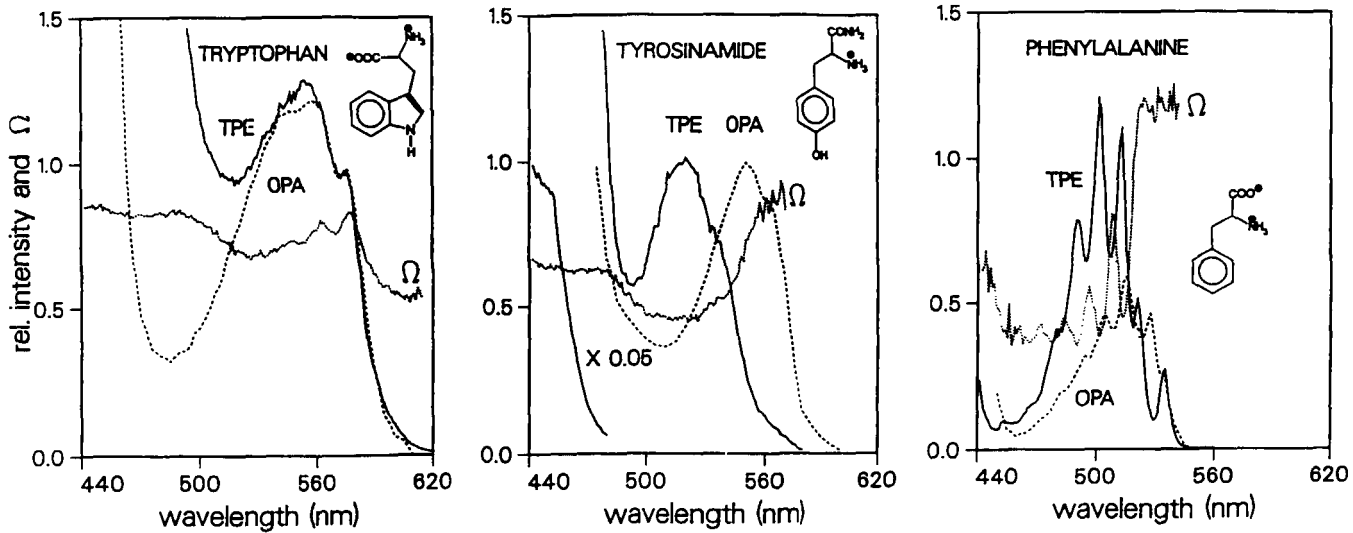


Figure 5.2. Two-photon excitation spectra (—) and one-photon absorption (OPA) spectra at the two-photon energy (— — —) and two-photon polarization, $\Omega = I_{\text{circular}}/I_{\text{linear}}$, (....) for tryptophan, tyrosinamide, and phenylalanine (as indicated) in 0.01 M neutral aqueous solution at room temperature. (Adapted from Ref. 34.)

Table 5.2. Relative Two-Photon Cross-Sections of Intrinsic and Extrinsic Probes of Proteins and Ratio of Their Fundamental Anisotropy for TPE (r_0^2) and for OPE (r_0^1).

Compound	Wavelength ^a (nm)	Concentration ^b (mM)	Relative cross section ^c (%)	r_0^2/r_0^1	Fluorescence probe	Refs.
bis-MSB	580	0.01	100	1.4	standard	20, 43
NATA	580	0.5	~0.7	0.7	intrinsic	18
NATyrA	580	5	<0.01	0	intrinsic	25
Indole	580	1	~0.1	1	intrinsic	18
NADH	580	1	0.001	1.4	extrinsic	29
	610	1	0.002	1.4	extrinsic	
	690	0.1	0.01	1.4	extrinsic	
Dansyl	720	0.1	~0.1	n.d.	extrinsic	d
	580	1	~0.01	n.d.	extrinsic	
Coumarin	720	0.01	~15	1.4	extrinsic	d

^aExcitation wavelengths of 580 and 720 (610 or 690) nm were obtained from rhodamine-6G and pyridine-2 dye lasers, respectively.

^bConcentration required for measurements.

^cEstimated by comparison with two-photon cross section of *p*-bis(*O*-methylstyryl)benzene (bis-MSB) standard ($700 \times 10^{-50} \text{ cm}^2 \text{ s}^{-1} \text{ photon}^{-1} \text{ molecule}^{-1}$)^(20,43) measured in the same experiment and taken as 100.

^dJ. R. Lakowicz, I. Gryczynski, and H. Malak, unpublished observations.

for most indole derivatives, but has been suggested to occur for 5-methylindole.⁽³⁷⁾ The emission spectra of 5-methylindole for OPE and TPE are presented in Figure 5.7, and exhibited a blueshift for TPE, which is consistent with emission from the 1L_b state.⁽³⁷⁾ Further experiments are needed to clarify this

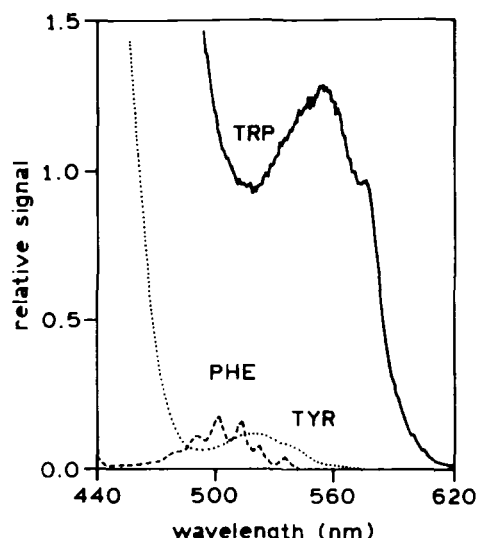


Figure 5.3. Relative two-photon excitation spectra observed for emission at 283, 303, and 356 nm for phenylalanine (PHE), tyrosinamide (TYR), and tryptophan (TRP), respectively. (Adapted from Ref. 34).

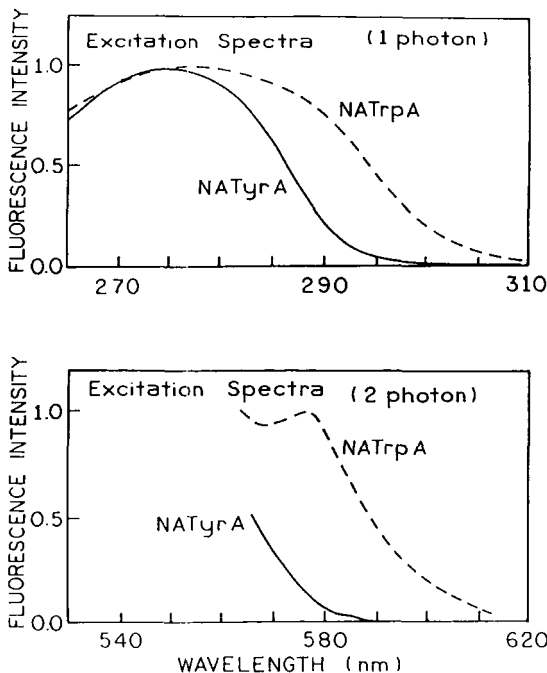


Figure 5.4. Fluorescence excitation spectra of *N*-acetyl-L-tryptophanamide (NATrpA) (— — —) and *N*-acetyl-L-tyrosinamide (NATyrA) (— — —) for OPE (top) and TPE (bottom) observed for emission at 355–364 nm (NATrpA) and 315 nm (NATyrA). (Adapted from Ref. 25).

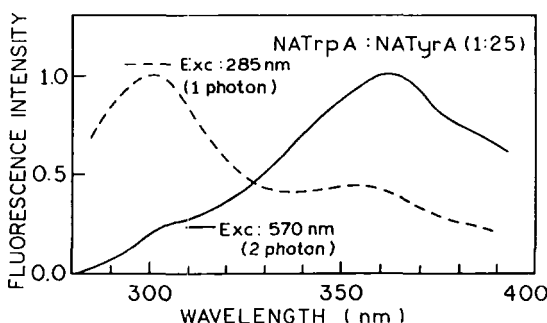


Figure 5.5. Fluorescence emission spectra of the mixture of *N*-acetyl-L-tryptophanamide (NATrpA) and *N*-acetyl-L-tyrosinamide (NATyrA) (1:25 by molar ratio) for OPE at 285 nm (— — —) and TPE at 570 nm (— — —). (Adapted from Ref. 25).

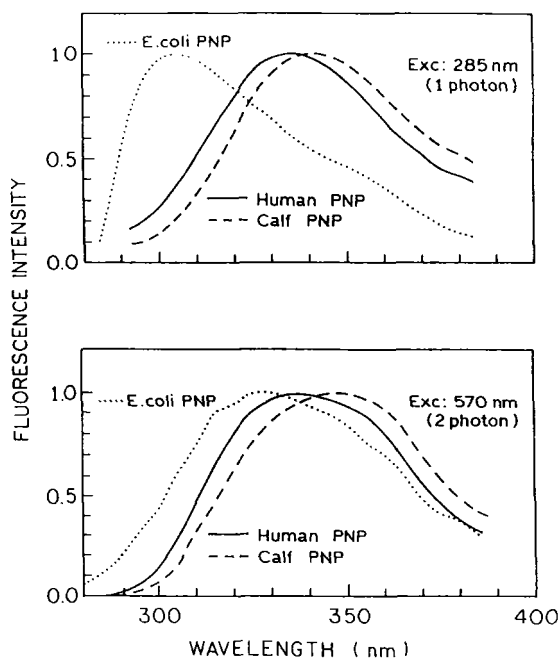


Figure 5.6. Fluorescence emission spectra of purine nucleoside phosphorylases (PNP) from *E. coli* (.....), human erythrocytes (—), and calf spleen (— —) in 50 mM Tris-HCl (pH 7.5) at 20°C, for OPE (top) and TPE (bottom). (Adapted from Ref. 25.)

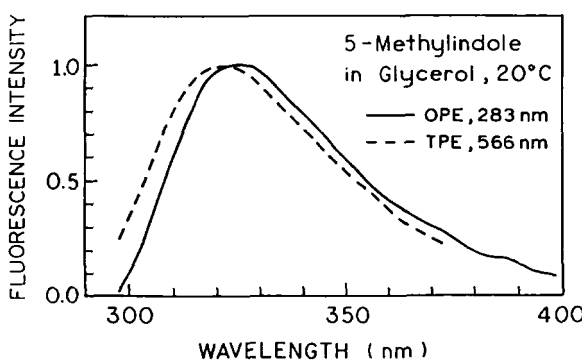


Figure 5.7. Fluorescence emission spectra of 5-methylindole obtained with one- (—) and two-photon excitation (— —) at resolution of 8 nm.

by examination of emission anisotropy spectra, which were shown to be a sensitive indicator of the relative emission of the 1L_a and 1L_b states.⁽³⁸⁾ This could be done in the solvents of different polarities, to investigate the solvent effect on the relative emission from these two states.

5.2.2. Tryptophan and Tyrosine in Proteins

As mentioned in the preceding section, TPE allows an interesting possibility of the selective excitation of tryptophan versus tyrosine residues in proteins. This possibility is illustrated by the comparison of human serum albumin (HSA) with one tryptophan residue and horse liver alcohol dehydrogenase (LADH) with two tryptophan residues (per identical subunit) in the dimmer. One tryptophan residue in LADH (Trp-314) is known to be present in a nonpolar site between the subunits, and the other residue (Trp-15) is in a polar region exposed to the solvent.⁽³⁹⁾ These proteins exhibited fluorescence emission spectra dominated by tryptophan components for both modes of excitation.^(21,28) The emission spectra (Figure 5.8) and intensity decay⁽²¹⁾ of HSA (data not shown) are the same for OPE and TPE.⁽²¹⁾ There is only a single tryptophan residue in HSA, and, like indole, it displays the same spectral properties independent of the mode of excitation. Remarkably, LADH has also displayed the same emission spectra for OPE and TPE (Figure 5.9), and indicated that both modes of excitation are equally sensitive to the environment of fluorophores. This observation was further confirmed by similar KI quenching of the long-wavelength part of both emission spectra dominated by exposed tryptophan residue (Trp-15).⁽²⁸⁾

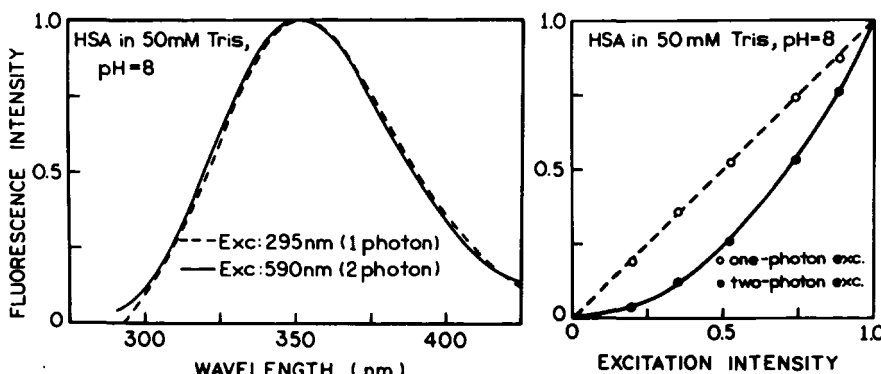


Figure 5.8. One- and two-photon-induced fluorescence spectra (left) and dependence of the fluorescence intensity on the excitation intensity of HSA (right) for excitation at 295 (---) and 590 nm (—). The maximum intensities for one- and two-photon excitation are both normalized to unity. (Adapted from Ref. 21.)

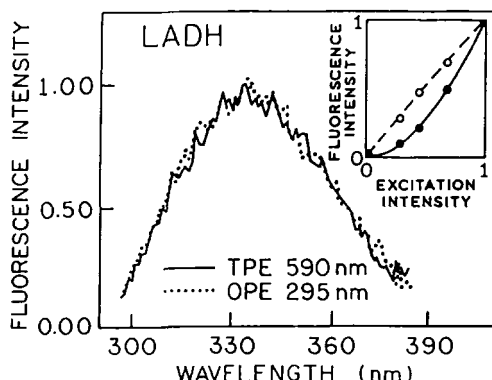


Figure 5.9. Fluorescence emission spectra of LADH for OPE (· · ·) and TPE (—). The insert shows the dependence of the one- (—○—) and two-photon-induced fluorescence intensity (—●—) on the intensity of the 295-nm (○) or 590-nm (●) incident light, both normalized to unity at the maximum, as indicated. (Adapted from Ref. 28.)

To further explore selective two-photon excitation, Kierdaszuk et al.⁽²⁵⁾ examined three varieties of purine nucleoside phosphorylase (PNP), which contain different amounts of tryptophan and tyrosine residues. For OPE of *E. coli* PNP, which contains six tyrosines per identical subunit in the hexamer,⁽⁴⁰⁾ tyrosine fluorescence was observed (Figure 5.6). For TPE this component is nearly absent and the emission is probably dominated by tyrosinate fluorescence (Figure 5.6). In the case of human and calf PNP, which contain both fluorophores, the emission for OPE and TPE appears to be dominated by tryptophan residues (Figure 5.6).

In recent studies on the tyrosine protein ribonuclease A,⁽²⁶⁾ different emission spectra from the tyrosine residues for OPE and TPE were observed (Figure 5.10, top). This difference could not be explained by emission from tryptophan-containing impurities, and suggests that TPE selectively excited redshifted tyrosine residues. Additional studies have shown that this effect depends on the secondary and tertiary structures of ribonuclease A, and no difference was observed for OPE and TPE emission of unfolded protein in the presence of 6 M guanidine hydrochloride (Figure 5.10, bottom). Similarly redshifted TPE fluorescence spectrum versus OPE fluorescence spectrum was also observed for tryptophan emission of hemoglobin (data not shown),⁽¹⁰⁾ although hemoglobin, as well as albumin and apohemoglobin, which also contain several tryptophans and tyrosines, exhibited TPE fluorescence spectra characteristic for tryptophan.⁽¹⁰⁾

5.3. Fluorescence Anisotropy of One- and Two-Photon Excitation of Tryptophan and Tyrosine

5.3.1. Limiting-Anisotropy Spectra

An important opportunity provided by TPE is the possibility of obtaining new information about the electronic spectra of fluorophores. For probes such

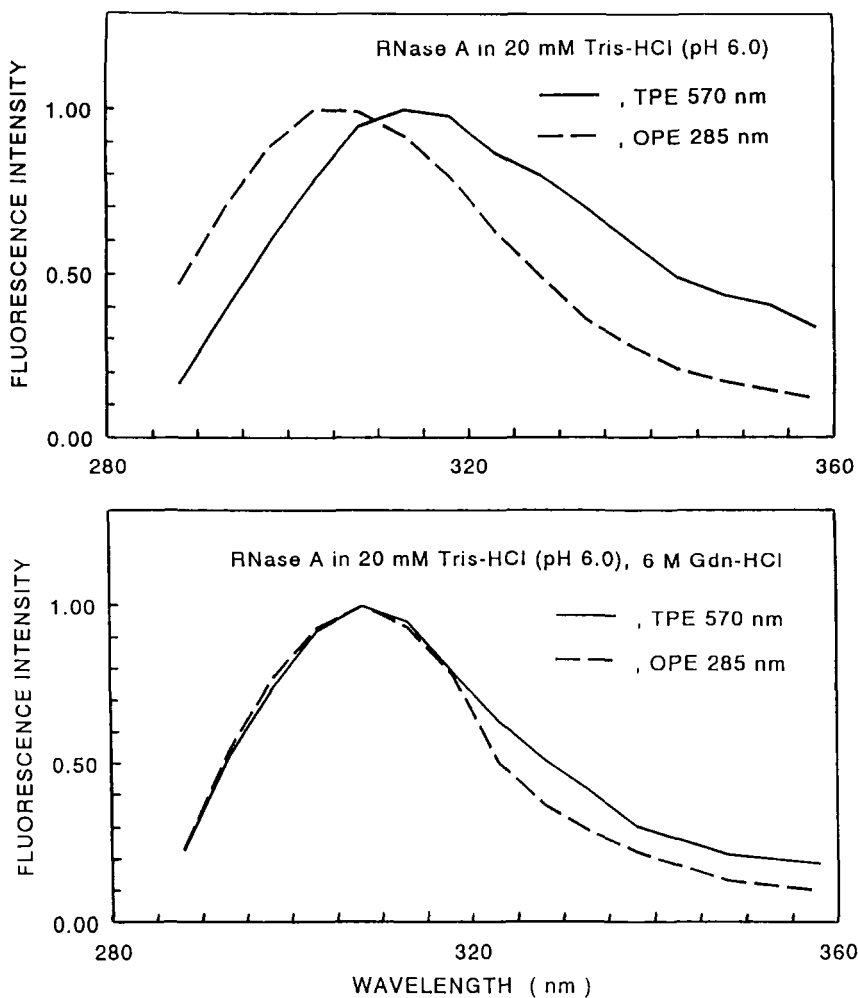


Figure 5.10. Fluorescence emission spectra of 1.5 mM ribonuclease A (RNase A) at 20°C obtained for one- (— — —) and two-photon excitation (—). (Top) RNase A in 20 mM Tris-HCl (pH 6.0) containing 80% glycerol. (Bottom) RNase A in 20 mM Tris-HCl (pH 6.0) containing 80% glycerol and 6 M guanidine hydrochloride (Gdn-HCl). (Adapted from Ref. 26.)

as 2,5-diphenyloxazole⁽¹⁶⁾ and diphenylhexatriene,^(15,17) Lakowicz *et al.* found that the TPE limiting anisotropies (r_0) could be explained by a $\cos^4 q$ photo-selection factor. However, such an increase in r_0 did not occur for indole or tryptophan, due to different cross sections of the 1L_a and 1L_b states for one- and two-photon absorption.⁽¹⁸⁾ The remarkable difference possible in the OPE and TPE anisotropy spectra is shown in Figure 5.11, which shows the excitation

anisotropy spectra of NATA in frozen solution. While the OPE anisotropy spectrum (---O---) shows the usual wavelength dependence due to the overlapping 1L_a and 1L_b absorptions, the TPE anisotropy spectrum is lower at all excitation wavelengths (---●---). These values are still lower following correction for the increased photoselection of TPE (--- ---). We concluded that these surprising results are due to a redshift of the 1L_b absorption spectrum for TPE, which results in initial absorption of two photons by the 1L_b state, followed by emission from 1L_a state, for which the transition moment is rotated by 90°. In fact, they are these exceptional cases that are more interesting, in that the excitation anisotropy spectra reflect the different OPE and TPE absorption spectra for the 1L_a and 1L_b states.

We used the anisotropy spectra in Figure 5.11, and the method proposed by Valeur and Weber,⁽⁴¹⁾ to resolve the 1L_a and 1L_b contributions to the two-photon absorption spectra. At any excitation wavelength the observed anisotropy is

$$r_0(\lambda) = f_a(\lambda)r_{0a} + f_b(\lambda)r_{0b} \quad (5.1)$$

where $f_i(\lambda)$ represents the fractional contribution of the i th state to the total absorption at the wavelength λ , and r_{0a} and r_{0b} represent the limiting anisotropies for the 1L_a and 1L_b states, respectively. The assumption was made that r_{0a} and r_{0b} are independent of wavelength and that emission occurs only from the 1L_a state. We also assumed that the transition moments for the 1L_a and 1L_b states are orthogonal (oriented 90° apart). This assumption is supported by the recent analysis of our two-photon anisotropy data, and the two-photon aniso-

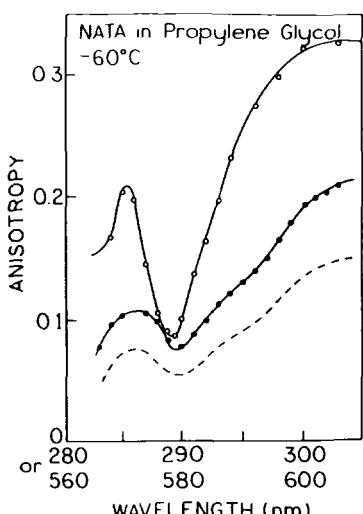


Figure 5.11. Excitation anisotropy spectra of 2 mM *N*-acetyl-L-tryptophanamide (NATA) in propylene glycol at -60°C obtained for OPE (---O---O---) and TPE (---●---●---). The dashed line shows the two-photon anisotropy spectrum corrected for higher photoselection resulting from TPE; i.e., TPE spectrum were divided by 1.429. (Adapted from Ref. 18.)

tropy parameter Ω , by Callis.^(34,42) Using these assumptions, it is possible to calculate the fractional absorption of each state as a function of wavelength. Rearrangement of Eq (5.1) yields

$$f_a(\lambda) = \frac{r_0(\lambda) - r_{0b}}{r_{0a} - r_{0b}} \quad \text{and} \quad f_b(\lambda) = \frac{r_{0a} - r_0(\lambda)}{r_{0a} - r_{0b}} \quad (5.2)$$

where we used $f_a(\lambda) + f_b(\lambda) = 1.0$. The necessary absorption (excitation) spectrum $A(\lambda)$ for NATA was obtained by comparison of the total intensity with that from the *p*-bis(methylstyryl)benzene (bis-MSB) standard⁽⁴³⁾ The absorption spectrum of each state is

$$A_a(\lambda) = f_a(\lambda)A(\lambda) \quad \text{and} \quad A_b(\lambda) = f_b(\lambda)A(\lambda) \quad (5.3)$$

where $A(\lambda)$ is the total absorption spectrum.

These resolved spectra (Figure 5.12) confirm the presence of a redshifted 1L_b spectrum in the two-photon spectrum of NATA, further interpreted by Callis⁽⁴²⁾ in terms of two-photon tensors and molecular orbital theory. This chapter describe how one can use the steady-state anisotropy spectra and the two-photon anisotropy $\Omega = \delta_{\text{circ}}/\delta_{\text{linear}}$, i.e., the ratio of absorption (fluorescence intensity) for circularly polarized (circ) and linearly polarized excitation (Figure 5.2),⁽³⁴⁾ to

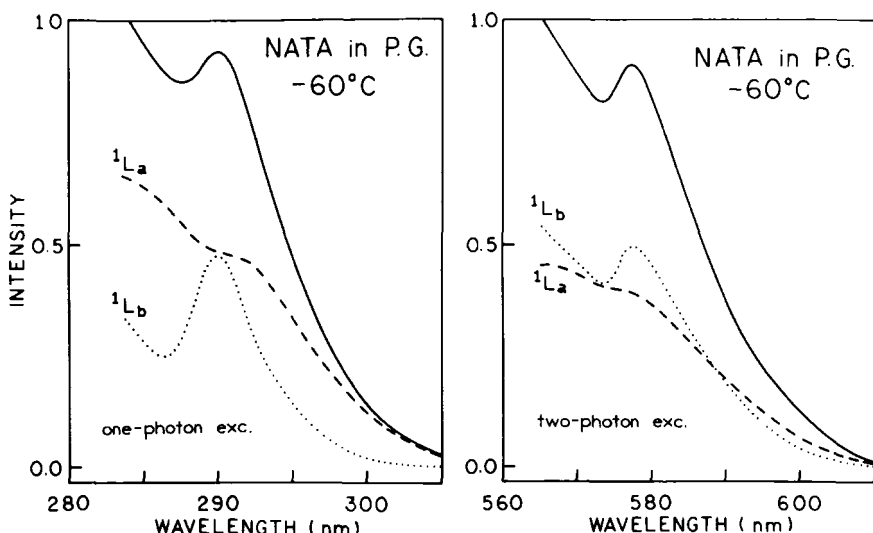


Figure 5.12. Resolution of the 1L_a and 1L_b states of *N*-acetyl-L-tryptophanamide (NATA) from the one-photon excitation (left) and two-photon excitation anisotropy spectra (right).

set limits on the angle between the principle angle of the two-photon tensor and the emission moment.

A rather surprising result was observed for the anisotropy spectrum of NATyrA and L-tyrosine,⁽²⁶⁾ where the TPE anisotropy was zero or slightly negative (Figure 5.13), as compared to near 0.3 for OPE. Theoretical considerations⁽²⁶⁾ do not negate the existence of such low anisotropy values for phenol analogs. Authors confirmed that the low anisotropy was not due to Forster homotransfer, which could occur at the high NATyrA concentration needed for these experiments. Low anisotropy values were also observed for phenol, tyrosine-containing peptide (Leu⁵-enkephaline), and ribonuclease A⁽²⁶⁾ (see below).

5.3.2. Anisotropy of Tryptophan- and/or Tyrosine-Containing Proteins

In recent years there has been considerable effort to use the potential advantage of higher limiting anisotropy (or initial anisotropy) values, which in principle should be obtained with TPE. Unfortunately, experimental results obtained for fluorophores in solution are far from theoretical predictions; i.e., some fluorophores (2,5-diphenyloxazole, diphenylhexatriene, NADH, coumarin) exhibited TPE anisotropy values related to OPE anisotropy by the simple factor of 10/7, reflecting higher photoselection for TPE;^(15-17,29) others have similar anisotropy values for TPE and OPE (indole).⁽²¹⁾ On the other hand, tryptophan and tyrosine have lower anisotropy for TPE than OPE (Table 5.2),^(18,21) and unexpectedly, TPE anisotropy of tyrosine is about zero (Figure 5.13). Furthermore, anisotropy of all fluorophores used so far for protein study (e.g., tryptophan, tyrosine, NADH, and dansyl) are known to depend on the protein environment and to be sensitive to resonance energy transfer and changes in protein conformation. Such effect of protein environment on the two-photon anisotropy was unequi-

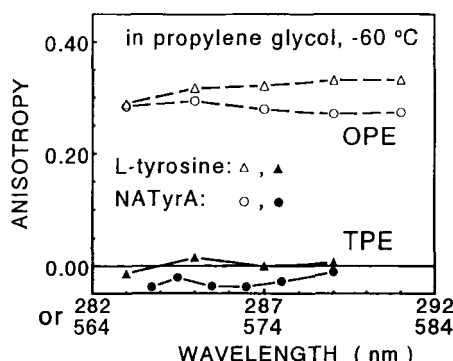


Figure 5.13. Excitation anisotropy spectra of 5 mM *N*-acetyl-L-tyrosinamide (NATyrA) (○, ●) and 2.5 mM L-tyrosine (Δ, ▲) in propylene glycol at -60°C obtained for one- (— — —) and two-photon (—) excitation. (Adapted from Ref. 26.)

vocally confirmed in the case of HSA and LADH, which contain one and two tryptophan residues, respectively. Similar values of the OPE and TPE limiting-anisotropy values were obtained for HSA with excitation at 298 and 596 nm, respectively, and TPE anisotropy was the same as for indole and 1.5-fold higher than for tryptophan (or NATA).⁽²¹⁾ In LADH, Lakowicz and co-workers⁽²⁸⁾ have shown that, although both nonidentical tryptophan residues exhibited similar fluorescence spectra for both modes of excitation, their limiting-anisotropy values measured with two-photon excitation from 585 to 610 nm appeared distinct from that obtained with one-photon excitation of LADH (Figure 5.14).⁽²⁸⁾ These observations strongly suggest that the relative one- and two-photon absorbance of the 1L_a and 1L_b transitions are different for tryptophan residue(s) in proteins, which is consistent with the data presented in the preceding section for NATA. To date, we are not able to exclude another possible explanation based on the assumption that additional state(s) are probed by TPE, which may also be affected by protein environment, including hydrogen bonding, stacking interactions, and hindered rotational motion of tryptophan residues(s).

Limiting-anisotropy spectra of tyrosine in proteins were studied by Lakowicz and co-workers,⁽²⁵⁾ using tyrosine protein, ribonuclease A, and the tyrosyl peptide Leu⁵-enkephaline. These data confirmed that a low anisotropy value is a basic feature of tyrosine residue, although it was slightly higher (near 0.06) for ribonuclease than for free tyrosine or tyrosine in peptide (Figure 5.15). In the same solution, OPE anisotropies were near the expected value. Except for the hypothesis considering depolarizing effect from TPE of another state(s) of tyrosine residue (as for tryptophan, see above), another possible reason for low anisotropy could be the presence of tyrosinate forms(s) in the native protein, which were expected to have redshifted two-photon absorption similarly to its

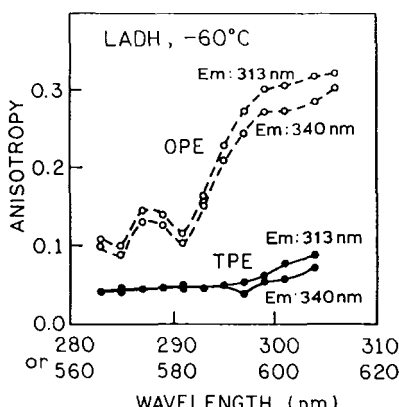


Figure 5.14. Excitation anisotropy spectra from 0.26 mM LADH in 20 mM phosphate buffer (pH 7.5) containing 70% glycerol at -60°C obtained for emission at 313 and 340 nm and for one- (○) and two-photon (●) excitation, respectively. (Adapted from Ref. 28.)

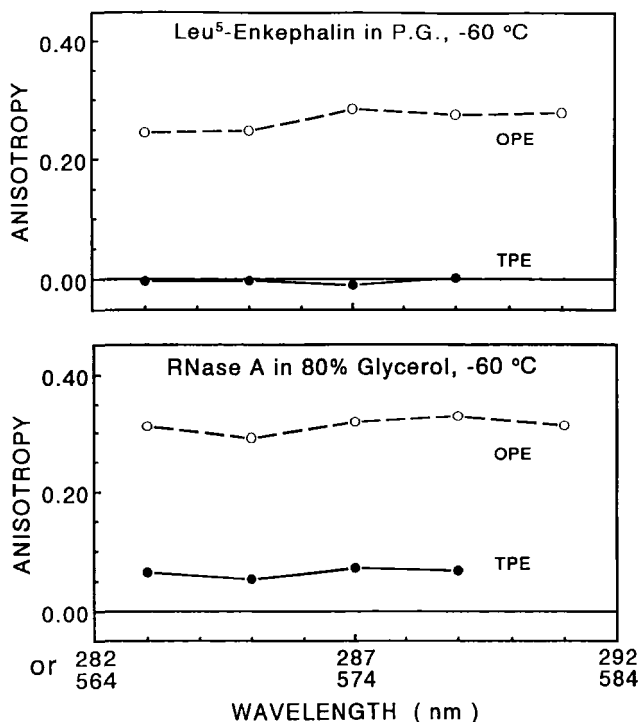


Figure 5.15. Excitation anisotropy spectra of 2 mM Leu⁵-enkephalin (top) in 90% propylene glycol and 2 mM ribonuclease A (RNase A) (bottom) in 20 mM Tris-HCl (pH 6.0) containing 80% glycerol obtained for one- (—○—) and two-photon (—●—) excitation at -60°C. (Adapted from Ref. 26.)

one-photon absorption, and higher cross section and anisotropy value, which were substantiated by theoretical data obtained for phenol.⁽²⁶⁾

5.4. Two-Photon Induced Fluorescence of Protein-Bound Chromophores

Very interesting results from the application of two-photon spectroscopy of protein-bound chromophores were obtained by Birge and co-workers^(7-9,12-13). They identified the retinal form in visual pigments based on comparison of the one-photon and two-photon absorption spectra, which revealed a stabilization of

the polar ${}^1B_u^*$ state by a local polar environment in visual pigments. Using knowledge of the excited state polarity of the symmetric low-lying nonpolar ${}^1A_g^*$ state^(9,44) (characterized by a symmetric charge distribution) and the polar ${}^1B_u^*$ state (displaying nonsymmetric charge distribution), Birge concluded that the retinal in the binding site of pigments is protonated and stabilized by a negatively charged environment^(8,9) (see Ref. 13 for review).

We applied two-photon spectroscopy in a fluorescence study of the reduced forms of β -nicotinamide adenine dinucleotide (NADH) and β -nicotinamide mononucleotide (NAMH) in solution and in a tertiary complex with LADH.⁽²⁹⁾ We observed similar OPE and TPE emission spectra of NADH and NAMH (Figure 5.16) and similar fluorescence intensity decay irrespective of the mode of excitation (data not shown). The limiting-anisotropy values of NADH and NAMH are both larger with TPE than OPE (Figure 5.17) and appear to be related by the $\cos^2 \theta$ to $\cos^4 \theta$ photoselection factor of 10/7 independently of excitation wavelength (Table 5.2). Depolarization of the NADH fluorescence observed for excitation wavelength below 300 nm for OPE and 600 nm for TPE (Figure 5.17) is due to an intramolecular interaction with the adenine part of NADH. Such depolarization is higher in the tertiary complex (Figure 5.18) of NADH, LADH, and the LADH inhibitor isobutyramide (IBA). These results indicate the

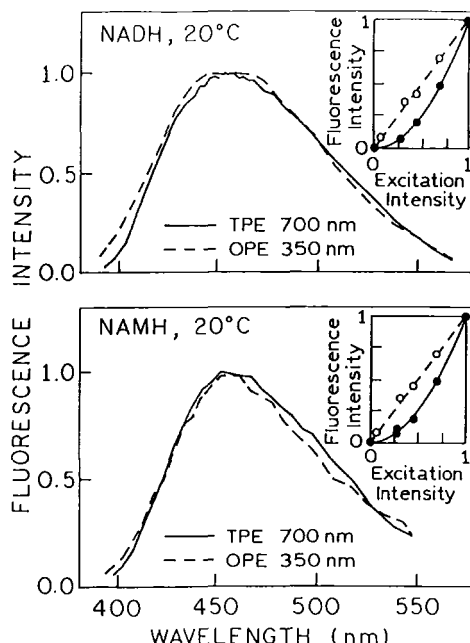


Figure 5.16. Fluorescence emission spectra of reduced forms of NADH (top) and NAMH (bottom) in 20 mM Tris-HCl (pH 7.5) at 20°C obtained for one- (---) and two-photon (—) excitation. The inserts shows the dependence of the one- (○) and two-photon-induced fluorescence intensity (●) on the intensity of the 350-nm (○) or 700-nm (●) incident light. The maximum intensities for OPE and TPE are both normalized to unity in the spectra and the inserts. (Adapted from Ref. 29.)

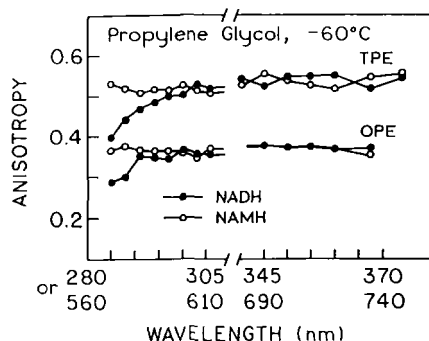


Figure 5.17. Excitation anisotropy spectra of 0.5 mM NADH (—●—) and 0.5 mM NAMH (—○—) in propylene glycol at -60°C measured for emission at 460 nm for OPE and TPE. (Adapted from Ref. 29.)

presence of another depolarizing factor due to a simultaneous two-photon excitation of LADH fluorophores in the NADH-LADH IBA complex. It seems likely that the decrease of the NADH anisotropy could be explained by a radiationless energy transfer from protein fluorophores or by conformational changes of coenzyme due to the complex formation with LADH.⁽⁴⁵⁾ One possibility is an energy transfer from tryptophan to NADH,⁽⁴⁵⁾ although all tryptophan residues are far from the active center of the enzyme.⁽⁴⁶⁾ Alternatively, Lowes and Shore⁽⁴⁷⁾ postulated that ionized tyrosine residues could be acceptors of the resonance energy transfer from Trp-314. Perhaps, ionized tyrosine could also be an energy donor for NADH.

Two-photon cross-sections for NADH (Table 5.2) in aqueous solution are one to two orders of values lower than for NATA, which suggests that fluorescence from NADH will be moderately difficult to observe with two-photon fluorescence microscopy and may not interfere with observations of TPIF of other extrinsic probes used to label cells.

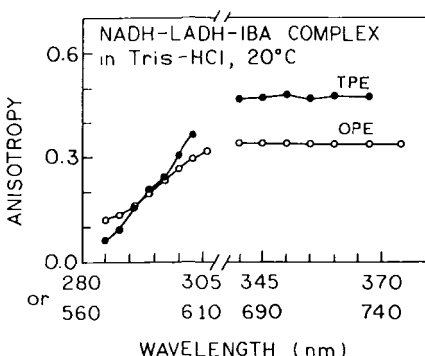


Figure 5.18. Excitation anisotropy spectra for the mixture of 20 μ M NADH, 20 μ M LADH, and 100 mM isobutyramide (IBA) in 20 mM Tris-HCl (pH 7.5) at 20°C obtained for emission at 460 nm and for one- (—○—) and two-photon excitation (—●—). (Adapted from Ref. 29.)

5.5. Experimental Methods

Several methods enable us to directly measure two-photon absorption spectra of fluorophores. They are based on direct absorption measurements,^(52–54) pump-probe methods,⁽⁵⁵⁾ thermal lensing,⁽⁵⁶⁾ and electronic second-harmonic detection.⁽⁵⁷⁾ Direct absorption measurement is difficult to perform due to small amounts of absorption out of the intense illumination, and most measurements rely on TPE spectra (see below).

Two-photon-induced fluorescence could be measured by using a lens to focus the fundamental outputs of cavity-dumped rhodamine-6G (570–620 nm) or pyridine-1 (or pyridine-2) (675–760 nm) dye lasers. These dye lasers are synchronously pumped by an argon-ion or Nd-Yag laser. The pulse full widths at half-maximum are about 5–10 ps at a repetition rate of about 4 MHz. The average power of the dye lasers is 80 to 100 mW, resulting in peak power near 4000 W. The excitation beam is passed through a Glan-Thompson vertical polarizer and focused by using a 5-cm focal length lens; a similar lens is usually used to collect the fluorescence. If the beam is focused to 10^{-4} cm², the peak power is estimated to be about 4×10^7 W/cm². For excitation in the range of 760–1000 nm the fs Ti:sapphire laser is usually used. One-photon-induced fluorescence and excitation anisotropy spectra should be measured with the same experimental system as for two-photon-induced fluorescence but equipped additionally with a frequency doubler and a polarization rotator. For reliable comparison of the fluorescence and excitation anisotropy spectra resulting from these two types of excitation, an instrument for time-correlated single-photon counting was used,^(58–59) and the steady-state intensity at each wavelength was obtained by integration of the area under the time-resolved decay curves. These allowed increased sensitivity and demonstrated the absence of scattered light in the detected emission by the absence of components with the same time profile as the excitation pulse.

For one-photon experiments, 0.5-cm × 0.5-cm cuvettes are used, with excitation and emission near a corner positioned at the center of a 1-cm × 1-cm cuvette holder. For two-photon experiments, 1.0-cm × 0.5-cm cuvettes are used, with the long axis aligned with the incident light and the focal point positioned about 0.5 cm from the surface facing the incident light. The position of the cuvette is adjusted so that the excitation laser beam crosses the solution near the observation window. Such a position practically eliminates trivial reabsorption, which could occur for a longer path length. Emission spectra are obtained with a monochromator of bandwidth 4–10 nm. The time-resolved and limiting-anisotropy values are measured without the monochromator by using glass cut-off filters or interference filters. Emission spectra and time-domain or frequency-domain intensity decays are measured under “magic-angle” conditions. To facilitate comparison between OPE and TPE data, both experiments are

performed on the same solutions. Because of the inefficient excitation with ps pulses, it is often necessary to use high probe concentrations and high optical densities. The concentration of the probes ranged from 0.02 to 1 mM for measurements performed on the dye laser systems, and it could be lower with the fs Ti:sapphire laser. For each two-photon measurement, the experimental system should be tested for square dependence of the fluorescence intensity on the intensity of incident light, which is unable to exclude an interference from the second- or third-harmonic components and other disturbing factors such as high electric fields.

Acknowledgments

This work was supported by grant GP04A03812 from the Committee for Scientific Research (KBN, Poland) and in part by an International Research Scholars Award of the Howard Hughes Medical Institute (grant No. HHMI 75195-543401), and by NIH grants RR-08119 and GM-35154.

References

1. D. M. Friedrich, and W. M. McClain, Two-photon molecular electronic spectroscopy, *Ann. Rev. Phys. Chem.* **31**, 559–577 (1980).
2. W. M. McClain, Two-photon molecular spectroscopy, *Acc. Chem. Res.* **7**, 129–135 (1974).
3. R. R. Birge, One-photon and two-photon excitation spectroscopy. in: *Ultrasensitive Laser Spectroscopy*, Academic Press, New York (1983).
4. L. Goodman and R. P. Rava, Two-photon spectra of aromatic molecules, *Acc. Chem. Res.* **17**, 250–257 (1984).
5. W. M. McClain, Excited state symmetry assignment through polarized two-photon absorption studies of fluids, *J. Chem. Phys.* **55**, 2789–2796 (1971).
6. M. J. Wirth, A. Koselko, and M. J. Sanders, Molecular symmetry and two-photon spectroscopy, *Appl. Spectrosc.* **35**, 14–21 (1981).
7. R. R. Birge and L. M. Hubbard, Molecular dynamics of *cis-trans* isomerization in rhodopsin, *J. Am. Chem. Soc.*, **102**, 2195–2205 (1980).
8. R. R. Birge, L. P. Murray, B. M. Pierce, H. Akita, V. Balogh-Nair, L. A. Findsen, and K. Nakanishi, Two-photon spectroscopy of locked 1 l-cis-rhodopsin: Evidence for a protonated Schiff base in a neutral protein binding site, *Proc. Natl. Acad. Sci. U.S.A.* **82**, 4117–4121 (1985).
9. R. R. Birge, J. A. Bennett, L. M. Hubbard, H. L. Fang, B. M. Pierce, D. S. Klier, and G. E. Leroi, Two-photon spectroscopy of all-trans-retinal. Nature of the low-lying singlet states, *J. Am. Chem. Soc.* **104**, 2519–2525 (1982).
10. S. P. Jing, S. H. Lian, K.-Ch. Ruan, L.-K. Hui, S.-H. Liu, Z. Zhang, and Q. Li, Two-photon excitation of proteins, *Chem. Phys. Lett.* **104**, 109–111 (1984).
11. Y.-W. Xu, J.-R. Zhang, Y.-M. Deng, L.-K. Hui, S.-P. Jiang, and S.-H. Lian, Fluorescence of proteins induced by two-photon absorption, *J. Photochem. Photobiol. B* **1**, 223–227 (1987).

12. R. R. Birge, B. M. Pierce, and L. P. Murray, Two-photon Spectroscopy of Biological Molecules, in: C. Sandorfy and T. Theophanides, eds., *Reidel, Spectroscopy of Biological Molecules*, pp. 473–486(1984).
13. R. R. Birge, Two-photon spectroscopy of protein-bound chromophores, *Acc. Chem. Res.* **19**, 138–146 (1986).
14. S. P. Jing, Two-photon spectroscopy of biomolecules, *Prog. Reaction Kinet.* **15**, 77–92 (1989).
15. J. R. Lakowicz, I. Gryczynski, J. Kusba, and E. Danielsen, Two-photon induced fluorescence intensity and anisotropy decays of diphenylhexatriene in solvents and lipid bilayers, *J. Fluoresc.* **2**, 247–257 (1992).
16. J. R. Lakowicz, I. Gryczynski, Z. Gryczynski, E. Danielsen, and M. J. Wirth, Time-resolved fluorescence intensity and anisotropy decays of 2,5 diphenyloxazole by two-photon excitation and frequency-domain fluorometry, *J. Phys. Chem.* **96**, 2096–3000 (1992).
17. J. R. Lakowicz, I. Gryczynski, and E. Danielsen, Anomalous differential polarized phase angles for two-photon excitation with isotropic depolarizing rotations, *Chem. Phys. Lett.* **191**, 47–53 (1992).
18. J. R. Lakowicz, I. Gryczynski, E. Danielsen, and J. Frisoli, Anisotropy spectra of indole and *N*-acetyl-L-tryptophanamide observed for two-photon excitation of fluorescence, *Chem. Phys. Lett.* **194**, 282–287 (1992).
19. J. R. Lakowicz and I. Gryczynski, Fluorescence intensity and anisotropy decay of the 4',6-diamidino-2-phenylindole-DNA complex resulting from one-photon and two-photon excitation, *J. Fluoresc.* **2**, 117–122 (1992).
20. J. R. Lakowicz and I. Gryczynski, Characterization of *p*-bis(β -methylstyryl) benzene as a lifetime and anisotropy decay standard for two-photon induced fluorescence, *Biophys. Chem.* **47**, 1–7 (1993).
21. J. R. Lakowicz and I. Gryczynski, Tryptophan fluorescence intensity and anisotropy decays of human serum albumin resulting from one-photon and two-photon excitation, *Biophys. Chem.* **45**, 1–6(1992).
22. H. Szmacinski, I. Gryczynski, and J. R. Lakowicz, Calcium-dependent fluorescence lifetimes of Indo-1 for one- and two-photon excitation of fluorescence, *Photochem. Photobiol.* **58**, 341–345 (1993).
23. I. Gryczynski and J. R. Lakowicz, Fluorescence intensity and anisotropy decays of the DNA stain Hoechst 33342 resulting from one-photon and two-photon excitation, *J. Fluoresc.* **4**, 331–336 (1994).
24. I. Gryczynski, J.R. Lakowicz, G. Gloyna, and A. Kawski, Picosecond fluorescence lifetime and anisotropy standards for one- and two-photon excitation, *Proc. SPIE* 2137 (1994).
25. B. Kierdaszuk, I. Gryczynski, A. Modrak-Wojcik, A. Bzowska, D. Shugar, and J. R. Lakowicz, Fluorescence of tyrosine and tryptophan in proteins using one- and two-photon excitation, *Photochem. Photobiol.* **61**, 319–324 (1995).
26. J. R. Lakowicz, B. Kierdaszuk, P. Callis, H. Malak, and I. Gryczynski, Fluorescence anisotropy of tyrosine using one- and two-photon excitation, *Biophys. Chem.* **56**, 263–271 (1995).
27. H. Szmacinski, I. Gryczynski, and J. R. Lakowicz, Three-photon induced fluorescence of the calcium probe Indo-1, *Biophys. J.* **70**, 547–555 (1996).
28. J. R. Lakowicz, B. Kierdaszuk, I. Gryczynski, and H. Malak, Fluorescence horse liver alcohol dehydrogenase using one- and two-photon excitation, *J. Fluoresc.* **6**, 51–59 (1996).
29. B. Kierdaszuk, H. Malak, I. Gryczynski, P. R. Callis, and J. R. Lakowicz, Fluorescence of reduced nicotinamides using one- and two-photon excitation, *Biophys. Chem.*, **62**, 1–13 (1996).
30. S.-Y. Chen and B. W. Van Der Meer, Theory for two-photon excitation in induced fluorescence anisotropy decay in membranes, *Biophys. J.* **64**, 1567–1575 (1993).
31. C. Wan and C. K. Johnson, Time-resolved anisotropic two-photon spectroscopy, *Chem. Phys.* **179**, 513–531 (1994).

32. W. Yu, P. T. C. So, T. French, and E. Gratton, Fluorescence generalization of cell membranes: A two-photon scanning microscopy approach, *Biophys. J.* 70, 626–636 (1996).
33. W. W. Webb, Non-linear laser microscopy, XIIth International Biophysics Congress, *Prog. Biophys. Mol. Biol.* 65, Suppl., p. 20, Elsevier (1996).
34. A. R. Rehms, and P. R. Callis, Two-photon fluorescence excitation spectra of aromatic amino acids, *Chem. Phys. Lett.* 208, 276–282 (1993).
35. B. E. Anderson, R. D. Jones, A. A. Rehms, P. Ilich, and P. R. Callis, Polarized two-photon fluorescence excitation spectra of indole and benzimidazole, *Chem. Phys. Lett.* 125, 106–112 (1986).
36. A. A. Rehms and P. R. Callis, Resolution of L_a and L_b bands in indoles by two-photon spectroscopy, *Chem. Phys. Lett.* 140, 83–89 (1987).
37. M. R. Eftink and Z. Chen, Evidence for dual L_a and L_b emission in 5-methylindole, *J. Fluoresc.* 4, 165–169 (1994).
38. B. Kierdaszuk, H. Malak, I. Gryczynski, and J. R. Lakowicz, unpublished observation.
39. J. A. Ross, C. Schmidt, and L. Brand, Time-resolved fluorescence of the two tryptophan in horse liver alcohol dehydrogenase, *Biochemistry* 20, 4369–4377 (1981).
40. M. S. Hirshfield, S. Chaffe, L. Koro-Johnson, A. Mary, A. A. Smith, and S. A. Short, Use of site-directed mutagenesis to enhance the epitope-shielding effect of covalent modification of proteins with polyethylene glycol, *Proc. Natl. Acad. Sci. U.S.A.* 88, 7185–7189 (1991).
41. B. Valeur and G. Weber, Resolution of the fluorescence excitation spectrum of indole into the 1L_a and 1L_b excitation bands, *Photochem. Photobiol.* 25, 441–444 (1977).
42. P. R. Callis, On the theory of two-photon induced fluorescence anisotropy with application to indoles, *J. Chem. Phys.* 99, 27–37 (1993).
43. S. M. Kennedy and F. E. Lytle, *p*-Bis(*o*-methylstyryl)benzene as a power-squared sensor for two-photon absorption measurements between 537 and 694 nm, *Anal. Chem.* 58, 2643–2647 (1986).
44. B. Hudson and B. Kohler, Linear polyene electronic structure and spectroscopy, *Ann. Rev. Phys. Chem.* 25, 437–460 (1974).
45. M. A. Abdallach, J.-F. Biellmann, P. Wiget, R. Joppich-Kuhn, and P. L. Luisi, Fluorescence quenching and energy transfer in complex between horse-liver alcohol dehydrogenase and coenzymes, *Eur. J. Biochem.* 89, 397–405 (1978).
46. H. Eklund, J.-P. Samamma, and T. A. Jones, Crystallographic investigation of nicotinamide adenine dinucleotide binding to horse liver alcohol dehydrogenase, *Biochemistry* 23, 5982–5996 (1984).
47. W. R. Lowes and J. D. Shore, The mechanism of quenching of liver alcohol dehydrogenase fluorescence due to ternary complex formation, *J. Biol. Chem.* 253, 8593–8597 (1978).
48. J. Eccles and B. Honig, Charged aminoacids as spectroscopic determinants for chlorophyll in vivo, *Proc. Natl. Acad. Sci. U.S.A.* 80, 4959–4962 (1983).
49. R. R. Birge, Photophysics of light transduction in rhodopsin and bacteriorhodopsin, *Ann. Rev. Biophys. Bioeng.* 10, 315–354 (1981).
50. C. Wan, Q. Song, and C. K. Johnson, Two-photon-induced anisotropic transient absorption in bacteriorhodopsin, *Chem. Phys. Lett.* 210, 94–100 (1993).
51. G. W. Stubbs, J. C. Saari, and S. J. Futterman, 11-Cis-retinal-binding protein from bovine retina: isolation and characterization, *J. Biol. Chem.* 254, 8529–8533 (1979).
52. B. Dick, H. Gonska, and G. Hohlneicher, Two-photon spectroscopy of dipole forbidden transitions. III. Experimental determination of two-photon absorption spectra including polarization control, *Ber. Bunsenges. Phys. Chem.* 85, 746–754 (1981).
53. R. L. Swofford, New two-photon absorption spectrometer and its application to diphenylbutadiene, *Rev. Sci. Instrum.* 46, 246–249 (1975).
54. B. Staginnus, D. Frohlich, and T. Caps, Automatic 2-photon spectrometer, *Rev. Sci. Instrum.* 39, 1129–1130 (1968).

55. G. J. Blanchard, Measurement of small absorbencies by picosecond pump-probe spectrometry, *Anal. Chem.* 58, 532–535 (1986).
56. A. J. Twarowski and D. S. Klier, Multiphoton absorption spectra using thermal blooming, *Chem. Phys.* 20, 253–258 (1977).
57. R. G. Freeman, D. L. Gilliland, and F. E. Lytle, Second harmonic detection of sinusoidally modulated two-photon excited fluorescence, *Anal. Chem.* 62, 2216–2219 (1990).
58. D. V O'Connor and D. Philips, *Time-Correlated Single Photon Counting*, Academic Press, London (1984).
59. D. J. S. Birch and R. E. Imhof, Time-domain fluorescence spectroscopy using time-correlated single-photon counting, in: *Topics in Fluorescence Spectroscopy, Volume 1: Techniques*, (J. R. Lakowicz, ed.), pp. 1–95, Plenum, New York, (1991).

This page intentionally left blank.

Fluorescence and Multiwave Mixing Induced by Photon Absorption of Excited Molecules

Valery L. Bogdanov

6.1. Introduction

It is generally assumed that fluorescence of polyatomic organic molecules (dyes, aromatics) in solutions is emitted from the lowest singlet excited state (S_1) according to the Kasha rule.⁽¹⁾ The absence of noticeable fluorescence from the highly excited electronic states (S_n , $n \geq 2$) is direct evidence that excitation energy excess (a difference between the excitation photon energy and the energy of S_1) dissipates in solution during a short time in comparison with lifetime of the state S_1 , which is usually 0.1–100 ns for organic fluorophores. Fundamental laws of molecular fluorescence in solutions—*independence of the fluorescence parameters, such as quantum yield and emission spectrum on the excitation wavelength,⁽²⁾ and the validity of Stepanov's relation between absorption and emission spectra⁽³⁾*—are also due to ultrafast nonradiative decay of the highly excited molecules.

This chapter presents data on emission and relaxation of the highly excited electronic states of polyatomic organic molecules in solution (HES). These data were predominantly obtained by nonlinear fluorescence and transient multiwave mixing techniques. The results are significant for elucidating the rigidity of Kasha's rule and the aforementioned fluorescence laws in solutions of organic molecules. Additionally, they indicate new analytical applications of molecular fluorescence and nonlinear optical spectroscopy.

The chapter is divided into two parts. The first part studies a weak short-wavelength emission of highly excited molecules. Observation of this emission in

Valery L. Bogdanov • Vavilov State Optical Institute, 199034 St. Petersburg, Russia; *present address:* Molecular Tool Inc., Hopkins Bayview Research Campus, Baltimore, Maryland 21224.

Topics in Fluorescence Spectroscopy; Volume 5: Nonlinear and Two-Photon-Induced Fluorescence, edited by J. Lakowicz. Plenum Press, New York, 1997.

practice is usually difficult due to its low quantum yield and a masked emission of a solvent and/or impurities. Subsequent two-photon absorption permits this experimental problem to be overcome and to reliably observe an emission from short-lived HES. Attention is focused on the results obtained with the stepped two-photon excitation method. Data on ultrafast internal conversion, vibrational relaxation, and energy transfer, which come from the stepped population of the highly excited states, are presented and discussed.

The second part demonstrates the possibilities of transient resonant multiwave mixing experiments for studies of ultrafast molecular photodynamics. Nonlinear multiwave mixing relates to stimulated coherent scattering, but fluorescence relates to spontaneous emission. Thus, transient multiwave mixing and short-wavelength fluorescence studies can be used as independent sources of information about molecular relaxations and HES properties. Experimental and theoretical results on nondegenerated multiwave mixing by excited molecules in steady-state and time-resolved regimes are presented. It is shown that transient multiwave mixing provides enhanced sensitivity of the mixing signal to the dynamics of excited molecules, in particular to orientational anisotropy decay.

6.2. Emission of Highly Excited Molecules

6.2.1. Methods of Excitation

Fluorescence from the states S_n corresponds to the optical transition between state S_n and electronic states with a lower energy, S_m ($m < n$) (Figure 6.1). The basic data on HES emission were obtained by studying short-wavelength fluorescence, which relates to the transition $S_n \rightarrow S_0$, where S_0 is a ground state. Emission spectra for transitions $S_n \rightarrow S_m$ ($n > m$, $m > 0$) are usually overlapped with the spectrum of strong fluorescence from S_1 and have so been studied somewhat.

The methods of excitation of HES emission can be separated into two groups. The first group includes methods in which, S_n is populated by the absorption of one photon with energy $\hbar v_N \geq \hbar v_{0n}$, where v_{0n} is the frequency of the electronic transition $S_n \rightarrow S_0$ and \hbar is Planck's constant. Methods in which subsequent absorption of two photons are used to populate S_n comprise the second group.

One-photon excitation is usually used for studying comparatively long-lived states S_n (with lifetime $\tau_n > 1$ ps and quantum yield of fluorescence $\eta_n > 10^{-3}$). In practice it is impossible to study fluorescence from HES with $\eta_n < 10^{-3}$ by

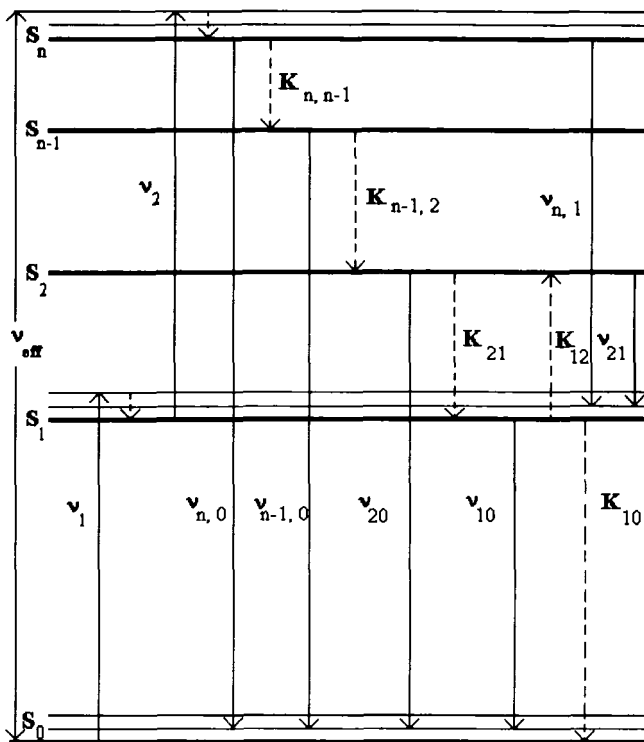


Figure 6.1. Diagram of singlet electronic states and molecular transitions accompanying the population of highly excited states. Arrows (\rightarrow) and (\leftrightarrow) show radiative and nonradiative transitions respectively.

one-photon methods without taking special precautions against impurities emission and scattering light.

Increasing the solution concentration can improve the ratio of intensities of the studied HES emission and the impurities emission. For instance, increasing the concentration of the solute to $10^{-2}\text{--}10^{-1} M$ enables us to observe emission from HES with one-photon excitation and quantum yield as small as 10^{-6} .⁽⁴⁾ However, the applicability of the high-concentration method is limited due to inadequate solubility of many compounds, the possibility of aggregation, and the emission spectrum distortion by reabsorption.

Modification of one-photon excitation, which enables separating short-lived fluorescence from highly excited states against the background of impurity emission in a low-viscosity solvent, was proposed in.⁽⁵⁾ HES fluorescence was excited by radiation with periodically varying polarization. With such excitation the

intensity of the HES fluorescence polarized due to the short lifetime of S_n , is modulated. The intensity of the long-lived depolarized impurity emission remains constant. The previous method, which is similar to time-resolved measurements, permitted recording the fluorescence spectra from HES with quantum yield as low as 7.5×10^{-5} in low-concentration solutions.⁽⁵⁾

The undesirable parasitic emission in the region of short-wavelength fluorescence for $S_n \rightarrow S_0$ is virtually eliminated by stepped excitation. In this method S_n is populated by the subsequent absorption of two photons: $S_0 + h\nu_1 \rightarrow S_1 + h\nu_2 \rightarrow S_n$ (Figure 6.1). Stepped excitation results in the population of S_n with electronic energy $h\nu_{0n} \leq h\nu_{\text{eff}}$, where $h\nu_{\text{eff}} = h\nu_{01} + h\nu_2$ is the effective excitation energy, $h\nu_{01}$ is the electronic energy of S_1 and $h\nu_1 \geq h\nu_{01}$. The advantages of stepped excitation relate to the selective population of S_n of molecules under study and the opportunity to vary effective excitation energy with detuning of ν_2 . A realization of two-photon stepped excitation in practice requires powerful laser pulses due to $h\nu_2$ photon absorption by the excited fluorophore during its lifetime, Q -switched and mode-locked lasers easily provide the needed pulses. The first observations of HES emission with stepped excitation method were made in Refs. 6 and 7.

Another modification of stepped HES population exploits the phenomenon of triplet-triplet annihilation,⁽⁸⁾ in which one of the interacted molecules in the lowest triplet state (T_1) goes into the highly excited state and the second molecule goes into the ground state. In this case the effective excitation energy $h\nu_{\text{eff}} = 2h\nu_T$, where $h\nu_T$ is the energy of the transition $T_1 \rightarrow S_0$. Significant drawbacks of the annihilation method are high-concentration solutions and the impossibility of varying the frequency $h\nu_{\text{eff}}$.

6.2.2. Radiationless Decay of Highly Excited States

It has long been known^(2,9) that spectrum and quantum yield of the intensive fluorescence from S_1 in solution of organic molecules are independent of the wavelength of excitation light. This independence stems from the high rate of nonradiative decay of highly excited vibronic states, as a result of which S_1 is efficiently populated and fluorescence S_n is quenched. Evidently, the high rate of nonradiative decay of S_n determines the short lifetime and low quantum yield of HES fluorescence.

The studies of HES emission completed with stepped excitation show that the fluorescence $S_n \rightarrow S_0$ is emitted from all of the electronic states S_n , transitions from which to the ground state are optically allowed and whose energy is less than $h\nu_{\text{eff}}$.^{10,11} Studies^(10,11) did not reveal significant deviations of the ratios of band intensities, corresponding to transitions from different states S_n from ν_{eff} . Based on these results, it was concluded in Ref. 11 that nonradiative decay of

highly excited states occurs by cascade way: $S_n \rightsquigarrow S_{n-1} \rightsquigarrow S_{n-2} \rightsquigarrow \dots \rightsquigarrow S_1$ (Figure 6.1).

The cascade nonradiative HES decay is due primarily to the dependence of the rate of intramolecular nonradiative deactivation K_{nm} on the energy gap between the neighboring electronic states with the same multiplicity. According to nonradiative decay theory,⁽²⁾

$$K_{nm} = (2\pi)^2 L_e^2 F \rho / h \quad (6.1)$$

where L_e is the electronic matrix element of the nonadiabatic operator, F is the Franck–Condon factor of the accepting vibrations, and ρ is the density of the vibrational levels of S_m with vibrational energy equal to the electronic energy gap between S_n and S_m .

When the electronic states are strongly coupled by a nonadiabatic operator, Eq. (6.1) implies an approximately exponential growth of K_{nm} as the energy gap ΔE_{nm} between S_n and S_m combined in the nonradiative transition decreases.⁽¹³⁾ This theoretical result is in agreement with experimental data^(14–16) and the model calculations of K_{nm} for polyatomic molecules.⁽¹⁷⁾ According to Refs. 14–16, the rate K_{nm} of internal conversion can reach $10^{10}–10^{13} \text{ s}^{-1}$, i.e., K_{nm} can greatly exceed the rate of allowed radiative molecular transitions ($\leq 10^9 \text{ s}^{-1}$). The strong dependence of K_{nm} on ΔE_{nm} leads to the fact that the main channel of HES depopulation is, as a rule, an internal conversion to the closest of the low-lying singlet state. Thus, the energy gap between neighboring excited states determines predominantly the depopulation of HES. We will examine the role of $\Delta E_{n,n-1}$ for fluorescence studies from S_2 for organic molecules.

1. The rate of internal conversion K_{21} is slow for molecules with a large energy gap ($\Delta E_{21} \geq 10^4 \text{ cm}^{-1}$). Therefore, fluorescence from S_2 can be easily observed due to the comparatively high quantum yield η_2 and long lifetime τ_2 . Thus, in experiments with azulene solutions, $\eta_2 = 0.03$ ⁽¹⁵⁾ and $\tau_2 = 1.4 \text{ ns}$.⁽¹⁴⁾ Quite intense fluorescence from S_2 is observed not only for azulene, which has $\Delta E_{21} \approx 14,000 \text{ cm}^{-1}$, but also for molecules with large ΔE_{21} belonging to other chemical classes: 1,2-Benzperylene,⁽¹⁸⁾ thioketones,⁽¹⁹⁾ annulenes.⁽²⁰⁾

An essential feature of the aforementioned molecules is low intensity of fluorescence from S_1 , which facilitates observation of fluorescence from S_2 . This feature is a result of a low K_{21} and a high K_{10} (for instance, $K_{21} \approx 10^8 \text{ s}^{-1}$ and $K_{10} \approx 10^{11} \text{ s}^{-2}$ in azulene solution).⁽²¹⁾ Studies of the intensity distribution in the emission spectra of transitions showed that the geometry of azulene molecules in S_1 and S_2 is approximately the same and differs substantially from the geometry in the ground state.⁽²¹⁾ These results suggested that the low (high) rate K_{21}

- (K_{10}) is determined by the small (large) number of accepting vibrational modes, which in turn determine the value of the Franck–Condon factor.
2. When the energy gap ΔE_{21} is small, K_{21} is high, the fluorescence can be observed simultaneously from the two close-lying states S_1 and S_2 . This is called double fluorescence, whose basic features are described in Ref. 22. The notion of smallness of an energy gap depends on the solution temperature, since the population of S_2 is determined by the population of the vibrational modes of S_1 with energy ΔE_{21} . At room temperature, double fluorescence of organic fluorophore solutions is usually observed with $\Delta E_{21} < 3000 \text{ cm}^{-1}$. In this case, the rate of thermally activated “back” nonradiative transition (K_{12}) is higher than the rate of depopulation of S_1 , while the ratio of the populations of S_2 and S_1 is determined by the Boltzmann factor ($\exp(-\Delta E_{21}/kT)$), where T is the solution temperature. The double-fluorescence spectrum does not depend on the excitation wavelength. This phenomenon was observed, for instance in a solution of 3,4-benzyprene above 190K.⁽²³⁾ Decreasing temperature results in diminishing K_{12} and elimination of the double fluorescence. At low temperature, fluorescence from S_2 is virtually absent for molecules with small energy gap due to very high K_{21} . Such a situation was observed for ovalene molecules, where $\Delta E_{21} = 1800 \text{ cm}^{-1}$, cooled in a supersonic jet.⁽²⁴⁾
 3. In the foregoing cases the relatively high intensity of fluorescence from S_2 was determined either by the low rate of internal conversion (large energy gap ΔE_{21}) or by the high rate of thermally induced “back” nonradiative transition between S_1 and S_2 due to a small ΔE_{21} and a high temperature. For most organic fluorophores ΔE_{21} is $\sim 3000\text{--}8000 \text{ cm}^{-1}$. Such a gap is not so large that the rate of internal conversion is low, but it is also not small enough to allow an effective thermal population of S_2 . Therefore, molecules with intermediate energy gap have, as a rule, a short lifetime ($<1 \text{ ps}$) and a low quantum yield ($<10^{-4}$) for fluorescence from S_2 .

The weak fluorescence from S_2 can be reliably recorded by the stepped excitation method^(6,7,25,26) or by one-photon excitation of substances whose quantum yield of fluorescence from S_2 is not too low.^(25,27) It was shown that the form of the fluorescence spectrum from S_2 of metal porphyrin solutions is independent of the excitation method (one-photon or stepped two-photon excitation).⁽²⁵⁾ Fluorescence from S_2 for metal porphyrins, which corresponds to the Soret band in absorption spectrum, has a relatively long lifetime ($\tau_2 \sim 1 \text{ ps}$) and high quantum yield ($\eta_2 \sim 10^{-3}$).^(25,27) These comparatively high values are in accord with the relatively large energy gap ($\Delta E_{21} \sim 8,000 \text{ cm}^{-1}$).

6.2.3. Emission Spectra and Relaxations of Short-Lived Highly Excited States

The density of molecular electronic states increases with increasing state energy. Therefore, the lifetimes of high-lying states S_n , with $n > 2$ are, as a rule, shorter than the lifetime of S_2 . To the best of our knowledge, the lifetimes of S_n , with $n > 2$ in all studied organic fluorophore solutions, are $\sim 0.01\text{--}1$ ps. Such ultrashort lifetimes decisively determine emission properties of highly excited molecules.

The emission spectrum, which is observed with stepped laser excitation of HES, usually includes all bands for allowed optical transitions from S_n whose energy is less than $h\nu_{\text{eff}}$. The spectra are shown in Figure 6.2 for 1,2-benzanthracene and in Figure 6.3 for coronene solutions. Two distinct regions can often be distinguished from a separate electronic state S_n : the long-wavelength region, in which the form and position of the emission band are correlated with the absorption spectrum of the transition $S_0 \rightarrow S_n$ (approximate mirror symmetry), and the short-wavelength region, consisting of a set of bands whose position is determined by the effective excitation frequency ν_{eff} ⁽²⁸⁻³⁰⁾.

The long-wavelength emission band from S_n is interpreted as the ordinary fluorescence spectrum, which is emitted with quasiequilibrium vibrational distribution of the molecules inside S_n . The form and position of this band in solutions usually demonstrated a smooth dependence on the excitation energy $h\nu_{\text{eff}}$ ^(30,31). If $h\nu_{\text{eff}}$ is close to the origin of $S_n \rightarrow S_0$ then the contours of the absorption and long-wavelength emission band are approximately mirror

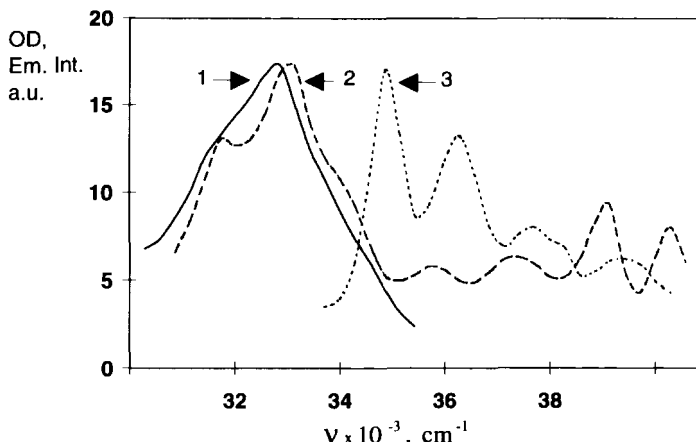


Figure 6.2. Short-wavelength spectra of 1,2-benzanthracene solution in heptane at $T = 300$ K: emission observed with stepped two-photon population of highly excited state at $\nu_2 = 18,800$ (1), $14,400\text{ cm}^{-1}$ (2), and absorption (3), respectively.

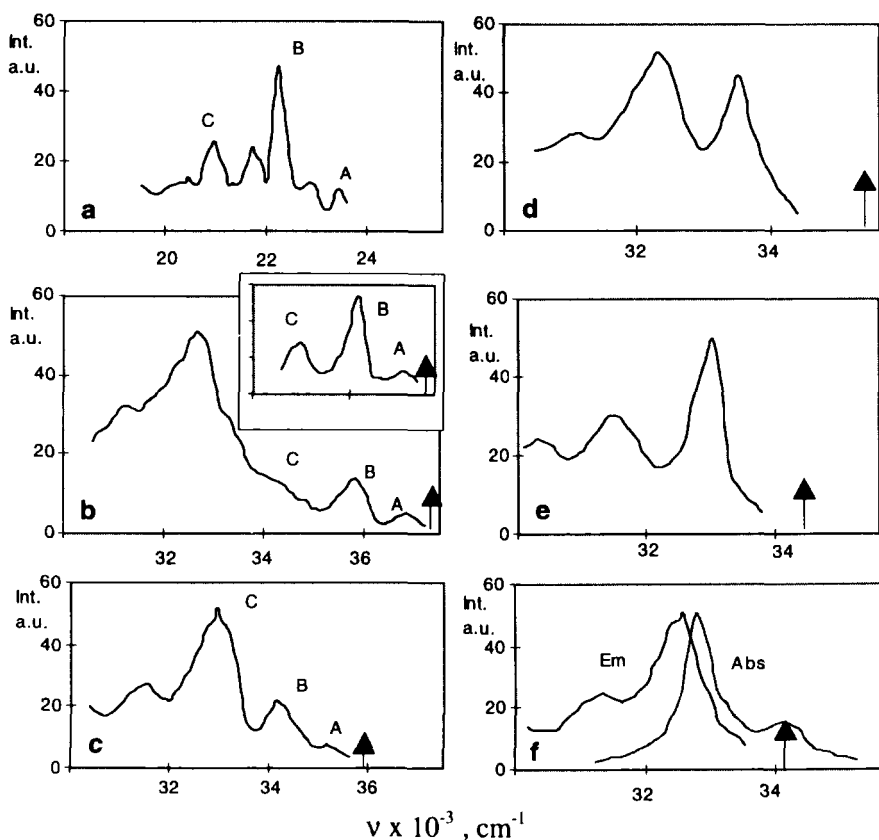


Figure 6.3. Spectra of coronene solution in ethanol at $T = 300 \text{ K}$: (a) fluorescence from S_1 and short-wavelength emission observed with stepped two-photon population of the highly excited state at (b) $\nu_2 = 14,400 \text{ cm}^{-1}$, (d) $12,600 \text{ cm}^{-1}$, $12,100 \text{ cm}^{-1}$, (e) $11,500 \text{ cm}^{-1}$, and (f) $10,850 \text{ cm}^{-1}$. Arrows indicate ν_{eff} : the Abs and Em curves in (f) show short-wavelength absorption and emission spectra of $S_0 \rightarrow S_n$. The insert in (b) shows the short-wavelength emission spectra of coronene solution in heptane at $T = 77 \text{ K}$.

symmetric^(28,30) (panel f in Figure 6.3). When $\hbar\nu_{\text{eff}} \gg \hbar\nu_{0n}$, smearing of the vibrational structure, distortion of mirror symmetry of absorption and fluorescence spectra, and a shift of the maximum of the emission band toward long wavelengths are observed^(28-30,32) (compare spectra 2 and 3 in Figure 6.2). Changes of this type in the fluorescence spectra accompanying variation of the excitation frequency are well known for fluorescence from S_1 for polyatomic organic molecules in the vapor phase under low pressure, provided there are no molecular collisions during the lifetime of S_1 .^(33,34) Observed

changes of the vapor fluorescence spectra correspond to the dependence of the vibration level population of S_1 on the stored excitation energy, which in turn determines the intramolecular vibrational temperature of excited molecules in the absence of the intermolecular exchange of vibrational energy during the lifetime of “isolated” excited molecules in the vapor phase.^(33,34)

A similar dependence of the long-wavelength emission band for transitions $S_n \rightarrow S_0$ in solution shows that the lifetime of highly excited states ($S_n, n > 2$) is shorter than the time of intermolecular vibrational energy exchange in solution. However, fluorescence spectra of relatively long-lived state S_2 , with lifetime more than 10 ps, does not depend on the excitation frequency.⁽²⁷⁾ Thus, one can conclude that the time interval needed for completed intermolecular vibrational energy exchange is approximately 10 ps in solution. This process results in equilibrium vibrational distribution of excited molecules with intramolecular temperature equal to the solvent temperature.

The short-wavelength group of the bands in the emission spectra from HES (for instance, A, B, C bands on panels b and c in Figure 6.3) was apparently first observed with stepped excitation of 3,4,9,10-dibenzpyrene solution.⁽²⁸⁾ Note, that the spectral position of these bands follows the change of v_{eff} . This group was interpreted in Ref. 28 as being the result of the excitation of separate centers inside inhomogeneous broadening absorption spectrum of $S_1 \rightarrow S_n$. Later, short-wavelength separate bands, whose positions follow v_{eff} were recorded for 1,2,5,6-dibenzanthracene solution⁽²⁹⁾ and were ascribed to fluorescence from high-lying vibrational levels of S_{n-1} , which are selectively populated via the internal conversion $S_n \rightsquigarrow S_{n-1}$.

The nature of these bands was also studied in.^(31,35,36) In Ref. 35 previous bands were observed with stepped two-photon excitation of polymethine dye solutions and were interpreted as belonging to the anti-Stokes electron-vibrational Raman scattering of the photon $\hbar\nu_2$ by excited (S_1) molecules (Figure 6.4). Further studies, with coronene and 1,2-benzanthracene solution,^(31,36) validated this explanation. The most convincing observation supporting scattering origin of the separate bands is the similarity of the intensity distribution in fluorescence spectra from S_1 (A, B, C marked fluorescence bands on panel a in Figure 6.3) and the intensity distribution along the separate bands of short-wavelength emission from HES (A, B, C marked short-wavelength emission bands on panel b in Figure 6.3). This similarity is distinctly observed for 1,2-benzanthracene solution in room-temperature and low-temperature (Shpol'skii matrices) solutions (Figure 6.5).

If the separate bands correspond to anti-Stokes Raman scattering by excited molecules, then the frequency of the scattered line is $v_{\text{sc}} = v_{01} + v_2 - \sum v_i v_i$, where v_i are the vibration frequencies in the ground electronic state and v_i are the vibrational quantum numbers. Since the vibrational structure of the fluorescence spectrum of $S_1 \rightarrow S_0$ contains the frequencies $v_{\text{fl}} - v_{10} - \sum v_i v_i$, then a simi-

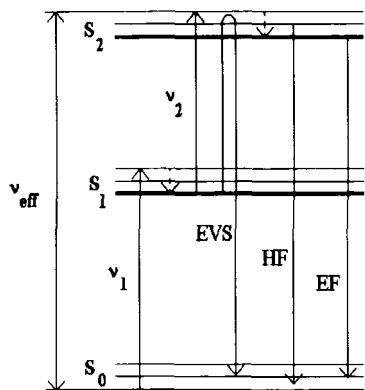


Figure 6.4. Diagram of stepped two-photon excitation and the principal three components in resonant emission spectrum from the highly excited state: anti-Stokes electronic–vibronical scattering (EVS), hot fluorescence (HF), and quasiequilibrium fluorescence (EF).

larity between the structure of the vibronic bands should be observed in the fluorescence spectrum from S_1 and the short-wavelength emission spectrum recorded with two-photon stepped excitation. Separate bands of short-wavelength scattering spectrum must be shifted relative to the corresponding fluorescence bands by an amount v_2 . This is indeed observed (Figure 6.5). Thus, short-wavelength bands can be interpreted as photon repetition (copy) of the fluorescent spectrum of excited molecules in S_1 . It is also important that the quasilinear structure of short-wavelength bands appear in frozen Shpolskii matrices as in the fluorescence spectrum of the transition $S_1 \rightarrow S_0$.

Complete similarity in the long-wavelength fluorescence spectra and the anti-Stokes electron-vibrational Raman spectra is not observed for molecules with a center of symmetry (spectra of coronene solutions in Figure 6.3; 1,2,5,6-dibenzanthracene⁽²⁹⁾). The fluorescence spectrum of such molecules has more bands than the short-wavelength emission spectrum (compare spectra in panel a and b, Figure 6.3). The difference between these spectra of symmetric molecules may be explained on the basis of selection rules for fluorescence and scattering processes.⁽³⁶⁾

In the region between the long-wavelength spectrum of quasiequilibrium fluorescence from S_n and short-wavelength separate bands (region 33,000–35,000 cm^{-1} in Figure 6.2 and panel b in Figure 6.3) there is a quite intensive continuous emission which is ascribed to emission from high-lying vibrational levels of HES.^(28,30,32) Anti-Stokes scattering and hot fluorescence, emitted in the process of intramolecular vibrational relaxation,⁽³⁷⁾ are responsible for the observed emission. It is difficult to distinguish the contributions of hot fluorescence and Raman scattering in this spectral region.

In interpreting these results, one can conclude that three fundamental components of the secondary resonant emission—quasiequilibrium fluorescence, hot fluorescence, and resonant Raman scattering⁽³⁷⁾—are all of the same order of

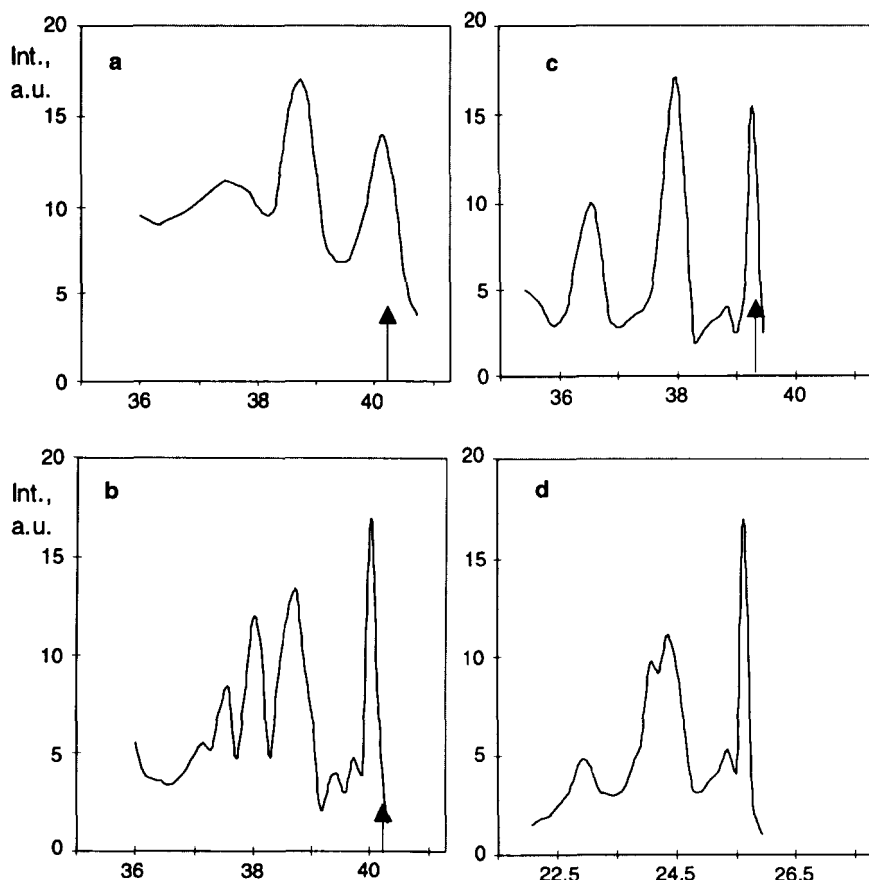


Figure 6.5. Spectra of short-wavelength emission (a–c) and fluorescence from the lowest excited state (d) of 1,2-benzanthracene solution in heptane at $T = 300$ K (a) and 77 K (b–d). Arrows indicate ν_{eff} for stepped two-photon excitation.

magnitude in the emission spectra from short-lived HES. This unique feature of short-wavelength emission permits observing quite simply the competition between fluorescence and resonant scattering. Figure 6.3 shows the complicated dependence of the secondary emission spectrum from HES on the frequency of exciting radiation. As the absorption bands of $S_0 \rightarrow S_n$ are approached when ν_{eff} is decreased, the relative intensity of those bands in the anti-Stokes Raman spectrum which are closest to resonance with absorption bands (the bands B and C in Figure 6.3) grows appreciably. Such changes in the spectrum are characteristic for resonant Raman scattering and thereby confirm the interpretation given in Refs 31, 35, and 36 for the observed group of the separate bands in the

short-wavelength region. The sharp changes in intensity, which occur in the spectrum of coronene (Figure 6.3, panels d–f) for ν_{eff} lying in the region of intensive vibronic absorption bands of $S_0 \rightarrow S_N$, are especially intriguing. For small alteration in ν_{eff} the ratio of the Raman scattering and fluorescence intensities changes markedly: Raman scattering makes the main contribution to the emission spectrum in Figure 6.3e, while fluorescence makes the main contribution to the spectrum Figure 6.3f. The high sensitivity of the secondary emission spectra accompanying stepped excitation of high-lying electronic states to a change in the frequency of exciting radiation can serve as a basis for development of new methods of spectral analysis of organic molecules.

6.2.4. Quantum Yield of Fluorescence from Highly Excited States

In studies of fluorescence from HES it is not always desirable to use the standard definition of the quantum yield η_n as the ratio of the number of photons emitted to the number of photons absorbed. This concerns primarily the measurements η_n with stepped excitation of the states S_n in which two photons must be absorbed in order to excite S_n . It is better to use the definition according to which the quantum yield of fluorescence is equal to the ratio of the number of molecules emitting fluorescence from S_n to the number of molecules excited in S_n . With this definition η_n is linked to the rates of depopulation of S_n by the well-known relation $\eta_n = A_n/(A_n + K_n)$, where A_n and K_n are the rates of radiative and nonradiative decay, respectively.

The choice of methods for measuring η_n depends on the excitation method used. If η_1 of fluorescence from the lowest excited state S_1 is known, then for one-photon excitation (or as a result of triplet-triplet annihilation⁽⁸⁾) of S_n , η_n and the fluorescence lifetime τ_n can be determined (assuming that $\tau_n \ll \tau_1$ and S_n predominately decays into S_1) from the relations

$$\eta_n = \eta_1 (F_n/F_1) \quad (6.2)$$

$$\tau_n = \tau_{\alpha n} \eta_n \quad (6.3)$$

where F_n and F_1 are the integrated intensities of fluorescence from S_n and S_1 , respectively, and $\tau_{\alpha n}$ is the radiative lifetime determined from the integrated absorption.⁽³⁸⁾

With stepped excitation in the system of singlet states the amount of η_n under stationary measurement conditions is

$$\eta_n = F_n (F_1 \sigma_{1n} P_2 \tau_{\alpha 1})^{-1} \quad (6.4)$$

where τ_{z1} is the radiative lifetime of S_1 , σ_{1n} is the absorption cross section for $S_1 \rightarrow S_n$, and P_2 is the power density of the exciting radiation with frequency ν_2 .

In Ref. 39 the population of S_n with the use of the stepped excitation was determined from the measurement of the absorbed energy of the radiation with frequency ν_2 by the photoacoustical method. The advantage of this method is that one need not know the adsorption cross section of excited molecules and P_2 . Table 6.1 shows η_n measured by the photoacoustic method.

As a rule, η_n is 10^{-4} – 10^{-6} .^(4,5,7,8,27,39) According to estimates made with measured values of η_n and Eq. (6.3), the HES lifetimes of different substances lie in a comparatively narrow range (~0.01–1 ps), if the few cases corresponding to small (double fluorescence) or very large intervals ΔE_{21} are excluded. Femtosecond lifetimes τ_n were obtained for the solutions studied in Ref. 8: $\tau_3 = 130$ fs for 1,2-dibenzanthracene; $\tau_4 = 26$ fs for fluoroanthrene; and $\tau_3 = 19$ fs for chrysene. For most metal porphyrines τ_2 is several picoseconds.⁽²⁷⁾ Estimates of τ_n , obtained for the same substances by different methods are usually in agreement. Thus, $\tau_3 = 0.2$ ps was obtained for rhodamine-6G solution in Ref. 7, and close values were presented in Refs. 40–42. Table 6.1 shows the rate of depopulation of the highly excited state $K_n = 1/\tau_n$ for a number of substances, which were estimated in Ref. 39 on the basis of τ_{an} values and η_n measured by the photoacoustical method.

Available experimental data demonstrate a tendency for η_n and τ_n to drop as the energy of S_n increases. This tendency for η_n was established in Ref. 43, in which the short-wavelength fluorescence of many dye solutions was studied, and for τ_n in Ref. 44, in which monotonous drop τ_n with increasing state energy in S_2 – S_6 was observed in 3,4,9,10-dibenzpyrene solution (τ_n drops monotonously from ~0.2 to ~0.04 ps for S_2 – S_6). Nevertheless, there are known cases when η_n and τ_n vary nonmonotonously as the energy of the excited state increases. This phenomenon was observed, for instance, for η_n in 3,4,9,10-dibenzpyrene solution⁽⁴⁴⁾ and for τ_n in tetrabenzporphyrin solution ($\tau_2 = 0.58$ ps, $\tau_3 = 1.14$ ps).

The nonmonotonous dependence of fluorescence quantum yield and lifetime on the energy of the highly excited electronic state shows that the rate of internal

Table 6.1. Fluorescence Quantum Yield (η_n) and Rate of Depopulation (k_n) for the Highly Excited States of Organic Compounds in Solution^a

Compounds	Solvent	η_n	$k_n \times 10^{-13} (\text{s}^{-1})$
9,10-Di- <i>n</i> -propylanthracene	Heptane	3×10^{-5}	3.3
2,1-Dibenzanthracene	Hexane	1×10^{-4}	1.8
Acridine	Ethanol	4×10^{-5}	3.3
9-Phenylacridine	Ethanol	1×10^{-5}	16.0
<i>n</i> -Methylacridone	Ethanol	5×10^{-5}	1.6

conversion is determined not only by the electronic energy gap but by other factors also (the number of accepted vibration modes, the magnitude of the shift of the potential curves, and so on). The tendency for η_n and τ_n to decrease monotonously with increasing energy of a highly excited state is evidently linked to the general tendency of the energy gap to decrease as the energy of the excited electronic state increases.

The values of η_n depend not only on the properties of the electronic state responsible for the observed fluorescence but also on v_{eff} when it varies within a band of a single electronic transition, i.e., on the amount of the stored vibrational energy $Q_n = hv_{\text{eff}} - hv_{0n}$. This phenomenon was observed, for instance, with excitation of S_6 in 3,4,9,10-dibenzpyrene solution.⁽⁴⁴⁾ The dependence of η_n on v_{eff} in fluorophore solutions may be linked to conservation of the vibrational energy of the highly excited state during its lifetime. As for “isolated” excited molecules at S_1 in the vapor phase,^(33,34) where Q_1 , obtained with excitation, is conserved, η_n from the short-lived HES of organic molecules in solution drops as Q_n increases. The dependence for η_1 in the vapor phase and similarly for η_n in solution can be explained by the increasing rate of internal conversion with the growth of the stored vibrational energy of excited molecules. Observation of the temperature-induced quenching of HES fluorescence in rhodamine-6G solution⁽⁴⁵⁾ also indicates that η_n in solution depends on Q_n .

6.2.5. Anisotropy of Fluorescence from Highly Excited States

The anisotropy of fluorescence from the lowest excited state is usually observed only in high-viscosity media, in which the rotation of excited molecules leading to fluorescence depolarization is suppressed. Fluorescence from highly excited states with $\tau_n < 1$ ps must be polarized in low-viscous solutions and in vapors. Experimental data confirm this conclusion: short-lived fluorescence from HES is always polarized.^(40,46,-50)

One of the important characteristics of polarized fluorescence from S_1 is the polarization spectrum P_e , which shows the dependence of the polarization degree on the frequency of the exciting radiation v_{exc} , with a fixed frequency of the recorded fluorescence, v_{rec} .⁽⁵¹⁾ HES fluorescence is also characterized by P_r , which shows the dependence of the polarization degree on v_{rec} with fixed v_{exc} . The form of P_r generally depends on v_{exc} .

Figure 6.6 illustrates the dependence of P_r on v_{exc} for hypothetical absorption and fluorescence bands belonging to different electronic transitions with mutually perpendicular direction of polarization (the relative direction of transition polarization is shown by the arrow). It is assumed that the bands belonging to the different electronic transitions slightly overlap. When S_n , for which the dipole moment of $S_n \rightarrow S_0$ is oriented parallel to the dipole moment of $S_1 \rightarrow S_0$ (band

III), is excited, P_r (curve 1) is similar in form to P_e but is shifted into the long-wavelength side in accordance with the Stokes shift of the fluorescence spectrum.⁽⁴⁸⁾ When S_n for which the dipole moment of $S_n \rightarrow S_0$ is oriented perpendicular to the dipole moment of $S_1 \rightarrow S_0$ (band IV), P_r corresponds to curve 2 in Figure 6.6.

For weakly overlapping absorption and fluorescence bands belonging to different electronic transitions, the form of P_r will be similar when excitation occurs in regions corresponding to transitions with the same transition dipole moment orientation, differing only in the frequency range ν_{rec} which depends on

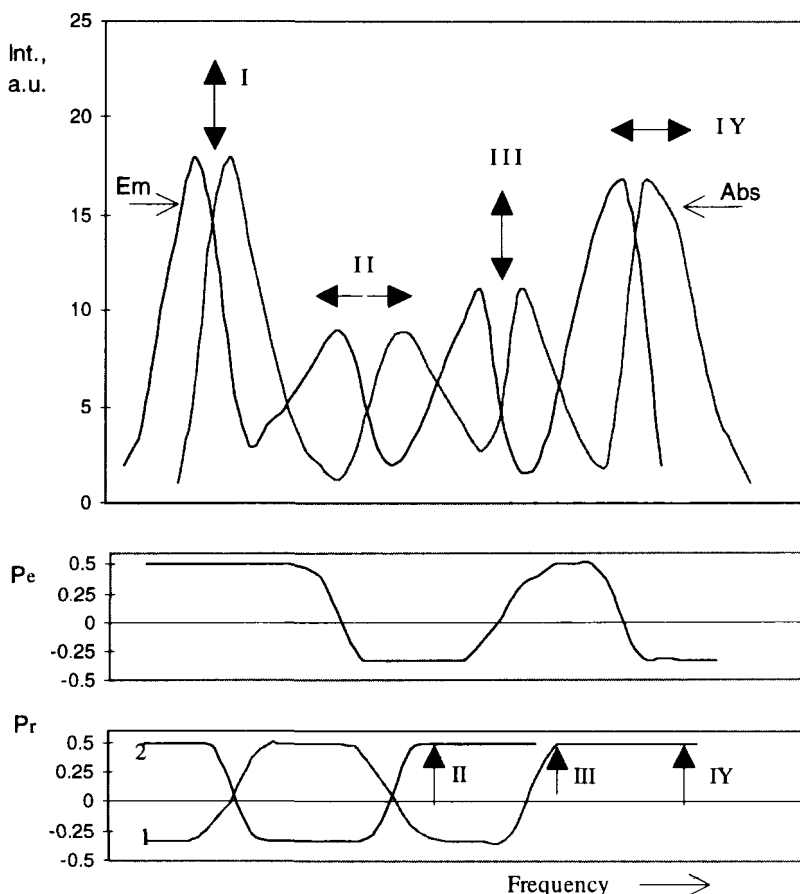


Figure 6.6. (top) Emission (Em) and absorption (Abs) spectra for transition I-IY; (middle) polarization spectrum P_e with registration frequency in the fluorescence region from the lowest excited state I (middle panel); (bottom) P_r with excitation state III (curve 1) and IY (curve 2). Top arrows show orientation of the transition dipole moment; bottom arrows show excitation frequencies.

ν_{exc} . Therefore P_r for excitation with $\nu_{\text{exc II}}$ and $\nu_{\text{exc IY}}$ are identical in the region $\nu_{\text{rec}} < \nu_{\text{exc II}}$ (curve 2 in Figure 6.6). If ν_{exc} falls into the absorption band region with a different direction of the transition dipole moment, the polarization degree at ν_{rec} varies with ν_{exc} (Figure 6.6). In the region of strong overlapping of the absorption bands with a different direction of transition dipole moment, even a small change in ν_{exc} can produce an appreciable change in polarization degree at ν_{rec} . Such dependence of P_r was observed in Ref. 48 and ascribed to the superposition of fluorescence signals from several excited states with overlapping spectra.

It is well known that P_e can be used to determine the relative dipole moment orientation for $S_0 \rightarrow S_n$ when the recording emission is fluorescence from S_1 .⁽⁵¹⁾ Information on the relative direction of the dipole moment for $S_1 \rightarrow S_n$ from the excited state S_1 can be obtained from P_r with the stepped excitation method. Thus, it was established in Refs. 46–50 that in rhodamine molecules the electronic transitions corresponding to transient absorption ($S_1 \rightarrow S_n$) have dipole moments closely parallel to the dipole moment of $S_0 \rightarrow S_1$ at $\nu_2 = 9400, 18,800, 22,200$, and $14,400 \text{ cm}^{-1}$ and perpendicular to it at $\nu_2 = 28,800 \text{ cm}^{-1}$.

Fluorescence anisotropy is often used for identifying short-lived fluorescence from highly excited states in low-viscosity solutions.^(46,47) The polarization of HES fluorescence was also used to create a method for registering fluorescence spectra from short-lived HES, whose emission is masked by the long-lived emission from impurities.⁽⁵⁾

6.2.6. Vibrational Relaxation and Fluorescence Spectra of Highly Excited Molecules

It was shown in Refs. 42,46, 52, and 53 that the lifetimes of high vibrational states τ_v of polyatomic organic molecules can be shorter than 1 ps; i.e., they can be of the same order of magnitude as the lifetimes of the high-lying electronic states τ_n . Therefore, emission studies in HES can provide valuable data on ultrafast vibrational relaxation of excited molecules.

For the rate of depopulation of HES close to the rate of intramolecular vibrational relaxation, we may expect that the contours of the fluorescence bands will depend on the ratio of τ_n and τ_v . When $\tau_v < \tau_n$, the intramolecular vibrational relaxation will be largely completed over the lifetime of S_n . This relation between τ_n and τ_v is usually satisfied for polyatomic molecules in high-temperature solution^(30,32) and it results in an approximate mirror symmetry of absorption and fluorescence spectra for $S_n \rightarrow S_0$ (Figures 6.2 and 6.3). The high diffuseness of the fluorescence spectrum, observed when $\nu_{\text{eff}} \gg \nu_{0n}$ is attributable to the high temperature of the excited molecules. The high vibrational “temperature” of excited molecules of S_n is provided by a large stored vibrational

energy, acquired via excitation, fast intramolecular vibrational relaxation, and slow intermolecular vibrational energy exchange in solution in comparison with the rate of depopulation of S_n .^(46,47)

Experimental data confirming that the rate of intramolecular vibrational relaxation of fluorophores in high-temperature solution exceeds the rate of HES depopulation were obtained in a study of fluorescence from S_n of 1,2-benzanthracene frozen solution in heptane at 77 and 4.2 K (Shpol'skii matrices).⁽³¹⁾ Molecular isolation in the Shpol'skii matrix causes a sharp change in the fluorescence band contour from the highly excited state. This phenomenon is most clearly observed for values of ν_{eff} which ensure that the high vibrational levels of S_n are populated. The short-wavelength fluorescence spectrum of 1,2-dibenzanthracene with $\nu_{\text{eff}} > 39,000 \text{ cm}^{-1}$ in the Shpol'skii matrix differs radically from the quasiequilibrium fluorescence spectrum, which is recorded in room-temperature solution (Figure 6.2): A trough is observed in the region corresponding to the maximum fluorescence spectrum in the solution. The observed change in the form of the short-wavelength fluorescence spectrum induced by the Shpol'skii matrix can be explained as the consequence of decreasing intramolecular vibrational relaxation accompanying molecular isolation in the matrix. If τ_v becomes longer than τ_n , emission from high vibrational levels will make the main contribution to the recording fluorescence spectrum. The observed change in fluorescence spectrum agrees with the expected one, derived from the calculation of the fluorescence spectrum emitted by highly vibronically excited molecules.⁽⁵⁴⁾

Studies of fluorescence from S_n lead to the following conclusions on the vibrational relaxation of polyatomic organic molecules in solution. In high-temperature solutions, two stages of relaxation with substantially different duration can be distinguished. Intramolecular redistribution of vibrational energy occurs at the first fast stage, while in the slower second stage the excess vibrational energy of the excited molecules is transferred to the solvent molecules. The intramolecular stage in liquid solvent occurs over subpicosecond time intervals (shorter or close to the lifetime of the highly excited electronic states). The intermolecular stage occurs over a picosecond time interval, which is substantially longer than τ_n . In Shpol'skii matrices the rate of the intramolecular stage decreases and its duration can be longer than the HES lifetime. A developed scheme of vibrational relaxation for polyatomic organic molecules in solution was confirmed by a direct time-resolved study of fluorescence spectrum dynamics with femtosecond resolution in time.⁽⁵⁵⁾

Photon absorption by excited molecules leads to population of the HES and subsequent electronic energy conversion into the vibrational energy of molecules in the lowest excited state S_1 . Fast randomization of the vibrational energy⁽⁵⁶⁾ results in light heating of excited fluorophores and appearance of hot fluorescence from S_1 on the short-wavelength edge of the emission spectrum.^(46,56)

Light heating of excited molecules can be very effective if the rate of photon absorption by excited molecules, determined by the parameter $\sigma_{1n}P_2$, is close to the rate of intermolecular vibrational relaxation in solution. In this case light heating results in smearing of the vibrational structure and long-wavelength displacement of the fluorescence spectrum.⁽⁵⁷⁾ Light heating of excited fluorophores is observed with the high-power density of the radiation with frequency ν_2 , and it may combine with light quenching of the fluorescence. The dependence of the amount of light quenching on the recording frequency in the fluorescence spectrum was observed in Ref. 58 as a result of interference of light heating and light quenching.

6.2.7. Energy Transfer from Highly Excited States

Nonradiative energy transfer is one possible way of depopulating highly excited states. This channel of conversion of HES energy is difficult to observe due to the short lifetimes of highly excited states. In early studies^(59,60) the conclusion that energy is transferred from HES, which process competes with depopulation of the HES via internal conversion, followed from an analysis of chemical reactions in the acceptor. Energy transfer from HES of aromatic solvents (excited by fast electrons) to scintillators (binaphthyl, oxazoles) was studied in Ref 61. Effective energy transfer occurs at a scintillator concentration of $\sim 1 M$, which, according to estimates, corresponds to a transfer rate of $\sim 10^{14} \text{ s}^{-1}$. Energy transfer from S_3 of rhodamine-6G (highly excited donor) to S_1 of benzophenone was observed in Ref. 62. The transfer was indicated by increasing triplet-triplet absorption of benzophenone. The lowest triplet state of benzophenone was populated via nonradiative intersystem conversion. The rate of transfer for rhodamine-6G-benzophenone was $\sim 10^{12} M^{-1} \text{ s}^{-1}$. Additionally, a broadening of the triplet-triplet absorption spectrum was also regarded as evidence of ultrafast energy transfer from the short-lived highly excited triplet states of triphenylene and naphthalene to the solvent (toluene) in Ref. 63.

Ultrafast energy transfer from HES can be effectively studied by two-photon stepped excitation of the highly excited state of the donor molecules (Figure 6.7). Significantly, this method provides an opportunity to choose photon frequencies ν_1 and ν_2 , whose individual energies are not high, to excite the acceptor S_1 . This method was first used in Ref 64. In this study the energy transfer in mixed crystal from the impurity (tetracene) to the matrix (anthracene) was observed. It was found that the transfer efficiency in mixed crystal depends strongly on ν_{eff} .

Nonradiative transfer from HES with stepped excitation of the donor molecules (9,10-di-*n*-propylanthracene) to the solvent (toluene) was studied in Ref. 65. The transfer was observed by the appearance of solvent luminescence. Back transfer from the solvent to the low-lying excited state of the donor molecules

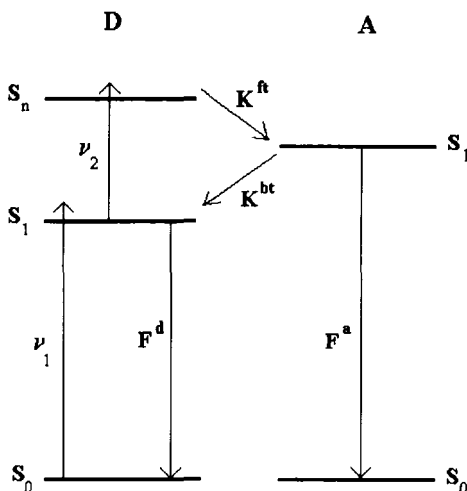


Figure 6.7. Diagram of processes accompanying nonradiative energy transfer with stepped two-photon population of highly excited donor state: K^{ft} and K^{bt} are the forward and back transfer rates, respectively, and F^d and F^a are fluorescences from the lowest excited state of the donor (D) and acceptor (A).

(Figure 6.7) was taken into account in estimating the rate of transfer. The rate of irreversible transfer was found to be $5 \times 10^{12} \text{ s}^{-1}$. It was assumed that an inductive-resonance mechanism was responsible for the observed phenomenon.

Nonradiative transfer from the high vibrational levels of HES in solution (hot transfer) was observed in Ref. 31. Energy donor molecules (1,2-benzanthracene) were excited into S_4 by the stepped method. Solvent (benzene, *n*-xylene) was used as the energy acceptor. Transfer was recorded by luminescence intensification in the solvent emission region. A strong spectral dependence of transfer efficiency on ν_{eff} was not observed. It was shown that the efficiency of hot transfer in solution is determined only by the overlap integral of the donor fluorescence spectrum and acceptor absorption spectrum. The hot origin of the observed transfer is due to the fact that the absorption bands of the solvent (acceptor) overlap with the emission spectrum of the donor at frequencies much higher than ν_{0n} . The rate of hot transfer to solvent was estimated as $\sim 10^{12} \text{ s}^{-1}$ in Ref. 31.

A general feature of the foregoing systems, in which nonradiative energy transfer from HES was observed, is the high acceptor concentration (as a rule, exceeding $10^{-2} M$). Hence, nonradiative transfer can successfully compete with internal conversion⁽⁶¹⁾ and vibrational relaxation of highly excited molecules. Nonradiative energy transfer from S_3 of rhodamine-6G (donor) to scintillator 2,5-bi5(5-tert-butyl-2-benzoxazolyl)thiophene (BBOT) (acceptor) at low acceptor concentration in solution ($3-7 \times 10^{-5} M$) was reported in Ref. 66. The data obtained for transfer efficiency allowed a calculation of $\eta_3 = 2.1 \times 10^{-6}$ and $\tau_3 = 30 \text{ fs}$. These values are approximately an order of magnitude lower than those reported in Refs. 7 and 40, where η_3 was determined

directly as the ratio of the number of emitted photons to the number of molecules excited into S_3

Uncertainty in the estimates of the HES fluorescence parameters in Ref. 66 could be attributed to the fact that the effective back transfer from the lowest singlet excited state of the acceptor (BBOT) to the lowest singlet excited state of the donor (rhodamine-6G) was neglected. Studies of rhodamine-6G + POPOP and rhodamine-6G + TOPOT systems in Ref. 67 (analogs of rhodamine-6G + BBOT) showed that reabsorption of the short-wavelength fluorescence from the donor highly excited state (rhodamine-6G) by the acceptor (oxazole), but not nonradiative energy transfer, is responsible for the observed appearance of acceptor fluorescence at a low acceptor concentration ($< 10^{-4} M$)

6.2.8. Stepped Excitation of Bifluorophore

Estimates of HES lifetimes show that τ_n can be as small as a few tens of femtoseconds (see Section 6.2.4). Extremely short lifetimes of highly excited molecules can hardly be explained in terms of relaxation caused by internal conversion because lifetimes of the HES are shorter than the period of molecular vibration. The latter promotes the nonradiative intermolecular transition, i.e., internal conversion.

This leads to the problem of seeking other channels for ultrafast depopulation of HES. The intramolecular nonradiative energy transfer between different fragments of one molecule seems to be a possible channel of ultrafast depopulation of highly excited electronic states in polyatomic molecules. The possibility of a needed localization of different electronic transitions on various intramolecular fragments has been discussed in the frame of the “molecule inside molecule” model.^(68,69)

Fluorescence study of bifluorophore solution has clarified the role of intramolecular nonradiative energy transfer in HES depopulation.^(70,71) In his study ultrafast energy transfer from HES in solution with a low acceptor concentration was also observed. A bifluorophore solution allows this due to the small distance between donor and acceptor fragments.

Synthesized bifluorophores consist of 3-aminophthalimide (PH) and *trans*-stilbene (TS) fragments bounded by a methylene group (CH_2). Figure 6.8 shows the absorption spectra of bifluorophore and the equimolar mixture of PH and TS solutions in ethanol. It appears that the long-wave absorption bands of the bifluorophore solution can be assigned to the transitions in the separate fragments. These bands are shifted to the long-wave region by a few (5–7) nanometers with respect to the position of the PH and TS absorption bands. Observed spectral shift can be induced by the substituting methylene group. Allowing for this shift, the absorption spectrum of the solution appears to be the sum of the fragment

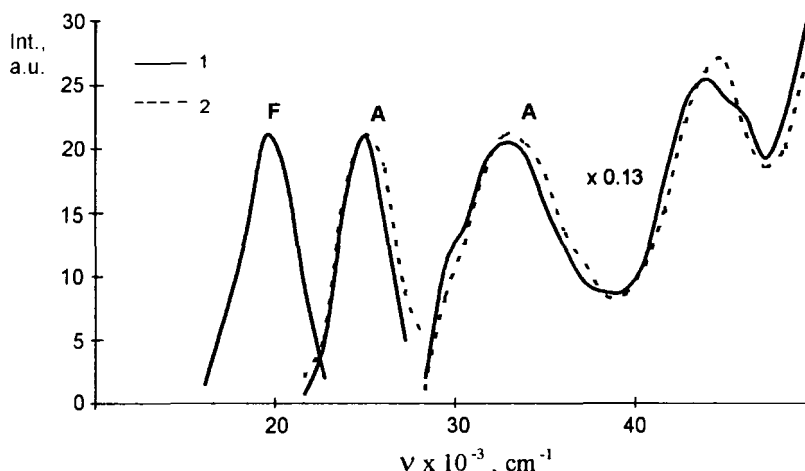


Figure 6.8. Absorption (A) and fluorescence (F) spectra of bifluorophore (1) and a mixture of 3-aminophthalimide and *trans*-stilbene (2) in ethanol solution at $T = 300\text{ K}$.

absorption spectra. The additivity of the absorption spectra and the existence of the separate bands related to PH and TS fragments point out the localization of the optical transitions in the different molecular fragments.

Fluorescence quantum yield of the PH fragment in the bifluorophore PH-(CH₂)-TS solution does not depend on the excitation wavelength from 250 to 350 nm. Hence, the efficiency of energy transfer from TS fragment to PH fragment is close to unity. Thus, the nonradiative energy transfer appears to be the basic depopulation channel of the TS fragment in the bifluorophore solution. The energy transfer rate is estimated to be $3.5 \times 10^{12}\text{ s}^{-1}$, which results from the rate stilbene radiative transition (about $7 \times 10^8\text{ s}^{-1}$, according to the integral absorption data) and the measured fluorescence quantum yield of the TS fragment in bifluorophore (about 2×10^{-4}).

The energy transfer from the highly excited states of the PH fragment was observed under two-photon stepped population of HES of the PH fragment by laser pulses with $\nu_1 = 28,800\text{ cm}^{-1}$ and $\nu_2 = 14,400\text{ cm}^{-1}$. The intensity of TS fragment fluorescence ($S_1 \rightarrow S_0$) greatly increased due to the stepped excitation ($\nu_1 + \nu_2$) of the PH fragment compared to excitation with ν_1 only. This result immediately shows the existence of the energy transfer from the highly excited states of PH fragment toward S_1 of the TS fragment. The observation of weak fluorescence of the TS fragment under excitation with ν_1 seems to be associated only with the stepped absorption of photon ν_1 by the PH fragment.⁽⁷⁰⁾

Fluorescence quantum yield of the TS fragment under direct one-photon excitation practically coincides with that under population of S_1 of the TS fragment via stepped excitation of the PH fragment (Table 6.2). Hence, the rate of energy transfer from HES of the PH fragment has to exceed significantly the rate of internal conversion from HES inside the PH fragment.

The rate of internal conversion of PH solution can be estimated as $8 \times 10^{11} \text{ s}^{-1}$ from measurements of the quantum yield of short-wavelength fluorescence by method⁽⁷²⁾ and integrated absorbance. Assuming the rates of internal conversion for PH molecules and the PH bifluorophore fragment are equal, it is possible to estimate the energy transfer rate as $\approx 2.3 \times 10^{12} \text{ s}^{-1}$, and the population efficiency of S_1 of the TS fragment via nonradiative energy transfer from highly excited states of the PH fragment as ≈ 0.75 . The results show that energy transfer from the HES of separate fragment can be a more effective way to depopulate these states than the intrafragment nonradiative transitions (internal and/or intersystem conversion). Intramolecular energy transfer from highly excited states is expected to take place not only in bifluorophores but also in many polyatomic molecules with the localization of electronic transitions (especially short-wavelength ones) in the different parts of polyatomic molecules.

Experimental data on the rate of ultrafast energy were used for the average distance between donor and acceptor fragments calculations.⁽⁷¹⁾ The obtained distance is 7.5 Å in PH-(CH₂)-TS and 11 Å in PH-(CH₂)₂-TS, respectively. A model calculation also showed that decreasing the interfragment distance to 5 Å provides nonradiative transfer rate larger than 10^{13} s^{-1} . Thus, intramolecular nonradiative energy transfer can be an effective channel of ultrafast depopulation of short-lived highly excited states.

Stepped photon absorption accompanying ultrafast energy transfer can be used to develop the site-selective method of excitation or damage the macro-

Table 6.2. Fluorescence Quantum Yields of 3-Aminophthalimide, trans-Stilbene, and Bifluorophore Solution Measured with One-Photon Excitation η_1 (transition $S_1 \rightarrow S_0$) and Stepped Two-Photon Excitation η_2 ($S_n \rightarrow S_0$ for 3-aminophthalimide and PH fragment, $S_1 \rightarrow S_0$ for trans-stilbene and TS fragment)^a

Substance	Emitted fragment	η_1	η_2	
			$v_2 = 14,400 \text{ cm}^{-1}$	$v_2 = 28,800 \text{ cm}^{-1}$
3-Aminophthalimide		0.6	1.2×10^{-4}	—
trans-Stilbene		2.2×10^{-2}	—	—
Bifluorophore	TS	2×10^{-4}	2.3×10^{-4}	2.1×10^{-4}
Bifluorophore	PH	0.29	3.2×10^{-5}	3.9×10^{-5}

^aData from Ref. 85.

molecule bounded with fluorescence labels. Selectivity of this method should be provided by the stepped population of the label HES, the ultrafast forward energy transfer from the label HES to the low-lying excited state of the closest macromolecule fragment, and the subsequent back transfer of excitation energy to the lowest excited state of the label. The last process eliminates the excitation energy migration inside the macromolecule. An additional selective possibility may be provided with the use of delay in time between the pulses with frequencies ν_1 and ν_2 .⁽⁷³⁾

6.3. Transient Third-Order Optical Nonlinearity and Relaxation of Excited Molecules

6.3.1. Preliminary Remarks

Resonant optical mixing studies give valuable information on the origin of optical nonlinearity and molecular photodynamics.⁽⁷⁴⁾ A theory of nondegenerated multiwave mixing for determinating ultrafast relaxation times with the use of two laser beams (the simplest experimental setup for frequency-domain measurement) was developed in Refs. 75 and 76. Briefly, two intersected laser pulses, which have wave vectors \mathbf{k}_1 , \mathbf{k}_2 and frequencies w_1 , w_2 in resonance with the absorption band of molecular electronic transition, record a moving grating inside the sample. Diffraction of the pulse with frequency w_1 by the moving grating provides a signal pulse with frequency $w_3 = 2w_1 - w_2$ and wave vector $\mathbf{k}_3 = 2\mathbf{k}_1 - \mathbf{k}_2$. This process is known as three-wave mixing. The signal pulse intensity depends on the ratio of the molecular relaxation rate and the detuning frequency of the pumping pulses $w_d = w_1 - w_2$. The diffraction efficiency goes down if w_d becomes larger than the relaxation rate. Thus, the dependence of self-diffracted signal intensity on the detuning frequency (i.e., dispersion of resonant nonlinearity) provides information on molecular relaxations.

Hitherto nonlinear optical mixing studies were predominantly accomplished with polyatomic molecules in the electronic ground state. In this contribution the experimental and simulated results for resonant multiwave mixing by excited molecules are presented. It is obvious that excitation of molecular species may provide great alteration of their nonlinear optical properties. The reason is the excited electronic state population and appearance of transient absorption bands. These well-known phenomena result in transient resonant nonlinearity.

The magnitude of the multiwave mixing signal is determined by the scattering efficiency of the moving grating, i.e., third-order susceptibility $\chi^{(3)}$.

Nonlinear mixing induced by a preliminary population of the lowest excited state (S_1) of organic molecules in solution can be easily observed when $\chi^{(3)}$ probe pulses are in resonance with a transient absorption spectrum. In this case a transient nonlinear mixing signal may be higher by a factor of $\sim 10^5$ than a signal of “nonresonant background” detected in an absence of the excitation pulse.⁽⁷⁷⁾ An enormous enhancement of transient susceptibility of approximately three orders of magnitude near resonance was observed in 3-hydroxy flavone solution.⁽⁷⁸⁾ The population of excited state and transient absorption appearance may provide an essential contribution to the third-order susceptibility of organic molecules, which is measured in resonance or in preresonance with the absorption band of unexcited molecules in the ground electronic state. For instance, such an enhancement of nonlinear susceptibility was found for fullerenes⁽⁷⁹⁾ and conjugated polymers.⁽⁸⁰⁾

Transient resonant susceptibility depends on the transition dipole moment and a phase memory of electronic optical resonance of excited molecules, and on the rate of depopulation of highly excited electronic states. Highly excited states of polyatomic organic molecules in condensed phase are usually extremely short-lived (HES lifetimes are $\leq 1\text{ ps}$, typically). Measurements of the $\chi^{(3)}$ dispersion provide a unique opportunity to elucidate ultrafast dynamics of highly excited molecules. This item is discussed in Section 6.3.2.

Nonlinear susceptibility of excited molecules displayed by the sum over molecular hyperpolarizabilities depends on the momentary state of the molecules in a low-lying excited electronic level (S_1). Consequently, one may expect that $\chi^{(3)}$ measurements with time delay after the excitation pulse would be a powerful method to control the dynamics of the excited molecules: depopulation, molecular structure or orientation relaxation, energy or particle transfer, solvent rearrangement, and so on. Importantly, transient multiwave mixing is a coherent nonlinear phenomenon. Therefore, it may provide a higher sensitivity of measured nonlinear optical response to the molecular dynamics in comparison with commonly used time-resolved fluorescence and transient adsorption measurements. Study of the dependence of transient $\chi^{(3)}$ on orientational anisotropy of excited molecules confirms this supposition (Section 6.3.3). Finally, a possibility for controlling spectral dynamics of excited molecules with time-resolved measurement of transient $\chi^{(3)}$ dispersion is discussed in Section 6.3.4.

6.3.2. Dispersion of Transient Susceptibility and Ultrafast Relaxation of Highly Excited Molecules

Nondegenerated three-wave mixing was extensively used for the study of molecular relaxation and hidden structure of absorption spectra of polyatomic

organic molecules in the ground electronic state.^(76,81,82) This method was applied later to the study of excited molecules of diphenylpolyenes, oxazoles, and polymethine dyes in solution.^(77,83,84)

The third-harmonic pulse of nanosecond Nd:YAG laser was used for population of S_1 of the studied molecules. Transient three-wave mixing signal was generated by excited molecules when the excitation pulse acted simultaneously with two dye laser pulses, which were in resonance with the $S_1 \rightarrow S_n$ absorption band. Pulses, which probed the transient nonlinearity, were generated by detuning dye lasers with a narrow spectrum (spectral width $\leq 0.3 \text{ cm}^{-1}$) pumped by the pulses at the second harmonic of the same nanosecond Nd:YAG laser. Dispersion of $\chi^{(3)}$ (dependence of a module of $\chi^{(3)}$ on the detuning frequency) was found from measurements of the mixing signal intensity (I_s) at the different values of detuning frequency ($|\chi^{(3)}| \sim I_s^{1/2}$). Dispersion of the transient $\chi^{(3)}$ of 1,4-diphenylbutadiene (DPB) in cyclohexane solution is shown in Figure 6.9, as plots of $\log |\chi^{(3)}|$ versus $\log(\nu_d)$, where $\nu_d = w_d/2\pi c$ and c is the velocity of light.

The left and right panels in Figure 6.9 correspond to negative and positive signs of the detuning frequency. The transient absorption spectrum of DPB solution is shown in Figure 6.10. Arrows on the transient absorption spectrum indicate three positions of the dye laser pumping frequency $\nu_1 = w_1/2\pi c$ which were used in the experiment.

The linear region of the dispersion curves ($\log |\chi^{(3)}| \sim -\log |\nu_d|$) in Figure 6.9, which can be seen at $|\nu_d| \geq 1.5 \text{ cm}^{-1}$, is evidence of a relatively

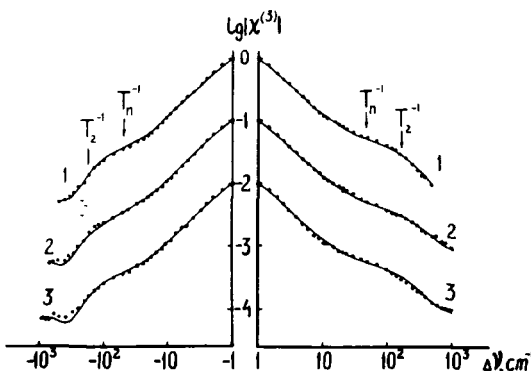


Figure 6.9. Dispersion of transient resonant third-order susceptibility $|\chi^{(3)}|$ of diphenylbutadiene solution in cyclohexane at $T = 300 \text{ K}$. The dots are experimental results, and the curves are calculated ones. The left and right panels show the dispersion at negative and positive detuning frequency ν_d , respectively. Arrows indicate the relative relaxation rates. Dispersion curves 1, 2, and 3 correspond to the different values of pumping frequency ν_d indicated on the transient absorption spectrum in Figure 6.10.

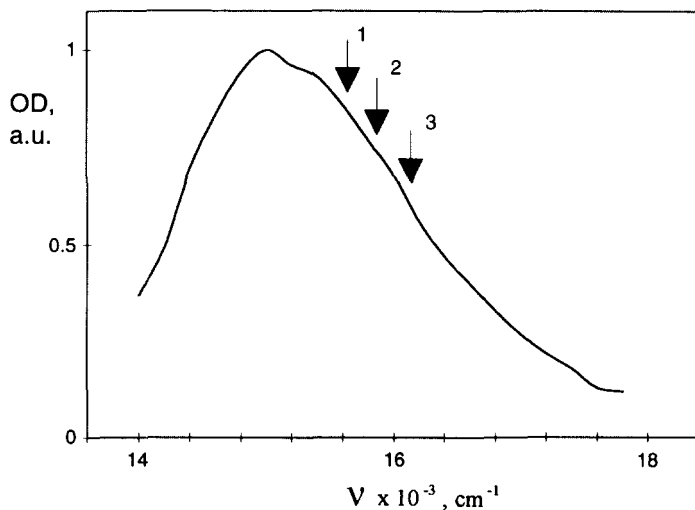


Figure 6.10. Transient absorption spectrum of diphenylbutadiene solution in cyclohexane at $T = 300$ K. Arrows 1–3 indicate the position of pumping frequency ν_1 used in the multiwave mixing experiment.

"slow" picosecond stage of the population of S_1 via internal conversion from S_n . The slope of the dispersion curves becomes gentler at ν_d deviations in the interval $10 \text{ cm}^{-1} \leq |\nu_d| \leq 100 \text{ cm}^{-1}$. This behaviour may be due to a realization of a three-level scheme of excited states (Figure 6.11), and also due to an inhomogeneous

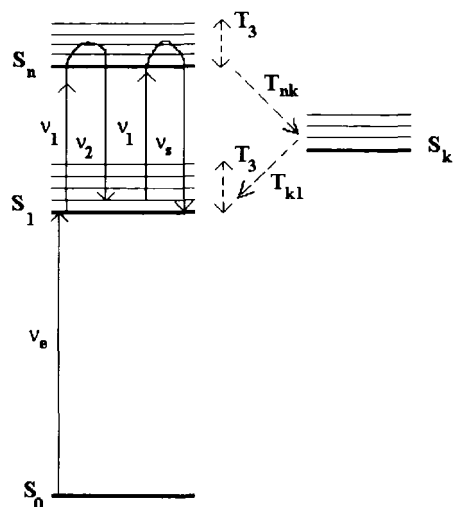


Figure 6.11. Diagram of transient three-wave mixing and three-level scheme of excited electronic states. S_1 , S_n , and S_k mark the lowest excited state, highest excited state, and intermediate excited state, respectively. $(T_3)^{-1}$ is the rate of spectral diffusion. $(T_{nk})^{-1}$ is the rate of internal conversion $S_n \longrightarrow S_k$. $(T_{k1})^{-1}$ is the rate of internal conversion $S_k \longrightarrow S_1$.

geneous broadening of the transient absorption band for $S_1 \rightarrow S_n$.⁽⁷⁶⁾ Finally, an asymmetry of $\chi^{(3)}$ dispersion curves with respect to the sign of the detuning frequency is apparently due to a distortion of the dispersion curve by the “nonresonant background,” which becomes predominant at large values of v_d .

Model-based calculations of transient dispersion curves were made to determine the pathway and relaxation rate of the highly excited states of DPB molecules. The calculations were carried out for a three-level (S_n , S_k , S_1) scheme (Figure 6.11) and a two-level (S_n , S_1) scheme of the excited states, taking into account an inhomogeneous broadening of the transient absorption spectrum and the spectral diffusion with rate T_3^{-1} . Fitting was accomplished with least-squares and global analysis methods. The solid curves in Figure 6.9 show the calculated dispersion of $\chi^{(3)}$.

The best agreement of the shape of experimental and calculated dispersion curves was found for three-level scheme with a real value of “nonresonant background” susceptibility, which was then equal to the experimental magnitude of $|\chi^{(3)}|$ at the extreme values of $v_d \geq 800 \text{ cm}^{-1}$. Calculated relaxation times are the dephasing time of $S_1 \rightarrow S_n$ ($T_2 \approx 20 \text{ fs}$), the spectral diffusion time ($T_3 \approx 20 \text{ fs}$), the lifetime of S_n ($T_n \approx 90 \text{ fs}$), the lifetime of S_k ($T_k \approx 9 \text{ ps}$), and the rate of population of S_k via internal conversion $S_n \rightsquigarrow S_k$ ($T_{nk}^{-1} \approx 10^{13} \text{ s}^{-1}$).

These results are consistent with the assumption of an inhomogeneous broadening of the transient absorption spectrum. They are also indicated because of the existence of a relaxation “bottle neck”: a relatively long-lived highly excited state S_k through which S_1 is populated primarily in nonradiative transition from S_n . An unusually slow depopulation rate of S_k was confirmed by an independent experiment, in which bleaching of the transient absorption band was observed during the exposure of the excited DPB molecules to a nano-second laser pulse with power density $P_2 \approx 100 \text{ MW/cm}^2$ at $v_2 = 16,200 \text{ cm}^{-1}$.

The long lifetime of S_k provides a high magnitude of hyperpolarizability of excited DPB molecules ($6 \times 10^{-29} \text{ esu}$). This magnitude is comparable to resonant hyperpolarizability of organic molecules in the ground electronic state. For instance, the ground-state hyperpolarizability of a malachite green molecule is $7 \times 10^{-29} \text{ esu}$. The existence of the bottleneck for population of the lowest excited state S_1 via internal conversion from the highly excited state seems important for an experimental observation of transient multiwave mixing. A large magnitude of transient nonlinear signal was observed in α -naphthyl-phenyloxazole solution, which also demonstrated photobleaching of a transient absorption. In contrast, transient nonlinear mixing signals were weak in 1,6-diphenylhexatriene and 1,2-benzanthracene solutions, which have no notable transient absorption photobleaching.⁽⁸⁵⁾ Considering these data one can assume that a low transient nonlinearity in the last solutions is due to ultrafast subpicosecond population of S_1 via internal conversion from S_n .

6.3.3. Transient Nonlinear Susceptibility and Orientational Anisotropy of Excited Molecules

Orientational anisotropy of excited molecules can be controlled by a few methods based on dependence of the probability of optical transition on a mutual orientation of the transition dipole moment and light polarization. The data about Orientational anisotropy and rotational motion of excited molecules may be obtained by measuring induced dichroism,⁽⁸⁶⁾ fluorescence anisotropy,^(86,87) light-induced grating,^(88,89) and birefringence.^(74,89)

A nonlinear method of light-induced grating provides the best sensitivity to anisotropy. A limit ratio of signal intensities R , which is observed with “parallel” and “perpendicular” polarization of a probe pulse, may be as high as 9:1 for the light-induced grating method. At the same time the commonly used fluorescence or dichroism methods provide $R = 3:1$ only.

Hitherto the induced grating method was predominantly applied for molecular systems in the ground electronic state with isotropic Orientational distribution. The possibility of the Orientational anisotropy control by transient resonant multiwave mixing with anisotropic initial distribution of excited molecules is presented in this section.

One can imagine three laser pulses interact with molecular solution. The first excitation pulse has frequency w_e in resonance with the absorption spectrum of $S_0 \rightarrow S_1$, and two probe transient susceptibility pulses have frequencies w_1 and w_2 in resonance with the transient absorption spectrum of $S_1 \rightarrow S_n$ and act simultaneously. The pulse width t_p is assumed to be short in comparison with the lifetime τ of S_1 and the time of rotational diffusion of excited molecules T_{or} , but longer than the dephasing time of the transient absorption band T_2 and lifetime τ_n of S_n . This assumption can be easily satisfied in the study of the room-temperature solution, which usually has $T_{\text{or}} \geq 50 \text{ ps}$ ⁽⁸⁹⁾ with the use of picosecond laser pulses.

The intensity of transient multiwave mixing signal pulse I_s is

$$I_s = \int_T^\infty \langle P^{(3)}(t) \rangle^2 dt \quad (6.5)$$

where $P^{(3)}(t)$ is the third-order macroscopic polarization, T is the delay in time between excitation and probe pulses, and $\langle \dots \rangle$ denotes angular averaging. The aforementioned assumptions permit us to calculate I_s with the use of standard formulas for resonant susceptibility related to an inhomogeneous broadening absorption spectrum in stationary approximation.⁽⁷⁵⁾ The calculated I_s is

$$I_s \sim [C_{01}]^2 [C_{12}]^2 [C(T)]^2 \quad (6.6)$$

where

$$C_{01} = N|\boldsymbol{\mu}_{01}|^2 P(w_e)/3 \quad (6.7)$$

$$\begin{aligned} C_{12} = & -2\pi T_n T_2 G(w_1) P(w_1) [P(w_2)]^{1/2} |\boldsymbol{\mu}_{12}|^4 \\ & \times \{9[h/2\pi]^3 [1 + (w_d T_n)^2]^{1/2} [1 + (w_d T_2)^2]^{1/2}\}^{-1} \end{aligned} \quad (6.8)$$

$$C(T) = \langle F(T, \tau, T_{\text{or}})(\boldsymbol{\mu}'_{12} \mathbf{e}_1)(\boldsymbol{\mu}'_{12} \mathbf{e}_2)(\boldsymbol{\mu}'_{12} \mathbf{e}_s) \rangle \quad (6.9)$$

In Eqs (6.6)–(6.9), N is the molecular concentration; $\boldsymbol{\mu}_{01}$ and $\boldsymbol{\mu}_{12}$ are the dipole moments of $S_0 \rightarrow S_1$ and $S_1 \rightarrow S_n$, respectively; $P(w_e)$, $P(w_1)$, and $P(w_2)$ are the power densities of the pulse with frequencies w_e , w_1 , and w_2 ; \mathbf{e}_1 , \mathbf{e}_2 , and \mathbf{e}_s are the polarization vector of the probe and signal pulses; $\boldsymbol{\mu}'_{ik} = \boldsymbol{\mu}_{ik}/|\boldsymbol{\mu}_{ik}|$; $F(T, \tau, T_{\text{or}})$ is an evolution function which describes time-dependent population and anisotropy of excited molecules during an interval T between excitation and probe pulses. In Eq. (6.8), $G(w_1)$ is a normalized function for inhomogeneous broadening of the transient absorption spectrum. Note that in the derivation of Eqs. (6.6)–(6.9), photobleaching of absorption spectra was not accounted for and propagation effects were neglected.

The evolution function $F(T, \tau, T_{\text{or}})$ can be easily determined in a one-exponential excited-state population decay with a temporal constant τ , isotropic rotational diffusion of excited molecules with relaxation constant T_{or} , and any angle γ between $\boldsymbol{\mu}_{01}$ and $\boldsymbol{\mu}_{12}$. One can assume that in a laboratory coordinate system the excitation pulse propagates along the y axis and has polarization vector parallel to the z axis. Let us introduce a molecular coordinate system x' , y' , z' with the y' axis perpendicular to the z axis, and the z' axis directed along $\boldsymbol{\mu}_{12}$. Then one may use the coordinate system transformation described in Ref. 90 and find that $F(T, \tau, T_{\text{or}})$ immediately after a short excitation pulse ($T = 0$) is

$$F(T = 0, \tau, T_{\text{or}}) = \frac{3}{4\pi} [\cos^2(\theta)L_2(\gamma) + \frac{1}{2}\sin^2(\gamma)] \quad (6.10)$$

and after a time delay T is

$$F(T, \tau, T_{\text{or}}) = \frac{1}{4\pi} \exp\left(\frac{-T}{\tau}\right) \left\{ 1 + \exp\left(\frac{-T}{T_{\text{or}}}\right) L_2(\gamma)[3 \cos^2(\theta) - 1] \right\} \quad (6.11)$$

where $L_2(\gamma)$ is the second Legendre polynomial and θ is the angle between $\boldsymbol{\mu}_{12}$ and the z axis.

The dependence of the multiwave mixing signal intensity on the time delay is provided by the function $C(T)$ (see Eqs. 6.4–6.9). The use of Eq. (6.11) and angle averaging gives

$$C(T) = A \exp(-T/\tau)[1 + B \exp(-T/T_{\text{or}})L_2(\gamma)] \quad (6.12)$$

where A and B are parameters which depend on the used pulse polarizations and the angle between transition dipole moments. The intensity of the nonlinear signal in the steady-state regime ($t_p \gg \tau, T_{\text{or}}$), determined by $C(T)^2$ over time delay T , is

$$I_s \sim A^2 \left\{ \frac{\tau}{2} + 2BL_2(\gamma)T_{\text{or}} \frac{\tau}{2}(T_{\text{or}} + \tau) + B^2[L_2(\gamma)]^2 T_{\text{or}} \tau / 2(T_{\text{or}} + \tau) \right\} \quad (6.13)$$

The values of A and B and the relative signal intensities for different probe pulse polarizations were published elsewhere⁽⁹¹⁾. Importantly, model-based calculations show that the limit ratio R for mixing signal intensities measured with “parallel” and “perpendicular” polarization of the probe pulses relative to the polarization of the excitation pulse may be as high as 25 : 1 if the angle between transition dipole moments $\gamma = 0$.⁽⁹¹⁾ Evidently, the same result is expected in the time-resolved experiment with $t_p \ll \tau, T_{\text{or}}$ at time delay between excitation pulse and transient nonlinearity probe pulses $T \ll T_{\text{or}}$.⁽⁹¹⁾ Thus, one may expect that the sensitivity of transient nonlinear measurement to orientational anisotropy of excited molecules exceeds the sensitivity of other optical anisotropy-controlled methods.

The high sensitivity of transient nonlinearity to orientational anisotropy of excited molecules was confirmed in experiments with DPB solutions. A dependence of transient nonlinear susceptibility on an angle α between polarization of excitation and probe pulses was measured with the experimental setup described in Section 6.3.2. The ideology of this experiment is explained in Figure 6.12. Third-order susceptibility of excited molecules was probed by a nondegenerate three-wave mixing technique ($w_2 \neq w_1$) in order to exclude a possible contribution of a scattering light produced by a thermal grating. In this steady-state experiment ($t_p > \tau$) excitation and probe pulses had a linear polarization, and polarization of probe pulses was identical.

DPB solutions in high-viscosity solvent (60% sugar solution in dimethyl sulfoxide) and low-viscosity solvent (cyclohexane) at room temperature were studied. Fluorescence anisotropy in viscous solution approached the 0.4, and fluorescence in cyclohexane solution was completely depolarized. Thus, a relation $\tau/T_{\text{or}} \ll 1$ was accomplished in viscous solvent, and $\tau/T_{\text{or}} \gg 1$ was accomplished in cyclohexane solution. Obtained angular dependencies of trans-

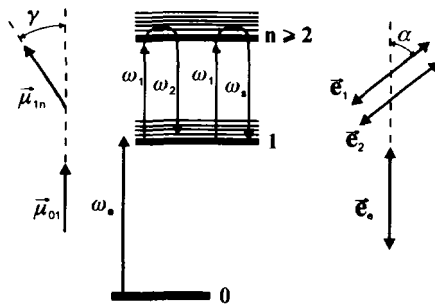


Figure 6.12. Control of orientation anisotropy of excited molecules by transient resonant nonlinearity: (left) orientation of transition dipole moments; (middle) optical processes; (right) polarization of excitation and probe pulses.

sient third-order susceptibility and transient absorption density in high- and low-viscosity solutions are presented in Figure 6.13.

The expected dependence of $|\chi^{(3)}|$ on α can be easily found for the simple molecular anisotropy model when excitation and probe pulses are coincident in time and have a rectangular temporal form. This dependence is given by

$$|\chi^{(3)}| = KC\{[F_1 - F_2] + F_2(10 \cos^2 \alpha + 2 \sin^4 \alpha + 9 \sin^2 \alpha \cos^2 \alpha)3/14\} \quad (6.14)$$

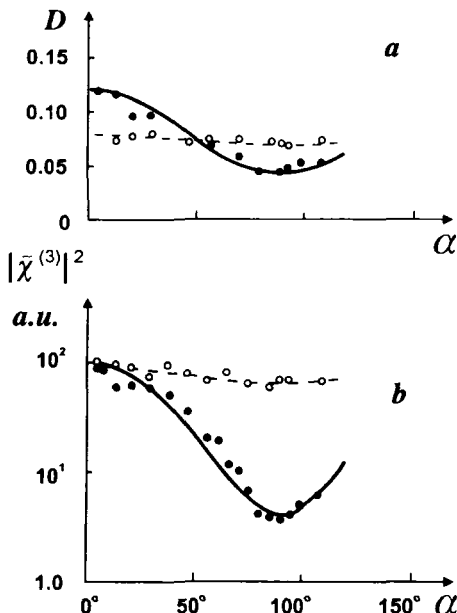


Figure 6.13. (a) Dependence of transient absorption density D and (b) transient third-order susceptibility $|\chi^{(3)}|$ on the angle α between excitation polarization and probe pulses of 1,4-diphenylbutadiene in high- (●) and low-viscosity (○) solution.

where K is constant, $C = \tau/5t_p$, $F_1 = 1 - \exp(-t_p/\tau)$, and

$$F_2 = 0.5 \left\{ 1 - \exp \left[-\frac{(T_{\text{or}} + \tau)t_p}{T_{\text{or}}\tau} \right] \right\} \left[\frac{T_{\text{or}}}{T_{\text{or}} + \tau} \right] [3 \cos^2 \lambda - 1] \quad (6.14a)$$

Experimental dependence of transient optical density and transient-squared susceptibility $|\chi^{(3)}|^2$ on α are shown in Figure 6.13a and b; respectively. Note that experimental angular dependencies are in good agreement with calculated ones. Data in Figure 6.13b demonstrate an achievement of $R = 25$ with transient nonlinearity measurement for DPB viscous solution. However, measurement of the dependence of transient optical density on α (i.e., induced dichroism) gives $R \leq 3$ for the same solution (Figure 6.13a). Comparison of the data in Figure 6.13a,b evidently shows the advantage of the transient multiwave mixing method. A high sensitivity of transient multiwave mixing to anisotropy is provided by nonlinear nature of this effect and anisotropic initial orientational distribution of excited molecules.

The limit value of the ratio $R = 25$ in DPB high-viscosity solution indicates that the DPB molecule has a close-to-parallel direction of μ_{01} and μ_{12} ; i.e., γ is a small angle. The dependency of $|\chi^{(3)}|^2$ on α was also calculated with a variable ratio of T_{or}/τ at $\gamma = 0$. The calculated curve with $T_{\text{or}}/\tau = 0.14$ was in best agreement with the measured one in the low-viscosity solution (Figure 6.13b). This ratio of T_{or}/τ and DPB fluorescence lifetime in cyclohexane solution ($\tau = 560$ ps⁽⁹²⁾) result in a magnitude of $T_{\text{or}} = 78$ ps. The determined T_{or} is close to DPB anisotropy decay time (69 ps), which can be determined with the use of an approximated relation between DPB anisotropy decay time and viscosity of hydrocarbon solvent proposed in Ref. 93. Thus, one can conclude that transient nonlinearity measurements provide the highest sensitivity to orientational anisotropy of excited molecules and may be successfully applied to studies of anisotropy decay in low-viscosity media.

6.3.4. Time-Resolved Dispersion of Transient Susceptibility and Spectral Dynamics of Excited Molecules

Polyatomic molecules in solution reach the nonequilibrium vibronic (Franck–Condon) state immediately after photon absorption. Consequently, various types of relaxation can occur during the lifetime of excited molecules. These relaxations may have different physical (radiationless transition, vibrational relaxation, energy transfer, solvent rearrangement) and chemical (isomerization, particle transfer) origins. These processes usually induce a temporal dependence of fluorescence and/or transient absorption spectra. Therefore, time-resolved measurements of fluorescence and transient absorption spectra are widely used in studies of molecular photodynamics.

A new experimental opportunity to control the spectral dynamics of excited molecules can be provided by time-resolved measurements of the dispersion of transient third-order susceptibility. This opportunity may be better understood by considering a simple experiment, in which the transient $\chi^{(3)}$ dispersion is measured with delayed probe pulses after preliminary population of the excited state by an ultrashort pulse. For fast spectral relaxation of excited molecules one may assume that a characteristic time of transient absorption spectrum relaxation T_r is shorter than lifetime τ . One may also assume exponential spectral dynamics of the transient absorption band. Then the temporal dependence of the transient optical density $D(v, t)$ is

$$D(v, t) = K_1 N_1 \left\{ |\mu_{12}^{(i)}|^2 \exp(-t/T_r) \{1 + [2\pi c(v_i - v)T_2^{(i)}]^2\}^{-1} + |\mu_{12}^{(f)}|^2 [1 - \exp(-t/T_r)] \{1 + [2\pi c(v_f - v)T_2^{(f)}]^2\}^{-1} \right\} \quad (6.15)$$

where K_1 is a constant, N_1 is the concentration of excited molecules; and $\mu_{12}^{(m)}$, v_m , and $T_2^{(m)}$ are transition dipole moment, frequency of the maximum of absorption spectrum, and dephasing time of the transient absorption band for initial ($m = i$) and final ($m = f$) relaxational states of the excited molecules, respectively. Note that Eq. (6.15) related to homogeneous broadening of the transient absorption spectrum at the initial and final relaxational states.

It is also assumed that excitation and transient nonlinearity probe pulses have a width t_p that is less than T_r but larger than the lifetimes of the highly excited state $T_n^{(m)}$ and dephasing times $T_2^{(m)}$ of the transient absorption band. The last assumption can easily be experimentally realized in the study of subnanosecond spectral relaxation of excited molecules with nanosecond lifetime τ by means of picosecond excitation and transient nonlinearity probe pulses.

This model of spectral relaxation was applied to a calculation of time-dependent dispersion of transient third-order susceptibility. It was found that time-dependent model of transient susceptibility, which determines the magnitude of the nonlinear mixing signal, is

$$|\chi^{(3)}(v_d, t)| \sim N_1 |\gamma_i^{(3)}(v_d) \exp(-t/T_r) + \gamma_f^{(3)}(v_d) [1 - \exp(-t/T_r)]| \quad (6.16)$$

where $\gamma_m^{(3)}(v_d)$ is a third-order hyperpolarizability of excited molecules in state m ($m = i, f$) at the detuning frequency v_d and is

$$\begin{aligned} \gamma_m^{(3)}(v_d) = & -iK_2 |\mu_{12}^{(m)}|^4 (T_2^{(m)})^2 T_n^{(m)} \\ & \times \{[1 + i2\pi c(v_m - v_1)T_2^{(m)}]^{-1} + [1 - i2\pi c(v_m - v_2)T_2^{(m)}]^{-1}\} \\ & \times [1 + i2\pi c(v_m - v_s)T_2^{(m)}]^{-1} [1 - i2\pi c v_d T_n^{(m)}]^{-1} \end{aligned} \quad (6.17)$$

Equation (6.17) describes the dispersion of third-order hyperpolarizability for a two-level system with homogeneous broadened absorption spectrum. This equation was derived on the basis of density matrix formalism in a case of unsaturated pumping intensity.⁽⁷⁵⁾ In equation (6.17) ν_1 and ν_2 are pumping frequencies and $\nu_s = 2\nu_1 - \nu_2$ is the frequency of the multiwave mixing signal.

Calculated dispersion curves for transient nonlinear susceptibility and transient absorption spectra with $\mu_{12}^{(i)} = \mu_{12}^{(f)}$, $T_2^{(i)} = T_2^{(f)} = 10$ fs, and $T_n^{(i)} = T_n^{(f)} = 1$ ps are shown in Figures 6.14 and 6.15 at different values of t/T_r . In Figure 6.14 one can see that a deep “hole” appears on the dispersion curve at $t/T_r = 0.15$. The hole shows a nonmonotonous alteration with a change of t/T_r . The hole disappears as t/T_r decreases and increases. Moreover, the spectral position of the hole and its depth and width depend on ν_d . The dispersion curve with the hole has asymmetric form with respect to the sign of ν_d : a distinct hole is observed if $\nu_d > 0$; but it is absent when $\nu_d < 0$. At the same time the transient absorption spectrum demonstrates monotonous dependence on t/T_r (Figure 6.15). Thus, one can conclude that time-resolved dispersion of transient third-order susceptibility has a high sensitivity to spectral relaxation of excited molecules.

The origin of this hole is evident. It is predominantly caused by interference of the real part of complex contributions of initial and final relaxational states to a summary transient susceptibility. Note that a similar hole was

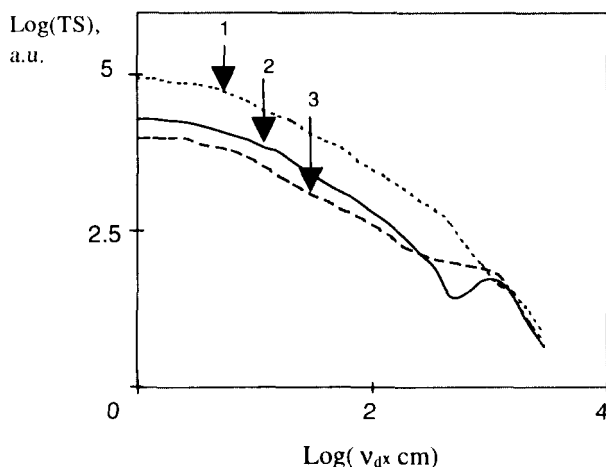


Figure 6.14. Dispersion of transient susceptibility (TS) at $t/T_r = 1$ (1), 0.15 (2), and 0.01 (3). Calculations were made at $\nu_i = 20,000$, $\nu_f = 18,500$, and $\nu_i = 18,500 \text{ cm}^{-1}$.

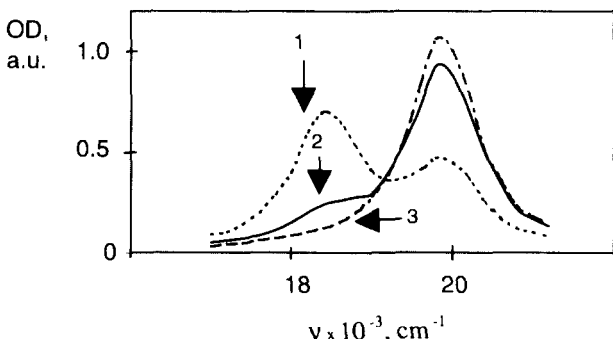


Figure 6.15. Spectra of transient optical density (OD) at $t/T_1 = 1$ (1), 0.15 (2), and 0.01 (3). Calculations were made at $v_f = 20,000$, $v_f = 18,500$, and $v_1 = 18,500 \text{ cm}^{-1}$.

observed early on the dispersion curve for third-order susceptibility of liquids and solutions due to interference of the contributions of nonresonant background and resonant Raman scattering.^(94,95) The last interference effect offers a valuable possibility of absolute measurement of two-photon absorption cross section in solution.^(94,95) The high sensitivity of the hole on the time-resolved transient dispersion curve to spectral dynamics of excited molecules seems very promising for detailed studies of the fast molecular photophysical and photochemical phenomena.

6.4. Summary

The use of powerful excitation sources, such as *Q*-switched and/or mode-locked lasers, results in the high concentration of excited molecules in solution and the population of highly excited electronic states due to stepped photon absorption. Weak short-wavelength emission from the highly excited states can be easily detected with stepped two-photon laser excitation. This "blue" emission usually has a very short lifetime, in the pico- to femtosecond region, caused by ultrafast depopulation of highly excited state via internal conversion to the low-lying electronic states. Importantly, the nonradiative decay of the highly excited states competes with intra- and intermolecular vibrational relaxation of studied molecules in solution. Thus, the short-wavelength emission relates predominantly to spontaneous optical transition from unrelaxed molecular vibronic states.

This peculiarity of the highly excited states determines unusual properties of short-wavelength emission of polyatomic organic molecules in solution:

dependencies of emission spectra, fluorescence lifetime, and quantum yield on the excitation frequency. These dependencies are similar to those observed for fluorescence from the lowest excited state in the vapor phase. This similarity comes from the slow rate of the intermolecular stage of vibrational relaxation in comparison with the studied excited-state decay in solution and in vapor, respectively.

Stepped photon absorption induces growth of the vibrational temperature of molecules in the lowest excited state. Light heating of excited fluorophores is the result of fast transformation of the electronic energy of the highly excited state into the vibrational one due to internal conversion. Powerful stepped excitation can provide a strong light heating of excited fluorophore and hot fluorescence appearance if the rate of light heating is close to the rate of intermolecular vibrational relaxation in solution.

Nonradiative energy transfer from the highly excited state can be easily observed with stepped excitation of donor molecules. The fast energy back transfer from acceptor to donor usually occurs if the acceptor was excited via energy transfer from the highly excited donor. This double-transfer effect can be used for site-selective excitation or photodamage of macromolecules bound to fluorophores.

Photon absorption by excited molecules results in transient third-order optical nonlinearity. Experimental study of transient three-wave mixing shows the high sensitivity of the measured mixing signal to the orientational anisotropy of excited molecules. This result comes from the multiphoton nature of nonlinear mixing and anisotropic initial orientational distribution of excited molecules. Measurements of dispersion of transient third-order susceptibility revealed the existence of a relatively long-lived excited state, which is an intermediate electronic state in the process of internal conversion of highly excited molecules. It was found that the lifetime of this state determines the efficiency of transient resonant multiwave mixing. Finally, the developed theory of time-resolved dispersion of transient third-order susceptibility revealed the appearance of a specific hole on the time-resolved dispersion curve, which is caused by spectral relaxation of excited molecules. Thus, time-resolved dispersion measurement can be a new powerful method in the study of molecular photodynamics.

Acknowledgment

This research was made possible in part by Grant R1W000 from the International Science Foundation and by Grant 95-02-06139 from the Russian Basic Research Foundation.

References

1. M. Kasha, Characterization of electronic transitions in complex molecules, *Discuss. Faraday Soc.* 9, 14–19 (1950).
2. S. I. Vavilov, Dependence of the fluorescence of dyes upon the wave length of the exciting light, *Phil. Mag.* 43, 307–320 (1922).
3. B. I. Stepanov and V. P. Gribkovskii, *Theory of Luminescence*, Iliffe, London. (1968).
4. F. Hirayama, T. A. Gregory, and S. Lipsky, Fluorescence from highly excited states of some aromatic molecules in solution, *J. Chem. Soc.*, 58, 4696–4697 (1973); T. A. Gregory, F. Hirayama and S. Lipsky, Fluorescence from highly excited states of some aromatic molecules in the vapor phase, *J. Chem. Soc.* 58, 4697–4698 (1973).
5. V. L. Ermolaev, I. P. Kotlyar, V. A. Lyubimtsev, and V. G. Maslov, Application of the polarization-modulation method to the study fluorescence from higher singlet excited electronic states, *Opt. Spectrosc.* (English trans.), 52, 1–2 (1982).
6. W. E. K. Gibbs, Excited state absorption in a saturable absorber, *Appl. Phys. Lett.* 11, 113–115 (1967).
7. M. D. Galanin and Z. A. Chizikova, Fluorescence from the second excited electronic level and absorption by excited rhodamine 6G molecules, *Bull. Acad. Sci. USSR, Phys. Ser.* (English transl.), 36, 850–853 (1972).
8. B. Nickel, Delayed fluorescence from upper excited singlet states S_n ($n > 1$) of the aromatic hydrocarbons 1,2-benzanthracene, fluoranthene and chrysene in methylcyclohexane, *Helv. Chim. Acta* 61, 198–222 (1978).
9. P. Pringsheim, *Fluorescence and Phosphorescence*, Interscience, New York (1949).
10. H.-B. Lin and M. R. Topp, Low quantum-yield molecular fluorescence: excitation energy dependence and fluorescence polarization in xanthene dyes, *Chem. Phys. Lett.* 47, 442–447 (1977).
11. V. L. Ermolaev and V. A. Lubimtsev, The Jablonski diagram and electronic energy relaxation processes from the high excited electronic level of organic molecules in solution, *Acta Phys. Polon. A* 71, 731–741 (1987).
12. B. R. Henry and W. Siebrand, in: *Organic Molecular Photophysics*, Vol. I (J. B. Birks, ed.), pp. 153–223, Wiley, London (1973).
13. E. S. Medvedev and V. I. Osherov, *Radiationless Transitions in Polyatomic Molecules*, Springer-Verlag, Berlin and New York (1995).
14. S. Murata, C. Iwanaga, T. Toda, and H. Kokubun, Fluorescence yields of azulene derivatives, *Chem. Phys. Lett.* 13, 101–104 (1972).
15. S. Murata, C. Iwanaga, T. Toda, and H. Kokubun, Erratum, *Chem. Phys. Lett.* 15, 152 (1972).
16. A. Olszowski, Pseudoazulenes: a new large group of compounds with anomalous fluorescence, *Chem. Phys. Lett.* 73, 256–262 (1980).
17. V. G. Plotnikov and B. A. Dolgikh, Processes of internal conversion in aromatic impurity molecules, *Opt. Spectrosc.* (English transl.) 43, 522–527 (1977).
18. A. Nakajima, Short-wavelength fluorescence of 1,2-benzperylene, *Chem. Phys. Lett.* 21, 200–204 (1973).
19. A. Mahaney and J. R. Huber, Fluorescence from the second singlet of aromatic thionketones in solution, *Chem. Phys.* 9, 371–378 (1975).
20. U. P. Wild, H. J. Griesser, and V. D. Tuan, Fluorescence from the second excited singlet states of [18] annulenes, *Chem. Phys. Lett.* 41, 450–455 (1975).
21. Y. Hirata and E. C. Lim, Radiationless transitions in azulene: evidence for the ultrafast $S_2 \rightarrow S_0$ internal conversion, *J. Chem. Phys.* 69, 3292–3296 (1978).

22. J. B. Birks, Photophysics of aromatic molecules—postscript, in: *Organic Molecular Photophysics*, Vol. 2 (J. B. Birks ed.) pp. 409–619, Wiley, London (1975).
23. P. A. M. Van der Bogaart, R. P. H. Retschnick and J. D. W. Van Voorst, Anomalous vibrational relaxation of a hot S_1^* state of 3,4-benzpyrene in 2-methylpentane, *Chem. Phys. Lett.* 18, 351–353 (1973).
24. A. Amirav, U. Even, and J. Jortner, Excited-state dynamics of the isolated ultracold ovalene molecule, *J. Chem. Phys.* 74, 3745–3756 (1981).
25. G. F. Stelmakh and M. R. Tsvirko, Two-quantum excitation of fluorescence from the higher excited electronic states in metalloporphyrin molecules, *Opt. Spectrosc. (English transl.)* 48, 105–106 (1980).
26. G. C. Orner and M. P. Topp, Biphotonic laser excitation of upper singlet state fluore in organic dyes, *Chem. Phys. Lett.* 36, 295–300 (1975).
27. M. P. Tsvirko, K. N. Solovev, G. F. Stelmach, V. E. Pyatosin, and T. F. Kachura, Fluorescence from the second excited π -electron state of porphyrin complexes with rare-earth ions, *Opt. Spectrosc. (English transl.)* 50, 300–303 (1981).
28. M. R. Topp and H.-B. Lin, Optical hole-burning in the ultraviolet spectrum of 3,4,9,10-dibenzpyrene at room temperature, *Chem. Phys. Lett.* 50, 412–417 (1977).
29. H.-B. Lin and M. R. Topp, Evidence for vibrational mode-selectivity in the radiationless relaxation of the large molecules, *Chem. Phys. Lett.* 67, 273–278 (1979).
30. V. L. Bogdanov and V. P. Klochkov, Luminescence from higher excited states and vibrational relaxation of polyatomic molecules in solutions, *Opt. Spectrosc. (English transl.)* 45, 51–54 (1978).
31. V. L. Bogdanov and V. P. Klochkov, Effect of temperature and medium on secondary luminescence of 1,2-benzanthracene during excitation of higher electronic states, *Opt. Spectrosc. (English transl.)* 52, 41–45 (1982).
32. H.-B. Lin and M. R. Topp, Low quantum yield molecular fluorescence. Aromatic hydrocarbons in solution at 300 K, *Chem. Phys. Lett.* 48, 251–255 (1977).
33. B. S. Neporent, Quenching of the fluorescence of β -naphthylamine vapors by foreign gases, *J. Phys. Chem. (USSR)* 21, 1111–1124 (1947). (in Russian).
34. N. A. Borisevitch, *Excited States of Complex Molecules in the Gas Phase*, Nauka i technika, Minsk 1967. (in Russian)
35. A. P. Veduta, M. D. Galanin, B. P. Kirsanov, and Z. A. Chizhikova, Two-quantum anti-Stokes processes in the excitation of dyes, *JETP Lett. (English transl.)* 11, 96–99 (1970).
36. V. L. Bogdanov and V. P. Klochkov, Secondary emission of coronene molecules with excitation of higher electronic states, *Opt. Spectrosc. (English transl.)* 50, 479–484 (1981).
37. K. K. Rebane, Resonant secondary emission by impurities in crystals, in: *Joint USA–USSR Symposium on Light Scattering in Condensed Matter* (J. L. Birman, H. Z. Cummins, and K. K. Rebane, eds.), pp. 257–267, Plenum Press, New York (1979).
38. S. J. Stricler and R. A. Berg, Relationship between absorption intensity and fluorescence lifetime of molecules, *J. Chem. Phys.* 37, 814–822 (1962).
39. A. A. Krasheninikov and A. V. Shablya, Determination of luminescence quantum yields from highly excited electronic states of molecules by the photo-acoustic effect, *Opt. Spectrosc. (English transl.)* 52, 159–162 (1982).
40. A. V. Aristov and V. S. Shevandin, Blue and ultraviolet luminescence of rhodamine 6G, *Opt. Spectrosc. (English transl.)* 44, 276–280 (1978).
41. W. Falkenstein, A. Penzkofer, and W. Kaiser, Amplified spontaneous emission in rhodamine dyes: generation of picosecond light pulses and determination of excited state absorption and relaxation, *Opt. Commun.* 27, 151–156 (1978).

42. C. V. Shank, E. P. Ippen, and O. Teschke, Sub-picosecond relaxation of large organic molecules, *Chem. Phys. Lett.* **45**, 291–294 (1977).
43. V. L. Ermolaev and V. A. Lubimtsev, Superfast processes of nonradiative transfer and relaxation of electronic energy from high singlet excited levels of organic molecules in solutions, *Bull. Acad. Sci. USSR, Phys. Ser.* (English transl.) **47**, 150–153 (1977).
44. M. R. Topp, H.-B. Lin, and K.-J. Choi, Fluorescence from subpicosecond states of 3,4,9,10-dibenzpyrene, *Chem. Phys.* **60**, 47–59 (1980).
45. M. D. Galinin and Z. A. Chizhikova, Applications of fluorescence from the second excited electronic level of rhodamine 6G, *J. App. Spectrosc.* (English transl.) **37**, 1440–1444 (1982).
46. V. L. Bogdanov, V. P. Klochkov, and B. S. Neporent, Hot luminescence of liquid solution of organic substances, *Opt. Spectrosc.* (English transl.) **43**, 701–702 (1977).
47. V. L. Bogdanov and V. P. Klochkov, Hot luminescence and vibrational relaxation in complex molecules with diffuse spectra, *Opt. Spectrosc.* (English transl.) **44**, 412–416 (1978).
48. A. V. Aristov and V. S. Shevandin, Short-wavelength luminescence of rhodamine solutions, *Opt. Spectrosc.* (English transl.) **45**, 825–826 (1978).
49. A. Penzkofer and J. Wiedmann, Orientation of transition dipole moments of Rhodamine 6G determined by excited state absorption, *Opt. Commun.* **35**, 81–86 (1980).
50. A. V. Aristov and V. S. Shevandin, Reasons of the similarity in the ultraviolet absorption spectra from the ground and fluorescent states of rhodamine molecules, *Opt. Spectrosc.* (English transl.) **48**, 266–268 (1980).
51. P. P. Feofilov, *The Physical Basis of Polarized Emission*, Consultants Bureau, New York (1961).
52. A. N. Rubinov, M. C. Richardson, K. Sala, and A. J. Alcock, Generation of single picosecond dye laser pulses using one and two-photon travelling wave excitation, *Appl. Phys. Lett.* **27**, 358–360 (1975).
53. R. B. Weisman and S. A. Rice, Vibrational relaxation in liquid diethylamine, *Chem. Phys. Lett.* **61**, 15–18 (1979).
54. G. R. Fleming, O. L. Gijzeman, K. F. Freed, and S. H. Lin, Theory for time resolved emission spectra, *J. Chem. Soc. Faraday Trans. 2* **71**, 773–780 (1975).
55. V. L. Bogdanov and V. P. Klochkov, Nuclear motion randomization and hot luminescence spectra of complex molecules, *Opt. Spectrosc.* (English transl.) **53**, 233–234 (1982).
56. A. Mokhtari, J. Chesnoy, and A. Lauberou, Femtosecond time- and frequency-resolved fluorescence spectroscopy of a dye molecule, *Chem. Phys. Lett.* **155**, 593–597 (1989).
57. V. L. Bogdanov, Light absorption and vibrational relaxation of electronically excited perylene molecules in a liquid solution and in a Spolskii matrix, *Opt. Spectrosc.* (English transl.) **55**, 270–275 (1983).
58. V. L. Bogdanov and A. B. Evdokimov, Light quenching and amplification of fluorescence of diphenylpolyene solutions, *Opt. Spectrosc.* (English transl.) **61**, 204–208 (1986).
59. G. K. Oster and H. Kallmann, Energy transfer from high-lying excited states. *J. Chim. Phys.* **64**, 28–32 (1967).
60. M. S. S. C. Leite and K. R. Nagvi, Intermolecular quenching of the second excited state of some aromatic molecules, *Chem. Phys. Lett.* **4**, 35–38 (1969).
61. D. L. Horrocks, Scintillation efficiencies at high solute concentrations: possible energy transfer from S_3 states of aromatic solvents, *J. Chem. Phys.* **52**, 1566–1572 (1970).
62. P. Peretti, P. Ranson and Y. Rousset, Singlet-singlet energy transfer in liquid solution between rhodamine 6G and benzophenone in presence of non-linear absorption, *Opt. Commun.* **9**, 106–111 (1973).
63. M. V. Alvimov, V. L. Gerko, L. S. Popov, and V. E. Razumov, Abnormal broadening in triplet-to-triplet absorption spectra caused by aromatic solvents, *Chem. Phys. Lett.* **50**, 398–401 (1977).

64. V. A. Benderski, V. Kh. Brikshtein, P. G. Filippov, and A. V. Yatsenko, Energy transfer over the highest vibronic levels in mixed molecular crystals, *Opt. Spectrosc.* (English transl.) 45, 287–290 (1978).
65. V. L. Ermolaev, A. A. Krasheninnikov, and A. V. Shablya, Transmission of energy from highly excited singlet states of aromatic molecules to a liquid solvent, *Dokl. Phys. Chem. Proc. Acad. Sci. USSR* (English transl.) 248, 768–770 (1979).
66. I. Kaplan and J. Jortner, Electronic energy transfer from S_2 state of rhodamine 6G, *Chem. Phys.* 32, 381–396 (1978).
67. V. L. Bogdanov and V. P. Klochkov, Transfer of excitation energy from the higher electronic states of organic molecules, *Opt. Spectrosc.* (English transl.) 61, 159–161 (1984).
68. M. Simonetta, A. Gamba, and E. Rusconi, Interpretation of the electronic spectra of azines by the molecules in molecules [MIM] method, in: *Quantum Aspects of Heterocyclic Compounds in Chemistry and Biochemistry*, Proc. 2nd Int. Symp., (E. D. Bergmann, ed.), pp. 213–224 (Israel Acad. Sci. Hum., Jerusalem (1970).
69. W. Von Niessen, A theory of molecules in molecules. I, *J. Chem. Phys.* 55, 1948–1957 (1971).
70. V. L. Bogdanov, V. P. Klochkov, and E. G. Korsakova, Relaxation of highly excited electronic states of bifluorophore molecules, *Opt. Spectrosc.* (English transl.) 70, 16–20 (1991).
71. V. L. Bogdanov, V. P. Klochkov, and E. G. Korsakova, Energy transfer and deactivation of the excited states of bifluorophores, *Opt. Spectrosc.* (English transl.) 71, 464–468 (1991).
72. E. G. Korsakova, E. B. Verkhovskii, and V. P. Klochkov, Fluorescence quantum yields and deactivation of high electronic states, *Opt. Spectrosc.* (English transl.) 59, 350–352 (1985).
73. A. Andreoni, R. Cubeddu, S. De Silvestri, P. Laporta, and O. Svelto, Time-delayed two-step selective laser photodamage of dye-biomolecule complexes, *Phys. Rev. Lett.* 45, 431–434 (1980).
74. B. Dick, R. M. Hochstrasser, and H. P. Trommsdorf, Resonant molecular optics, in: *Nonlinear Optical Properties of Organic Molecules and Crystals*, Vol. 2, (D. S. Chemla and J. Zyss, eds.), Academic Press, Orlando (1987).
75. T. Yajima and H. Souma, Study of ultrafast relaxation processes by resonant Rayleigh-type optical mixing, *Phys. Rev. A* 17, 309–323 (1978).
76. H. Souma, E. J. Heiweil, and R. M. Hochstrasser, Resonant nonlinear optical mixing using the phase conjugate configuration, *J. Chem. Phys.* 76, 5693–5702 (1982).
77. V. L. Bogdanov, S. V. Kulya, B. S. Neporent, and A. G. Spiro, Four-wave spectroscopy of excited organic molecules, *JETP Lett.* (English transl.) 51, 540–543 (1990).
78. T. Hoffer, P. Kruck, and W. Kaiser, Dynamics of photochemical reactions studied by degenerated four-wave mixing, *Chem. Phys. Lett.* 224, 411–416 (1994).
79. W. Ji, S. H. Tang, G. O. Li, H. S. O. Chan, and W. W. Ng, Resonant optical nonlinearity of fullerenes in free-standing polymethyl methacrylate films, *J. Appl. Phys.* 74, 3664–3672 (1993).
80. J. Yan, J. Mu, H. Zhu, D. Sun, Y. Hi, and F. Li, Excited-state enhancement of the third-order nonlinear optical susceptibility of nonether polyphenylquinoxaline, *Opt. Lett.* 20, 255–257 (1995).
81. V. M. Petnikova, S. A. Pleshakov, and V. V. Schuvalov, Method of biharmonic pumping in nonlinear spectroscopy of solutions of organic dyes, *Opt. Spectrosc.* (English transl.) 55, 270–275 (1983).
82. B. S. Neporent, S. V. Kulya, and A. G. Spiro, Direct determination of the difference in the nature of the band broadening in relaxational and configurational continuous vibronic spectra of complex molecules by four-photon spectroscopy, *JETP Lett.* (English transl.) 48, 406–409 (1988).
83. S. V. Kulya, V. L. Bogdanov, A. A. Ishenko, and A. G. Spiro, Relaxation of highly excited states of polymethine dye molecules studied by four-wave and luminescence spectroscopy, *Opt. Spectrosc.* (English transl.) 70, 173–177 (1991).

84. V. L. Bogdanov, S. V. Kulya, and A. G. Spiro, *Ultrafast Optical Dynamics and Nonlinear Susceptibility for Resonant Transitions of Excited Molecules and Aggregates*, Vol. 126, The Institute of Physics, (1992), pp. 485–498.
85. V. L. Bogdanov, V. P. Klochkov, and A. G. Spiro, Luminescence properties and relaxation of organic molecules under excitation of high electronic states, *Bull. Acad. Sci. USSR, Phys. Ser.* (English transl.) 56, 256–262 (1992).
86. V. A. Gaysenok and A. M. Sarshevskii, *Anisotropy of Absorption and Luminescence of Polyatomic Molecules*, Universitetskoe, Minsk (1986). (in Russian)
87. J. R. Lakowicz, *Principles of Fluorescence Spectroscopy*, Plenum, New York (1983).
88. H. J. Richler, P. Gunter, and D. M. Pohl, *Laser-Induced Dynamic Grating*, Springer Series in Optical Sciences, Vol. 50, Berlin (1986).
89. A. B. Myers and P. M. Hochstrasser, Comparison of four-wave mixing technique for studying orientational relaxation, *IEEE J. Quantum Electron.* 22, 1482–1492 (1986).
90. T. Tao, Time-dependent fluorescence depolarization and Brownian rotational diffusion coefficients of macromolecules, *Biopolymers* 8, 609–632 (1969).
91. V. L. Bogdanov, Resonant four-photon scattering and dynamics of excited molecules, *SPIE Proc.* 2324, 243–249(1994).
92. S. P. Velsko and G. R. Fleming, Photochemical isomerization in solution. Photophysics of diphenylbutadiene, *J. Chem. Phys.* 76, 35–53 (1982).
93. R. J. Anderton and J. F. Kauffman, Temperature-dependent rotational relaxation of diphenylbutadiene in *n*-alcohols: a test of the the quasihydrodynamic free space model, *J. Phys. Chem.* 98, 12117–12124 (1994).
94. R. T. Lynch, Jr., and H. Lotem, Two-photon absorption measurements in organic liquids via nonlinear light mixing spectroscopy, *J. Chem. Phys.* 66, 1905–1913 (1977).
95. R. J. Anderson, C. R. Hotton, and Wm. M. McClain, Two-photon absorptivities of all trans α , ω -diphenylpolyenes from stilbene to diphenyloctatetraene via three wave mixing, *J. Chem. Phys.* 70, 4310–4315(1979).

This page intentionally left blank.

Ultrafast Stimulated Emission Spectroscopy

G. J. Blanchard

For stationary states in an atomic or molecular system, there are four possible ways in which transitions between two states can occur. These are spontaneous absorption, stimulated absorption, spontaneous emission, and stimulated emission. We are used to thinking of spontaneous absorption in the context of the thermal population of an excited state according to the Boltzmann distribution function. For transitions between states separated in energy by several electron volts ($1\text{ eV} = 8065\text{ cm}^{-1}$), spontaneous absorption becomes important only at very high temperatures, such as those found in a flame or an inductively coupled plasma. Stimulated absorption differs from spontaneous absorption because the electric field used to stimulate absorption defines the final state of the transition. We take advantage of this level of spectral resolution in common linear absorption measurements. Spontaneous emission (fluorescence) is a technique used widely for understanding the transient and steady-state responses of many atomic and molecular systems. In a spontaneous-emission measurement, the final state of the transition is not determined, *per se*, for a given molecule. Rather, the molecule relaxes spontaneously and the identity of the final state in the transition is determined statistically, with the statistical weighting of the distribution of final states being determined by the magnitude of the transition dipole moment for each possible state pair. Stimulated emission, like absorption, differs from spontaneous emission in the sense that an electric field couples two states and mediates the transfer of population between the two states. Einstein recognized in 1917 that these four processes (spontaneous emission and absorption, stimulated emission and absorption) determined the optical response of a two-level system, and

G. J. Blanchard • Department of Chemistry, Michigan State University, East Lansing, Michigan 48824.

Topics in Fluorescence Spectroscopy; Volume 5: Nonlinear and Two-Photon-Induced Fluorescence, edited by J. Lakowicz. Plenum Press, New York, 1997.

he described the relationship among them.⁽¹⁾ Specifically, he considered that the two energy levels, 1 and 2 in an ensemble of isolated atoms, were at thermodynamic equilibrium at temperature T . He used, for convenience, a blackbody radiator as the light source in his description of stimulated emission and absorption. The rate equations describing the spectroscopically important processes of absorption, spontaneous emission, and stimulated emission are

$$\begin{aligned} -\frac{dN_1}{dt}\Big|_{\text{abs}} &= B_{12}N_1\rho(v) && \text{stimulated absorption} \\ -\frac{dN_2}{dt}\Big|_{\text{spont. em}} &= A_{21}N_2 && \text{spontaneous emission} \\ -\frac{dN_2}{dt}\Big|_{\text{stum. em}} &= B_{21}N_2\rho(v) && \text{stimulated emission} \\ \sum_i \frac{dN_i}{dt} &= 0 && \text{thermodynamic equilibrium} \end{aligned} \quad (7.1)$$

$$\frac{N_2}{N_1} = \exp\left(-\frac{E_{12}}{k_B T}\right) \quad \rho(v) = \frac{8\pi h v^3}{c^3(\exp(hv/k_B T) - 1)} \quad (7.2)$$

From these equations, Einstein derived the expressions relating the rate constants for these transitions:

$$B_{12} = B_{21} \quad A_{21} = \frac{8\pi h v^3 B_{21}}{c^3} \quad (7.3)$$

Thus, in principle, for a given homogeneously broadened transition, if one could determine the transition cross section (and therefore the rate constant) for a particular transition, then one could calculate the analogous quantities for all of the other transitions.

The Einstein coefficients A_{ij} and B_{ij} are fundamental parameters used to describe transition probabilities. These rate constants are related to more familiar quantities, such as the strength of absorption or intensity of (spontaneous) emission,^(2,3)

$$\begin{aligned} I_{\text{sp. em}}^{21} &= N_2 h c v_{21} A_{21} & I_{\text{abs}}^{12} &= \rho_{12} N_1 x h c v_{12} B_{12} \\ A_{21} &= \frac{64\pi^4 v_{21}^3 |\mu_{21}|^2}{3h} & I_{\text{st. em}}^{21} &= \rho_{21} N_2 x h c v_{21} B_{21} \\ B_{12} &= B_{21} = \frac{8\pi^3 |\mu_{12}|^2}{3h^2 c} \end{aligned} \quad (7.4)$$

where ν_{ij} is the frequency of the transition, $|\mu_{ij}|^2$ is the square of the magnitude of the transition moment for the $i \leftrightarrow j$ transition, and x is the thickness of the sample. The terms N_1 and N_2 are the populations of states 1 and 2, respectively. While absorption and fluorescence spectroscopies have been developed extensively and used widely for the characterization and understanding of myriad atomic and molecular systems, the use of stimulated emission as a spectroscopic tool has come into its own somewhat more recently. Indeed, the stimulated emission response of a molecular system can contain significantly more information than the corresponding spontaneous emission signal, and the details of this difference in information content depend, to some extent, on the way in which the stimulated emission measurements are made. We will elaborate on this point later. As mentioned, a key difference between stimulated emission and spontaneous emission is that, for the former process, the initial and final states in the transition are defined by an external variable (the incident electric field), whereas for spontaneous-emission measurements there is no corresponding external variable available.

This chapter is divided into four sections. In the first section we provide an overview of the stimulated-emission spectroscopic tools used and the chemical information available from certain of these measurements. We then describe the ultrafast stimulated-emission spectroscopy technique developed in our laboratories and those of others over the past several years. Next, we present a discussion of the chemical information content of the ultrafast time-resolved stimulated-emission measurements, and highlight the utility of stimulated emission, in conjunction with other techniques, to measure rotational diffusion and vibrational population relaxation. We hope that this chapter will guide and stimulate further work in this emerging area of ultrafast spectroscopy.

7.1. Stimulated-Emission Pumping Spectroscopies

There are a variety of means available to measure stimulated emission. One class of measurements involves monitoring a diminution of a different optical or molecular process, such as spontaneous emission or multiphoton ionization, resulting from the occurrence of stimulated emission, where the magnitude of the diminution is related to the efficiency of stimulated emission.⁽⁴⁻³³⁾ The second important class of stimulated-emission measurements senses the gain in intensity of an electric field due to stimulated emission directly.⁽³⁴⁻⁴³⁾ This type of measurement is the on-resonance analog of stimulated Raman scattering.⁽⁴⁴⁻⁵⁰⁾

Stimulated emission spectroscopy has been used, for the most part, to make spectroscopic state and transition assignments or to measure transient population relaxations. For the former class of measurements, the important attribute of

stimulated-emission measurements is that, because two electric fields are involved in the measurement, the simultaneous satisfaction of selection rules for both transitions is required, and therefore the assignment or determination of transition symmetry is simplified to some extent. For spectroscopic assignment measurements, high spectral resolution is required, and thermal congestion serves to complicate the experimental response. Thus, most stimulated-emission measurements that are done for spectroscopic assignment purposes use ns pulsed lasers with high peak powers and comparatively narrow linewidths ($\sim 0.001 \text{ cm}^{-1}$) and are performed in supersonic jet expansions. The second class of stimulated-emission measurements, where the kinetic response of the system under examination is the quantity of interest, typically employ short-pulse lasers, where the limiting-response function of the laser system is picoseconds (ps). For such measurements, the effective bandwidth of the measurement is large enough to make selection of specific rotational bands impossible, but such spectroscopic resolution is of little importance for condensed phase measurements, where inhomogeneous broadening processes dominate the measured spectral linewidths. The spectral resolution of this class of measurements is perfectly satisfactory for vibrational and electronic spectroscopies in liquids. This family of measurements is the focus of this chapter. We describe two types of measurement in detail; rotational diffusion dynamics measured by both stimulated emission and ground-state absorption depletion recovery^(36–40) and a vibrational population relaxation scheme based on the time evolution of stimulated emission from organic chromophores.^(51–53)

7.2. Experimental Implementation of Ultrafast Stimulated-Emission Pump-Probe Spectroscopy

The general form of an ultrafast stimulated-emission experiment is a pump–probe configuration, where the energy in the individual short light pulses typically ranges from pJ to μJ . The goal of all such measurements is to create a population in the medium of interest at a known time and monitor the time course of that population. Many different spectroscopic processes can be accessed using a pump–probe configuration, depending on the wavelengths, polarization conditions, and time registration of the pump and probe laser pulses.⁽⁵⁴⁾ The laser system we use for the pump–probe measurements we discuss here employs pJ to nJ pulses⁽⁵⁵⁾ (Figure 7.1). The primary motivation for using comparatively low power lasers is to avoid accessing unwanted nonlinear optical responses in our samples. The consequent disadvantage of this approach is that the stimulated signal is small, making detection of the transient gain or loss challenging. To help overcome the low power per pulse

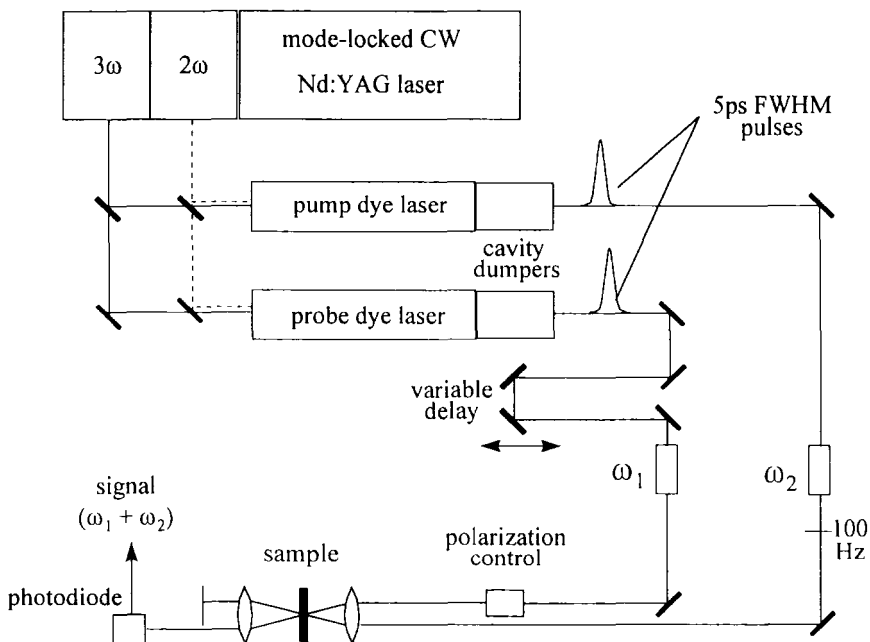


Figure 7.1. Schematic of picosecond pump–probe laser spectrometer. The mode-locked CW Nd:YAG laser light source allows excitation of the synchronously pumped dye lasers at either 532 nm (2 ω) or 355 nm (3 ω). Modulation frequencies are indicated as ω_1 and ω_2 , and the signal is detected as the sum of the modulation frequencies ($\omega_1 + \omega_2$). Typical time resolution of this spectrometer is ~ 2 pulse widths, ~ 10 ps.

typical of these laser systems, we take advantage of their high repetition rates for efficient signal averaging. For most picosecond time-resolved pump–probe experiments, synchronously pumped dye lasers^(56–58) are the light sources of choice because of the excellent time registration between the individual dye lasers combined with their broad, independent tunability, high long-term stability, and low-noise characteristics. For these experiments, the time resolution limit is determined by the temporal jitter between the two laser pulse trains, which is typically about one pulse width.^(55,59) This minimal instrumental response function compares favorably with detection systems that achieve time resolution electronically, such as time-correlated single-photon counting, where 25–40ps is a practical minimum instrumental response time.^(60,61) For rotational diffusion and vibrational population relaxation pump–probe measurements, the population of interest is created by a resonant electronic excitation. The signal of interest appears as a gain or loss on the probe laser beam, with

the magnitude of the gain or loss depending on the time registration of the two laser pulses, their wavelengths, and their relative polarizations. These transient gains or losses are usually small; for our experimental conditions, changes in probe laser intensity are about 10^{-4} – 10^{-5} of the probe laser intensity, and signal lifetime is significantly less than the laser repetition rate, so no cumulative gain or loss can be used to advantage. Because the low-frequency fluctuations of the probe laser can be as high as several percent of the average output intensity, a detection scheme is required that can separate the transient response from background noise. It is therefore important to understand the noise spectrum of the laser light sources used in these measurements. For synchronously pumped dye lasers, low (audio)-frequency noise scales approximately as f^{-1} , with the noise diminishing to the shot-noise “floor” by ~ 1 – 2 MHz (Figure 7.2). Depending on the output power of the synchronously pumped dye lasers, the magnitude of the shot noise on the output is between $\sim 10^{-6}$ and 10^{-9} of the laser beam intensity.⁽⁶²⁾ The key to the successful execution of these experiments lies in the ability to shift the detection frequency into a region of the laser noise spectrum dominated by shot noise. This signal shift can be accomplished in several ways. For such a frequency shift to be possible, each laser must interact linearly with the sample.

The first successful demonstration of frequency-shifted detection for pump-probe measurements was reported by Heritage *et al.*⁽⁴⁹⁾ In that work,

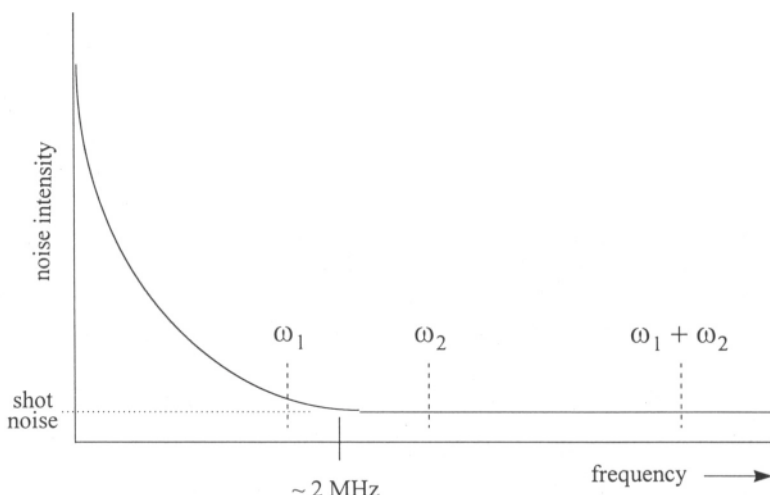


Figure 7.2. Diagram of the noise spectrum of a synchronously pumped dye laser. The low-frequency region of this noise spectrum is dominated by f^{-1} noise. The shot noise floor is achieved by ~ 2 MHz. The modulation frequencies ω_1 and ω_2 are indicated on the diagram.

a 10.7-MHz radio frequency (RF) amplitude modulation was applied to the pump laser pulse train, and the magnitude of the amplitude modulation transferred to the probe laser pulse train was the signal of interest. Using this scheme, Heritage obtained stimulated Raman gain responses as small as $\Delta T/T \approx 10^{-8}$.^(48,49) Despite this extremely high detection sensitivity, several experimental factors conspired to limit the utility of this detection scheme. Most notably, the electronics required to impose the ~10-MHz modulation on the pump laser broadcast enough RF signal to be picked up electronically by the ultrasensitive detection system. Also, stray capacitive effects in the room which housed the experiment could, and did, give rise to unpredictable variations in the magnitude of the detected RF signal. An additional mechanical modulation helped to reduce, but not eliminate, broadcast, capacitive, and scattering limitations to the single-RF-modulation approach.

The next significant advance in this detection technology was developed by the Wilson group.⁽⁶³⁾ They imposed an amplitude modulation on both the pump and probe laser pulse trains, each at a different radio frequency. As before, both the pump and probe electric fields interact with the sample, but in this case the magnitude of the mutual interaction is sensed by measuring the extent to which the two RF modulations mix. The mixing or multiplication of the two modulations by the sample results in new RF modulations at the sum and difference of the two initial modulation frequencies:

$$\cos(\omega_1 t) \cos(\omega_2 t) = \frac{1}{2} \cos((\omega_1 + \omega_2)t) + \frac{1}{2} \cos((\omega_1 - \omega_2)t) \quad (7.5)$$

where the (new) frequency components at the sum and difference of the modulation frequencies exist against a background that is optically and electronically “dark.” The Wilson group demonstrated AM demodulation of the resulting signal as the decoding method, resulting in a square-law output of the detection electronics. Later, the Rice group demonstrated single-sideband detection based on the same modulation scheme,⁽⁶⁴⁾ and the Kenney–Wallace,⁽⁶⁵⁾ Blanchard,⁽⁵⁹⁾ and Wirth⁽⁶²⁾ groups have used simple lock-in amplifier detection. In addition to amplitude modulation, frequency modulation (FM) schemes have been demonstrated to achieve the same highly sensitive detection of small coherent gains or losses on laser beams.⁽⁴⁶⁾ While these schemes work as well as AM techniques, their experimental implementation and diagnosis is comparatively more involved. The multiple-AM detection method, while slightly more complex electronically than the single-modulation approach, is significantly more robust in its experimental implementation and has been demonstrated to be shot-noise-limited in sensitivity.⁽⁶²⁾ We will discuss the specific information available from the stimulated-emission response of probe molecules, measured with a pump–probe spectrometer such as the one described.

7.3. Applications of Stimulated-Emission Spectroscopy to Rotational Diffusion Dynamics Measurements

The orientational relaxation behavior of a molecule dissolved in a liquid can reveal a significant amount of information about the interactions between that molecule and its surroundings. Indeed, reorientation dynamics measurements have been used to probe local molecular environments in a wide variety of neat and binary liquids, membranes, and interfacial systems. The idea behind such measurements is to photoselect an anisotropic orientational distribution of optically accessible “probe” molecules within the medium of interest by using a polarized light pulse and then to monitor the rate(s) at which this subset of probe molecules re-randomizes by using a second polarized pulse of light. In interfacial media and membranes, the probe molecule cannot achieve a completely random orientational distribution, and these data can be treated in the context of the probe molecule reorienting within a cone.^(66–68) In liquids there is usually no such restriction on the motion of the molecule. Understanding the reorientation dynamics of many molecules, both polar and nonpolar, has been accomplished by considering the shape of the rotating solute molecule, the strength of frictional interactions between the solvent and solute, and the dielectric “drag” imposed on the rotating solute by the local solvent dielectric field.

The first theoretical description of rotational diffusion in solution via Brownian motion appeared in 1929, in the context of a dipole reorienting in a microwave cavity.⁽⁶⁹⁾ The essential physics of this problem are identical to that of a molecule reorienting in solution. The Debye–Stokes–Einstein (DSE) equation was derived to treat a dipole in a spherical cavity reorienting in a continuum medium:

$$\tau_{\text{OR}} = \frac{1}{6D} = \frac{\eta V}{k_B T} \quad (7.6)$$

where τ_{OR} is the orientational relaxation time constant of the rotating species, η is the bulk viscosity of the surrounding medium, V is the hydrodynamic volume of the reorienting moiety,^(70,71) k_B is the Boltzmann constant, T is the temperature, and D is the rotational diffusion constant. Despite the significant oversimplifications employed in the derivation of this model, the DSE equation has proven to be remarkably useful as a *qualitative* predictor of molecular reorientation times for a multitude of chemical systems. The DSE equation considers the interaction between the solvent and the solute as frictional, as expressed through the direct dependence of the reorientation time on the solvent viscosity. The most obviously limiting assumptions in the DSE treatment are

first that the majority of molecules is not represented accurately as spheres and, second, that the frictional interactions between the solvent and solute are assumed to be the same as those between identical solvent molecules. To account for these limitations, the DSE equation has been modified by several groups^(72–78) to be of the general form

$$\tau_{\text{OR}} = \frac{\eta V}{k_B T} \frac{f}{S} \quad (7.7)$$

In this model, S is a shape factor and f is a frictional term. For strong solvent–solute interactions, where the probe molecule and the solvent “stick” as they move past one another, $f=1$, the “sticking boundary condition” or “stick limit.” Where the frictional interactions are weaker, the solvent and solute are said to slip past one another, giving rise to the “slip limit.” While $f=1$ for all S in the stick limit, $f=f(S)$ in the slip limit.^(76,77) In this model the volume swept out by a reorienting molecule is described in terms of ellipsoids (i.e., distorted spheres). For a flattened sphere the resulting shape is termed an oblate ellipsoid, and for a sphere that is elongated along a single Cartesian axis the rotor shape is said to be a prolate ellipsoid. The shape factor, S , is related to the ratio of the axial dimensions, ρ , for the probe molecule⁽⁷⁹⁾ by

$$S = \frac{3}{2} \frac{(2 - \rho^2)(\rho^2 / \sqrt{\rho^2 - 1}) \tan^{-1}(\sqrt{\rho^2 - 1}) - \rho^2}{1 - \rho^4} \quad \text{oblate ellipsoid}$$

$$S = \frac{3}{2} \frac{(2 - \rho^2)(\rho^2 / \sqrt{1 - \rho^2}) \ln\left(\frac{1 + \sqrt{1 - \rho^2}}{\rho}\right) - \rho^2}{1 - \rho^4} \quad \text{prolate ellipsoid}$$

$$\rho = \frac{a}{b} \quad (7.8)$$

where b is the length of the rotational symmetry axis, and a is the length of either of the minor axes of rotation. For a prolate ellipsoid $b > a$, and for an oblate ellipsoid $a > b$. Using these corrections to Eq. (7.6), many studies of molecular reorientation in solution have been modeled accurately, and a significant body of chemical information has been advanced through these works. In addition to frictional interactions between solvent and solute, there can also be a dielectric contribution to molecular reorientation, where dipole–dipole interactions serve to place a torque on the reorienting molecule that acts counter to its rotary motion.^(79–84) This additive “dielectric friction” effect, with a characteristic

time constant τ_{df} , operates for polar systems where dipole–dipole interactions are thought to dominate the intermolecular interactions.⁽⁷⁹⁾

$$\tau_{df} = \frac{\mu^2}{a^3 k_B T} \left[\frac{\varepsilon - 1}{(2\varepsilon + 1)^2} \right] \tau_D \quad (7.9)$$

In Eq. (7.9), μ is the solute permanent dipole moment, a^3 is the volume occupied by the solute, ε is the solvent zero-frequency dielectric constant, and τ_D is the solvent Debye dielectric relaxation time, a quantity related to the reorientation time of the individual solvent molecules. We thus expect there to be at least two contributions to the rotational diffusion time of a (polar) probe molecule in a polar liquid. Neither of these treatments, however, considers explicitly any moiety-specific interactions between the solvent and the solute. Stimulated-emission measurements of rotational diffusion dynamics, in conjunction with ground-state depletion recovery measurements, can be used to determine the contribution(s) of each of these processes and to detect the occurrence of site-specific solvent-excited solute complex formation.^(36,37,39,40)

While a variety of experimental means to measure rotational diffusion dynamics have been developed, the majority of these methods sense the dynamics of an excited molecule, where the dominant intermolecular interactions are between the (ground state) solvent and solute in its lowest excited singlet electronic state. To relate these measurements to ground-state processes, such as chemical reactions or surface adsorption, it is necessary to assume that the probe molecule interacts with its surroundings identically in both its ground and excited electronic states. This assumption is not always valid. One consequence of electronic excitation is the redistribution of charge density about the molecule, and therefore the magnitude and possibly the direction of the permanent dipole moment changes with excitation for many polar chromophores.^(59,85) Such a change can, in principle, give rise to a state-dependent dielectric friction term, or state-dependent association between solvents and solutes could occur under certain circumstances. In order to evaluate the validity of the assumption that ground-state and excited-state reorientation are identical, we studied the state dependence of the rotational diffusion dynamics of several different families of molecules in selected solvent systems.^(36–40,86) We used stimulated-emission to interrogate the excited-state response of these molecules and ground-state depletion recovery measurements, where both the pump and probe laser wavelengths are tuned to be coincident with the absorption band of the chromophore, to measure their ground-state dynamical response directly. The raw experimental data, taken as the magnitude of gain (stimulated-emission) or change in loss (transient ground-state absorption depletion) on the probe laser pulse, for polarizations parallel and perpendicular to the

pump laser pulse, are converted into the induced orientational anisotropy decay function, $R(t)$:

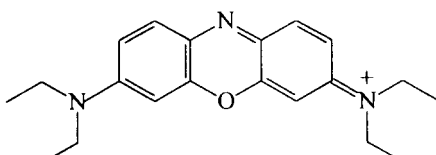
$$R(t) = \frac{I_{\parallel}(t) - I_{\perp}(t)}{I_{\parallel}(t) + 2I_{\perp}(t)} \quad (7.10)$$

The functionality of $R(t)$ is related to the rotational diffusion constant and spectroscopic properties of the probe molecule. To first approximation, and under many experimental conditions, where the probe molecule is polar, of low symmetry, or fulfills certain spectroscopic and geometric conditions,

$$R(t) \approx R(0) \exp(-t/\tau_{\text{OR}}) \quad (7.11)$$

The form of $R(t)$ is, in fact, more complex than is implied by Eq. (7.11), and can contain up to five exponential decays.⁽⁸⁷⁾ While it is possible to obtain multiple exponential decays of $R(t)$ under certain circumstances, the most common experimental form is shown in Eq. (7.11). For conditions where multiple exponential decays are observed, the individual time constants are related to permutations of the Cartesian components of the rotational diffusion constant. We discuss this point later, for rotational diffusion measurements of 1-methylperylene in a series of *n*-alkanes.

For many molecules, the change in dipole moment and/or charge distribution on excitation is not sufficient to alter its interactions with the surrounding medium. For some systems, however, the state dependence of rotational diffusion dynamics can be significant.^(36–40,43) The oxazines are one such family of molecules (Figure 7.3). The experimental manifestation of the state dependence is that



oxazine 725

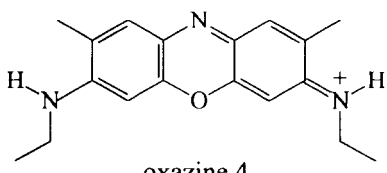


Figure 7.3. Structures of the two oxazines discussed in the chapter. For both compounds, no counter ion is indicated and only one resonance structure is shown.

the excited oxazines reorient more slowly than ground-state oxazines in hydrogen-bonding solvents (Figure 7.4 and Table 7.1).

The state-dependent difference in reorientation time for a particular oxazine depends sensitively on the identity of the solvent medium, and the reorientation behavior of oxazines is state independent to within the experimental uncertainty in polar aprotic, non-hydrogen-bonding solvents such as 2-butanone, dimethyl sulfoxide, and acetonitrile.^(36,37,39,40) Based on these experimental data there are, in principle, two explanations. The first is solvent attachment, and the second is an additive contribution due to dielectric friction. Semiempirical calculations of oxazines indicate that the electron density of the heterocyclic nitrogen nonbonding orbital increases significantly ($\sim 0.25\text{ e}$) on excitation due to the overlap of this orbital with the π^* molecular orbital.⁽⁸⁵⁾ This increase in electron density, in addition to creating a larger static dipole moment in the S_1 electronic state, gives rise to stronger H-bonding interactions with the surrounding medium, thereby increasing the effective volume of the reorienting species. Simon's group put forth an alternative explanation for the state-dependent reorientation behavior seen for the oxazines, suggesting that the state-dependent change in the static dipole moment of the oxazine is responsible for changes in the strength of

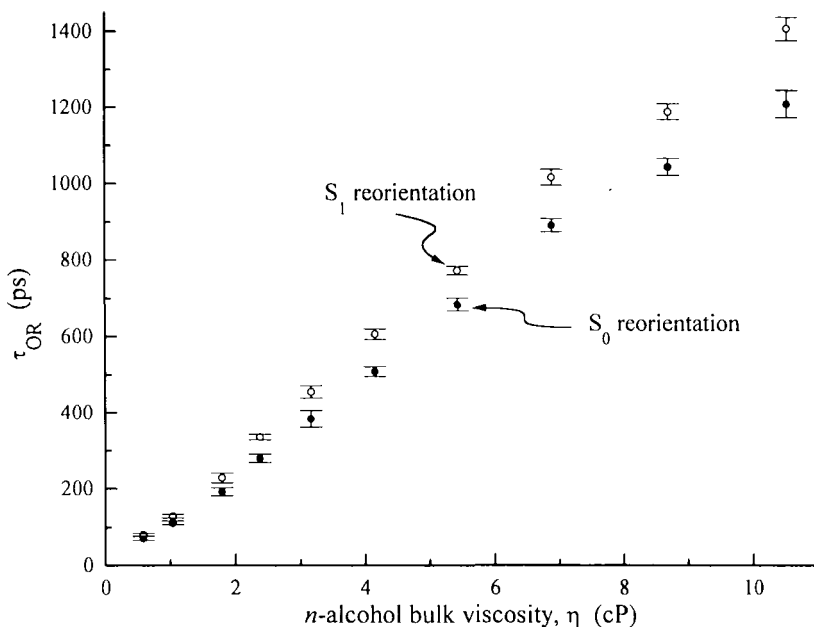


Figure 7.4. Reorientation times for S_0 and S_1 oxazine 725 in the n -alcohols methanol through n -decanol. (Reprinted (in part) with permission from *J. Phys. Chem.* 92, 6303–6308 (1988), ©1988 American Chemical Society.)

Table 7.1. State-Dependent Rotational Diffusion Times for Oxazine 725 in *n*-Alcohols^a

Solvent	$S_0 \tau_{\text{OR}}$ (ps)	$S_1 \tau_{\text{OR}}$ (ps)
CH ₃ OH	72 ± 5	82 ± 3
C ₂ H ₅ OH	112 ± 5	129 ± 5
<i>n</i> -C ₃ H ₇ OH	193 ± 10	229 ± 13
<i>n</i> -C ₄ H ₉ OH	281 ± 11	337 ± 7
<i>n</i> -C ₅ H ₁₁ OH	385 ± 22	456 ± 16
<i>n</i> -C ₆ H ₁₃ OH	509 ± 13	607 ± 14
<i>n</i> -C ₇ H ₁₅ OH	685 ± 17	773 ± 11
<i>n</i> -C ₈ H ₁₇ OH	892 ± 17	1017 ± 21
<i>n</i> -C ₉ H ₁₉ OH	1045 ± 22	1190 ± 21
<i>n</i> -C ₁₀ H ₂₁ OH	1210 ± 36	1409 ± 31
(CH ₃) ₂ SO	266 ± 20	279 ± 14

^aReprinted (in part) with permission from *J. Phys. Chem.* 92, 6303–6308 (1988), ©1988 American Chemical Society.

dielectric frictional contributions to the interaction between the solvent and the solute.⁽⁸⁴⁾ This explanation, while not at odds with the data on oxazine 725, fails to account for the larger body of data on oxazine reorientation in many solvents. The dielectric friction contribution to the reorientation of the molecule depends on the magnitude of the solute dipole moment and the longitudinal relaxation time of the solvent, as indicated in Eq. (7.9). Solvents that exhibit strong H-bonding interactions have long longitudinal relaxation times, and the effects of dielectric friction on the solute reorientation time should be maximized. There are several ways to determine experimentally whether a site-specific solvent–solute interaction or state-dependent changes in the dielectric friction explain the state-dependent reorientation behavior seen for the oxazines. One method is to measure reorientation times for both ground-state and excited-state oxazines in a binary solvent system, where the reorientation dynamics of a particular oxazine are observed to be state independent in one constituent and state dependent in the other.⁽³⁹⁾ Controlling the concentration of the “active” solvent in the solution and monitoring the state-dependent reorientation behavior allow the determination of a formation constant for the solvent-excited solute complex responsible for the state-dependent reorientation behavior. We performed this experiment for oxazine 4 in acetonitrile–methanol solutions (Figure 7.5 and Table 7.2).

Our data demonstrated that the reorientation dynamics of oxazine 4 in acetonitrile are state independent, and the addition of a H-bonding solvent, such as methanol, to the acetonitrile–oxazine solution causes the reorientation dynamics of the probe molecule to become state dependent.⁽³⁹⁾ This result is significant for two reasons. First, the reorientation time of the oxazine 4 molecule in either solvent is ~50 ps, and this time constant is significantly faster

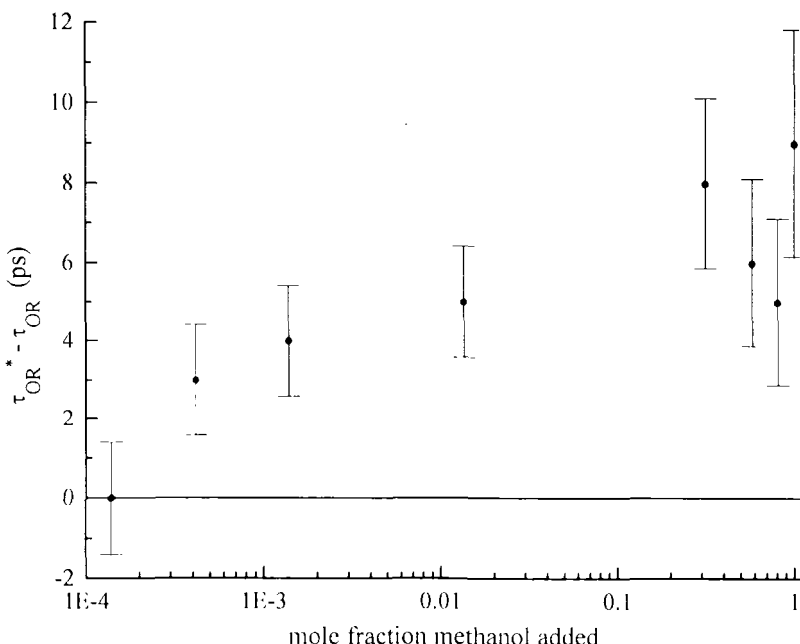


Figure 7.5. Difference between S_1 and S_0 reorientation times for oxazine 4 in the acetonitrile-methanol binary solvent system. The data indicate the presence of a complex between methanol and excited oxazine 4. For neat acetonitrile, $\Delta\tau_{\text{OR}} = 0 \pm 2$ ps, and this point is not shown because of the logarithmic scale used for X_{MeOH} . (Reprinted (in part) with permission from *Anal. Chem.* 61, 2394–2398 (1989), ©1989 American Chemical Society.)

Table 7.2. State-Dependent Reorientation Time of Oxazine 4 in Methanol/Acetonitrile Solutions^a

Mole fraction CH_3OH in CH_3CN	$S_0\tau_{\text{OR}}$ (ps)	$S_1\tau_{\text{OR}}$ (ps)
0	57 ± 2	57 ± 3
0.000138	49 ± 1	49 ± 1
0.000414	48 ± 1	51 ± 1
0.00138	48 ± 1	52 ± 1
0.0136	51 ± 1	46 ± 1
0.0315	55 ± 2	63 ± 1
0.0580	61 ± 1	67 ± 2
0.0805	69 ± 1	74 ± 2
1	88 ± 2	97 ± 2

^aReprinted (in part) with permission from *Anal. Chem.* 61, 2394–2398 (1989), ©1989 American Chemical Society.

than the time expected for a diffusion-limited complex formation to occur for these dilute solutions; $[O \times 4^*] \sim 10^{-7} M$, $[MeOH] \sim 10^{-3} M$ at the onset of complexation. Therefore, the distribution of methanol in the oxazine–acetonitrile solution is not uniform, but there is aggregation of the methanol about the polar (ionic if dissociated) probe molecule. The second reason that this result is important is that it provides direct proof that dielectric friction is not the operative mechanism for the state-dependent reorientation behavior seen for the oxazines. While the Debye longitudinal relaxation time, τ_D is longer for methanol (56 ps) than it is for acetonitrile (4.3 ps),⁽⁸⁸⁾ the permanent dipole moment for acetonitrile (3.9 D) is significantly larger than for methanol (1.7 + D).⁽⁸⁹⁾ Thus, despite these differences, the expected state-dependent increase in τ_{OR} from τ_{df} is close to the same for acetonitrile and methanol, because the large ϵ_0 for each solvent makes the τ_{df} contribution very small compared to the frictional τ_{OR} term. If dielectric friction does account for the experimental state-dependent reorientation, then we should observe it in both methanol and acetonitrile. The absence of state-dependent reorientation of oxazine 4 in acetonitrile and its presence in methanol is a direct demonstration of the unimportance of dielectric friction to these data. From our reorientation measurements of oxazine 4 in the methanol–acetonitrile binary system, we found that K_f for the excited oxazine/methanol complex is $\sim 350 M^{-1}$. While this is a comparatively small value for a formation constant, it is important to understand how these comparatively subtle effects can be detected sensitively using ultrafast stimulated-emission spectroscopy in conjunction with other measurements.

Another experiment that can be used to determine the importance, or not, of dielectric friction to state-dependent reorientation dynamics is to determine the extent to which the reorientation of the cationic oxazine chromophore depends on the identity of its counterion in solution.⁽⁴⁰⁾ Evidence for ionic association in solution suggests that intermolecular complexation rather than nonspecific dielectric effects would be responsible for the observed behavior. In order to test this hypothesis we measured the ground-state and excited-state reorientation times of oxazine 725 perchlorate and oxazine 725 chloride in several polar organic solvents. The concentration of the chromophore is low enough ($\sim 10^{-5} M$) that the ions should be dissociated completely. The experimental data indicated that ionic complexation is important in some solvents but not others. The demonstration of this ionic association indicates that site-specific solvent–solute as well as ionic interactions can be important to rotational diffusion measurements. There is little direct evidence for the dominance of dielectric friction in these systems. Understanding the reorientation behavior of oxazines at this level of detail is possible because of the direct comparison of S_0 and S_1 dynamics that ground-state depletion recovery and stimulated-emission measurements offer.

7.4. Measuring Vibrational Population Relaxation Using Stimulated Emission

Measurements of vibrational population relaxation using ultrafast stimulated-emission spectroscopy require a more detailed understanding of the form of the stimulated-emission signal than do the rotational diffusion experiments. For rotational diffusion measurements, it is the difference between stimulated signal intensities parallel and perpendicular to the excitation polarization that yields the information of interest (see Eq. 7.10). For T_1 measurements, it is important to ensure the absence of reorientation contributions to the stimulated-emission signal. For such measurements the polarization of the probe laser electric field is adjusted to be at 54.7° with respect to that of the pump laser electric field. The quantity of interest related to T_1 relaxation in the stimulated-emission response of a given molecule is the time course of the population of a state pair rather than the orientational re-randomization of an ensemble of molecules. If the stimulated- and spontaneous-emission responses of a given molecule were identical, then the form of the stimulated-emission population relaxation signal would be

$$I(t) = I_0 \exp(-t/\tau_{\text{ste}}) \quad (7.12)$$

where

$$\tau_{\text{fl}} = \frac{\phi_{\text{fl}}}{k_{\text{rad}}} = \frac{c^3}{8\pi\hbar\nu^3} \tau_{\text{ste}} \quad (7.13)$$

and τ_{ste} is the stimulated-emission time constant. The experimental stimulated-emission intensity decay would be that of a single exponential. Experimentally, the pump–probe stimulated response is invariably more complex than that of the spontaneous response for times well beyond the instrumental response function, and we understand this added complexity in the context of the higher degree of state specificity inherent to stimulated measurements, as noted. The starting point for interpreting most stimulated-emission measurements is, however, to assume that the signal is, at least qualitatively, the same as that of a spontaneous-emission measurement; i.e., despite the fact that the final state of the emission process is defined, its population does not play a role in the observed experimental signal. A closer examination of the measurement indicates that the population of the final (vibrational) state does indeed play a deterministic role in the evolution of the stimulated-emission signal shortly after excitation.

Our initial investigations of stimulated-emission spectroscopy, using the nonpolar probe molecule perylene, indicated the presence of transient structure

in its stimulated-emission spectrum (Figure 7.6).⁽⁵¹⁾ This transient structure, with maxima present at frequencies shifted from the spectroscopic origin by Raman resonances, persisted for less time than the excited state (S_1) lifetime but significantly longer than the instrumental response function. This apparently anomalous response, not seen in corresponding spontaneous-emission measurements, cannot be due to either excited state-absorption or stimulated Raman gain because its persistence time is intermediate between that expected for these processes. To understand the nature of this response, we consider that both spontaneous and stimulated-emission from S_1 contribute to the population of the ground-state vibrational levels of the perylene molecule. After initial excitation of the S_1 state with a short laser pulse, spontaneous emission begins to populate the ground-state vibrational levels of perylene according to the Franck–Condon factors for each vibronic transition. The equilibrium fractional population of

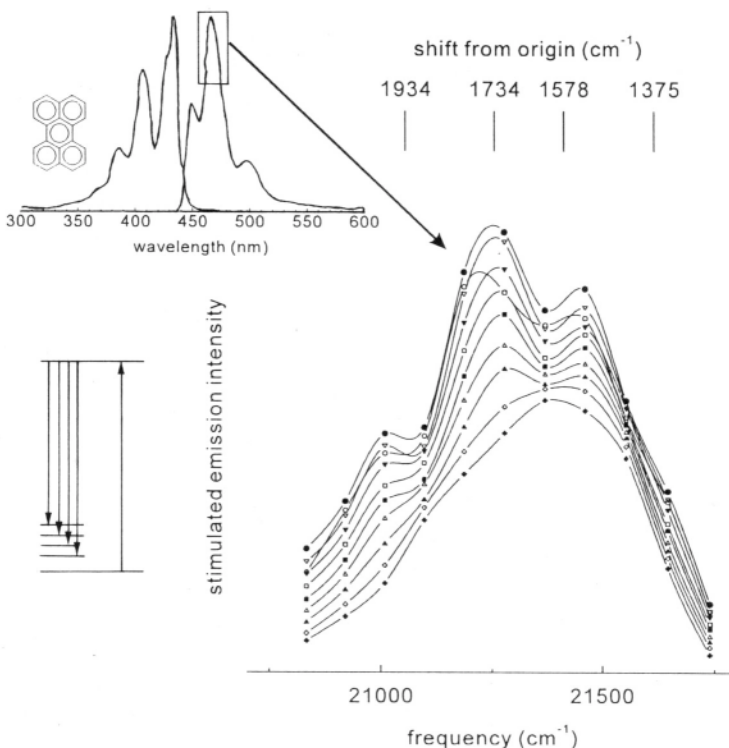


Figure 7.6. Stimulated-emission response of perylene in *n*-octane. Family of stimulated spectra shown are for time delays of 10 ps and 100 ps to 900 ps in 100-ps intervals. The transient resonances are shifted from the spectroscopic origin of perylene by Raman resonance frequencies. The boxed region of the linear response spectrum indicates the region over which the stimulated spectra were taken.

each ground-state vibration will be given by $(k_{\text{spe}}/k_{\text{vib}}) \times N(S_1)$, where k_{spe} is the spontaneous-emission rate constant for S_1 depopulation and k_{vib} is the vibrational population relaxation rate constant for the mode of interest. The time it takes a given vibrational state to achieve this equilibrium population will be determined approximately by k_{vib} for $k_{\text{vib}} \gg k_{\text{spe}}$. The time evolution of the population of the ground-state vibration does, in fact, contribute substantially to the stimulated-emission response, and we describe this contribution in detail.

For the stimulated-emission experiments outlined, the probe laser electric field couples the vibrationless excited state to the ground-state vibrational level. Because the ensemble of probe molecules that interact with the probe electric field will be distributed between those in $S_1^{v=0}$ and $S_0^{v=1}$, both stimulated-emission and absorption transitions will occur, with the relative population of the two states determining the contribution of each process to the overall response. In any such measurement, the form of the stimulated signal is necessarily gain (stimulated-emission) – loss (absorption), and it is the time course of the fractional contribution of each of these processes that gives rise to the nonexponential form of the stimulated response in the time domain (Figure 7.7). Because of the way in which the pump (excitation) and probe (stimulating) laser pulse trains are modulated, the form of the signal is actually the sum of the stimulated-emission and absorption

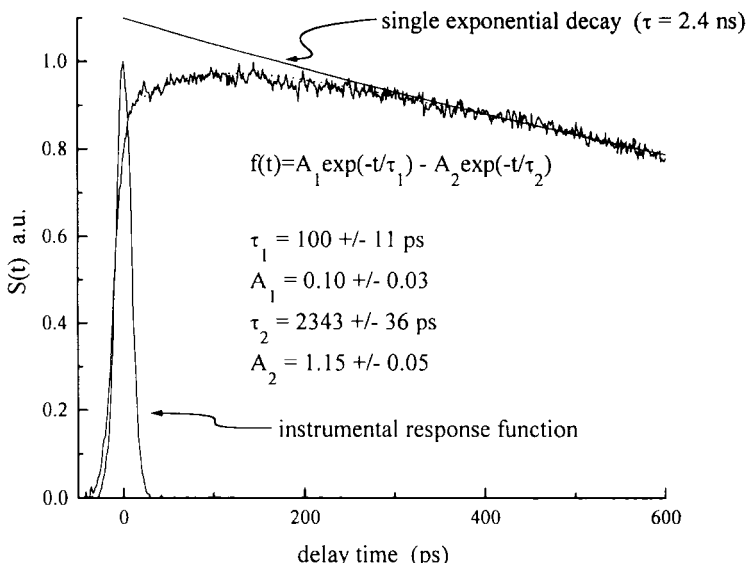


Figure 7.7. Stimulated response $S(t)$ of the v_5 mode (1578 cm^{-1}) of perylene in n -octane. The straight line indicates the form of a single-exponential decay response. The instrumental cross correlation and the fitted data are also shown.

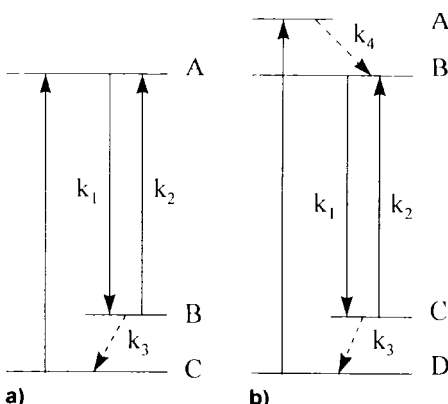
processes. Although the details of the experimental laser beam modulation scheme are more complex,⁽⁶²⁻⁶⁵⁾ as we discussed, we consider for conceptual purposes that the pump laser electric field imposes a sinusoidal amplitude modulation, ω_{mod} , on the excited-state population (level A in Figure 7.8a). For an unmodulated probe laser electric field applied at a time t after excitation, the stimulated-emission signal ($A \rightarrow B$) will appear as a sinusoidal gain at ω_{mod} , and the absorption component of the signal $I(B \rightarrow A)$ will appear as a sinusoidal loss, also at ω_{mod} , but because of the sign of the population change with respect to the ambient conditions for the emitting and absorbing states, the phase of the gain modulation is shifted by π from the phase of the loss modulation. That is, when stimulated-emission from A to B is maximized, absorption from B to A will be minimized, and *vice versa*.

$$\begin{aligned} \text{Gain}(\omega_{\text{mod}}, t) &= A(t) \sin(\omega_{\text{mod}}t) & \text{Loss}(\omega_{\text{mod}}, t) &= B(t) \sin(\omega_{\text{mod}}t + \pi) \\ S(\omega_{\text{mod}}, t) &= \text{Gain}(\omega_{\text{mod}}, t) - \text{Loss}(\omega_{\text{mod}}, t) \\ S(\omega_{\text{mod}}, t) &= A(t) \sin(\omega_{\text{mod}}t) - B(t) \sin(\omega_{\text{mod}}t + \pi) = (A(t) + B(t)) \sin(\omega_{\text{mod}}t) \end{aligned} \quad (7.14)$$

With synchronous demodulation detection, $S(t) = A(t) + B(t)$ can be obtained. The coupled differential equations that describe the time-dependent population changes for the three-level system Figure 7.8a are⁽⁹⁰⁾

$$\begin{array}{l} A \xrightleftharpoons[k_2]{k_1} B \xrightarrow{k_3} C \\ \frac{dA}{dt} = -k_1 A + k_2 B \\ \frac{dB}{dt} = k_1 A - (k_2 + k_3) B \\ \frac{dC}{dt} = k_3 B \end{array} \quad (7.15)$$

Figure 7.8. (a) Schematic three-level system for stimulated-emission measurements where the 0–0 is excited. In this diagram, k_1 is the sum of the stimulated- and spontaneous-emission rate constants, k_2 is the absorption rate constant for the $A \leftrightarrow B$ transition, and k_3 is the vibrational population relaxation rate constant. (b) Schematic four-level system for stimulated-emission measurement where a vibronic transition is pumped instead of the origin. The rate constants k_1 , k_2 , and k_3 are analogous to those in (a), and k_4 is the relaxation rate constant for the excited-state vibration.



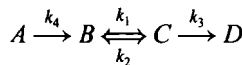
For this model, k_1 is the sum of the spontaneous- and stimulated-emission rate constants. Assuming instantaneous population of state A at time $t = 0$, integration of Eqs. (7.15) yields expressions for $A(t)$ and $B(t)$, which are combined to produce $S(t)$.^(51,90)

$$S(t) = A(t) + B(t) = \frac{k_2 + k_3}{k_3 - k_1} A_0 \exp(-k_1 t) - \frac{k_2 + k_1}{k_3 - k_1} A_0 \exp(-k_3 t) \quad (7.16)$$

Here, A_0 is the initial population placed in state A by $\sim \delta(t)$ excitation from the pump electric field. We assume implicitly that $k_3 > k_1 \sim k_2$, and for cases where this condition does not hold, the exponential terms do not correspond simply to k_1 and k_3 relaxations. The negative sign preceding the exponential term containing k_3 indicates the measured signal should exhibit an initial buildup followed by a decay, and this is the form of the signal we observe experimentally. The magnitudes of the preexponential factors give the relative contribution of the two terms, and because $k_3 > k_1$ the second term in Eq. (7.15) will appear as a small initial buildup compared to the dominant k_1 term.

Experimental techniques have been developed to measure T_1 relaxation in the time and frequency domains.^(91–112) Most time-domain techniques use short infrared laser pulses to populate the vibrational state of interest selectively, and several schemes have been devised to monitor this population subsequent to its creation. While IR lasers are a useful light source for populating molecular vibrations, tunability is often limited with these systems. The stimulated-emission technique populates the vibrational state of interest using easily tunable visible lasers, making it possible to populate probe molecule vibrational resonances selectively that are functionally degenerate with vibrational resonances in the surrounding solvent.^(51–53) Such an experiment is not feasible with IR lasers because, for such a condition, the solvent would absorb virtually all of the incident radiation rather than the probe molecule of interest. Also, using visible lasers, it is possible to select vibrational resonances between $\sim 300\text{ cm}^{-1}$ and $\sim 3000\text{ cm}^{-1}$ by tuning over a $\sim 100\text{-nm}$ probe laser wavelength range.

The description of vibrational population relaxation measurement in a coupled three-level system presumes that the initial excited electronic state is the vibrationless excited electronic state, and not a higher vibronic level in the S_1 manifold. In addition, T_1 relaxation can be measured for vibrations in the S_1 electronic state of a probe molecule by using this stimulated-emission technique. The essential form of the relaxation process is similar to that in Eqs. (7.15) and (7.16), but with a different initial population condition and with an additional state to consider (Figure 7.8b).^(43,53)



$$\begin{aligned}\frac{dA}{dt} &= -k_4 A & \frac{dB}{dt} &= k_3 A - k_1 B + k_2 C \\ \frac{dC}{dt} &= k_1 B - (k_3 + k_2) C & \frac{dD}{dt} &= k_3 C\end{aligned}\quad (7.17)$$

For the three-level system, it was assumed implicitly that $k_3 > k_1 \sim k_2$ and we apply this same assumption plus one other, $k_4 \sim k_3$, for the solution of the four-level system. Integration of these equations yields

$$S(t) = B(t) + C(t)$$

$$\begin{aligned}S(t) &= A_0 k_4 \left\{ \frac{k_2 + k_3}{(k_3 - k_1)(k_4 - k_1)} \exp(-k_1 t) + \frac{k_2 + k_1}{(k_3 - k_1)(k_3 - k_4)} \exp(-k_3 t) \right. \\ &\quad \left. + \frac{k_1 + k_2 + k_3 - k_4}{(k_4 - k_1)(k_4 - k_3)} \exp(-k_4 t) \right\}\end{aligned}\quad (7.18)$$

The experimental signal from our experiments contains three exponential terms. In principle, one can fit the experimental decay curve by using Eq. (7.18), but with five variable parameters and a finite signal-to-noise ratio it is difficult to obtain fits to the data where the fitted parameters are sufficiently independent of one another. This problem is easily overcome. Because of the information obtained from experiments exciting the origin, we can determine k_4 with acceptable certainty. With k_1 and k_3 data from the 0–0 excitation experiments, either the raw data from the blue excitation experiments can be fitted directly or the difference between blue and red excitation data can be taken and fitted. It is possible for a ground-state vibrational mode and an excited-state vibrational mode to decay with the same time constant (i.e., $k_3 = k_4$). If this condition were to occur, it would lead to undefined preexponential terms in Eq. (7.18). Such a condition does not pose a problem experimentally because the ground-state and excited-state vibrational modes used in the measurements can be different, as long as the same ground-state vibrational mode is used for both excitation frequencies in the determination of the excited-state T_1 time. In fact, we use that approach for acquiring T_1 times in the first excited singlet electronic state (S_1) of perylene. This additional ability to measure the relaxation of vibrational energy in different electronic states is useful in determining the role that the electronic excitation plays in the relaxation of energy both to its surroundings and through intramolecular dissipation.

7.4.1. Chemical Information Content of Ultrafast Stimulated-Emission T_1 Measurements: Perylene and 1-Methylperylene in *n*-Alkanes

With this understanding of the transient stimulated-emission response, we now consider the chemical information content of T_1 measurements. We first consider the role that electronic excitation plays in the relaxation of vibrational energy for perylene in *n*-alkanes. Next we examine in detail how perylene dissipates vibrational energy to surrounding *n*-alkanes, and we conclude with a discussion of the coupling mechanism(s) that operate in nonpolar systems.

7.4.2. T_1 Relaxation in Different Electronic States

There have been a number of studies of both ground-state T_1 relaxation and vibrational population relaxation in excited electronic-state manifolds.⁽⁹¹⁻¹¹⁷⁾ A basic question that must be addressed to understand whether there is a correspondence between T_1 times for different electronic states is whether the T_1 times measured for a vibrational mode depend on the electronic state of the molecule. It is not unreasonable to expect T_1 in different electronic states to be different because, for many molecules, the excited-state vibrational frequencies differ slightly from those in the ground electronic state. Changes in the vibrational resonance frequencies for a given molecule could give rise to state-dependent resonance detuning effects, but significantly more important than this small effect is that the state-dependent change in vibrational frequencies implies that the potential energy surfaces for the two electronic states are different for a given vibration, and therefore the anharmonic coupling between individual vibrational modes will be, in general, different for the two electronic states. Any significant change in T_1 relaxation times for a vibration in two electronic states will be dominated by state-dependent differences in intramolecular relaxation processes rather than intermolecular energy transfer. We describe how ultrafast stimulated-emission measurements of T_1 in the S_0 and S_1 states of perylene demonstrate state-dependent vibrational population relaxation behavior, and that both intermolecular and intramolecular relaxation contributions can be inferred, depending on the vibrational mode and electronic state accessed.⁽⁵³⁾

To make these measurements, a necessary first step is to determine the appropriate pump and probe wavelengths. From the linear optical response of perylene in the solvents used, we can determine its spectroscopic origin. This information, in conjunction with the Raman response of perylene, allows us to select specific vibrational resonances. The steady-state absorption and emission spectra of perylene in *n*-hexane are shown in Figure 7.9. For excitation of the perylene 0-0 transition, the pump laser is set to the wavelength indicated by the arrow labeled “0-0” in Figure 7.9, and for excitation of the v_7^* mode the pump

laser wavelength is at $\sim 1400 \text{ cm}^{-1}$ above the origin, indicated by arrow “0- v ” in Figure 7.9. While the v_7 mode has a characteristic frequency of 1373 cm^{-1} in S_0 , it shifts to $\sim 1390 \text{ cm}^{-1}$ in S_1 .⁽¹¹⁸⁾ The v_7 mode in perylene is an in-plane α_g Raman active ring distortion mode. As discussed, the difference in vibrational resonance frequencies between the ground and excited electronic states indicates that the potential surface for this vibration differs for the two electronic states.

Before we discuss our results for the v_7 and v_7^* population relaxation times, we return briefly to consider the acquisition and analysis of the raw data. As noted, the determination of ground-state and excited-state T_1 relaxation times is done by performing two groups of experiments. First, the v_7 mode T_1 time is determined by exciting at the 0-0 transition, and, second, measurements containing information on the v_7^* mode are made by exciting at $v_{0-0} + 1390 \text{ cm}^{-1}$. In the first group of experiments, the v_7 mode (state B in

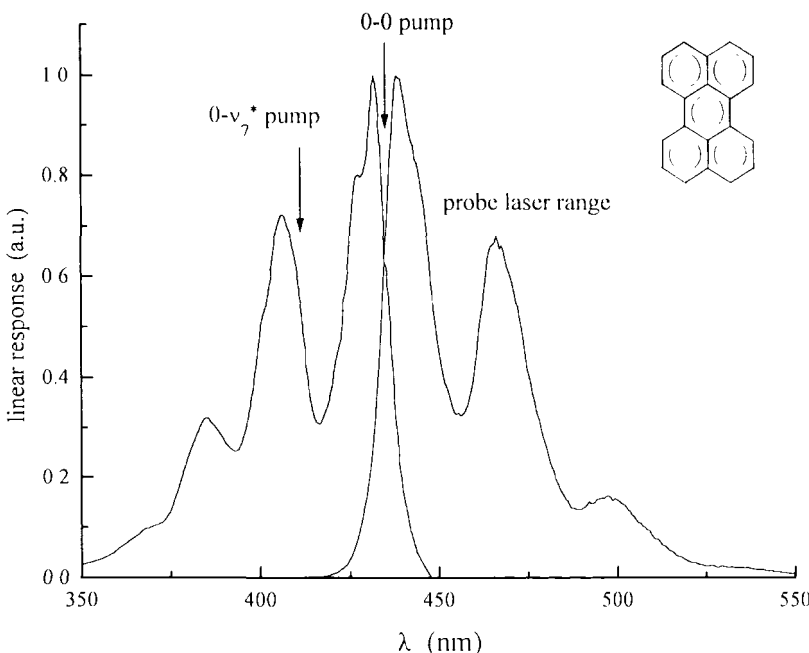


Figure 7.9. Absorption and emission spectra of perylene in *n*-hexane. The arrows indicate the transitions excited and the boxed region indicates the spectral region probed. (Reprinted (in part) with permission from *J. Phys. Chem.* 98, 9411–9416 (1994), ©1988 American Chemical Society.)

Figure 7.8a) was accessed directly. For the second group of experiments, the ground-state v_5 mode (state C in Figure 7.8b) was used instead of the v_7 mode. For a given vibrational mode, it is possible that T_1 and T_1^* can be the same, and if this condition exists it leads to a difficulty in the extraction of T_1 information from our data (see Eq. 7.18). By using different ground- and excited-state vibrational modes, the possibility of $k_3 = k_4$ is diminished but not eliminated. In fact, for perylene in *n*-pentane, $k_3(v_5) \sim k_4(v_7^*)$, but because the agreement is not exact, we are able to extract information about v_7^* from the stimulated signal. For the 0–0 excitation experiments on both the v_7 and v_5 modes, T_1 information is extracted from the raw data by least-squares fitting. For the v_7^* mode, the k_1 and $k_3(v_5)$ data are used to fit the data from the v_7^* excitation experiments to obtain k_4 . The difference signal $\Delta S(t)$ (0– v_7^* excitation response – 0–0 excitation response) is of the form (Eqs. 7.18–7.16),

$$\begin{aligned}\Delta S(t) = & \left(\frac{k_2 + k_3}{k_3 - k_1} \right) \left(\frac{k_4 A_0}{k_4 - k_1} - B_0 \right) \exp(-k_1 t) \\ & + \left(\frac{k_2 + k_1}{k_3 - k_1} \right) \left(\frac{k_4 A_0}{k_3 - k_4} - B_0 \right) \exp(-k_3 t) \\ & + \left(\frac{k_4 A_0 (k_1 + k_2 + k_3 - k_4)}{(k_4 - k_1)(k_4 - k_3)} \right) \exp(-k_4 t)\end{aligned}\quad (7.19)$$

Both the 0–0 and v_7^* excitation time scans are shown in Figure 7.10a for stimulation of the transition between the $S_1^{v=0}$ and $S_0^{v=v_5}$ mode in *n*-hexane; $\Delta S(t)$ is shown in Figure 7.10b. The $T_1 (= k_3^{-1})$ and $T_1^* (= k_4^{-1})$ population relaxation times for v_5 , v_7 , and v_7^* in the three *n*-alkanes we studied are given in Table 7.3. The v_5 mode exhibits a solvent-dependent T_1 relaxation time and v_7 mode does not. These data on the perylene v_5 and v_7 modes are consistent with the solvent- and mode-dependent T_1 relaxation behavior seen for other modes in a wider range of solvents. We discuss these data in the next section.

T_1 for the perylene v_7 mode is the same for the three *n*-alkanes (pentane, hexane, and heptane) to within the experimental uncertainty. Likewise, T_1^* for the v_7^* mode is the same for perylene in each of the three solvents, and in all cases $T_1^* < T_1$. As discussed, there are two possible reasons for the difference between T_1 and T_1^* for these modes. The first is that the state dependence arises from intramolecular changes in the coupling between the vibrational modes of interest and lower-energy modes. A difference in anharmonic coupling between modes in the two electronic states is possible, as indicated by the $\sim 17\text{-cm}^{-1}$ blueshift of v_7 on excitation. Indeed, there are several vibrational modes, some IR active and some Raman active, in close energetic proximity to v_7 and v_7^* ,^(118–122) and the state-dependent frequency shifts seen for these modes are not, in general, the

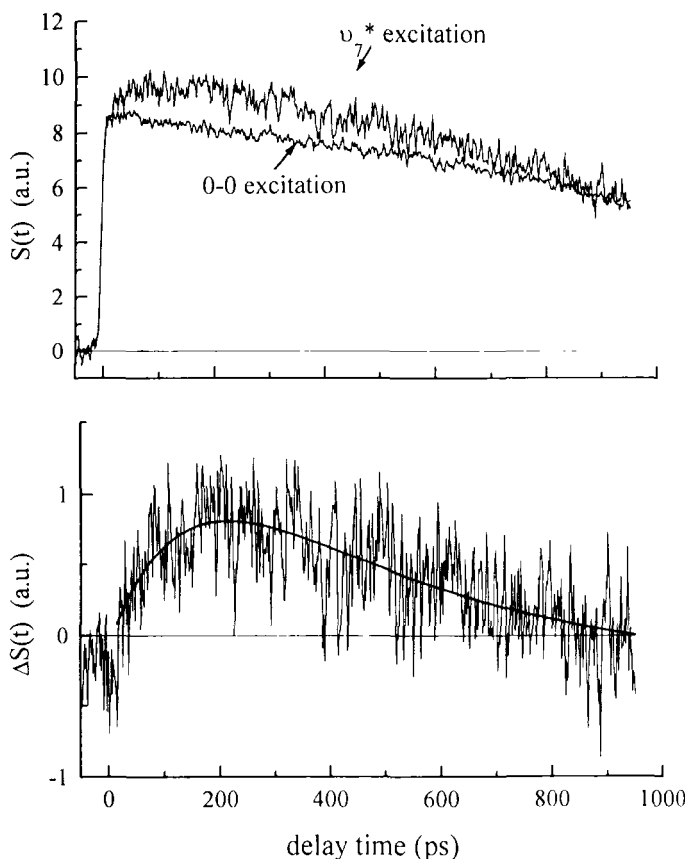


Figure 7.10. (a) Experimental $S(t)$ data for excitation at the $0-0$ transition and the $0-v_7^*$ transition. (b) Difference signal, $\Delta S(t)$ with fitted line. (Reprinted (in part) with permission from *J. Phys. Chem.* 98, 9417–9421 (1994), ©1994 American Chemical Society)

Table 7.3. Ground- and Excited-State T_1 Times for Perylene in Selected n -Alkanes^a

Solvent	$T_1(v_5)$ (ps) 1578 cm^{-1}	$T_1(v_7)$ (ps) 1375 cm^{-1}	$T_1^*(v_7^*)$ (ps) 1390 cm^{-1}
$n\text{-C}_5\text{H}_{12}$	160 ± 37	276 ± 46	141 ± 2
$n\text{-C}_6\text{H}_{14}$	300 ± 100	281 ± 177	150 ± 17
$n\text{-C}_7\text{H}_{16}$	308 ± 41	355 ± 100	129 ± 71

^aReprinted (in part) with permission from *J. Phys. Chem.* 98, 9417–9421 (1994), © 1994 American Chemical Society.

same as those seen for ν_7 and ν_7^* . Any coupling between these modes will necessarily vary with the potential energy surface anharmonicity characteristic of each mode as well as their frequency differences. We note that, because we are working in a room-temperature liquid and the spectral resolution of our system is $\sim 10 \text{ cm}^{-1}$, it is not possible to separate anharmonic coupling effects from the nonselective simultaneous excitation of several nearly degenerate modes. The second possible reason for the difference in T_1 and T_1^* is that the *intermolecular* relaxation pathways available to ν_7 and ν_7^* differ significantly. If intermolecular relaxation does, in fact, change significantly for the two electronic states, then a noncollisional $v-v$ energy transfer process must be operative, because the frequency of solvent-solute collisions does not depend on the electronic state of either the solute or the solvent. Any state-dependent change in the inelastic collisional rate would require substantial local heating on excitation and, for our experimental conditions, the transient temperature rise does not exceed several Kelvins. A prerequisite for the dominance of a noncollisional energy transfer mechanism is, of course, that there be a solvent vibrational resonance in the energetic vicinity of the perylene $\sim 1375 \text{ cm}^{-1}$ (ν_7) mode(s). Linear alkanes exhibit an IR active vibrational resonance at 1378 cm^{-1} , assigned as a rocking motion of the terminal CH_3 groups, and thus there is a virtually degenerate acceptor state available to the perylene ν_7 mode. Due to the linewidths of the donor and acceptor transitions, it is likely that ν_7 and ν_7^* are essentially at a $\Delta\nu = 0$ condition, and state-dependent differences in the potential energy surfaces of these modes which give rise to electronic state-specific intramolecular relaxation dominate this response. In the next section, we examine T_1 relaxation in S_0 perylene under conditions where solvent-dependent variations in *intermolecular* relaxation dominate the experimental data.

7.4.3. Solvent-Dependent T_1 Relaxation Dynamics of S_0 Perylene

As discussed in the previous section, measuring the state-dependent T_1 relaxation behavior of a specific vibrational resonance in two electronic states can provide at least some insight into the role of intramolecular vibrational population relaxation. While intramolecular processes can be important in determining the fate of the population in a given vibrational mode, it is clear that, at some point, the molecule excited originally will dissipate the excess energy into its surroundings, and therefore intermolecular energy transfer is the important physical process.⁽¹²³⁻¹³²⁾ In order to examine intermolecular relaxation, it is necessary to find experimental conditions where the intramolecular contribution to T_1 relaxation is nominally constant for a solvent series. We have chosen a series of *n*-alkanes because of the absence of strong polar intermolecular inter-

actions in these solvents. For the alkanes, any solvent-dependent change in perylene T_1 relaxation will be dominated by intermolecular processes.

The experimental form of the T_1 data for S_0 perylene is the same as described previously. While there are a variety of Raman active vibrational modes accessible to our measurement scheme, we have focused on the relaxation dynamics of two specific vibrational resonances: the ν_7 fundamental mode at 1375 cm^{-1} and a combination mode composed of the ν_7 and the ν_{15} (358 cm^{-1}) modes at 1733 cm^{-1} . The ν_7 mode is an a_g in-plane ring deformation mode, and the ν_{15} mode (also a_g) is dominated by the in-plane stretching motion of the center ring between the two naphthalene moieties. It is necessary to use the $\nu_7 + \nu_{15}$ combination mode instead of accessing the ν_{15} mode directly because of spectral overlap of the steady-state absorption and emission bands, which prevents the experimental separation of ground-state depletion and stimulated-emission responses in the region of the $\nu_{0-0} - \nu_{15}$ probe laser resonance. The relaxation times we measure for the ν_7 and $\nu_7 + \nu_{15}$ modes depend sensitively on the identity of the *n*-alkane solvent, and this aliphatic-chain-length dependence is direct evidence for solvent structure around the perylene solute molecule.

Figure 7.7 provides an example of the experimental stimulated signal, $S(t)$. The vibrational relaxation times, $T_1 = k_3^{-1}$, in eight *n*-alkanes, pentane through hexadecane, are presented in Figure 7.11 and Table 7.4 for the perylene ν_7 and $\nu_7 + \nu_{15}$ modes. Each T_1 time is determined by regression of the average of at least 15 individual time scans. The large uncertainty in these values is reflective of the comparatively small contribution of the k_3 process to the overall transient gain response (Eq. 7.16). For the ν_7 mode, T_1 ranges from $30 \pm 3\text{ ps}$ in *n*-octane and $< 10\text{ ps}$ in *n*-hexadecane to $\sim 300\text{ ps}$ in the other *n*-alkanes. We have not attempted to determine the exact T_1 values for the few cases where the relaxation is complete in less than the instrumental response time. The nonmonotonic relationship between the T_1 times and solvent aliphatic chain length indicates that noncollisional (v-v) energy transfer is the dominant intermolecular relaxation process. For the $\nu_7 + \nu_{15}$ combination mode, the measured T_1 times are qualitatively similar to those for the ν_7 mode but exhibit additional efficient relaxation pathways, which are the result of relaxation via the perylene ν_{15} mode (Figure 7.11).

We interpret these data in the context of the intermolecular energy transfer mechanism and the (transient) organization of the solvent about the perylene molecule. The experimental T_1 data provide insight into intermolecular vibrational energy transfer over Angstrom-length scales. For dilute solutions, intermolecular energy exchange between perylene molecules will be insignificant because of the large average perylene-perylene intermolecular distance. We therefore center our attention on the interactions between perylene and the *n*-alkane molecules in close spatial proximity. While anharmonic coupling within

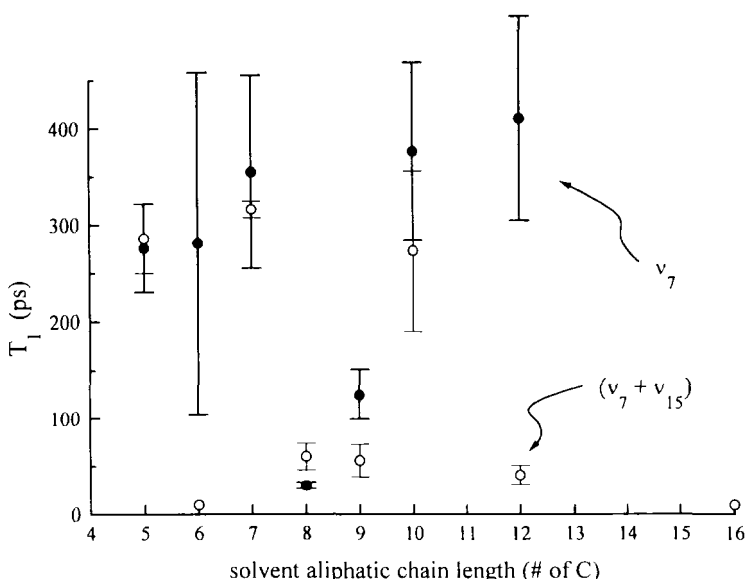


Figure 7.11. T_1 relaxation times for the perylene v_7 (●) and $v_7 + v_{15}$ (○) modes as a function of solvent aliphatic chain length. (Reprinted (in part) with permission from *J. Phys. Chem.* 98, 9411–9416 (1994), ©1994 American Chemical Society.)

perylene is significant, as is apparent from the prominence of the $v_7 + v_{15}$ combination mode and the state-dependent T_1 relaxation behavior discussed in the previous section, intramolecular energy transfer to low-energy modes will contribute little to solvent-chain-length dependence in the T_1 times that we measure,

Table 7.4. T_1 Relaxation Times for the Perylene v_7 and $v_7 + v_{15}$ Modes in *n*-Alkanes^a

Solvent	$T_1(v_7)$ (ps) 1275 cm^{-1}	$T_1(v_7 + v_{15})$ (ps) 1733 cm^{-1}
<i>n</i> -C ₅ H ₁₂	276 ± 46	286 ± 26
<i>n</i> -C ₆ H ₁₄	281 ± 177	< 10
<i>n</i> -C ₇ H ₁₆	355 ± 100	316 ± 9
<i>n</i> -C ₈ H ₁₈	30 ± 3	60 ± 14
<i>n</i> -C ₈ D ₁₈	298 ± 102	—
<i>n</i> -C ₉ H ₂₀	125 ± 26	56 ± 17
<i>n</i> -C ₁₀ H ₂₂	376 ± 92	273 ± 183
<i>n</i> -C ₁₂ H ₂₆	410 ± 106	41 ± 10
<i>n</i> -C ₁₆ H ₃₄	< 10	< 10

^aReprinted (in part) with permission from *J. Phys. Chem.* 98, 9411–9416 (1994), ©1994 American Chemical Society.

because the linear optical responses of perylene and, therefore, the relevant potential energy surfaces are virtually solvent independent. The separation of intermolecular and intramolecular relaxation processes is more likely to be accurate for a rigid molecule such as perylene than for a labile molecule, where photoisomerization or other large-amplitude molecular motions can alter the potential surface(s)^(42,133) and thereby influence the efficiency of intramolecular decay pathways.

In principle, intermolecular energy relaxation from one molecule to another can proceed by collision-mediated short-range ($v\text{-}t$, v , r) inelastic exchange processes or by longer-range resonance polar ($v\text{-}v$) coupling where no intermolecular collisions are required to execute the energy transfer.⁽¹³⁴⁾ In the gas phase, the probability of collisional ($v\text{-}t$, r) processes is typically much smaller ($\langle\langle P\rangle\rangle \sim 10^{-5}$) than for collisional ($v\text{-}v$) processes ($\langle\langle P\rangle\rangle \sim 10^{-3}$).¹³⁴ For most experimental conditions, especially in the liquid phase, the dominant relaxation pathway will be through ($v\text{-}v$) coupling ($\langle\langle P\rangle\rangle \sim 0.1^{-1}$).⁽¹³⁴⁾ For perylene in the *n*-alkanes, the dominant relaxation processes must be ($v\text{-}v$) because, in *n*-alkanes, the terminal CH₃ rocking mode resonance occurs at 1378 cm⁻¹, and this resonance exhibits no discernible variation among the different *n*-alkanes. The perylene ν_7 mode is centered at 1375 cm⁻¹, functionally degenerate with the solvent CH₃ rocking bath mode. Unfortunately, we are aware of no theoretical work that treats the relative efficiency of different ($v\text{-}v$) processes in room-temperature liquids, and therefore it is necessary to borrow the essential points from gas-phase theoretical treatments in attempting to distinguish between long-range polar and short-range collisional relaxation processes. Obviously, vibrational energy transfer in liquids will be more complex than in gases. In liquids, the relevant length scales are not well defined, and intermolecular energy transfer processes between solvent molecules will have some, largely undetermined, effect on the solute–solvent energy transfer process. Nonetheless, in the absence of a theoretical treatment of liquid-phase T_1 processes, we are left to assume that the essential physics of the energy transfer process are the same in both media, save for an unknown and likely system-specific scaling factor.

With these caveats in mind, we attempt to estimate the average distance between the donor and acceptor chromophores. In gases, the probability of a ($v\text{-}v$) energy transfer event for short-range collisional transfer from donor to acceptor at exact resonance is⁽¹³⁴⁾

$$\langle\langle P\rangle\rangle = \frac{8\mu L^2 kT}{\hbar^2} |U_{if}|^2 \quad (7.20)$$

where U_{if} is a vibrational matrix element for the collisional interaction, μ is the reduced mass of the two molecules experiencing the collisional interaction, and L is the length scale over which the collisional interaction can take place; i.e., L is

the effective intermolecular distance of the colliding species when (v-v) energy transfer takes place. The value of L will depend on the chemical identities of the colliding species, and is typically taken as 0.2 Å for both (v-t) and (v-v) gas-phase collisional interactions. While the value of L may not be precisely the same in liquids, it is not likely to be much different because the fundamental nature of the interaction responsible for the energy transfer is the same in both the liquid and the gas phases. A critical point to note here is that, given the small value of L , it is clearly not representative of an internuclear distance, but rather is a point of closest contact between the van der Waals radii of the individual species. As mentioned, $\langle P \rangle \sim 10^{-3}$ for collisionally mediated short-range energy transfer. For short-range collisional processes, the probability of energy transfer does not vary smoothly with the distance between molecules. For an energy transfer event to occur, the donor and acceptor molecules must be in direct contact. In contrast, for long-range interactions, polar coupling between donor and acceptor species is the mechanism by which energy transfer takes place.⁽¹³⁴⁾

$$\langle \langle P \rangle \rangle = \frac{4\mu C^2}{\hbar^2 d^4 kT} \quad (7.21)$$

There are several formulations for long-range (v-v) energy transfer, and all yield qualitatively the same result. The term C contains information on the magnitude and relative orientations of matrix elements for the donor and acceptor vibrational transitions between which the energy is transferred. In this model $\langle P \rangle$ scales as d^{-n} , with the exact distance dependence being determined by the order of the polar intermolecular interaction (i.e., dipole-dipole, dipole-quadrupole, quadrupole-quadrupole). The length scale over which the energy transfer takes place depends sensitively on the symmetry of the vibrational resonances of both the probe and solvent molecules. We discuss this important point in the next section. At exact resonance in a condensed-phase system, where d is small, $\langle P \rangle$ is about unity. Polar energy transfer is significantly more efficient than short-range, collision-mediated (v-v) energy transfer for perylene in the *n*-alkanes, and this assertion is fully consistent with our experimental data.

The data in Figure 7.11 show that T_1 for the v_7 mode does not vary regularly with the length of the aliphatic solvent. We begin our examination of these data with a consideration of the role that intermolecular collisional energy transfer processes may or may not play in the observed data. If collisional interactions did contribute significantly to the (intermolecular) relaxation sensed by the T_1 measurements, then a smooth progression of T_1 times, proportional to the frequency of collisions between perylene and the terminal methyl groups of the alkane solvent molecules, would be expected. The frequency of inelastic collisions between the solvent and the solute varies with the solvent viscosity and

density, both of which are well-behaved functions of aliphatic chain length. In addition, the fractional concentration of CH_3 group acceptor modes will decrease smoothly as a function of aliphatic chain length. If short-range (v-v) energy transfer were responsible for the data in Figure 7.11 and Table 7.4, then inelastic collisions between perylene and *n*-octane would have to be a factor of ~ 10 more frequent than they are for either *n*-hexane or *n*-decane, which is a physically unreasonable proposition.

Long-range polar (v-v) energy transfer must therefore be the dominant intermolecular relaxation process for these chemical systems, and the solvent dependence of the T_1 data implies that the solvent exhibits some of local organization around the perylene molecule. Eq. (7.21) shows that the probability of long-range energy transfer is inversely proportional to some power of the distance between the donor and acceptor and the term C in Eq. (7.21) accounts for intermolecular alignment between the donor and acceptor transition moments.⁽³⁴⁾ The solvent acceptor mode is significantly localized on the terminal methyl groups of the alkane chains, and the efficiency of (v-v) transfer will be proportional to the distance between the perylene v_7 normal mode coordinate and the terminal methyl groups of the solvent. The anomalously fast T_1 times we measured for the perylene v_7 mode in *n*-octane and *n*-hexadecane indicate that the terminal methyl groups of these solvents are, on average, closer to the perylene molecule than the terminal methyl groups of the other *n*-alkane solvents. We consider next how to estimate the proximity of these donor and acceptor moieties.

The perylene $v_7 + v_{15}$ combination mode T_1 relaxation behavior should be a superposition of the responses of each fundamental constituent mode in the limit of modest anharmonicity. Experimentally, the solvent dependence of the T_1 times of the $v_7 + v_{15}$ mode is the same as for the v_7 mode; in addition, there is efficient coupling to the solvents *n*-hexane and *n*-dodecane, and to a lesser extent for *n*-nonane. The efficient coupling of the v_{15} mode to the surrounding bath modes is also due to (v-v) long-range resonance processes, but, in contrast to the v_7 mode, the solvent and solute resonances are not at exactly the same frequency and the length scale of the coupling may be different from for the v_7 mode because coupling may proceed from the perylene Raman active v_{15} mode to either Raman ($\Delta\alpha$) or infrared ($\Delta\mu$) active modes of the solvent. Despite these possible differences in the order of the coupling, the qualitative information content of the data on the $v_7 + v_{15}$ combination mode is similar to that for the v_7 mode. The enhanced coupling of the v_{15} mode to the solvents *n*-hexane and *n*-dodecane comes about as a result of arrangements of the solvent around the perylene molecule that are sensitive to the motions of the perylene molecule along its v_{15} normal mode coordinate. Because these motions are significantly different than those for the v_7 mode, a different solvent dependence for the relaxation of this mode is an expected result.

It is important to verify that the processes we measure are sensitive to the donor-acceptor resonance detuning. To establish the existence of a detuning dependence for T_1 relaxation, especially under conditions of efficient intermolecular energy transfer, we have measured T_1 for the perylene v_7 mode in *n*-octane- d_{18} (*n*-C₈D₁₈). For this system, $T_1 = 298 \pm 102$ ps, compared to 30 ± 3 ps in *n*-octane- h_{18} . For *n*-octane- d_{18} the CD₃ rocking mode resonance occurs at 1050 cm⁻¹, $\Delta\nu = 325$ cm⁻¹ for (v-v) relaxation from the perylene v_7 mode to this mode. We can use this detuning dependence to estimate d . The detuning dependence of $\langle P \rangle$ is⁽¹³⁴⁾

$$\langle\langle P \rangle\rangle = \frac{2\pi^2 C^2 \Delta\omega \mu}{\sqrt{12\hbar^2 d^3 \nu^* kT}} \exp\left(-\frac{\mu\xi^{*2}}{2kT}\right) \quad (7.22)$$

where

$$\xi^* = \left(\frac{2d\Delta\omega kT}{\mu}\right)^{1/3}$$

The experimental T_1 values, in conjunction with Eqs. (7.21) and (7.22), allow the estimation the average perylene-solvent methyl group spacing. For a frequency difference of ~ 300 cm⁻¹, $\langle P \rangle \sim 0.07$ for $d = 1$ Å and $\langle P \rangle \sim 0.0005$ for $d = 2$ Å. These values of $\langle P \rangle$ for perylene in *n*-octane- d_{18} yield $T_1 \sim 430$ ps for the perylene v_7 mode in *n*-octane- d_{18} for $d = 1$ Å and $T_1 \sim 4.2$ ns for $d = 2$ Å, based on the assumption that $T_1 = 30$ ps for perylene in *n*-octane- h_{18} represents $\langle P \rangle = 1$. In order to infer any solvent organization information, it is necessary to assume that the deuteration of *n*-octane does not alter the way it solvates the perylene molecule to any significant extent. Provided this assumption is valid, Eq. (7.22) provides a value of the perylene-methyl group spacing of $d \sim 0.9$ Å in the *n*-octanes. This value is based on the ratio of the perylene $v_7 T_1$ times in the two octanes, $\langle P \rangle_{\Delta\omega=0 \text{ cm}^{-1}} \sim 10 \langle P \rangle_{\Delta\omega=300 \text{ cm}^{-1}}$. The functional form of Eq. (7.22) is shown in Figure 7.12 for the two detunings.

Using this estimate of d for the *n*-octanes and *n*-hexadecane and the T_1 time of ~ 300 ps for the perylene v_7 mode in other *n*-alkanes, the average perylene-methyl group separation for these solvents can be estimated as ~ 1.7 Å (Figure 7.12). It is critical to note that if these distances were internuclear separations they would be physically unrealistic. These distances refer to the separation between the closest contact point of the two van der Waals volumes for the two molecules. There is an additional stoichiometric uncertainty involved in the interpretation of these numbers. It is not clear to what extent the terminal CH₃ rocking mode in *n*-alkanes behaves as a collective motion of both CH₃ groups, or if each CH₃ group acts as a doubly degenerate but spatially separated vibrational chromophore within an individual *n*-alkane molecule. Despite this stoichiometric

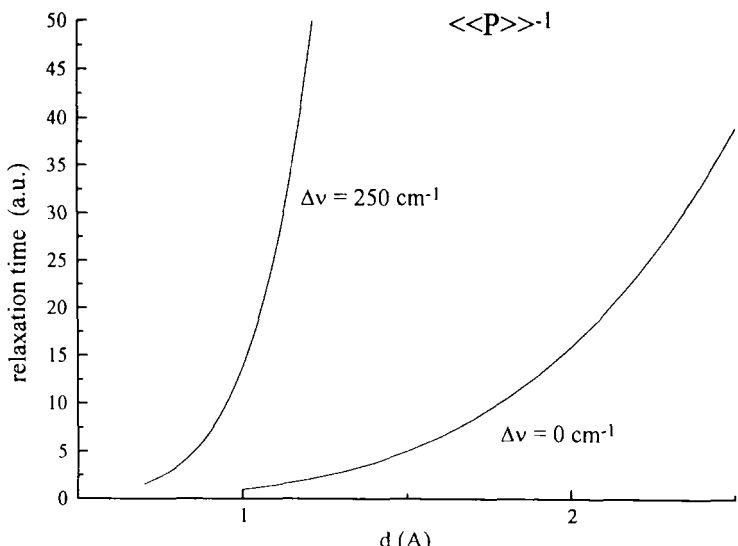


Figure 7.12. Relative relaxation time as a function of distance between donor and acceptor for resonant ($v-v$) energy transfer, from Eq. (7.22) for two donor-acceptor resonance detuning conditions.

ambiguity, the foregoing *estimates* of d seem entirely plausible for a liquid-phase system, provided that d is the point of closest proximity between van der Waals volumes.

Additionally, for *n-octane-d*₁₈ there is another vibrational mode, the CD₂ scissors motion at 1080 cm⁻¹ ($\Delta v = 295 \text{ cm}^{-1}$) which will necessarily contribute to the measured relaxation time. Both solvent modes act as acceptors for the perylene v_7 mode. Because of the resonance detuning of *n-C*₈D₁₈, we consider the role that inelastic collisional energy transfer processes may play in the data. For a frequency difference of $\Delta v \sim 300 \text{ cm}^{-1}$, $\langle P \rangle$ for collisionally mediated ($v-v$) transfer falls to $\sim 10^{-5}$, indicating that, for perylene in *n-octane-d*₁₈, the dominant relaxation mechanism remains long-range resonant ($v-v$) coupling. By way of comparison, for gas-phase T_1 relaxation, the crossover point between polar noncollisional and inelastic collisional ($v-v$) relaxation is at $\Delta v \sim 250 \text{ cm}^{-1}$.⁽¹³⁵⁾ Clearly the density of the bath medium alters this value significantly. Most liquids possess a large number of vibrational modes, and despite the high frequency of collisions in this medium it is likely that essentially all vibrational population relaxation processes in liquids are dominated by noncollisional polar energy transfer.

It is important to consider the organization of the solvent about the solute. Mode- and solvent-specific intermolecular interactions have been observed

before, and the key question in all cases is whether these intermolecular interactions can be resolved to the extent of providing transient spatial relationships between the molecules involved. The fact that perylene exhibits mode- and solvent-dependent coupling to *n*-alkanes⁽⁵¹⁻⁵³⁾ invites speculation on geometric organization of the solvent surrounding the solute. In this context, there are two observations we wish to make. The dominant motion of the ν_7 mode is a distortion of the individual naphthalene moieties, and this mode is found experimentally to couple efficiently to *n*-octane and *n*-hexadecane. The "length" of *n*-octane, if it were in an all-*trans* conformation, is quite close to that of the perylene long axis, which spans both of the naphthalene moieties. In contrast, the dominant motion of the ν_{15} mode is an in-plane stretching of the perylene central ring, and this mode is observed to couple strongly to *n*-hexane and *n*-dodecane. Because the solvent resonances to which the ν_{15} mode couples are not as well isolated on specific portions of the solvent molecules as those to which the ν_7 mode couples, the geometric implications of these data are not completely clear, but we note that the "length" of an all-*trans* *n*-hexane molecule is similar to the length of a naphthalene molecule. For both perylene modes examined, the coupling efficiency exhibits what is apparently a periodic effect; i.e., ν_7 couples to *n*-C₈H₁₈ and *n*-C₁₆H₃₄, and ν_{15} couples to *n*-C₆H₁₄ and *n*-C₁₂H₂₆. The molecular origin(s) of such a "magic number" effect are, at present, unclear, but suggest a regularity in the way aliphatic chains organize around a solute molecule. These postulations are reminiscent in some sense of Shpol'skii's work on perylene in cryogenic *n*-alkane crystals.⁽¹²²⁾ Shpol'skii observed absorption and emission spectral line narrowing for perylene in frozen *n*-alkane matrices. For a low-temperature crystalline system, local structure will persist for the lifetime of the emitting state (several nanoseconds). In liquids there is a significant body of information that points to short-range solvent structure⁽¹³⁶⁻¹⁴⁰⁾ (*vide infra*), but with a persistence time likely on the order of picoseconds at most.

The T_1 data for the ν_7 and $\nu_7 + \nu_{15}$ modes underscore the importance of solvent local organization in vibrational energy relaxation processes. The length scale over which such structure persists is not clear from the T_1 measurements alone, but other dynamical measurements, such as the rotational diffusion measurements discussed earlier, can serve to place an upper bound on the persistence length of any solvent organization. The rotational diffusion dynamics of perylene in these same *n*-alkane solvents show that, while the boundary condition changes between the solvent and the solute at ~*n*-octane, there is no discontinuous change in the viscosity dependence of the reorientation time (Figure 7.13).⁽⁸⁶⁾ A discontinuous response is expected only if there is a substantial solvent-chain-length-dependent change in solvent ordering in the vicinity of the solute. The reorientation data are sensitive to changes in the relative hydrodynamic volumes of the solute and the solvent but show no evidence of comparatively long-range solvent structure. Thus, the local structure we sense

with the T_1 measurements persists on a length scale much shorter than the perylene molecule ($\sim 10 \text{ \AA}$).

7.4.4. Understanding the Length Scales over Which Intermolecular Vibrational Energy Transfer Operates

In order to obtain a more thorough understanding of the local organization which T_1 measurements sense, it is important to understand the nature of polar coupling and the length scale over which these processes operate. 1-Methylperylene⁽⁴¹¹⁻¹⁴³⁾ is an ideal probe molecule for a comparative study aimed at achieving this understanding. We have examined 1-methylperylene in the same series of alkanes used for perylene. In contrast to the data on perylene, for 1-methylperylene the solvent dependence of the T_1 and τ_{OR} dynamical responses are correlated.⁽¹⁴⁴⁾ The significant difference between the dynamical responses for the two probe molecules can be understood at a qualitative level in terms of the symmetries of the two chromophores. We first consider the vibrational popu-

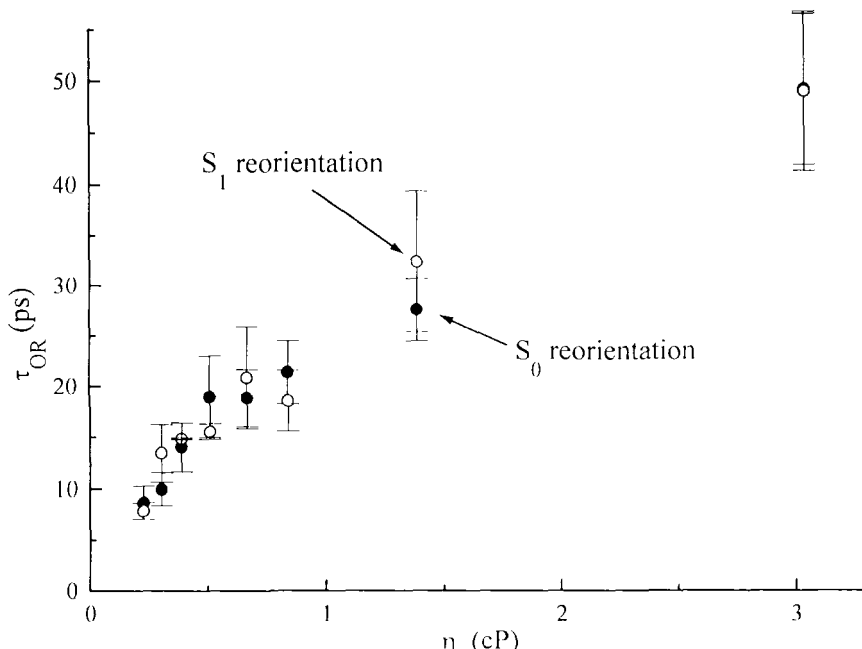


Figure 7.13. Rotational diffusion times for S_0 (●) and S_1 (○) perylene in the *n*-alkanes. The change in the dependence of τ_{OR} on solvent viscosity near C_8H_{18} indicates a change in the solvent-solute frictional boundary condition. (Reprinted (in part) with permission from *J. Phys. Chem.* 98, 6436-6440 (1994), ©1994 American Chemical Society.)

lation relaxation dynamics of 1-methylperylene and then its orientational relaxation dynamics. Comparison of these data on 1-methylperylene to those on perylene provides an understanding of the length scales over which local solvent organization is sensed using these two molecules.

7.4.5. 1-Methylperylene Vibrational Population Relaxation

As discussed, we chose to measure the perylene ν_7 vibrational mode at 1375 cm^{-1} because of its functional degeneracy with the *n*-alkane solvent terminal methyl group rocking mode. The T_1 data for perylene indicated that, for the ν_7 mode, the solvent *n*-octane organized in such a way as to place its methyl groups in closer spatial proximity to the perylene vibrational coordinate than the other alkanes, and that other vibrational modes revealed preferential organization of different *n*-alkanes along their vibrational coordinates. These results were significant in the sense that they showed the existence of local organization in *n*-alkane solutions, but their lack of correspondence with τ_{OR} data, where the length scale of the measurement is comparatively well defined, precluded the extraction of information on intermolecular distances with any degree of certainty. We expect the structural aspects of interactions between 1-methylperylene and *n*-alkanes to be essentially the same as those between perylene and *n*-alkanes, but with vibrational spectroscopic selection rules that are relaxed significantly for 1-methylperylene compared to perylene.⁽¹⁴⁵⁾ Thus, the differences in polar interactions between the two chromophores and the *n*-alkane solvents should provide information on the role of polar coupling processes in these solvents.

As a first step, it is important to understand the linear electronic and vibronic spectral responses of 1-methylperylene. The absorption and emission spectra of 1-methylperylene are shown in Figure 7.14. The electronic response of 1-methylperylene is very similar to that of perylene, except that individual features for 1-methylperylene are blueshifted by $\sim 300\text{ cm}^{-1}$ compared to perylene for a given solvent, consistent with other literature reports on this molecule.⁽¹⁴²⁾ This blue-shift is a result of steric strain imposed on the perylene rings by the methyl group at the 1-position. Semiempirical molecular orbital calculations of 1-methylperylene show that the internaphthalene dihedral angles are 13° and 23° for the dihedrals without and containing the 1-methyl group, respectively.⁽¹⁴¹⁾ Because of this distortion from planarity, we expect the rotational diffusion dynamics of this molecule to differ from that of the planar perylene chromophore.

The infrared and Raman spectra of 1-methylperylene and perylene differ significantly. The basis for this difference lies in the reduction of symmetry that results from the addition of the methyl group. Perylene (D_{2h}) contains a center of inversion. For any molecule with a center of inversion, a Raman active vibrational

mode is infrared inactive, and *vice versa*.⁽¹⁴⁵⁾ The addition of the CH_3 group to perylene lifts the center of inversion, and therefore all vibrational modes are both Raman and infrared active for 1-methylperylene. The infrared and Raman spectra of 1-methylperylene (Figure 7.15) show that the 1370-cm^{-1} mode is present in both spectra. The 1370-cm^{-1} 1-methylperylene mode is derived from the perylene 1375-cm^{-1} mode, and we base this assertion on the both experimental energies of the resonances and semiempirical calculation results.

The time constants T_1 for the 1-methylperylene 1370-cm^{-1} mode are presented in Figure 7.16 and Table 7.5. These data are significantly different from those we reported earlier for perylene. Clearly, the addition of a methyl group to the perylene chromophore alters the coupling between the solvent and the solute significantly. For short-chain solvents, *n*-pentane through *n*-octane, T_1 is fast (~ 20 ps) and changes little as the solvent aliphatic chain length increases. For the solvents *n*-decane through *n*-hexadecane, T_1 is significantly slower and slightly more solvent dependent. A transition in T_1 relaxation behavior occurs between *n*-octane and *n*-decane. The T_1 times for 1-methylperylene are, for the most part, faster than they are for perylene, indicating efficient coupling of the 1-methylperylene normal coordinate to the solvent environment. Perhaps more informative is the difference in the dependencies of T_1 on solvent aliphatic chain length for the two probe molecules.

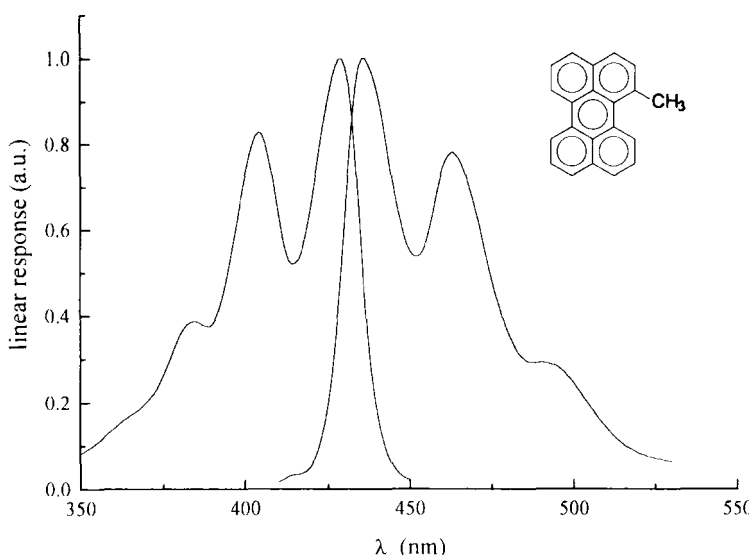


Figure 7.14. Absorption and emission spectra of 1-methylperylene in *n*-hexane. The boxed region indicates the spectral region probed. (Reprinted (in part) with permission from *J. Phys. Chem.* 99, 7904–7912 (1995), © 1995 American Chemical Society.)

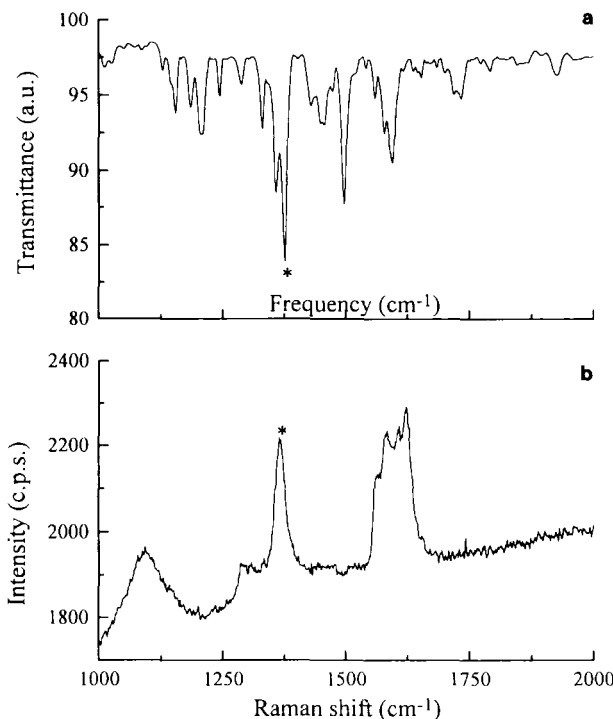


Figure 7.15. (a) Infrared and (b) Raman spectra of 1-methylperylene between 1000 cm^{-1} and 2000 cm^{-1} . The resonances marked by (*) are the 1370 cm^{-1} mode for which T_1 times were measured. (Reprinted (in part) with permission from *J. Phys. Chem.* 99, 7904–7912 (1995), ©1995 American Chemical Society.)

The T_1 relaxation times for these two molecules are determined to a significant extent by the mechanism of the polar intermolecular coupling. Local molecular organization within the solvent surrounding the chromophore is reflected in the modest solvent-dependent variations in T_1 we detect experimentally for each molecule. As discussed for perylene in the *n*-alkanes, any solvent dependence we measure in T_1 will arise from intermolecular relaxation processes. The form of the solvent dependence of the T_1 data for 1-methylperylene indicates the dominance of polar coupling over collisional relaxation processes. As before, if collisional energy transfer processes dominate, T_1 will vary continuously with increasing solvent alkane chain length because of the direct relationship between solvent-solute collision rate and solvent viscosity. We do not observe this trend experimentally, implying the dominance of polar (v-v) coupling.

The T_1 times for the 1-methylperylene 1370-cm⁻¹ mode increase with solvent aliphatic chain length, but there is an abrupt increase in T_1 starting with *n*-nonane. This solvent dependence in T_1 implies the existence of local organization around 1-methylperylene. In solvents shorter than the 1-methylperylene 1370-cm⁻¹ normal-mode coordinate, both solvent CH₃ groups are likely in close spatial proximity to the probe molecule, permitting efficient intermolecular energy transfer. For longer-chain solvents, where the length of a solvent molecule is similar to or greater than the maximum dimension of the 1-methylperylene vibrational coordinate, it is possible for the solvent terminal CH₃ groups to interact with the probe molecule, but the average distance between probe molecule and solvent terminal CH₃ groups will be greater, on average, than they are for the shorter solvents. This argument is, of course, qualitative, and in room-temperature liquids there is necessarily a broad distribution of *n*-alkane molecular conformations. Nonetheless, the predictions of this model are in qualitative agreement with the experimental data. The interactions between 1-methylperylene and the alkane solvents should be similar to those between perylene and the alkanes.

The T_1 relaxation of 1-methylperylene in *n*-alkanes differs from that of perylene. The dominant reason for this difference is the reduction in the symmetry of the probe molecule by the addition of the CH₃ group. The associated change in *vibrational* selection rules allows our experimental access to vibrations in 1-methylperylene that are both infrared and Raman active. For perylene, only Raman active, infrared inactive vibrational modes are accessible to our experimental excitation scheme. Raman active modes exhibit a change in polarizability on vibrational motion, while infrared active

Table 7.5. Reorientation (τ_{OR}) and Vibrational Relaxation (T_1) Times for 1-Methylperylene in *n*-Alkanes^a

Solvent	$\tau_{\text{OR}}(1)$ (ps) [%]	$\tau_{\text{OR}}(2)$ (ps) [%]	T_1 (ps)
<i>n</i> -C ₅ H ₁₂	12 ± 1 [100]	—	14 ± 3
<i>n</i> -C ₆ H ₁₄	13 ± 2 [100]	—	14 ± 3
<i>n</i> -C ₇ H ₁₆	15 ± 1 [100]	—	18 ± 2
<i>n</i> -C ₈ H ₁₈	16 ± 1 [100]	—	18 ± 1
<i>n</i> -C ₉ H ₂₀	14 ± 2 [75]	49 ± 14 [25]	28 ± 8
<i>n</i> -C ₁₀ H ₂₂	17 ± 3 [86]	70 ± 26 [14]	70 ± 8
<i>n</i> -C ₁₂ H ₂₆	21 ± 2 [85]	126 ± 29 [15]	77 ± 8
<i>n</i> -C ₁₆ H ₃₄	25 ± 3 [70]	152 ± 23 [30]	105 ± 7

^aReprinted (in part) with permission from *J. Phys. Chem.* 99, 7904–7912 (1995). © 1995 American Chemical Society.

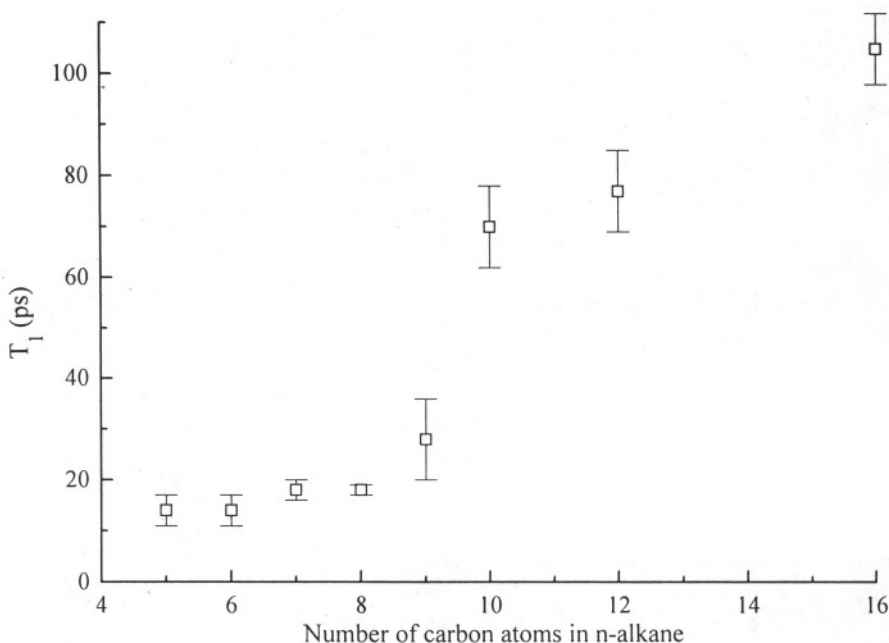


Figure 7.16. T_1 times for the 1-methylperylene 1370-cm^{-1} vibrational mode as a function of solvent aliphatic chain length. (Reprinted (in part) with permission from *J. Phys. Chem.* 99, 7904–7912 (1995), © 1995 American Chemical Society.)

modes exhibit a change in dipole moment on excitation. Because of the center of inversion present in perylene, the lowest order moment that Raman active modes will modulate will be the quadrupole moment. For 1-methylperylene, absent the center of inversion, the corresponding vibrational mode will modulate the molecular dipole moment on excitation. In both experiments, the dominant solvent bath mode is the infrared active *n*-alkane terminal CH_3 rocking mode. Thus, for perylene, intermolecular relaxation is through quadrupole-dipole coupling (interaction potential $\propto r^{-7}$), and for 1-methylperylene the analogous relaxation occurs through dipole-dipole coupling (interaction potential $\propto r^{-6}$).⁽¹⁴⁶⁾ Because of this fundamental difference in direct intermolecular coupling, the local environment sensed by perylene T_1 relaxation measurements is in substantially closer proximity to the chromophore than for 1-methylperylene. To establish this chromophore-dependent difference in the length scale over which solvent organization is detected, we next compare the T_1 results to τ_{OR} data for 1-methylperylene.

7.4.6. Reorientation Dynamics of 1-Methylperylene in the Alkanes

Without a comprehensive theoretical treatment of T_1 relaxation processes in liquids, and absent a calibration of the length scales over which intermolecular vibrational relaxations operate, it is essential to compare the T_1 data to a different dynamical response where the length scale of the dynamics is better understood. Rotational diffusion measurements are just such a response. Because rotational diffusion measurements sense the motion of the entire electronic chromophore, only a limited number of systems yield information on site-specific intermolecular interactions (*vide infra*). For comparatively nonpolar chromophores, the length scale sensed by rotational diffusion measurements is reasonably well related to the hydrodynamic volume of the probe molecule. Having this “ruler” provides some level of insight into the length scale over which (v-v) T_1 relaxation processes operate.

As discussed earlier, a single exponential decay of $R(t)$ is the most common form of the experimental response, and therefore significant ambiguity exists in the interpretation of experimental data. In cases where only limited information is available about the probe molecule transition moment orientation(s) or where a single exponential decay of $R(t)$ is observed, the viscosity dependence of the $R(t)$ decay time constant is typically measured to extract information on the frictional interaction between solvent and solute (Eq. 7.7). For 1-methylperylene it is important to understand that our primary focus is on the effective rotor shape, S , of the reorienting moiety and not on the solvent-solute boundary condition, f . The reorientation data on 1-methylperylene in the *n*-alkanes are of a functionality that allows information on rotor shape to be extracted. Reorientation measurements of perylene in these same solvents present a significantly different experimental $R(t)$ function. This difference comes about as a result of the addition of a methyl group to the perylene chromophore, a portion of which may be the result of the torsional strain introduced to the aromatic ring system by the addition of the CH_3 group.⁽¹⁴¹⁾ The rotational diffusion constant can be decomposed into its Cartesian components, and Chuang and Eisenthal⁽⁸⁷⁾ have related the anisotropy decay determined experimentally (Eq. 7.10) to the relative directions of the pumped and probed transition dipoles and the Cartesian components of the rotational diffusion constant (D) for a general ellipsoid. For 1-methylperylene the z axis is perpendicular to the molecular π system quasiplane, with the transition dipole moment(s) along the long (x) axis of the electronic chromophore. For an oblate ellipsoid the most rapid reorientation occurs along the axis perpendicular to the molecular plane ($D_z > D_x = D_y$), and for a prolate ellipsoid the dominant reorientation axis lies within the molecular plane, usually along the longest in-plane axis ($D_x > D_y = D_z$). For 1-methylperylene the experimental $R(t)$ functionality is determined by the effective rotor shape:⁽⁸⁷⁾

$$\text{oblate} \quad R(t) = \frac{3}{10} \exp(-(2D_x + 4D_z)t) + \frac{1}{10} \exp(-6D_x t) \quad (7.23)$$

$$\text{prolate} \quad R(t) = \frac{4}{10} \exp(-6D_z t) \quad (7.24)$$

The reorientation dynamics of 1-methylperylene in the *n*-alkanes are such that we can extract substantial information on the effective rotor shape of the probe molecule. In *n*-pentane, *n*-hexane, *n*-heptane, and *n*-octane, $R(t)$ decays as single exponential in time, and in *n*-nonane, *n*-decane, *n*-dodecane, and *n*-hexadecane, $R(t)$ decays as a double-exponential function. The $R(0)$ values and decay times, τ_{OR} , are shown in Table 7.5. The viscosity dependence of these data (Figure 7.17) show that the motional dynamics of 1-methylperylene in short- ($\leq C_8$) and long-chain ($\geq C_9$) alkane solvents are very different. There are several ways in which this solvent-dependent change in the functionality of $R(t)$ could be interpreted. We consider these data in the context of a solvent-dependent change in the effective rotor shape of the molecule. Information on the solvent dependence of the frictional boundary condition from these data cannot be extracted easily because of the different information content of the two forms of $R(t)$. As the solvent chain length increases, the effective rotor shape of the chromophore changes from prolate to oblate. Using the preexponential factors from the data in Table 7.5 and Eqs. (7.23) and (7.24), we estimate the anisotropy of the 1-methylperylene rotor shape for the longer-chain solvents. For short-chain solvents, where 1-methylperylene behaves as a prolate rotor, we can extract only D_x from the experimental data. As a consequence, there is little “shape” information available from these data. For the longer-chain solvents, where there are two exponential decays, it is straightforward to extract D_x and D_z and, thus, the major-to-minor axial ratio of the ellipsoid of rotation (Table 7.6). While we cannot provide detailed information on the effective rotor shape of 1-methylperylene in *n*-pentane through *n*-octane, the ratio D_z/D_x for the longer-chain solvents shows that the anisotropy of the rotational ellipsoid increases with solvent length to a limiting value in *n*-dodecane. These data represent a quasilamellar confinement of 1-methylperylene in the long-chain solvents.

7.4.7. Comparison of T_1 and τ_{OR} Data for 1-Methylperylene

The solvent-dependent change of rotational diffusion rotor shape and the onset of the increase in T_1 both occur between *n*-octane and *n*-nonane. Interpreting the reorientation data in terms of solvent local organization is consistent with the solvent local organization suggested by the T_1 solvent-chain-length dependence. In short *n*-alkanes the 1-methylperylene rotor shape is prolate; i.e., the dominant rotational motion is about one of the 1-methylperylene long in-

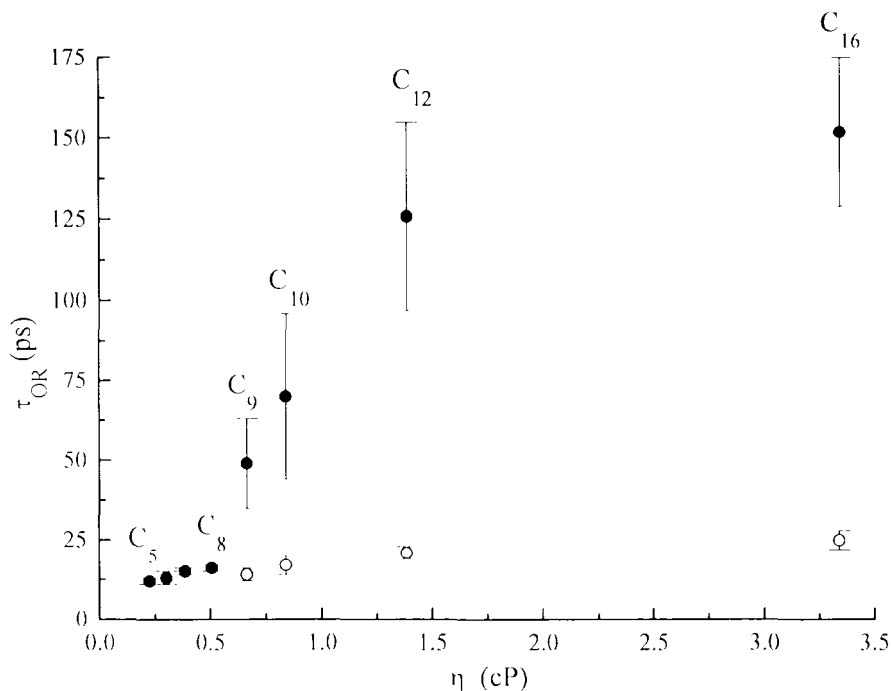


Figure 7.17. S_1 Reorientation times of 1-methylperylene as a function of solvent viscosity. A single exponential decay of $R(t)$ is observed for *n*-pentane through *n*-octane, and a double exponential decay functionality is observed for longer-chain aliphatic solvents. (Reprinted (in part) with permission from *J. Phys. Chem.* 99, 7904–7912 (1995), © 1995 American Chemical Society.)

Table 7.6. Rotational Diffusion Constant(s) for 1-Methylperylene in *n*-Alkanes^a

Solvent	D_x (GHz)	D_z (GHz)	D_z/D_x
<i>n</i> -C ₅ H ₁₂		23.9 ± 1.2	< 1
<i>n</i> -C ₆ H ₁₄		12.8 ± 2.3	< 1
<i>n</i> -C ₇ H ₁₆		11.1 ± 0.8	< 1
<i>n</i> -C ₈ H ₁₈		10.4 ± 0.7	< 1
<i>n</i> -C ₉ H ₂₀	3.40 ± 0.75	16.2 ± 1.9	4.8 ± 1.3
<i>n</i> -C ₁₀ H ₂₂	2.38 ± 0.64	13.5 ± 1.9	5.7 ± 1.8
<i>n</i> -C ₁₂ H ₂₆	1.32 ± 0.24	11.2 ± 0.9	8.5 ± 1.9
<i>n</i> -C ₁₆ H ₃₄	1.10 ± 0.15	9.5 ± 1.2	8.6 ± 1.9

^aReprinted (in part) with permission from *J. Phys. Chem.* 99, 7904–7912 (1995), © 1995 American Chemical Society.

plane axes. The solvent molecules are small enough that both terminal CH₃ groups for a particular molecule are in close spatial proximity to the probe molecule, and fast T₁ relaxation is expected. For longer *n*-alkanes, 1-methylperylene behaves as an oblate rotor, where the dominant rotational motion is around the axis perpendicular to its molecular quasiplane. This solvent-dependent change of rotor shape for 1-methylperylene comes about because the probe molecule is confined between solvent “layers.” This confinement can also be described as a result of individual solvent molecules that are sufficiently long to span the 1-methylperylene long axis, significantly reducing the structural freedom of individual solvent molecules on the probe molecule length scale. If such an environment were to exist, the solvent terminal CH₃ groups would be further away from the probe molecule, on average, than in the shorter *n*-alkanes, and a longer T₁ relaxation time in such an environment is an expected result. The change in both the reorientation and T₁ data between *n*-octane and *n*-decane indicates that the “length” of the 1-methylperylene 1370-cm⁻¹ vibrational coordinate is similar to the average “length” of the ensemble of these solvent molecules. These data also indicate that the dipolar (v-v) coupling processes responsible for relaxation proceed over ~10 Å.

7.5. Summary and Overview

We have discussed the application of stimulated-emission spectroscopy to solving chemical problems in three different chemical systems and for two photophysical processes: orientational relaxation dynamics and vibrational population relaxation. For the rotational diffusion measurements, it was the ability of the stimulated-emission measurements to provide a direct comparison to data from ground-state depletion measurements that allowed insight into intermolecular complex formation in polar H-bonding solvents. For measurements of vibrational population relaxation, ultrafast stimulated-emission measurements allowed the direct acquisition of T₁ times for individual vibrational resonances from ~300 to ~3000 cm⁻¹. This broad tunability, high information content of the raw experimental data, and an excitation scheme that allows the direct examination of (v-v) relaxation in systems where Δv ~ 0 cm⁻¹ offers a significant opportunity in our ability to understand transient local organization in condensed phases. We expect that this type of measurement will find increasing use in time because of its combination of versatility, sensitivity, and the comparatively high information content of the signal.

References

1. A. Einstein, Zur Quantentheorie der Strahlung, *Phys. Z.* **18**, 121–128 (1917).
2. G. Herzberg, *Molecular Spectra and Molecular Structure, Volume I. Spectra of Diatomic Molecules*, Krieger, Malabar, FL (1989), p. 383.
3. J. D. Ingle, Jr., and S. R. Crouch, *Spectrochemical Analysis*, Prentice Hall, Englewood Cliffs, NJ (1988), pp. 564–567.
4. J. Dods, P. Brumer, and M. Shapiro, Two color coherent control with SEP preparation: Electronic branching in Na_2 photodissociation, *Can. J. Chem.* **72**, 958–965 (1994).
5. M. Takayanagi and I. Hanazaki, Intermolecular vibrations and dynamics of the anisole-benzene complex studied by multiresonance spectroscopy, *Spectrochim. Acta 50A*, 1435–1442 (1994).
6. P. G. Smith and M. R. Topp, Vibrational relaxation of isomerizing alkyl halide complexes of perylene measured by stimulated emission spectroscopy, *Chem. Phys. Lett.* **229**, 21–28 (1994).
7. A. Geers, J. Kappert, F. Temps, and J. W. Wiebrecht, Rotation-vibration state resolved unimolecular dynamics of highly vibrationally excited CH_3O ($X^2\text{E}$). I: Observed stimulated emission pumping spectra, *J. Chem. Phys.* **101**, 3618–3633 (1994).
8. M. F. Hineman, E. R. Bernstein, and D. F. Kelley, Measurement of vibrational energy redistribution rates in molecular clusters by time-resolved stimulated emission pumping, *J. Chem. Phys.* **101**, 850–851 (1994).
9. R. Sussmann, R. Neuhauser, and H. J. Neusser, Stimulated Raman adiabatic passage with pulsed lasers: High resolution ion dip spectroscopy of polyatomic molecules, *J. Chem. Phys.* **100**, 4784–4789 (1994).
10. T. Baumert and G. Gerber, Fundamental interactions of molecules (Na_2 , Na_3) with intense femtosecond laser pulses, *Israel J. Chem.* **34**, 103–114 (1994).
11. D. M. Jonas, S. A. B. Solina, B. Rajaram, R. J. Silbey, and R. W. Field, Intramolecular vibrational redistribution of energy in the stimulated emission pumping spectrum of acetylene, *J. Chem. Phys.* **99**, 7350–7370 (1993).
12. M. Takayanagi and I. Hanazaki, Dynamics of vibrationally excited van der Waals complex: Stimulated emission pumping laser induced fluorescence spectroscopy of the anisole–Ar complex, *J. Chem. Phys.* **98**, 6958–6964 (1993).
13. Y. Murata, C.-H. Lin, and T. Imasaka, Comparison of stimulated emission pumping fluorescence dip spectrometry and conventional fluorescence spectrometry in application to supersonic jet spectrometry, *Fres. J. Anal. Chem.* **346**, 543–544 (1993).
14. D. W. Neyer, X. Luo, and P. L. Houston, CO product distribution from metastable levels of HCO $X^2\text{A}'$ prepared by stimulated emission pumping, *J. Chem. Phys.* **98**, 5095–5098 (1993).
15. P. G. Smith and J. D. McDonald, Picosecond stimulated emission pumping: Intramolecular vibrational relaxation in the excited electronic state of *p*-cyclohexylaniline, *J. Chem. Phys.* **96**, 7344–7351 (1992).
16. M. Takayanagi and I. Hanazaki, SEP-LIF study on dynamics of vibrationally excited states of van der Waals complexes: The anisole–Ar complex, *Chem. Phys. Lett.* **190**, 115–118 (1992).
17. G. V. Hartland, P. W. Joireman, L. L. Connell, and P. M. Felker, High resolution Fourier transform stimulated emission and molecular beam hole-burning spectroscopy with picosecond excitation sources: Theoretical and experimental results, *J. Chem. Phys.* **96**, 179–197 (1991).
18. W. Xie, C. Harkin, and H.-L. Dai, Bending overtones and barrier height of a ${}^1\text{A}_1$, CH_2 by flash photolysis stimulated emission pumping, *J. Chem. Phys.* **93**, 4615–4623 (1990).
19. M. Takayanagi and I. Hanazaki, Fluorescence dip and stimulated emission pumping laser induced fluorescence spectra of van der Waals molecules containing benzonitrile, *J. Opt. Soc. Am. B* **7**, 1898–1904 (1990).

20. S. A. Reid, H. L. Kim, and J. D. McDonald, A stimulated emission pumping study of jet cooled methyl glyoxal, *J. Chem. Phys.* 92, 7079–7086 (1990).
21. M. Broyer, G. Delacretaz, G.-Q. Ni, R. L. Whetten, J.-P. Wolf, and L. Woste, Vibronic structure of the Na_3 ground state by stimulated emission spectroscopy, *Phys. Rev. Lett.* 62, 2100–2103 (1989).
22. M. Broyer, G. Delacretaz, G.-Q. Ni, R. L. Whetten, J.-P. Wolf, and L. Woste, Stimulated emission spectroscopy of the ground state of Na_3 , *J. Chem. Phys.* 90, 4620–4622 (1989).
23. Y. S. Choi and C. B. Moore, Evidence for mode-specific dynamics in the stimulated emission pumping spectra of HFCO, *J. Chem. Phys.* 90, 3875–3876 (1989).
24. D. Frye, P. Arias, and H.-L. Dai, Stimulated emission spectroscopy of van der Waals vibrational levels of glyoxal! X^1A_g -Ar, *J. Chem. Phys.* 88, 7240–7241 (1988).
25. T. Suzuki, M. Hiroi, and M. Ito, Stimulated emission spectroscopy of jet-cooled polyatomics: $S_1 \rightarrow S_0$ two color ionization dip spectra of m-fluorotoluene and aniline, *J. Phys. Chem.* 92, 3774–2778 (1988).
26. K. Yamanouchi, H. Yamada, and S. Tsuchiya, Vibrational level structure of highly excited SO_2 in the electronic ground state as studied by stimulated emission pumping spectroscopy, *J. Chem. Phys.* 88, 4664–4670 (1988).
27. P. M. Felker, B. F. Henson, T. C. Corcoran, L. L. Connell, and G. V. Hartland, Fourier transform stimulated emission pumping spectroscopy, *Chem. Phys. Lett.* 142, 439–445 (1987).
28. H. L. Kim, S. Reid, and J. D. McDonald, Intramolecular vibrational state mixing in glyoxal by stimulated emission pumping spectroscopy, *Chem. Phys. Lett.* 13, 525–527 (1987).
29. D. Frye, H. T. Liou, and H. L. Dai, Stimulated emission polarization spectroscopy of $v_2 = 2X^1A_g$ glyoxal, *Chem. Phys. Lett.* 133, 249–253 (1987).
30. C. E. Hamilton, J. L. Kinsey, and R. W. Field, Stimulated emission pumping: new methods in spectroscopy and molecular dynamics, *Ann. Rev. Phys. Chem.* 37, 493–524 (1986).
31. J. I. Selco, P. L. Holt, and R. B. Weisman, Direct stimulated emission spectroscopy of gas phase polyatomics; pyridazine, *J. Chem. Phys.* 79, 4083–4085 (1983).
32. P. H. Vaccaro, J. L. Kinsey, R. W. Field, and H. L. Dai, Electric dipole moments of excited vibrational levels in the X^1A_1 state of formaldehyde by stimulated emission spectroscopy, *J. Chem. Phys.* 78, 3659–3664 (1983).
33. C. Kittrell, E. Abramson, J. L. Kinsey, S. A. McDonald, D. E. Reisner, and R. W. Field, Selective vibrational excitation by stimulated emission pumping, *J. Chem. Phys.* 75, 2056–2059 (1981).
34. G. J. Blanchard and M. J. Wirth, A critical comparison of molecular reorientation in the ground and excited electronic states: cresyl violet in methanol, *J. Chem. Phys.* 82, 39–44 (1985).
35. D. Ben-Amotz and T. W. Scott, Microscopic frictional forces on molecular motion in liquids. Picosecond rotational diffusion in alkanes and alcohols, *J. Chem. Phys.* 87, 3739–3748 (1987).
36. G. J. Blanchard and C. A. Cihal, Orientational relaxation dynamics of oxazine 118 and resorufin in the butanols. Valence and state dependent solvation effects, *J. Phys. Chem.* 92, 5950–5954 (1988).
37. G. J. Blanchard, A study of the state dependent reorientation dynamics of oxazine 725 in primary n-aliphatic alcohols, *J. Phys. Chem.* 92, 6303–6307 (1988).
38. G. J. Blanchard, The state dependent reorientation of methylene blue: the role of dipolar solvent-solute interactions, *J. Phys. Chem.* 93, 4315–4319 (1989).
39. G. J. Blanchard, Detection of a transient solvent-solute complex using time-resolved pump-probe spectroscopy, *Anal. Chem.* 61, 2394–2398 (1989).
40. G. J. Blanchard, Counter-ion dependent reorientation dynamics of an oxazine in polar protic and aprotic solvents, *J. Phys. Chem.* 95, 5293–5299 (1991).
41. G. J. Blanchard, Time-resolved measurement of the stimulated emission stokes shift in LDS750: evidence for inhomogeneous relaxation kinetics, *J. Chem. Phys.* 95, 6317–6325 (1991).

42. M. M. Awad, P. K. McCarthy, and G. J. Blanchard, Photoisomerization of cyanines: a comparative study of oxygen and sulfur containing species, *J. Phys. Chem.* 98, 1454–1458 (1994).
43. Y. Jiang, P. K. McCarthy, and G. J. Blanchard, The role of multiple electronic states in the dissipative energy dynamics of coumarin 153, *Chem. Phys.* 183, 249–267 (1994).
44. A. Owyong, Sensitivity limitations for CW stimulated Raman Spectroscopy, *Opt. Commun.* 22, 323–328(1977).
45. A. Owyong, Coherent Raman gain spectroscopy using CW laser sources, *IEEE J. Quant. Electron. QE-14*, 192–203 (1978).
46. B. F. Levine and C. G. Bethea, Frequency-modulated shot noise limited stimulated Raman gain spectroscopy, *Appl. Phys. Lett.* 36, 245–247 (1980).
47. B. F. Levine and C. G. Bethea, Ultrahigh sensitivity stimulated Raman gain spectroscopy, *IEEE J. Quant. Electron. QE-16*, 85–88 (1980).
48. J. P. Heritage and D. L. Allara, Surface picosecond Raman gain spectra of a molecular monolayer, *Chem. Phys. Lett.* 74, 507–510 (1980).
49. J. P. Heritage, J. G. Bergman, A. Pinczuk, and J. M. Worlock, Picosecond Raman gain Spectroscopy of a monolayer of cyanide on silver, *Chem. Phys. Lett.* 67, 229–232 (1979).
50. B. F. Levine, C. V. Shank, and J. P. Heritage, Surface vibrational spectroscopy using stimulated Raman scattering, *IEEE J. Quant. Electron. QE-15*, 1418–1432 (1979).
51. S. A. Hambir, Y. Jiang, and G. J. Blanchard, Ultrafast stimulated emission spectroscopy of perylene in dilute solution: measurement of ground state vibrational population relaxation, *J. Chem. Phys.* 98, 6075–6082 (1993).
52. Y. Jiang and G. J. Blanchard, Vibrational population relaxation of perylene in n-alkanes. The role of solvent local structure in long range vibrational energy transfer, *J. Phys. Chem.* 98, 9411–9416(1994).
53. Y. Jiang and G. J. Blanchard, Vibrational population relaxation of perylene in its ground and excited electronic states, *J. Phys. Chem.* 98, 9417–9421 (1994).
54. G. R. Fleming, *Chemical Applications of Ultrafast Spectroscopy*, Oxford University Press (1986).
55. Y. Jiang, S. A. Hambir, and G. J. Blanchard, Synchronous pumping of two dye lasers using a single UV excitation source, *Opt. Commun.* 99, 216–220 (1993).
56. J. M. Harris, R. W. Chrisman, and F. E. Lytle, Pulse generation in a cw dye laser by mode-locked synchronous pumping, *Appl. Phys. Lett.* 26, 16–18 (1975).
57. J. M. Clemens, J. Najbar, I. Bronstein-Bonte, and R. M. Hochstrasser, Dual picosecond dye lasers synchronously pumped by a mode locked CW YAG laser, *Opt. Commun.* 47, 271–277 (1983).
58. P. A. Elzinga, R. J. Kneisler, F. E. Lytle, Y. Jiang, G. B. King, and N. M. Laurendeau, Pump/probe method for fast analysis of visible spectral signatures utilizing asynchronous optical sampling, *Appl. Opt.* 26, 4309–4309 (1987).
59. G. J. Blanchard, Picosecond spectroscopic measurement of a solvent dependent change of rotational diffusion rotor shape, *J. Chem. Phys.* 87, 6802–6808 (1987).
60. G. R. Holtom, Artifacts and diagnostics in fast fluorescence measurements, *Proc. SPIE 1204*, 2–12 (1990).
61. L. DeWitt, G. J. Blanchard, E. LeGoff, M. E. Benz, J. H. Liao, and M. G. Kanatzidis, Determination of ground and excited state isomerization barriers for the oligothiophene: 3',4'-dibutyl-2,2':5',2'-terthiophene, *J. Am. Chem. Soc.* 115, 12158–12164(1993).
62. G. J. Blanchard and M. J. Wirth, Measurement of small absorbances by picosecond pump-probe spectrometry, *Anal. Chem.* 58, 532–535 (1986).
63. P. Bado, S. B. Wilson, and K. R. Wilson, Multiple modulation for optical pump-probe spectroscopy, *Rev. Sci. Instrum.* 53, 706–707 (1982).

64. L. Andor, A. Lorincz, J. Siemion, D. D. Smith, and S. A. Rice, Shot noise limited detection scheme for two beam laser spectroscopies, *Rev. Sci. Instrum.* **55**, 64–67 (1984).
65. E. L. Quitevis, E. F. Gudgin-Templeton, and G. A. Kenney-Wallace, Multiple modulation spectroscopy at radiofrequencies for picosecond laser spectroscopy, *Appl. Opt.* **24**, 318–321 (1985).
66. G. Lipari and A. Szabo, Effect of librational motion on fluorescence depolarization and nuclear magnetic resonance relaxation in macromolecules and membranes, *Biophys. J.* **30**, 489–506 (1980).
67. K. Kinosita, S. Kawato, and A. Ikegami, A theory of fluorescence polarization decay in membranes, *Biophys. J.* **20**, 289–304 (1977).
68. A. Szabo, Theory of fluorescence depolarization in macromolecules and membranes, *J. Chem. Phys.* **81**, 150–167 (1984).
69. P. Debye, Polar Molecules, Chemical Catalog, New York (1929), p. 84.
70. J. T. Edward, Molecular volumes and the Stokes-Einstein equation, *J. Chem. Ed.* **47**, 261–270 (1970).
71. A. Bondi, Van der Waals volumes and radii, *J. Phys. Chem.* **68**, 441–451 (1964).
72. F. Perrin, Mouvement Brownien d'un ellipsoïde. I: Dispersion dielectrique pour des molécules ellipsoidales, *J. Phys. Radium* **5**, 497 (1934).
73. F. Perrin, Mouvement Brownien d'un ellipsoïde. II: Rotation libre et depolarisation des fluorescences. Translation et diffusion de molécules ellipsoidales, *J. Phys. Radium* **7**, 1–11 (1936).
74. L. D. Favro, Theory of the rotational Brownian motion of a free rigid body, *Phys. Rev.* **119**, 53–62 (1960).
75. T. Tao, Time-dependent fluorescence depolarization and Brownian rotational diffusion coefficients of macromolecules, *Biopolymers* **8**, 609–632 (1969).
76. C.-M. Hu and R. Zwanzig, Rotational friction coefficients for spheroids with the slipping boundary condition, *J. Chem. Phys.* **60**, 4354–4357 (1974).
77. G. K. Youngren and A. Acrivos, Rotational friction coefficients for ellipsoids and chemical molecules with the slip boundary condition, *J. Chem. Phys.* **63**, 3846–3848 (1975).
78. E. W. Small and I. Isenberg, Hydrodynamic properties of a rigid molecule: rotational and linear diffusion and fluorescence anisotropy, *Biopolymers* **16**, 1907–1928 (1977).
79. L. A. Philips, S. P. Webb, and J. H. Clark, High pressure studies of rotational reorientation dynamics: the role of dielectric friction, *J. Chem. Phys. S3*, 5810–5821 (1985).
80. J. B. Hubbard and P. G. Wolynes, Dielectric friction and molecular reorientation, *J. Chem. Phys.* **69**, 998–1006 (1978).
81. P. Madden and D. Kivelson, Dielectric friction and molecular reorientation, *J. Phys. Chem.* **86**, 4244–4256 (1982).
82. D. Kivelson and K. G. Spears, Dielectric friction as a source of rotational drag on charged noncentrosymmetric molecules, *J. Phys. Chem.* **89**, 1999–2001 (1985).
83. A. J. Cross and J. D. Simon, Rotational dynamics of a solvated dipole: a molecular dynamics study of dielectric friction, *J. Chem. Phys.* **86**, 7079–7083 (1987).
84. J. D. Simon and P. A. Thompson, Spectroscopy and rotational dynamics of oxazine 725 in alcohols: a test of dielectric friction theories, *J. Chem. Phys.* **92**, 2891–2896 (1990).
85. G. J. Blanchard, An MNDO calculational study of selected oxazine, thiazine and oxazone dyes, *Chem. Phys.* **138**, 365–375 (1989).
86. Y. Jiang and G. J. Blanchard, Rotational diffusion dynamics of perylene in n-alkanes. Observation of a solvent length-dependent change of boundary condition, *J. Phys. Chem.* **98**, 6436–6440 (1994).
87. T. J. Chuang and K. B. Eisenthal, Theory of fluorescence depolarization by anisotropic rotational diffusion, *J. Chem. Phys.* **57**, 5094–5097 (1972).

88. E. W. Castner, M. Maroncelli, and G. R. Fleming, Subpicosecond resolution studies of solvation dynamics in polar aprotic and alcohol solvents, *J. Chem. Phys.* **86**, 1090–1097 (1987).
89. John A. Dean (ed.), *Lange's Handbook of Chemistry*, 13th ed., McGraw-Hill (1985), pp. 10–102–10–111.
90. Z. G. Szabo, in: *Comprehensive Chemical Kinetics*, Vol. 2, (C. H. Bamford and C. F. H. Tipper, eds.), Elsevier, New York (1969), pp. 24–26.
91. T. P. Dougherty and E. J. Heilweil, Ultrafast transient infrared absorption studies of $M(CO_6)$ ($M = Cr, Mo$ or W) photoproducts in *n*-hexane solution, *Chem. Phys. Lett.* **227**, 19–25 (1994).
92. T. A. Germer, J. C. Stephenson, E. J. Heilweil, and R. R. Cavanagh, Hot carrier excitation of adlayers: time-resolved measurement of adsorbate-lattice coupling, *Phys. Rev. Lett.* **71**, 3327–3330 (1993).
93. E. J. Heilweil, M. P. Casassa, R. R. Cavanagh, and J. C. Stephenson, Picosecond vibrational energy transfer studies of surface adsorbates, *Ann. Rev. Phys. Chem.* **40**, 143–171 (1989).
94. E. J. Heilweil, R. R. Cavanagh, and J. C. Stephenson, CO ($v = 1$) population lifetimes of metal-carbonyl cluster compounds in dilute CHCl₃ solution, *J. Chem. Phys.* **89**, 230–239 (1988).
95. E. J. Heilweil, R. R. Cavanagh, and J. C. Stephenson, Population relaxation of CO ($v = 1$) vibrations in solution phase metal carbonyl complexes, *Chem. Phys. Lett.* **134**, 181–188 (1987).
96. E. J. Heilweil, M. P. Casassa, R. R. Cavanagh, and J. C. Stephenson, Population lifetimes of OH ($v = 1$) and OD ($v = 1$) stretching vibrations of alcohols and silanols in dilute solution, *J. Chem. Phys.* **85**, 5004–5018 (1986).
97. H. J. Bakker, P. C. M. Planken, and A. Lagendijk, Ultrafast vibrational dynamics of small organic molecules in solution, *J. Chem. Phys.* **94**, 6007–6013 (1991).
98. P. A. Anfinrud, C. Han, T. Lian, and R. M. Hochstrasser, Evolution of the transient vibrational spectrum following short-pulse excitation, *J. Phys. Chem.* **94**, 1180–1184 (1990).
99. T. Elsaesser and W. Kaiser, Vibrational and vibronic relaxation of large polyatomic molecules in liquids, *Ann. Rev. Phys. Chem.* **42**, 83–107 (1991).
100. N. H. Gottfried, A. Seilmeyer, and W. Kaiser, Transient internal temperature of anthracene after picosecond infrared excitation, *Chem. Phys. Lett.* **111**, 326–332 (1984).
101. A. Seilmeyer, P. O. J. Scherer, and W. Kaiser, Ultrafast energy dissipation in solutions measured by a molecular thermometer, *Chem. Phys. Lett.* **105**, 140–146 (1984).
102. F. Wondrazek, A. Seilmeyer, and W. Kaiser, Ultrafast intramolecular redistribution and intermolecular relaxation of vibrational energy in large molecules, *Chem. Phys. Lett.* **104**, 121–128 (1984).
103. H. Graener and A. Laubereau, Ultrafast overtone excitation for the study of vibrational population decay in liquids, *Chem. Phys. Lett.* **102**, 100–104 (1983).
104. N. H. Gottfried and W. Kaiser, Redistribution of vibrational energy in naphthalene and anthracene studied in liquid solution, *Chem. Phys. Lett.* **101**, 331–336 (1983).
105. W. Zinth, C. Kolmeder, B. Benner, A. Irgens-Defragger, S. F. Fischer, and W. Kaiser, Fast and exceptionally slow vibrational energy transfer in acetylene and phenylacetylene in solution, *J. Chem. Phys.* **78**, 3916–3921 (1983).
106. W. Kaiser and A. Laubereau, Picosecond time resolved measurements of vibrational energy transfer and relaxation phenomena in large polyatomic molecules, *Pure Appl. Chem.* **50**, 1231–1238 (1978).
107. A. Laubereau and W. Kaiser, Vibrational dynamics of liquids and solids investigated by picosecond light pulses, *Rev. Mod. Phys.* **50**, 607–665 (1978).
108. A. Laubereau, G. Wochner, and W. Kaiser, Ultrafast coherent excitation and probing of molecular vibrations with isotopic substructure, *Phys. Rev. A* **13**, 2212–2225 (1976).
109. A. Laubereau, G. Wochner, and W. Kaiser, Collective beating of molecular vibrations in liquids on the picosecond timescale, *Opt. Commun.* **17**, 91–94 (1976).

110. A. Laubereau, A. Seilmeier, and W. Kaiser, A new technique to measure ultrashort vibrational relaxation times in liquid systems, *Chem. Phys. Lett.* **36**, 232–237 (1975).
111. A. Laubereau, G. Wochner, and W. Kaiser, Direct observation of the relaxation time of the symmetric molecular CO_3^{2-} vibration of calcite, *Opt. Commun.* **14**, 75–78 (1975).
112. A. Laubereau and W. Kaiser, Picosecond spectroscopy of molecular dynamics in liquids, *Ann. Rev. Phys. Chem.* **26**, 83–99 (1975).
113. M. L. Nowlin and M. C. Heaven, Energy transfer rate constants for highly excited rovibrational levels of $^1\text{D}_2(\text{X})$, *J. Chem. Phys.* **99**, 5654–5660 (1993).
114. J. M. Price, J. A. Mack, C. A. Rogaski, and A. M. Wodtke, Vibrational state-specific self-relaxation rate constant. Measurements of highly vibrationally excited O_2 ($\nu = 19\text{--}28$) *Chem. Phys.* **175**, 83–98 (1993).
115. X. Yang, J. M. Price, J. A. Mack, C. G. Morgan, C. A. Rogaski, D. McGuire, E. H. Kim, and A. M. Wodtke, Stimulated emission pumping studies of energy transfer in highly vibrationally excited molecules, *J. Phys. Chem.* **97**, 3944–3955 (1993).
116. S. H. Kable and A. E. W. Knight, Temperature dependence of vibrational relaxation in the very low energy collision regime: the ground electronic state of p-difluorobenzene prepared by stimulated emission pumping, *J. Chem. Phys.* **93**, 3151–3159 (1990).
117. W. D. Lawrence and A. E. W. Knight, Vibrational relaxation in ground state *p*-difluorobenzene: single level preparation by stimulated emission pumping, *J. Chem. Phys.* **77**, 570–571 (1982).
118. S. Matsunuma, N. Akamatsu, T. Kamisuki, Y. Adachi, S. Maeda, and C. Hirose, $S_n \leftarrow S_1$ and $S_1 \rightarrow S_0$ resonance CARS spectra of perylene in the S_1 state, *J. Chem. Phys.* **88**, 2956–2961 (1988).
119. S. J. Cyvin, B. N. Cyvin, and P. Klaeboe, Condensed aromatics. Part XIX Perylene, *Spectrosc. Lett.* **16**, 239–248 (1983).
120. M. A. Kovner, A. A. Terekhov, and L. M. Babkov, Calculation of the planar vibrational frequencies and interpretation of the infrared spectrum and the vibrational structure of the fluorescence spectrum of the perylene molecule, *Opt. Spectrosc.* **26**, 38–40 (1972).
121. M. M. Valdman and R. I. Personov, Quasi-line fluorescence and absorption spectra of perilene at 20° and 4°K, *Opt. Spectrosc.* **19**, 296–298 (1965).
122. E. V. Shpol'skii and R. I. Personov, Emission and absorption spectra of perylene in solid solutions at 77°K, *Opt. Spectrosc.* **8**, 172–176 (1960).
123. H. Kim and D. D. Drrott, Molecular dynamics simulation of nanoscale thermal conduction and vibrational cooling in a crystalline naphthalene cluster, *J. Chem. Phys.* **94**, 8203–8209 (1991).
124. T.-C. Chang and D. D. Drrott, Vibrational cooling in large molecular systems: pentacene in naphthalene, *J. Chem. Phys.* **90**, 3590–3602 (1989).
125. J. R. Hill and D. D. Drrott, Theory of vibrational cooling in molecular crystals: application to crystalline naphthalene, *J. Chem. Phys.* **89**, 842–858 (1988).
126. J. R. Hill and D. D. Drrott, A model for ultrafast vibrational cooling in molecular crystals, *J. Chem. Phys.* **89**, 830–841 (1988).
127. T.-C. Chang and D. D. Drrott, Picosecond vibrational cooling in mixed molecular crystals studied with a new coherent Raman scattering technique, *Chem. Phys. Lett.* **147**, 18–24 (1988).
128. J. R. Hill, E. L. Chronister, T.-C. Chang, H. Kim, J. C. Postlewaite, and D. D. Drrott, Vibrational relaxation of a guest and host in mixed molecular crystals, *J. Chem. Phys.* **88**, 2361–2371 (1988).
129. J. Rodriguez, C. Kirmaier, and D. Holten, Time resolved and static optical properties of vibrationally excited porphyrins, *J. Chem. Phys.* **94**, 6020–6029 (1991).
130. J. Rodriguez and D. Holten, Ultrafast photodissociation of a metalloporphyrin in the condensed phase, *J. Chem. Phys.* **92**, 5944–5950 (1990).

131. O. Bilsel, J. Rodriguez, and D. Holten, Picosecond relaxation of strongly coupled porphyrin dimers, *J. Phys. Chem.* **94**, 3508–3512 (1990).
132. J. Rodriguez and D. Holten, Ultrafast vibrational dynamics of a photoexcited metalloporphyrin, *J. Chem. Phys.* **91**, 3525–3531 (1989).
133. C. Rulliere, Laser action and photoisomerization of 3,3'-diethyloxadicarbocyanine iodide (DODCI): Influence of temperature and concentration, *Chem. Phys. Lett.* **43**, 303–308 (1976).
134. J. T. Yardley, *Introduction to Molecular Energy Transfer*, Academic Press, New York (1980).
135. J. C. Stephenson, R. E. Wood, and C. B. Moore, Near-resonant energy transfer between infrared-active vibrations, *J. Chem. Phys.* **48**, 4790–4791 (1968).
136. D. Brown, J. H. R. Clarke, M. Okuda, and T. Yamazaki, A molecular dynamics study of chain configurations in *n*-alkane-like liquids, *J. Chem. Phys.* **100**, 1684–1692 (1994).
137. A. H. Narten, A. Habenschuss, K. G. Honnell, J. D. McCoy, J. G. Curro, and K. S. Schweizer, Diffraction by macromolecular fluids, *J. Chem. Soc. Faraday Trans.* **88**, 1791–1795 (1992).
138. Y. Marcus, The structuredness of solvents, *J. Sol. Chem.* **21**, 1217–1230 (1992).
139. M. Iwahashi, Y. Yamaguchi, Y. Ogura, and M. Suzuki, Dynamical structures of normal alkanes, alcohols, and fatty acids in the liquid state as determined by viscosity, self-diffusion coefficient, infrared spectra and ¹³C NMR spin-lattice relaxation time measurements, *Bull. Chem. Soc. Jpn.* **63**, 2154–2158 (1990).
140. A. Habenschuss and A. H. Narten, X-ray diffraction study of some liquid alkanes, *J. Chem. Phys.* **92**, 5692–5699 (1990).
141. S. Grimme and H.-G. Lohmannsroben, MO theoretical investigation of strained PAH molecules: effects of methyl substituents in ground and excited states, *J. Phys. Chem.* **96**, 7005–7009 (1992).
142. F. Lewitzka, H.-G. Lohmannsroben, M. Strauch, and W. Luttko, Photophysical properties of methylperylene and bromoperylene in solution, *J. Photochem. Photobiol A: Chem.* **61**, 191–200 (1991).
143. H. E. Ziegler and E. M. Laski, The alkylation of perylene with methylolithium, *Tetrahedron Lett.* **32**, 3801–3804 (1966).
144. Y. Jiang and G. J. Blanchard, Vibrational population and orientational relaxation of 1-methylperylene in *n*-alkanes. The effective range of dipolar energy relaxation in solution, *J. Phys. Chem.* **99**, 7904–7912 (1995).
145. F. A. Cotton, *Chemical Applications of Group Theory*, 2nd ed., Wiley-Interscience (1971).
146. P. W. Atkins, *Physical Chemistry*, 4th ed., W. H. Freeman, New York (1990), p. 656.

This page intentionally left blank.

Fluorescence Quenching by Stimulated Emission

Joseph R. Lakowicz and Ignacy Gryczynski

8.1. Introduction

Time-resolved fluorescence spectroscopy, following one-pulse excitation, is often used to obtain structural and dynamic information from the complex intensity and anisotropy decays which are characteristic of biological macromolecules.⁽¹⁻³⁾ Such measurements can be performed by time-domain (TD)⁽⁴⁻⁸⁾ or frequency-domain (FD)^(9,10) methods. The information available from these “one-pulse” experiments is determined by the mean lifetime of the excited state, which determines the time available for dynamic processes to affect the emission spectral parameters, and by the extent of orientation photoselection ($\cos^2 \theta$) possible with one-pulse optical excitation. At present, time-resolved fluorescence relies on the use of one pulse, or a single amplitude-modulated beam, for excitation of the sample, followed by measurement of the resulting intensity or anisotropy decay of the emission. In this chapter “one-pulse” or “one beam” refers to a continuous train of excitation pulses, which is the type of light source routinely used for TD or FD fluorescence.

In recent years there has been an increased emphasis on nonlinear processes, such as two- (2PE), three- (3PE), or multiphoton excitation (MPE). Simultaneous absorption of two or more photons has become possible, and practical, as the result of commercially available ps and fs lasers. The use of ps dye lasers and fs Ti:sapphire lasers have enabled 2PE of biochemical fluorophores,⁽¹¹⁻¹⁴⁾ and provide localized “confocal” excitation in fluorescence microscopy.^(15,16) In the past two years there have been several reports of 3PE under spectroscopic condi-

Joseph R. Lakowicz and Ignacy Gryczynski • Center for Fluorescence Spectroscopy and Department of Biochemistry and Molecular Biology and Medical Biotechnology Center, University of Maryland at Baltimore School of Medicine, Baltimore 21201.

Topics in Fluorescence Spectroscopy; Volume 5: Nonlinear and Two-Photon-Induced Fluorescence, edited by J. Lakowicz. Plenum Press, New York, 1997.

tions⁽¹⁷⁻¹⁹⁾ and in fluorescence microscopy.⁽²⁰⁻²²⁾ Three-photon excitation allows excitation of UV-absorbing fluorophores and tryptophan residues in proteins using the fundamental output of a Ti:sapphire laser.⁽¹⁷⁾

The use of intense pulses can result in other nonlinear effects, such as depletion of the ground-state population,^(23,24) local photobleaching of the sample using one-photon^(23,24) or two-photon⁽²⁵⁾ processes. Photobleaching or ground-state depletion can result in low apparent anisotropy values.⁽²⁶⁾ We now describe the use of time-delayed laser pulses, at longer wavelengths than the excitation wavelength, to quench the excited-state population by the process of stimulated emission. For example, if the wavelength of the quenching pulse (450 nm) overlaps the emission spectrum of the previously excited fluorophore (DPH in Figure 8.1), then the fluorophore can be stimulated to emit.⁽²⁷⁾ The emitted photon is directed along the path of the quenching beam. This photon is not observed with right-angle observation, resulting in a decrease (quenching) of the observed intensity. An accurate name for this phenomenon is fluorescence quenching by stimulated emission (FQ by SE). We will refer to FQ by SE as light quenching (LQ). For clarity we note that we are observing the residual fluorescence not quenched by light and that we are not observing the stimulated emission itself. Hence, our experiment is different from other pump-probe methods, such as induced stimulated emission (ISE), in which one observes the stimulated emission itself. Also, our experiment does not require a high concentration of fluorophore population inversion, as is needed to observe ISE or for transient absorption measurements.

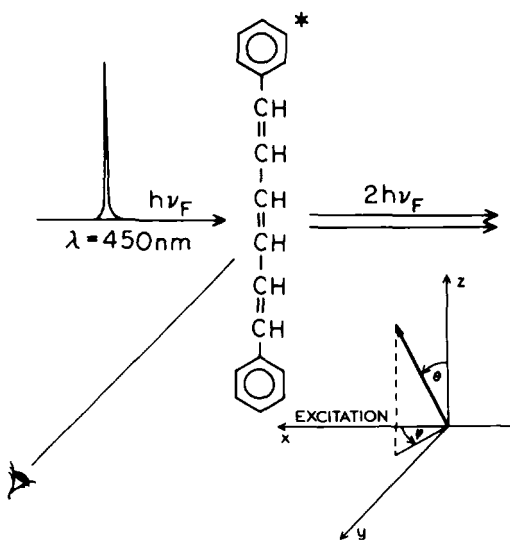


Figure 8.1. Intuitive description of light quenching. (From Ref. 44.)

The phenomenon of light quenching is illustrated in more detail in Figure 8.2. Suppose the fluorophore absorbs a photon of energy $\hbar\nu_A$. While the fluorophore is in the excited state, it can be stimulated to return to the ground state by a photon of energy $\hbar\nu_F$, which overlaps the emission spectrum of the fluorophore. The Jablonski diagram for light quenching (Figure 8.2, lower panel) illustrates how light quenching provides an additional rate process returning the fluorophore to the ground state, but this route is only active during the quenching pulse. A population inversion is not required for light quenching because an externally applied quenching pulse acts on the excited-state population, and no amplification is needed. The excitation pulse need not deplete the ground state. In our experiments we use low-intensity excitation pulses which have similar intensities to those used routinely for time-resolved fluorescence spectroscopy. In fact, light quenching may protect the fluorophore against photobleaching by decreasing the time spent in the excited state. Such protection occurs in fluorescence microscopy where energy transfer donors are bleached more slowly in the presence of acceptors which depopulate the excited state.⁽²⁸⁾

The origin of light quenching can be traced to the prediction of stimulated emission by Einstein in 1917.⁽²⁷⁾ However, observation of light quenching, outside of a laser cavity, were not reported until 1969 by Galanin *et al.*⁽²⁹⁾ These researchers were studying 2PE with a ruby laser. The expected quadratic

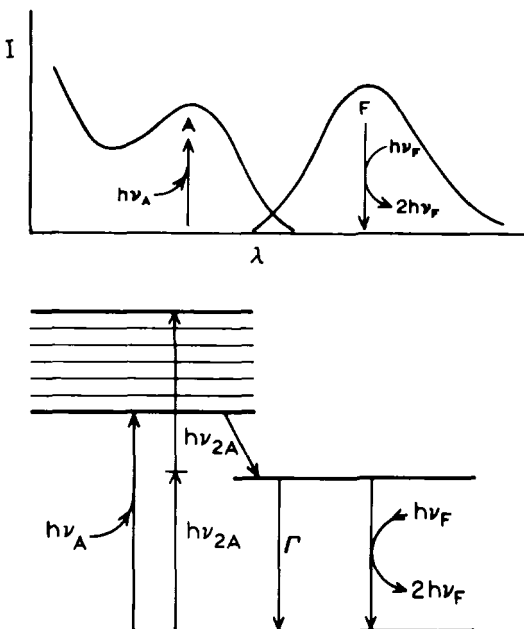


Figure 8.2. Jablonski diagram for LQ. (From Ref. 44.)

dependence on excitation intensity was observed at low illumination intensities but not for the highest intensities where the emission intensity displayed a more linear dependence. Since the laser wavelength overlapped with the red side of the emission spectra of the fluorophore, the effect was interpreted as light quenching. Light quenching was also detected indirectly by the effects of intense illumination, at nonabsorbed wavelengths, on the emission spectra of solvent-sensitive fluorophores.⁽³⁰⁻³³⁾ The blueshifts upon long-wavelength quenching suggested that the mean excited-state lifetime of the phthalimide probe was decreased by light quenching. Almost all of the published studies use a frequency-doubled ruby laser at 347 nm for excitation, and simultaneously illumination with the ruby fundamental at 694 nm. Until recently, light quenching has been primarily a laboratory curiosity and has not been applied to problems in biophysical chemistry. Prior to our experiments there were no time-resolved studies of light quenching.

A promising aspect of light quenching is that it depends on polarization and fluorophore orientation,⁽³⁴⁾ that is, the dot-vector product of the electric vector of the polarized quenching light and the emission transition moment. Mazurenko *et al.*⁽³⁵⁾ observed depolarization at high illumination intensities, apparently due to selective stimulated decay of the vertically polarized component of the excited-state population. These early reports used the giant pulses from ruby lasers, and it was not known whether significant light quenching could be observed with modern high-repetition-rate ps lasers. We now know that light quenching can be observed with cavity-dumped dye lasers,⁽³⁶⁻³⁸⁾ and that light quenching results in profound changes in the steady-state and time-resolved fluorescence intensity and anisotropy.^(39,40) By selection of the direction of propagation and polarization of the excitation and quenching beams, it may be possible to selectively deplete part of the excited-state population. This effect may be used to increase the time-zero anisotropy or to break the usual *z*-axis symmetry of the emission field. One may then apply steady-state, TD, or FD methods to the population remaining after light quenching.

Light quenching may be valuable in studies of multichromophore macromolecules. Since the extent of light quenching depends on spectral overlap of the quenching wavelength and emission spectra, it should be possible to selectively quench fluorophores in macromolecules. For instance, consider a solution or microscopic sample which contains a fluorophore which is present free in solution and bound to a protein or membrane. Depending on the quenching wavelength, light quenching may allow selective quenching of the macromolecule-bound (blueshifted) fluorophores, whereas collisional quenchers typically quench the unbound (redshifted) fluorophores. In fact, such an experiment has been performed to selectively quench the emission of free Prodan in a solution also containing Prodan bound to human serum albumin.⁽⁴¹⁾ One can imagine similar experiments using light quenching to selectively quench the buried (blue-

shifted) or exposed (redshifted) tryptophan residue in proteins. In contrast to collisional quenchers, the quenching light can be instantly removed from the sample, and thus light quenching can be used with sensitive lock-in detection schemes when the quenching beam is passed through a light chopper. Light quenching depends on the polarization of the sample and quenching beam, whereas there is no known dependence on orientation in collisional quenching. Importantly, light quenching and collisional quenching rely on different phenomena and should thus provide complementary, rather than similar, information. Light quenching with time-delayed quenching pulses may prove valuable in studies of photosynthetic proteins such as phycobiliproteins.⁽⁴²⁾ By varying the time delay and wavelengths of the quenching pulses, it may be possible to obtain additional information on the transfer of energy among the bilin pigments.

Light quenching can be regarded as a new type of fluorescence experiment, in which multiple light pulses are used to “prepare” the sample for the steady-state or time-resolved measurements. Depending on the experimental conditions, light quenching can increase or decrease the anisotropy. The extent of light quenching and changes in anisotropy are different for continuous or pulsed illumination. The effects on the anisotropy are different for quenching pulses which are co-incident or time-delayed relative to the excitation pulse and depend on the polarization orientation of the quenching beam and the angle of observation. Light quenching depends on the emission wavelength, lifetime, and cross section for quenching. The high sensitivity of fluorescence detection will allow measurements with over 95% quenching, and light quenching is not destructive. The phenomena of light quenching appears to offer new opportunities for time-resolved fluorescence.

8.2. One-Pulse and Two-Pulse Light Quenching

We will consider two types of light-quenching experiments. The simplest experimental situation is when the excitation and quenching are provided by the same light pulse (Figure 8.3, left), in which case the excitation and quenching beam is coincident in time and direction of propagation. In one-pulse experiments, ground-state depletion does not occur if the cross section for light quenching is much larger than that of light absorption,⁽³⁶⁾ which is achievable with red-edge or two-photon excitation. The second type of experiment involves excitation of the population with a low intensity pulse, followed by a more intense longer-wavelength pulse at a delay time t_d (Figure 8.3). The quenching pulse can be polarized parallel (Figure 8.3, center) or perpendicular (right) to the excitation pulse. These different experimental conditions result in distinct effects on the excited-state population.

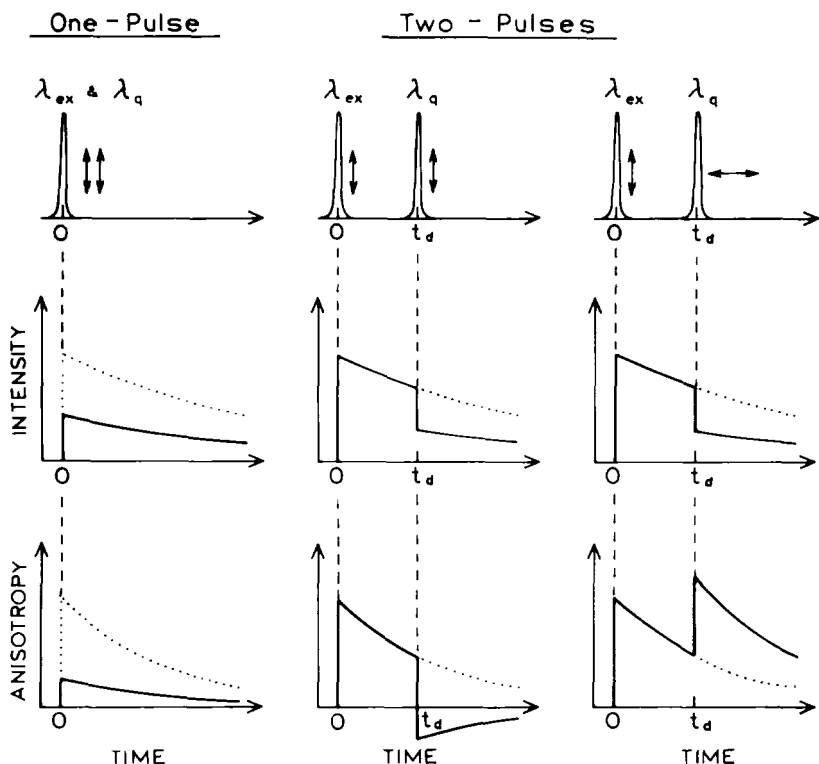


Figure 8.3. Intuitive description of the effects of LQ on the intensity and anisotropy decays of fluorescence for one-beam (left) and two-beam (center and right) experiments. The effects caused by LQ of different intensity are shown by the solid or dashed lines. The dotted lines after the quenching pulse show the shape of the intensity or anisotropy decays in the absence of LQ. (From Ref. 43.)

8.2.1. One-Pulse Time-Coincident Light Quenching

We first consider the effects of light quenching during the excitation pulse, one-pulse light quenching. Assume the sample is illuminated with a single beam (Figure 8.3, left), which is understood to be a train of intense laser pulses from a high-repetition-rate laser. For light quenching to occur, the incident wavelength must overlap with the fluorescence emission.⁽²⁹⁾ Hence, the incident excitation wavelength must be either at the extreme long-wavelength side of the absorption of a fluorophore with a small Stokes' shift or must rely on 2PE at wavelengths beyond the absorption spectrum but overlapping the emission spectrum. One-pulse light quenching is expected to decrease the intensity at time zero and the time-zero anisotropy (Figure 8.3, left).

We recently described the theory of one- and two-pulse light quenching,⁽⁴³⁾ which allows calculation of the orientation distribution of the excited-state fluorophores. The effect of one-pulse light quenching is to decrease the time-zero anisotropy. This effect can be seen as a more spherical excited-state population (Figure 8.4, middle), compared to an excited-state population preferentially aligned along the z axis in the absence of light quenching (Figure 8.4, top). Since light quenching occurs only during the pulse, we do not expect any change in the intensity or anisotropy decays following the quenching pulse. Recent experimental studies of light quenching have confirmed this prediction and demonstrated decreases in the time-zero anisotropy and intensity, with no change in the excited-state lifetime.⁽³⁶⁻³⁸⁾

One-beam light quenching decreases the time-zero (r_0) or steady-state (r) anisotropy.⁽³⁶⁻³⁸⁾ This effect is due to θ -dependent light quenching of the excited-state population, where θ is the angle between the transition direction in the fluorophore and the electric vector of the quenching beam. Excitation photo-

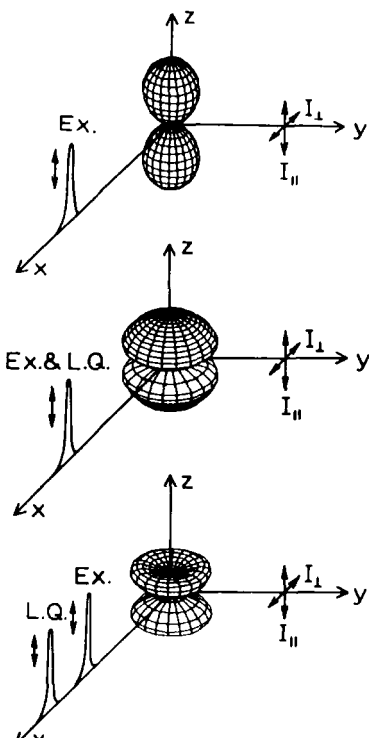


Figure 8.4. Light quenching with parallel excitation and quenching pulses. Excited-state population without light quenching (top), with time-coincident or one-pulse light quenching (middle), and with time-delayed light quenching (bottom).

selection results in a $\cos^2 \theta$ distribution of excited molecules due to the $\cos^2 \theta$ dependence of the probability of light absorption. Light quenching displays the same $\cos^2 \theta$ dependence on fluorophore orientation. For vertically polarized quenching, those fluorophores which are most closely aligned with the z axis have the highest probability of light quenching.^(43,44) In the absence of light quenching, the usual $\cos^2 \theta$ distribution is obtained (Figure 8.4, top). As the extent of light quenching increases, the distribution becomes compressed along the z axis (Figure 8.4, middle). At higher levels of quenching, the distribution becomes nearly spherical (middle), suggesting that the anisotropy approaches zero. This decreased anisotropy does not require ground-state depletion. The excited-state population around the z axis remains symmetrical because the quenching rate does not depend on the azimuthal angle ϕ . The dependence of the polarization on the extent of one-beam light quenching (Q) is shown in Figure 8.5. As Q increases, the polarization approaches zero, which is expected for a spherical distribution (Figure 8.4, middle). It is evident that the extent of light quenching will change if the absorption and emission moments are not collinear ($r_0 < 0.4$), and will depend on the rate of motion of the transition moment and the laser pulse width. We are presently developing the theory for these more complex cases.

8.2.2. Two-Pulse Time-Delayed Light Quenching

Light quenching can also be accomplished by using pulses with two different wavelengths. For 1PE the excitation pulse is typically a shorter wavelength, and the quenching pulse a longer wavelength which overlaps the emission spectrum of the fluorophore (Figure 8.3, middle and right).

When we initiated our studies of light quenching, we were not aware of the different effects of time-delayed and time-coincident quenching pulses. We now know rather different effects are expected for time-delayed pulses, which provide additional opportunities to modify the time-dependent intensity or anisotropy. The time-dependent intensity is expected to show a decrease upon arrival of the quenching pulse at time t_d (Figure 8.3, middle and right). The time-dependent anisotropy is expected to decrease for vertical polarization of the quenching beam because of selective quenching along the z axis. Remarkably, in contrast to one-beam quenching (Figure 8.4, middle), the excited-state population does not approach a spherical distribution as the extent of quenching increases. The distribution becomes selectively depleted along the z axis (Figure 8.4, bottom). At high amounts of light quenching the anisotropy can decrease below zero, as suggested by the dominant population being below a 45° angle. This is a unique property of a two-beam experiment. With a single-beam experiment, the anisotropy can only change to a spherical distribution ($r = 0$) for either pulsed or continuous illumina-

nation. For two-beam light quenching selective depletion along the z axis can cause the anisotropy to become negative for larger values of Q . In fact, the polarization approaches -1.0 (Figure 8.5). We use the polarization instead of anisotropy in Figure 8.5 because z -axis symmetry of the emission field is lost for quenching with horizontally polarized light. We have already observed anisotropy changes to less than zero using for two-pulse light quenching TD and FD⁽⁴⁴⁾ methods, demonstrating that light quenching is the origin of the observed effects. Ground-state depletion can only result in a decrease in the anisotropy to zero.

Our theoretical studies of polarized quenching^(43,44) revealed that the polarization can be increased to unity under selected conditions. This is seen in Figure 8.6 (top), where we show the excited-state population following quenching with a

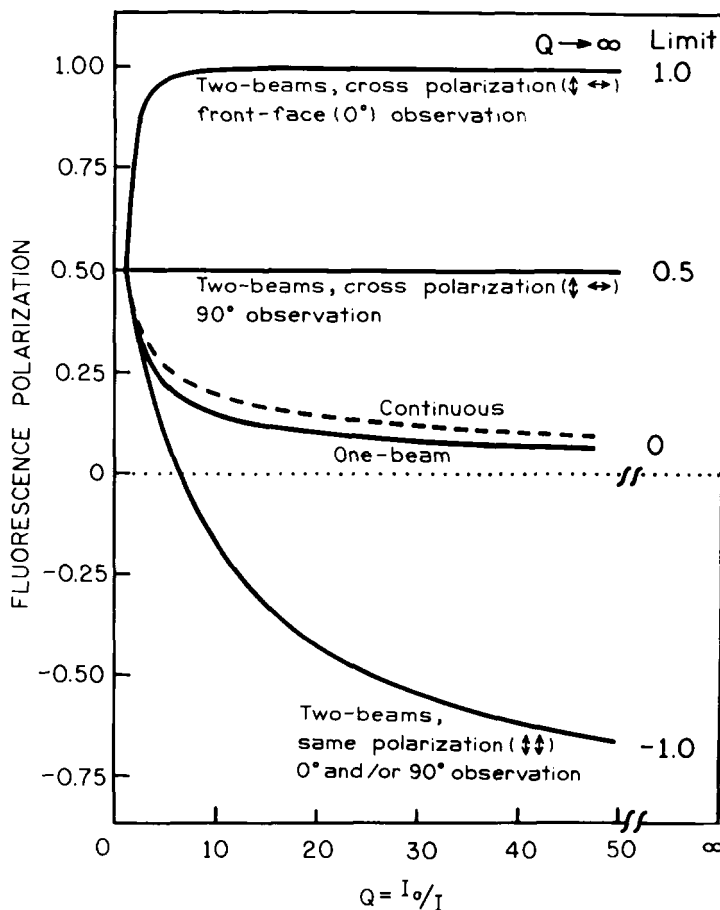


Figure 8.5. Emission polarization in the presence of light quenching. (From Ref. 44.)

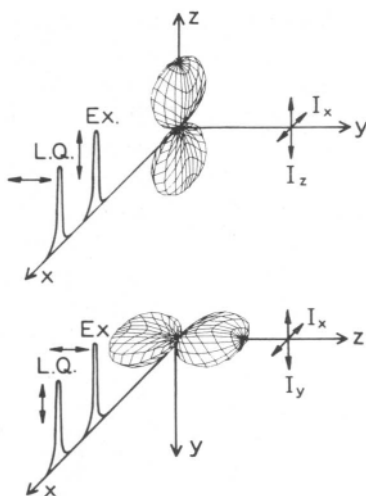


Figure 8.6. Perpendicular two-pulse light quenching. All three components of the emission can be observed with the use of vertically or horizontally polarized excitation. (From Ref. 43.)

horizontally polarized quenching pulse. This pulse results in selective depletion of excited fluorophores characterized by larger values of the projection of their transition moment on the y axis. If the emission is observed at a small angle from the x axis, then the population appears to be highly oriented. When observed along the x axis, horizontally polarized quenching results in polarization values as high as 1.0 (Figures 8.5 and 8.6). This effect can be observed experimentally with the usual experimental geometry by using horizontally polarized excitation and vertically polarized quenching (Figure 8.6, bottom). In this case the polarization approaches -1.0. High polarization values can be achieved for modest amounts of light quenching ($Q < 10$), where $Q = I_0/I$, for which I_0 and I are the intensities in the absence and presence of quenching, respectively. The results in Figures 8.4–8.6 assume that the absorption and emission moments are collinear and that the fluorophore is not rotating. Future studies will consider the effects of non-collinear transitions and rotational diffusion of nonsymmetric biomolecules.

The oriented excited-state populations obtainable with one- and two-pulse light quenching are summarized in Figure 8.7. For one-pulse light quenching the excited-state population approaches a spherical distribution. Contrasting results are obtained for two-pulse quenching. If the excitation and quenching beam have the same polarization, then the excited-state population is compressed along the z axis. At high extents of LQ the polarization approaches -1. If the excitation and quenching beams are perpendicularly polarized, the polarization can increase to +1 as observed along the excitation axis. For right-angle observation with perpendicularly polarized quenching the polarization is unchanged. Hence, polarized light quenching can result in diverse effects on the excited-state orientation.

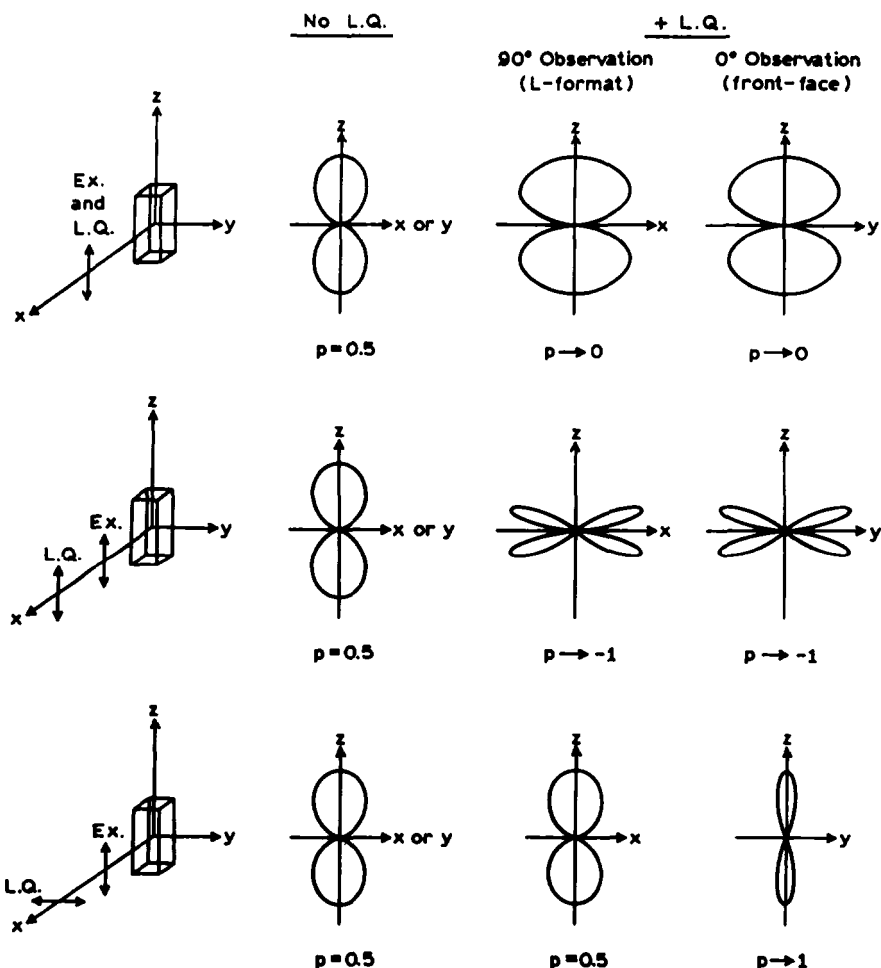


Figure 8.7. Oriented excited-state population obtainable with one- and two-photon light quenching. (From Ref. 44.)

8.3. Effects of Light Quenching on Time-Resolved Intensity and Anisotropy Decays

In the case of one-pulse light quenching the effects occur during the excitation pulse, and the width of these pulses is typically shorter than the time resolution of the instrumentation. Since the intensity and anisotropy decays are measured mostly after the excitation pulse, the decays are mostly unchanged by

one-pulse light quenching. However, time-delayed light quenching can have profound effects on the time-resolved decays.

If the time-delayed pulse arrives during the intensity decay, then the excited-state population can be decreased abruptly ($q = 50\%$ in Figure 8.8). Time-resolved measurements are often performed using frequency-domain methods,⁽⁴⁵⁾ so it is of interest to consider the effects of a step decrease in the intensity decay on the frequency-domain data. Simulated time-domain and frequency-domain data for a 50% decrease in the excited-state population are shown in Figure 8.8. The step decrease in intensity at $t_d = 1$ ns is expected to result in oscillations in the frequency response. The frequency of the oscillations is related to the time delay t_d between the excitation and quenching pulses.⁽³⁹⁾

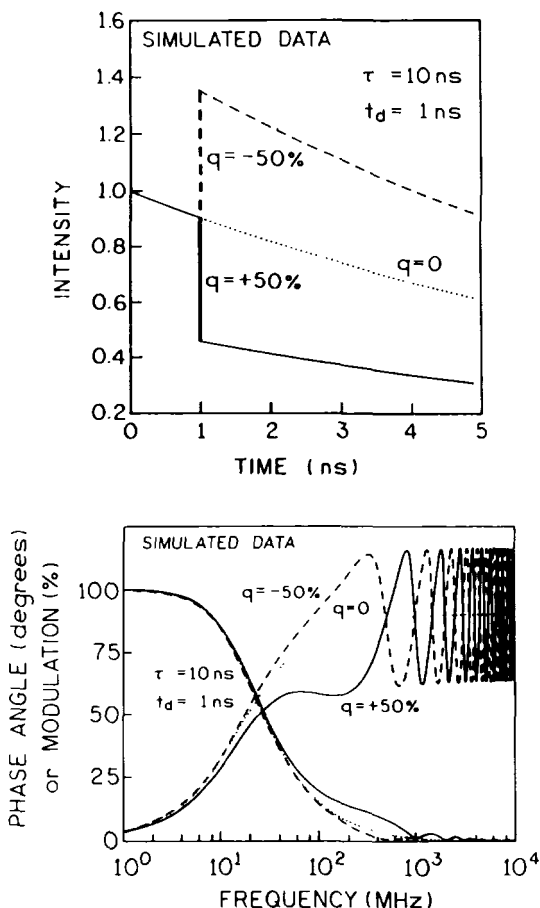


Figure 8.8. Simulated TD (top) and FD (bottom) data for a time-delayed quenching pulse for a fluorophore with a 10-ns decay time. The delay time is 1 ns. The dashed line ($q = -50\%$) indicates excess excitation over quenching by the delayed pulse. (From Ref. 44.)

It is important to consider the possibility of excitation by the quenching beam, which could occur by one-photon or two-photon excitation. Depending upon the relative magnitude of the cross sections for excitation and quenching, the second pulse could result in more excitation than quenching ($q = -50\%$). In this case the oscillations in phase angle will start in the opposite manner, with the phase (— —) initially becoming larger than the unperturbed frequency response ($q = 0$), so light quenching can be distinguished from excitation. We found that the sign and magnitude of the extent of quenching (q) can be accurately recovered from analysis of the FD data and that this parameter is essentially not correlated with the intensity decay parameters (lifetimes and amplitudes).⁽³⁹⁾

Two-beam light quenching also results in a profound alteration of the frequency-domain anisotropy decay. Simulated results for 50% light quenching, with a lifetime $\tau = 1.0$ and a correlation time $\theta = 0.1$ ns, are shown in Figure 8.9. In this simulation we assumed a step decrease in anisotropy of $\Delta r = -0.2$. The step change in the anisotropy results in oscillations in the differential polarized phase angles and the modulated anisotropy. The depth of the oscillations is sensitive to the extent of quenching (not shown), and the rate of oscillations depends on the time delay. The oscillations in Figure 8.9 are unique properties of a two-beam experiment. If the time delay is decreased to 0.001 ns, the frequency-domain anisotropy data becomes identical to that observed for a fluorophore with the same lifetime and correlation time but with a decreased time-zero anisotropy (— —).

It is also important to notice that time-delayed light quenching can result in differential phase angles larger than 30° and modulated anisotropies in excess of 0.4. Such values are outside the range possible for any fluorophore with 1 PE.^(46,47)

It appears that polarized light quenching may provide additional information on complex anisotropy decays. Consider the simplest case of parallel two-pulse light quenching with a short time delay of the quenching pulse which is polarized parallel to the excitation pulse. The initial distribution of the transition dipoles is given by $n_0(\theta) = \cos^2 \theta \exp\{-S_p \cos^2 \theta\}$, where θ is the angle from the z axis, $n_0(\theta)$ is the excited-state population, and S_p is a parameter proportional to the time-integrated power of the quenching pulse.⁽⁴³⁾ This distribution can be expressed by the surface harmonics of zero and second order, but only when the parameter S_p describing the power of the quenching pulse is small (i.e., in the absence of light quenching). When S_p is not negligible, expansion of the exponent into the Maclaurin series shows that $n_0(\theta)$ also contains the surface harmonics of order higher than 2 (fourth, sixth, eighth,...). For larger values of S_p these higher-order components may become dominant, indicating the possibility of additional information in the anisotropy decay.

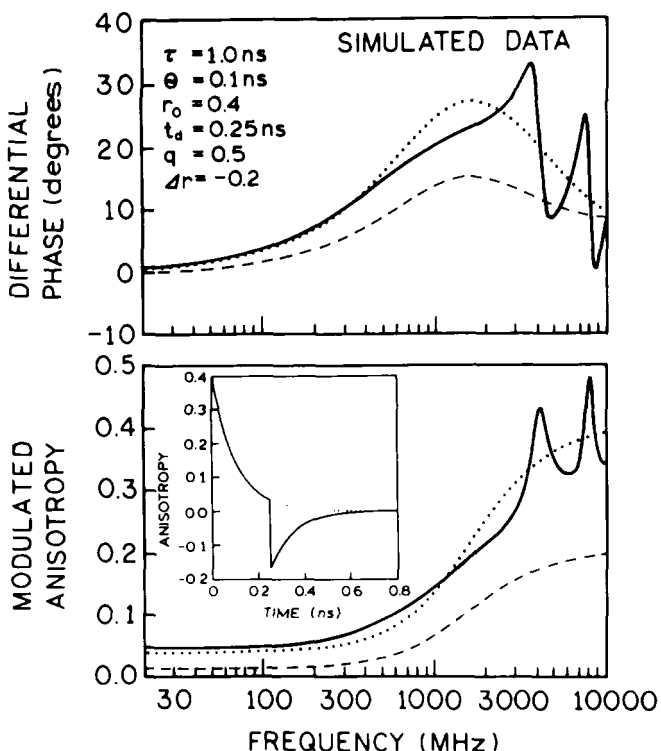


Figure 8.9. Simulated FD anisotropy data with a time-delayed quenching pulse (—) with $t_D = 0.25$ ns, $q = 0.5$ and $\Delta r = -0.2$. The dotted (· · · · ·) line represents no LQ. The dashed lines show the effect of $\Delta r = -0.2$ with $t_D = 0.001$ ns. (From Ref. 44.)

8.4. Lifetime-Resolved Experiments by Two-Beam Light Quenching

In any fluorescence experiment, the information available from the fluorophore is determined by the lifetime of the fluorophore. Several laboratories have used collisional or energy transfer quenching to decrease the excited-state lifetime. The steady-state anisotropy and emission spectra measured for various lifetimes of the fluorophore can be used to determine the rotational correlation time or solvent relaxation times, respectively.⁽⁴⁸⁻⁵²⁾ Such experiments are referred to as lifetime-resolved measurements. Hence, one can also imagine a general class of light-quenching experiments where information about the time-dependent processes is obtained by steady-state measurements as the mean lifetime is decreased by light quenching. For instance, two-beam light quenching can be

used to decrease the mean lifetime ($\bar{\tau}$) and thus obtain information on processes which occur in this time scale. The mean lifetime can be calculated as

$$\bar{\tau} = \frac{\int_0^\infty t I(t) dt}{\int_0^\infty I(t) dt} \quad (8.1)$$

In light quenching, the intensity decay is

$$I(t) = \begin{cases} I_0 e^{-t/\tau_0} & \text{for } 0 < t < t_q \\ I_0(1-q)e^{-t/\tau} & \text{for } t > t_q \end{cases} \quad (8.2)$$

where the extent of quenching when the quenching pulse arrives at the sample is

$$q = \frac{I_b - I_a}{I_b} \quad (8.3)$$

In this expression I_b and I_a are the intensities immediately before and after the quenching pulse. For these conditions the mean lifetime $\bar{\tau}$ is

$$\bar{\tau} = \tau \frac{1 - (1 + t_d/\tau)qe^{-t_d/\tau}}{1 - qe^{-t_d/\tau}} \quad (8.4)$$

Hence, the mean lifetime may be shortened by the time-delayed pulse.

The effect of q and t_d on the mean lifetime is shown in Figure 8.10. By the use of short time delays, it should be possible to reduce the mean lifetime several-fold by light quenching. A decrease in the mean lifetime, or the form of the

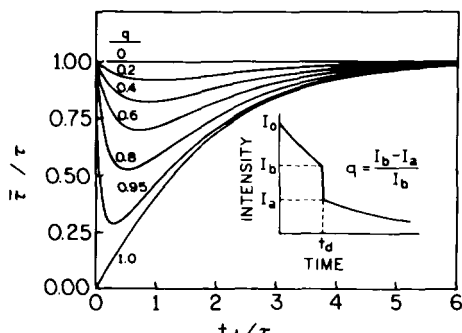


Figure 8.10. Effect of the extent $LQ(q)$ and the time delay (t_d) between the excitation and the quenching pulse on the mean lifetime of a fluorophore. (From Ref. 44.)

intensity decay, is expected to alter the steady-state anisotropy. The steady-state anisotropy is related to the intensity decay ($I(t)$) and the anisotropy decay ($r(t)$) by

$$r = \frac{\int_0^\infty r(t)I(t) dt}{\int_0^\infty I(t) dt} \quad (8.5)$$

In the case of a single exponential intensity and anisotropy decay, use of Eq. (8.5) results in the well-known Perrin equation

$$r = \frac{r_0}{1 + \tau/\Theta} \quad (8.6)$$

If the fluorescence lifetime is decreased by collisional quenching, the correlation time can be estimated by the changes in steady-state anisotropy. In light quenching it will also be necessary to consider the effects of the quenching pulse on the anisotropy of the remaining fluorophores, as well as the change in mean lifetime. Nonetheless, it is evident that information about the anisotropy decay may be obtained by alterations of the intensity decay by light quenching.

Similarly, the lifetime-resolved steady-state emission spectra can be used to estimate the solvent or spectral relaxation time. According to Bakhshiev and co-workers,⁽⁵³⁻⁵⁵⁾ the emission center of gravity (\bar{v}_{cg}) is

$$\bar{v}_{cg} = \frac{\int_0^\infty \bar{v}_{cg}(t)I(t) dt}{\int_0^\infty I(t) dt} \quad (8.7)$$

where $\bar{v}_{cg}(t)$ is the time-dependent emission center of gravity. For a single-exponential decay of $\bar{v}_{cg}(t)$,

$$\bar{v}_{cg}(t) = \bar{v}_\infty + (\bar{v}_0 - \bar{v}_\infty)e^{-t/\tau_R} \quad (8.8)$$

and a single-exponential intensity decay (Eq. 8.7) becomes

$$\bar{v}_{cg} = \bar{v}_\infty + (\bar{v}_0 - \bar{v}_\infty) \frac{\tau_R}{\tau_R + \tau} \quad (8.9)$$

where \bar{v}_0 and \bar{v}_∞ are the centers of gravity at $t = 0$ and at long times ($t = \infty$) respectively, τ is the decay time, and τ_R is the solvent or spectral relaxation time.

The precise values of \bar{v}_{cg} will depend on the values of τ , t_D , and q , but can be readily calculated for known values of τ and τ_R . It is important to recognize that information on the dynamic processes can be available from steady-state measurements while the sample is simultaneously illuminated to the excitation and quenching pulses. Since the quenching beam can be periodically interrupted

with a light chopper, it should be possible to detect small changes in the intensity by using lock-in detection. This suggests that there are many opportunities to combine the use of pulse lasers and steady-state methods to study the dynamics of fluorophores and biological macromolecules.

8.5. Experimental Results on One-Pulse Light Quenching

8.5.1. One-Pulse Light Quenching of DCM

Prior to the studies of LQ in this laboratory, all previous experiments were performed with the giant pulses from ruby lasers.⁽²⁹⁻³⁵⁾ Hence, it was of interest to determine if LQ could be observed with modern high-repetition-rate lasers. Initial LQ experiments were one-pulse because they are technically easier to accomplish. In contrast to two-beam light quenching, one-beam experiments do not require effort to obtain spectral and temporal overlap, as this occurs automatically.

Our experimental arrangement for one-beam light quenching is shown in Figure 8.11. The light source in these experiments was the cavity-dumped output of a rhodamine-6G (R6G) dye laser, which was synchronously pumped by the 514-nm output of a mode-locked argon-ion laser. The pulse width was near 5 ps, with a repetition rate of 3.795 MHz. Hence, an incident power of 50 mW corresponds to an approximate peak power of 2.5 kW. This light was focused (L_1) to a spot size of about 20 μm in diameter (Figure 8.12), resulting in a maximum intensity of about $1.0 \times 10^9 \text{ W/cm}^2$. Without focusing, the spot size was about 0.2 cm in diameter. For the initial studies of LQ⁽³⁷⁾ we selected the dye DCM for

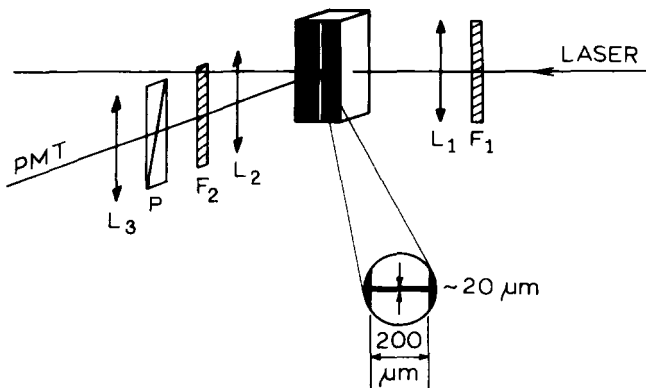


Figure 8.11. Sample and focusing configurations used for light-quenching studies of DCM. (From Ref. 37.)

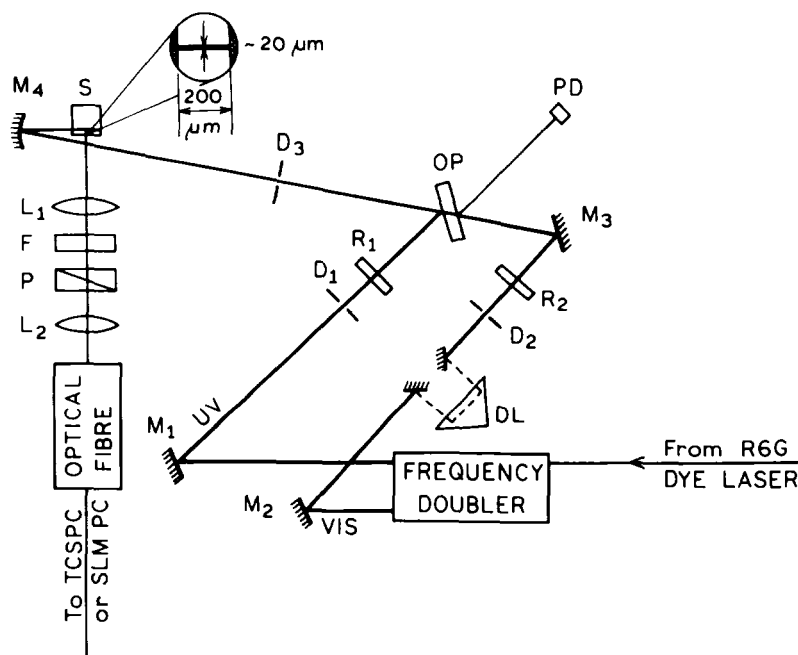


Figure 8.12. Experimental arrangement for the two-pulse FQ by SE experiment. L are lenses, P are polarizers, D are diaphragms, M are mirrors, R are polarization rotators, and F are optical filters. The delay line (DL) is placed in the quenching beam. OP is a coated optical plate (dichroic filter), and PD is a reference photodiode, used in time-resolved measurements. (From Ref. 59.)

its absorption at wavelengths available from our R6G dye laser and its ability to excite DCM in the anti-Stokes region due to a long-wavelength tail in the absorption spectrum (Figure 8.13). Additionally, DCM displays a substantial Stokes shift, which allows observation of a substantial fraction of its emission at wavelengths greater than 650 nm, allowing rejection of the incident light from 560 to 600 nm. It is important to recognize that light quenching requires that the quenching wavelength overlap the emission spectrum. Without such overlap, light quenching due to stimulated emission is not expected or observed.⁽²⁹⁾

Light quenching of DCM in glycerol is shown in Figure 8.14. For excitation with the less intense unfocused laser beam, the DCM intensity is linear with incident power up to the highest power of about 34 mW (—, lower panel). If this same light beam is focused, the DCM intensity is sublinear with incident power (• —). By sublinear we mean that the intensity does not increase linearly with increasing intensity of the incident light but rather increases more slowly.

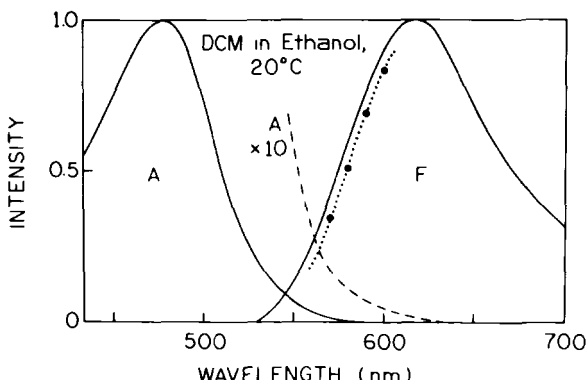


Figure 8.13. Absorption and emission spectra of DCM in ethanol. The closed circles represent relative values of the LQ constant. The emission spectra of DCM were the same for excitation ranging from 500 to 600 nm. (From Ref. 44.)

This effect can be presented as a Stern–Volmer plot (middle panel) by assuming I_0 to be the DCM intensity in the absence of light quenching (—, lower panel), or, equivalently, dividing laser power by the DCM intensity and normalizing to unity at low incident power. Specifically, for pulsed illumination the extent of quenching is approximately

$$\frac{I_0}{I} = 1 + \sigma_{lq} t_p P \quad (8.10)$$

where I_0 and I are the intensities in the absence and presence of LQ, t_p is the pulse width, σ_{lq} is the cross section for light quenching, and P is the laser power. The extent of quenching is linear with laser power, and no quenching is observed for the unfocused laser beam (Figure 8.14, middle panel). Importantly, the steady-state anisotropy of DCM decreases over the same range of intensities where light quenching occurs (Figure 8.14, top) and does not decrease for unfocused excitation that does not cause light quenching. A decrease in anisotropy is expected for the single-beam configuration (Figure 8.3), and r_0 values are greater than zero. Similar decreases in anisotropy were observed previously for phthalimide derivatives by using the fundamental output of pulsed ruby lasers.^(33,35) The results of DCM suggest that significant amounts of light quenching can be observed with modern high-repetition-rate dye lasers.

Illumination of fluorophores with high-intensity laser light can result in a wide range of undesirable photochemical and photophysical processes, such as sample decomposition, heating, and other effects. Results of the type in Figure 8.14 could also be due to decomposition or heating of the sample by the high local light intensity. To exclude this possibility we decreased the average incident

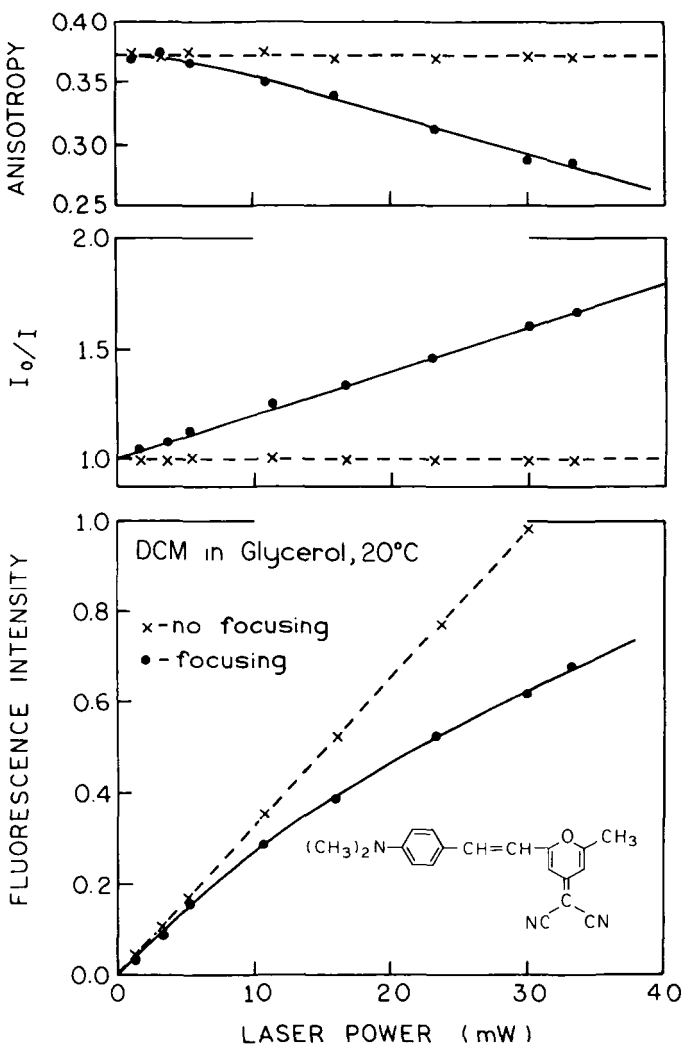


Figure 8.14. Dependence of the fluorescence intensity of DCM in glycerol on the excitation power (lower panel). The middle panel shows a Stern-Volmer representation of the light-quenching data. The upper panel shows the steady-state anisotropy. (From Ref. 37.)

power using a mechanical light chopper. The same power-dependent intensities and anisotropies for DCM (Figure 8.14) were observed when the average power was decreased 100-fold.

To further eliminate the possibility of unwanted effects as the origin of light quenching, we examined the effects of incident wavelength on the extent of light

quenching. These data (Figure 8.15) show that the amount of light quenching increases at longer wavelengths. Since the amount of light absorbed decreases with longer incident wavelength, these results suggest that the quenching effect of the high-intensity illumination is not due to absorption of excessive amounts of light or depletion of the ground-state DCM population.

The amount of light quenching is expected to depend on the extent of overlap of the incident light with the fluorescence emission spectrum. More specifically, the cross section for quenching is expected to be proportional to the emission spectra $I(\bar{v})$ and inversely proportional to the natural (radiative) lifetime (τ_N) by

$$\delta_{\text{LQ}} = \frac{k'}{\tau_N} \frac{I(\bar{v})}{\int I(\bar{v}) d\bar{v}} \quad (8.11)$$

where k' is a constant. This suggests that the amounts of quenching should scale as the emission spectrum.

The wavelength-dependent quenching constants are shown in Figure 8.13 along with the DCM emission spectrum. The amount of quenching clearly follows the DCM emission spectrum. To the best of our knowledge, these data represent the first measurement of light-quenching spectrum of a fluorophore. This observation of a quenching spectrum corresponding to the emission spectrum indicates that this spectrum already exists within the 5-ps duration of the excitation pulse. More explicitly, this result suggests that the excited-state of

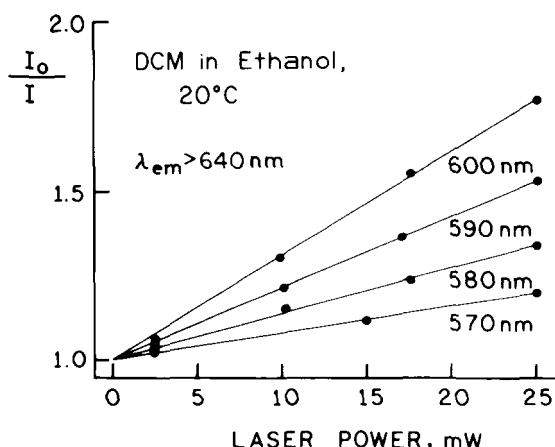


Figure 8.15. Wavelength-dependent quenching of DCM in ethanol. (From Ref. 44.)

DCM has already relaxed from the Franck–Condon state to the solvent relaxed state during the laser pulse.

As a final confirmation of our observation of light quenching we examined the FD intensity and anisotropy decays of DCM for low- and high-power illumination (Figure 8.16). As discussed, light quenching is expected to decrease the steady-state intensity and anisotropy but not to change the decay time or rotational correlation time. While the fluorescence quantum yield of DCM is decreased by high-power illumination, its decay time is not changed (Figure 8.16, top). The inserts show the intensity decays reconstructed from the FD data.

The bottom of Figure 8.16 shows the FD anisotropy decay. The correlation times are identical for low- and high-intensity illumination, which argues strongly against the presence of any heat-dependent effects of the observed light quenching. Heating of the sample is expected to decrease the rotational correlation time. Importantly, the time-zero anisotropy ($r(0)$) is decreased for high laser power, as predicted for coincident excitation and quenching pulses (Figure 8.3).

Although not shown, similar results for one-pulse light quenching were observed for rhodamine-B.⁽³⁶⁾ That is, the extent of RhB quenching was proportional to the amplitude of the emission spectrum, the lifetime and correlation times were unchanged by LQ, and the steady-state and time-zero anisotropy were decreased by LQ.

8.5.2. One-Pulse Light Quenching with Two-Photon Excitation

Two-photon excitation is now widely used for confocal fluorescence microscopy.^(15,16) The intense focused illumination needed for 2PE may result in light quenching and a decrease in the time-zero intensity or polarization in multiphoton microscopy. Additionally, one group has already started using light quenching in an attempt to improve the spatial resolution of light microscopy. Dr. S. Hell and co-workers are using light quenching to break the diffraction resolution limit in fluorescence microscopy.⁽⁵⁶⁾ They are using light quenching to remove emission in the outer regions of the excitation point-spread function. The principles of light quenching have already been used to provide lifetime imaging microscopy.⁽⁵⁷⁾ Hence, we asked whether LQ might occur with 2PE.

For studies of LQ with 2PE we selected tetraphenylbutadiene (TPB) because of its high two-photon cross section and its emission spectrum, which overlaps with the wavelength used for excitation and quenching (514 to 610 nm, Figure 8.17). Since the two-photon absorption is low, we do not expect significant depletion of the ground state or other undesirable thermal or photochemical effects.

As a control molecule we chose PPO because of its known large cross section for 2PE.⁽¹¹⁾ The emission of PPO does not overlap with the excitation

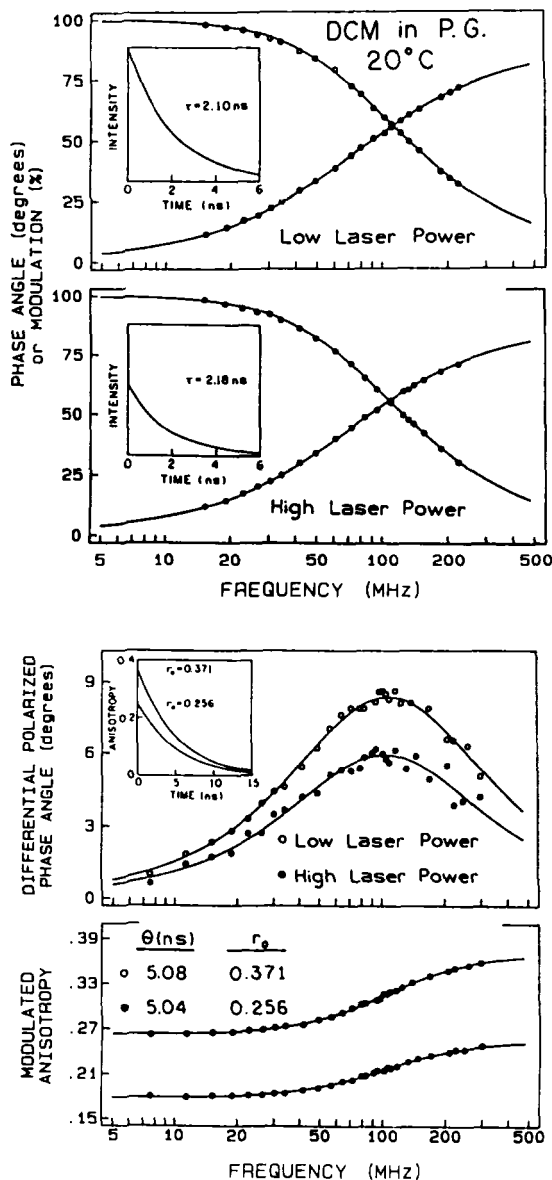


Figure 8.16. Frequency-domain intensity (top) and anisotropy decays (bottom) of DCM in propylene glycol at low (\circ) and high (\bullet) laser power.

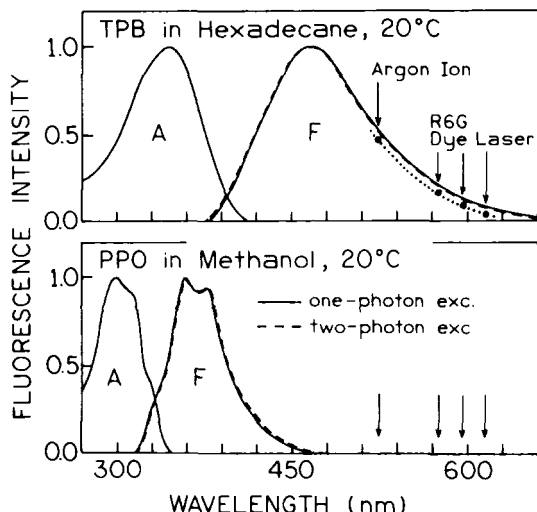


Figure 8.17. Absorption (A) and emission (F) spectra of TPB in hexadecane (top) and PPO in methanol (bottom). In each case the solid line shows the emission spectrum for 1PE (360 nm for TPB and 290 nm for PPO), and the dashed line the emission spectrum for 2PE at 575 nm. The filled circles show the relative cross section for quenching, obtained from Figure 8.19. (From Ref. 38.)

(quenching) wavelength, so light quenching is not expected during 2PE of PPO. The fluorescence intensities of PPO for increasing incident power are shown in Figure 8.18. As expected, the PPO intensity depends quadratically on laser power (---x---). In contrast, the fluorescence intensities of TPB display a less-than-quadratic dependence (—●—). This difference between PPO and TPB is due to the longer-wavelength emission of TPB and its overlap with the incident wavelength.

The relative cross sections for quenching can be obtained from “quadratic” Stern–Volmer plots. For 2PE the intensity in the absence of light quenching is proportional to the square of the incident intensity. Hence, one can rewrite Eq. (8.10) as

$$\frac{P^2}{I} = 1 + \sigma_{lq} t_p P \quad (8.12)$$

Hence, a plot of P^2/I versus P is expected to give a slope proportional to the cross section for light quenching. In this plot (Figure 8.19) the data for PPO appear as a horizontal line due to its pure quadratic dependence on the incident power and the absence of light quenching. Our interpretation of the subquadratic TPB intensities as being due to light quenching is supported by lesser amounts of quenching observed at longer wavelengths (Figure 8.19). Progressively smaller cross sections for quenching are seen at 514, 575, 595, and 615 nm (Figure 8.17), which corresponds to decreasing overlap with the emission spectrum of TPB. In fact, the slopes of the “quadratic” Stern–Volmer plots (relative cross section

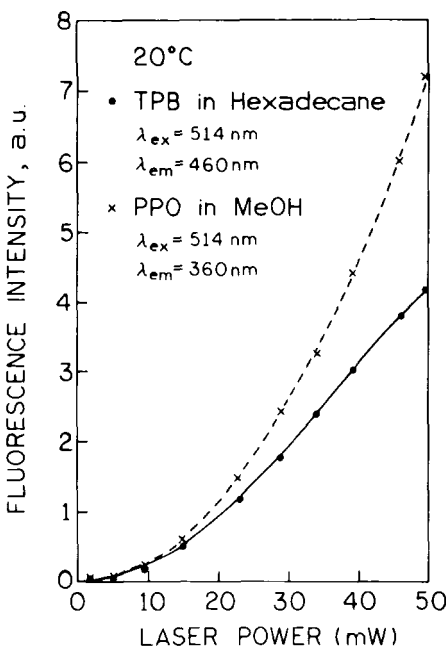


Figure 8.18. Fluorescence intensity of PPO and TPB for increasing laser power. The dashed line is the square of the laser power normalized to the intensity of PPO at low incident power. (From Ref. 38.)

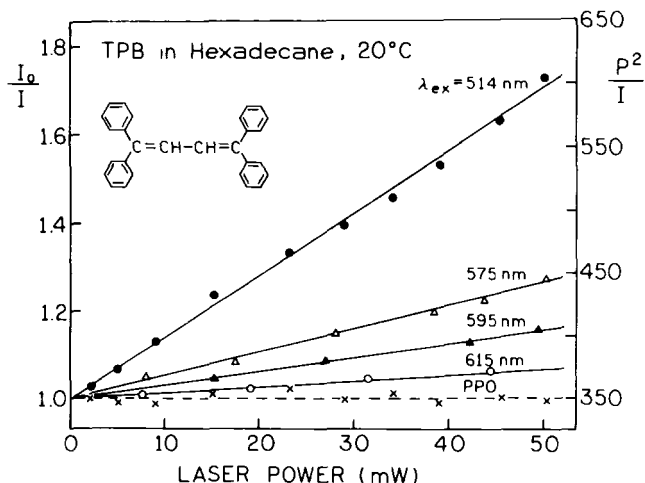


Figure 8.19. "Quadratic" Stern-Volmer light quenching plots for PPO (---) and TPB (—). No quenching is seen for PPO, whose emission spectrum does not overlap with the quenching wavelength. The excitation and quenching wavelengths are indicated. (From Ref. 38.)

for quenching) closely follow the emission spectrum, as expected for the phenomena of stimulated emission.

While the fluorophores described (DCM, RhB, and TPB) are not used as biochemical probes, we note that one-beam light quenching of biochemical probes has been observed. Light quenching was observed with a Ca^{2+} probe, Fura-Red.⁽⁴⁴⁾ The extent of quenching was proportional to the amplitude of the emission spectrum at the quenching wavelength. Light quenching has also been observed for DAPI and Hoechst 33342 bound to DNA.⁽⁴⁴⁾ The presence of observable light quenching of these Ca^{2+} and DNA probes with 1PE indicates the need to consider this possibility in two-photon microscopy.^(15,16)

8.6. Experimental Results on Two-Pulse Light Quenching

We now describe results for two-pulse light quenching. Our experimental apparatus for two-pulse light quenching is shown in Figure 8.12. Two-pulse light quenching requires precise timing of the quenching beam relative to the excitation beam, which is possible with the fundamental and frequency-doubled outputs of a single dye laser. The probe 4-dimethylamino-4'-cyanostibene (DCS) was selected for these initial light-quenching experiments because of its favorable spectral properties compared to the R6G laser. Absorption and emission spectra are shown in Figure 8.20. The large Stokes shift of DCS allows excitation with the frequency-doubled output of the R6G laser (290 to 310 nm) and light quenching with the fundamental output of this same laser. DCS displays an emission maxima near 540 nm with a tail to over 600 nm. This allows use of the R6G dye laser to quench the emission by illumination from 580 to 620 nm. The emission can be observed at 540 nm with a monochromator or interference filter without interference from the longer-wavelength quenching beam. DCS displays a high fundamental anisotropy for UV excitation, as seen by the steady-state anisotropy spectrum in glycerol (Figure 8.20, lower panel). This is desirable because we wish to observe the decrease in anisotropy due to light quenching. In the present experiment we also want the quenching pulse to arrive during the anisotropy decay. This condition is met in dimethylformamide (DMF), where the correlation time is near 124 ps. An additional advantage of DCS is that it displays a single-exponential decay in a range of solvents, allowing detection of light quenching as deviations from the single-exponential model. Finally, the emission spectrum of DCS is highly sensitive to solvent polarity. This feature allows us to examine the effects of quenching wavelength and solvent relaxation on the emission spectra of the unquenched DCS molecules.

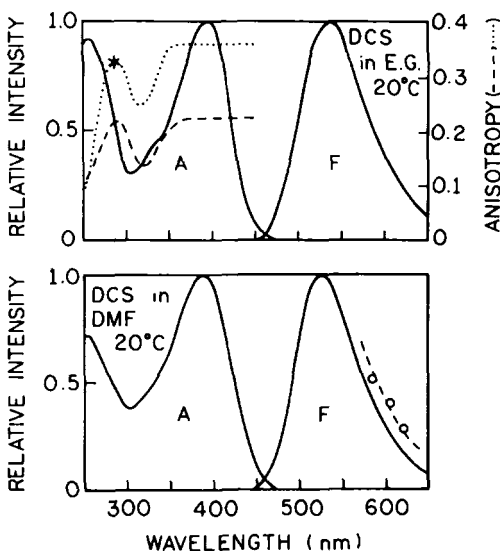


Figure 8.20. Absorption and emission spectra of DCS in EG (top) and DMF (bottom). The open circles (\circ) show the relative cross section for LQ in DMF. The dashed (—) and dotted (···) lines (top panel) show the steady-state anisotropy spectra in EG and glycerol, respectively. The star (*) shows the time-zero anisotropy recovered from the FD anisotropy data (Figures 8.24 and 8.26). (From Ref. 44.)

8.6.1. Steady-State Measurements with Two-Beam Light Quenching

We first examined whether the steady-state intensity of DCS could be decreased by illumination with 590-nm light. For these measurements the sample was illuminated with the 2-MHz pulse train of excitation pulses or a combined pulse train of both excitation (295 nm) and quenching (590 nm) pulses. Illumination at 295 and 590 nm results in a substantial decrease in intensity (Figure 8.21). The decrease in the intensity of DCS was proportional to the laser power at the quenching wavelength. If the quenching beam is blocked, and if the excitation and quenching beams are not synchronized, there is no quenching.

It is interesting to observe the effects of the time delay between the excitation and quenching pulses on the extent of quenching. No change in intensity was observed if the quenching pulse preceded the excitation pulse (Figure 8.22). This result suggests that there are no effects of the quenching beam unless an excited-state population is present, and it argues against thermal or photochemical effects of the quenching beam. The quenching effect was completely and immediately reversible upon blocking the quenching beam. The emission spectra are nearly identical in the absence and presence of light quenching (Figure 8.21), but we did observe spectral shifts in more viscous solvents (below).

The total amount of quenching, as observed in the steady state, is expected to depend on the time delay. As the time delay increases, the excited-state population decays and there is less fluorescence to quench. The dependence of the

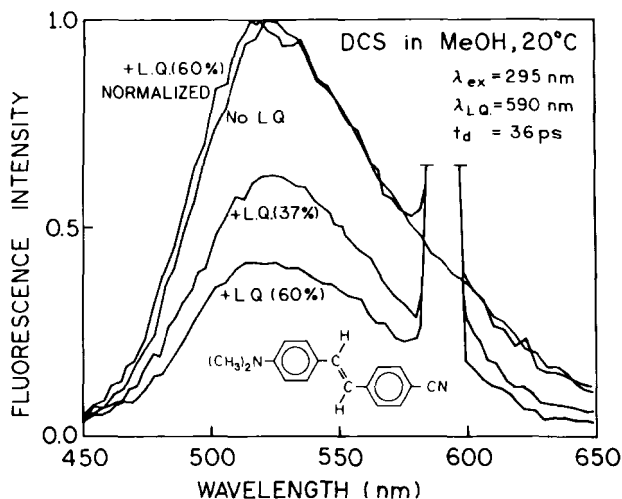


Figure 8.21. Emission spectra of DCS in the absence of light quenching (LQ 0%) and with light quenching. The peak near 590 nm is the scattered quenching light. (From Ref. 39.)

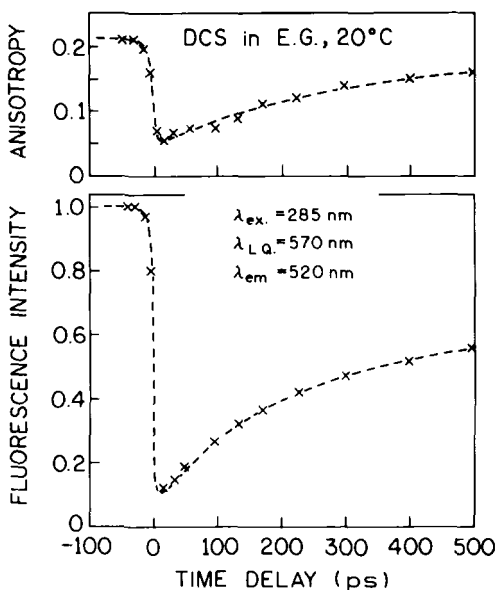


Figure 8.22. Effect of time-delayed light quenching on the steady-state anisotropy (top) and intensity (bottom) of DCS. (From Ref. 59.)

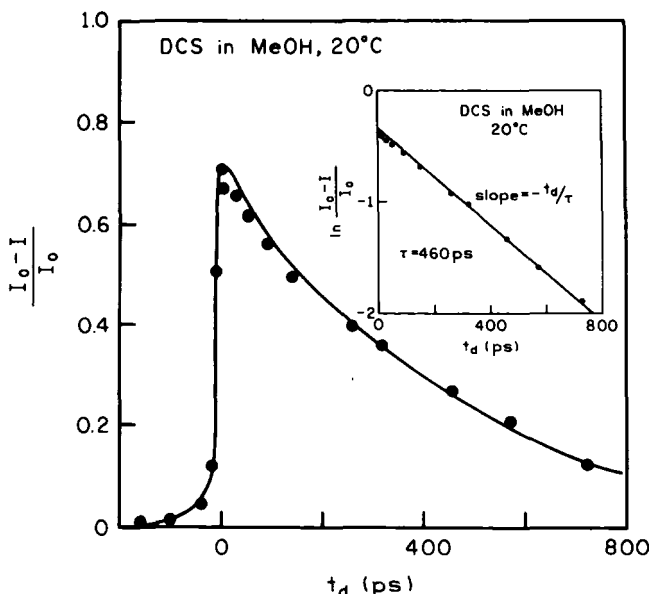


Figure 8.23. Steady-state measurements of the extent of LQ for various delay times. (From Ref. 44.)

extent of quenching on time delay is shown in Figure 8.23. As expected, there is no light quenching for $t_d < 0$ because the fluorophores are not yet excited. The extent of quenching, as measured by $(I_0 - I)/I_0$, appears to decrease exponentially with time delay, where I_0 and I are the steady-state intensities in the absence and presence of LQ, respectively. In fact, using Eq. (8.2), one obtains

$$\frac{I_0 - I}{I_0} = q \exp\left(-\frac{t_d}{\tau}\right) \quad (8.13)$$

A plot of $\ln(I_0 - I)/I_0$ versus t_d yields the decay time as the slope; such data can be used to measure the excited-state lifetime. In other systems multiexponential decays have been resolved by time-delayed light quenching.⁽⁵⁸⁾ Given the short pulse widths of laser sources and the ability to accurately set short delay times, light quenching may prove valuable for studies of fast components in complex decay processes.

8.6.2. Time-Domain and Frequency-Domain Studies of Light Quenching

In the introduction we described the unusual intensity and anisotropy decays possible in the presence of time-delayed light quenching. We now show data

which confirm these predictions. Time-resolved intensity and anisotropy decays of DCS with time-delayed light quenching are shown in Figure 8.24. In the absence of light quenching, the decays are single exponentials. The presence of a time-delayed quenching pulse results in a steep decrease in the DCS intensity (Figure 8.24, left) and anisotropy decay (right). This effect was immediately reversible on blocking the quenching beam. The amplitudes of the intensity and anisotropy changes depended upon laser power. To the best of our knowledge no mechanism, other than light quenching, could result in these effects.

We examined the frequency-domain intensity and anisotropy decays to detect the oscillations predicted in Figures 8.20 and 8.9. Frequency-domain data of DCS in DMF are shown in Figure 8.25. In the absence of a time-delayed quenching pulse, we observed the usual frequency response for the single-exponential intensity decay of DCS, which displayed a 675-ps lifetime in DMF (dotted line). Upon illumination with the long-wavelength pulses, the intensity decay displays a profound change in shape. The extent of the changes in the frequency response can be seen by comparison of these data for light-quenched DCS (bottom, $-●-$) with the single-exponential frequency response observed upon blocking the quenching beam (top). It is obviously impossible to fit these data to the single-exponential model (bottom, $- - -$). If the time delay is increased, the shape of the FD data changes, with an apparent increase in oscillation frequency.⁽³⁹⁾ Such oscillations provide an unambiguous demonstration of light quenching.

We also measured the FD anisotropy decay of DCS in DMF (Figure 8.26). In the absence of light quenching, the anisotropy decay was a single correlation time of 124 ps. The data display oscillations in the presence of a time-delayed

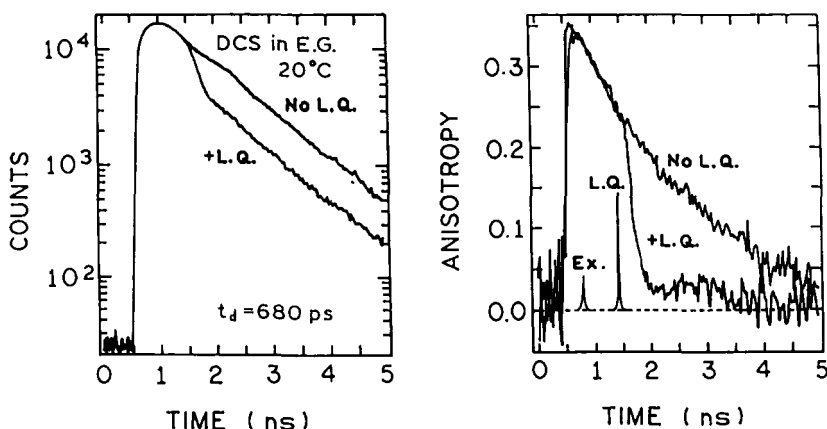


Figure 8.24. Time-domain measurements of the two-pulse LQ of the DCS intensity (left) and anisotropy (right) decay.

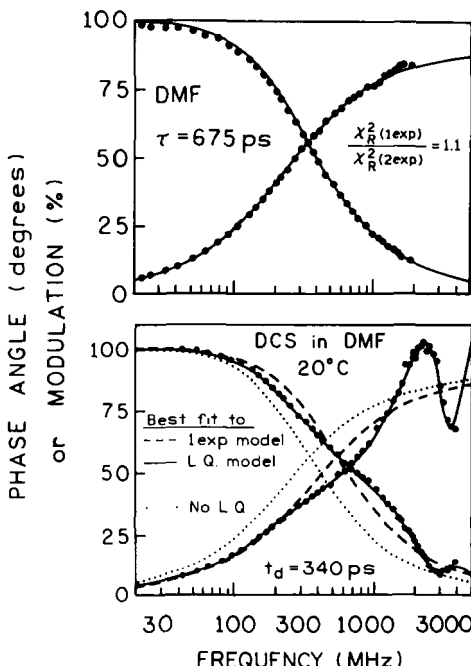


Figure 8.25. Frequency-domain intensity decay of DCS in DMF in the absence (top) and presence (bottom) of the time-delayed LQ. (From Ref. 44.)

quenching pulse (—●—). The recovered time-zero anisotropy, which exists before the quenching pulse, was the same in the absence and presence of time-delayed light quenching, and agrees with the anisotropy observed in viscous glycerol (Figure 8.20). In contrast to one-beam light quenching, two-beam light quenching does not decrease the time-zero anisotropy but changes the anisotropy after the pulse. Importantly, light quenching can cause the anisotropy to decrease to below zero, as can be seen from the time-domain anisotropy decay reconstructed from the FD data (Figure 8.26, insert). This result strongly suggests that light quenching, and not ground-state depletion or photobleaching, is the origin of the observed effects. Light quenching can also be used to induce the anisotropy in originally isotropic (low anisotropy) excited systems, allowing a time-resolved anisotropy decay measurement.

8.6.3. Wavelength-Selective Light Quenching with Time-Dependent Spectral Relaxation

One possible biochemical application of light quenching is wavelength-selective quenching in the presence of solvent relaxation or energy transfer, as illustrated in Figure 8.27. Light quenching on the long-wavelength side of the emission is expected to selectively quench the relaxed emission (middle),

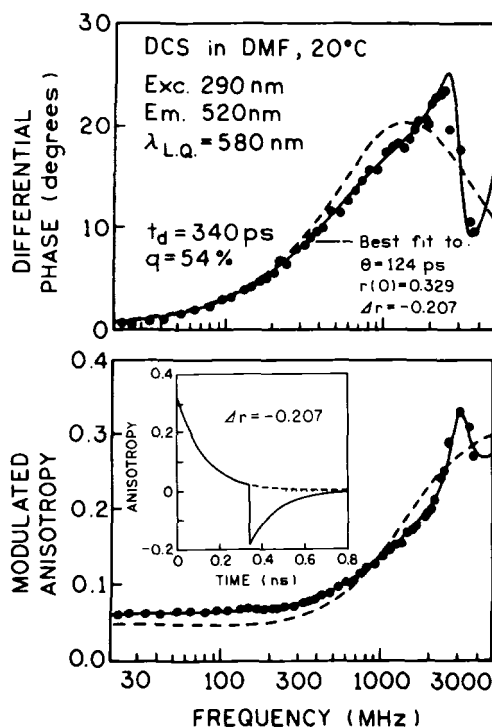


Figure 8.26. Frequency-domain anisotropy decay of DCS in the presence of time-delayed light quenching.

resulting in a blueshift of the emission spectrum. Additionally, for vertically polarized excitation and quenching, the anisotropy is expected to become dependent on emission wavelength due to photoselective quenching of the vertically polarized and relaxed emission (Figure 8.27, bottom).

To examine these possibilities, we chose to examine DCS in more viscous solvents such as propylene glycol and glycerol, which display time-dependent spectral relaxation. We questioned whether light quenching on the long-wavelength side of the emission would result in selective quenching of the solvent relaxed state or in uniform quenching of DCS at all emission wavelengths. Emission spectra are shown in Figure 8.28 for unquenched DCS and for light quenching at 570 nm. The intensity-normalized spectra show that the emission spectra are blueshifted by light quenching at 570 nm. Light quenching selectively occurs for the solvent relaxed state whose emission wavelength overlaps with the light-quenching wavelength. The extent of blueshift depends on the time delay t_d (Figure 8.29). In fact, one can use the dependence of the spectral shift on the delay time to obtain information on the rate of spectral relaxation.⁽⁵⁹⁾ The emission center of gravity for various delay times revealed the presence of at least two relaxation times for DCS (Figure 8.29).

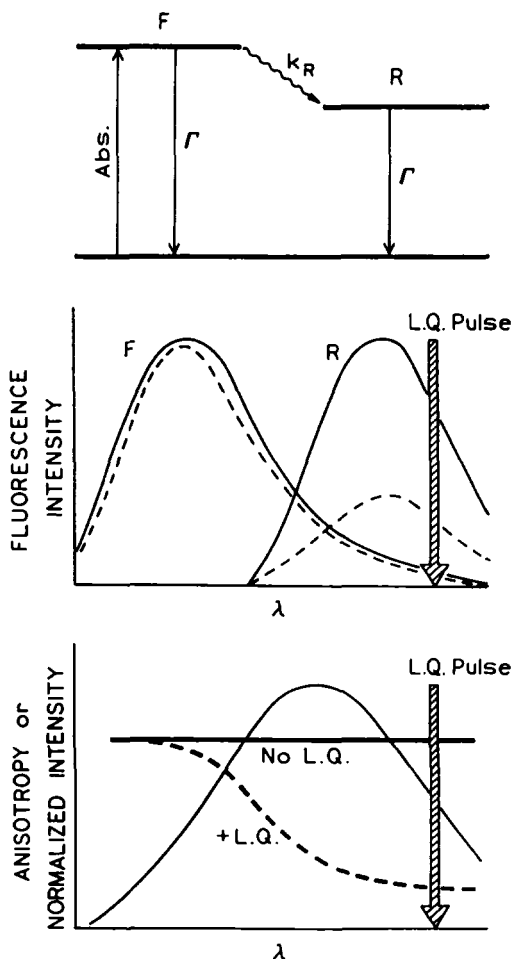


Figure 8.27. Effect of light quenching on the emission and anisotropy spectrum in the presence of spectral relaxation.

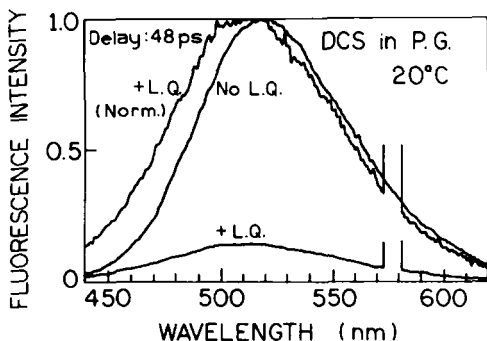


Figure 8.28. Light quenching of DCS in propylene glycol at 20°C. (From Ref. 59.)

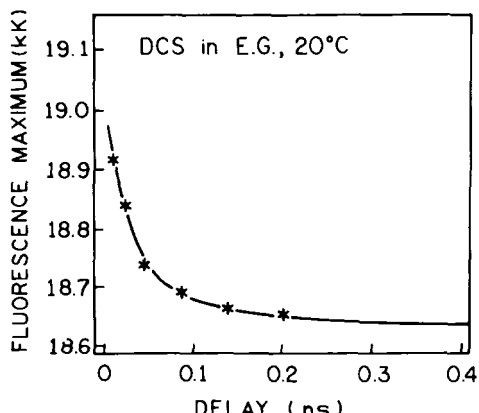


Figure 8.29. Effect of t_d on the emission maximum of DCS. (From Ref. 59.)

We questioned whether the spectral shifts in Figure 8.28 were due to the effects of spectral relaxation and wavelength-selective light quenching or had some other origin. We examined samples where solvent relaxation was either complete prior to arrival of the quenching pulse or where time-dependent spectral shifts were not expected to be significant. To obtain complete relaxation we chose DCS in the highly fluid solvent methanol, where spectral relaxation is essentially complete prior to arrival of the quenching pulse. In this case light quenching decreased the emission intensity but did not result in any spectral shift (Figure 8.30, top). Hence, for a fluorophore in a single or dynamically averaged environment one expects uniform quenching across its emission spectrum. Additionally, we examined acridine orange in propylene glycol at 20°C. Acridine orange is relatively insensitive to solvent polarity. No spectral shift was seen for acridine orange with light quenching (Figure 8.30, bottom), which displays a uniform decrease in intensity across the emission spectrum. These results demonstrate that light quenching is sensitive to the rates and extent of spectral relaxation and can be used to selectively deplete those fractions of the fluorophore population which overlap with the quenching wavelength.

We next examined the emission anisotropy spectra of DCS. In the absence of light quenching the anisotropy of DCS was found to be essentially independent of emission wavelength. Upon illumination at 570 nm the emission anisotropy spectrum displays a strong dependence on emission wavelength (Figure 8.31, top). The decreased anisotropy at long wavelengths indicates that light quenching can selectively deplete the relaxed state. Although not possible with our present lasers, light quenching on the blue side of the emission should selectively quench the unrelaxed state. Control experiments on the solvent-insensitive fluorophore acridine orange show a decrease in anisotropy due to light quenching

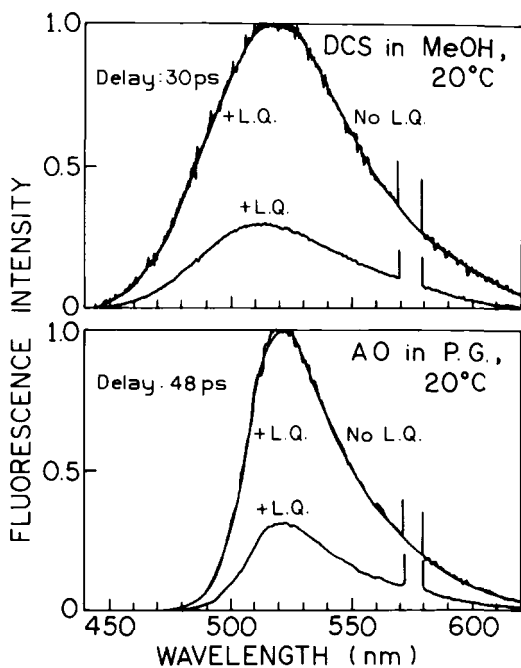


Figure 8.30. Light quenching of DCS in methanol (top) and of acridine orange in propylene glycol (bottom). (From Ref. 59.)

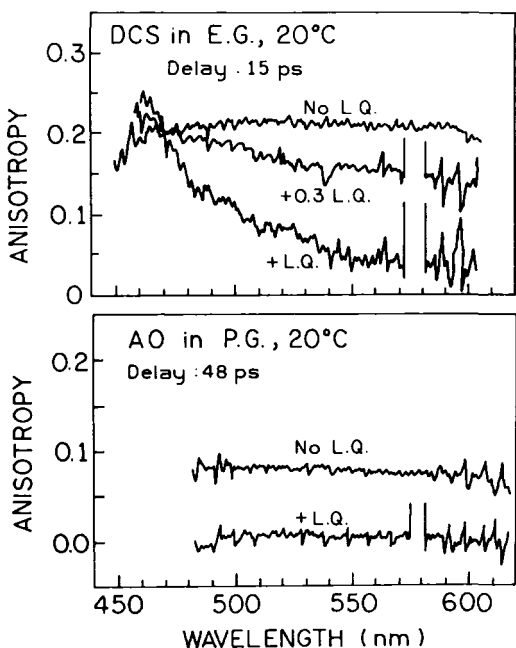


Figure 8.31. Emission anisotropy spectrum of DCS in ethylene glycol (top) and AO in PG (bottom) in the absence of (no LQ) and presence (+ LQ) of light quenching.

(Figure 8.31, bottom). However, the anisotropy remains constant across its emission spectrum independent of the extent of light quenching.

We have already started development of the theory, which showed that the spectral shift is highly sensitive to t_d and the presence of one or more relaxation times.⁽⁵⁹⁾ The method appears to be highly sensitive to processes occurring on the 10-ps time scale, even in the presence of a second slower process. Light quenching may thus provide an ability to measure components in the relaxation process normally hidden by more dominant effects. For instance, our simulations for the DCS system⁽⁵⁹⁾ showed that the small-amplitude slower component of the spectral relaxation becomes the dominate component following the quenching pulse (Figure 8.32). The relaxation appears to be slower because light quenching does not create the *F* state but removes part of the redshifted population. In the remaining population the fast part of the relaxation is already complete. Hence, following light quenching at long wavelengths, one can expect to selectively observe the slower components in the relaxation process. Additionally, the spectral shift due to light quenching depends strongly on whether spectral relaxation is a single (· · · ·) or double (—) exponential (Figure 8.33). These simulations suggest that time-delay and wavelength-dependent light quenching can provide a new method to examine complex relaxation processes in biopolymers.

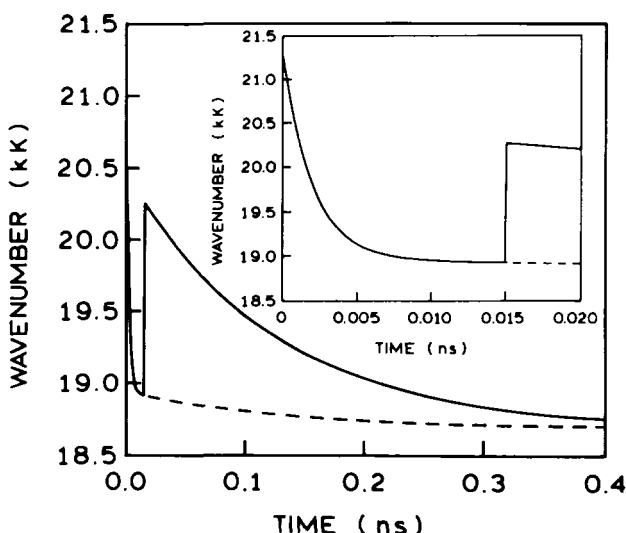


Figure 8.32. Dependence of the position of the center of gravity of the emission spectrum on time in the presence (solid line) and absence (dashed line) of light quenching. The insert shows the first 20 ps in more detail. (From Ref. 59.)

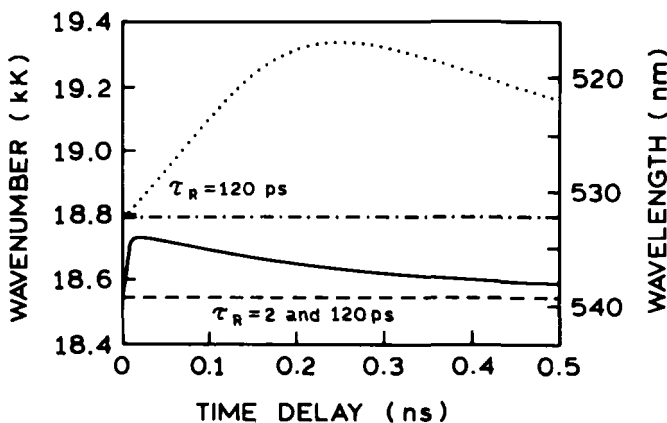


Figure 8.33. Effect of time delay of the quenching pulse on the position of the steady-state emission center of gravity for a single- (· · · · ·) and double- (—) exponential spectral relaxation. (From Ref. 59.)

8.7. Applications of Light Quenching

8.7.1. Wavelength- or Lifetime-Selective Light Quenching

Light quenching appears to provide opportunities for studies of multichromophoric systems. For each fluorophore the extent of light quenching is expected to depend on its cross section for quenching, decay time and time delay, emission spectrum, and quenching wavelength. Hence, it appears that light quenching can be used to selectively quench one fluorophore in a mixture of fluorophores. We examined this possibility in both the one-pulse and two-pulse experiments. In one-pulse quenching we examined a mixture of DCM and ethidium bromide (EB) in methanol. The emission spectra of DCS and EB are similar (Figure 8.34). Because of its higher cross section for light quenching, DCM ($\tau = 1.2$ ns) was more sensitive to one-beam light quenching at 600 nm than EB ($\tau = 5.8$ ns and a natural lifetime near 30 ns). Under light-quenching conditions the FD intensity decay displayed a larger amplitude of the 5.8-ns lifetime of EB compared with the 1.2-ns lifetime of DCM (Figure 8.35). We observed changes in the emission spectra and intensity decay of several other mixtures for one-pulse light quenching,⁽⁶⁰⁾ demonstrating that light quenching can alter the information content of the time-resolved data.

For time-delayed two-pulse light quenching we examined mixtures such as of DCS and 2-AF (Figure 8.36). We found that fluorophores with similar emission spectra can be selectively quenched. For instance, 3-aminofluoranthene

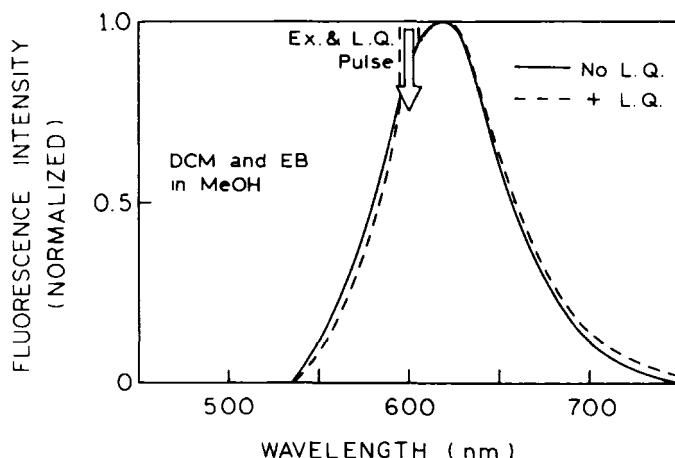


Figure 8.34. Emission spectra of a mixture of DCM and EB in methanol without (—) and with (---) one-beam light quenching at 600 nm.

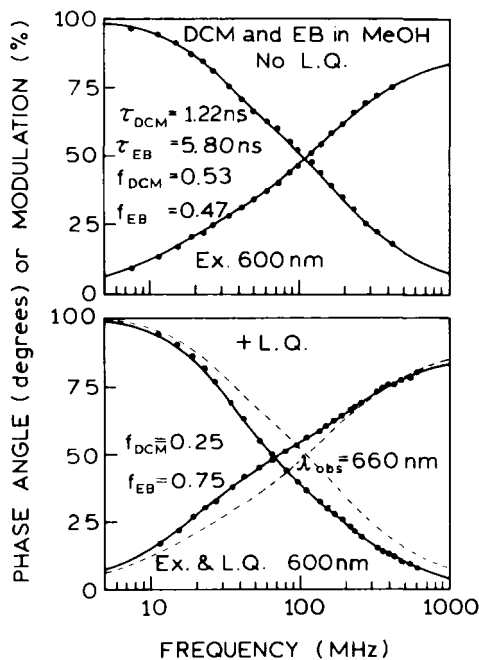


Figure 8.35. Frequency-domain intensity decay of the DCM-EB mixture without (top) and with (bottom) light quenching. The dashed line (lower panel) is the frequency response of the unquenched mixture.

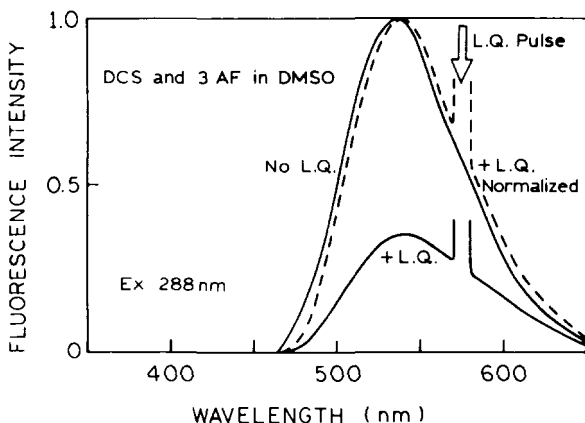


Figure 8.36. Emission spectra of a mixture of DCS and 3-AF.

(3-AF), which has an emission spectrum similar to DCS, is more resistant to 570-nm light quenching than DCS is (Figure 8.37). Because of its longer natural lifetime, 3-AF ($\tau = 11.7$ ns) is expected to show a smaller cross section for light quenching than does DCS ($\tau = 0.87$ ns). The frequency-domain intensity decay data indicate that the fractional intensity of 3-AF increases in the mixture after the light-quenching pulse (Figure 8.37). The changes in frequency response due to light quenching are substantial, much greater than the experimental uncertainties. Wavelength-selective quenching was demonstrated for several other mixtures.⁽⁶⁰⁾ These results demonstrate that light quenching of mixtures, and probably multi-fluorophore macromolecules, can be selective based on wavelength, delay time, or cross section for light quenching.

We explored the biochemical usefulness of light quenching by examining the solvent-sensitive fluorophore Prodan when partially bound to human serum albumin. The light-quenching pulse at 570 nm overlaps more strongly with the

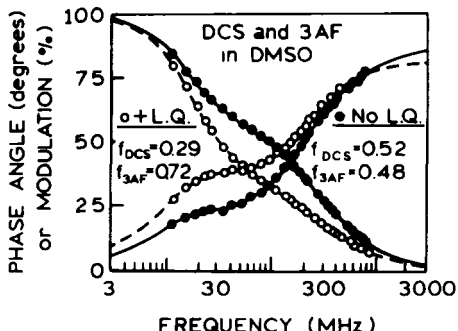


Figure 8.37. Frequency-domain intensity decay of a mixture of DCA and 3-AF.

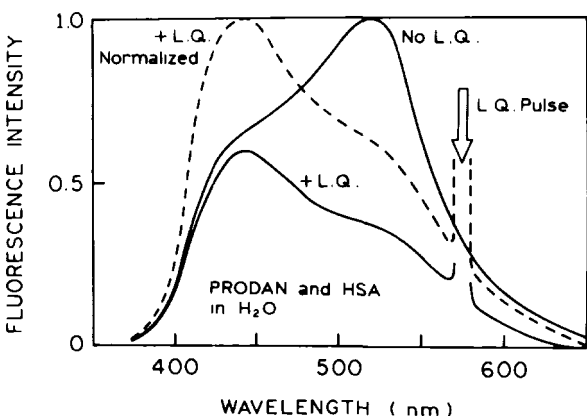


Figure 8.38. Emission spectra of Prodan partially bound to HSA.

emission spectrum of free Prodan than with the blueshifted emission of the bound form (Figure 8.38). Light quenching at 570 nm results in a remarkable blueshift, indicating extensive quenching of free Prodan. The frequency-domain intensity decay data revealed that the fractional contribution of the bound form from $\tau = 3.9$ ns more than doubled upon light quenching (Figure 8.39). Selective quenching of free Prodan ($\tau = 0.57$ ns) can be seen by the more rapid decrease in modulation with increasing frequency. The decrease in phase angle at high frequency is due to the oscillations described earlier for time-delayed light quenching. Hence, selective quenching of fluorophores is possible for fluorophores in different microenvironments.

An important potential application of light quenching is for resolution of the heterogeneous emission from multityptophan proteins. To model this situation we use a mixture of two proteins: ribonuclease T₁ (RNase I₁) with a buried tryptophan residue and ACTH with a solvent-exposed residue.⁽⁵⁰⁾ We demonstrated selective quenching of the buried tryptophan residue in RNase T₁ in the presence of an exposed residue in ACTH.⁽⁶¹⁾ The single tryptophan residue in RNase T₁ displays an emission spectrum blueshifted relative to ACTH (Figure 8.40). Due to limitations of our laser we could only perform one-beam light quenching. For excitation on the red edge of the absorption spectrum, the emission spectrum of the mixture shows a redshift consistent with light quenching of the buried tryptophan residue in RNase T₁ (Figure 8.41). We also observed that the frequency response of the mixture displayed changes consistent with a higher contribution of the exposed residue of ACTH after light quenching. The decay intensity of RNase T₁ is a single exponential ($\tau = 3.44$ ns), and the intensity decay of ACTH is reasonably approximated as a single exponential ($\tau = 2.36$ ns). Light quenching resulted in a shift of the frequency response to

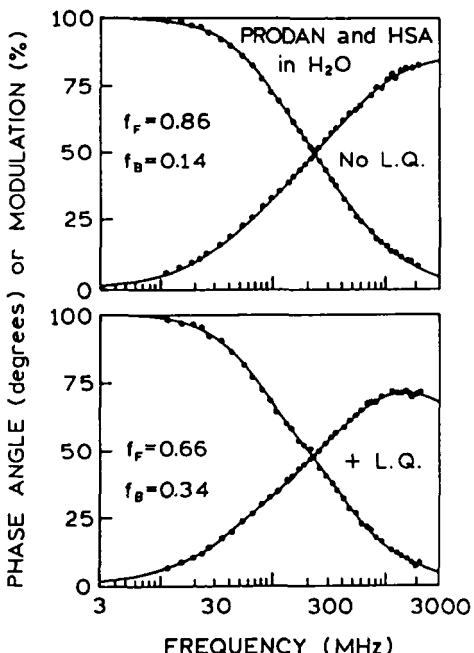


Figure 8.39. Frequency-domain intensity decays of Prodan partially bound to HSA.

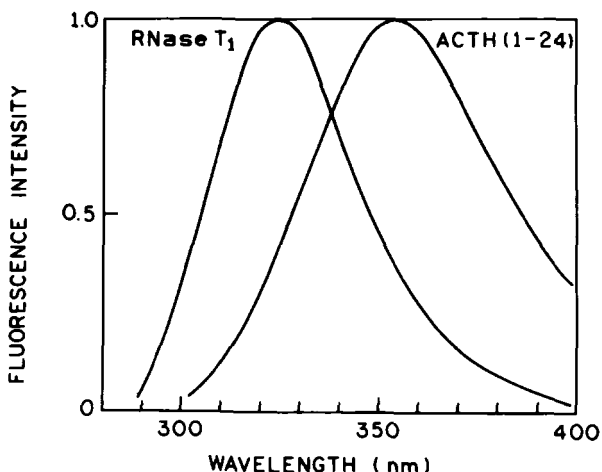


Figure 8.40. Emission spectra of RNase T₁ and ACTH.

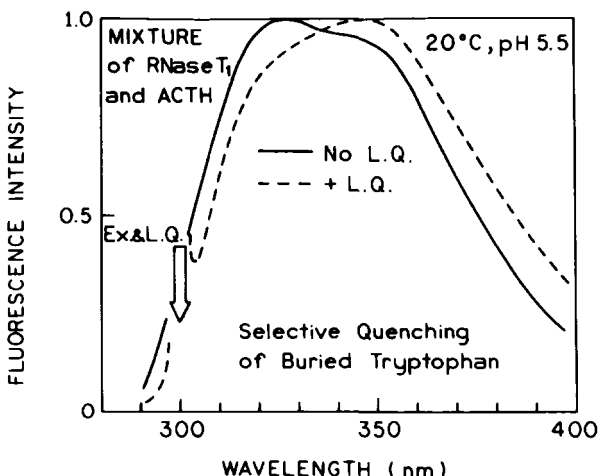


Figure 8.41. Emission spectra of a mixture of RNase T₁ and ACTH with (---) and without (—) light quenching.

higher frequencies (Figure 8.42) resulting from the substantial increase in the fractional intensity of ACTH from 0.397 to 0.626. These results demonstrate selective quenching of tryptophan residues in different environments and suggest that wavelength-selective light quenching should occur in multityptophan proteins.

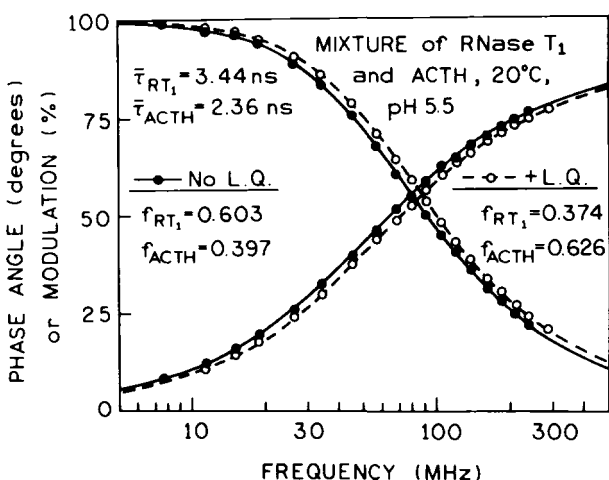


Figure 8.42. Frequency response of a mixture of RNase T₁ and ACTH without (—●—) and with (—○—) one-beam light quenching.

It is important to notice that light quenching has different properties than collisional quenching. Light quenching can be accomplished without addition of quenchers, that is, without changes in chemical composition, which can potentially alter the conformation of sensitive biomolecules. Additionally, the effect is rapidly reversible by blocking the illumination, and removal of the “quencher” does not require purification or dialysis. Finally, little photochemical damage is expected because the quenching light is not absorbed by the fluorophores.

It is important to emphasize that LQ can be effective under conditions where collisional quenching is not practical, such as in viscous or vitrified solution where diffusion is slow. Additionally, fluorophores occasionally are inaccessible to collisional quenchers, as found for the single tryptophan residue of RNase T₁,^(50,62) or for dyes intercalated into DNA.⁽⁶³⁾ For such systems we cannot use collisional quenchers. However, LQ will most probably be insensitive to the local environment of the probe and can thus be used to control the decay times of even inaccessible fluorophores. The ability to decrease the lifetime by LQ may increase our ability to resolve complex phenomena in rigid or inaccessible environments.

8.7.2. Light Quenching with Total Internal Reflectance

We recently applied light quenching to total internal reflectance (TIR) and demonstrated that the evanescent wave can result in light quenching.⁽⁶⁴⁾ Excitation of fluorophores or macromolecules at a glass–liquid interface can be accomplished by using the principle of total internal reflection at the glass–water interface.⁽⁶⁵⁾ It is well known that the optical field propagates into the aqueous phase for a distance comparable to the wavelength of the light and that the depth of penetration depends on the angle of incidence (θ_i), the wavelength (λ_e), and values of the refractive index of the glass or quartz (n_2) and water (n_1).⁽⁶⁵⁾ This phenomenon has been widely used to study the adsorption or interactions of macromolecules with solid surfaces⁽⁶⁶⁾ and has been used with photobleaching, whereby the recovery of fluorescence reveals the rates of molecular diffusion or transport into the photobleached area.⁽⁶⁷⁾ One important application of TIR Fluorescence (TIRF) is with fluorescence microscopy, in which the evanescent wave can be used for excitation of cellular components adjacent to the glass–water interface.^(68,69) One limitation of TIRF with microscopy is that the fluorophores closest to the solid–liquid interface are preferentially excited. The macromolecules of interest may be located in the cytoplasm and not detectable in the presence of a much larger signal from molecules adjacent to the interface.

The phenomenon of total internal reflectance and penetration of the evanescent wave has been described by many authors. Suppose the light beam is traveling in the solid phase with a refractive index n_2 . Depending on the angle of incidence (θ_I) relative to an axis normal to the interface, the beam can penetrate the aqueous phase with a refraction angle or undergo total internal reflectance. The latter occurs for angles greater than the critical angle θ_c . The critical angle is

$$\theta_c = \sin^{-1}(n_1/n_2) = \sin^{-1} n \quad (8.14)$$

where n_1 is the refractive index of the aqueous phase and $n = n_1/n_2$. For total internal reflection to occur, n_1 must be less than n_2 , or $n < 1$. If $\theta_I < \theta_c$, the beam passes into the aqueous phase. However, when $\theta_I > \theta_c$, the beam is totally reflected back into the solid phase. However, some of the energy propagates into the aqueous phase in the form of an evanescent wave. The intensity of this wave decreases exponentially with distance z from the surface:

$$I(z), \theta = I(0)\exp(-z/d) \quad (8.15)$$

where d describes the characteristic distance. The depth of penetration is related to the incident wavelength (λ) and angle of incidence by

$$d = \frac{\lambda}{4\pi} (n_2^2 \sin^2 \theta - n_1^2)^{-1/2} \quad (8.16)$$

The value of d is typically comparable to or smaller than the incident wavelength.

We now consider a TIR experiment with different excitation and quenching beams. The intensity of the excitation evanescent wave is

$$I(z, \theta_{\text{ex}}) = I_{\text{ex}}(0) \exp(-z/d_{\text{ex}}) \quad (8.17)$$

and the intensity of the quenching evanescent wave is

$$I(z, \theta_q) = I_q(0) \exp(-z/d_q) \quad (8.18)$$

Hence, the fluorescence intensity in the presence of the quenching beam is

$$F(z) = \frac{I_{\text{ex}}(z, \theta_{\text{ex}})}{1 + I_q(z, \theta_1)P} \quad (8.19)$$

In this expression the maximum values of $I_{\text{ex}}(z, \theta_{\text{ex}})$ and $I_q(z, \theta_q)$ at $z=0$ are taken as unity, so P is a scaling factor for the quenching intensity distribution.

Light quenching with an evanescent wave was accomplished with the experimental arrangement in Figure 8.43. The excitation and light-quenching beams were from the frequency-doubled and fundamental output of a pyridine 2 cavity-dumped ps dye laser, at 368 and 736 nm, respectively. The pulse width was near 7 ps. The sample was a solution of pyridine 2 in water which was contained in a 0.5-nm-thick compartment attached to the side of a 1×1 cm cuvette, 3.5 cm high. One side of the 1×1 cm quartz cuvette was thinner than usual, 0.2 mm thick. This cuvette was filled with toluene with a refractive index of 1.49 and serves as a coupling prism to the 0.5-mm-thick side compartment containing the fluorophore. Total internal reflection occurs at the quartz-water interface of the prism compartment which contains pyridine 2 in water.

We questioned whether the intensities of the evanescent wave would be adequate for light quenching using available laser sources. The sample was an aqueous solution of pyridine 2 which was excited by an evanescent wave at 368 nm. Upon 368-nm illumination a red fluorescent spot could be seen localized at the quartz-water interface. Upon illumination with both 368 and 736 nm the intensity of this spot was visibly reduced.

Light quenching by the 736-nm evanescent wave is shown quantitatively in Figure 8.44. When the 736-nm beam is blocked, the emission of pyridine 2 is observed. Upon simultaneous illumination at 368 and 736 nm the intensity of pyridine 2 decreases in proportion to the intensity of the 736-nm beam. These results demonstrate that the intensity of the evanescent wave is adequate to obtain light quenching with currently available laser sources.

We questioned the spatial distribution of the excited fluorophores relative to the solid-liquid interface. For these calculations we chose wavelengths of 450 and

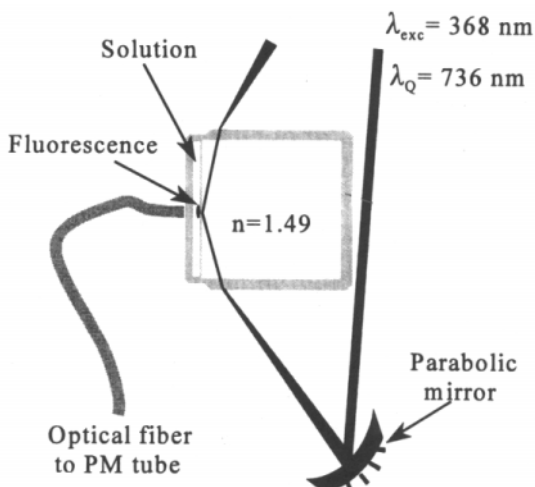


Figure 8.43. Experiment arrangement for light quenching at an interface. (From Ref. 64.)

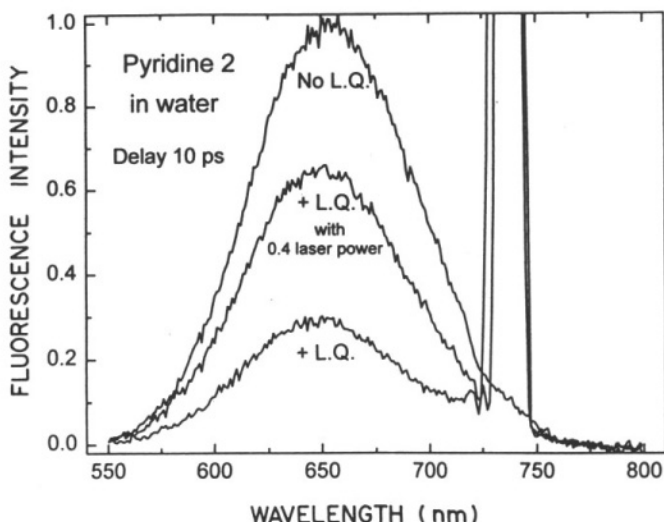


Figure 8.44. Light quenching of pyridine 2 at a quartz–water interface. Excitation and light quenching were at 368 and 736 nm, respectively.

600 nm, which are typical of the excitation and emission wavelengths of many fluorophores used in biochemical research. For these wavelengths at a quartz–water interface the critical angles are 66.189° and 66.053° , respectively. Figure 8.45 shows the intensity of the evanescent waves at a quartz–water interface when the incident angles are 66.389° and 80° for the 450-nm excitation and 600-nm quenching beams, respectively. The incident angle of the excitation beam was chosen to be 0.2° larger than the critical angle, a degree of precision readily accessible with laser light sources. At this angle of incidence $d_{ex} = 4820 \text{ \AA}$, providing excitation to $10,000 \text{ \AA}$ (Figure 8.45, top). The incident angle for the quenching beam was chosen to be 80° , resulting in $d_a = 890 \text{ \AA}$. One notices that the short-wavelength 450-nm excitation at 66.389° penetrates much more deeply the aqueous phase than the 600-nm quenching beam with an incident angle of 80° . This suggests that the effect of the quenching beam will be localized closer to the interface than the excitation.

We used the calculated evanescent-wave intensities to predict the distribution of fluorescence at various distances from the interface. The effect of light quenching on the spatial distribution of the fluorescence is shown in Figure 8.45 (lower panel). In the absence of light quenching the emission intensity decreases exponentially from the surface, reaching $1/e$ of the maximum at 4820 \AA . Increasing the quenching power results in selective quenching of the emission from the area closest to the interface. At lower laser power ($P = 5$) the maximum

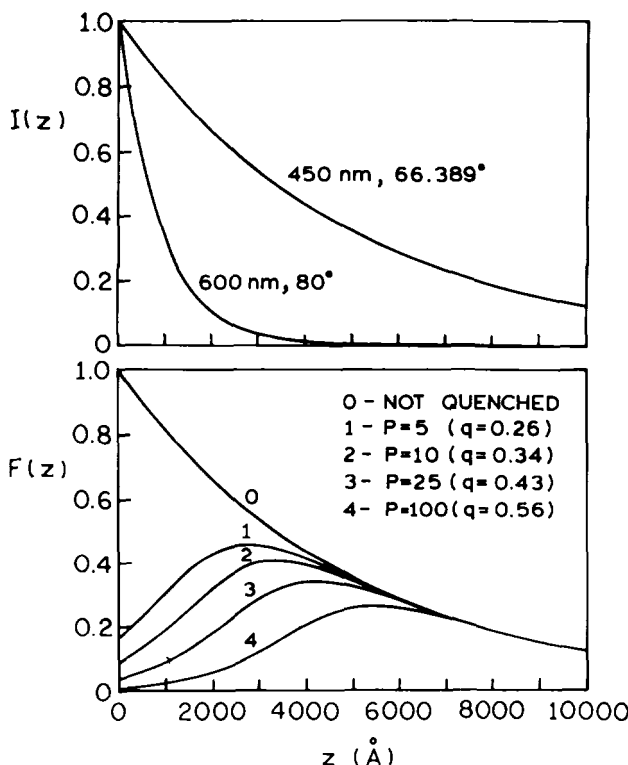


Figure 8.45. (Top) Spatial distribution of the evanescent wave for excitation at 450 nm and for light quenching at 600 nm. (Bottom) Spatial distribution of the fluorescent for increasing amounts of optical power at the quenching wavelength.

intensity occurs from about 2700 Å into the solution. Increasing the laser power causes the region of maximal intensity to be displaced to over 5000 Å (Figure 8.45, lower panel). It is important to notice that this displacement of the excited volume is accomplished with only modest amounts of total quenching. The distances of maximal fluorescence are considerably longer than the thickness of a cell membrane near 80 Å. Hence, fluorophores located in membranes adjacent to the interface will be quenched, and the emission can be expected from the cytoplasmic region of cells.

Light quenching by an evanescent wave suggests several experimental opportunities. In the use of TIRF to study cellular systems one should be able to selectively observe fluorescence at distances of 5000 Å into the aqueous or cellular phase, without the signal being dominantly due to fluorophores located adjacent to the interface. This possibility suggests the use of TIRF to study

intracellular phenomena such as Ca^{2+} , pH, and other ion concentrations, with minimal contributions from the extracellular or cell contact region.

Another possible advantage of TIRF with light quenching could be realized in the use of fluorescence sensors based on evanescent-wave excitation. The response times of such sensors are limited to the diffusion times of analytes to the interface.⁽⁷⁰⁾ Suppose the reagent is present at a range of distances from the interface, as may occur with surface irregularities, or a range of orientations of surface-adsorbed antibodies. By the use of TIRF with light quenching the signal can be due primarily to those molecules most distant from the surface, which are also those likely to display the most rapid interactions with analytes. Hence, the response times of TIRF sensors may be improved.

8.8. Discussion

8.8.1. Comparison of Light Quenching and Induced Stimulated Emission

It should be recognized that there is a significant difference between light quenching and ISE. In the latter case it is necessary to excite most of the ground-state molecules to create the population inversion. After inversion, a probe pulse can be used to obtain ISE. The probe pulse must arrive very quickly following excitation, otherwise the population inversion will have been lost by the excited-state decay. Consequently, ISE can only be observed at the earliest times following excitation. In contrast, light quenching can be used at any point throughout the intensity decay. Additionally, the creation of a population inversion requires a high-intensity pump pulse which necessarily depletes the ground state, with the loss of information concerning the anisotropy. The two-pulse light-quenching experiments are completely different in that a weak-intensity excitation pulse is used to create the excited-state population. It is not necessary that the ground-state population be depleted to any significant extent. After excitation the photoselected excited-state population is then modified by a high-intensity photo-selective quenching pulse. The high-intensity pulse causes stimulated emission. However, the pulse is not absorbed by the sample, and light quenching only serves to decrease the excited-state population. Light-quenching experiments are routinely performed with low concentrations of fluorophores, as is necessary with biomolecules.

8.8.2. Biophysical Applications of Light Quenching

It is important to consider the types of information which can be available from light-quenching experiments. Light quenching may be useful in studies of

time-resolved energy transfer. Such experiments typically involve use of the donor decay kinetics, which depend on the distance to the acceptor(s). In this laboratory we have emphasized the recovery of distance distributions.⁽⁷¹⁻⁷³⁾ The acceptor decay kinetics are rarely used because they contain contributions from both the transferred energy and directly excited acceptors. Only the acceptors excited by transferred energy contain information on the distance or distance distribution. Light quenching can be used to selectively deplete the initially excited acceptor population. One then expects the acceptor emission to rise due to transfer from the donor followed by spontaneous decay of the acceptor. These acceptor data can then be used to recover the distance or distance distribution.

We have recently been investigating distance-dependent rate constants for quenching.⁽⁷⁴⁾ The distance dependence occurs over a short distance, only to 1–3 Å beyond the contact distance of the fluorophore and quencher. Consequently, the desired information is contained at the earliest times following excitation. Also, these effects are most easily seen in viscous or vitrified solution where diffusion is slow. The ability to decrease the lifetime by light quenching may increase our ability to resolve such complex phenomena.

Another potential use of light quenching in biophysical chemistry is exemplified by the phycobilisomes.⁽⁷⁵⁾ These proteins serve to funnel absorbed light into the photosynthetic reaction centers, and consist of a variety of subunits and spectral classes.⁽⁷⁵⁾ Briefly summarized, the main spectral classes in phycobilisomes are the three phycobiliproteins: phycoerythrin (PE), phycocyanin (PC), and allophycocyanin (AP). Energy absorbed by PE can be transferred to PC and in turn, to AP. Each protein contains many bilin chromophores. Because of their high chemical stability and photostability, these proteins are being used as fluorescent labels.^(75,76) Time-resolved fluorescence methods have been used to study energy transfer between phycobiliproteins in the phycobilisomes, and in the isolated phycobiliproteins.⁽⁷⁷⁻⁸⁰⁾ The intensity decay kinetics are complex and depend on emission wavelength and display decay times from picoseconds to nanoseconds.

The advantages of light quenching over experiments requiring a strong excitation can be seen by consideration of the energy transfer dynamics of phycobiliproteins. The long-wavelength absorption and emission of the phycobiliproteins make light quenching readily accessible with dye and Ti:sapphire lasers. The fluorescence intensity or quantum yields depend strongly on excitation intensity because these multichromophore proteins can have more than one excited-state donor. The relative quantum yields depend on the excitation intensity, which is thought to be a result of singlet-singlet annihilation in phycobiliproteins containing more than one excited state chromophore.^(81,82) Consequently it is impractical to use high excitation intensities in examining these proteins. In contrast, light quenching requires only excitation at low inten-

sites, which does not result in exciton annihilation. Because light quenching depends on spectral overlap of the quenching wavelength with the emission spectrum, a subsequent quenching pulse can be used to selectively quench various chromophores in the phycobiliproteins. Importantly, the time scale of energy migration among the phycobiliproteins is on the picosecond-to-subnanosecond time scale, which is ideal for light-quenching experiments where such time delays can be easily accomplished with optical delays. If an intermediate species is present between the donor and acceptor, it may be quenched by timing the quenching pulse to arrive when the intermediate displays its highest concentration. It is important to notice that both excitation and quenching occur with orientation photoselection. Hence, additional information might be available by using quenching pulses which are oriented parallel or perpendicular to the excitation pulse.

Light quenching has also been used to study the transfer of vibrational energy in anthracene vapor.⁽⁸³⁾ In this case absorption of vibrational quanta were detected by changes in the emission spectra of anthracene.⁽⁸³⁾ This effect suggests an opportunity to study the time-dependent transfer of vibrational energy, as calculated by Hochstrasser and co-workers for heme proteins.⁽⁸⁴⁾ We have used phase-sensitive emission spectra to detect a similar phenomena in anthracene derivatives, this being time-dependent changes in spectral shape due to torsional motions of side groups.⁽⁸⁵⁾ Hence, one can imagine measurements of vibrational energy transfer based on time-delayed quenching pulses.

8.8.3. Pulse-Width-Dependent Light Quenching

Light quenching may provide unique opportunities to study rapid processes using stationary measurements. We expect polarized light quenching to depend on the rate of rotational diffusion and on the presence of noncollinear transitions which displace the emission moment from the absorption moment. Such methods may be valuable in studies of protein fluorescence, where the indole residues display overlapping 1L_a and 1L_b states.⁽⁸⁶⁻⁸⁹⁾ These transitions are thought to be nearly perpendicular within the indole plane. In polar solvents emission occurs from the more-solvent-sensitive 1L_a state. Comparison of the amounts of polarized light quenching may reveal the rates of $^1L_a - ^1L_b$ interconversion. It is relatively easy to obtain small delay times for the quenching pulse. The extent of two-pulse light quenching with polarized quenching beams may reveal the rate of conversion between these states. One-pulse experiments may also be informative to probe the interconversion rate within the laser pulse. For instance, suppose the electronic state exchange in 1 ps. Then for a 5-ps pulse, the change occurs within the pulse width but is not yet complete for a 100-fs pulse.

From this point of view, light quenching is analogous to the variety of methods which obtain their time resolution from the pulse width of the laser rather than the speed of the detector, as illustrated by the real-time probing of reactions by Zewail and colleagues.^(90,91)

8.8.4. Perspectives on Light Quenching

The use of light to control the decay time of fluorophores can be regarded as a subset of the increasing use of light to control processes which were previously controlled by mechanical, electrical, or chemical means. Examples include light-controlled switching of molecular elements, the use of light to control chemical reactions,⁽⁹²⁻⁹⁴⁾ and the use of intense light beams to act as “optical tweezers” which provide controlled trapping or movement of bacteria or subcellular organelles.^(95,96) Light quenching is far less developed than these topics, but one cannot predict the long-range applications of controlling decay times by long-wavelength illumination.

In summary, the advantages of light quenching include the use of weak excitation pulses, nondestructive nonabsorbed quenching pulses, low concentration samples, wavelength-selective quenching, and orientation-selective quenching. Light quenching can occur in vitrified solvents, and buried fluorophores should be accessible. The time resolution of light quenching is determined by the pulse width and delay time, so processes occurring from femtoseconds to picoseconds to nanoseconds can be examined in a single experiment.

Acknowledgments

This work was supported by the NIH Research Center for Research Resources, RR-08119 and RR-10416.

References

1. T. G. Dewey (Ed.), *Biophysical and Biochemical Aspects of Fluorescence Spectroscopy*, Plenum, New York (1991).
2. D. M. Jameson and G. D. Reinhart (Eds.), *Fluorescent Biomolecules: Methodologies and Applications*, Plenum, New York (1989).
3. J. R. Lakowicz, (Ed.), Time-Resolved laser spectroscopy in biochemistry. III, *Proc. SPIE 2137* (1994).
4. D. V O'Connor and D. Phillips, *Time-Correlated Single Photon Counting*, Academic Press, London (1984).
5. J. N. Demas, *Excited State Lifetime Measurements*, Academic Press, London (1983).

6. G. R. Fleming, *Chemical Applications of Ultrafast Spectroscopy*, Oxford University Press, New York (1986).
7. D. S. Birch and R. E. Imhof, Time-domain fluorescence spectroscopy using time-correlated single-photon counting, in: *Topics in Fluorescence Spectroscopy, Vol. 1: Techniques* (J. R. Lakowicz, ed.), pp. 1–95, Plenum, New York (1991).
8. T. M. Nordlund, Streak cameras for time-domain fluorescence, in: *Topics in Fluorescence Spectroscopy, Vol. 1: Techniques* (J. R. Lakowicz, ed.), pp. 183–260, Plenum, New York (1991).
9. J. R. Lakowicz and I. Gryczynski, Frequency-domain fluorescence spectroscopy, in: *Topics in Fluorescence Spectroscopy: Vol. 1 Techniques* (J. R. Lakowicz, ed.), pp. 293–235, Plenum, (1991).
10. E. Gratton and J. R. Lakowicz, Ultrafast dynamics in proteins and membranes by time-resolved fluorescence spectroscopy, in: *Structure and Motion: Membranes, Nucleic Acids and Proteins* (E. Clementi, G. Corongiu, M. H. Sarma and R. H. Sarma, eds.), pp. 155–168, Adenine Press (1985).
11. J. R. Lakowicz, I. Gryczynski, Z. Gryczynski, E. Danielsen, and M. J. Wirth, Time-resolved fluorescence intensity and anisotropy decays of 2,5-diphenyloxazole by two-photon excitation and frequency-domain fluorometry, *J. Phys. Chem.* 96, 3000–3006 (1992).
12. J. R. Lakowicz, I. Gryczynski, E. Danielsen, and J. K. Frisoli, Unexpected anisotropy spectra of indole and N-acetyl-L-tryptophanamide observed for two-photon excitation of fluorescence, *Chem. Phys. Lett.* 194, 282–287 (1992).
13. J. R. Lakowicz and I. Gryczynski, Fluorescence intensity and anisotropy decay of the 4',6-diamidino-2-phenylindole-DNA complex resulting from one-photon and two-photon excitation, *J. Fluoresc.* 2, 117–122 (1992).
14. J. R. Lakowicz, I. Gryczynski, J. Kušba, and E. Danielsen, Two-photon induced fluorescence intensity and anisotropy decays of diphenylhexariene in solvents and lipid bilayers, *J. Fluoresc.* 2, 247–258 (1992).
15. W. Denk, J. H. Strickler, and W. W. Webb, Two-photon laser scanning fluorescence microscopy, *Science* 248, 73–76 (1990).
16. D. W. Piston, D. R. Sandison, and W. W. Webb, Time-resolved fluorescence imaging and background rejection by two-photon excitation in laser scanning microscopy, *Proc. SPIE 10*, 379–389 (1992).
17. I. Gryczynski, H. Malak, and J. R. Lakowicz, Three-photon excitation of a tryptophan derivative using a fs Ti:sapphire laser, *Biospectroscopy* 2, 9–15 (1996).
18. I. Gryczynski, H. Malak, and J. R. Lakowicz, Three-photon induced fluorescence of 2,5-diphenyloxazole with a femtosecond Ti:sapphire laser, *Chem. Phys. Lett.* 245, 30–35 (1995).
19. H. Szmacinski, I. Gryczynski, and J. R. Lakowicz, Three-photon induced fluorescence of the calcium probe indo-1, *Biophys. J.* 70, 547–555 (1996).
20. S. W. Hell, M. Schrader, K. Bahlmann, F. Meinecke, J. R. Lakowicz, and I. Gryczynski, Stimulated emission on microscopic scale: light quenching of pyridinium 2 using a Ti:sapphire laser, *J. Microsc.* 180(2), RP1–RP2 (1995).
21. S. W. Hell, K. Bahlmann, M. Schrader, A. Soini, H. Malak, I. Gryczynski, and J. R. Lakowicz, Three-photon excitation in fluorescence microscopy, *J. Biomed. Opt.* 1(1), 71–74 (1996).
22. W. W. Webb, Three-photon excited fluorescence and applications in nonlinear laser scanning microscopy, *Biophys. J.* 70(2), A429 (1996).
23. D. E. Koppel, P. Primakoff, and D. G. Myles, Fluorescence photobleaching analysis of cell surface regionalization, in: *Applications of Fluorescence in the Biomedical Sciences*, (D.L. Taylor, A. S. Waggoner, R. F. Murphy, F. Lanni, and R. R. Birge, eds.), pp. 477–97, A. R. Liss, New York (1986).
24. Y. Yuan and D. Axelrod, Photobleaching with a subnanosecond laser flash, *J. Fluoresc.* 4, 141–151 (1994).

25. Z. Huang and N. L. Thompson, Theory for two-photon excitation in pattern photobleaching with evanescent illumination, *Biophys. Ghent.* 47, 241–249 (1993).
26. E. H. Hellen and T. P. Burghardt, Saturation effects in polarized fluorescence photobleaching recovery and steady state fluorescence polarization, *Biophys. J.* 66, 891–897 (1994).
27. A. Einstein, On the quantum theory of radiation, *Phys. Z.* 18, 121 (1917). (This paper has been reprinted in *Laser Theory* by F.S. Barnes, IEEE Press, New York, 1972.)
28. U. Kubitscheck, M. Kircheis, R. Schweitzer-Stenner, W. Dreybrodt, T. M. Jovin, and I. Pecht, Fluorescence resonance energy transfer on single living cells, *Biophys. J.* 60, 307–318 (1991).
29. M. D. Galanin, B. P. Kirsanov, and Z. A. Chizhkov, Luminescence quenching of complex molecule in a strong laser field, *Soviet Phys. JETP Lett.* 9(9), 502–507 (1969).
30. A. N. Rubinov, V. I. Tomin, and V. A. Zhivnov, Shift in the fluorescence spectrum of molecules in a non-resonant-laser field, *Opt. Spectrosc. (USSR)* 35(4), 451–452 (1973).
31. O. P. Girin, Effect of intermolecular relaxation of the luminescence spectra of solutions under powerful excitation, *Izv. Akad. Nauk (USSR)* 42(3), 550–553 (1987) (English transl., pp. 86–89).
32. N. G. Bakhshiev, E. S. Voropai, V. A. Gaisenok, O. P. Girin, and A. M. Sarzhevskii, Influence of intermolecular relaxation processes on the absorption and emission spectra of solutions with high-intensity optical excitation, *Opt. Spectrosc. (USSR)* 50(6), 614–618 (1981).
33. N. G. Bakhshiev and O. P. Girin, Description of the displacement kinetics of vibronic spectra of solutions under different conditions of optical excitation within the framework of the Debye model of intermolecular relaxation, *Opt. Spectrosc. (USSR)* 52(1), 7–8 (1982).
34. A. I. Butko, E. S. Voropai, V. A. Gaisenok, V. A. Saechnikov, and A. M. Sarzhevskii, Manifestation of intermolecular relaxation in the spectroluminescent characteristics of molecular solutions in the presence of light quenching of luminescence, *Opt. Spectrosc. (USSR)* 52(2), 153–156 (1982).
35. Y. T. Mazurenko, V. V. Danilov, and S. I. Vorontsova, Depolarization of photoluminescence by powerful excitation, *Opt. Spectrosc. (USSR)* 35(1), 107–108 (1973).
36. J. R. Lakowicz, I. Gryczynski, V. Bogdanov, and J. Kuśba, Light quenching and fluorescence depolarization of rhodamine B and applications of this phenomenon to biophysics, *J. Phys. Chem.* 98, 334–342 (1994).
37. I. Gryczynski, V. Bogdanov, and J. R. Lakowicz, Light quenching and depolarization of fluorescence observed with a high repetition rate picosecond dye laser, *Biophys. Chem.* 49, 273–232 (1994).
38. I. Gryczynski, V. Bogdanov, and J. R. Lakowicz, Light quenching of tetraphenylbutadiene fluorescence observed during two-photon excitation, *J. Fluoresc.* 3, 85–92 (1993).
39. I. Gryczynski, J. Kuśba, and J. R. Lakowicz, Light quenching of fluorescence using time-delayed laser pulses as observed by frequency-domain fluorometry, *J. Phys. Chem.* 98, 8886–8895 (1994).
40. I. Gryczynski, J. Kuśba, V. Bogdanov, and J. R. Lakowicz, Control of excited state population by light quenching of fluorescence, *Proc. SPIE* 2137, 742–760 (1994).
41. I. Gryczynski, J. Kuśba, and J. R. Lakowicz, Wavelength-selective light quenching of biochemical fluorophores, *J. Biomed. Opt.* 2, 80–87 (1997).
42. A. N. Glazer, Light harvesting by phycobilisomes, *Ann. Rev. Biophys. Chem.* 14, 47–77 (1985).
43. J. Kusba, V. Bogdanov, I. Gryczynski, and J. R. Lakowicz, Theory of light quenching: effects of fluorescence polarization, intensity, and anisotropy decays, *Biophys. J.* 67, 2024–2040 (1994).
44. J. R. Lakowicz, I. Gryczynski, J. Kuśba, and V. Bogdanov, Light quenching of fluorescence: a new method to control the excited state lifetime and orientation of fluorophores, *Photochem. Photobiol.* 60, 546–562 (1994).
45. J. R. Lakowicz and I. Gryczynski, Frequency domain fluorescence spectroscopy, in: *Topics in Fluorescence Spectroscopy, Vol. 1: Techniques* (J. R. Lakowicz, ed.), pp. 293–355, Plenum, New York (1991).

46. J. R. Lakowicz, I. Gryczynski, and E. Danielsen, Anomalous differential polarized phase angles for two-photon excitation with isotropic depolarizing rotations, *Chem. Phys. Lett.* 9(1,2), 47–53 (1992).
47. J. R. Lakowicz and I. Gryczynski, Characterization of *p*-bis(*O*-methylstyryl)benzene as a lifetime and anisotropy decay standard for two-photon induced fluorescence, *Biophys. Chem.* 47, 1-7 (1993).
48. J. R. Lakowicz, Fluorescence spectroscopic investigations of the dynamic properties of proteins, membranes and nucleic acids, *J. Biochem. Biophys. Meth.* 2, 91–119 (1980).
49. J. R. Lakowicz, F. G. Prendergast, and D. Hogen, Fluorescence anisotropy measurements using oxygen quenching conditions as a method to quantify the depolarizing rotations of fluorophores. Application to diphenylhexatriene in isotropic solvents and in lipid bilayers, *Biochemistry* 18, 520–527 (1979).
50. M. R. Eftink, Fluorescence quenching: theory and applications, in: *Topics in Fluorescence Spectroscopy. Vol. 2: Principles* (J. R. Lakowicz, ed.), pp. 53–126, Plenum, New York (1991).
51. J. R. Lakowicz, B. P. Maliwal, H. Cherek, and A. Baiter, Rotational freedom of tryptophan residues in proteins and peptides quantified by lifetime-resolved fluorescence anisotropies, *Biochemistry* 22, 1741–1752 (1983).
52. J. R. Lakowicz and D. Hogan, Dynamic properties of the lipid-water interface region of model membranes as revealed by lifetime-resolved fluorescence emission spectra, *Biochemistry* 20, 1366–1373 (1981).
53. N. G. Bakhshiev, Y. T. Masurenko, and I. V. Piterskaya, Luminescence decay in different portions of the luminescence spectrum of molecules in viscous solution, *Opt. Spectrosc.* 31, 307–309 (1986).
54. Y. T. Masurenko and N. K. Bakhshiev, Effect of orientation dipole relaxation on spectral time and polarization characteristics of the luminescence of solution, *Opt. Spectrosc.* 28, 490–494 (1970).
55. N. K. Bakhshiev, Y. T. Masurenko, and I. V. Piterskaya, Relaxation effects in the luminescence characteristics of viscous solutions, *Akad. Nauk USSR, Bull. Phys. Sci.* 32, 1262–1266 (1969).
56. S. W. Hell and J. Wichmann, Breaking the diffraction resolution limit by stimulated emission: stimulated-emission depletion fluorescence microscopy, *Opt. Spectrosc.* 19, 780–782 (1994).
57. C. Y. Dong, T. C. So, T. French, and E. Gratton, Fluorescence lifetime imaging by asynchronous pump-probe microscopy, *Biophys. J.* 69, 2234–2242 (1995).
58. I. Gryczynski, J. Kuśba, and J. R. Lakowicz, unpublished observations.
59. I. Gryczynski, J. Kuśba, Z. Gryczynski, H. Malak, and J. R. Lakowicz, Effect of fluorescence quenching by stimulated emission on the spectral properties of a solvent-sensitive fluorophore, *J. Phys. Chem.* 100(24), 10135–10144 (1996).
60. I. Gryczynski, J. Kuśba, and J. R. Lakowicz, Effects of light quenching on the emission spectra and intensity decays of fluorophore mixtures. *J. Fluoresc.* (in press).
61. I. Gryczynski, J. Kuśba, and J. R. Lakowicz, Wavelength-selective light quenching on biochemical fluorophores, *J. Biomed. Opt.* 2, 80–87 (1997).
62. J. R. Lakowicz, I. Gryczynski, H. Szmacinski, H. Cherek, and N. Joshi, Anisotropy decays of single tryptophan proteins measured by GHz frequency-domain fluorometry with collisional quenching, *Eur. Biophys. J.* 19, 125–140 (1991).
63. J. R. Lakowicz and G. Weber, Quenching of fluorescence by oxygen. A probe for structural fluctuation in macromolecules, *Biochemistry* 12, 4161–4170 (1973).
64. J. R. Lakowicz, Z. Gryczynski, and I. Gryczynski, On the possibility of evanescent wave excitation distal from a solid-liquid interface using light quenching, *Photochem. Photobiol.* 64, 636–641 (1996).

65. D. Axelrod, E. H. Hellen, and R. M. Fulbright, Total internal reflection fluorescence, in: *Topics in Fluorescence Spectroscopy, Vol. 3: Biochemical Applications* (J. R. Lakowicz, ed.), pp. 289–343, Plenum, New York (1992).
66. G. K. Iwamoto, L. C. Winterton, R. S. Soker, R. A. VanWagenen, J. D. Andrade, and D. F. Mosher, Fibronectin absorption detected by interfacial fluorescence, *J. Colloid Interface Sci.* 106, 459–463 (1985).
67. N. L. Thompson, T. P. Burghardt, and D. Axelrod, Measuring surface dynamics of biomolecules by total internal reflection fluorescence with photobleaching recovery or correlation spectroscopy, *Biophys. J.* 33, 435–454 (1981).
68. D. Gingell, I. Todd, and J. Bailey, Topography of cell-glass apposition revealed by total internal reflection fluorescence of volume markers, *J. Cell Biol.* 100, 1334–1338 (1985).
69. R. J. Bloch, M. Velez, J. Krikorian, and D. Axelrod, Microfilaments and actin-associated proteins at sites of membrane-substrate attachment within acetylcholine receptor clusters, *Exp. Cell Res.* 182, 583–596 (1989).
70. B. K. Lok, Y-L. Cheng, and C. R. Robertson, Protein adsorption on crosslinked polydimethylsiloxane using total internal reflection fluorescence, *J. Colloid Interface Sci.* 91(1), 104–116 (1983).
71. H. C. Cheung, I. Gryczynski, H. Malak, W. Wiczk, M. L. Johnson, and J. R. Lakowicz, Conformational flexibility of the Cys 697-Cys 707 segment of myosin subfragment-1: distance distribution by frequency-domain fluorometry, *Biophys. Chem.* 40, 1–17 (1991).
72. J. R. Lakowicz, W. Wiczk, I. Gryczynski, M. Fishman, and M. L. Johnson, End-to-end distance distributions of flexible molecules: frequency-domain fluorescence energy transfer measurements and rotational isomeric state model calculations, *Macromolecules* 26, 349–363 (1993).
73. P. S. Eis, J. Kusba, M. L. Johnson, and J. R. Lakowicz, Distance distributions and dynamics of a zinc finger peptide from fluorescence energy transfer measurements, *J. Fluoresc.* 3, 23–31 (1993).
74. B. Zelent, J. Kusba, I. Gryczynski, and J. R. Lakowicz, Distance-dependent quenching of anthracene fluorescence by *N,N*-diethylaniline observed by frequency-domain fluorometry, *Appl. Spectrosc.* 49(1), 43–50 (1995).
75. J. C. White and L. Stryer, Photostability studies of phycobiliprotein fluorescence labels, *Anal. Biochem.* 161, 442–452 (1987).
76. V. T. Oi, A. N. Glazer, and L. Stryer, Fluorescence phycobiliprotein conjugates for analyses of cells and molecules, *J. Cell Biol.* 93, 981–986 (1982).
77. A. R. Holzwarth, J. Wendler, and W. Wehrmeyer, Studies on chromophore coupling in isolated phycobiliproteins. I: Picosecond fluorescence kinetics of energy transfer in phycocyanin 5 from CHROOMONAS sp., *Biochem. Biophys. Acta* 724, 388–395 (1983).
78. A. R. Holzwarth, J. Wendler, and G. W. Suter, Studies on chromophore coupling in isolated phycobiliproteins. II: Picosecond energy transfer kinetics and time-resolved fluorescence spectra of C-phycocyanin from *Synechococcus 6301* as a function of the aggregation state, *Biophys. J.* 51, 1–12 (1987).
79. R. MacColl, D. Guard-Friar, T. J. Ryan, K. Csatorday, and P. Wu, The route of exciton migration in phycocyanin 612, *Biochem. Biophys. Acta* 934, 275–281 (1988).
80. I. Yamazaki, M. Mimuro, T. Murao, T. Yamazaki, K. Yoshihara, and Y. Fujita, Excitation energy transfer in the light harvesting antenna system of the red alga *Porphyridium cruentum* and the blue-green alga *Anacystis nidulans*: Analysis of time-resolved fluorescence spectra, *Photochem. Photobiol.* 39, 233–240 (1984).
81. D. Wong, F. Pellegrino, R. R. Alfano, and B. A. Zilinskas, Fluorescence relaxation kinetics and quantum yield from the isolated phycobiliproteins of the blue-green alga *nostoc* sp. measured as a function of single picosecond pulse intensity, i. *Photochem. Photobiol.* 33, 651–662 (1981).

82. G. F. W. Searle, J. Barber, G. Porter, and C. J. Tredwell, Picosecond time-resolved energy transfer in *Porphyridium cruentum*. II: In the isolated light harvesting complex (phycobilisomes). *Biochem. Biophys. Acta* **501**, 246–256 (1978).
83. G. A. Abakumov, S. A. Vorobev, V. F. Pikelni, and A. P. Simonov, Distortion of the shape of the fluorescence spectrum of anthracene vapor in the presence of intense radiation, *Opt. Spectrosc. (USSR)* **44**(3), 283–285 (1978).
84. E. R. Henry, W. A. Eaton, and R. M. Hochstrasser, Molecular dynamics simulations of cooling in laser-excited heme proteins, *Proc. Natl. Acad. Sci.* **83**, 8982–8986 (1986).
85. G. Laczko and J. R. Lakowicz, Torsional rearrangements of fluorophore: a possible probe of volume fluctuations in macromolecules, *Biophys. Chem.* **19**, 227–232 (1984).
86. M. R. Eftink, L. A. Selvidge, P. R. Callis, and A. A. Rehms, Photophysics of indole derivatives: experimental resolution of L_a and L_b transitions and comparison with theory, *J. Phys. Chem.* **94**, 3469–3479 (1990).
87. B. Albinsson and B. Nordén, Excited-state properties of the indole chromophore. Electronic transition moment directions from linear dichroism measurements: effect of methyl and methoxy substituents, *J. Phys. Chem.* **96**, 6204–6612 (1992).
88. M. R. Eftink and Z. Chen, Evidence for dual L_a and L_b emission in 5-methylindole, *J. Fluoresc.* **4**, 165–168 (1994).
89. B. Albinsson, M. Kubista, B. Nordén, and E. W. Thulstrup, Near-ultraviolet electronic transitions of the tryptophan chromophore: linear dichroism, fluorescence anisotropy, and magnetic circular dichroism spectra of some indole derivatives, *J. Phys. Chem.* **93**, 6646–6655 (1989).
90. J. L. Herek, S. Peersen, L. Bnares, and A. H. Zewail, Femtosecond real-time probing of reactions. IX: Hydrogen-atom transfer, *J. Chem. Phys.* **91**(12), 9046–9061 (1992).
91. J. S. Baskin, L. Bnares, S. Pedersen, and A. H. Zewail, Femtosecond real-time probing of reactions. 20: Dynamics of twisting, alignment, and IVR in the trans-stilbene isomerization reaction, *J. Phys. Chem.* **100**, 11920–11933 (1996).
92. E. D. Potter, J. L. Herek, S. Pedersen, Q. Liu, and A. H. Zewail, Femtosecond laser control of a chemical reaction, *Nature* **355**, 66–68 (1992).
93. J. Maddox, Towards real-time molecular demolition? *Nature* **360**, 103 (1992).
94. Ian W. M. Smith, Probing the transition state, *Nature* **358**, 279–280 (1992).
95. S. M. Block, D. F. Blair, and H. C. Berg, Compliance of bacterial polyhooks measured with optical tweezers, *Cytometry* **12**(6), 492–496 (1991).
96. A. Ashkin, J. M. Dziedzic, and T. Yamane, Optical trapping and manipulation of single cells using infrared laser beams, *Nature* **330**, 769–771 (1987).

Increasing the Resolution of Far-Field Fluorescence Light Microscopy by Point-Spread-Function Engineering

Stefan W. Hell

9.1. Introduction

Microscopy plays a key role in many areas of modern science. This is probably because for humans visual perception is the most important way of obtaining information. Therefore, the visualization of minute structures has contributed a great deal to the better understanding of many phenomena in nature. The most important property of the microscope is the resolution, which is the ability to distinguish closely positioned objects. The resolution determines the smallest observable structure of a specimen. Therefore, most of the developments in microscopy aimed at higher resolution, and increases in resolution have always led to new discoveries in science. A good example is the improvement of resolution in light microscopy at the end of the 19th century. In those days, the resolution of the light microscope was limited by chromatic and spherical aberrations. Mastery of aberrations improved the resolution by a factor of 2, thus allowing the first observation of chromosomal behavior during cell mitosis.⁽¹⁾

This progress was primarily due to the efforts of Ernst Abbe working in close collaboration with Carl Zeiss. Studying the image formation in light microscopy, Abbe realized the importance of the wave nature of light and its central role in the resolution issue.⁽²⁾ He found a fundamental limit that still bears his name. When imaging a pointlike object with a lens, the point is imaged into a blurred spot whose radius depends on the wavelength of the light λ and the angular aperture α of the lens. Abbe argued that objects ‘closer than about half the wavelengths should not be distinguishable in a light microscope’. In fact, a

Stefan W. Hell • High Resolution Optical Microscopy Group, Max-Planck-Institute for Biophysical Chemistry, D-37070 Göttingen, Germany.

Topics in Fluorescence Spectroscopy; Volume 5: Nonlinear and Two-Photon-Induced Fluorescence, edited by J. Lakowicz. Plenum Press, New York, 1997.

distinct value for the smallest distance Δr cannot be given; however, it has become customary to take an expression derived by Lord Rayleigh,⁽³⁾ quantifying the radius of the blurred spot:

$$\Delta r = \frac{0.61\lambda}{n \sin \alpha} \quad (9.1)$$

The parameter n is the refractive index of the specimen, and the product $n \sin \alpha$ is called the numerical aperture, NA. To obtain a high resolution, a short wavelength and a high numerical aperture are desirable. However, the use of short wavelengths and high apertures is technically constrained since the shortest usable wavelength λ is around 350 nm and the highest available numerical aperture is about 1.4. Even under very favorable conditions the lateral resolution of the focusing light microscope is limited to about $\Delta r = 150$ nm. Objects closer than 150 nm should not be distinguishable.

This resolution limit severely restricts the applicability of light microscopy. For example, viruses, single genes, and a myriad of cell organelles cannot be resolved with a standard light microscope.⁽¹⁾ As Abbe's resolution limit has been considered fundamental, it has been a great stimulus to pursue different approaches in microscopy. The most prominent examples are electron microscopes⁽⁴⁾ and scanning probe microscopes such as scanning tunneling,⁽⁵⁾ atomic force,⁽⁶⁾ and the near-field optical microscope.⁽⁷⁾ The electron microscope focuses accelerated electrons rather than light. The de Broglie wavelength of the electrons can be as small as 0.005 nm and is easily controllable by an acceleration voltage of typically 50–100 kV so that the wave nature of the electrons hardly plays a limiting role. Presently, electron microscopes are limited by spherical and chromatic aberrations rather than by the wavelength, somewhat paralleling the situation of light microscopes in the middle 19th century. Electron microscopes provide a resolution ranging from tens of nanometers down to the atomic scale depending on the imaging mode (e.g., scanning or transmission) and on the sample. For biological applications a typical resolution of 0.1 nm is obtained.⁽⁸⁾ Atomic resolution can be achieved in a high voltage transmission electron microscope for specimens thinner than 0.1 μm.

In contrast to electron microscopes which are still based on focusing, scanning probe microscopes have assumed a more radical approach by abandoning the idea of focusing altogether. Scanning probe microscopes rely on the interaction of a narrow tip scanned across the surface of the object. The scanning tunneling microscope (STM), for example, measures a tunneling current between a conducting tip and a conducting surface of a specimen. The STM employs a single atom as a probe and achieves atomic resolution. The atomic force microscope (AFM) measures the force between a tip, usually made of Si₃N₄, and the specimen surface, thus offering the possibility of investigating nonconducting

material such as biological samples.⁽⁶⁾ The distance between the tip and the surface of an AFM in contact mode is in the range of fractions of a nanometer. The resolution of the AFM is primarily determined by the chemical environment and the size of the tip, which ranges from tens of nanometers down to the molecular scale.

The optical counterpart of the scanning probe microscope is the scanning near-field optical microscope (SNOM).⁽⁷⁾ The principles of the SNOM⁽⁹⁾ had been recognized before the advent of the AFM and STM, but the development of the SNOM technique was stimulated by the latter.⁽⁷⁾ A common version of the scanning near-field optical microscope consists of tapered aluminum-coated glass fiber with a tip opening of about 50–100 nm.⁽¹⁰⁾ The tip is used either as a tiny light source or as a probe for measuring the light emitted at the specimen surface. The fiber is brought as close as 5–15 nm to the specimen surface. Again, the resolution is determined by the diameter of the tip rather than by the wavelength. The resolution of scanning near-field optical microscopes ranges from 150 nm down to about 30 nm.⁽⁷⁾ Near-field means that the distance between the tip and the specimen surface is in the order of one to several percent of the wavelength. This is in contrast to the lens-based focusing light microscope, where the distances between the investigated object and the lens are at least several thousands of wavelengths. The invention of the near-field optical microscope demanded a new name for light microscopes based on focusing optics. In recent years it has become customary to name them light microscopes working in the *far-field*.

9.1.1. Why Far-Field Light Microscopy?

There is no doubt that electron and scanning probe microscopes feature a much higher resolution than focusing light microscopes. Despite this fact, electron and scanning probe microscopes have not replaced the far-field light microscope, and probably never will. Users of electron or scanning probe microscopes face inherent drawbacks in these techniques. In electron microscopy the sample has to be dehydrated and kept in an evacuated chamber to provide an unattenuated flow of electrons. This excludes the investigation of living cells.^(1,8) Furthermore, most of the electrons are absorbed on the specimen surface within a depth of a micron. In many cases, this urges metal coating of the sample to avoid charging of the specimen. Likewise, scanning probe microscopes are considered slow, and the scanning tip is not always easy to control. In addition, the image is not always easy to interpret. This applies also to the optical near-field microscope where the optical signal generated by the sample (e.g., fluorescence emission)⁽¹⁰⁾ also depends on the tip-sample interaction.

The most striking drawback of electron and scanning probe microscopes, however, is that they are restricted to investigations *on the specimen surface*. The interior of an intact specimen is accessible to neither of them. This is particularly serious in biomedical research, for in most of biomedical applications it is less exciting to investigate the specimen surface, than the *interior*. The most attractive feature of a far-field light microscope is its ability to gather information from the inside of the specimen. Focused light penetrates translucent specimens without harming them. The most sophisticated far-field light microscope in common use, the *confocal microscope*, can also deliver *three-dimensional images* of whole specimens and living biological samples.⁽¹¹⁾

Another important aspect of far-field fluorescence imaging is the considerable progress that has taken place in fluorescence labeling over the last decades. New fluorescent labels have offered biologists an efficient tool to mark the regions of concern inside the specimen. In biomedical applications, fluorescence is generally more specific than reflectance or absorbance.⁽¹²⁾ Fluorescence has become the most important mode of imaging in biological light microscopy, ranging from the investigations of DNA conformation to the observations of various biochemical mechanisms in living cells. It becomes clear that for many applications it would be highly interesting to have a far-field light microscope with a fundamentally increased resolution, say between 20 and 80 nm. Such a microscope could reveal, for example, the structure of DNA or the role and conformation of genes.⁽¹³⁾ Bearing diffraction in mind, the realization of such a microscope could not be considered a straightforward task.⁽¹⁴⁾ In fact, for many years, a large part of the scientific community has considered such an endeavor as ill-fated right from the outset.

Our studies, however, have shown that it should be possible to design novel types of far-field light microscopes with fundamentally increased lateral⁽¹⁵⁻¹⁷⁾ and axial resolution.⁽¹⁸⁻²⁰⁾ How can we overcome Abbe's resolution barrier? The answer is that we shape the spatial extent of the focus of the fluorescence microscope by implementing selected physical phenomena into the focusing process. We call this *method point-spread-function engineering*. The aim of this chapter is to outline the ideas of point-spread-function (PSF) engineering for increasing the resolution in the far field.

9.1.2. Imaging with a Lens: The Point-Spread Function

Let us assume a pointlike light source S is imaged to F by a lens (Figure 9.1). Due to the wave nature of light, the light emanating from S is spread around F , forming a three-dimensional distribution.⁽²¹⁾ The function describing the distribution of the intensity around F is called the *intensity point-spreadfunction*. In a

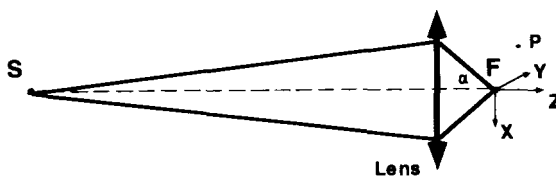


Figure 9.1. Imaging with a lens. The point S is imaged into F , and vice versa.

scalar theory, the intensity PSF is described by

$$h(u, v) = C \left| \int_0^1 J_0(v\rho) \exp\left(\frac{1}{2}iu\rho^2\right) \rho \, d\rho \right|^2 \quad (9.2)$$

The variables u , v are optical units representing the spatial coordinate along the optical axis (z) and in the lateral direction (x , y), respectively. The real spatial coordinates x , y , and z are related to the optical units by $u = 8\pi nz \sin^2(\alpha/2)/\lambda$, and $v = 2\pi nr \sin(\alpha)/\lambda$ with $r = \sqrt{x^2 + y^2}$. J_0 is the zero-order Bessel function of the first kind and C is a normalization constant.⁽²²⁾ The intensity PSF $h(u, v)$ is cylindrical symmetric and determined by the semiaperture angle α and the wavelength λ . The focal point F has the coordinates $(u = 0, v = 0)$. The intensity PSF is displayed in Figure 9.2a where one can also note its elongation along the optical axis. Figure 9.3 shows the profile of the intensity PSF in the focal plane, $h(0, v)$ where it is narrowest. The focal plane intensity distribution has a pronounced main maximum and two minima on either side at $v = 1.22\pi$ which is equivalent to the distance $\Delta r = 0.61\lambda/(n \sin \alpha)$ of Eq. (9.1). The region in the focal plane covered by the main maximum is called the Airy disk. For obtaining a deeper insight into the resolution issue it is not necessary to derive Eq. (9.2), but it is very useful to get a feel for the physical significance of $h(u, v)$. A good explanation of the PSF $h(u, v)$ can be given through a simple photon optics interpretation.⁽²³⁻²⁵⁾ From this viewpoint, the intensity PSF is a measure of the probability that a photon emitted by S reaches any given point (u, v) in the focus. Thus Figure 9.2a can be regarded as a map showing the likelihood that a given point is illuminated. Normalized to unity, the probability is 1.0 in the focal point $F = (0, 0)$, whereas in the arbitrarily chosen point P , a photon is encountered with a lower relative probability, e.g., of only 0.1. The integral $\int_0^\infty h(u, v)v \, dv$ is constant, thus accounting for a constant flux of photons in a plane perpendicular to the optical axis.

There is another interpretation of $h(u, v)$ which is equally interesting. As the light paths are reversible, we can also argue that the intensity PSF $h(u, v)$ is a measure for the probability that a photon emanating from (u, v) is able to arrive at the point S . Let us assume the reversed situation where the point like light source is at F so that the image of F is formed at S . Let us further assume that we have an additional point source at P . As the light travels equally well from P to S as from S

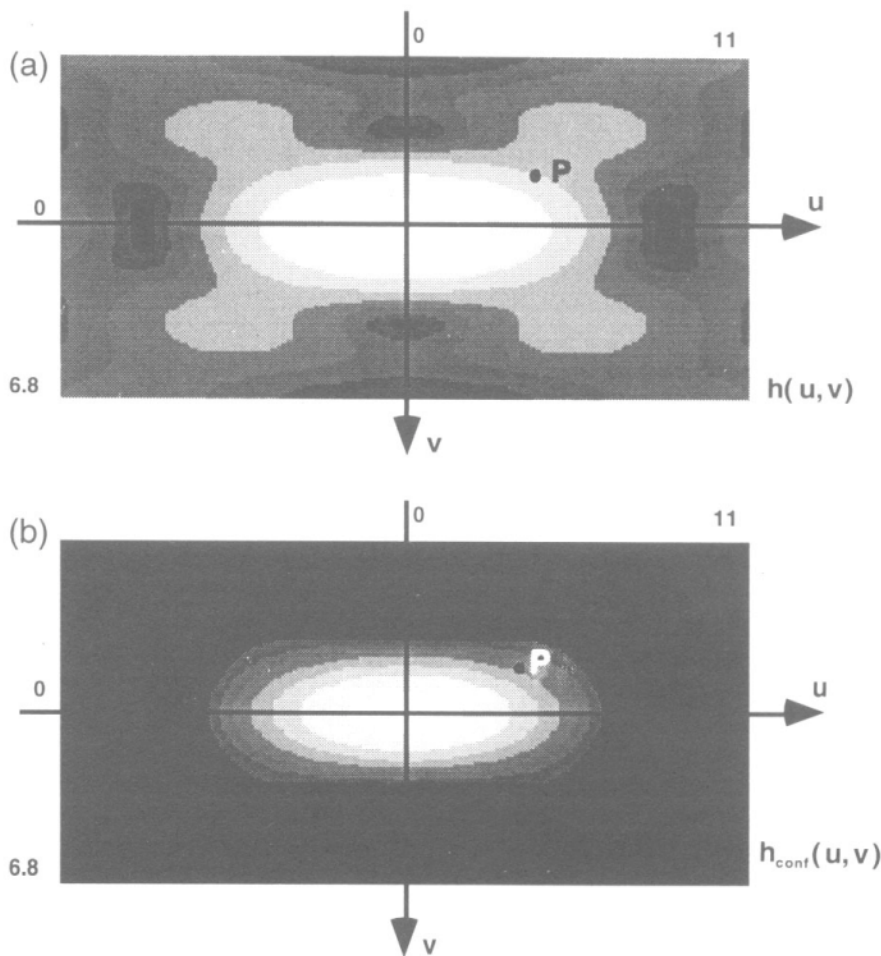


Figure 9.2. Intensity PSF, $h(u, v)$, of a lens (a), and the corresponding PSF $h_{\text{conf}}(u, v)$ of a confocal arrangement. The intensity PSF is normalized to unity and shows the distribution of focal intensity when an aberration-free lens is illuminated with an unpolarized wave free of aberrations. The u axis corresponds to the optical axis, whereas the v axis denotes the focal plane. The range from $-11 < u < 11$ and $0 < v < 6.8$ is shown. For a wavelength of 500 nm and a numerical aperture of 1.35 (oil) the size of the image is $0.8 \times 1.6 \mu\text{m}$. The look-up table has eight gray levels with contour lines at relative intensities of 0.7, 0.32, 0.13, 0.07, 0.03, 0.01, and 0.004. The PSFs are cylindrically symmetric around the u axis.

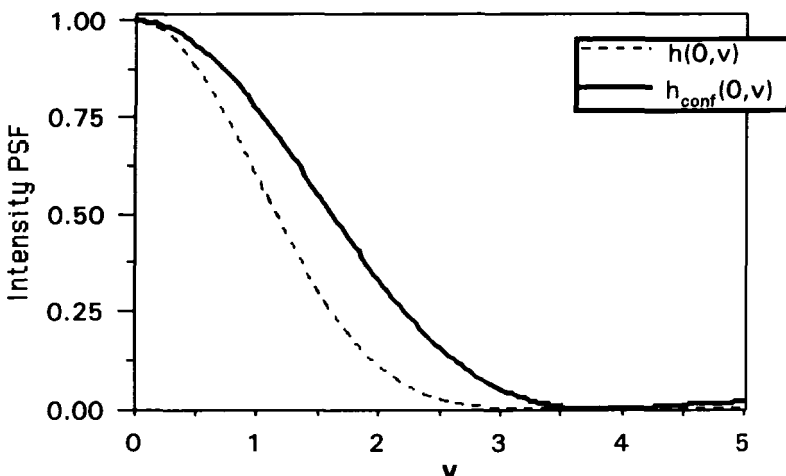


Figure 9.3. Intensity PSF $h(0, v)$ and confocal PSF $h_{\text{conf}}(0, v)$ in the focal plane describing the lateral resolution of a conventional and confocal fluorescence microscope. The first minimum of $h(0, v)$ is located at $v = 1.22\pi$, thus defining the main maximum, which is also referred to as the Airy disk.

to P , the intensity S consists not only of light from F , but also of contributions from P . The contribution from P is weaker than that of F because it is weighted by $h(\bar{u}, \bar{v})$, with \bar{u}, \bar{v} , being the optical units at P . Clearly, a lens is not able to distinguish self luminous points that are well within the main maximum of the intensity PSF $h(u, v)$, because these points contribute to the formation of the same image point, here at S , with almost equal strength.

Although a light microscope uses several lenses, we can reduce imaging of a compound system to that of a single lens. Thus, the lateral resolution of a conventional microscope imaging self-luminous objects is limited by the lateral extent of the intensity PSF, $h(0, v)$ shown in Figure 9.3. A good measure of the extent of $h(0, v)$ is the diameter of the Airy disk as described by Eq. (9.1). The function $h(0, v)$ and Eq. (9.1) describe the classical lateral resolution limit.

9.1.3. Scanning Fluorescence Microscopy

Whereas in conventional fluorescence microscopy the object is illuminated uniformly by a lamp, in scanning fluorescence microscopy^(26–29) it is illuminated by a pointlike light source (Figure 9.4). Thus, one obtains a single focal illumination intensity PSF in the specimen space, denoted by $h_{\text{ill}}(u, v)$ which is the image of the pointlike light source. The fluorescence light from the specimen is collected by the same objective lens, separated by a dichroic mirror and directed

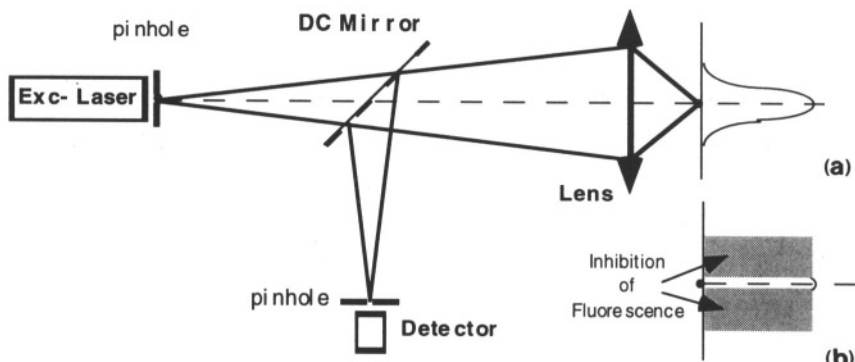


Figure 9.4. Scanning fluorescence microscope using a pointlike light source. In a *confocal* scanning fluorescence microscope the detector is also pointlike. Indent (b) sketches the idea of increasing the lateral resolution by inhibiting the fluorescence process at the outer region of the focus.

into a detector, e.g., a photomultiplier. To obtain a whole image in a scanning microscope, the focused illumination light has to be scanned across and inside the specimen.^(27–31) This is a technical procedure and ideally does not affect imaging. Scanning is usually performed by movable mirrors deflecting the beam so that the pivot is in the entrance pupil of the objective lens.⁽³¹⁾ An alternative approach is to scan the specimen stage with respect to a fixed illumination beam.^(26–30)

The *confocal* scanning microscope is the most popular version of the scanning microscope. In addition to pointlike illumination the confocal microscope also uses *pointlike* detection. Pointlike detection is achieved by placing a pinhole in front of the photomultiplier. The illumination and detection pinholes are imaged into the object plane, lined up along the optical axis and are optically symmetrical to each other (Figure 9.4).

In a confocal fluorescence microscope the contribution of any point (u, v) to the signal depends on two independent events. The first event is that an illumination photon has to arrive at the point (u, v) which is described by the illumination PSF $h_{\text{ill}}(u, v)$. The second event is that the fluorescence photon emitted from (u, v) has to propagate to the detector pinhole. As discussed in the previous section, the propagation to the detector is described by a similar intensity PSF which is here called detection PSF $h_{\text{det}}(u, v)$. Since both illumination and detection have to take place, the confocal imaging is determined by the product of both point-spread functions:^(23–29)

$$h_{\text{conf}}(u, v) = h_{\text{ill}}(u, v)h_{\text{det}}(u, v) \cong h_{\text{ill}}^2(u, v) \quad (9.3)$$

The right-hand side of Eq. (9.3) takes into account that the illumination and the detection PSF are approximately equal; there are slight differences between

$h_{\text{ill}}(u, v)$ and $h_{\text{det}}(u, v)$ stemming from the different illumination and fluorescence wavelengths. The Stokes shift can be accounted for by calculating the detection PSF as $h_{\text{det}}(u\lambda_{\text{exc}}/\lambda_{\text{fl}}, v\lambda_{\text{exc}}/\lambda_{\text{fl}})$. For typical Stokes shifts of 50–70 nm we can set $\lambda_{\text{exc}}/\lambda_{\text{fl}} \cong 1$ and imply that confocal fluorescence imaging is well described by the square of a single-lens PSF. In the previous example, the point P had a relative illumination probability of 0.1. The final probability that P contributes to the image signal is the square of the initial value, or 0.01. The same applies for all other points in the focal region.

The squaring effect has two major consequences. First, the confocal PSF is narrower than its conventional counterpart (Figure 9.2b and Figure 9.3). This is because the values at the outer region of the PSF are reduced. For instance, the value of 0.1 at P turned into 0.01. The second consequence is a discrimination effect; i.e., points outside the inner region of the confocal PSF have a much lower probability of contributing to the signal. The integral $\int_0^\infty h_{\text{conf}}(u, v)v dv$ is not constant along the optical axis but falls off with increasing values of $|u|$. However, this applies not only to optical axis; as generally contributions from outer regions of the confocal focus are suppressed. As a result of the quadratic intensity dependence, the confocal PSF $h_{\text{conf}}(u, v)$ forms as a three-dimensional probe for investigating the object. Only the fluorescence molecules inside the probe are recorded so that three-dimensional images of transparent specimens can be generated through scanning the PSF through the specimen in all directions.

In conclusion, in scanning microscopes imaging is accomplished with well-defined PSFs. The confocal fluorescence microscope features a quadratic PSF defining three-dimensional volumes. In contrast to conventional microscopes, the PSF of a scanning (confocal) microscope acts as a probe whose signal is recorded in a detector and whose extent determines the resolution. This is an excellent precondition for implementing physical processes in order to shape the extent of the PSF and finally break the diffraction resolution barrier.

9.2. PSF Engineering through Fluorescence Inhibition

Let us consider a scanning fluorescence microscope such as the one sketched in Figure 9.4. For the sake of simplicity it should not be confocal one so that the imaging is entirely described by the illumination PSF $h(u, v)$ shown in Figure 9.2a and Figure 9.3. The lateral resolution of this microscope is given by the lateral extent of $h(0, v)$ which is Airy's intensity distribution. When reconsidering the interpretation of $h(0, v)$ as the probability of an excitation photon to reach $(0, v)$, it becomes clear that $h(0, v)$ is also proportional to the probability that a fluorescent molecule *emits* a photon at $(0, v)$. As the lateral resolution is determined by the spatial extent of the fluorescing area, any inhibition of the

fluorescence process at the outer region of $h(0, v)$ increases the resolution of a scanning fluorescence microscope. By sharply confining the fluorescence process to the inner region of the PSF, we can overcome Abbe's resolution limit and enhance the resolution significantly^(16,17) (see Figure 9.4, indent). In principle, *any mechanism preventing fluorescence emission* is a potential candidate for reducing the extent of the effective focus, but suitable candidates include those mechanisms not resulting in destruction of the fluorescing molecule. Candidates for inhibiting fluorescence can be found by studying the process of fluorescence emission.

Figure 9.5 displays the energy levels involved in the excitation and emission process of a typical fluorophore.⁽³²⁾ S_0 and S_1 are the ground and the first excited singlet state, respectively; T_1 is the first triplet state; S_0^{vib} , S_1^{vib} , and T_1^{vib} are higher vibronic levels of these states. The excitation of the dye takes place from the relaxed state S_0 to the state S_1^{vib} obeying the Franck–Condon principle, whereas fluorescence is described by the radiative relaxation $S_1 \rightarrow S_0^{\text{vib}}$. The transitions $S_1 \rightarrow T_1^{\text{vib}}$ and $T_1 \rightarrow S_0^{\text{vib}}$ represent intersystem crossing. The transitions $S_1^{\text{vib}} \rightarrow S_1$, $T_1^{\text{vib}} \rightarrow T_1$, and $S_0^{\text{vib}} \rightarrow S_0$ are vibrational relaxations. The transition $S_1 \rightarrow S_0^{\text{vib}}$ can also be induced through stimulated emission, that is, a photon whose wavelength matches the energy gap between S_0^{vib} and S_1 interacts with the molecule in the excited state and generates a photon that is indistinguishable from itself.⁽³³⁾

Figure 9.5 also indicates the rates for these processes. The rates for the spontaneous processes are given by the inverse of the lifetimes τ of the source states; e.g., the fluorescence rate is given by $k_f = 1/\tau_f$, and the rate for vibrational decay by $k_{\text{vib}} = 1/\tau_{\text{vib}}$. The rates for excitation and stimulated emission are given by the product of the photon fluxes of the beams and molecular cross sections, i.e., $h_{\text{exc}}\sigma_{\text{exc}}$ and $h_{\text{sted}}\sigma_{\text{sted}}$ for excitation and stimulated emission, respectively. Typical values for σ_{exc} and σ_{sted} are 10^{-16} – 10^{-18} cm^2 . The fluorescence

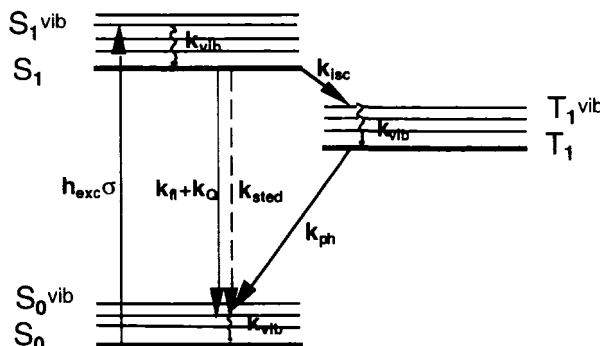


Figure 9.5. Energy states (Jablonski diagram) of an organic fluorophore.

lifetime τ_f is about 1 ns, and τ_q is about 10 ns. The intersystem crossing transitions are spin-forbidden and therefore slower than fluorescence, namely about 10–500 ns for τ_{isc} and 10^4 – 10^7 ns for τ_{ph} . The lifetimes of the vibrationally excited states are very short, $\tau_{vib} \leq 1$ ps. Hence, the vibrational relaxations $S_0^{vib} \rightarrow S_0$, $T_1^{vib} \rightarrow T_1$, and $S_1^{vib} \rightarrow S_1$ are the fastest relaxations in the fluorophore, three orders of magnitude faster than fluorescence. The triplet state T_1 is the most stable excited state, having a life time of 10^5 – 10^7 ns.

One consequence of the rapid vibrational decay is that the excited molecules in the Franck–Condon state S_1^{vib} rapidly come down to the relaxed state S_1 before emitting a photon. The state S_1 is the actual source of fluorescence photons, and the effective number of emitted fluorescence photons is directly proportional to the population of S_1 . We can even argue that at ambient temperature, S_1 is a *bottleneck* every molecule has to pass before undergoing fluorescence. Clearly, any mechanism depopulating S_1 leads to the required inhibition of fluorescence.

When considering the lifetime and the transitions of Figure 9.5, two phenomena appear to be of interest, the first being stimulated emission. For high enough intensities, one can expect the depopulation rate by stimulated emission to be stronger than that by spontaneous decay. A strong stimulating beam can make it more likely for a molecule to suffer stimulated emission than to emit a fluorescence photon. Fluorescence normally occurs in a broad spectrum of several tens of nanometers in wavelength. However, the stimulated photon has the same wavelength, polarization, and direction of propagation as its stimulating counterpart. The stimulated photon intermingles with the photons of the stimulated-emission beam and cannot be distinguished from the stimulating beam. However, the effect of stimulated emission can be observed as a loss of fluorescence intensity in the remaining part of the fluorescence spectrum. Meanwhile this is well investigated in fluorescence spectroscopy where it is referred to as *light quenching*.^(34–38) In our case, we are interested in generating this loss at the outer region of the focus. Light quenching by stimulated emission can inhibit the fluorescence signal and is therefore highly interesting for PSF engineering.

Figure 9.5 suggests that another mechanism could also be suitable for inhibiting the fluorescence process. Usually, the fluorescence molecule in the focus is excited many times, thus undergoing a fast circuit from the ground state to the excited state and back to the ground state. It remains in the singlet system for many excitation–fluorescence processes and rarely crosses to the triplet state. However, if the intersystem crossing rate k_{isc} is high, the molecule can be trapped in T_1 . As the triplet state is long-lived the molecule is efficiently excluded from the excitation–fluorescence circuit and is not able to emit fluorescence photons. Along with depletion of the excited state by stimulated emission, building up a high triplet-state population at the outer region of the focus is an interesting approach to inhibit the fluorescence process and engineer the PSF in the far-field.⁽¹⁷⁾

9.2.1. STED Fluorescence Microscopy

Figure 9.6 outlines the concept of the stimulated emission depletion (STED) fluorescence scanning microscope.⁽¹⁶⁾ It is designed for increasing the resolution by inhibiting the fluorescence process through stimulated emission. The light exciting the dye from $S_0 \rightarrow S_1^{\text{vib}}$ originates from a point-like light source consisting of a laser focused onto a pinhole. Its wavelength is denoted by λ_{exc} . The point source is imaged into the specimen by the objective lens, thus generating a classical distribution of $h(0, v) \equiv h(v)$ in the focal plane. But in contrast to the latter, the STED fluorescence microscope uses offset beams able to quench the excited molecules by light. We call them STED beams. In the ideal case, the STED beam forms a concentric annulus around the focal point, overlapping with the outer region of the Airy disk. The role of the STED beam is to stimulate the transition $S_1 \rightarrow S_0^{\text{vib}}$ at the outer region of the illumination PSF.

The spectroscopic properties of the fluorophore are crucial for the functioning of the STED fluorescence microscope. Shape and extent of the final PSF will strongly depend on the properties of the energy states involved. To find the potential resolution of a STED fluorescence microscope, an investigation is required of the behavior of the fluorescence molecules when excited by a strongly focused beam, $h_{\text{exc}}(v, t)$, and quenched by a second focused beam, $h_{\text{sted}}(v, t)$. The excitation wavelength λ_{exc} is preferably in the absorption maximum whereas the wavelength of the quenching beam, λ_{sted} , is centered in the emission spectrum of the dye. The photon fluxes of the focused beams have to be considered as functions of space and time when calculating the population probabilities $n_i^{\text{vib}}(v, t)$. The following set of differential equations describes the

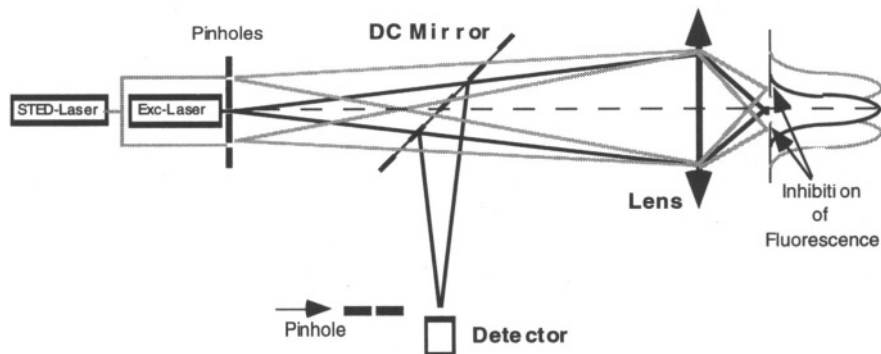


Figure 9.6. STED microscope. The excitation beam is centered along the optical axis, whereas the stimulating beams are laterally offset in order to quench the excited molecules at the outer region of the focus. A doughnut-shaped PSF is preferably used for depletion (not shown here). The optional detection pinhole provides a three-dimensional imaging capability and suppresses scattered light.

interplay among absorption, thermal quenching, vibrational relaxation, inter-system crossing, spontaneous emission, and stimulated emission:

$$\frac{dn_0}{dt} = h_{\text{exc}}\sigma_{\text{exc}}(n_1^{\text{vib}} - n_0) + k_{\text{vib}}n_0^{\text{vib}} \quad (9.4\text{a})$$

$$\frac{dn_0^{\text{vib}}}{dt} = h_{\text{sted}}\sigma_{\text{sted}}(n_1 - n_0^{\text{vib}}) + (k_{\text{fl}} + k_Q)n_1 - k_{\text{vib}}N_0^{\text{vib}} + k_{\text{ph}}n_2 \quad (9.4\text{b})$$

$$\frac{dn_1}{dt} = k_{\text{vib}}n_1^{\text{vib}} + h_{\text{sted}}\sigma_{\text{sted}}(n_0^{\text{vib}} - n_1) - (k_{\text{fl}} + k_Q + k_{\text{isc}})n_1 \quad (9.4\text{c})$$

$$\frac{dn_1^{\text{vib}}}{dt} = h_{\text{exc}}\sigma_{\text{exc}}(n_0 - n_1^{\text{vib}}) - k_{\text{vib}}n_1^{\text{vib}} \quad (9.4\text{d})$$

$$\frac{dn_2}{dt} = k_{\text{vib}}n_2^{\text{vib}} - k_{\text{ph}}n_2 \quad (9.4\text{e})$$

$$\frac{dn_2^{\text{vib}}}{dt} = k_{\text{isc}}n_1 - k_{\text{vib}}n_2^{\text{vib}} \quad (9.4\text{f})$$

with $\sum_i n_i^{(\text{vib})}(v, t) = 1$. The notation (v, t) was left out for clarity, but it is evident that the population probabilities of a molecule in the focal region of a lens are functions of space and time, with the temporal dependence becoming relevant when pulsed lasers are employed. Equation (9.4) also includes re-excitation of the vibrationally excited ground state S_0^{vib} by λ_{sted} and stimulated emission by the excitation wavelength λ_{exc} .

9.2.1.1. Depletion of the Excited Singlet State through Stimulated Emission

Although the phenomenon of stimulated emission is well known, it is not at all clear that it can be efficiently used to deplete the excited state of a fluorescent molecule. Of course, stimulated emission is used in dye lasers,⁽³⁹⁾ but the operational requirements in a laser and those for depletion are different. In a dye laser, the dye is pumped to S_1 to achieve the highest possible population.⁽³⁹⁾ The intent is to supply as many excited molecules as possible to obtain the highest possible flux of stimulated photons. For laser operation, it is sufficient to keep the excited state populated highly enough to have many molecules contributing with a stimulated photon. Depletion of the excited state is not required; moreover it would interrupt the lasing process. In our case, we do not want to strengthen the laser beam by stimulated photons and do not require a high population of S_1 . We do require the ability of the stimulating beam to quench the excited state before the

molecules emit a fluorescence photon. In simple terms, the quenching beam should generate an ambience in which spontaneous emission cannot take place.

The lifetimes and transition rates of the fluorophore suggest that it is highly advantageous to employ pulsed lasers.^(16,34–38) This becomes evident when considering Eq. (9.4c), suggesting that depletion by stimulated emission, or light quenching, prevails for

$$h_{\text{sted}} \sigma_{\text{sted}} n_1 \gg k_{\text{vib}} n_1^{\text{vib}} \quad (9.5a)$$

$$h_{\text{sted}} \sigma_{\text{sted}} n_1 \gg (k_{\text{fl}} + k_Q + k_{\text{isc}}) n_1 \quad (9.5b)$$

$$h_{\text{sted}} \sigma_{\text{sted}} n_1 \gg h_{\text{sted}} \sigma_{\text{sted}} n_0^{\text{vib}} \quad (9.5c)$$

Equation (9.5) suggests that light quenching faces three competing mechanisms. The first competing mechanism is the supply from the higher vibronic level S_1^{vib} given by $k_{\text{vib}} n_1^{\text{vib}}$. The second competing mechanism is the spontaneous decay of S_1 described by $(k_{\text{fl}} + k_Q + k_{\text{isc}}) n_1$. The supply from the higher state and the spontaneous decay can be outperformed by using *pulsed* excitation and *pulsed* STED beams. Employing an excitation pulse that is immediately followed by a stimulating pulse temporally separates excitation from stimulated emission. Thus, the fluorescent level S_1 is not supplied by fresh molecules from S_1^{vib} while being quenched. In this case, quenching is very efficient. The excitation pulse width τ_p should be about $\tau_{\text{vib}} \leq 1 \text{ ps}$, thus ensuring a vanishing fluorescence decay during excitation.

Another aspect of pulsed excitation is that the supply from the higher vibrational level S_1^{vib} to S_1 vanishes a picosecond after the excitation pulse has passed. To avoid spontaneous emission from S_1 , the stimulating pulse has to closely follow the excitation pulse. This condition makes it beneficial to use stimulating pulses in the picosecond range or shorter. Furthermore, to surpass this spontaneous decay a high intensity is required. Pulsed lasers help in this respect, because they provide a high peak intensity at a rather low average power. The latter is important for keeping the irradiation doses low, especially when considering potential biological applications. The shorter the pulse, the higher is the peak power at a given average intensity.

However, there is a clear restriction concerning the duration of the pulse. This restriction traces back to the population n_0^{vib} of S_0^{vib} , which is the final state of the quenching process. Equation (9.5c) shows that efficient depletion requires a vanishing population n_0^{vib} . A quenching pulse facing a high population n_0^{vib} would reexcite the dye to the first singlet state S_1 , so quenching would not be efficient. There must be a drain for the quenched molecules in S_0^{vib} to keep n_0^{vib} low, otherwise the stimulating beam would pump the molecule up and down. This problem does not occur when the rate $S_1 \rightarrow S_0^{\text{vib}}$ is lower than the vibrational decay

$S_0^{\text{vib}} \rightarrow S_0$. In other words, the stimulated-emission rate should be low enough to allow the state S_0^{vib} to relax vibrationally. Since the lifetime of vibrational states is about ≤ 1 ps, the duration of the STED pulses should be in the range of several picoseconds to allow sufficient time for S_0^{vib} to relax.

At this stage, we can calculate the PSF of a STED fluorescence microscope by solving Eq. (9.4), and assuming pulsed excitation and STED beams with the STED pulses immediately following the excitation pulse. The excitation and the STED pulses should have Gaussian temporal pulse shape:^(16,39)

$$\begin{aligned} h_{\text{exc}}(v, t) &= \tilde{h}_{\text{exc}}(v) e^{-((t-t_0)/\tau_p)^2 \ln 2} \\ h_{\text{sted}}(v, t) &= \tilde{h}_{\text{sted}}(v) e^{-((t-t_0)/\tau_p)^2 \ln 2} \end{aligned} \quad (9.6)$$

It is interesting to initially restrict our investigation to the depletion process. Let us assume that the fluorescence molecules are already excited, i.e., $n_1(t=0)=1$, and that the excitation pulse is switched off. We chose $\tau_{\text{fluor}}=2$ ns, $\tau_Q=0.1$ ns, $\tau_{\text{vib}}=1$ ps, $\lambda_{\text{exc}}=500$ nm, $\lambda_{\text{sted}}=600$ nm, $\sigma_{\text{sted}}=10^{-16}$ cm 2 , and NA=1.4(oil) for our numerical studies.

Figure 9.7 shows the temporal dependence of the population probability of S_1 , when subject to a STED pulse of $\tau_p=100$ ps duration (FWHM), reaching its maximum at $t=0.2$ ns after the subpicosecond excitation pulse has passed. We can also safely neglect the triplet state because intersystem crossing is too slow to

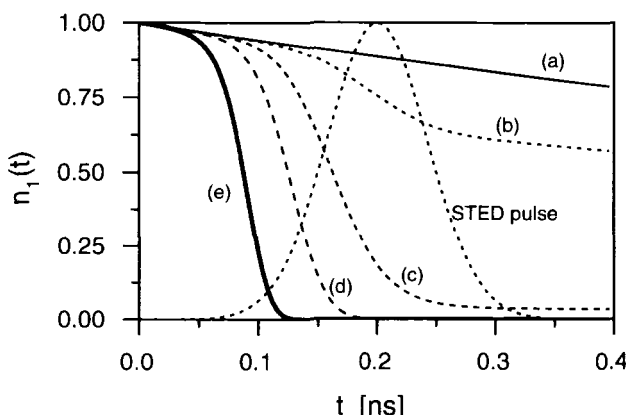


Figure 9.7. Population of the first excited state as a function of time when subject to a quenching pulse of 100-ps duration reaching its maximum 0.2 ns after the excitation pulse has left. For increasing peak intensities: (b) 10, (c) 100, (d) 500, (e) 1000 MW/cm 2 , depletion by stimulated emission or light quenching occurs increasingly fast, thus strongly reducing the lifetime of the excited state. Curve (a) shows the spontaneous decay of the fluorophore without light quenching.

play a role in this time scale. We calculate $n_1(t)$ for different peak intensities \tilde{h}_{sted} corresponding to peak photon fluxes of (a) 0, (b) 3.0×10^{25} , (c) 3.0×10^{26} , (d) 1.5×10^{27} , and (e) 3.0×10^{27} photons/(s cm²). Curve (a) describes the regular fluorescence decay of S_1 with the STED beam switched off. Curves (b–e) show how the STED beam depletes the population of S_1 . For low intensities (b, c) the depletion by stimulated emission is not complete. After the STED pulse has passed, the decrease of $n_1(t)$ is governed by spontaneous emission and thermal quenching. For higher pulse intensities (d, e), depletion is strong, and for a peak intensity of 500 MW/cm² the state S_1 is depleted after 200 ps. Light quenching of S_1 can also be interpreted as an enforced reduction of the lifetime of S_1 by stimulated emission.^(36–39)

Figure 9.7 clearly shows how depletion depends on the intensity of the STED beam for a given pulse length. As the pulse length is much shorter than the lifetime of the dye, and the rate of stimulated emission is linear with regard to intensity, depletion becomes stronger as the number of stimulating photons in the pulse increase, i.e., depletion depends on the pulse energy. Therefore, one can also expect that depletion will be stronger for longer pulses as long as the pulse is shorter than the lifetime of S_1 .

Figure 9.8 quantifies the efficiency η of light quenching for increasing intensities. For a Gaussian temporal shape of the STED pulse reaching its maximum at $t = 2\tau_p$, after a time interval $t = 4\tau_p$, the pulse has left the focus almost entirely. Therefore we define the depletion efficiency η as the ratio between the population of S_1 after $t = 4\tau_p$, as given with and without exposure to the STED pulse:

$$\eta = \frac{n_1^{\text{with sted}}(t = 4\tau_p)}{n_1(t = 4\tau_p)} \quad (9.7)$$

Figure 9.8 shows the depletion efficiency η with increasing peak intensity of the STED pulse \tilde{h}_{sted} for different pulse durations τ_p . For low intensities, the depletion process is linear and the probability of stimulating the molecule to the ground state increases linearly with increasing STED intensity. This can be recognized from the linear negative slope of η . The curve flattens at higher intensities (about 50 MW/cm²) suggesting that the saturation point of depletion is being reached.

As the next step, we consider the spatial distribution of the depletion process.⁽¹⁶⁾ Let us assume a spatially uniform distribution of excited molecules in the focal region: $n_1(v, t = 0) = 1$. A uniform distribution of excited molecules could be obtained by exciting a layer of fluorescent molecules with a weakly focused excitation beam. Let us further assume that this uniform distribution of excited molecules is subject to a focused STED beam of Gaussian *temporal*

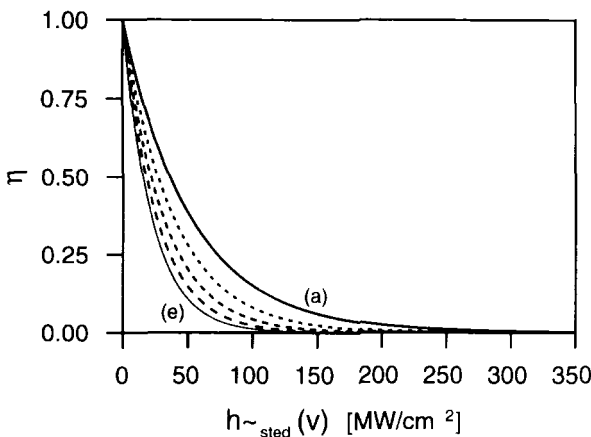


Figure 9.8. Efficiency of depletion η as a function of the peak intensity calculated for pulse durations of (a) 60, (b) 80, (c) 100, (d) 120, and (e) 140 ps.

shape. The *spatial* distribution of the STED beam is given by the illumination PSF, $h_{\text{sted}}(v, t)$, at λ_{sted} which is of the Airy type (Figure 9.3). Figure 9.9 shows how the STED pulse leaves depleted areas in the initially uniform distribution of excited molecules. The values are calculated for increasing peak intensities h_{sted} . For low intensities (a, b), the STED beam essentially carves its own profile into the distribution of excited molecules, so that the curves resemble inverted classical focal intensity distributions. For higher intensities the depleted area increases in diameter and the depleted area features increasingly steeper edges.⁽¹⁶⁾ The reason is that depletion by stimulated emission reaches saturation, as predicted in Figure 9.8. Whereas the high intensity around the focal point ($v = 0$) almost totally depletes the molecules located around $v = 0$, the areas at the minima of the STED beam ($v = 1.22\pi$) remain mostly unaffected. This explains why the edges become sharper with increasing STED-beam intensity. For higher STED-beam intensities the center of the focused beam reaches the saturation level of depletion, whereas the strongest spatial change in population occurs at the rim of $h_{\text{sted}}(v, t)$. The increase of the sharpness of the edges is desirable since it opens up possibility of a sharp limitation of the illumination PSF at the outer region of the focus.

9.2.1.2. Resolution in the Concept of STED Fluorescence Microscopy

As the molecules in the first minimum of $h_{\text{sted}}(v, t)$, ($v = 1.22\pi$) are hardly affected by the STED beam, we can outline a fluorescence microscope—that is focusing excitation light $h_{\text{exc}}(v)$ at $v = 0$ and two STED beams laterally offset

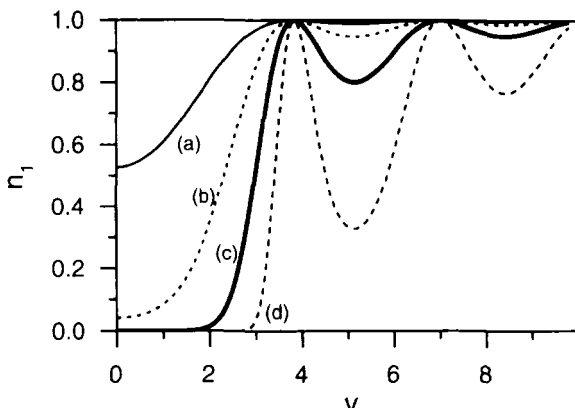


Figure 9.9. Spatial depletion profile as produced in a uniform distribution of excited molecules by a diffraction-limited beam, $h(0, v)$. The population of the excited state n_1 is calculated for increasing peak intensities h_{sted} of the quenching pulse: (a) 10, (b) 50, (c) 200, (d) 1000 MW/cm². For increasing intensities, saturation is reached. This can be recognized by the steep edges of depletion and pronounced lobes. For Gaussian-shaped quenching beams, the edges are not as steep as with diffraction-limited beams and no sidelobes occur.

along one axis, say in the x direction, focused at $v = \pm 1.22\pi$ (see also Figure 9.6). The offset by $v = \pm 1.22\pi$ makes the first minimum of $h_{\text{sted}}(v)$ coincide with the maximum of $h_{\text{exc}}(v)$. To increase the resolution in the y direction one would use a similar arrangement of STED beams, also in the y direction. The ideal solution, of course, is an annular STED beam intensity distribution around the excitation focus as could be possibly provided by an **axicon**⁽⁴⁰⁾ or a higher mode of a glass fiber or laser.

In the following, we investigate the extent of the effective PSF for different intensities of the STED-beam. The STED beams are focused with an offset $\Delta v = \pm 1.22\pi$ with respect to the excitation beam focused at $v = 0$. As we intend to excite the dye molecules with pulses that are immediately followed by STED pulses, we can separate the excitation and the depletion process, so that the effective PSF of the STED fluorescence microscope with two STED beams along, say the x axis, is readily calculated by multiplying the excitation PSF at λ_{exc} and the depletion curves:

$$h_{\text{eff}}(v_x) = h_{\text{exc}}(v_x)n_1(v_x) \quad (9.8)$$

Figure 9.10 shows the effective PSF for the peak intensities of the STED beam of (a) 0, (b) 500, (c) 1000, (d) 5000, and (e) 20,000 MW/cm². One can note a sharp decrease of lateral FWHM and therefore a strong increase in lateral resolution up to one order of magnitude, which is achieved for the high intensity in (e). The

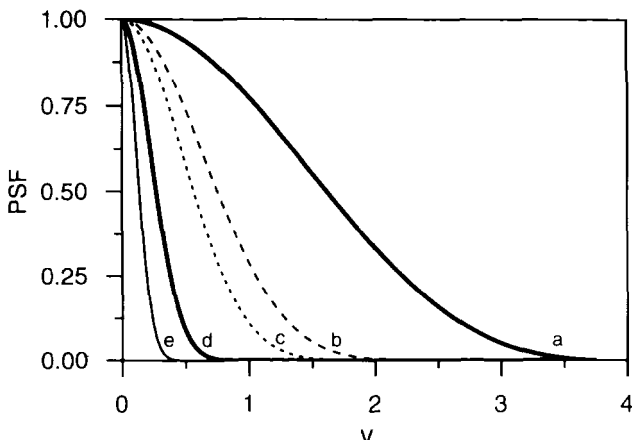


Figure 9.10. Effective PSF $h_{\text{sted}}(v_x)$ in a STED fluorescence microscope as predicted for quenching beams focused at $v = \pm 1.22\pi$, featuring pulse lengths of 100 ps and peak intensities of (a) 0, (b) 500, (c) 1000, (d) 5000, and (e) 20,000 MW/cm². Curve (a) represents the classical resolution limit. A strong increase in lateral resolution is predicted.

FWHM of the effective PSFs in optical units is (a) 3.2, which is the conventional resolution, (b) 1.5, (c) 1.14, (d) 0.54, and (e) 0.27. For an assumed excitation wavelength of 500 nm and a numerical aperture of 1.4 (oil) these values amount to a lateral resolution of (a) 182 nm, (b) 85 nm, (c) 65 nm, (d) 31 nm, and (e) 15 nm.

In our model, the minimum of the excitation PSF coincides spatially with the maximum of the STED beam. In this case the first side maximum of each STED beam overlaps with the main maximum of the other STED beam, thus strengthening depletion. However, the side maxima of the STED beam are not required; they rather support the depletion of the excited state. At an excitation wavelength of 500 nm and an aperture of 1.4 (oil) the offset $\Delta v = 1.22\pi$ is equivalent to a spatial offset of $\Delta x = 220$ nm in the focus. This offset can be realized technically by displacing the STED rays by the factor $M \Delta x$ in the space of the light sources, with M being the magnification of the microscope. The offset is readily changed by altering the distance from the illumination pinholes to the objective lens (see Figure 9.6). With typical magnifications of $M = 100\text{--}300$, the lateral offset of the STED beams is 50–150 μm , which is easily handled in practice.

In the original publication introducing the STED fluorescence concept,⁽¹⁶⁾ a beam with a Gaussian spatial distribution was considered. A Gaussian beam does not have side maxima and displays a depletion curve similar to that of Figure 9.9, except that it renders a single depletion area. The increase in resolution, does not however, depend solely on the STED beam intensity but also on the slope of the

STED PSF $h_{\text{sted}}(v, t)$. In this respect it is better to employ an Airy intensity distribution because it is steeper than a Gaussian-shaped focus, thus leading to steeper edges. In addition, one can expect that the molecules in the minima of the STED beam are not affected by depletion; this favors a higher fluorescence yield. Annularly shaped apertures would probably even amplify this effect. Annularly shaped apertures lead to pronounced minima, with up to a 30% narrower main maximum and somewhat higher sidelobes.⁽⁴¹⁾

The fluorescence signal depends on the area where the molecules do not undergo stimulated emission. Inevitably, a higher resolution reduces the detectable signal. Figure 9.11 shows the dependence of the detectable signal on the peak intensity of the STED pulse. Curve (a) shows the detectable signal from the focal plane in the case that the resolution is increased only along one axis. Curve (b) is calculated for a doughnut-shaped STED beam. Both curves are normalized to unity representing the signal obtained with a conventional focus. Figure 9.12 displays the increase in resolution as a function of the peak intensity. In theory, the STED fluorescence concept has the potential of decreasing the full-width-half-maximum of the effective focus by up to one order of magnitude.

The resolution is clearly not diffraction limited if the intensity is increased even further. Besides increasing the intensity, the STED beams can also be brought closer together, i.e., closer than 1.22π . Bringing the STED beams closer⁽¹⁶⁾ further increases the resolution but also goes at the expense of the signal strength. This is because for closer STED beams, the STED beam minima no longer coincide with the maximum of the excitation beam. The practical limit of resolution is determined by the intensity the sample can with-

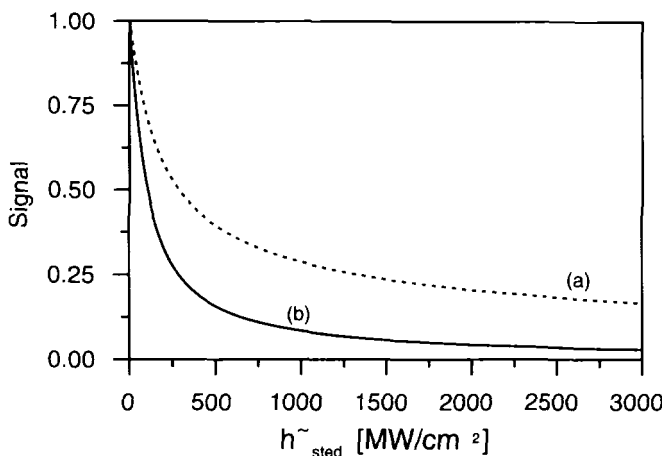


Figure 9.11. Signal in the STED fluorescence microscope as a function of the quenching beam peak intensity for a single direction (a) and (b) an annularly shaped beam.

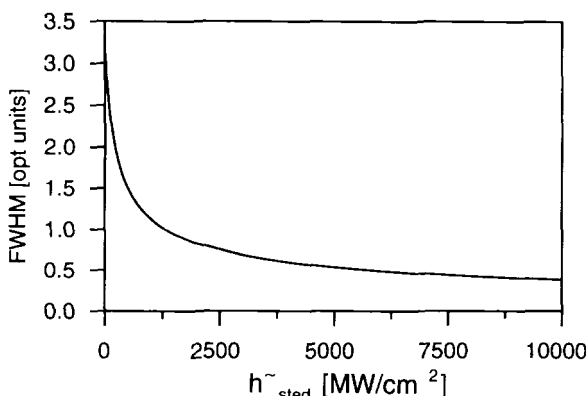


Figure 9.12. Resolution (FWHM) as a function of the peak intensity of the quenching beams calculated for the focusing parameters given in the text.

stand without being damaged and the number of fluorescence photons that can be collected in a reasonable time interval. As the stimulating beam is assumed to not be absorbed by the fluorophore, quenching by stimulated emission should be a “cool” depopulation of the excited state.

The theoretically predicted resolution of 20–50 nm is well within the range of the resolution provided by near-field optics. It is clear that the focal intensities in this concept are governed by diffraction; so that both the excitation and the STED beams are regular diffraction-limited beams. There is no possibility of avoiding diffraction in a far-field light microscope. However, by engineering the PSF of a scanning fluorescence microscope we reduce the effective area of the PSF probe so that it is spatially narrower in the sample. The fact that lenses have a limited bandwidth when transferring spatial frequencies does not play any role.

9.2.1.3. STED Fluorescence Microscopy with Incomplete Depletion

The model of Eq. (9.4) describes the dye as a four-level system. Normally, four-level systems satisfactorily quantify fluorophores and other organic molecules. The operation of a dye laser is sufficiently described by a four-level model.⁽³⁹⁾ However, for a considerable thermal excitation of the states and a *small Stokes shift*, we expect a simple four-level model to fail. At ambient temperature, there is a finite probability that S_0 and S_1 are in a higher vibrational state. How does this affect the above model? We do not expect this to concern the stimulation process. A lower vibronic state being emptied by stimulated emission would be filled by relaxing higher vibrational states within a picosecond, so

thermally excited states of S_1 will also be depleted. However, a similar effect does not take place in the ground state. A drain for the thermally excited level does not exist, unless the excitation beam is pumping the dye very strongly. In principle, the molecules in a stable higher vibronic level of the ground state could absorb a low-energy photon, assumed to perform stimulated emission. For dyes of a short Stokes shift, a strong STED beam intensity can lead to a considerable excitation by the STED beam.

Thermal excitation can be phenomenologically accounted for in the model by subtracting a term $\alpha h_{\text{sted}} \sigma_{\text{exc}} n_1$ from the right-hand side of Eq. (9.4a) and adding the same term on the right-hand side of Eq. (9.4d). The parameter $\alpha < 1$ considers the lower probability of this process, as compared with that of excitation by λ_{exc} . A factor of $\alpha = 0.1$ means that the possibility of exciting the ground state is about $1/\alpha$ times less with λ_{sted} than with λ_{exc} . Because of the excitation by the STED beam, depletion of S_1 cannot be total. Whereas for $\alpha = 0$ the population n_1 converges to zero at high STED beam intensities, for finite α a finite n_1 is reached. This is shown in Figure 9.13 for $\alpha = 0.1$, a high value. This value of α might not be typical, but was chosen to clearly illustrate the effect. For a strong excitation with the STED beam, one can use the STED beam for depletion only if the excitation pulse populates the molecules to a very high level, close to unity. Otherwise, the fluorescence induced by the STED-beam could be stronger than that of the excitation beam.

Figure 9.14 shows the effective PSF for increasing STED beam peak intensities h_{sted} for $\alpha = 0.1$. One notices that the incomplete depletion of S_1 leads to a

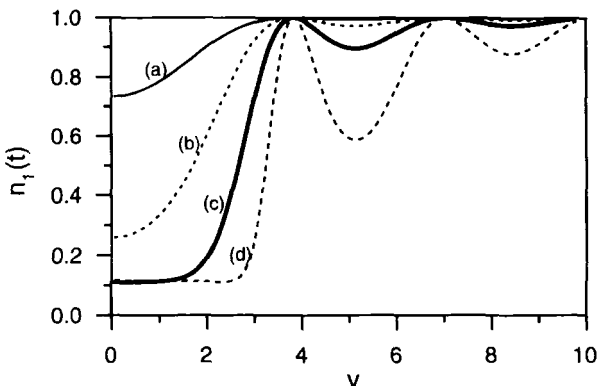


Figure 9.13. Spatial depletion profile as produced by a diffraction-limited beam, $h(0, v)$, in a uniform distribution of excited molecules calculated for a quenching beam able to excite molecules in the ground state ($\alpha = 0.1$). The population of the excited state n_1 is calculated for increasing peak intensities h_{sted} of the quenching pulse: (a) 10, (b) 50, (c) 200, (d) 1000 MW/cm². For increasing intensities, saturation is reached at a higher level of population and depletion is incomplete.

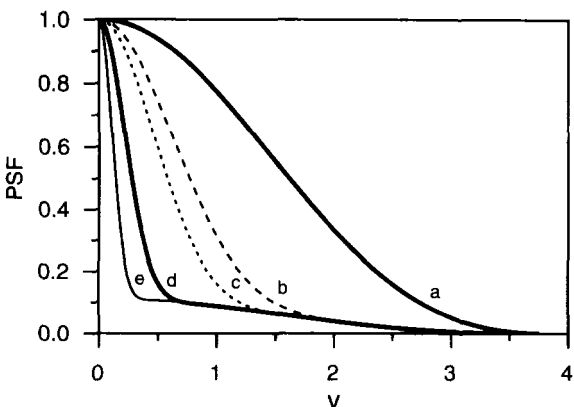


Figure 9.14. Effective PSF $h_{\text{sted}}(v_x)$ in a STED fluorescence microscope as predicted for incomplete light quenching ($\alpha = 0.1$). Depletion parameters are the same as in Figure 9.10.

shoulder, diminishing the benefit of decreased FWHM. The decrease in lateral extent of the focus is present, but it is reached at higher STED beam intensities. We can therefore conclude that a possible excitation of the dye by the stimulating beam compromises the resolution improvement. Under these less favorable conditions, the FWHM decreases and the increase in resolution still takes place, but wavelength-dye combinations showing a high absorption at the stimulating wavelength should be avoided. A large Stokes shift is preferable.

9.2.1.4. Toward the Practical Realization of STED Fluorescence Microscopy: Studies on Quenching of the Excited State by Stimulated Emission

The theoretical analysis reveals the importance of careful selection of the appropriate combination of wavelengths λ_{exc} , λ_{sted} and fluorophores when developing a STED fluorescence microscope. At present, mode-locked or cavity-dumped dye lasers are probably the most suitable light sources since they provide picosecond light pulses throughout the visible range. Practical realization of a STED fluorescence microscope would preferably include two dedicated, synchronized dye lasers, one for excitation and one for stimulated emission. A different approach is to use the fundamental wavelength of a laser and its second harmonic.^(42,43) The second harmonic is gained by focusing the laser light into a frequency-doubling crystal. Using a single laser is less flexible than two lasers, but the advantage of this approach is the corresponding lower cost and straightforward synchronization of the pulses.

An experiment based on the use of a mode-locked Ti:sapphire laser is sketched in Figure 9.15. The Ti:sapphire laser (Coherent Mira 900F) provides

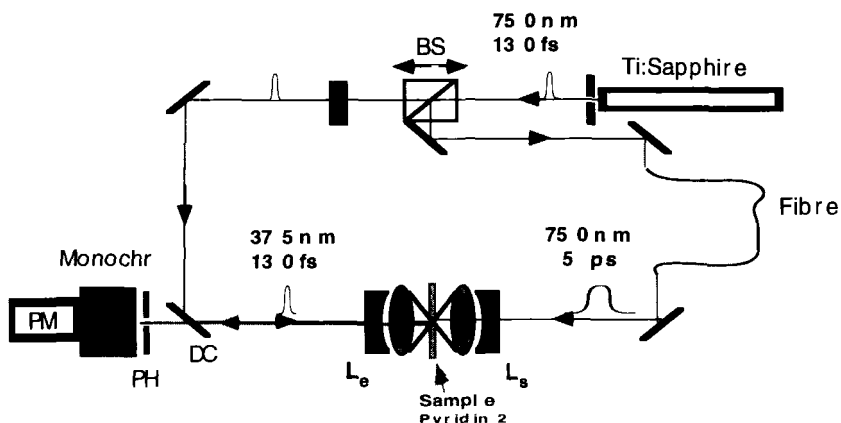


Figure 9.15. Experimental arrangement to study light quenching by stimulated emission on a microscopic scale. L_e and L_s are the lenses used for excitation and stimulated emission, respectively. BS represents a beam splitter, DC a dichroic mirror, and PH is a pinhole placed optically conjugate to the sample and the pinhole in front of the laser. PM represents a photomultiplier.

130-fs pulses at a repetition rate of 76 MHz and a central wavelength of 750 nm. The laser light is split into two beams, one of which is frequency-doubled to 375 nm by a BBO crystal with a conversion efficiency of about 3%. The other beam is coupled into a glass fiber. The duration of the frequency-doubled pulses is largely unaffected by the BBO crystal. This is not so with the infrared pulses passing through the fiber. The purpose of the fiber is to stretch the temporal pulse width through dispersion. The fiber is 5 m long, so an infrared pulse of initially 130 fs duration has a duration of about 5 ps at the end of the fiber. With such an arrangement one can employ the near-UV femtosecond pulse for excitation, and the picosecond infrared pulse for stimulated emission. The excitation light of $\lambda_{\text{exc}} = 375 \text{ nm}$ is focused by the objective denoted with L_e , whereas the light for stimulated emission at $\lambda_{\text{sted}} = 750 \text{ nm}$ is focused by the opposite objective L_s . The lenses have a specified numerical aperture of 1.4 (oil) and share a common focus. L_e is fixed whereas the other lens L_s is lined up with respect to L_e . Moreover, the objective lens L_s can be scanned with a precision of 10 nm with respect to the focus of the lens L_e .

In an experiment studying depletion by stimulated emission^(42,43) a drop of pyridine 2 (Radiant Dyes, Wermelskirchen, Germany)⁴⁴ dissolved in glycerol was mounted between two cover slips forming a 10-μm thick layer. Pyridine 2 is excitable at 375 nm and shows susceptibility to stimulated emission at 750 nm.^(42,43,45) Besides, pyridine 2 is commonly used in dye lasers operating in the 700–780 nm range.⁽⁴⁴⁾ The fluorescence of pyridine 2 is collected by the same objective lens L_e and focused on a pinhole placed in front of a double

monochromator adjusted to a maximum transmission at 670 nm. The spectral opening of the monochromator is about 2 nm which is a fraction of the emission spectrum of pyridine 2. Fluorescent light passing the monochromator was recorded in a photomultiplier working in the photon counting mode. The excitation beam filled the entrance aperture of lens L_e . The detection pinhole had a diameter equivalent to the magnified back projected Airy disk to provide a confocal operation of the setup. A long-wave-pass dichroic mirror with an edge at 700 nm was placed directly behind the fiber to remove any other light coming out of the glass fiber. Similarly, a short-wave-pass dichroic mirror with an edge at 700 nm was placed in front of the monochromator to further suppress the infrared light. The total path length of the 375-nm pulse was matched to that of the 750-nm pulse. One mirror was placed on a translation stage to allow for a precision change of the path length.

The illumination pinhole together with the detection pinhole define a confocal point-spread function of L_e . Therefore, the arrangement of Figure 9.15 features a probe volume, from which the fluorescence light is registered. Since the probe is inside a uniform solution of fluorophore, the fluorescence signal registered in the detector is independent of the spatial coordinate of the probe volume of L_e . The fluorescence signal is constant as shown in Figure 9.16a. When overlapping the excitation focus of L_s with that of the 750-nm light of L_e , the fluorescence signal is reduced. Moreover, when scanning the lens L_s with respect to L_e , one expects a profile of depletion⁽¹⁶⁾ carved into the constant fluorescence signal of curve (a). Such a profile is shown in curve (c) where the lens L_s scanned with respect to L_e , 15 μm back and forth. The focused power of the infrared beam was 20 mW, corresponding to a peak intensity of about $\tilde{h}_{\text{sted}} = 18.6 \text{ GW/cm}^2$, assuming a beam diameter of

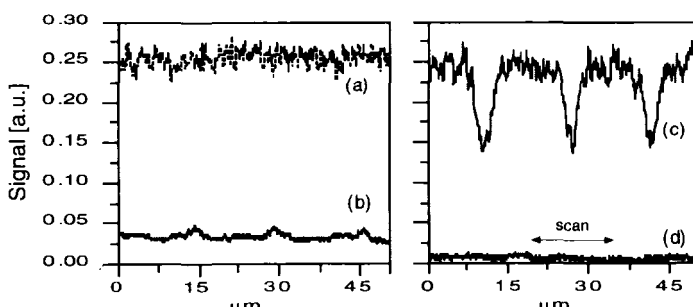


Figure 9.16 Fluorescence signal (a) measured at 670 nm when exciting with 375 nm, (b) the background with blocked excitation light and opened quenching beam, (c) the fluorescence signal when exposed to the 750-nm light from the scanning lens L_s , and (d) the background when both beams were blocked. All curves were measured with the lens L_s scanning laterally 15 μm back and forth.

0.6 μm. Each pixel was 10 nm, the speed of the scanning stage 10 μm/s, and the pixel dwell time 1 ms.

One can notice that the fluorescence signal drops with increasing overlap of the two focal intensities as a result of stimulated emission. The phenomenon is stable over periods of 1 h, which was the longest period of observation. Curve (d) shows the background signal when both laser beams were completely blocked. Curve (b) shows the signal with only the 750-nm light being switched on, revealing a background that is mostly due to the incomplete suppression of the 750-nm light in the monochromator. One can also notice small peaks at the coordinates where the foci overlap best, which is probably due to the higher transmission intensity here. In this initial experiment, the FWHM of the depletion signal is larger than the theoretically expected value. We found that this can be mostly attributed to the limited focusing capabilities of the used objective lens at 375 nm rather than to any other process. Special UV objective lenses providing a sharper excitation PSF will be more suitable for further experiments with pyridine 2. An alternative is to study dye-wavelength combinations in the visible range, e.g., rhodamines with excitation around 500 nm and stimulated emission around 620 nm. In this range, the lenses are corrected.

To check if the reduction of fluorescence signal is due to stimulated emission rather than to photothermally induced damage, we carefully altered the path lengths of the two beams and measured the efficiency of the depletion process. The efficiency of depletion was defined as the ratio between the signal given by the difference between the fluorescence with and without depletion beam, and the fluorescence signal with the depletion beam switched off.⁽⁴⁵⁾ In Figure 9.16 the depletion efficiency for overlapping beams is $\varepsilon = 0.5$:

$$\varepsilon = \frac{P_{\text{fl}} - P_{\text{fl+depl}}}{P_{\text{fl}}} \quad (9.9)$$

Figure 9.17 shows the normalized depletion efficiency as a function of the delay Δt between the two pulses. For a negative delay Δt , the infrared pulse precedes the near-UV pulse and no depletion takes place; i.e., $\varepsilon = 0$. With a delay near zero, depletion becomes efficient, reaching its maximum with a steep slope determined by the pulse length of the stimulating beam. With increasing delay Δt , the depletion efficiency drops continuously. The drop corresponds to an average lifetime of $\tau = 1.1 \pm 0.2$ ns. It can be interpreted by the fluorescence decay of the excited state. This is a further evidence for stimulated emission. For the infrared pulse arriving immediately after the excitation pulse, the efficiency of depletion is highest because shortly after excitation the excited state has not undergone any significant spontaneous decay. With increasing delay Δt , a considerable part of the excited molecules have already decayed before the 750-nm pulse reaches the focus. In consequence the depletion rate decreases with the lifetime of the excited

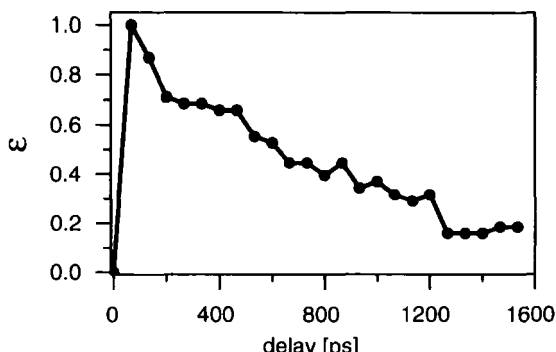


Figure 9.17. Normalized depletion efficiency ϵ versus the delay of the stimulating pulse with respect to the excitation pulse.

state. The steep slope is due to the 5-ps length of the infrared pulses, and the flat slope is due to spontaneous decay. Evidently, quantifying the lifetime of the excited state by measuring the depletion efficiency $\epsilon(\Delta t)$ is possible. Furthermore, we measured the change of fluorescence signal when chopping the infrared beam. Rise times of typically 50 μ s of the fluorescence signal identical with those of the chopped stimulating beam were observed. This experiment provides further evidence for the fact that the reduction of fluorescence intensity is due to stimulated emission. In these experiments the maximum average power available from the fiber was 20 mW. No single- or two-photon excitation by the infrared beam was observed, so one can conclude that the parameter α of pyridine 2 is vanishingly small. This is not surprising since pyridine 2 has a Stokes shift of about 250 nm. As the incomplete depletion in Figure 9.16 can be mostly attributed to the limited focusing performance of the high-aperture lenses used in the near-UV and infrared, the initial results of Figure 9.16 are encouraging. The measurements confirm the theoretical prediction that it should be possible to deplete the excited state of a population of fluorescence molecules through stimulated emission.

9.2.2. Ground-State-Depletion Fluorescence Microscopy

As pointed out, any nondestructive process inhibiting fluorescence is suitable for cutting the excitation PSF and increasing the resolution, but in order to obtain a more-than-two-fold resolution increase one has to employ saturation. An efficient depletion of the excited state requires a stimulation rate that is stronger than spontaneous decay but slower than vibrational relaxation. Picosecond pulses are needed for efficient depletion by stimulated emission. However, picosecond lasers are not as easily available as their low-power continuous wave counterparts. It is therefore interesting to investigate whether PSF engineering could be done with continuous-wave lasers. As pointed out, a

suitable mechanism could be depletion of the ground state^{*17)} through triplet-state saturation.

In the STED fluorescence concept the triplet state plays a rather minor role, since depletion by stimulated emission takes place within a fraction of the lifetime of the excited state. This is five to six orders of magnitude faster than intersystem crossing. When focusing continuous-wave light of 1 mW power through a high-aperture lens, one obtains focal intensities of the order of 1 MW/cm². We can safely neglect the higher vibronic levels S_0^{vib} , S_1^{vib} , and T_1^{vib} because populating picosecond states with such intensities is not possible. Stimulated emission can also be ignored, especially if one takes into account that the excitation wavelength is not suitable for significant stimulated emission. However, there is a high probability of the excited molecule crossing to the triplet state T_1 .^(32,39,46) We therefore concentrate our study on the relaxed states S_0 , S_1 , and T_1 . With an excitation photon flux of h_{exc} , the population probabilities $n_{0,1,2}$ of the fluorophore are:

$$\begin{aligned}\frac{dn_0}{dt} &= -h_{\text{exc}}\sigma n_0 + (k_{\text{fl}} + k_Q)n_1 + k_{\text{ph}}n_2 \\ \frac{dn_1}{dt} &= +h_{\text{exc}}\sigma n_0 - (k_{\text{fl}} + k_Q)n_1 - k_{\text{isc}}n_1 \\ \frac{dn_2}{dt} &= +k_{\text{isc}}n_1 - k_{\text{ph}}n_2\end{aligned}\quad (9.10)$$

again with $\sum_i n_i = 1$. Having lifetimes of $\tau_{\text{ph}} = 1 \mu\text{s}$ –1 ms, the triplet decay rate k_{ph} is the slowest rate involved in the process. When switching on the continuous-wave excitation light, we can assume that a stationary state will be reached after $t \approx 5\tau_{\text{ph}}$ and that the population probabilities n_i of the fluorophore do not undergo any further changes: $dn_i/dt = 0$. In contrast to the previous case, we find an analytical expression for the stationary values of the population probabilities:

$$\begin{aligned}n_0 &= \frac{k_{\text{ph}}(k_{\text{fl}} + k_Q + k_{\text{isc}})}{D} \\ n_1 &= \frac{h_{\text{exc}}\sigma k_{\text{ph}}}{D} \\ n_2 &= \frac{h_{\text{exc}}\sigma k_{\text{isc}}}{D}\end{aligned}\quad (9.11)$$

with $D = (h_{\text{exc}}\sigma + k_{\text{fl}} + k_Q)(k_{\text{ph}} + k_{\text{isc}}) + k_{\text{isc}}(k_{\text{ph}} - k_{\text{fl}} - k_Q)$.

Figure 9.18 displays the population probabilities n_i as a function of the excitation intensity for fluorescein which is one of the most frequently used dyes for biological fluorescence labeling. The typical lifetimes for the energy states of fluorescein⁽⁴⁶⁾ are $\tau_{\text{fl}} = 4.5 \text{ ns}$, $\tau_{\text{isc}} = 100 \text{ ns}$, and $\tau_{\text{ph}} = 1 \mu\text{s}$. Further, an excitation wavelength of 488 nm and a numerical aperture of 1.4 (oil) is assumed. Figure 9.18 reveals that for an intensity higher than 10 MW/cm^2 , almost 89% of the fluorophore molecules are in the long-lived triplet state T_1 , 11% are in the singlet state, and the ground state is depleted. An intuitive explanation is that for high intensities the molecules undergo fast circular processes from S_0 to S_1 and back to S_0 . After each circuit, a fraction of $k_{\text{isc}}/(k_{\text{isc}} + k_{\text{fl}} + k_Q)$ is caught in the long-lived triplet state, ultimately depleting the ground state. The population of the ground state lacks the molecules in the triplet state as long as the excitation beam is switched on and for its average lifetime τ_{ph} after it has been switched off.

How can the effect of ground-state depletion be employed for reducing the extent of the effective PSF in a far-field fluorescence light microscope? Again we first assume an uniform distribution of molecules. But this time all the molecules should be in the ground state. We assume two beams being symmetrically offset by $\pm \Delta v_x$ with respect to the geometric focus, say along the x -axis. Again, for an offset of $\Delta v_x = 1.22\pi$, the first minima of the beams coincide at the geometrical focus, whereas the main maximum of one beam partly overlaps with the first side maximum of the other. Figure 9.19 shows the intensity $h_{\text{dep1}}(v_x) = h_{\text{beam1}}(v_x - \Delta v_x) + h_{\text{beam2}}(v_x + \Delta v_x)$ of the resulting beam. Figure 9.19 shows also the effect of the different intensities of $h_{\text{dep1}}(v_x)$ on the probability

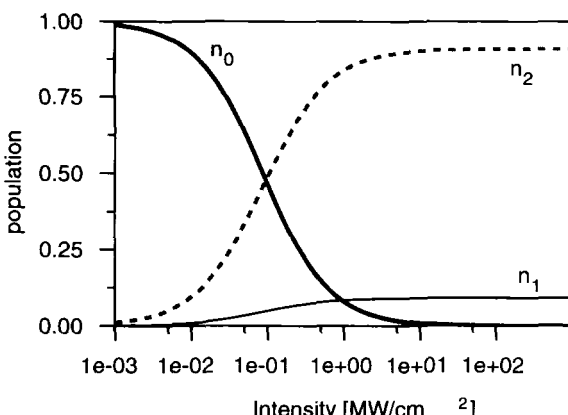


Figure 9.18. Population of the ground state (n_0), the first singlet state (n_1), and the triplet state (n_2) as a function of the excitation intensity for $\tau_{\text{fl}} + \tau_Q = 4.5 \text{ ns}$ and $\tau_{\text{isc}} = 100 \text{ ns}$, which is typical for fluorescein.

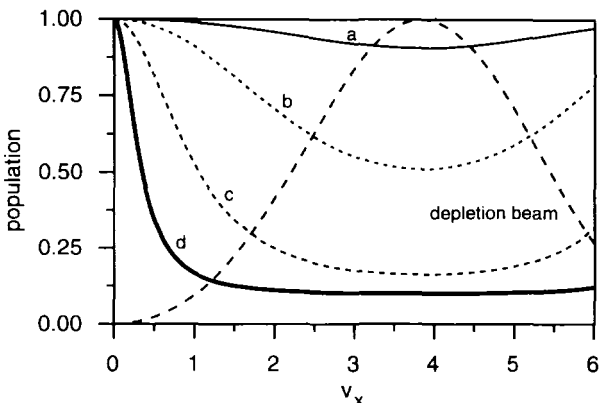


Figure 9.19. The effect of the depletion beam $h_{\text{depl}}(v)|_x$ (dashed) on the probability of the dye to be in a singlet state, $1 - n_2(v)$, for the maximum of $h_{\text{depl}}(v)|_x$ of (a) 0.01, (b) 0.1, (c) 1, and (d) 10 MW/cm^2 . In contrast to Figure 9.9, the beams are focused to $v = \pm 1.22\pi$.

$1 - n_2(v_x)$, which is the probability that the dye is not caught in the triplet state. For lower intensity values, $h_{\text{depl}}(v_x)$ leaves a hole resembling its own shape. For higher intensities, the saturation of the triplet state becomes evident, but at $v = 0$, $h_{\text{depl}}(v_x)$ has a minimum and the molecules near $v = 0$ remain in the ground state. Due to saturation the unaffected regions around $v = 0$ are bordered by steep edges of depletion. Apparently, ground-state depletion renders a similar situation to the effect of depletion by stimulated emission. We can exploit this effect for engineering the effective PSF in a similar way as by stimulated emission. We can decrease the extent of the effective PSF by preventing the molecules at the outer regions of the focus from emitting fluorescence.

Let us assume that the point of interest is at $v = 0$. The first step of the PSF-forming process is to expose the area surrounding to a beam exciting the molecules and shift them to the triplet state. After about $\tau_{\text{ph}} = 5 \mu\text{s}$ the depletion beam $h_{\text{depl}}(v_x)$ is switched off, and after $\tau_{\text{fl}} \approx 5 \text{ ns}$ nearly all the molecules from the first singlet state are relaxed. Yet for a time of about $\tau_{\text{ph}}/5$ the molecules in the triplet state have still not returned to the ground state. The population distribution of excitable molecules is given by $1 - n_2(v_x)$. When a beam centered at $v = 0$ is focused, the effective excitation point-spread function is

$$h_{\text{eff}}(v_x) = h_{\text{exc}}(v_x)(1 - n_2(v_x)) \quad (9.12)$$

and thus reduced in its lateral extent. Figure 9.20 shows the calculated effective PSF $h_{\text{eff}}(v_x)$ along the axis of the offset. Notice that the FWHM decreases with increasing maximum intensities of $h_{\text{depl}}(v_x)$. For maximum intensities $h_{\text{depl}}(v_x)$ of

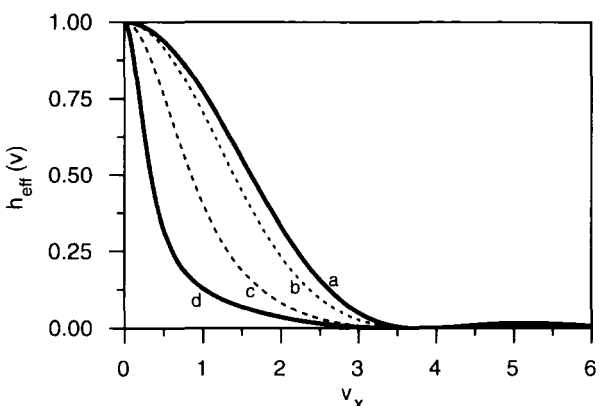


Figure 9.20. The calculated effective point-spread function along the axis of the offset for peak intensities of (b) 0.01, (c) 0.1, and (d) 10 MW/cm^2 of the depletion beam as calculated for fluorescein, compared with the (a) point-spread function of a classical scanning fluorescence microscope.

0.1, 1, and 10 MW/cm^2 one obtains lateral FWHM of 2.76, 1.68, and 0.66 in optical units. For $h_{\text{depl}}(v_x) = 10 \text{ MW/cm}^2$ the resolution is considerably enhanced, and the FWHM is five times smaller than that of a classical scanning fluorescence microscope. However, also notice that the width of the peak is not significantly reduced at the bottom because the ground state is not entirely depleted in our example.

The depletion efficiency depends primarily on $k_{\text{isc}}/(k_{\text{isc}} + k_n + k_Q)$. For a fluorophore with a faster intersystem crossing time of $k_{\text{isc}} = (10 \text{ ns})^{-1}$, the ground state can be depleted to 2%. This leads to an efficient reduction in the extent of the effective excitation PSF, as shown in Figure 9.21. A comparison of the PSF obtained for a focal intensity of 10 MW/cm^2 with that of a classical scanning fluorescence microscope shows an increase of resolution by a factor of 13. Assuming an excitation wavelength of 400 nm and a numerical aperture of 1.4, one obtains a lateral FWHM of about 10 nm.

When illuminating a 1.4-NA oil immersion lens with a power of 10 mW, an average focal intensity of 10 MW/cm^2 is obtained. The intensities required for GSD fluorescence microscopy are rather low. An intrinsic limitation of GSD fluorescence microscopy is that the maximum pixel rate will be determined by the relaxation of the dye from the triplet state. One has to wait until all the molecules have returned to the ground state before one can record the neighboring point. This delay is approximately $5\tau_{\text{ph}} \approx 5 \mu\text{s}$, thus confining the maximum recording speed to about 200 kHz. However, this delay is of the same order as that of a standard beam-scanning confocal microscope. A further aspect is that the molecules in the long-lived triplet state might undergo chemical reactions, thus causing a bleaching of the fluorescence molecules.

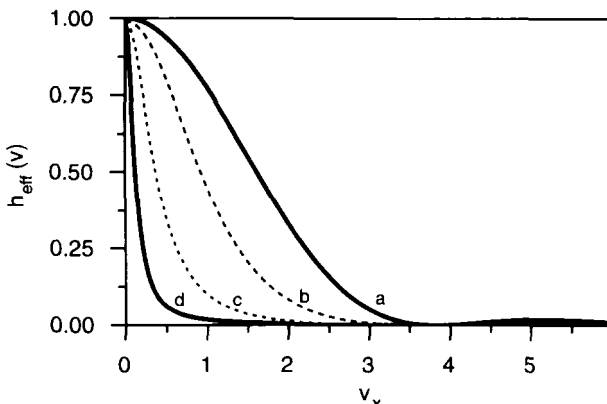


Figure 9.21. The calculated effective point-spread function along the axis of the offset for the same parameters as in Figure 9.20 but with a (fast) intersystem crossing rate of $(10 \text{ ns})^{-1}$.

In the worst case, the molecules in the triplet state are photochemically disrupted, especially in the presence of high concentrations of oxygen. As these phenomena depend strongly on the environment, a carefully chosen chemical environment will be required for saturating the triplet state. Furthermore, excitation wavelengths generating absorption from the first to higher triplet states should be avoided. Selecting a dye that shows the most favorable conditions for ground state depletion is a useful approach in the practical development of a GSD fluorescence microscope. As in the STED fluorescence concept, an additional pair of depletion beams can be used to obtain an equivalent resolution increase in the y axis or a doughnut-shaped depletion intensity around the geometric focal point. Employing continuous-wave low-power lasers, the concept of GSD fluorescence microscopy is an interesting alternative to the STED concept for increasing resolution in far-field light microscopy to the tens of nanometer range.

9.3. PSF Engineering through Aperture Increase: 4Pi Confocal Microscopy

As shown earlier, the role of the objective lens is to convert an incoming wave front into a spherical wave front propagating toward the focal point, and *vice versa*. The resolution in scanning far-field fluorescence microscopy is well described by a three-dimensional effective PSF describing the probability of each focal coordinate to contribute to the signal. Increasing resolution therefore aims at decreasing the extent of the PSF. The STED and GSD fluorescence

concepts are conceived to reduce the lateral extent of the PSF and increase the lateral resolution; but in three-dimensional microscopy the axial resolution is as important as the lateral resolution. Therefore, an increase in axial resolution is equally desirable.

The PSFs in Figure 9.2 are about 3.5 times longer axially. The axial elongation is even stronger with lower-numerical-aperture lenses^(21, 22) so that the axial resolution of a far-field light microscope is never as good as that of its lateral counterpart. This applies both to the conventional as well as to the confocal microscope⁽²⁸⁾ The reason is that the lens only produces a segment of a spherical wave rather than a complete spherical wave front. For such a complete wavefront of a full solid angle of 4π , the illumination PSF would be spherical and its axial extent the same as in lateral direction^(18, 22) This would dramatically improve axial resolution. A similar consideration applies also to detection. If we had a pointlike light source emitting a spherical wave front and collected the complete emitted spherical wave front we would obtain better information about the localization of the point source.^(18, 19, 23) The benefits of using a spherical wave front generated by a hologram and propagating toward a single point, had been considered in the late seventies.⁽⁴⁷⁾ It has not been pursued or worked out theoretically because producing aberration-free wave fronts with spherical holograms is hardly possible. However, a fundamental increase of the overall aperture can be achieved by using two opposing objectives of high numerical aperture sharing a common focus^(18, 19, 23) (see Figure 9.22).

Use of two objective lenses does not by itself increase the aperture. The best that can be achieved is that the signal is enhanced. For increasing the *illumination* aperture, the illumination wave fronts have to be coherent and interfere constructively in the common focal point. Similarly, increasing the *detection* aperture requires two separately collected wavefronts adding up coherently in a point-like detector.^(18, 19, 23) Pointlike detection also confocalizes the microscope. Scanning microscopy using two high-aperture lenses for coherent illumination and/or coherent detection of the same object point is called a 4Pi confocal microscopy.^(18, 19) With two high-aperture lenses, a solid angle of about 3π is reached, however, the name 4Pi was chosen as a simple reminder of the idea. In similarity to STED and GSD fluorescence microscopy, the philosophy of 4Pi confocal microscopy is to alter the shape of the point-spread function, ultimately reducing the spatial extent of an effective PSF. 4Pi confocal microscopy is another example of increasing the resolution by PSF engineering.

9.3.1. 4Pi Illumination and Detection PSF

The focal intensity distribution of a 4Pi illumination PSF is calculated by the coherent summation of the two focal electric fields of the two opposing lenses.

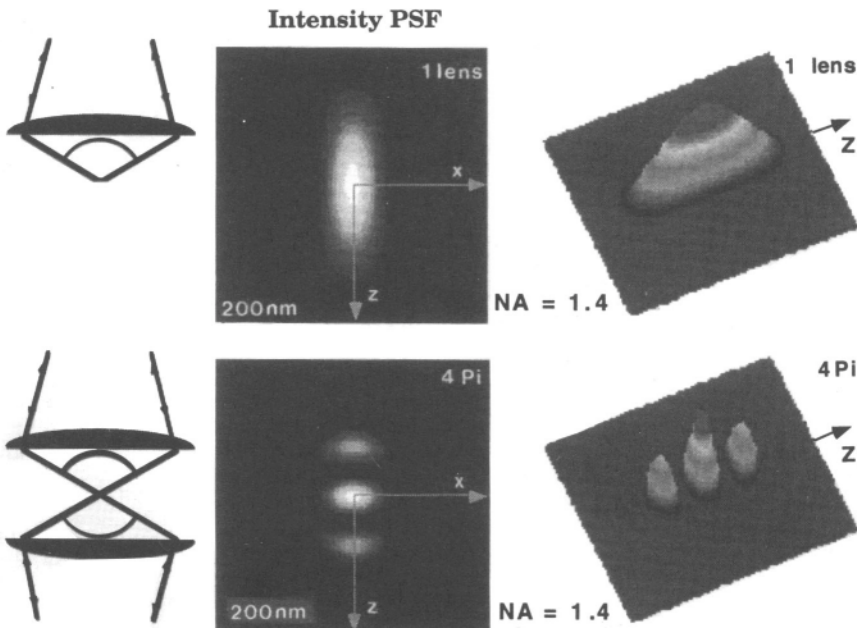


Figure 9.22. The calculated PSF of a single lens (above) compared with a calculated PSF of a 4Pi arrangement (below). 4Pi microscopy employs two opposing objective lenses of high numerical aperture (here NA = 1.4 oil and $\lambda = 500$ nm) with a common focus. The coherent addition of the electric fields yields a steep main maximum and two lobes in axial direction. The center panels outline the focal intensities in a plane containing the optical axis, whereas the right-hand panels show the corresponding surface plots. As with the single-lens PSFs of Figure 9.2, the 4Pi PSF gives the relative probability that a photon from a pinhole arrives at a certain point in the focal region when propagating simultaneously through both lenses. Similarly, the 4Pi PSF describes the relative probability that a photon emanating from a given point succeeds in propagating to a remote pinhole coherently collecting the light in a 4Pi manner. The 4Pi PSF is shown for constructive interference of the illuminating-detected waves at the focal point.

We could use a scalar theory as in Eq. (9.22) for calculating the 4Pi PSF. However as 4Pi confocal microscopy uses high-numerical aperture lenses and relies on interferences, it is more appropriate to employ an electromagnetic theory taking the polarization properties of the focused electric field into account.^(19, 20) Following Richards and Wolf⁽⁴⁸⁾ the electric field in the focal region of a single lens is

$$\mathbf{E}(u, v, \varphi) - (e_x, e_y, e_z) = -i(I_0 + I_2 \cos(2\varphi), I_2 \sin(2\varphi), -2il_1 \cos \varphi) \quad (9.13)$$

with $I_{0,1,2} = I_{0,1,2}(u, v)$ being integrals over the lens aperture:

$$I_0 = \int_0^\alpha \sqrt{\cos \theta} \sin \theta (1 + \cos \theta) J_0\left(\frac{v \sin \theta}{\sin \alpha}\right) \exp\left(iu \frac{\cos \theta}{\sin^2 \alpha}\right) d\theta$$

$$I_1 = \int_0^\alpha \sqrt{\cos \theta} \sin^2 \theta J_1\left(\frac{v \sin \theta}{\sin \alpha}\right) \exp\left(iu \frac{\cos \theta}{\sin^2 \alpha}\right) d\theta$$

$$I_2 = \int_0^\alpha \sqrt{\cos \theta} \sin \theta (1 - \cos \theta) J_2\left(\frac{v \sin \theta}{\sin \alpha}\right) \exp\left(iu \frac{\cos \theta}{\sin^2 \alpha}\right) d\theta$$

Again, u and v are optical units, but here u is somewhat differently defined, namely as $u = (2\pi/\lambda)n_z \sin^2 \alpha$. Angle φ is the angle between the direction of vibration of the incident electric field and the direction of observation. $J_{0,1,2}$ are Bessel functions of the first kind. The focal intensity for a single lens is given by the modulus square of the electric field:

$$h(u, v, \varphi) = |\mathbf{E}(u, v, \varphi)|^2 = |I_0|^2 + |I_2|^2 + 4|I_1|^2 \cos^2 \varphi + 2 \operatorname{Re}\{I_0 I_2^*\} \cos 2\varphi \quad (9.14)$$

with Re denoting the real part of the expression in braces. For randomly or circularly polarized light, dependence on φ vanishes, and the normalized PSF is

$$h(u, v) = |I_0|^2 + 2|I_1|^2 + |I_2|^2 \quad (9.15)$$

The 4Pi PSF is given by the coherent summation of the electric field of the wave fronts of the objective lenses.⁽¹⁸⁻²⁰⁾ Constructive interference in the common focal point yields a 4Pi PSF:

$$h^{4\text{Pi}}(u, v, \varphi) = |\mathbf{E}_1(u, v, \varphi) + \mathbf{E}_2(-u, v, \varphi)|^2 \quad (9.16)$$

the evaluation of which results in⁽¹⁹⁾

$$\begin{aligned} h^{4\text{Pi}}(u, v, \varphi) = & \operatorname{const} (\operatorname{Re}\{I_0\}^2 + \operatorname{Re}\{I_2\}^2 + 2 \operatorname{Re}\{I_0\} \operatorname{Re}\{I_2\} \cos 2\varphi \\ & + 4 \operatorname{Re}\{I_1\}^2 \cos^2 \varphi) \end{aligned} \quad (9.17)$$

For random polarization, we obtain

$$h^{4\text{Pi}}(u, v) = \operatorname{const} (\operatorname{Re}\{I_0\}^2 + 2 \operatorname{Re}\{I_1\}^2 + \operatorname{Re}\{I_2\}^2) \quad (9.18)$$

Figure 9.22 depicts the 4Pi PSF for a numerical aperture of 1.4, oil immersion ($n = 1.518$) for constructively interfering wavefronts along with that of a single lens. Notice that coherent illumination through both objective lenses renders a PSF that has a main maximum four times narrower in axial direction than that produced by a single-lens, and two pronounced axial lobes. The narrower main maximum opens up the prospect on an increased axial resolution; but the lobes are undesirable. These lobes stem from the fact that the total wave front produced by the two objective lenses does not reach a full solid angle. With two objective lenses with numerical apertures of 1.4, the semiaperature angle is only 68° , so there is still a missing part of the full solid angle in the lateral direction. It is evident that using lower-numerical-aperture lenses would increase the lobes, in relative height and number. Increasing the aperture angle, however, reduces the lobes and renders a more spherical PSF. For a complete wave front of 4π the lobes vanish.

Due to symmetry, a 4Pi PSF can also be realized by a coherent detection of the light with both lenses. When calculating the 4Pi or regular detection PSF in a confocal scanning arrangement, we can assume as a general approximation that the fluorescence is depolarized. Therefore, the detection PSF of a confocal system, h_{det} is described by Eqs. (9.15) and (9.18). The only difference is that for fluorescence imaging we have to take into account the Stokes shift of the fluorescence light, which can be considered by scaling the optical coordinates: $h_{\text{det}}(u(\lambda_{\text{exc}}/\lambda_{\text{fl}}), v(\lambda_{\text{exc}}/\lambda_{\text{fl}}))$. For a short Stokes shift, the same PSF can be used for describing illumination with circularly polarized light and detection.

9.3.2. The 4Pi Confocal Microscope and Its Imaging Modes

Figure 9.23 sketches the basic arrangement of a 4Pi confocal microscope.^(18,19,49-55) The sample is mounted between two cover slips and placed into the common focus of the objective lenses. The lens on the left-hand side, L_2 , is fixed, whereas the other lens, L_1 , can be adjusted with a precision of 10–20 nm with respect to the first one by means of a piezoelectric stage. The light from a common point source is split into two coherent parts, each part illuminating one objective lens. A piezoelectrically controlled mirror allows for alteration of the relative phase of the two illuminating wave fronts. The light collected by the two lenses is combined by another beam splitter and directed toward the common point detector. The point detector, the illumination pinhole and the focus of the two lenses are in optically conjugated planes.

In principle, the 4Pi confocal microscope offers four modes of imaging.^(18,19,23,49-55) Blocking one of the lenses reduces the 4Pi confocal microscope to the status of a regular confocal microscope. Another option is to use both lenses for coherent illumination but with regular detection.

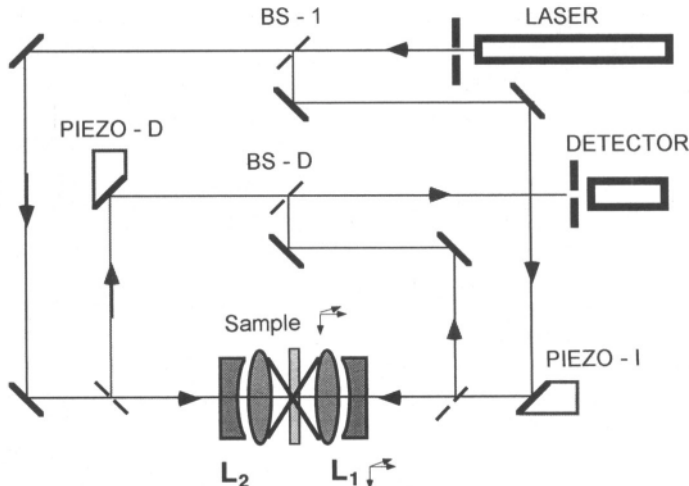


Figure 9.23. Sketch of a 4Pi confocal microscope. Laser light coming from a pinhole is split in two parts by a beam splitter (BS-I), thus illuminating simultaneously two opposing high-aperture lenses. The light originating from the sample can be collected by both lenses, combined at a beam splitter (BS-D), and directed toward a common detector pinhole. The relative phases of the illumination and detection wave fronts are adjusted by means of piezoelectrically driven mirrors, denoted PIEZO-I and PIEZO-D, respectively. While lens L_1 is fixed, lens L_2 is adjusted with a precision of 10–20 nm with respect to L_1 . The sample is scanned with a piezoelectric stage of high precision to render a three-dimensional image. The 4Pi confocal setup allows four types of imaging: regular confocal, 4Pi illumination in conjunction with regular detection (4Pi type A), 4Pi detection with regular illumination (4Pi type B), and 4Pi illumination with 4Pi detection (4Pi type C). The latter features the highest aperture in far-field light microscopy.

This imaging mode is called 4Pi of type A. The corresponding PSF is given by the product of the 4Pi illumination PSF and a single-lens PSF describing detection, which are both depicted in Figure 9.22.

$$h_{\text{conf}}^{\text{4Pi,A}} = h_{\text{ill}}^{\text{4Pi}} h_{\text{det}} \quad (9.19)$$

Similarly, one has the option of illuminating through a single lens and coherently detecting the light through both objective lenses. This imaging mode is termed 4Pi confocal microscopy of type B, and its PSF is

$$h_{\text{conf}}^{\text{4Pi,B}} = h_{\text{ill}} h_{\text{det}}^{\text{4Pi}} \quad (9.20)$$

As illumination and detection are generally optically similar, theory predicts similar PSFs for the 4Pi type A and type B imaging mode. Eqs. (9.19) and (9.20)

suggest that the 4Pi imaging mode strongly differs from its confocal counterpart. The interferences of the illumination or detection wave fronts lead to marked changes in the PSF. The strongest change to be expected when the lenses are used coherently in illumination *and* detection, a technique referred to as 4Pi confocal imaging of type C. The type C 4Pi confocal PSF is mathematically described by

$$h_{\text{conf}}^{\text{4Pi,C}} = h_{\text{ill}}^{\text{4Pi}} h_{\text{det}}^{\text{4Pi}} \quad (9.21)$$

4Pi confocal microscopy of type C offers the highest aperture available in far-field light microscopy at present.^(50–52) Therefore, one can expect a strong increase in axial resolution. This can be investigated by measuring the PSF of a 4Pi confocal microscope of types A, B, and C and comparing them with the PSF of a regular confocal microscope.

A good method of measuring the focus of a scanning confocal microscope is to record the scattered light of a tiny gold bead when scanned through the focus.^(50–52) We obtained single beads by drying a suspension of colloidal gold of 30-nm particle size on a cover slip. The beads were immobilized on the surface, immersed in oil, and covered with a second cover slip. The objective lenses were the 100x magnifying, infinity-corrected, oil-immersion Planapochochromats by Leica (Wetzlar; Germany). The wavelength used was 632.8 nm, namely that of a red He–Ne laser. We employed the highest possible numerical aperture of 1.4 (oil). The sample was scanned using a piezoelectric three-dimensional stage (Melles Griot, Cambridge, England) moving the sample in a closed-loop control, with a precision of 10–15 nm. The common focus of the two lenses was maintained by a similar piezoelectric stage. The studies were performed with linearly polarized light. The scattered light was separated from the transmitted light by placing a crossed polarizer in front of the detector.

The results of a PSF measurement are depicted as surface plots in Figure 9.24 for the confocal imaging and the three 4Pi imaging types.⁽⁵²⁾ The confocal PSF is elongated as predicted by theory for a single lens. The FWHM are 490 ± 15 nm and 200 ± 15 nm in the axial and lateral direction, respectively. The panel denoted with 4Pi type A shows the 4Pi confocal PSF which is obtained when both objectives are used with constructively interfering illumination. When recording the type A 4Pi confocal PSF one of the detection paths was blocked, so that detection was performed through a single lens. The interference strongly changes the PSF. The main maximum is about 3.5 times narrower than in the regular confocal case, reaching a FWHM of 130 ± 15 nm. The pronounced axial lobes originating from interference can also be seen. The height of the lobes is between 55% and 60%. The 4Pi confocal PSF of type B was obtained by illuminating through a single lens but collecting the scattered light of the bead simultaneously from both sides, so the light scattered both forward and backward

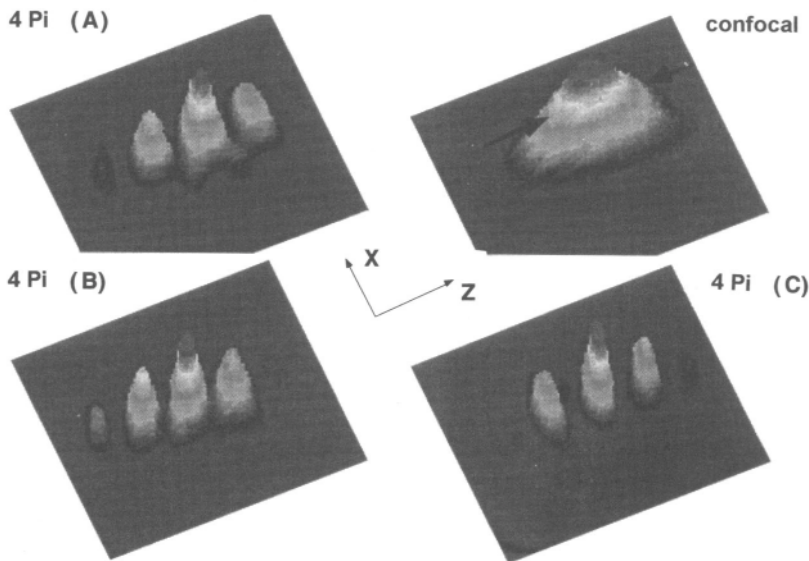


Figure 9.24. Surface plots of the measured PSFs in a 4Pi confocal microscope. The PSFs were probed with scattering gold beads with subresolution size (30 nm). The FWHM of the main maximum of the type A and B PSF is 135 ± 10 nm and 120 ± 10 nm, respectively. This is about three to four times narrower than that of the confocal PSF. The 4Pi type C recording shows the sharpest main maximum with an axial width of 85 ± 10 nm, thus promising a strong increase in axial resolution.

was added coherently. The interference in the point detector was constructive. The theoretical prediction that the 4Pi imaging mode of type B is similar to that of type A is nicely confirmed within the given accuracy by the experiment. The axial FWHM of the main maximum was determined to be 120 ± 15 nm. The lobes are also between 55% and 60%.

A simple explanation of the nature of the 4Pi PSF is given through a photon optics interpretation⁽²³⁻²⁵⁾ when bearing in mind that in the 4Pi confocal microscope, the photons propagate simultaneously through both objectives lenses. In a 4Pi *illumination* PSF, the photons have a reduced chance of arrival at the minima due to destructive interference. The minima of the 4Pi confocal PSF of type B stem from the fact that the photons originating from these points have a low probability of arriving in the point detector. In 4Pi confocal microscopy of type B, there is no interference pattern in the focus itself, as in 4Pi type A, because the illumination is carried out through a single lens. The interference structure of the 4Pi type B PSF is formed by the probabilities to be detected in the pointlike detector. Finally, the strongest change in the PSF occurs in the 4Pi case of type C

where both illumination and detection wave fronts interfere constructively in the sample and in the detector, respectively. As a result of the coherent use of both illumination *and* detection, the minima are more pronounced.^(19, 52) (Figure 9.24). The axial FWHM of the 4Pi confocal PSF of type C is 85 ± 15 nm. This is about six to seven times narrower than in a regular confocal microscope.^(50–52)

The advantage of using gold beads for measuring the focus is the high signal-to-noise ratio. However, there is a difference between imaging fluorescence and recording scattering or reflection. In fluorescence imaging the phase of the light is lost during absorption of the illumination. While fluorescence has a different wavelength, in scattering or reflection the phase of the light is preserved. For instance, when imaging two or more adjacent gold beads, or other multiple scattering centers, the light from adjacent scatterers is able to add up coherently in the pinhole. Interference occurs because of the high spatial coherence in a confocal arrangement.⁽²⁸⁾ With *multiple* scatterers, defining a PSF in the focus is not possible, but one can use *single* pointlike scatterers (e.g., single gold beads) for measuring the PSF. For single point objects the (absolute) phase of the light does not play any role because interferences with other sources cannot occur. Apart from slight differences in wavelength, a single subresolution scattering particle gives the same result as a single subresolution fluorescent particle. As they provide a high signal-to-noise ratio they are very well suited for PSF studies.

In principle, all three 4Pi confocal contrasts shown in Figure 9.24 (type A, B, and C) are obtainable with fluorescence samples. So far, 4Pi confocal microscopy of types A and B have been most commonly used. The latter requires that the detection paths are matched within the coherence length of the fluorescence, which is about 20 μm . While such distances are controllable with piezoelectric positioning equipment, experiments with the first-generation 4Pi confocal setup⁽⁵¹⁾ showed that it is more challenging to obtain a high interference contrast in fluorescence. Although the interference of the fluorescence light was well pronounced in the common point detector, the minima of the 4Pi confocal *fluorescence* PSF of type B did not reach the zero value.⁽⁵¹⁾ This is most probably because of the higher technical effort to align the lenses using a weak fluorescent signal. However, there is no reason why proper coherent detection should not be realizable with fluorescence, and it will be interesting to investigate 4Pi confocal PSF of type B and C with second-generation 4Pi confocal microscopes.^(52, 86) At present, 4Pi confocal microscopy of type A is the method of choice when increasing the axial resolution in a practical system.

The derivation of the optical transfer functions (OTF) of the 4Pi confocal microscope also reveals the superior axial resolution of the 4Pi confocal microscope. Theoretical predictions of the OTF,^(53–55) such as the increase in axial bandwidth were experimentally confirmed⁽⁵²⁾ by deriving the OTFs from the experimental PSF measurements of Figure 9.24.

The use of interference in light microscopy goes back to the end of the last century. While interferences were mainly used for measuring axial height differences and changes in refractive index of the sample, in the standing-wave microscope (SWM) they were probably first used to reveal greater axial detail in fluorescence imaging.^(56–58) The SWM uses a plane-wave, wide-field illumination as in a conventional microscope. The field of standing plane waves is produced along the optical axis either by redirecting the excitation light back to the lens using a mirror or by illuminating through two objective lenses. The regions of constructive and destructive interference appear as stratified layers in the object. The excitation of the fluorophore is restricted to the layers of constructive interference, which can be as thin as 80 nm (FWHM). By varying the relative phase of the waves, different parts of the objects become visible. The unrivaled strength of the SWM is its simplicity and its ability to obtain an image of the whole object. The SWM does not require scanning, but the axial lobes are higher than in the 4Pi confocal microscope, so the fluorescence comes from several layers of the object. As the fluorescence of different layers cannot be kept apart, a rigorous deconvolution of the image is required. This is the case also in the 4Pi confocal microscope, but in the latter confocality renders a quadratic PSF that is axially narrower than in the SWM. The 4Pi has just two axial lobes that are reduced in height, so the focus is better defined. The intrinsic axial discrimination of the 4Pi confocal microscope also eases the deconvolution of 4Pi images. Both the SWM and the 4Pi confocal microscope share the use of interferences, but the philosophy in the 4Pi is different: 4Pi confocal microscopy aims at increasing the aperture and engineering the extent of a well-defined PSF in order to form a single sharp focal peak^(18–20) that is three to seven times narrower than that of a single lens.

9.3.3. Two-Photon Excitation 4Pi Microscopy

The confocal and 4Pi confocal microscope feature a point spread function obeying a quadratic dependence on intensity. Such a behavior can also be achieved by exciting the dye in the two-photon mode.^(59–69) In two-photon excitation (TPE), the excitation energy is provided by the simultaneous absorption of two photons of half the energy, i.e., with twice the wavelength. The PSF of a TPE microscope is

$$h^{\text{TPE}}(u, v) = h_{\text{ill}}^2(u, v) \quad (9.22)$$

The quadratic dependence of TPE stems from the fact that two independent photons have to arrive at the same place in the focus. As the probability of each of them is $h_{\text{ill}}(u, v)$, the total PSF is the product of two identical illumination

PSFs. Two-photon excitation microscopy (TPEM) is a powerful fluorescence imaging approach.^(59,60) Because of the quadratic dependence of excitation on the intensity the TPE-PSF also defines a focal probe volume, therefore allowing for three-dimensional imaging without a pinhole. The dye is excited only in the inner focal volume, thus leading to a reduced amount of total bleaching of the sample.^(60,63-67)

TPEM is particularly interesting for 4Pi (confocal) microscopy because of the intensity-squared dependence of the TPE 4Pi PSF: $h_{\text{ill}}^{\text{4Pi,TPE}}(u, v) = [h_{\text{ill}}^{\text{4Pi}}(u, v)]^2$. The intensity-squared behavior makes the 4Pi illumination PSF similar to that of an ideal 4Pi confocal PSF of type c.^(20,61,62) Figure 9.25 shows the normalized axial excitation intensity $h_{\text{ill}}^{\text{4Pi}}(u, 0)$ in (a), along with the TPE PSF, $h_{\text{ill}}^{\text{4Pi,TPE}}(u, 0) = [h_{\text{ill}}^{\text{4Pi}}(u, 0)]^2$ in (b), calculated for a numerical aperture of 1.35 (oil) and a typical excitation wavelength of 750 nm. Figure 9.25 also shows the axial profile of the 4Pi *confocal* PSF with considerably reduced axial lobes, an effect to be discussed later.

A major goal in the development of the 4Pi confocal microscope is to remove the lobes and to obtain a sharper focus of a single peak. But it is important to note also that a PSF with lobes is more sensitive to axial changes in the object. This is demonstrated in an experiment recording *xz* images of clustered fluorescence beads. Figure 9.26a shows a standard, single lens TPEM *xz* image of the fluorescence bead cluster. The beads had a specified diameter of 100 nm and were mounted in Aquatex (Merck, Darmstadt, Germany) between

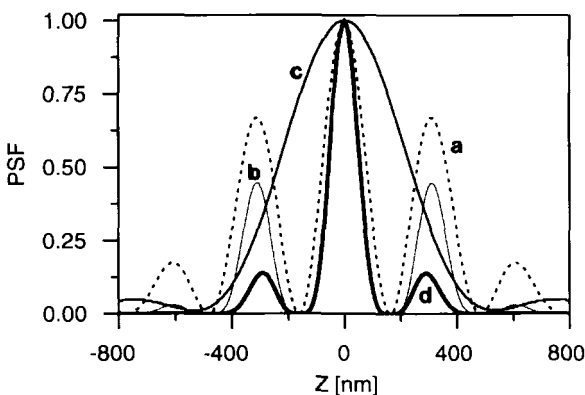


Figure 9.25. Axial resolution in an ideal two-photon 4Pi (confocal) microscope of type A with constructive interference calculated for a numerical aperture of 1.35 (oil), an excitation wavelength of 750 nm, and fluorescence at 450 nm. The curves show (a) the 4Pi excitation intensity, (b) squared excitation intensity corresponding to the 4Pi PSF, (c) regular detection PSF at 450 nm, (d) TPE confocal PSF. Note that the multiplication with a narrow (c) detection PSF suppresses the outer region of the 4Pi PSF thus reducing the lobes (d).

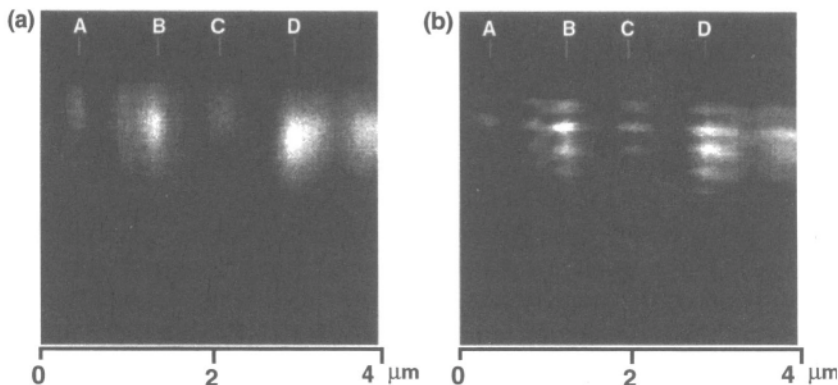


Figure 9.26. Two-photon excitation axial image (xz) of clustered fluorescent beads of 100-nm diameter as found with a single lens (a) and 4Pi illumination (b).

two cover slips. After a drying period, Aquatex has an index of refraction of about 1.5 which is close to the immersion system. The excitation maximum of the fluorophore was 360 nm and the maximum fluorescence emission around 430 nm (Molecular Probes, Eugene, Oregon). Two-photon excitation was performed with a mode-locked titanium–sapphire laser operating at a wavelength of 750 nm. No confocal pinhole was used.

Figure 9.26a shows that the images of the beads are elongated in the axial direction as expected from a single lens recording. In addition, different intensities in different areas of the image are found, e.g., those marked with A, B, and C. These differences could be due to a defocus in the y direction but may also be due to clustering of the beads. A detailed analysis of the single lens image shows that in Figure 9.26a, the axial extent of the intensity patches in A, B, and C are similar, so that the single-lens recording cannot give any further information about potential clustering in these regions.

Figure 9.26b shows the recording of the same site in the 4Pi mode with constructively interfering illumination. Figure 9.27 (left) compares the 4Pi axial profile (bold) with that of the single-lens recording (dashed), as found in C. The 4Pi is clearly different as a result of the interference of the illumination beams. It strongly resembles the typical axial response as found for a pointlike object in a TPE 4Pi microscope (compare Figure 9.25). This allows us to conclude that region C features a single fluorescent bead. But the 4Pi is able to reveal more: The dashed line on the right-hand side of Figure 9.27 is a 4Pi recording in region B. It looks entirely different from the axial profile in region C, so it cannot consist just of a single bead; but must represent a bead cluster. The most probable explanation is that B represents two beads of comparable intensity that are axially offset by a certain distance Az . This can be verified by adding the

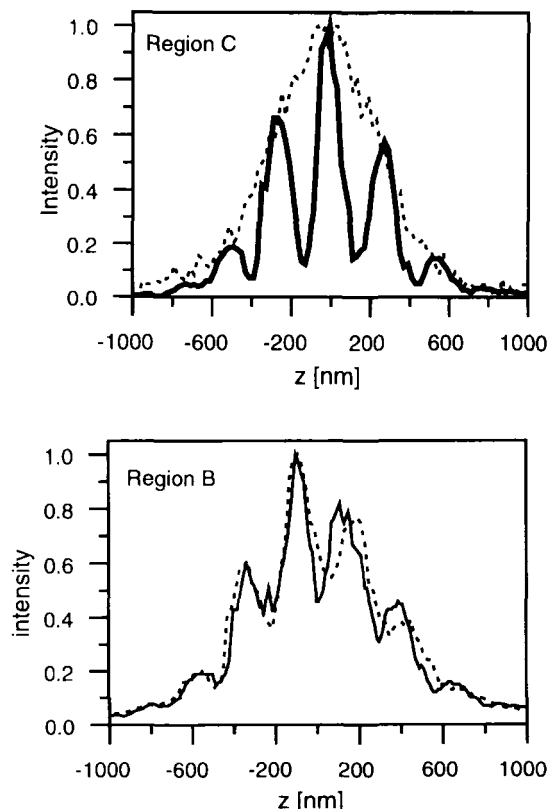


Figure 9.27. (Top) Axial profile of the signal of region C as found for the single lens (dashed) and the 4Pi recording (bold). The profiles correspond to the axial profiles of a PSF of a single-lens TPE (dashed), and a TPE 4Pi PSF (bold). (Bottom) 4Pi microscopy allows for better axial resolution of a cluster of fluorescent beads. The dashed line shows the measured axial profile in region B, whereas the continuous line is the sum of two (bold) TPE 4Pi profiles offset by 170 nm. The comparison of both reveals that region B features two beads axially offset by 170 ± 15 nm.

signal of two single beads with varying axial offset Δz and comparing the sum with the measured profile in the 4Pi image at B. The single-bead signal is readily retrieved from the 4Pi image as it is given by the bold axial profile of Figure 9.27 (left). By calculating and comparing the profiles, it is possible to show that for an offset of $\Delta z = 170 \pm 15$ nm, the summed signal (Figure 9.27 right, continuous line) agrees very well with the (dashed) original 4Pi axial profile of B. Thus, we can conclude that region B features two fluorescence beads that are axially offset by $\Delta z = 170 \pm 15$ nm. While the single-lens recording was not able to give any further axial information for bead at such distances, the 4Pi microscope is able to resolve them. The reason is the high axial sensitivity of the 4Pi PSF. A resolution of this order is remarkable, especially if we take into account that the wavelength used was 750 nm, which is in the near-infrared.

The analysis of Figure 9.26 relies on the comparison of normalized intensity profiles from an xz plane. Such an analysis can be carried out with

confidence for microscopes with a PSF of quadratic, or higher, intensity dependence, but not in a conventional microscope. The reason is that these microscopes have the ability to discriminate by intensity, in the axial *and* lateral directions. It is important to note that the confocal or TPE PSF faints with increasing lateral defocus, but the axial FWHM hardly broadens. The axial profile $h^{\text{TPE}}(u, v)$ with $0 < v < 0.6\pi$ is reduced in intensity compared to the profile along the optical axis $h^{\text{TPE}}(u, 0)$, but both feature nearly the same FWHM. Thus, the TPE axial profile in the above example contains the information of “one bead” or “two beads” even if the beads are slightly out of the xz plane of imaging. Thus we are able to reliably obtain this information by analyzing the axial profiles. Still, three-dimensional data stacks further increase the amount and precision of retrievable information in confocal and TPE microscopy. When recording 3D data stacks more complicated structures can be resolved. Indeed, stunning images of very dense bead clusters are given in Ref. 70.

A potentially interesting approach to analyze 4Pi images is to use the 4Pi PSF, such as the one in region C, and deconvolve the image with the inverse of the 4Pi PSF. The disadvantage of many deconvolution algorithms is the repeatedly applied subtraction operations leading to noisy results. Therefore, restoration approaches have attracted attention. They rely on the comparison between the experimentally gained image, with an estimated image gained by convolving an estimated object with an experimentally achieved PSF, much the same as performed with the image of Figure 9.26b. The increase in computational speed with modern computers will significantly reduce the time required for these methods.

9.3.4. Confocal Two-Photon Excitation 4Pi Microscopy

Despite the mathematical option of deconvolving 4Pi images it is highly desirable to find physical approaches to reduce the axial lobes. In addition, the comparison of the theoretical (Figure 9.25b) and the experimental 4Pi response of Figure 9.27 (top), although remarkable at first sight, shows that in the experiment the lobes are slightly higher than in theory. This can be attributed to the fact that the calculations of Figure 9.25 are for an ideal system. They did not take into account a possible mismatch in refractive index between the immersion medium and the sample,^(72–74) as it often encountered in practice. Refractive index changes further stress the need to eliminate the axial lobes.

The lobes can be reduced by applying a confocal detection pinhole. As pointed out, the use of a confocal pinhole means that the excitation PSF is multiplied by a detection PSF (Eq. 9.3) calculated at the fluorescence wavelength.

A confocal pinhole results in a reduction of the axial extent of the TPE PSF.^(59, 60) In the TPE 4Pi confocal case we obtain an effective PSF of

$$h_{\text{conf}}^{\text{TPE}}(u, v) = [h_{\text{ill}}^{\text{4Pi}}(u, v)]^2 h_{\text{det}} \left(u \frac{\lambda_{\text{exc}}}{\lambda_{\text{fl}}}, v \frac{\lambda_{\text{exc}}}{\lambda_{\text{fl}}} \right) \quad (9.23)$$

As the excitation wavelength is almost twice as large as the detection wavelength, $\lambda_{\text{exc}}/\lambda_{\text{fl}} \approx 2$, in TPE, the detection PSF is almost twice as narrow as the illumination PSF. Thus, the axial lobes are multiplied with rather low values of the detection PSF.^(20, 67) This is illustrated in Figure 9.28 and also in Figure 9.25. Curve c in Figure 9.25 represents the axial profile of the detection PSF. Curve d shows the axial 4Pi *confocal* PSF according to Eq. (9.23), revealing that the axial lobes are reduced to about 12%. Although a reduction to 12% cannot be achieved with a real specimen, the confocal pinhole promises a strong reduction in the height of the lobes.

Figure 9.29 shows an axial response to a thin layer of fluorophore⁽⁶¹⁾ as obtained with a (a) single-lens TPE confocal microscope and (b) the correspondent 4Pi. The height of the lobes is about 30%, and the FWHM about 130 ± 10 nm, typical for a wavelength of 750 nm. A comparison between Figures 9.29a and b clearly reveals the potential for an axial resolution increase by TPE 4Pi *confocal* microscopy. Nevertheless, the presence of the lobes can be a source of ambiguities in the image, unless the image is deconvolved or carefully analyzed. An interesting method of removing the lobes is described in Ref. 61. This method is based on the assumption that the axial profile of the 4Pi confocal

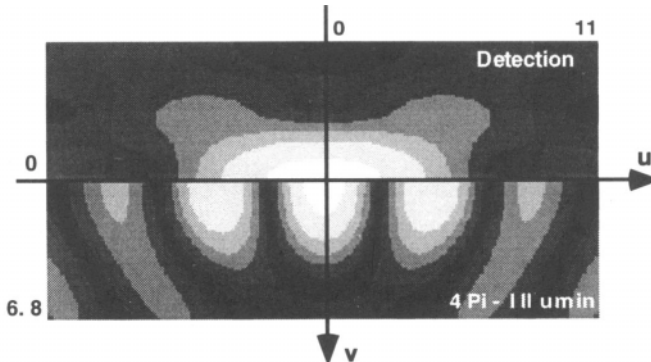


Figure 9.28. In two-photon *confocal* 4Pi microscopy the detection PSF (above) is about twice as narrow as the 4Pi illumination PSF (below). Thus, multiplication with a narrow-detection PSF cuts out the inner part of the illumination PSF in a confocal arrangement. The contour lines are the same as in Figure 9.2.

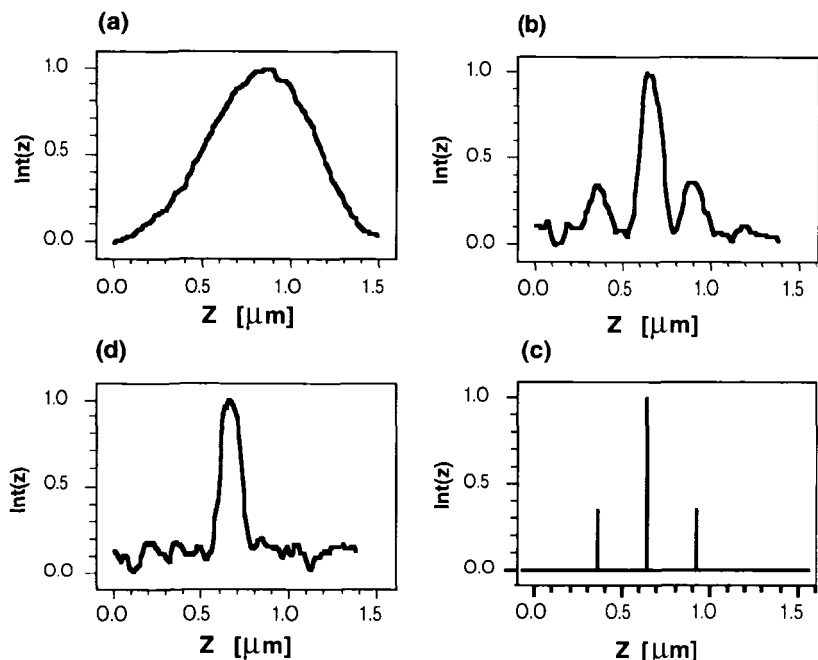


Figure 9.29. The axial responses to a thin layer as recorded in a two-photon (a) confocal, (b) 4Pi confocal microscope of type A. (c) The lobe function, $l(r, z)$; (d) the peak function h_{peak} . The peak function shows the resolution of a two-photon excitation 4Pi confocal microscope with deconvolution by the inverse of $l(r, z)$. A comparison of (d) with (a) shows the 4.5-fold increase of the axial resolution in 4Pi confocal microscopy.

PSF is a convolution of two functions: the lobe function $l(r, z)$ (Figure 9.29c) and the peak function h_{peak} (Figure 9.29d). The lobe function is a product of (three) offset δ functions weighted by the height of the ordinary TPE confocal PSF, describing the location of the lobes and their relative height. The peak function quantifies the intensity distribution of a single peak as it is encountered in the 4Pi axial response.

$$h^{4\text{Pi}}(r, z) = l(r, z') \otimes_{z'} h_{\text{peak}}(r, z') \quad (9.24)$$

In Fourier space, Eq. (9.24) is given by $H^{4\text{Pi}} = LH_{\text{peak}}$. The lobe function and thus the lobes can be computationally removed by multiplying the 4Pi response by the inverse of the lobe function in Fourier space. The resulting response is the function of a single peak, namely the main maximum in the Fourier space

$H_{\text{peak}} = H^{4\text{Pi}} L^{-1}$. An efficient, approximated spatial inverse filter is a three-point filter given by

$$l^{-1}(z) = [C_i \delta(z - z_i)]|_{z_i=\{-d, 0, d\}} \quad \text{with } C_i = \{-C, 1, -C\} \quad (9.25)$$

C is the relative height of the lobes; e.g., $C = 0.4$ for lobes of 40%. Parameter d is the distance between lobes. The inversion of the lobe function is carried out in the spatial domain:

$$h_{\text{peak}}(r, z) \approx h^{4\text{Pi}}(r, z') \otimes_{z'} l^{-1}(z') \quad (9.26)$$

With the object function $O(r, z)$ the image from a 4Pi microscope is described by

$$I(r, z) = h_{\text{peak}}(r, z') \otimes_{z'} O(r, z') = [h^{4\text{Pi}}(r, z'') \otimes_{z''} O(r, z'')] \otimes_{z'} l^{-1}(r, z') \quad (9.27)$$

This filter performs well when the lobes are significantly below 50%. For a relative height of about 50% to 70% more points are needed, such as five or seven. The fact that the filter is based on a few points allows for a rapid on-line application of the deconvolution shortly after image recording. Following Eq. (9.25), the only information needed for performing such a three-point deconvolution is the distance between the lobes and their relative height. Figure 9.29d is actually the result achieved by the application of the three-point inverse filtering. After deconvolution, the axial resolution of the 4Pi confocal microscope is described by Figure 9.29d. A comparison between Figure 9.29d and its single lens counterpart of Figure 9.29a shows an experimental axial resolution improvement of a factor of 4.5 in the 4Pi confocal microscope.

The simplicity of this filter is attractive for removing the axial lobes and producing well-defined, unambiguous axial images. The three-point deconvolution is expected to be the method of choice for improving images recorded in the 4Pi mode. To further evaluate the applicability of this method, images were recorded of DAPI-labeled human lymphocyte chromosomes mounted in glycerol. The thickness of the sample was about 4–5 μm in this case. Figure 9.30a shows an xy image as an overview of the sample. We first recorded TPE confocal axial images (xz images) of pointlike agglomerations of fluorophore with a single lens (Figure 9.30b). One can clearly notice the elongation along the optical axis as it is typical for a single lens axial image; the axial FWHM is $630 \pm 10 \text{ nm}$. Figure 9.30c shows its 4Pi confocal counterpart for constructive interference featuring a main maximum of $140 \pm 10 \text{ nm}$ (FWHM) and two axial lobes. Since the system is no longer aberration-free due to refractive index variations introduced by the sample, the lobes were about 40%. Figure 9.30d shows the 4Pi confocal recording for destructive interference. Here the relative phases of the two interfering wave

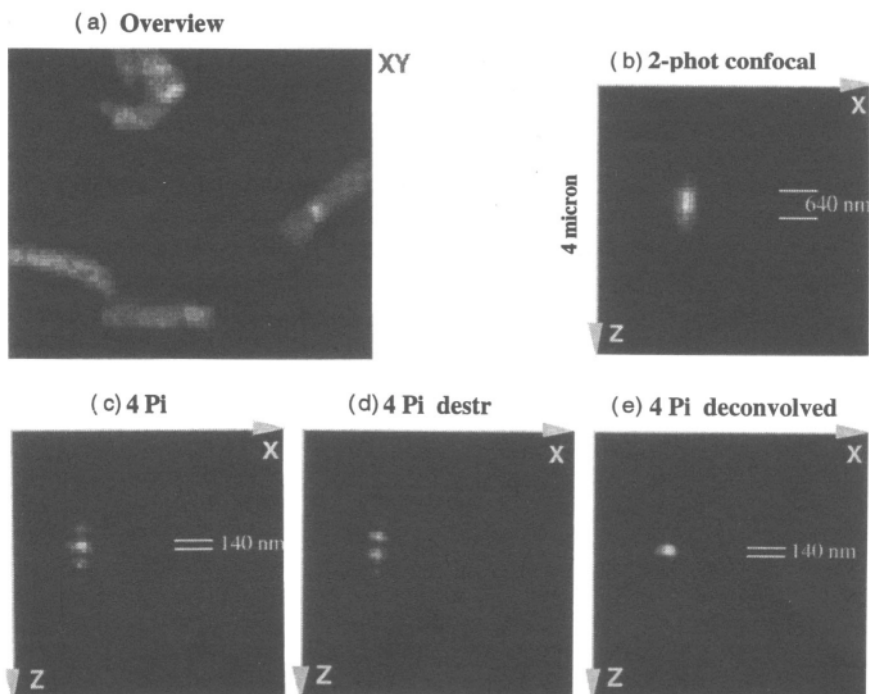


Figure 9.30. (a) XY overview of a chromosome sample; (b) XZ cut performed with a single lens through a pointlike fluorophore label showing the axial and lateral resolution of a standard confocal two-photon excitation microscope, (c) the corresponding 4Pi with constructive interference, (d) the 4Pi with destructive interference, and (e) the constructive 4Pi with subsequent three-point deconvolution. A comparison between (b) and (e) shows that the 4Pi confocal microscope with subsequent three-point deconvolution features a sharp focus, the most localized PSF currently available in far-field light microscopy.

fronts were adjusted to a phase difference of a multiple of π . As a result, the signal vanishes at the geometric focal point and two pronounced peaks are present. Figure 9.30e again shows the 4Pi confocal image for constructive interference, but this time with the lobes removed by the three-point deconvolution technique. A striking difference is observable when comparing Figure 9.30e with the standard TPE confocal image of Figure 9.30b. A comparison of the single-lens recording of Figure 9.30b and e reveals that the TPE 4Pi confocal microscope features the highest resolution in far-field light microscopy.

Figure 9.31a shows a TPE confocal axial image in the DAPI-labeled chromosome sample, whereas Figure 9.31b shows its 4Pi confocal counterpart with subsequent three-point deconvolution. The two images show an axial cut through

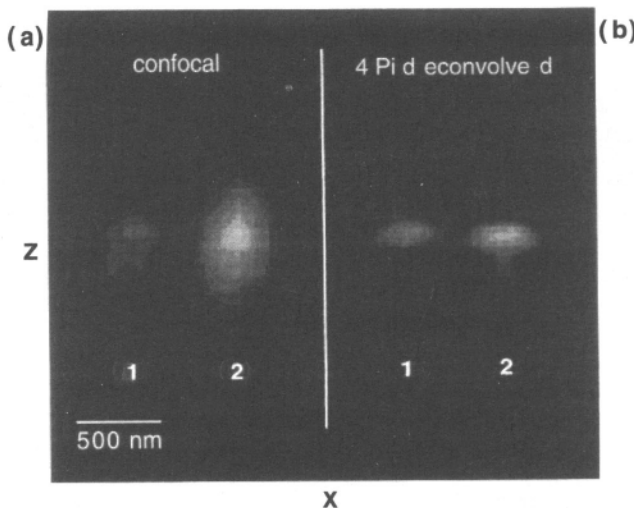


Figure 9.31. Two-photon excitation confocal (a) and three-point deconvolved 4Pi confocal axial images (b) through DAPI-labeled chromosomes. A striking increase in axial resolution is observed in the 4Pi microscope.

two adjacent objects. In (a) the objects are extended along the optical axis. In (b) the 4Pi confocal section from the same position is shown. The objects in Figure 9.31b are localized axially with an accuracy of 140 nm. From the results it becomes apparent that TPE 4Pi confocal microscopy has reached a level where it can be applied to microscopic research of simple, thin biological objects. The four- to fivefold increase in axial resolution should be applicable to high-resolution studies of simple subcellular organelles and their structure.

9.3.5. Limitations and Further Potentials of 4Pi Confocal Microscopy

Despite its superior axial resolution, the 4Pi confocal microscope faces several challenges, one of them being the unknown relative phase of the interfering wave fronts. In our studies, the interference was either constructive or destructive. However, the interference can also have an intermediate state.^(18,19) This uncertainty can be addressed by recording several images with different relative phase of the interfering wave fronts.⁽¹⁸⁾ The image with the least amount of peaks is the one with constructive interference. Another approach is to record or even include a pointlike object in the sample, as it has been done in Figure 9.26. Including pointlike objects can be accomplished by standard labeling techniques. In many cases, fluorescent labels are already pointlike

fluorophore agglomerations. A pointlike object automatically renders the real PSF in the sample and the measured PSF can be used for analyzing the image.^(20,69,86,87) If the PSF is known, it is not necessary to have constructive interference because any PSF can be used for deconvolution. However, limitations due to sudden changes in the index of refraction are expected in certain biological specimens, especially in cell nuclei. In such specimens, the PSF analysis will be restricted to a confined area, e.g., in the order of several microns where the index of refraction does not display significant changes.

For specimens with strongly varying refractive indices one can expect the 4Pi concept to be applicable to investigations of particular labels within the distance of a micron or less, otherwise not resolvable with a standard microscope. While potential differences in the intensities between the interfering beams can be neglected, wave front distortions induced by refractive index mismatches between the sample and the immersion medium can lead to less pronounced interferences. This problem can be addressed by using lenses with an immersion medium with an index of refraction close to that of the specimen, such as the newly developed water-immersion objective lenses (Leica, Germany; Nikon, Olympus, Japan; Zeiss, Germany). A more recent and promising way to reduce the lobes is to use a phase conjugate mirror for producing the wave front of the second lens.⁽⁷⁵⁾ In this case, the excitation light transmitted through the lenses is reflected back into the second objective lens by the phase conjugate mirror. The reflected wave front re-enters the sample again and arrives in the focal region without additional aberration. The need for pumping of the phase conjugate mirror makes this setup additionally complex but this might be outweighed by the advantage of reduced aberrations.

Besides biological applications, there are other areas where the 4Pi confocal microscope may prove very valuable. Such areas include optical data storage⁽⁷⁵⁾ and also single fluorescence molecule detection.⁽⁷⁶⁻⁷⁸⁾ The field of single-molecule detection through confocal fluorescence microscopy has developed very rapidly in the last two years. This technique employs the very narrow volume defined by the PSF of a high-aperture confocal or TPE microscope. As the extent of the confocal or TPE PSF is roughly 100–200 nm in radius and 700–1000 nm in axial distance, the PSF-defined volume is as small as one femtoliter. Single-fluorescence molecules can be studied by using a strongly diluted solution of molecules in a water droplet attached to the objective lens. Due to diffusion in the watery droplet, single molecules cross the focal volume with a typical dwell time of 1 ms. During this time, the molecule is excited by the laser, emitting a burst of photons that are detected in the (confocal) detector. Single-molecule detection is a fascinating field because it allows photophysical and photochemical studies of independent molecules in solution. Furthermore, novel biotechnological methods, such as evolutionary molecular biotechnology, are based on the detection of single-fluorescence molecules tagged to specific parts of biomolecules of

interest.^(76,77) 4Pi confocal microscopy could be very valuable for single-molecule detection, due not only to its doubled photon collection efficiency but also because it allows reduction of the focal volume by a factor of 2–3. In addition, fast phase changes in the 4Pi PSF could be used for studying rapidly diffusing molecules.⁽⁷⁶⁾

9.4. Other Examples of PSF Engineering

Perceiving the PSF of a scanning (confocal) microscope as a probe capable of exploring the sample in three dimensions is a very powerful way of altering the imaging mode of a far-field light microscope. The PSF can be engineered for different purposes such as resolution improvement but also for increasing the working distance of high-resolution microscopes. Figure 9.28 nicely shows that the narrow-detection PSF of a confocal pinhole is able to suppress the outer region of the illumination PSF, thus reducing the height of the lobes in 4Pi microscopy. The multiplication of the illumination PSF with a spatially different detection PSF in order to obtain a narrower or differently shaped effective PSF is an exemplary case of PSF engineering. It has been described in Ref. 20; in this section we discuss two novel and promising developments in microscopy in which this method was applied: *offset-beam overlap microscopy*^(15,72) and *theta-(4Pi) confocal microscopy*.^(80–82)

9.4.1. Offset-Beam Overlap Microscopy

As pointed out, the lateral resolution of a scanning microscope is determined by the lateral extent of the PSF, and the resolution increase aims at the reduction of the lateral extent of the PSF. The *multiplication of two laterally offset but still overlapping PSFs* $h_1(v_x - \Delta v_x)$ and $h_2(v_x + \Delta v_x)$ leads to a resultant PSF $\bar{h}_{\text{offs}}(v_x)$ that is laterally narrower along the axis of the offset than that of a single PSF:

$$\bar{h}_{\text{offs}}(v_x) = h_1(v_x - \Delta v_x)h_2(v_x + \Delta v_x) \quad (9.28)$$

The FWHM of the resultant PSF $\bar{h}_{\text{offs}}(v_x)$ depends on the offset Δv_x and is, under ideal conditions one half of the FWHM of the initial, standard PSF (Figure 9.32 and Figure 9.33). The image intensity is reduced up to two orders of magnitude in such a microscope because the signal originates only from the region of overlap of the two PSFs.⁽¹⁵⁾ The fact that the multiplication of laterally offset PSFs results in a narrower PSF exploitable for resolution increase has been proposed in Ref. 15 and confirmed in Ref. 78, which also shows an application to simple fluorescent objects. A multiplication of two PSFs can be realized through two-photon

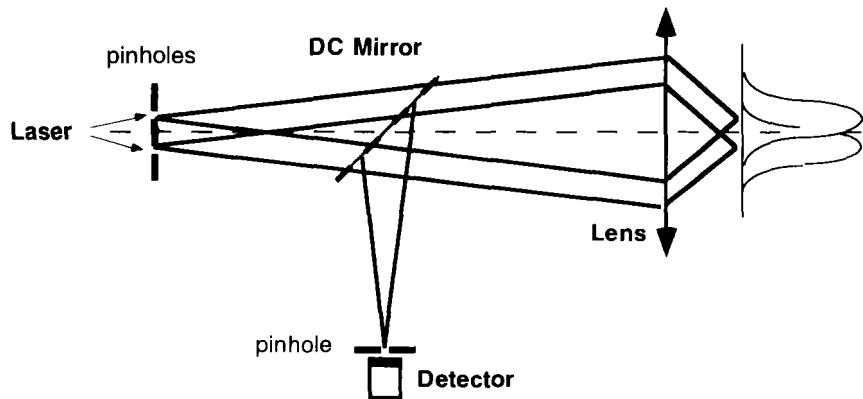


Figure 9.32. Sketch of a microscope with laterally offset overlapping beams and centered point detector.

excitation with one of the photons stemming from the PSF $h_1(v_x - \Delta v_x)$ and the other from $h_2(v_x + \Delta v_x)$. The decrease in FWHM is accompanied by increased lateral lobes compromising the decrease in FWHM. However, this problem can be solved⁽¹⁵⁾ by a standard PSF engineering method: the resultant PSF $\bar{h}_{\text{offs}}(v_x)$ is multiplied by a centered detector PSF $h_{\text{det}}(v)$ suppressing the outer regions of

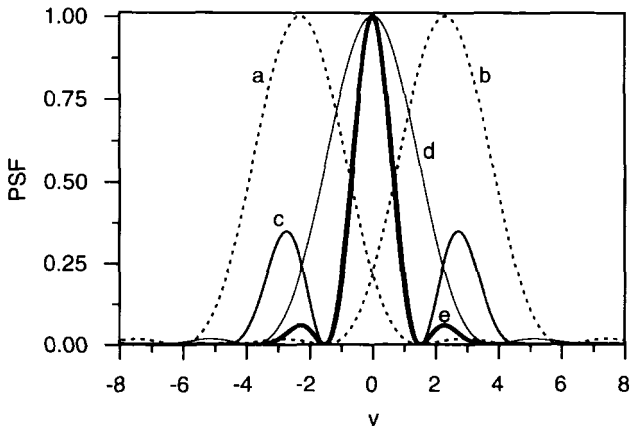


Figure 9.33. Multiplication of two offset PSFs (a) $h_1(v_x - \Delta v_x)$ and (b) $h_2(v_x + \Delta v_x)$ results in a narrower PSF $\bar{h}_{\text{offs}}(v_x)$ with high sidelobes (c). The resultant PSF $\bar{h}_{\text{offs}}(v_x)$ is weaker in intensity; here it is normalized to unity. By applying an additional pinhole centered at $v = 0$, the lobes are suppressed so that the final PSF (e) is laterally narrower and almost lobe free. Note that the main maxima of (c) and (e) coincide. This method results in a resolution increase in direction of the lateral offset up to a factor of 2, as can be found by comparing (e) with the original PSFs (a) or (b).

$\bar{h}_{\text{offs}}(v_x)$. This centered detector PSF is generated by a confocal pinhole lined up in the center of the two offset beams ($v=0$), so

$$\bar{h}_{\text{offs}}^{\text{conf}}(v_x) = h_1(v_x - \Delta v_x)h_2(v_x + \Delta v_x)h_{\text{det}}(v) \quad (9.29)$$

The two offset PSFs are shown in Figure 9.33 along with the resultant PSF $\bar{h}_{\text{offs}}(v_x)$, and the lobe-free PSF $\bar{h}_{\text{offs}}^{\text{conf}}(v_x)$

9.4.2. Theta-4Pi Confocal Microscopy

The theta-4Pi confocal microscope was introduced by Lindek and Stelzer as a modification of the 4Pi confocal concept⁽⁸⁰⁻⁸²⁾. In this concept, these authors have adopted the idea of multiplying spatially differently arranged detection and multiplication PSF to achieve a narrower-resultant PSF.⁽²⁰⁾ One of the initial motivations of introducing the theta confocal concept was the reduction of the axial lobes in 4Pi confocal microscopy. The 4Pi-*theta* confocal microscope uses two opposing lenses of *low* aperture, e.g., water-immersion lenses with numerical aperture 0.75. The aperture angle of such an objective lens is about 34°, so enough space is left to place a third objective lens orthogonally to the two opposing lenses⁽⁸⁰⁻⁸²⁾ (Figure 9.34). The orthogonally arranged third lens is employed for detection using the normal spectrometry arrangement. As a confocal pinhole is used for detection, we can assert that the orthogonal lens defines a detection PSF that is crossed with respect to its illumination counterpart. The crossed arrangement of the illumination and detection PSF is interesting because, as with Figures 9.28 and 9.33, the detection PSF cuts out a part of the illumination PSF. This arrangement has been termed the “Theta-confocal microscope”. The PSF of a theta confocal microscope is given by the product of an illumination and a (crossed) detection PSF, which is found by exchanging the variables u and v :

$$h_{\text{conf}}^{\text{Theta}} = h_{\text{ill}}(u, v)h_{\text{det}}\left(v \frac{\lambda_{\text{exc}}}{\lambda_{\text{det}}}, u \frac{\lambda_{\text{exc}}}{\lambda_{\text{det}}}\right) \quad (9.30)$$

As the PSFs are elongated, the illumination and detection PSFs overlap just in the center of the two PSFs, so the resulting PSF, $h_{\text{conf}}^{\text{Theta}}$, is considerably narrower than that of objective lenses of *low numerical aperture*. It has been pointed out that the reduced region of overlap in a theta confocal microscope can be used for increasing the resolution in far-field fluorescence light microscopy.⁽⁷⁹⁻⁸¹⁾ Indeed, with water-immersion lenses of numerical aperture 0.75, the *axial* resolution of a theta confocal microscope is predicted to be narrower by 30% as

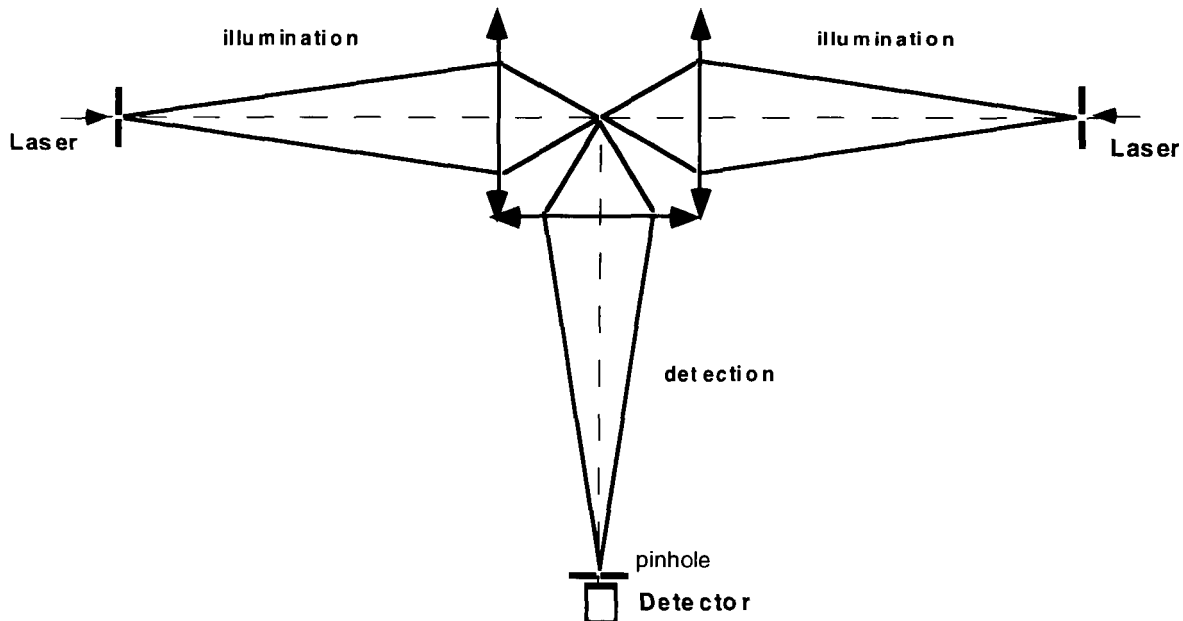


Figure 9.34. Sketch of the theta-4Pi confocal microscope. Three objective lenses of low numerical aperture are employed. The orthogonally arranged lens collects the fluorescence of the fluorophore excited through the horizontal lens(es) either in the 4Pi or single-lens mode. Mechanical constraints enforce the use of low-aperture lenses. This arrangement achieves a high working distance at a resolution almost as good as that of a standard high-aperture confocal microscope.

compared with that of a regular confocal microscope of high aperture.⁽⁸⁰⁾ This is equivalent to an axial resolution of about 360 nm for a wavelength of 633 nm. Thus, the axial resolution of a theta confocal microscope is about two to three times poorer than that of a 4Pi confocal microscope. Unfortunately, a consequence of low numerical apertures is a resultant deterioration of the lateral resolution in both the x and y -directions. The lateral resolution is decreased almost by a factor of 2 when compared with a high-aperture immersion lens, so the area of the Airy disk is about four times larger than in a standard high-numerical confocal microscope. Taking into account the 30% improvement in the axial direction, the three-dimensional extent or volume of a theta confocal PSF is about three times larger than that of a high-numerical-aperture standard confocal microscope (Figure 9.35) which is equivalent to a poorer performance in resolution.

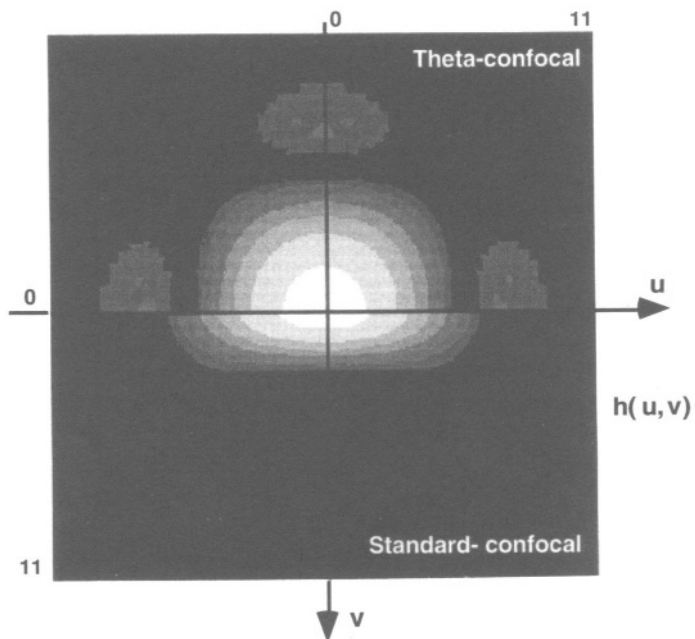


Figure 9.35. PSFs of the theta confocal microscope for single-lens illumination and orthogonal detection ($NA = 0.75$ water immersion) compared with the PSF of a standard confocal fluorescence microscope with an aperture of 1.35 (oil). The PSFs are cylindrically symmetrical around the optical axis (u). Theta confocal microscopy has a slightly improved axial resolution but a noticeably decreased lateral resolution. The PSF volume defined, for example, by the FWHM criterion is about three times larger than that of the standard confocal setup, thus accounting for the poorer overall three-dimensional resolution.

The axial resolution can be improved further by using 4Pi illumination, resulting in theta-4Pi confocal microscopy. The lateral resolution cannot be improved because the theta confocal microscope needs low-aperture lenses due to mechanical constraints. With aperture angles higher than 34°, the orthogonal arrangement is not feasible because the lenses would overlap in space. The low lateral resolution is the main drawback of orthogonal detection. Another disadvantage is the loss of fluorescence due to low angle collection and the fact that the orthogonal arrangement of the detecting lens requires the specimen to be mounted on a pipette; the usual mounting on a cover slip has to be abandoned.^(80–82) It has also been pointed out that the theta arrangement reduces the axial lobes of the 4Pi illumination PSF, thus helping to solve the problem of the unknown phase.^(80–82) However, one has to take into account that the use of low aperture lenses in two-photon 4Pi illumination produces seven or eight high axial lobes that have to be suppressed entirely. Still, the theta confocal microscope is a highly interesting development in 3D-microscopy because the use of low-numerical-aperture lenses provides a uniquely large working distance in the order of a millimeter. This allows the investigation of large biological specimens. Theta-4Pi confocal microscopy is an exemplary case of PSF engineering increasing the working distance of high-resolution confocal microscopes.

9.5. Recent Developments

9.5.1. STED 4Pi Confocal Microscopy

The reduction or removal of the axial lobes is of great interest since achieving a PSF consisting of a single peak is a primary goal in the development of 4Pi confocal microscopy. A potential approach to removing the axial lobes is to apply stimulated emission in 4Pi confocal microscopy. Selective quenching of fluorescence in the area of the lobes without affecting the main maximum of the 4Pi PSF is very attractive. This could be achieved by illuminating both objective lenses with the stimulating light so that a 4Pi PSF with destructive interference is produced similar to that in Figure 9.29d. If the stimulating light has twice the wavelength of the excitation light, as is the case in the example in Figure 9.15, the peaks of the stimulating destructive 4Pi PSF perfectly coincide with the axial lobes (Figure 9.36). In a STED 4Pi confocal microscope, mathematical deconvolution will be redundant. The main maximum of the excitation 4Pi PSF is not affected by the stimulating destructive phase 4Pi PSF because the intensity minimum is in the geometric focus. The destructive 4Pi PSF of doubled wavelength is well suited for the inhibition of fluorescence at the site of the lobes.

Figure 9.36 shows how the PSF is engineered in a STED 4Pi confocal microscope with $\lambda_{\text{exc}} = 375 \text{ nm}$ and $\lambda_{\text{sted}} = 750 \text{ nm}$, constructive interference

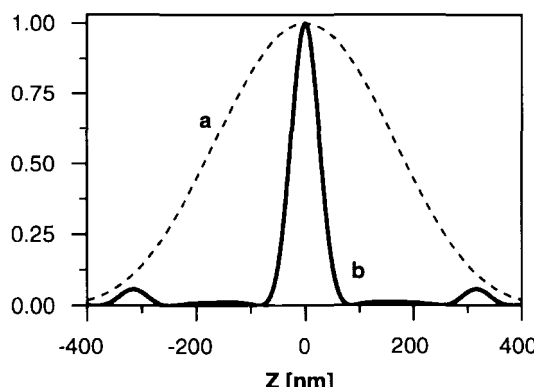


Figure 9.36. STED 4Pi confocal microscope. The axial lobes of the constructive 4Pi illumination PSF (a) calculated for an excitation wavelength of 375 nm, and (b) a stimulating intensity generated by a destructive 4Pi PSF at 750 nm. As the stimulating wavelength is twice the excitation wavelength, the lobes of the 4Pi illumination excitation PSF overlap with the maxima of the destructive stimulating 4Pi PSF. Thus, the fluorescence from the lobes is minimized, and the main maximum remains virtually unaffected.

for λ_{exc} and destructive interference for λ_{sted} . Figure 9.37 shows the resulting PSF as compared with a single lens confocal PSF. One can see that for higher intensities the 4Pi lobes vanish and a sharp peak remains. For higher intensities of the stimulating beam the main maximum is further narrowed. As in the STED fluorescence concept, saturation of the depletion process reduces the width of the axial main maximum, so one can expect an additional increase in axial resolution by stimulated emission. In Figure 9.37, the FWHM of the STED 4Pi axial PSF is 60 nm. It is important to note that the decrease of the spatial extent of the PSF is performed *exclusively by physical effects*. No mathematical deconvolution is employed. The STED 4Pi confocal concept is a good example of PSF engineering, i.e., implementing physics in the focusing process in order to change the spatial extent of the PSF and improve the resolution.

9.5.2. 4Pi Confocal Microscopy Combined with Image Restoration Provides 3D-Resolution in the 100 nm Range

The simple point-deconvolution described previously removes the lobes and is fast. However, it must not be confused with 3D-image restoration algorithms such as the Tikhonov or the Maximum-Likelihood-Estimation algorithm.^(70, 83–85) Point deconvolution uses the information of the location and height of the lobes but does not fully exploit the knowledge of the PSF for increasing resolution. On

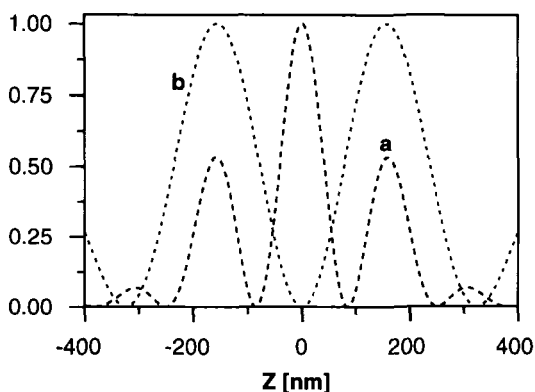


Figure 9.37. Effective PSF of a STED 4Pi microscope (b) as compared with that of a single lens confocal (a). One can notice that the 4Pi lobes can be removed by stimulated emission.

the other hand, the purpose of image restoration or 3D-deconvolution is to correct the diffraction blur by mathematically considering the PSF of the microscope. 3D-image restoration is probably the most common method for improving the resolution in conventional and confocal microscopy. In fact, these methods do not deconvolve the image but approach the real structure of the object iteratively by relying on the PSF which has to be established separately in a measurement. In spite of being popular in microscopy, restoration algorithms have only recently succeeded in significantly improving the resolution.^(83,84) This is due to increased computational speed which now enables the implementation of efficient and stable algorithms. In particular, the combination of high sensitivity detection with piezoelectric stage scanning microscopy has made possible an increase in resolution by 1.5 and 3 in the lateral and axial directions, respectively, as demonstrated by imaging F-actin fibers in mouse fibroblast cells.⁽⁸⁵⁾

An obvious advantage of the 4Pi confocal microscope is the sharper PSF with which the image is taken. This is particularly true for multiphoton 4Pi confocal images since the combination of multiphoton excitation with confocal detection leads to a strongly pronounced main maximum of the effective focus. Hence, when restoring 4Pi confocal images with the 4Pi PSF the resolution should be considerably increased.⁽⁸⁶⁻⁸⁸⁾ Recently, this was demonstrated with densely clustered fluorescence beads as well as by imaging fluorescently labeled F-actin in mouse skin fibroblast cells. The restoration was carried out with a two-photon excitation 4Pi PSF that was measured precisely by using a subresolution fluorescence bead.

Restoration with the 4Pi confocal PSF not only removes the axial lobes but further improves the axial and lateral resolution of 4Pi confocal microscopy.

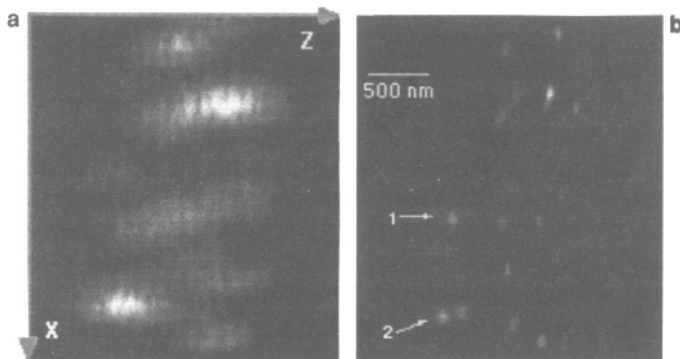


Figure 9.38. Comparison of two axial images of the same site of a sample containing clusters of beads of 110 nm diameter: two-photon (a) confocal and (b) 4Pi confocal with subsequent restoration by a Maximum-Likelihood-Estimation algorithm. In (b) the lateral FWHM is reduced by a factor of 2–3 and its axial counterpart by 7–8.

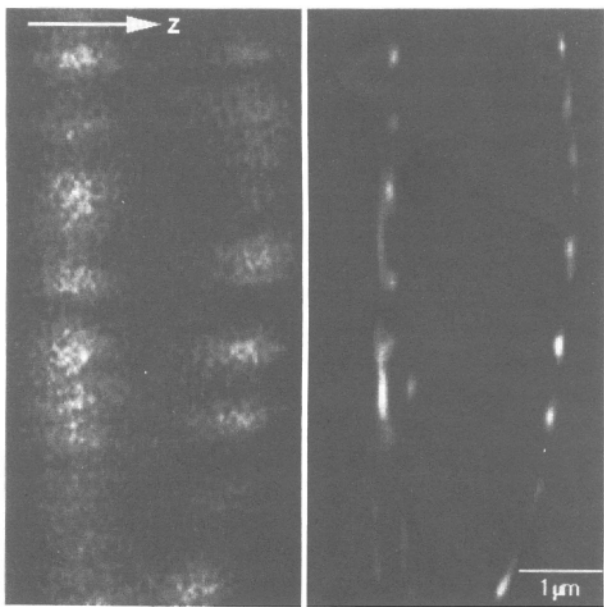


Figure 9.39. Two-photon fluorescence axial images of Rhodamine-phalloidin labeled actin filaments of a mouse skin fibroblast cell: (a) confocal, (b) 4Pi confocal restored. The comparison reveals a 3D-resolution of the order of 100 nm, i.e., a decrease of the uncertainty volume of the effective PSF by a factor of up to 15.

Using a 2-photon excitation wave length of 810 nm a lateral resolution of the order of 100–150 nm and an axial resolution of the order of 70–100 nm was demonstrated.⁽⁸⁷⁾ Figure 9.38 compares axial images of fluorescence beads as recorded with a two-photon (a) confocal and (b) 4Pi confocal microscope using image restoration. A strong increase in 3D-resolution is observed. Whereas, the single lens image in (a) is unable to separate the beads, the restored 4Pi images clearly separate the beads in the sample. If the uncertainty volume as defined by the FWHM of the effective PSF is taken as a measure, the resolution in (b) is improved over (a) by a factor of 15.

Figure 9.39 shows a similar comparison for axial images of F-actin filaments of a mouse fibroblast cell. The axial FWHM is about 600 nm in the standard confocal and 85 nm in the 4Pi confocal restored case. The increase in 3D-resolution by restoration is however accomplished at the expense of increased computational complexity and cannot be carried out online to date. However, the rapidly increasing performance of computers will greatly alleviate this drawback in the future.

9.6. Conclusion

In scanning fluorescence microscopy the resolution is determined by an effective point-spread function which can be interpreted in terms of probabilities. The effective PSF quantifies the probability that a given focal spatial coordinate contributes to the detector signal. The lateral resolution of a scanning microscope is determined by the lateral extent of the effective PSF. For scanning microscopes featuring a PSF with quadratic intensity dependence, such as the confocal fluorescence and TPE microscopes, we can specify an axial resolution that is given by the axial extent of the effective PSF. Moreover, PSFs with quadratic dependence on intensity define a three-dimensional focal volume acting as a probe when scanned through a sample, thus allowing for three-dimensional imaging. The resolution of a scanning microscope can be increased by reducing the probability of contribution of the outer region of the PSF. This can be accomplished by the implementation of selected (photo) physical effects in PSF formation. Changing and shaping the spatial extent of the PSF is called *PSF engineering*.

PSF engineering can be performed by arranging the optics of the scanning microscope so that the effective PSF is given by the product of PSFs of different extent, location, or photophysical impact. PSF engineering is applied in two-photon excitation 4Pi confocal microscopy and offset-beam overlap microscopy, and is the basic idea behind the concepts of STED, GSD fluorescence, and theta-4Pi confocal microscopy. The effective PSF of these microscopes is different in extent, when compared to the PSF of a regular microscope. Thus, PSF engi-

neering opens up the prospect of far-field light microscopy with fundamentally improved resolution.

4Pi confocal microscopy is designed for increasing the axial resolution by three to seven times. The 4Pi confocal microscope is the far-field light microscope with the highest three-dimensional resolution at present. When combined with image restoration, 4Pi confocal microscopy is able to provide lateral resolution in the 100 nm and axial resolution in the 50–100 nm range. STED and GSD fluorescence microscopies are novel concepts for increasing the lateral resolution by up to one order of magnitude. The concepts of STED and GSD fluorescence microscopy are the first methods to show a potential for largely overcoming the diffraction resolution barrier. Both concepts rely on the decrease of the lateral extent of the effective PSF of the scanning fluorescence microscope by inhibiting the fluorescence process at the outer region of the focus. The success of realization will depend on the efficiency of fluorescence inhibition and the signal to noise ratio obtained. Their experimental elaboration is one of the most exciting developments taking place in modern light microscopy. Due to its potential, PSF engineering is likely to evolve as one of the main developments in microscopy at the end of this decade. Moreover, it appears to be a path to a class of microscopy that seemed unfeasible for more than a century: far-field light microscopy with tens of nanometers resolution.

Acknowledgments

A large part of this manuscript was written while the author was a recipient of a grant by the European Commission. The author also would like to thank his collaborators M. Kroug for participating in the theoretical evaluation of the STED and GSD concepts, and M. Schrader and K. Bahlmann for experimental work on 4Pi confocal microscopy and stimulated emission.

References

1. B. Alberts, D. Bray, J. Lewis, M. Raff, K. Roberts, and J. D. Watson, *Molecular Biology of the Cell*, 2nd ed., Garland Publishing, (1989), 136–138.
2. E. Abbe, Beiträge zur Theorie des Mikroskops und der mikroskopischen Wahrnehmung, *Arch. Mikrosk. Anat.* 9, 413 (1873).
3. L. Rayleigh, *Scientific Papers*, Vol. 4, Cambridge University Press, (1903), p. 235.
4. S. Wischnitzer, *Introduction to Electron Microscopy*, 3rd ed. Pergamon Press (1981).
5. J. Chen, *Introduction to Scanning Tunneling Microscopy*, Oxford University Press (1993).
6. G. Binnig, C. F. Quate, and Ch. Gerber, *Phys. Rev. Lett.* 49, 57–59 (1982).
7. D. W. Pohl and D. Courjon (eds.) Proc. NFO1, NATO AS1 Series E 242 (1993).

8. J. Darnell, H. Lodish, and D. Baltimore, *Molecular Cell Biology*, 2nd ed., Freeman, New York (1990), p. 126.
9. E. H. Synge, *Phil. Mag.* 6, 356–362 (1928).
10. E. Betzig and R. Chichester, *Science* 262, 1422–1424 (1993).
11. M. Terasaki and M. E. Dailey, Confocal microscopy of living cells, in: *Handbook of Biological Confocal Microscopy*, 2nd ed. (J. Pawley, ed.), pp. 327–344, Plenum, New York (1995),
12. R. Y. Tsien and A. Waggoner, Fluorophores for confocal microscopy, in: *Handbook of Biological Confocal Microscopy*, 2nd ed. (J. Pawley, ed.), pp. 267–277, Plenum, New York (1995).
13. T. Cremer, A. Kurz, R. Zirbel, S. Dietzel, B. Rinke, E. Schröck, M. R. Speicher, U. Mathieu, A. Jauch, P. Emmerich, H. Scherthan, T. Ried, C. Cremer, and T. Lichten, *Cold Spring Harbor Symp. Quant. Biol.*, 58, 777–792 (1993).
14. R. Kopelman and W. Tan, *Science* 262, 1382 (1993).
15. S. W. Hell, Improvement of lateral resolution in far-field fluorescence light microscopy by using two-photon excitation with offset beams, *Opt. Commun.* 106, 19–24 (1994).
16. S. W. Hell and J. Wichmann, Breaking the diffraction resolution limit by stimulated emission; stimulated emission depletion fluorescence microscopy, *Opt. Lett.* 19, 780–782 (1994).
17. S. W. Hell and M. Kroug, Ground-state-depletion fluorescence microscopy: a concept for breaking the diffraction resolution limit, *Appl. Phys. B* 60, 495–497 (1995).
18. S. Hell, European Patent EP0491289 (filed 1990) published 1992.
19. S. Hell and E. H. K. Stelzer, Properties of a 4Pi-confocal microscope, *J. Opt. Soc. Am. A* 9, 2159–2164 (1992).
20. S. Hell and E. H. K. Stelzer, Fundamental improvement of resolution with a 4Pi-confocal microscope using two-photon excitation, *Opt. Commun.* 93, 277–281 (1992).
21. M. Born and E. Wolf, *Principles of Optics*, 6th ed., Pergamon Press, Oxford (1993), pp. 438–442.
22. C. J. R. Sheppard and H. J. Matthews, Imaging in high-aperture optical systems, *J. Opt. Soc. Am. A* 4, 1354–1360 (1987).
23. S. Hell, Physical basis of confocal fluorescence microscopy, *Soluobiologi* (Jyväskylä, Finland) 3, 183–185 (1991).
24. S. Hell, E. Lehtonen, and E. Stelzer, Confocal fluorescence microscopy: wave optics considerations and applications to cell biology, in: *New Dimensions of Visualization in Biomedical Microscopies* (A. Kriete, ed.), pp. 145–160, Verlag Chemie, Weinheim (1992).
25. S. W. Hell, J. Soukka, and P. E. Hänninen, Two- and multiphoton detection as an imaging mode and means of increasing the resolution in far-field light microscopy: a study based on photon optics, *Bioimaging* 3, 1–6 (1995).
26. C. J. R. Sheppard, and A. Choudhury, Image formation in the scanning microscope, *Opt. Ada* 24, 1051–1073 (1977).
27. G. J. Brakenhoff, P. Blom, and P. Barends, Confocal scanning light microscopy with high aperture immersion lenses, *J. Microsc.* 117, 219–232 (1979).
28. T. Wilson and C. J. R. Sheppard, *Theory and Practice of Scanning Optical Microscopy*, Academic Press, London (1984).
29. T. Wilson, *Confocal Microscopy*, Academic Press, London (1990).
30. R. W. Wijnands van Resandt, H. J. B. Marsman, R. Kaplan, J. Davoust, E. H. K. Stelzer, and R. Stricker, Optical fluorescence microscopy in three dimensions: microtomoscopy, *J. Microsc.* 138, 29–34 (1985).
31. N. Åslund, A. Liljeborg, P. O. Forsgren, and S. Wahlsten, Three-dimensional digital microscopy using the PHOIBOS scanner, *Scanning* 9, 227–235 (1987).
32. J. R. Lakowicz, *Principles of Fluorescence Spectroscopy*, Plenum, New York, (1983), pp. 4–10.
33. A. Einstein, On the quantum theory of radiation, *Phys. Z.* 18, 121–128 (1917).

34. M. D. Galanin, B. P. Kirsanov, and Z. A. Chizhikova, Luminescence quenching of complex molecules in a strong laser field, *Sov. Phys. JETP Lett.* 9, 502–507 (1969).
35. I. Gryczynski, V. Bogdano, and J. R. Lakowicz, Light quenching of tetraphenylbutadiene fluorescence observed during two-photon excitation, *J. Fluoresc.* 3, 85–92 (1993).
36. J. R. Lakowicz, I. Gryczynski, V. Bogdano, and J. Kusba, Light quenching and fluorescence depolarization of rhodamine and applications of this phenomenon to biophysics, *J. Phys. Chem.* 98 (1), 334–342 (1994).
37. J. R. Lakowicz, I. Gryczynski, J. Kusba, and V. Bogdano, Light quenching of fluorescence: a new method to control the excited state lifetime and orientation of fluorophores, *Photochem. Photobiol.* 60, 546–562 (1994).
38. J. Kusba, V. Bogdano, I. Gryczynski, and J. R. Lakowicz, Theory of light quenching; effects on fluorescence polarization, lutensit, and anisotropy decays, *Biophysics J.*, 67, 2024–2040 (1994).
39. F. P. Schäfer (ed.), *Dye Lasers*, 3rd ed., Topics in Applied Physics, Vol 1, Springer, Berlin (1990).
40. K. H. Drexhage, Siegen, Germany, private communication (1994).
41. C. J. R. Sheppard, The use of lenses with annular aperture in scanning optical microscopy, *Optik* 48, 329 (1977).
42. S. W. Hell, P. E. Hänninen, M. Schrader, T. Wilson, and E. Soini, Resolution beyond the diffraction limit: 4Pi-confocal, STED and GSD, *Zool. Stud.* 34, Suppl I (1995).
43. S. W. Hell, M. Schrader, K. Bahlmann, F. Meinecke, J. R. Lakowicz, and I. Gryczynski, Stimulated emission on a microscopic scale: light quenching of pyridinium 2 using a Ti:sapphire laser, 180, RP1-RP2 (1995).
44. U. Brackmann, *Lambdachrome Laser Dyes*, 2nd ed., Lambda Physik, Göttingen, Germany (1985).
45. M. Schrader, F. Meinecke, K. Bahlmann, C. Cremer, and S. W. Hell, Monitoring the excited state by stimulated emission depletion, *Bioimaging* 3, 147–153 (1995).
46. R. Gandin, Y. Lion, and A. Van de Horst, *Photochem. Photobiol.* 37, 271 (1983).
47. C. Cremer and T. Cremer, Considerations on a laser-scanning-microscope with high resolution and depth-of-field, *Microsc. Acta* 81, 31–44 8 (1978).
48. B. Richards and E. Wolf, *Proc. R. Soc. London, Ser. A* 253, 349 (1959).
49. S. W. Hell, S. Lindek, and E. H. K. Stelzer, Enhancing the axial resolution in far-field light microscopy: two-photon excitation 4Pi-confocal fluorescence microscopy, *J. Mod Opt.* 41 (4), 675–681 (1994).
50. S. W. Hell, S. Lindek, C. Cremer, and E. H. K. Stelzer, Measurement of the 4Pi-confocal point spread function proves 75 nm resolution, *Appl. Phys. Lett.* 64, 1335–1338 (1994).
51. S. W. Hell, S. Lindek, C. Cremer, and E. H. K. Stelzer, Confocal microscopy with enhanced detection aperture: type B 4Pi-confocal microscopy, *Opt. Lett.* 19, 222–224 (1994).
52. M. Schrader, M. Kozubek, S. W. Hell, and T. Wilson, Optical transfer functions of 4Pi confocal microscopes: theory and experiment, *Opt Lett.* 22, 436–438 (1997).
53. C. J. R. Sheppard and C. J. Cogswell, in: *Optics in Medicine. Biology and Environmental Research* (G. v. Bally, ed.) Elsevier, Amsterdam (1993).
54. M. Gu and C. J. R. Sheppard, Three-dimensional transfer-functions in 4Pi confocal microscopes, *J. Opt. Soc. Am. A*, 11, 1619–1627 (1994).
55. M. Gu, and C. J. R. Sheppard, Optical transfer-function analysis for 2-photon 4pi confocal fluorescence microscopy, *Opt. Commun.* 114, 45–49 (1995).
56. F. Lanni, *Applications of Fluorescence in the Biological Sciences*, (D. L. Taylor, ed.) Liss, New York (1986) pp. 505–521.
57. B. Bailey, D. L. Farkas, D. L. Taylor, and F. Lanni, Enhancement of axial resolution in fluorescence microscopy by standing-wave excitation, *Nature* 366, 44–46 (1993).

58. F. Lanni, B. Bailey, D. L. Farkas, and D. L. Taylor, Excitation field synthesis as a means for obtaining enhanced axial resolution in fluorescence microscopy, *Bioimaging 1*, 187–192 (1994).
59. C. J. R. Sheppard and R. Kompfner, Resonant scanning optical microscope, *Appl. Opt.* 17, 2879–2883 (1978),
60. W. Denk, J. H. Strickler, and W. W. Webb, Two-photon fluorescence scanning microscopy, *Science* 248, 73–75 (1990).
61. P. E. Hänninen, S. W. Hell, J. Salo, C. Cremer, and E. Soini, Imaging at 140 nm axial resolution with a two-photon excitation 4Pi-confocal fluorescence microscope, *Appl. Phys. Lett.* 66 (13), 1698–1700(1995).
62. S. W. Hell, A. R. Utz, M. Schrader, P. E. Hänninen, and E. Soini, Pulsed laser fluorophore deposition: a method for measuring the axial response of two-photon excitation microscopes, *J. Opt. Soc. Am. A*, 12 (9) 2072–2076 (1995).
63. D. W. Piston, R. G. Summers, and W. W. Webb, Observation of nuclear division in living sea urchin embryos by two photon fluorescence microscopy, *Biophys. J.* 63A, 110 (1993).
64. E. H. K Stelzer, S. Hell, S. Lindek, R. Stricker, R. Pick, C. Storz, G. Ritter, and N. Salmon, Non-linear absorption extends confocal fluorescence microscopy into the ultra-violet regime and confines the illumination volume, *Opt. Commun.* 104, 223–228 (1994).
65. W. Denk, Two-photon scanning photochemical microscopy: mapping ligand-gated ion channel distributions, *Proc. Natl. Acad. Sci. U.S.A.* 91, 6629-6633 (1994).
66. D. W. Piston, B. R. Masters, and W. W. Webb, Three-dimensionally resolved NAD(P)H cellular metabolic redox imaging of the *in situ* cornea with two-photon excitation laser scanning microscopy, *J. Microsc.* 178, 20–27 (1995).
67. P. E. Hänninen, E. Soini, and S. W. Hell, Continuous wave excitation two-photon fluorescence microscopy, *J. Microsc.* 176, 222–225 (1994).
68. S. W. Hell, P. E. Hänninen, M. Schrader, and E. Soini, Annular aperture two-photon excitation fluorescence microscopy, *Opt. Commun.* 117, 20–24, 1995.
69. S. W. Hell, M. Schrader, P. E. Hänninen, and E. Soini, Resolving fluorescence beads at 100–200 distance with a two-photon 4Pi-microscope working in the near infrared, *Opt. Commun.* 117, 20–24 (1995)
70. M. Schrader and S. W. Hell, 4Pi-confocal images with axial superresolution, *J. Microsc.* 183, 189–193 (1996).
71. W. A. Carrington, R. M. Lynch, E. D. W. Moore, G. Isenberg, K. E. Fogarty, and F. S. Fay, Superresolution three-dimensional images of fluorescence in cells with minimal light exposure, *Science* 268, 1483–1487, (1995).
72. S. Hell, G. Reiner, C. Cremer, and E. Stelzer, Refractive index mismatch induced aberrations in confocal fluorescence microscopy, *J. Microsc.* 169, 391–405, (1993).
73. H. Jacobsen, P. E. Hänninen, and S. W. Hell, Effect of refractive index mismatch in two-photon confocal fluorescence microscopy, *J. Microsc.* 176, 226–230 (1994).
74. H. Jacobsen and S. W. Hell, Effect of refractive index mismatch on the resolution and image brightness in confocal fluorescence microscopy, *Bioimaging 3*, 39–47, (1995).
75. Y. Kawata, K. Fujita, O. Nakamura, and S. Kawata, 4Pi confocal optical system with phase conjugation, *Opt. Lett.* 21, 1415–1417 (1996)
76. M. Eigen and R. Rigler, Sorting single molecules: Application to diagnostics and evolutionary biotechnology, *Proc. Natl. Acad. Sci. U.S.A.* 91, 5740–5747 (1994).
77. Ü. Mets and R. Rigler, Submillisecond detection of single rhodamine molecules in water, *J.Fluoresc.* 4, 259–264 (1994).
78. S. Nie, D. T. Chiu, and R. N. Zare, Probing individual molecules with confocal fluorescence microscopy, *Science* 266, 1018–1021 (1994).

79. M. Vaez-Iravani and D. I. Kavaldfje\itv, Resolution beyond the diffraction limit using frequency-domain field confinement in scanning microscopy, *Ultramicrosc.* 61, 105–110 (1995).
80. S. Lindek, N. Salmon, C. Cremer, and E. H. K. Stelzer, Theta microscopy allows phase regulation in 4Pi(A)-confocal two-photon fluorescence microscopy, *Optik* 98, 15–20 (1994).
81. S. Lindek, R. Pick, and E. H. K. Stelzer, Confocal theta microscope with three objective lenses, *Rev. Sci. Instrum.* 65, 3367–3372 (1994).
82. S. Lindek, E. H. K. Stelzer, and S. W. Hell, Two new high-resolution confocal fluorescence microscopies (4Pi, Theta) with one and two-photon excitation, in: *Handbook of Biological Confocal Microscopy* (J. Pawley, ed.), Plenum, New York (1995).
83. H. T. M. van der Voort and K. C. Strasters, Restoration of confocal images for quantitative analysis, *J. Microsc.* 178, 165–181 (1995).
84. W. A. Carrington, R. M. Lynch, and E. D. W. Moore, Superresolution in three-dimensional images of fluorescence in cells with minimal light exposure, *Science* 268, 1483–1487 (1995).
85. H. Kano, H. T. M. van der Voort, M. Schrader, G. van Kempen, and S. W. Hell, Avalanche photodiode detection with object scanning and image restoration provides 2–4 fold resolution increase in two-photon fluorescence microscopy, *Bioimaging* 4, 187–197 (1996).
86. M. Schrader, S. W. Hell, and H. T. M. van der Voort, Potential of confocal microscopes to resolve in the 50–100 nm range, *Appl. Phys. Lett.* 69, 3644–3646 (1996).
87. S. W. Hell, M. Schrader, and H. T. M. van der Voort, Far-field fluorescence microscopy with resolution in the 100 nm range, *J. Microsc.* 187, 1–5 (1997).

Time-Resolved Stimulated-Emission and Transient-Absorption Microscopy and Spectroscopy

P. T. C. So, C. Y. Dong, K. M. Berland, T. French, and E. Gratton

10.1. Introduction

Time-resolved pump–probe spectroscopy is routinely used to study ultrafast phenomena in biological systems. Important systems such as photosynthetic reaction centers, rhodopsins, and hence proteins exhibit functionally important processes on femtosecond and picosecond time scales.^(1–3) This chapter describes the application of pump–probe spectroscopy techniques to time-resolved microscopy. In addition to the well-known advantages associated with time-resolved microscopy^(4–6) pump–probe microscopy can facilitate functional studies of ultrafast protein reactions and motions in native environments (i.e., cells and tissues).

10.1.1. Pump–Probe Spectroscopy

Pump–probe spectroscopy uses a light pump pulse to promote the sample to an excited state and then monitors the relaxation back to the ground state with a probe pulse (Figure 10.1a and 10.1b). Transient absorption studies are the most common implementation.^(7–9) In this approach, when a sample is excited (pumped), there are fewer molecules in the ground state to absorb the probe beam, thus increasing the transmitted probe beam power. As the molecules

P. T. C. So, C. Y. Dong, K. M. Berland, T. French, and E. Gratton • Laboratory for Fluorescence Dynamics, Department of Physics, University of Illinois at Urbana-Champaign, Urbana, Illinois 61801.

Topics in Fluorescence Spectroscopy; Volume 5: Nonlinear and Two-Photon-Induced Fluorescence, edited by J. Lakowicz. Plenum Press, New York, 1997.

relax back to the ground state, the absorption increases, eventually returning to its original value. Another approach uses a probe beam to cause stimulated emission. As the excited molecules relax, the probability for stimulated emission decreases until the excited-state population is completely depleted. Measurements using stimulated emission can either directly observe stimulated emission or the resulting decrease in fluorescence intensity emitted in directions different from the stimulated emission beam. Here, this fluorescence intensity decrease is the experimentally observed quantity.

To monitor the time course of molecular relaxation, the time between pump and probe pulses is varied, typically using a variable delay line in the time domain. The main purpose of pump–probe experiments is to measure ultrafast relaxation by exploiting the inherent time resolution of ultrashort laser pulses without the need for ultrafast optical detectors. MicroChannel plates with about 5–10 GHz bandwidth are the fastest available detectors, but these devices are inherently limited by the response of electronics. For pump–probe experiments, the time resolution is essentially given by the pulse width of the laser, which has bandwidth of hundreds of gigahertz to terahertz. At present, the shortest pulse width achieved is less than 10 fs.⁽¹⁰⁾ For the probe beam to monitor the sample populations excited by the pump beam, it is necessary that the two beams overlap at the sample. A pump–probe signal is generated only from the part of the sample where the two beams coincide spatially. This is the basis for the spatial resolution which will be discussed.

There are other pump–probe techniques, such as fluorescence up-conversion, in which two beams are combined outside the sample that serves as an optical gate. These methods have high time resolution but no spatial resolution, and are thus not considered here.

Pump–probe techniques are well established in the time domain. In the frequency domain, the same concept can be applied to better utilize the harmonic content of pulsed lasers. This method was first demonstrated by Lytle.^(11,12) A high-repetition-rate pulsed laser (the pump) is focused to excite a fluorescent sample. A second pulsed laser (the probe) is focused onto the same spot to monitor the ground-state population by using absorption measurements. The repetition rates of the two lasers are slightly offset from each other, introducing a variable delay between the pump and probe pulses. The effect of this delay is to repeatedly sample (probe) the population of the molecular ground state (excited state) at multiple times after the pump-beam excitation. The interaction of the two beams causes a mixing in the sample, resulting in “modulation” of the probe beam. In frequency space the transmitted probe beam (transient absorption) or fluorescence intensity (stimulated emission) has a low-frequency component at the difference of laser repetition (cross-correlation) frequencies. Since pulsed laser systems have harmonic content, cross-correlation signals at higher laser harmonics are also present in the probe beam, and these cross-correlation signals

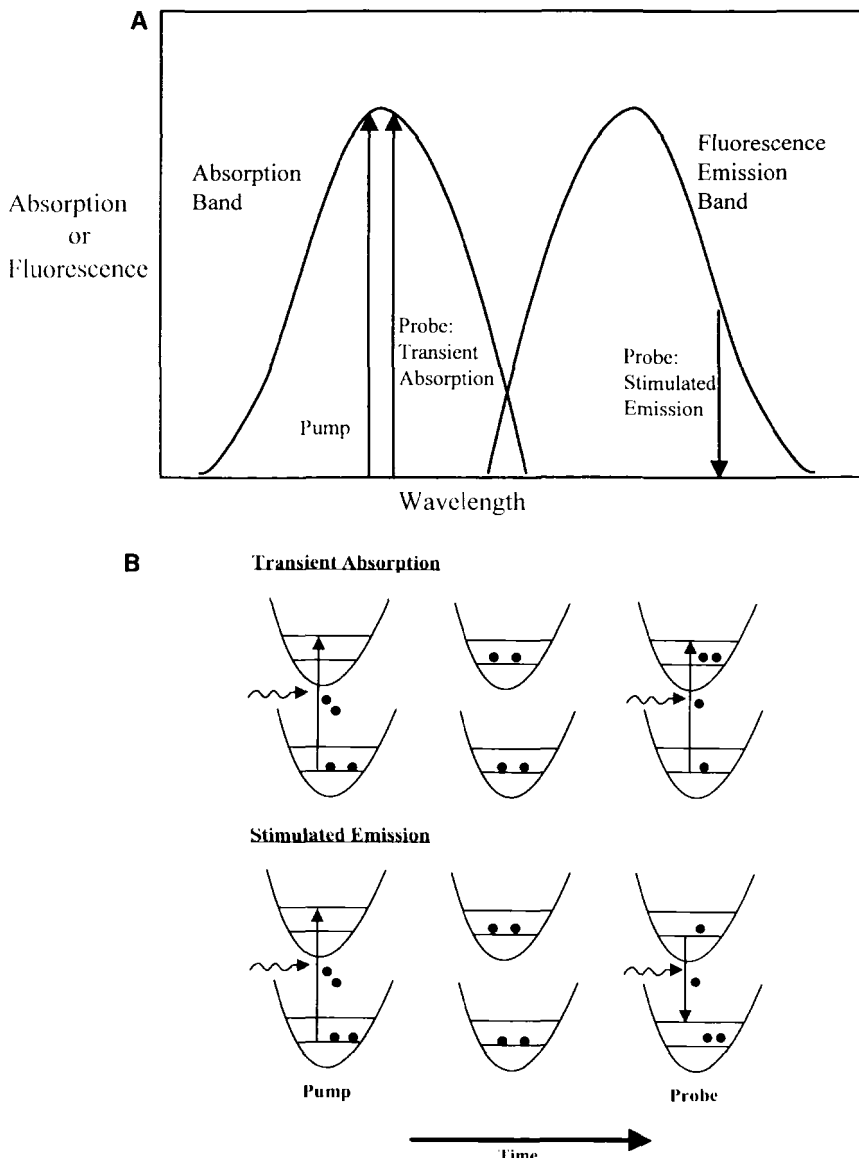


Figure 10.1. Principles of pump-probe fluorescence microscopy. (a) In stimulated emission, the pump beam excites the molecules in the absorption band and the probe causes stimulated emission in the emission band. In transient absorption, the pump and probe beams excite the molecules. (b) For both pump-probe methods, the pump pulse excites a fraction of ground-state molecules into the excited state. When the probe pulse arrives sufficiently quickly and the excited molecules have not emitted, the probe beam in the stimulated-emission case brings a fraction of the excited-state molecules back to the ground state. On the other hand, the probe beam in the absorption case monitors the fewer molecules in the ground state. The excited-state kinetics of the molecule can be deduced from the time-dependent probe-beam modulation by using either method.

can be analyzed to obtain lifetime information of the sample. One of the important advantages of implementing the pump–probe method in the frequency domain is the elimination of slow-moving mechanical delay lines and the automation of the data acquisition processes. This important simplification permits easy integration of the pump–probe technique for use in microscopy.

10.1.2. Time-Resolved Fluorescence Microscopy

Different approaches to time-resolved fluorescence microscopy have been devised for over two decades; all of these techniques relied on gated fast detectors. The development of time-resolved microscopy started with single-point measurements using time-domain single-photon counting.^(13,14) These measurements were performed at a few selected cellular positions to deduce important information about cellular events, such as calcium concentration or cytoplasm matrix viscosity.

Methods have since been developed—two of which are mentioned here—to obtain lifetime resolved image of entire cells. The first method uses charge-coupled device cameras equipped with gain-modulated image intensifiers to collect data simultaneously over the whole image. Both frequency-domain^(4,6,15–20) and time-domain⁽²¹⁾ versions have been constructed. The other approach modifies traditional confocal scanning microscopes and obtains time-resolved information on a point-by-point basis^(5,22) with fast photomultipliers or microchannel plates.

These time-resolved microscopes enable the study of chromophore fluorescence, which is a sensitive monitor of their local cellular environments. Many novel applications of fluorescence lifetime imaging have been demonstrated: important cellular information, such as calcium concentration or pH, have been measured with time-resolved methods.^(23,24) Measurement of cellular autofluorescence intensity and lifetime have been used to monitor the mechanism responsible for cell damage due to ultraviolet A (UVA; 320 to 400 nm) exposure.^(25–27) Fluorescence lifetime has also been used to assess antigen processing stages in mouse macrophage cells.^(28,29) Furthermore, lifetime imaging can provide useful contrast between chromophores with similar emission spectra but different lifetimes. These conventional time-resolved microscopes are limited to the nanosecond regime because of slow detector responses.

The development of a pump–probe fluorescence microscopy can potentially increase the time resolution of lifetime microscopy into the range of picoseconds and femtoseconds.^(30,31) Today the ultrafast dynamics of photosystems or heme groups are investigated at the molecular level in solution.^(32–35) A few pioneering time-resolved studies of these fast systems in whole cells are the exceptions.⁽³⁶⁾ Using pump–probe microscopy, ultrafast spectroscopy of biological molecules

can be performed in their native surroundings. Moreover, many interesting cellular systems with dynamics in the subnanosecond time range were studied at the limit of conventional time-resolved microscope technology. These subnanosecond studies should benefit from the over two-orders-of-magnitude time-resolution improvement achievable using the pump–probe approach. The monitoring of rotational diffusion in cytoplasm and membranes is an important example.⁽³⁷⁾ An improvement in time resolution would allow picosecond rotational components to be resolved, providing accurate microviscosity information in cellular organelles. Another application is for the use of time-resolved resonance energy transfer to monitor protein aggregation in cell membrane or organelles.^(38,39) Instruments with very high time resolution can be used to study energy transfer over smaller distances and better characterize distance distribution between energy transfer pairs. Recent studies have shown that single molecules can be observed by optical microscopy.^(40–42) The pump–probe fluorescence microscope is a promising platform to study picosecond and femtosecond dynamics of single molecules.

10.1.3. Overview

We start with a review of the theory of fluorescence pump–probe spectroscopy in the frequency domain. In particular, the heterodyning method using two asynchronous laser sources will be presented. A major benefit of applying pump–probe fluorescence techniques in microscopy is the improvement in the image spatial resolution. The theoretical analysis of the point-spread function will be presented. The essential components of the experimental apparatus for pump–probe spectroscopy in the frequency domain will be described. The additional optics and electronics required to adapt pump–probe spectroscopy to the fluorescence microscope will also be described. Finally, the spatial and temporal resolution of the frequency-domain pump–probe technique will be evaluated. The power of this new instrument will be illustrated in examples of cellular lifetime-resolved images using pump–probe methods.

10.2. Theory

10.2.1. Pump–Probe Spectroscopy

Frequency-domain pump–probe spectroscopy can be implemented by either monitoring transient absorption or fluorescence intensity following stimulated emission. Absorption spectroscopy studies the dynamics of the ground-state recovery after excitation. Stimulated-emission spectroscopy measures the

time-dependent population of the excited state. Using a combination of these techniques, one can obtain information of radiative and nonradiative decay processes and gain a more complete picture of molecular behavior. In principle, the absorption and the stimulated-emission methods can be utilized for ultrafast microscopy. The theoretical derivation of the laser heterodyning technique is quite similar in both cases and will be developed in parallel here.

Pump-probe spectroscopy in the frequency-domain requires the use of intensity-modulated light sources. In the simplest case, the light source is sinusoidally modulated. Pulsed excitation is composed of multiple sinusoidal Fourier components and will be discussed later. For chromophores with a single exponential lifetime τ , concentration c , quantum efficiency q , and absorption cross section σ , $F(\mathbf{r}, t)$, the density of fluorescence photons at position \mathbf{r} and time t obeys the differential equation

$$\frac{dF(\mathbf{r}, t)}{dt} = -\frac{1}{\tau} F(\mathbf{r}, t) + cq\sigma I(\mathbf{r}, t) \quad (10.1)$$

$I(r, t)$ is the excitation photon flux which is sinusoidal with modulation frequency ω and modulation depth m_e . Separating spatial and temporal parts, $I(r, t) = [1 + m_e \sin(\omega t + \phi)]I(r)$. The fluorescence signal $F(\mathbf{r}, t)$ is proportional to the excited-state population, $E(\mathbf{r}, t)$. The sum of the ground-state population, $G(\mathbf{r}, t)$, and the excited-state population is a constant due to particle number conservation.

The integrated fluorescence signals responds at the same angular frequency as the excitation, but with a phase delay, ϕ , and decreased modulation m_f , due to the lifetime of the fluorescent sample:

$$F(t) \propto cq\sigma(1 + m_f \sin(\omega t + \phi)) \int I(r) d^3r \quad (10.2)$$

where c is chromophore concentration (assumed constant for simplicity), and σ is the absorption cross section.

In solving Eqs. (10.1) and (10.2) and in the absence of saturation, the lifetime from the phase delay, ϕ , and modulation, m_f , can be determined.⁽⁴³⁾

$$\tan(\phi) = \omega\tau \quad (10.3)$$

$$M = \frac{1}{\sqrt{1 + \omega^2\tau^2}} \quad (10.4)$$

For both absorption and stimulated emission, a sinusoidally modulated probe beam of intensity $I'(\mathbf{r}, t) = I(\mathbf{r})I(t) = I(\mathbf{r})[1 + m'_e \sin(\omega't + \phi')]$, is introduced.

We will make two assumptions at this point. First, the attenuation of the pump and probe beams by the sample is negligible. This may not be true for conventional pump–probe spectroscopy, but it is certainly valid for a micron-thick sample. Second, the dynamics of either the ground- or excited-state populations are slow compared to the transit time of light through the sample. For a sample with a thickness around 10 microns, the transit time is about 30 fs.

In absorption measurements, the attenuation of the probe beam depends on the transient ground-state population $G(\mathbf{r}, t)$. In stimulated-emission measurements, the amount of stimulated emission depends on the transient excited-state population $E(\mathbf{r}, t)$. The respective detected signals can be expressed as

$$\Delta I'(t) \propto \int \sigma I'(\mathbf{r}, t) G(\mathbf{r}, t) d^3 r \quad (\text{ground-state absorption}) \quad (10.5a)$$

$$\Delta F(t) \propto \int \sigma' I'(\mathbf{r}, t) E(\mathbf{r}, t) d^3 r \quad (\text{excited-state stimulated emission}) \quad (10.5b)$$

where σ' is the stimulated-emission cross section. The time-dependent ground- and excited-state populations can be deduced from Eqs. (10.1)–(10.4). Neglecting constant terms, the previous equation can be simplified and all time-dependent terms isolated:

$$\begin{aligned} \Delta I'(t) &\propto cq\sigma^2[1 + m'_e \sin(\omega't + \phi')] \\ &\cdot \left[1 + m_e \frac{1}{\sqrt{1 + \omega^2\tau_m^2}} \sin(\omega t + \phi) \right] \int I(\mathbf{r})I'(\mathbf{r}) d^3 r \end{aligned} \quad (10.6a)$$

$$\begin{aligned} \Delta F(t) &\propto cq\sigma\sigma'[1 + m'_e \sin(\omega't + \phi')] \\ &\cdot \left[1 + m_e \frac{1}{\sqrt{1 + \omega^2\tau_m^2}} \sin(\omega t + \phi) \right] \int I(\mathbf{r})I'(\mathbf{r}) d^3 r \end{aligned} \quad (10.6b)$$

The temporal product term in Eq. (10.6) may be rewritten as two terms containing the sum and difference of frequencies, respectively. If the frequencies of the pump

and probe beams are $\Delta\omega = |\omega' - \omega|$ apart, then Eq. (10.6), and therefore the detected fluorescence, contains a low-frequency, cross-correlation term

$$\Delta I'(t) \propto cq\sigma^2 m_e m'_e \cdot \frac{1}{\sqrt{1 + \omega^2 \tau_m^2}} \cos[|\omega' - \omega|t + (\phi' - \phi)] \int I(\mathbf{r}) I'(\mathbf{r}) d^3 r \quad (10.7a)$$

$$\Delta F(t) \propto cq\sigma\sigma' m_e m'_e \cdot \frac{1}{\sqrt{1 + \omega^2 \tau_m^2}} \cos[|\omega' - \omega|t + (\phi' - \phi)] \int I(\mathbf{r}) I'(\mathbf{r}) d^3 r \quad (10.7b)$$

With electronic filtering, the cross-correlation signal can be isolated, and the lifetime of the sample in the excitation volume can be obtained from the amplitude and phase of the cross-correlation signal.

The preceding discussion examines the pump–probe spectroscopy at a single frequency. The ultimate time resolution of pump–probe spectroscopy depends on the maximum usable frequency available in the laser light sources. The harmonic content of picosecond and femtosecond lasers can extend to gigahertz to terahertz. Consider the ideal case where the pulses of the laser system are infinitely narrow:

$$I_1(t) \sum_{n=0}^N \delta(t - nT_0) \quad (10.8a)$$

The Fourier transform of this signal gives its harmonic content:

$$I_1(\omega) = \sum_{n=0}^N e^{in\omega T_0} \quad (10.8b)$$

For large N ,

$$I_1(\omega) \propto \frac{\sin(N\omega T_0/2)}{\sin(\omega T_0/2)} \quad (10.9)$$

One can observe that this function has contributions only at frequency multiples of $2\pi/T_0$. The widths of these harmonic peaks are proportional to $1/N$. In the limit that N approaches infinity, this is just a series of Dirac delta functions at equal frequency separated by $2\pi/T_0$. This series of peaks extend to infinity

in frequency space. The bandwidth of a train of infinitely narrow pulses is unlimited.

We can account for the finite width of real laser pulse train by modifying Eq. (10.8) as

$$I_2(t) = I_1(t) \otimes S(t) \quad (10.10)$$

where $S(t)$ is the functional form of the finite-width laser pulse and \otimes denotes convolution operation. The Fourier transform of $I_2(t)$ is easily evaluated since the Fourier transform of two convoluted functions is just the product of the Fourier transform of the individual functions. The Fourier transform of $I_1(t)$ is an infinite series of pulses in frequency space. $S(t)$ can be roughly approximated as a Lorentzian of width t_w . The Fourier transform of a Lorentzian is just an exponential function with a decay constant of $1/t_w$. Therefore, the finite-width laser pulses limit the infinite series in frequency space. This envelope function has a frequency cutoff at $f_w = 1/t_w$. This is the bandwidth limit for pump-probe spectroscopy in the time domain. For a laser pulse width of about 1 ps, the frequency cutoff is about 1 THz.

In the frequency domain the pump-probe method requires the use of two lasers operating at different frequencies. Although these lasers can be phase-locked, some random phase jitter between the pulses from the two lasers is unavoidable. The effect of phase jitter is also a relevant consideration in the two-color pump-probe experiment in the time domain when autocorrelation of the same laser pulse is not used.

The jitter of typical mode-locked lasers is tens of picoseconds. The effect of phase jitter on the ultimate bandwidth of the frequency-domain pump-probe technique can be evaluated by a modification of Eq. (10.10):

$$I(t) = \left[\sum_{n=0}^N \delta(t - nT_0 + \sigma_n) \right] \otimes S(t) \quad (10.11)$$

where σ_n is a random phase jitter which is uncorrelated from pulse to pulse. More precisely,

$$\lim_{M \rightarrow \infty} \sum_{m=0}^M \sigma_m = 0 \quad (10.12a)$$

$$\lim_{M \rightarrow \infty} \sum_{m=0}^M \sigma_m^2 = \langle \sigma^2 \rangle \quad (10.12b)$$

where $\langle \sigma^2 \rangle$ is the mean-square amplitude of the jitter.

Since the effect of convolving with $S(t)$ gives a known envelope function, to evaluate the effect of the phase jitter we will only consider the first term. The Fourier transform is

$$I(\omega) = \sum_{n=0}^N e^{-nT_0\omega} e^{-i\sigma_n\omega} \quad (10.13)$$

To evaluate this sum, we take an ensemble average of $I(\omega)$. This ensemble average corresponds to taking multiple time series of the fluorescence intensity, Fourier-transforming these series, and averaging the result in phase. This is exactly how the data are processed by either the spectrum analyzer or the digital data acquisition electronics described here.

Let $I_m(t)$ be the m th series and $I_m(\omega)$ its Fourier transform. The ensemble average is then

$$\langle I(\omega) \rangle = \lim_{M \rightarrow \infty} \sum_{m=0}^M I_m(\omega) = \lim_{M \rightarrow \infty} \sum_{m=0}^M \sum_{n=0}^N e^{-inT_0\omega} e^{-i\sigma_n^m\omega} \quad (10.14)$$

The only m dependence of $I_m(\omega)$ is in the random phase jitter σ_n^m . After Taylor expansion and keeping only the leading terms,

$$\langle I(\omega) \rangle = \sum_{n=0}^N e^{-inT_0\omega} \lim_{M \rightarrow \infty} \sum_{m=0}^M [1 - i\sigma_n^m\omega - \frac{1}{2}\omega^2(\sigma_n^m)^2 + \dots] \quad (10.15)$$

For random fluctuations, the linear term in σ drops out, and we can approximate the series as another exponential function:

$$\langle I(\omega) \rangle = \sum_{n=0}^N e^{-inT_0\omega} [1 - \frac{1}{2}\langle \sigma^2 \rangle \omega^2] = e^{-(\sigma^2)\omega^2} \sum_{n=0}^N e^{-inT_0\omega} \quad (10.16)$$

Therefore, phase jitter introduces a second exponential envelope function and limits the signal bandwidth to the time scale of the mean-square phase jitter. The typical phase-jitter magnitude of mode-locked lasers is about 10 ps. This derivation is modeled after the formulation of the Debye–Waller factor in X-ray diffraction theories.^(44,45) The limitation on the frequency bandwidth of pump–probe spectroscopy as a result of pulse width and phase jitter is summarized pictorially in Figure 10.2.

10.2.2. Pump–Probe Microscopy

Superior time resolution is not the only distinctive advantage of pump–probe microscopy. It also has an inherent 3D sectioning capability and a spatial resolution comparable to the confocal method.

10.2.2.1. Radial and Axial Resolution

The effective spatial resolution in a microscopic fluorescence imaging system depends on the focusing of the excitation source and collection of the fluorescence signal. For an incoherent fluorescence imaging system using a large detector, the image at the object space F is

$$F = |h|^2 \otimes f \quad (10.17)$$

where h is the amplitude point-spread function of the focusing lens, f is the spatial distribution of the fluorescence sample, and \otimes represents the three-dimensional convolution operation.^(46,47)

In the pump–probe system described in Eqs. (10.7), the spatial dependence of the cross-correlation signal depends on the overlap integral of the pump and probe intensity involved in the transition

$$\int I(\mathbf{r})I'(\mathbf{r}) d^3r \quad (10.18)$$

The point-spread function (PSF) is the integrand of Eq. (10.18). Different pump and probe mechanisms can result in different intensity profiles near the focal point. For example, in a one-photon pump (1 pu) and one-photon probe (1 pr) system using the same wavelength, the PSF is

$$I_{1\text{pu}, 1\text{pr}}(u, v) = I(u, v)I'(u, v) \quad (10.19)$$

where $I(u, v) = |2 \int J_0(v\rho)e^{-iup^2/2}\rho d\rho|^2$ is the intensity distribution of light with wavelength λ near the focal point of a circular objective with numerical aperture $\sin(\alpha)$, $u = 4k \sin(\alpha/2)^2 z$ and $v = k \sin(\alpha)r$ are the dimensionless radial and axial coordinates respectively, and $k = 2\pi/\lambda$ is the magnitude of the wave

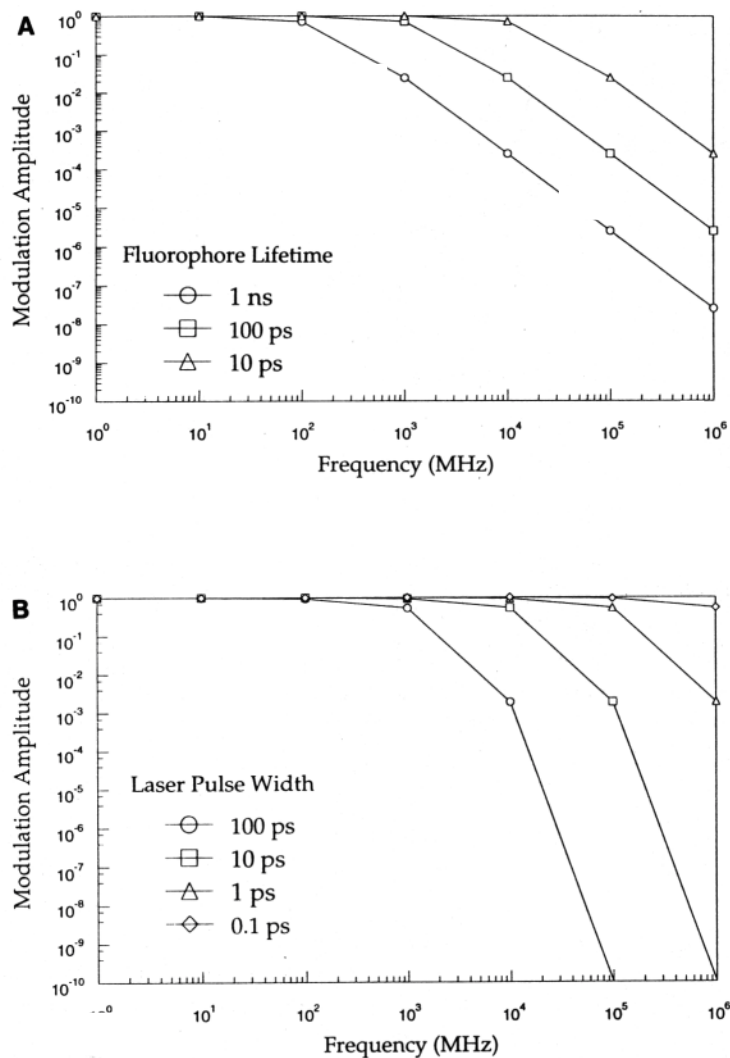


Figure 10.2. Bandwidth of frequency domain pump-probe spectroscopy. (a) The effect of fluorophore lifetime on pump-probe bandwidth. (b) The effect of laser pulse width on pump-probe bandwidth. Where two lasers are used, the bandwidth is limited by the laser with the wider pulses.

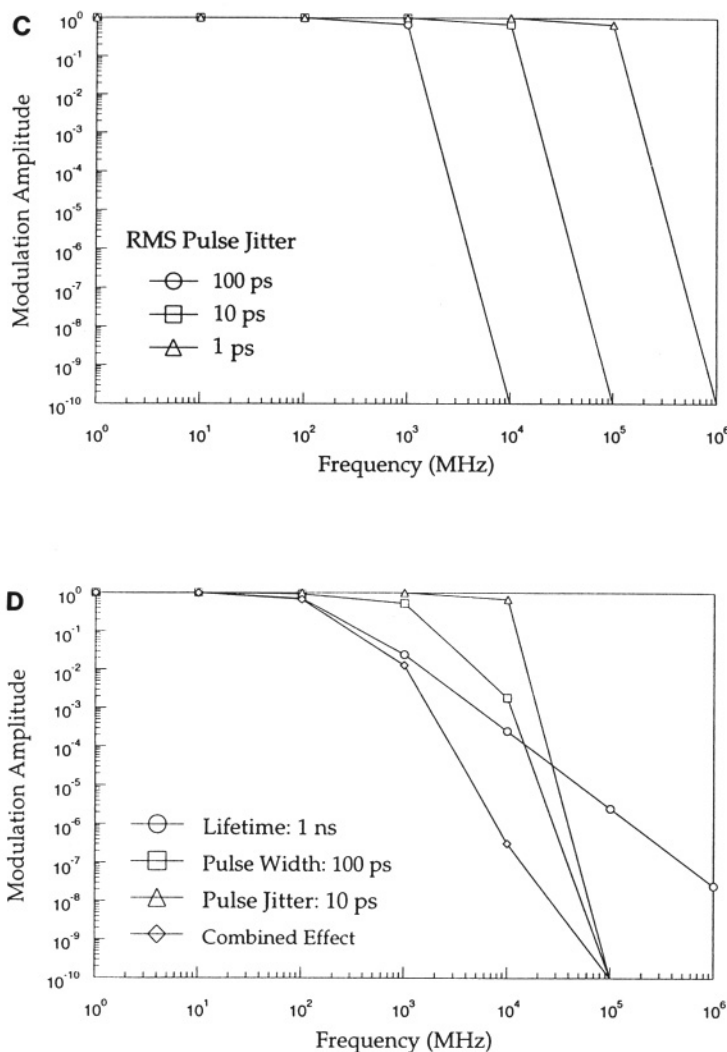


Figure 10.2. *Continued* (c) The effect of laser pulse jitter on pump-probe bandwidth. (d) The bandwidth of the experiments described in this chapter (fluorophore of 1 ns lifetime, laser pulse width of 100 ps, and laser jitter of 10 ps).

vector.^(48,49,50) If, instead, a two-photon mechanism is used in the pump, the probe, or both light sources, there are two additional PSFs to consider:

$$I_{2\text{pu},1\text{pr};1\text{pu},2\text{pr}}(u, v) = I^2\left(\frac{u}{2}, \frac{v}{2}\right)I'(u, v) \quad (10.20)$$

$$I_{2\text{pu},2\text{pr}}(u, v) = I^2\left(\frac{u}{2}, \frac{v}{2}\right)I'^2\left(\frac{u}{2}, \frac{v}{2}\right) \quad (10.21)$$

In each case, the excitation and stimulated-emission cross sections σ and σ' expressed in Eqs. (10.2), (10.5), and (10.7) must correspond to the appropriate one- or two-photon process.^(51,52)

To demonstrate the improved spatial resolution introduced by the pump-probe arrangement, the PSFs given by Eqs. (10.19)–(10.21) are plotted in Figures 10.3 and 10.4 along with the one-photon and two-photon excitation distributions $I(u, v)$ and $I_{2p}(u, v) = I^2(u/2, v/2)$. In our analysis, we have assumed for simplicity that the pump laser, probe laser, and signal detection are at the same wavelength. This assumption is reasonable since, for a typical chromophore, a spectral bandwidth of 100 nm is sufficient to include the wavelengths used in pump-probe microscopy.

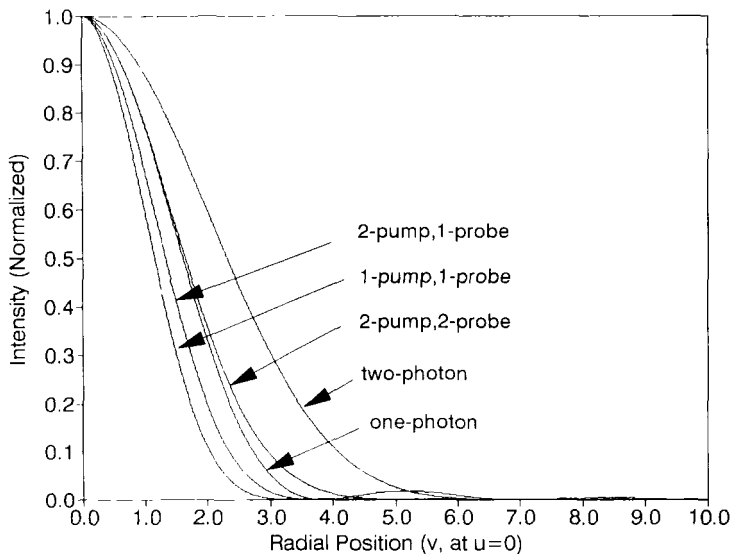


Figure 10.3. Theoretical radial intensity distributions at the focal plane for pump-probe microscopy using one- and two-photon excitation.

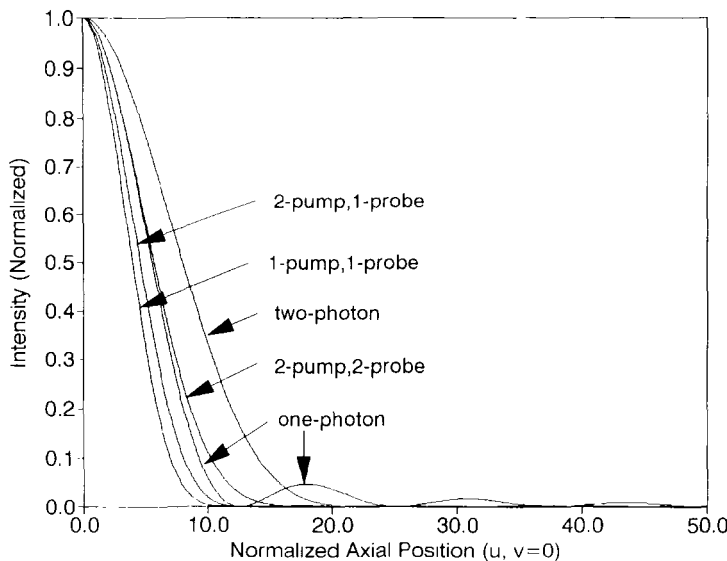


Figure 10.4. Theoretical axial intensity distributions at the focal plane for pump–probe microscopy using one- and two-photon excitation.

From Figures 10.3a and 10.4a, we can see that in this group of PSFs, the one-photon pump-and-probe approach offers the narrowest width (FWHM). Along the radial direction, FWHM of the PSF in one-photon pump-and-probe fluorescence microscopy is $1.16\text{ }v$, and it is 0.716 of that in conventional one-photon microscopy. The axial FWHM is $8.02\text{ }u$, which is 0.819 of the conventional one-photon case. Furthermore, examination of the secondary peaks in Figures 10.3b and 10.4b shows that in all cases of the pump–probe fluorescence microscopy, the secondary peaks are much smaller in amplitude than those of conventional microscopy.

10.2.2.2. Confocal Pump–Probe Fluorescence Microscopy

Further improvements in pump–probe fluorescence microscopy can be achieved if confocal detection is used. The point-spread functions for the various pump–probe microscopy cases then become

$$I_{c,1pu,1pr}(u, v) = I(u, v)I'(u, v)I(u, v) \quad (10.22)$$

$$I_{c,2pu,1pr;c,1pu,2pr}(u, v) = I^2(u/2, v/2)I(u, v)I(u, v) \quad (10.23)$$

$$I_{c,2pu,2pr} = I^4(u/2, v/2)I(u, v) \quad (10.24)$$

The PSFs in the radial and axial directions for confocal pump–probe fluorescence microscopy of Eqs. (10.22)–(10.24) are plotted in Figures 10.5 and 10.6, respectively. Confocal one- and two-photon PSFs are also shown for comparison. The figures show that the confocal one-photon pump-and-probe PSF has the narrowest radial and axial FWHM at 0.952 ν and 6.58 u , respectively. These values are 0.586 (radial) and 0.591 (axial) of the FWHM for standard one-photon microscopy.

10.2.2.3. Optical Transfer Function

The convolution operation described in Eq. (10.17) provides an opportunity to analyze an imaging system by Fourier methods. Fourier analysis has the advantage that it can separate the optical properties of the imaging system from the imaged object. For conventional one-photon fluorescence microscopy, the 3D optical transfer function (OTF) is

$$C(l, s) = \frac{1}{l} \operatorname{Re} \left[1 - \left(\frac{|s|}{l} + \frac{l}{2} \right)^2 \right]^{1/2} \quad (10.25)$$

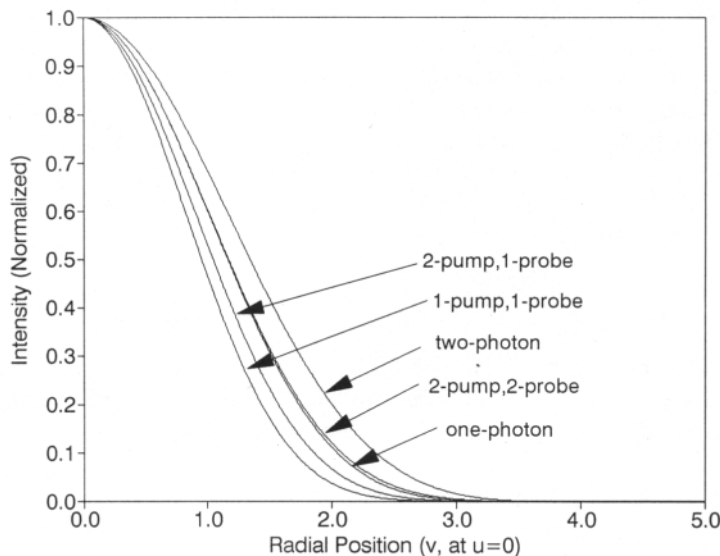


Figure 10.5. Theoretical radial intensity distribution at the focal plane for pump–probe microscopy with confocal detection using one- and two-photon excitation.

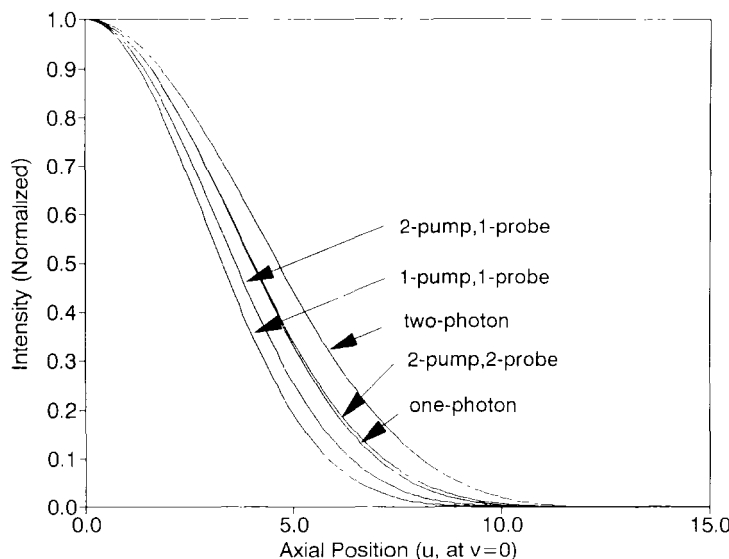


Figure 10.6. Theoretical axial intensity distribution at the focal plane for pump–probe microscopy with confocal detection using one- and two-photon excitation.

where $l = l'\lambda/\sin(\alpha)$ and $s = s'\lambda/4\sin^2(\alpha)$ are the normalized radial and axial spatial frequencies, respectively. The primed units denote the corresponding spatial frequencies. The OTFs for one-photon confocal, two-photon, and two-photon confocal fluorescence microscopy have been investigated and are

$$C_{c,1\text{photon}} = C(l, s) \otimes C(l, s) \quad (10.26)$$

$$C_{2\text{photon}} = C(2l, 2s) \otimes C(2l, 2s) \quad (10.27)$$

$$C_{c,2\text{photon}} = C(2l, 2s) \otimes C(2l, 2s) \otimes C(l, s) \quad (10.28)$$

where \otimes represents the three-dimensional convolution operation.^(47,50–52)

Extension of Fourier analysis to pump–probe microscopy is straightforward, and by applying the convolution theorem to Eqs. (10.19)–(10.21), OTFs for different pump–probe approaches can be expressed with

$$C_{1\text{pu},1\text{pr}}(l, s) = C(l, s) \otimes C(l, s) \quad (10.29)$$

$$C_{2\text{pu},1\text{pr};1\text{pu},2\text{pr}}(l, s) = C(2l, 2s) \otimes C(2l, 2s) \otimes C(l, s) \quad (10.30)$$

$$C_{2\text{pu},2\text{pr}}(2l, 2s) = C(2l, 2s) \otimes C(2l, 2s) \otimes C(2l, 2s) \otimes C(2l, 2s) \quad (10.31)$$

The OTFs for the corresponding confocal cases (from Eqs. 10.22 to 10.24) can be similarly obtained:

$$C_{c,1pu,1pr}(l, s) = C(l, s) \otimes C(l, s) \otimes C(l, s) \quad (10.32)$$

$$C_{c,2pu,1pr;c,1pu,2pr}(l, s) = C(2l, 2s) \otimes C(2l, 2s) \otimes C(l, s) \otimes C(l, s) \quad (10.33)$$

$$C_{c,2pu,2pr} = C(l, s) \otimes C(2l, 2s) \otimes C(2l, 2s) \otimes C(2l, 2s) \otimes C(l, s) \quad (10.34)$$

The cutoff frequencies for Eqs. (10.25), (10.27), (10.29)–(10.31) are plotted in Figure 10.7 and their confocal counterparts (Eqs. 10.26, 10.28, 10.32–10.34) are plotted in Figure 10.8. The OTFs exterior to the boundaries have zero values. Without confocal detection, the cutoff frequency for the different variations of pump–probe microscopy are the same as confocal one- or two-photon detection; the radial and axial cutoffs in those cases are 4 and 1 normalized frequencies respectively. With confocal detection, the cutoff frequencies in pump–probe microscopy increase to 6 (radial) and 1.5 (axial) normalized frequencies. One can thus conclude that pump–probe fluorescence microscopy can provide comparable spatial resolution to one-photon confocal microscopy, and superior resolution can be accomplished by combining pump–probe fluorescence microscopy with confocal detection.

10.2.2.4. Axial Depth Discrimination

In this section, the ability of the pump–probe microscopy to reject the background fluorescence contribution from off-focal axial planes is investigated. The question addressed is how much cross-correlation signal is detected from off-focal planes compared to conventional microscopy. To answer this question, we need to integrate Eqs. (10.19)–(10.21) over the radial coordinate and then compare the signal at each axial position. For conventional microscopy, the normalized fluorescence from each axial plane of interest is⁽⁵³⁾

$$F_{\text{axial}}(u) = \frac{\int_0^{\infty} I(u, v)v dv}{\int_0^{\infty} I(0, v)v dv} \quad (10.35)$$

Equation (10.35) may be applied to intensity profiles for pump and probe beams and the result, compared to the conventional microscopy and two-photon cases, is

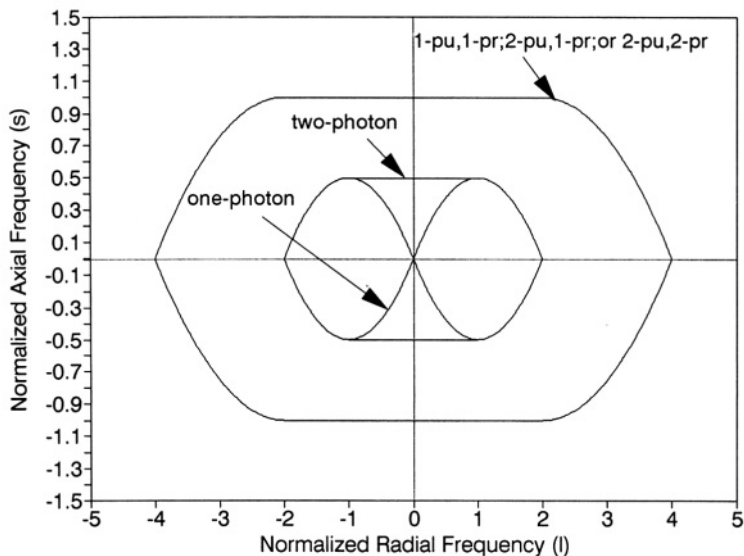


Figure 10.7. Theoretical optical transfer functions (cutoff frequencies) for pump-probe microscopy using one- and two-photon excitation.

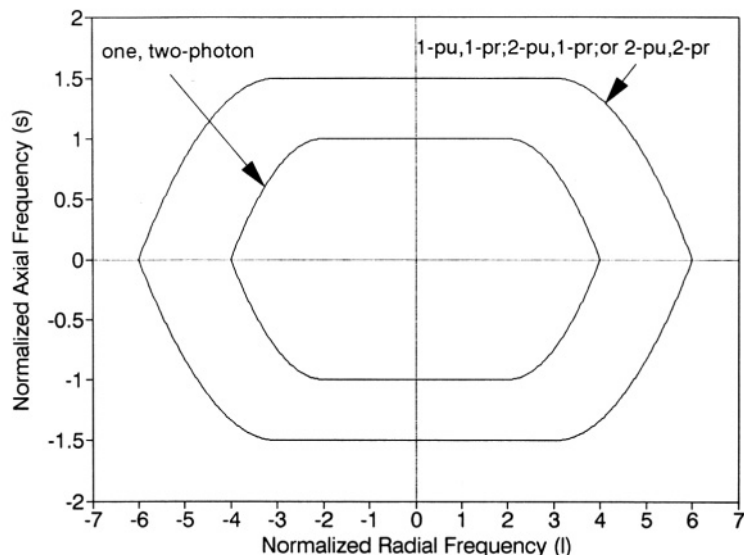


Figure 10.8. Theoretical optical transfer functions (cutoff frequencies) for pump-probe microscopy with confocal detection using one- and two-photon excitation.

shown in Figure 10.9. One sees that all versions of pump-probe microscopy offer better depth discrimination than conventional one-photon microscopy, which provides no depth discrimination due to the conservation of energy at different axial planes. The corresponding confocal cases are plotted in Figure 10.10. By combining pump-probe techniques and confocal microscopy, greater background fluorescence rejection can be achieved. The narrowest width is with the confocal one-photon pump-probe case; the FWHM is 6.66μ , which is 0.783 of the width (8.51μ) is one-photon pump-probe and one-photon confocal.

A summary of spatial resolution comparisons between conventional and pump-probe microscopes is presented in Table 10.1.

10.3. Instrumentation and Methods

10.3.1. Pump-Probe Light Sources

The most important components in any ultrafast pump-probe experiment are the excitation light sources. In a frequency-domain pump-probe experiment, two high-repetition synchronous lasers with adjustable repetition rates are used. These lasers should have short pulse width, high peak power, and low phase jitter. The high peak power is required for efficient depletion of either the excited state or the

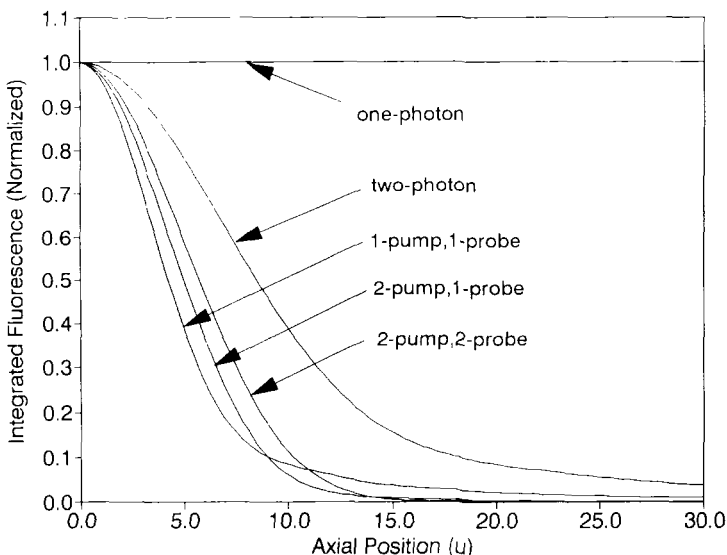


Figure 10.9. Integrated axial intensity distribution for pump-probe microscopy using one- and two-photon excitation.

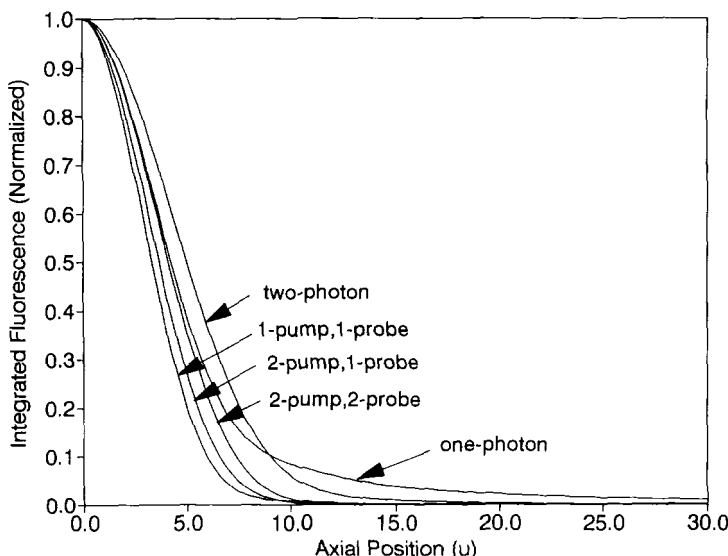


Figure 10.10. Integrated axial intensity distribution for pump-probe microscopy with confocal detection using one- and two-photon excitation.

ground state. The short pulse width ensures high harmonic content of the light sources. Low phase jitter is critical to maintain the harmonic content up to very high frequency.

For one-photon experiments, the two-mode locked neodymium-YAG (Nd-YAG, Antares, Coherent Inc., Santa Clara, CA) lasers are used. The Nd-YAG laser is either applied to the sample directly at 532 nm or synchronously pumps a DCM dye laser (Model 700, Coherent Inc.) to obtain wavelengths from 580 to 680 nm. The typical repetition rate of the YAG lasers is 76.2 MHz, but it can be easily adjusted within a range of 5 kHz. For the two-photon excitation experiment, we have used a titanium-sapphire laser (Mira 900, Coherent Inc.) pumped by an 8 W argon-ion laser (Innova 310, Coherent Inc.). A master synthesizer which generates a 10-MHz reference signal actively synchronizes the YAG lasers. For the passive mode-locked titanium-sapphire laser, the laser is used as the master clock of the system as previously described.⁽⁵⁴⁾

10.3.2. Optics for Absorption-Mode Measurement

The goal in the absorption measurement is to measure a modulation in the probe-beam intensity due to the pumping of the system under study. We must prevent the more intense pump beam from saturating the detector. Since the

Table 10.1. Comparison of Spatial Resolution between Conventional and Pump-Probe Microscopy with Nonconfocal and Confocal Detection Geometry

	Radial FWHM at $u = 0$ (v)	Axial FWHM $v = 0$ (u)	Radial cutoff frequency (normalized)	Axial cutoff frequency (normalized)	Axial Depth Discrimination (FWHM, u)
Nonconfocal					
1-photon	1.617	11.140	2.000	0.000	None
2-photon	2.320	16.040	2.000	0.500	17.020
1-photon pump/probe	1.160	8.020	4.000	1.000	8.510
2,1-photon pump/probe	1.339	9.250	4.000	1.000	10.010
2,2-photon pump/probe	1.653	11.440	4.000	1.000	11.500
Confocal					
1-photon	1.160	8.020	4.000	1.000	8.510
2-photon	1.339	9.250	4.000	1.000	10.010
1-photon pump/probe	0.952	6.580	6.000	1.500	6.660
2,1-photon pump/probe	1.043	7.210	6.000	1.500	7.330
2,2-photon pump/probe	1.167	8.070	6.000	1.500	8.250

pump and probe laser wavelengths are tuned within the absorption band of the chromophore, their wavelengths are close (or the same) and they cannot be isolated by their color. However, the pump and probe beams can be isolated spatially with the proper geometry. The apparatus schematic is presented in Figure 10.11. The intensity of both beams can be independently adjusted by using Glan-Thompson polarizers. The beams are then focused onto the sample via a 5-cm focal length lens. The sample is a free-flowing rhodamine-6G slab jet or a quartz flow cell. We used the jet to avoid difficulties from thermal lensing. The two beams are incident at the dye jet at a slightly different angle but are adjusted such that their focal point coincides within the diffraction-limited volume of the lens. A low-numerical-aperture lens is used in this case, but a higher numerical lens is desirable for better spatial localization. However, the requirement to spatially separate the pump and probe beams precludes using a high-numerical-aperture lens because of its large divergence angle. A narrow-band interference filter (Oriel) was used to cut out sample

fluorescence. The photodetector was a Hamamatsu R928 side-on photomultiplier tube.

10.3.3. Optics for Stimulated-Emission Mode

For stimulated emission, the pump and probe beams can be selected to be widely separated in wavelength. This opens up the opportunity to simplify the optical arrangement. In our implementation of pump–probe stimulated-emission spectroscopy, we have designed our instrument around a high-performance research microscope which features high excitation throughput and high collection efficiency (Figure 10.12).

Glan–Thompson polarizers are again used to control the laser power reaching the sample. The pump and probe laser beams are combined at a dichroic mirror (Chroma Technology Inc., Brattleboro, VT). The combined collinear laser beams enter the microscope system (Zeiss Axiovert 35, Thornwood, NY) via its epiluminescence light path. The combined beams are focused at the field aperture plane of the objective by a scan lens which ensures diffraction-limited focusing at the object plane. After recollimation by the tube lens and deflection by a second dichroic mirror, both beams are directed to the objective. The objective used in these studies is a well-corrected Zeiss 63X Plan–Neofluar with numerical aperture (NA) of 1.25. The pump and probe beams are focused onto a fluorescent sample, and a modulated stimulated-emission signal is generated. Quantum mechanics dictates that the stimulated-emission photons propagate in the same direction as the probe-beam photons, collinear with the pump-beam photons. The remaining excited-state molecules emit fluorescent photons isotropically. Since the sum of photons emitted in stimulated-emission mode and fluorescence mode is constant, equivalent information can be obtained by monitoring either the fluorescence photons or the stimulated-emission photons. We choose to detect the fluorescence photons as collected by the same objective in epi-illumination geometry. Since these fluorescence photons travel in the opposite direction of either the pump or probe beams, the fluorescence signal is largely free from interference of the much stronger signals. Signal-to-noise ratio is significantly enhanced with this detection method. The fluorescence signal transmitted through the objective, the second dichroic mirror, and two 640-nm bandpass filters is refocused onto the detector (R928 or R1104 photomultiplier tube, Hamamatsu, Bridgewater, NJ).

In the alignment of a typical pump–probe apparatus, the proper overlap of the pump and probe beams is often the most difficult and time-consuming procedure. The use of collinear beams in this geometry greatly simplifies the alignment procedure. Removing the scan lens at the entrance of the microscope allows the laser beams to exit the objective as collimated rays. Since the objective magnifies small angular deviation, collinearity can be easily observed and corrected.

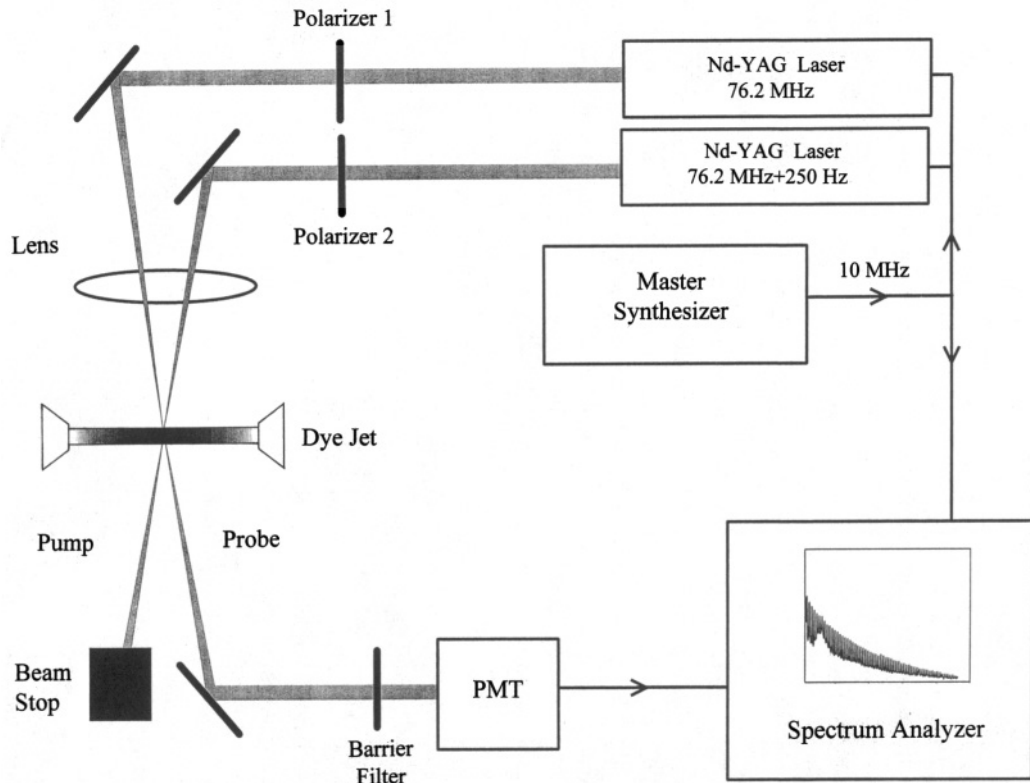


Figure 10.11. Schematics of pump-probe transient absorption spectrometer.

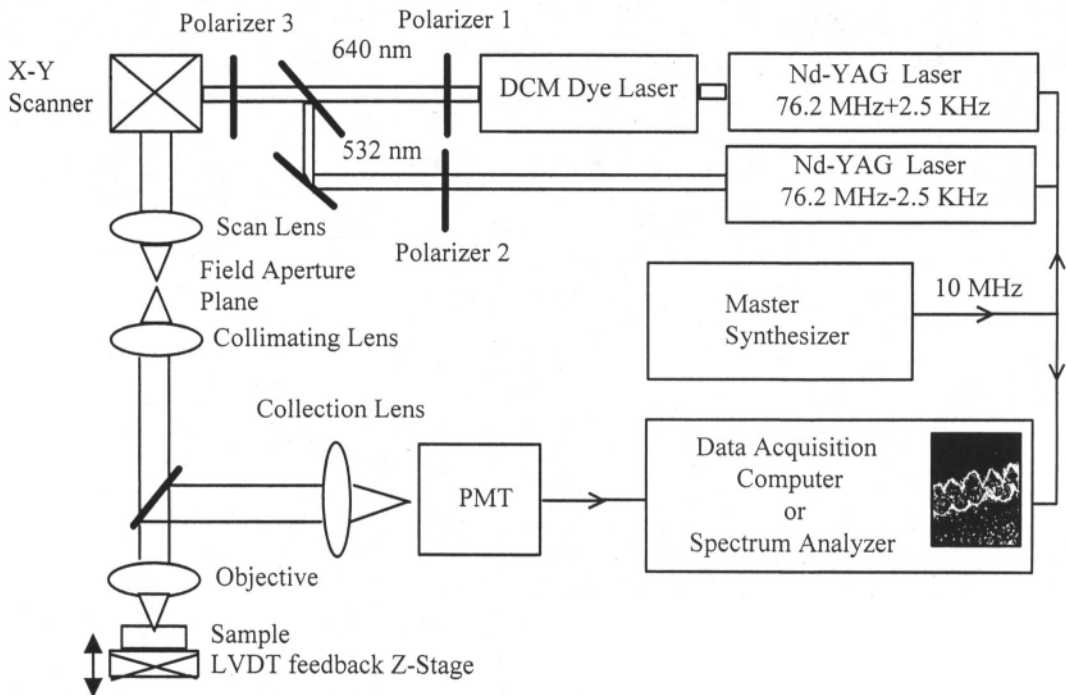


Figure 10.12. Schematics of pump-probe stimulated-emission spectrometer and microscope.

10.3.4. Scanner Optics for Microscopy

The modification of the pump–probe stimulated emission fluorometer for microscopy is relatively straightforward. This microscope uses beam scanning to obtain an image. An x-y scanner (Cambridge Technology, Watertown, MA) is inserted before the combined pump and probe beams enter the epi-illumination port of the microscope. The scanning mirrors can be driven by both analog and digital signals. We used the digital scheme to perform raster scans. The x and y scanners have a scanning range of ± 60 degrees; each angular position is specified by a 16-bit binary number, but only the middle 8 bits are used for scanning. This results in images composed of 256×256 pixels. The epi-illuminated light path of the microscope has been further modified to include a 10X eyepiece as the scan lens. It is positioned such that the x-y scanner is at its eyepoint while the field aperture plane is at its focal point. The eyepiece has the proper optical property to linearly transform the angular deviation of the input laser beam controlled by the x-y scanner to a lateral translation of the focal point position at the field aperture plane. Since the field aperture plane is telecentric to the object plane of the microscope objective, the movement of the focal point on the object plane is proportional to the angular deviation of the scanned beam.⁽⁵⁵⁾

For normal operation the pixel spacing in the images was $0.14 \mu\text{m}$. A smaller stepping size of $0.035 \mu\text{m}$ can be achieved for high-resolution experiment such as PSF measurements. The smaller step size was generated by specifying bits 1–9 instead of bits 3–11 of the scanner driver.

For z-sectioning studies it was necessary to vary the relative distance between the objective and the sample. Axial displacement of the objective is controlled by a stepping motor coupled to the objective manual adjustment mechanism and monitored by a linear variable differential transformer (LVDT, Schaevitz Engineering, Camden, NJ). This control system is designed to have a position resolution of $0.2 \mu\text{m}$ over a total range of $200 \mu\text{m}$.

10.3.5. Signal Detection and Processing

With pulsed lasers the frequency-domain heterodyning method samples the complete temporal dynamics simultaneously. In contrast, the time-domain technique requires a mechanical delay line, and time evolution is sampled on a point-by-point basis. In the frequency domain the fundamental of the excitation frequency is mapped to the fundamental of the cross-correlation frequency. The higher harmonic responses are mapped to the harmonics of the cross-correlation frequency. The cross-correlation frequency can be chosen for convenience or to avoid noisy spectral regions. A constraint on this flexibility is that one must select

a sufficiently low cross-correlation frequency in order to observe very high harmonics. For spectroscopy, a cross-correlation frequency from tens to hundreds of Hertz is often picked. For microscopy, 5-kHz cross-correlation is used to maintain a reasonable frame acquisition rate.

The full spectrum of the cross-correlated signal as detected by the PMT can be conveniently collected by a HP 35655A spectrum analyzer (Hewlett Packet, Rolling Meadows, IL) synchronized to the cross-correlation frequency. All synthesizers and detectors were phase-locked to the mode-locking frequency synthesizers. The low-noise spectrum analyzer is a convenient instrument to obtain the entire frequency-domain spectra at once.

For microscopic applications the spectrum analyzer is less convenient for collecting a large matrix of data and displaying it. Hence, the signal is sent to a computer for custom analysis. The analog photomultiplier tube (PMT) signal is electronically filtered by a preamplifier (Stanford Research, Sunnyvale, CA) to isolate the cross-correlation signal. The filtered signal is then digitized by a 100-kHz, 12-bit sampling digitizer (A2D-160, DRA Laboratories, Sterling, VA). The Shannon sampling theorem dictates that at least two points per waveform need to be acquired to determine a sinusoidal signal. The determination of the n th harmonic requires getting at least $2n$ time points within each time period of the cross-correlation frequency. For this first-generation pump-probe microscope, only the first-harmonic signal was acquired. In this case, only two points at each cross-correlation period are needed, but we typically digitize four points per waveform to reduce harmonic noise. With four waveforms integrated per pixel, a pixel dwell time of 800 μ s and a corresponding frame acquisition time of 52 s result for 5-kHz cross-correlation. After digital processing, the amplitude and phase of the cross-correlation signal are then displayed and stored by the data acquisition computer.

10.4. Spectroscopy Applications and Performance

10.4.1. Pump-Probe Absorption Spectroscopy

As a demonstration of frequency-domain absorption spectroscopy using the pump-probe technique, we have studied the fluorescence decay of rhodamine-6G in ethylene glycol.⁽⁵⁶⁾ Two YAG lasers operating at 532 nm are used, and the repetition rates are offset by 40 Hz. We have measured a single-component lifetime of 3.6 ns, consistent with results using conventional techniques. Note that this is a measurement of the ground-state recovery; we do not observe the fluorescence emission. The modulation data are presented in Figures 10.13 and 10.15. The excellent signal-to-noise ratio suggests that we should be able to detect

significantly smaller signals without being overburdened by noise. The signal-to-noise consideration is important for measuring shorter lifetimes. We are able to achieve excellent resolution through signal averaging. Typically, we took about 500 samplings for each figure. Since we trigger each measurement from the same phase-locked electronics that generate the laser pulses, any random noise was averaged out. We still see some systematic noise, perhaps due to cross talk between the two lasers or other electronic components, but this noise does not seem to be significant.

The measurement of the phase proved to be somewhat more difficult than the modulation. We see much more noise in our signal. The phase of each of the harmonics is still clearly resolvable, however. We adjusted the base line of the data so that the high-frequency data approach the 90° phase. The data then yield the same lifetime as the modulation measurements. Figures 10.14 and 10.15 show this phase data.

We also investigated the upper limit of frequencies observed for each decay. We can see harmonics up to 12.2 GHz. Figure 10.16 shows the resolution of these higher-frequency harmonics. This limit is due to the long lifetime of the rhodamine and the width of the laser pulses and is not an inherent limit of the apparatus.

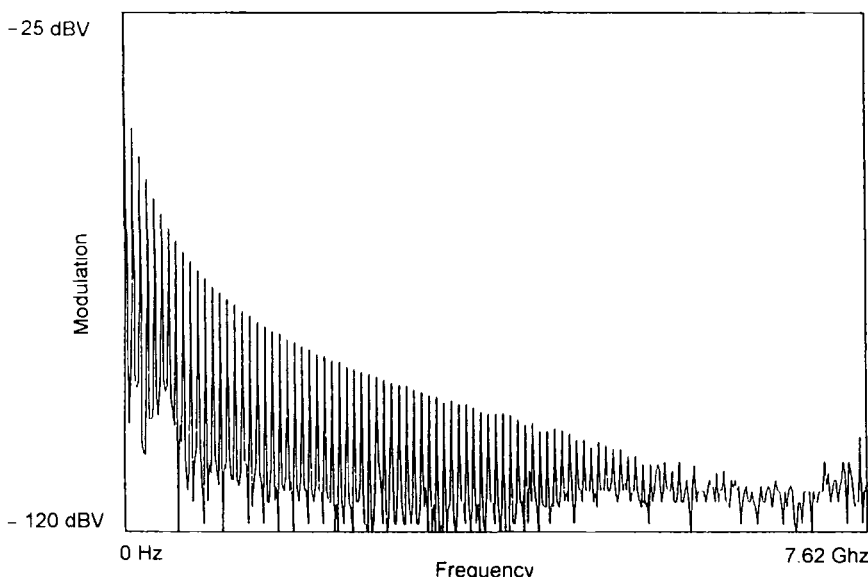


Figure 10.13. Modulation versus cross-correlation frequency of rhodamine-6G in ethylene glycol as detected by frequency-domain transient absorption pump-probe technique.

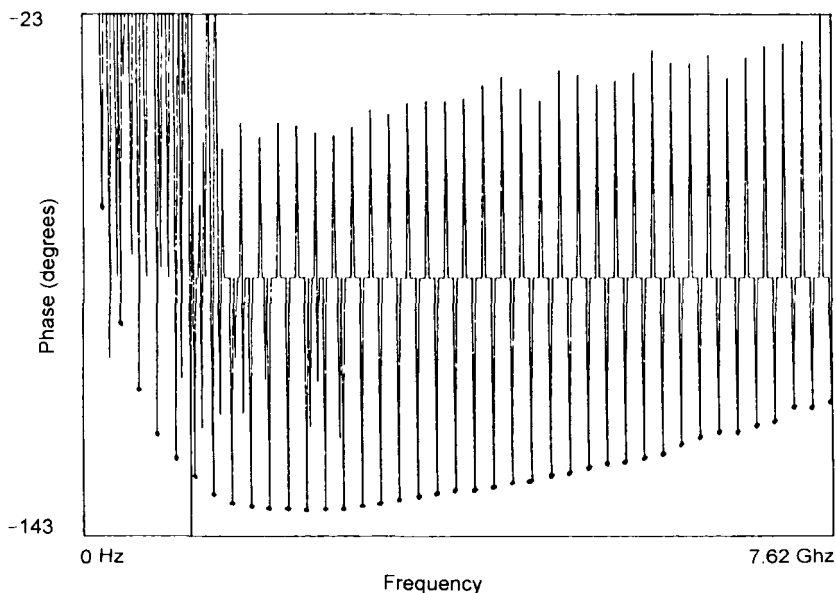


Figure 10.14. Phase shift versus cross-correlation frequency of rhodamine-6G in ethylene glycol as detected by frequency-domain transient-absorption pump-probe technique. The dots identify the phase values of interest.

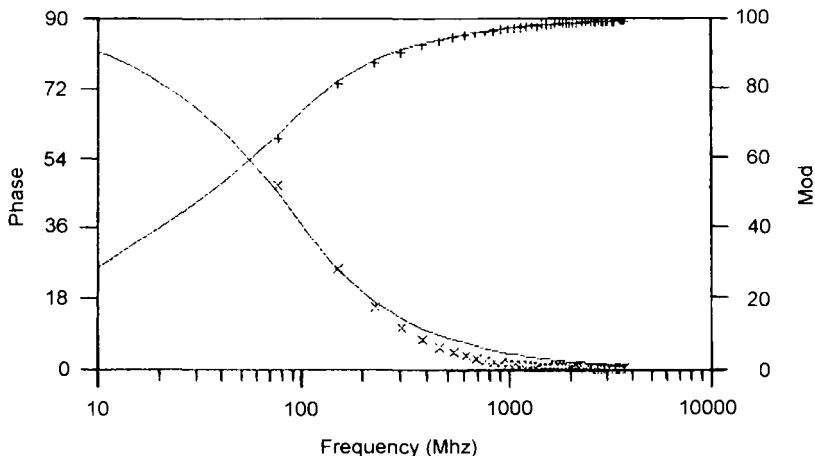


Figure 10.15. Phase and modulation signals calculated from the data in Figures 10.12 and 10.13. Curves represent a single exponential fit of 3.6 ns.

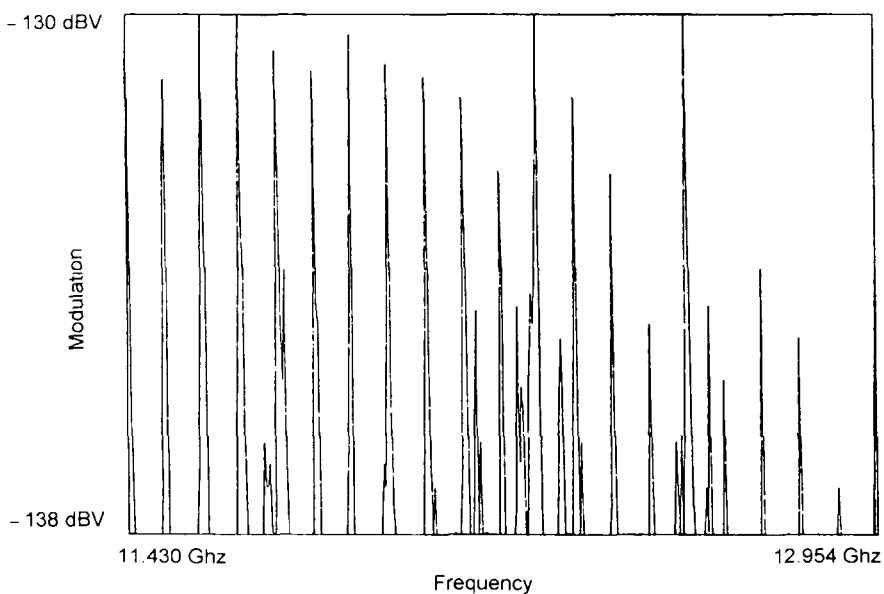


Figure 10.16. Logarithmically displayed harmonic amplitudes centered around 4 kHz with $\Delta f = 25$ Hz. The 4-kHz center frequency corresponds to the 160th harmonic of the 76.2-MHz probe-beam frequency, i.e., 12.2 GHz in real time.

10.4.2. Stimulated-Emission Pump-Probe Spectroscopy

10.4.2.1. One-Photon Stimulated-Emission Spectroscopy

Performing ultrafast pump-probe Spectroscopy in the stimulated-emission mode has received much interest lately.⁽⁵⁷⁻⁵⁹⁾ The dynamics of rhodamine-B in water was studied to characterize the time resolution of stimulated-emission pump-probe Spectroscopy. In this case, the 532-nm YAG pump laser is operated at 76.2 MHz, and the 610-nm DCM probe laser has repetition frequency of at 76.2 MHz + 210 Hz. Good signal-to-noise ratio at high cross-correlation harmonics of 8 GHz can be obtained with pump laser power of 35.6 μ W and probe laser power of 2.75 mW. The fluorescence signal was collected and optically filtered in the same manner as for imaging, and the photomultiplier signals were fed directly into the spectrum analyzer where the harmonics were displayed and stored at a bandwidth of 16 Hz. The result of this measurement is presented in Figure 10.17. A fluorescence lifetime of 1.4 ns was measured, which agrees with the lifetime measured with a conventional fluorometer.

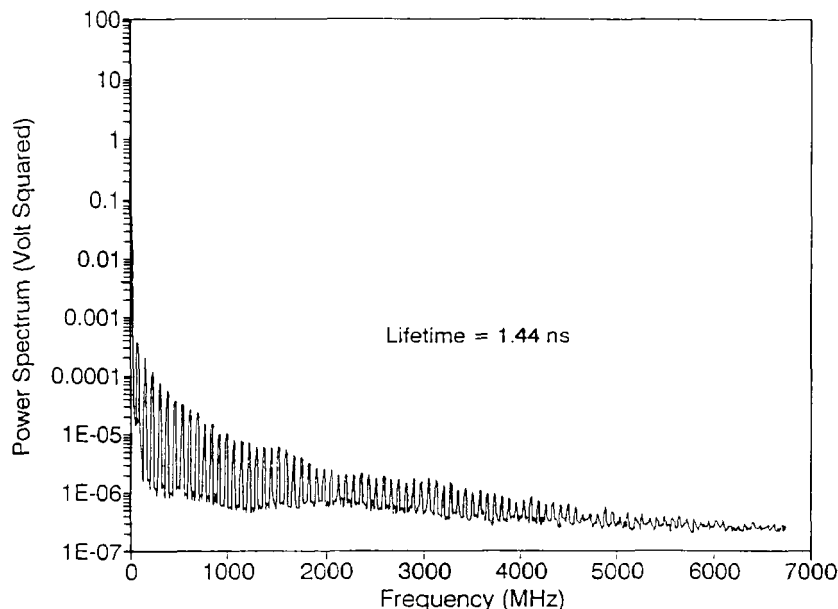


Figure 10.17. Modulation versus excitation frequency for rhodamine-B in water as detected by frequency-domain stimulated-emission pump-probe technique.

10.4.2.2. Two-Photon Stimulated-Emission Spectroscopy

One of the most important variants of pump-probe Spectroscopy is the introduction of two-photon excitation.⁽⁶⁰⁾ The advantages of two-photon excitation in time-resolved microscopy have been discussed in detail elsewhere.^(61,62) In the context of pump-probe spectroscopy, the wavelength separation of the two-photon mode is particularly relevant. First, the small separation between the pump and probe wavelengths has made absorption measurement difficult in the microscope as previously discussed. On the other hand, if either the pump or probe beam operates in the two-photon mode, the probe beam can be effectively isolated due to its color difference. Collinear optical geometry will become feasible and allow relatively easy adaptation to a microscope. Second, the large color separation allows either the pump- or probe-beam wavelength to be varied without overlapping and interfering with the detection wavelength. This feature should facilitate future wavelength-dependent experiments. Third, the combination of two-photon excitation and the pump-probe method would further improve spatial resolution in microscopy.

Although two-photon excitation has been used extensively in femtosecond spectroscopy of solid-state or solution systems,^(63,64) it has rarely been applied in

biology. Stimulated-emission measurement using two-photon pump and one-photon probe configuration has been used to measure the lifetime of 3.8 mM 4'-6-diamidino-2-phenylindole (DAPI) in ethanol. A Ti-sapphire laser tuned to 790 nm with a power of 20 mW is the excitation source. A Nd-YAG laser at 532 nm at a power of 2.5 mW causes stimulated emission at the sample. Because the Ti-sapphire laser has a repetition rate of 80 MHz and the YAG laser has a repetition rate of 76.2 MHz, the cross-correlation signal appears at harmonics of 3.8 MHz. For more accurate analysis of this signal, it is further down-translated to 210 Hz by a superheterodyning scheme using a gated PMT at 3.8 MHz + 210 Hz. The frequency spectrum of the cross-correlated signal is presented in Figure 10.18. Harmonics up to 5 GHz can be obtained by using a spectrum analyzer with a bandwidth of 16 Hz. The lifetime of DAPI has been determined to be 2.35 ns, which is consistent with literature values.⁽⁶⁵⁾

10.5. Applications and Performances of Pump-Probe Fluorescence Microscope

All the experiments in the stimulated-emission pump-probe microscope are performed with one YAG laser as the pump source and one DCM laser at 610 nm as the probe source. The repetition rates of these lasers are offset by 5 kHz.

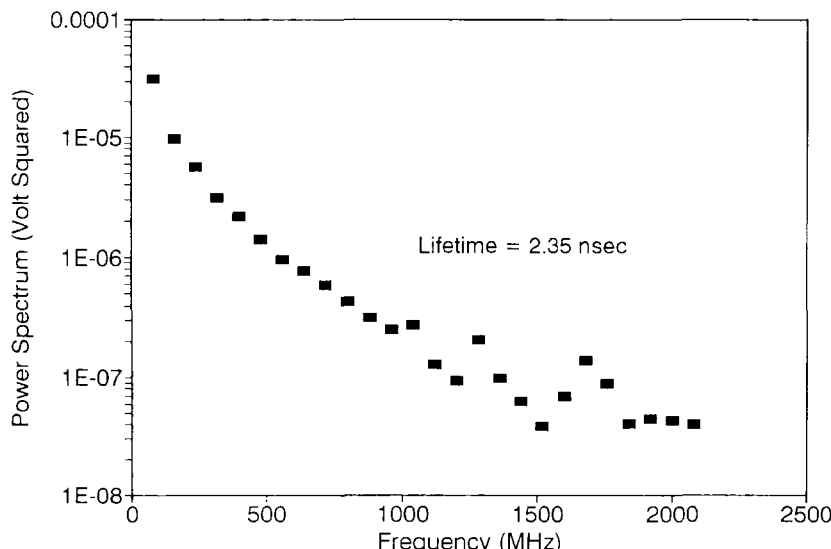


Figure 10.18. Modulation versus excitation frequency for DAPI in ethanol using one-photon pump, two-photon probe-stimulated emission method.

10.5.1. Linearity of Pump–Probe Signal Response on Laser Power Level

We have investigated the dependence of the cross-correlation signal on the pump and probe laser powers. As the pump or probe laser power is increased, eventually the signal will saturate due to depletion of chromophores in the focal volume available for the pump–probe process. An off-focal signal can begin to contribute significantly, resulting in broadening of the PSF and deterioration of the spatial resolution. It is important to determine the linear response region in pump–probe microscopy.

For the saturation test, aqueous rhodamine-B (4.16 mM) sealed between the cover slip and a microscope slide was used. The test was performed in two steps. First, the fluorescence saturation effect due to the pump source is determined by focusing a different intensity of the excitation laser onto the rhodamine-B sample and recording the PMT output induced by the fluorescence. The result is shown in Figure 10.19a, where the effect of saturation is evident starting at about $10\text{ }\mu\text{W}$. Second, the probe laser was also focused onto the rhodamine-B sample, and the first-harmonic amplitude at 5 kHz was recorded at pump laser settings of 1.75 , 3.18 , and $5.12\text{ }\mu\text{W}$, all of which are in the linear region of the fluorescence curve in Figure 10.18a. The three calibration curves are plotted in Figure 10.19b along with best linear fits, using the first five points of each data set. The slopes of the three calibration curves are plotted as a function of pump power in Figure 10.19c. Figure 10.19b shows that the pump–probe signal deviates from linearity, starting at about 7 mW of the probe laser at 640 nm . The linearity in the slope plot of Figure 10.18c confirms that the cross-correlation signal is proportional to the intensity of the pump and probe sources if the power levels used do not exceed $10\text{ }\mu\text{W}$ (pump) and 7 mW (probe). These values also represent the upper limits in power levels used in our experiments. Note that the beginning power for the probe laser saturation is roughly two orders of magnitude higher than that for the pump laser. The difference in power may be due to several factors. First, the absorption and stimulated-emission cross sections may be quite different at the wavelengths chosen. For rhodamine-6G the absorption (at 532 nm) and stimulated emissions (at 640 nm) are about $2.6 \times 10^{-16}\text{ cm}^2$ and $4.0 \times 10^{-17}\text{ cm}^2$ respectively.⁽⁶⁶⁾ The difference in cross sections can contribute to an order-of-magnitude-higher probe laser power, which is needed to observe saturation effects. Other factors such as pump- and probe-beam overlapping efficiency, molecular rotational effects, and quantum efficiency can also contribute to the higher probe laser power needed to observe saturation effects in the cross-correlation signal.

The linearity calibration data are only valid for rhodamine-B in water at the wavelengths chosen. The estimation of the power for pump saturation may be extended to other chromophores if their extinction coefficients are known. To estimate the probe-beam saturation power for other chromophores, their cross

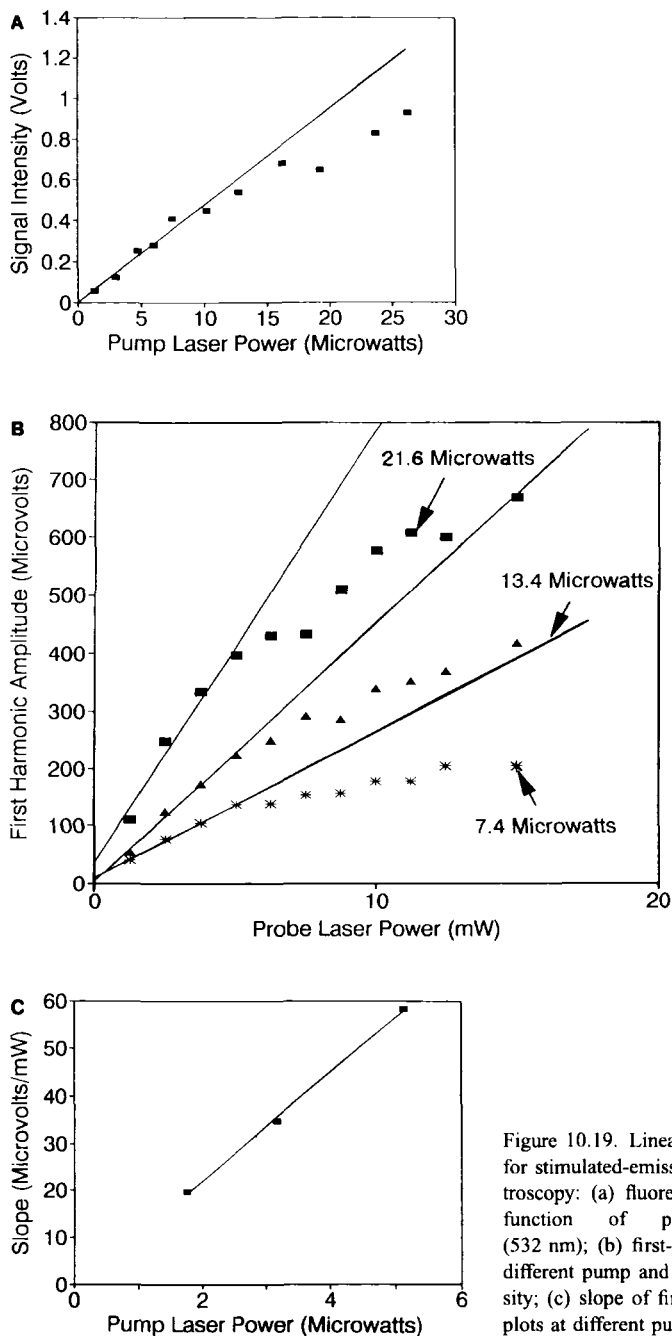


Figure 10.19. Linearity of signal response for stimulated-emission pump-probe spectroscopy: (a) fluorescence generated as a function of pump-beam intensity (532 nm); (b) first-harmonic amplitude at different pump and probe (640 nm) intensity; (c) slope of first-harmonic amplitude plots at different pump powers.

sections relative to that of rhodamine-B in water need to be determined. Since rhodamine-B has relatively strong absorption compared to many other dyes, to avoid PSF broadening in imaging experiments where the chromophores' spectroscopic properties are not always known, the power levels chosen were below 10 μW for the pump beam and 7 mW for the probe beam, both in the linear region for rhodamine-B's pump-probe signal.

10.5.2. Experimental Verification of Pump–Probe Microscopy Resolution

To characterize the radial and axial spatial resolution of the system, orange fluorescent latex spheres of 0.28 μm in diameter (absorption maximum 530 nm, emission maximum 560 nm; Molecular Probes, Eugene, OR) were imaged. These spheres were immobilized between a cover slip and a flat microscope slide with Fluoromount G mounting medium (Southern Biotechnology, Birmingham, AL). The slide was left to dry at room temperature for one day before the spheres were imaged. The size of the spheres was uniform and calibrated by the manufacturer, using electron microscopy. Since the dimensions of the spheres are comparable to the FWHM of the theoretical pump–probe PSF at the wavelengths chosen, the fluorescence intensity measured is compared with the convolution of the theoretical PSF to the sphere size given by

$$I_{\text{sphere}}(z, r) = \frac{I(z, r)I'(z, r) \otimes S(z, r)}{I(0, 0)I'(0, 0) \otimes S(0, 0)} \quad (10.36)$$

where $S(z, r)$ characterizes the physical dimension of the spheres in the axial (z) and radial (r) dimensions; it has the value of 1 for $\sqrt{z^2 + r^2} \leq 0.14 \mu\text{m}$, 0 otherwise. Data from 36 spheres were analyzed, and the experimental and theoretical intensity distributions are plotted in Figure 10.20. While the axial data agree well with the Fraunhofer diffraction theory, there is slight deviation of the radial data from the theoretical prediction. This deviation is probably due to slight misalignment of the pump and probe lasers. Other possible effects include chromatic aberrations and polarization effect of the focusing objective.

10.5.3. Time-Resolution of Pump–Probe Microscopy

We obtained lifetime-resolved images of a mixture of 2.3 μm orange and 1.09 μm Nile red (absorption maximum 520 nm, emission maximum 580 nm) fluorescent latex spheres (Molecular Probes). The two types of spheres were known to have different lifetimes. The measured lifetimes using standard frequency-domain phase fluorometry are 2.7 ns for 1.09- μm spheres and 4.3 ns

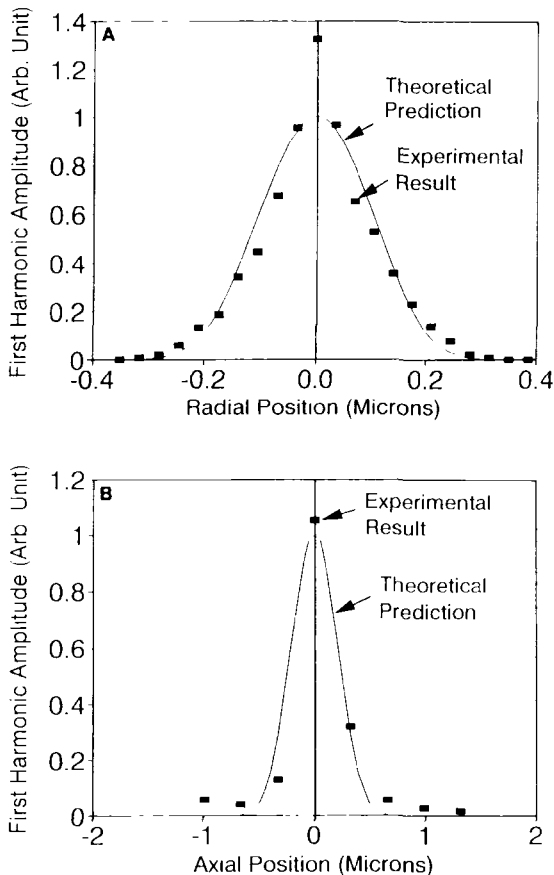


Figure 10.20. A determination of pump-probe microscopy point-spread function by imaging 0.28- μm orange fluorescent latex spheres: (a) radial intensity response; (b) axial intensity response.

for 2.3- μm spheres. In our images, the first-harmonic amplitude and phase are measured in (Figure 10.21). The phase image was referenced to that of a 4.16-nm rhodamine-B slide for the purpose of lifetime calculations. From the histograms of lifetime values, the lifetimes of the spheres were determined to be 3.2 ± 1.0 ns (1.09 μm) and 4.2 ± 1.4 ns (2.3 μm). These values agree within error to the results obtained with a conventional frequency-domain phase fluorometer.

10.5.4. Comparison between Conventional Microscopy and Pump-Probe Fluorescence Microscopy in Human Erythrocytes and Mouse Fibroblasts

To demonstrate the superior spatial resolution achieved by pump-probe fluorescence microscopy compared to conventional one-photon microscopy, we

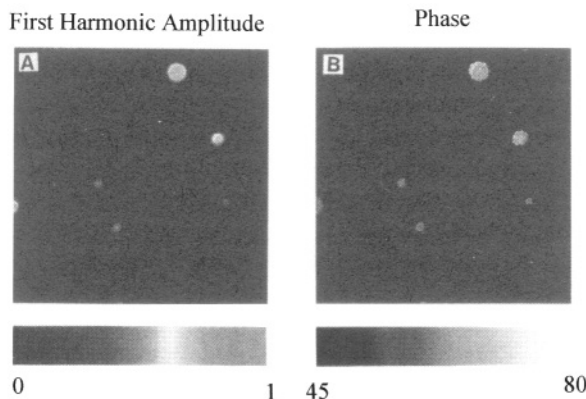


Figure 10.21. Using pump-probe microscopy, time-resolved images of 1.09- μm Nile red ($\tau_p = 3.2 \pm 1.0$ ns) and 2.3- μm orange ($\tau_p = 4.2 \pm 1.4$ ns) fluorescent latex spheres were obtained: (a) image of normalized first-harmonic amplitude; (b) image of phase values in degrees.

imaged two commonly used biological systems: human erythrocytes and mouse fibroblast cells.

The human erythrocytes were labeled with the membrane dye rhodamine-DHPE (Molecular Probes). A small amount of erythrocytes was mixed with Hanks balanced salt buffer (HBSB with NaHCO_3) to make a 1-mL mixture. The solution was spun at 1000 rpm for 5 min before the top buffer was removed. The erythrocytes were then shaken and diluted to 1 mL with HBSB. Six microliters of rhodamine-DHPE (at 5 mg/rnL DMSO) were injected into the solution containing the cells and allowed to incubate for 30 min. After incubation, the cells were again spun down and washed with HBSB two more times to remove residual dye before being mounted on a microscope slide. Nail polish was used to seal the cover slip.

The mouse fibroblast cells were grown on a cover slip. For fixation, they were placed in acetone for 5 min and allowed to air-dry. Then a few drops of a solution containing 10 $\mu\text{g/mL}$ of rhodamine-DHPE (diluted in PBS, 0.1% Triton X-100) were placed onto the cover slip and incubated for 30 min. After incubation, the dye was removed by rinsing the cover slip in PBS buffer twice before mounting onto a flat microscope slide. For mounting, a drop of the mounting medium Prolong (Molecular Probes) was placed between the cover slip and a slide. In a few hours, the mounting medium dries and the slide was ready for viewing.

The images at the first harmonic of 5 kHz are presented in Figure 10.22 along with the corresponding one-photon images. The one-photon images were obtained by blocking the probe beam and recording only the fluorescence intensity due to the pump beam. In this manner, the cells were not moved relative to

the microscope objective, and a comparison between the two techniques can be made. From the image of the erythrocytes, it is apparent that the pump-probe images can better reject the fluorescence from off-focal planes. The one-photon images show much more background fluorescence from the central region of the erythrocytes than does pump-probe microscopy. Similarly, the pump-probe image of the mouse fibroblast shows superior spatial resolution compared to the corresponding one-photon image by revealing the finer details of the cell's structure.

10.5.5. Multiple-Dye-Labeling Application

We examined mouse fibroblast cells doubly labeled with the nucleic acid stain ethidium bromide (EB) and the membrane stain rhodamine-DHPE (Molecular Probes). The pump-probe image is shown in Figure 10.23. These cells

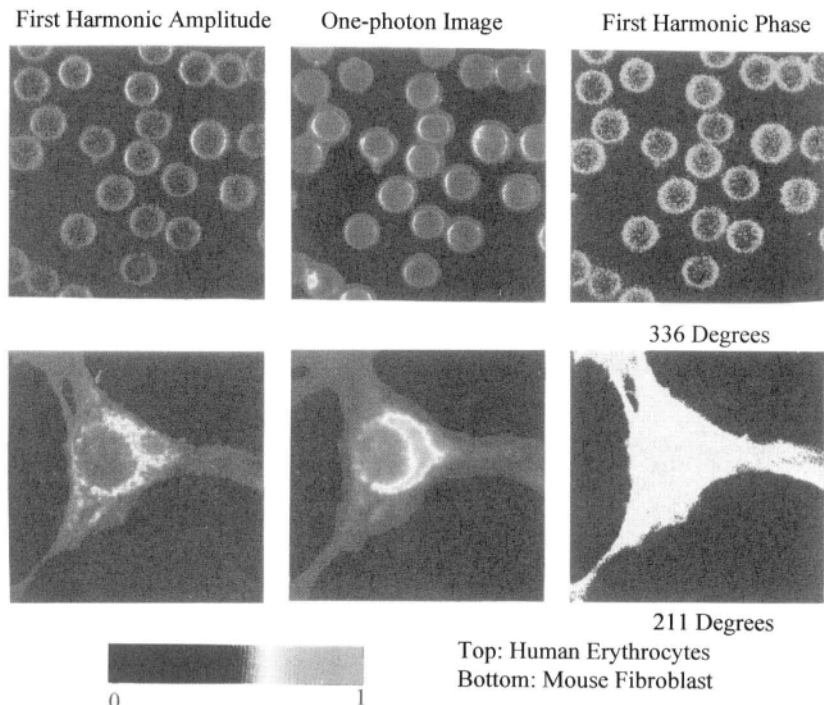


Figure 10.22. Normalized first-harmonic amplitude images using pump-probe microscopy is compared with intensity images' using conventional laser scanning microscopy: (Top) human erythrocytes; (Bottom) a mouse fibroblast cell (staining: rhodamine-DHPE).

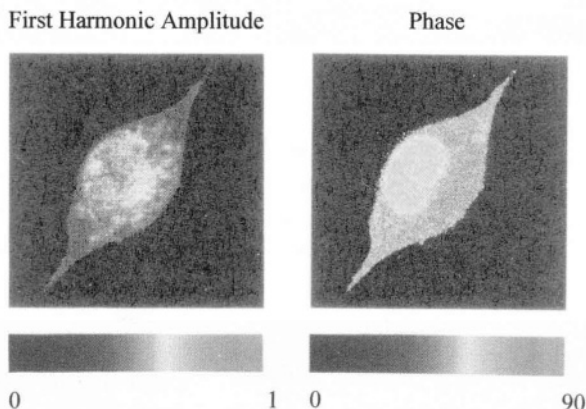


Figure 10.23. Time-resolved images of a mouse fibroblast cell labeled with rhodamine-DHPE and ethidium bromide (membrane and cytoplasm: $\tau_p = 2.0 \pm 0.5$ ns; nucleus: $\tau_p = 6.6 \pm 4.8$ ns). Images of normalized first-harmonic amplitude and phase in degree were shown.

(grown on a cover slip) are fixed and stained in the same manner as the mouse fibroblast cell. The only difference is that the cover slip was incubated first with EB (1 mM PBS, 0.1% Triton X-100) for 30 min and then stained by rhodamine-DHPE (10 $\mu\text{g}/\text{mL}$ in PBS, 0.1% Triton X-100) for another 30 min before it was rinsed twice in PBS and mounted for viewing. The lifetimes of the cytoplasmic and nuclear region were determined from the phase image. The reference phase was obtained from a slide of 4.16-mM rhodamine-B in water. It was found that the average and the full width at half-maximum of lifetime histograms in the cytoplasm and nucleus are 2.0 ± 0.5 ns and 6.6 ± 4.8 ns, respectively. For comparison, the lifetime of rhodamine-B in water was determined from standard frequency-domain phase fluorometry to be 1.44 ns. Furthermore, the lifetimes of the unbound EB and bound EB to nucleic acid are 1.7 and 24 ns, respectively. Our measurements of lifetime in the cytoplasm show that there was significant staining of cytoplasmic structures by rhodamine-DHPE. The average lifetime in the nucleus is between that of bound and unbound EB, indicative of the fact that both populations of the chromophores exist in the nucleus. Nonetheless, the lifetime contribution from bound EB is sufficient to distinguish the different lifetimes in the nucleus and cytoplasm as demonstrated by the phase image.

This example demonstrates one advantage of lifetime-resolving imaging. From intensity imaging, it is difficult to distinguish the cytoplasmic and nuclear regions since these chromophores have similar emission spectra. With lifetime imaging, sharp contrast between the two species of chromophores can be generated.

10.6. Conclusion

We have demonstrated the first application of the stimulated-emission technique to fluorescence microscopy. By measuring the fluorescence signal at the cross-correlation frequency, pump-probe fluorescence microscopy can provide superior spatial resolution and effective off-focal background rejection compared to conventional one-photon microscopy. Due to the wavelengths used in the one-photon pumping and probing processes, this technique has better spatial resolution than two-photon excitation microscopy, and comparable spatial resolution to confocal microscopy. Furthermore, imaging at low-frequency harmonics eliminates the need of using a fast optical detector in time-resolved imaging of biological systems. The technical development of pump-probe microscopy is still in its early stages. Substantial future improvements are expected. The implementation of transient absorption mode in pump-probe microscopy will allow ground-state kinetics to be directly monitored. The addition of two-photon excitation would improve the microscope spatial resolution as well as making wavelength-dependent spectroscopy possible. The implementation of the pump-probe technique in the time domain would make the microscopy alignment and automation more difficult but may take time-resolved microscopy solidly into the femtosecond time scale. The pump-probe microscopy technique has the potential to radically transform the field of time-resolved microscopy.

Acknowledgment

We would like to thank Dr. Matt Wheeler, Dr. Laurie Rund, Ms. Linda Grum, and Ms. Melissa Izard for providing us with mouse fibroblast cells. This work was supported by the National Institute of Health (RR03155).

References

1. M. A. El-Sayed, I. Tanaka, and Y. Molin (eds.), *Ultrafast Process in Chemistry and Photobiology*, Blackwell Science, Oxford, England (1995).
2. W. Kaiser (ed.) *Ultrashort Laser Pulses*. Springer-Verlag, New York (1993).
3. R. M. Hochstrasser and C. K. Johnson, Biological processes studied by ultrafast laser techniques, in: *Ultrafast Laser Pulses* (W. Kaiser, ed.), pp. 357–417, Springer-Verlag, New York (1988).
4. G. Marriott, R. M. Clegg, D. J. Arndt-Jovin, and T. M. Jovin, Time- resolved imaging microscopy, *Biophys. J.* 60, 1347–1387 (1991).
5. E. P. Buurman, R. Sanders, A. Draaijer, H. C. Gerritsen, J. J. F. Van Veen, P. M. Houpt, and Y. K. Levine, Fluorescence lifetime imaging using a confocal laser scanning microscope, *Scanning* 14, 155–159 (1992).

6. J. R. Lakowicz, H. Szmacinski, K. Nowaczyk, and M. L. Johnson, Fluorescence lifetime imaging of calcium using Quin-2, *Cell Calcium* 13, 131–147 (1992).
7. D. K. Evans (ed.), *Laser Applications in Physical Chemistry*, Marcel Dekker, New York (1989).
8. G. R. Fleming, *Chemical Applications of Ultrafast Spectroscopy*, Oxford University Press, New York (1986).
9. F. E. Lytle, R. M. Parrish, and W. T. Barnes, An introduction to time-resolved pump/probe Spectroscopy, *Appl. Spectrosc.* 39, 444–451 (1985).
10. J. Zhou, G. Taft, C. P. Huang, I. P. Christov, H. C. Kapteyn, and M. M. Murnane, Sub-10 fs pulse generation in Ti: sapphire: capabilities and ultimate limits, in: *Ultrafast Phenomena IX* (P. F. Barbara, W. H. Knox, G. A. Mourou, and A. H. Zewail, eds.), pp. 39–40, Springer-Verlag, Berlin (1994).
11. P. A. Elzinga, R. J. Kneisler, F. E. Lytle, G. B. King, and N. M. Laurendeau, Pump/probe method for fast analysis of visible spectral signatures utilizing asynchronous optical sampling, *Appl. Opt.* 26, 4303–4309 (1987).
12. P. A. Elzinga, F. E. Lytle, Y. Jian, G. B. King, and N. M. Laurendeau, Pump/probe spectroscopy by asynchronous optical sampling, *Appl. Spectros.* 41, 2–4 (1987).
13. J. A. Dix and A. S. Verkman, Pyrene excimer mapping in cultured fibroblasts by ratio imaging and time-resolved microscopy, *Biochemistry* 29, 1949–1953 (1992).
14. S. M. Keating and T. G. Wensel, Nanosecond fluorescence microscopy: emission kinetics of fura-2 in single cells, *Biophys. J.* 59, 186–202 (1990).
15. J. R. Lakowicz, H. Szmacinski, K. Nowaczyk, K. W. Berndt, and M. L. Johnson, Fluorescence lifetime imaging, *Anal. Biochem.* 202, 316–330 (1992).
16. M. vandeVen M. and E. Gratton, in: *Optical Microscopy: Emerging Methods and Applications*, Academic Press, New York, (1993); pp. 373–402.
17. W. W. Mantulin, T. French, and E. Gratton, Optical imaging in the frequency domain, in: *Proc. SPIE, Medical Lasers and Systems II*, Vol. 1892 (D. M. Harris, ed.), pp. 158–166, SPIE, Bellingham (1993).
18. P. T. C. So, T. French, and E. Gratton, A frequency domain time-resolved microscope using a fast-scan CCD camera, in: *Proc. SPIE, Time-Resolved Laser Spectroscopy IV*, Vol. 2137 (J. R. Lakowicz, ed.), pp. 83–92, SPIE, Bellingham (1994).
19. J. R. Lakowicz, H. Szmacinski, and M. L. Johnson, Calcium imaging using fluorescence lifetimes and long-wavelength probes, *J. Fluoresc.* 2, 47–62 (1992).
20. D. W. Piston, D. R. Sandison, and W. W. Webb, Time-resolved fluorescence imaging and background rejection by two-photon excitation in laser scanning microscopy, in: *Proc. SPIE*, Vol. 1640, pp. 379–389, SPIE, Bellingham (1992).
21. T. Oida, Y. Sako, and A. Kusumi, Fluorescence lifetime imaging microscopy (filmscopy), *Biophys. J.* 64, 676–685 (1993).
22. C. G. Morgan, A. C. Mitchell, and J. G. Murray, Prospects for confocal imaging based on nanosecond fluorescence decay time, *J. Microsc.* 165, 49–60 (1991).
23. R. Sanders, A. Draaijer, H. C. Gerritsen, P. M. Houpt, and Y. K. Levine, Quantitative pH imaging in cells using confocal fluorescence lifetime imaging microscopy, *Anal. Biochem.* 227, 302–308 (1995).
24. A. Draaijer, R. Sanders, and H. C. Gerritsen, Fluorescence lifetime imaging, a new tool in confocal microscopy, in: *Handbook of Biological Confocal Microscopy* (J. Pawley, ed.), pp. 491–505, Plenum, New York (1995).
25. H. Schneckenburger, P. Gessler, and I. Pavenstadt-Grupp, Measurement of mitochondrial deficiencies in living cells by microspectrofluorometry, *J. Histochem. Cytochem.* 40, 1573–1578 (1992).

26. H. Schneckenburger and K. Koenig, Fluorescence decay kinetics and imaging of NAD(P)H and flavins as metabolic indicators, *Opt. Eng.* 31, 1447–1451 (1992).
27. K. Koenig and H. Schneckenburger, Laser-induced autofluorescence for medical diagnosis, *J. Fluoresc.* 4, 17–40 (1994).
28. E. Voss, Anti-fluorescein antibodies as structure-function models to examine fundamental immunological and spectroscopic principles, *Comm. Mol. Cell Biophys.* 6, 197–221 (1990).
29. T. French, P. T. C. So, D. J. Weaver, Jr., T. Coelho-Sampaio, E. Gratton, E. W. Voss, Jr., and J. Carrero, Two-photon fluorescence lifetime image microscopy of macrophage-mediated antigen processing, *J. of Microscopy* 185, 339–353 (1997).
30. C. Y. Dong, P. T. C. So, T. French, and E. Gratton, Fluorescence lifetime imaging by asynchronous pump-probe microscopy, *Biophys. J.* (in press).
31. C. Y. Dong, P. T. C. So, and K. Gratton, Spatial resolution in scanning pump-probe fluorescence microscopy, *Appl. Opt.* (in press).
32. Y. W. Jia, D. M. Jonas, T. H. Joo, Y. Nagasawa, M. J. Lang, and G. R. Fleming, Observation of ultrafast energy transfer from the accessory bacteriochlorophylls to the special pair in photosynthetic reaction centers, *J. Phys. Chem.* 99, 6263–6266 (1995).
33. M. Du, X. L. Xie, L. Mets, and G. R. Fleming, Direct observation of ultrafast energy transfer process in light harvesting complex, *J. Phys. Chem.* 98, 4736–4741 (1994).
34. S. Savikhin, P. I. Vannoort, Y. W. Zhu, S. Lin, R. E. Blankenship, and W. S. Struve, Ultrafast energy transfer in light-harvesting chlorosomes from the green sulfur bacterium *Chlorobium tepidum*, *Chem. Phys.* 194, 245–258 (1995).
35. T. Q. Lian, B. Locke, Y. Kholodenko, and R. M. Hochstrasser, Energy flow from solute to solvent probed by femtosecond IR spectroscopy—malachite green and heme protein solutions, *J. Phys. Chem.* 98, 11648–11656 (1994).
36. D. Foguel, R. M. Chaloub, J. L. Silva, A. R. Crofts, and G. Weber, Pressure and low temperature effects on the fluorescence emission spectra and lifetimes of the photosynthetic components of cyanobacteria, *Biophys. J.* 63, 1613–1622 (1992).
37. H. P. Kao, J. R. Abney, and A. S. Verkman, Determinants of the translational mobility of a small solute in cell cytoplasm, *J. Cell Biol.* 120, 175–184 (1993).
38. T. W. Gadella and T. M. Jovin, Oligomerization of epidermal growth factor receptors on A431 cells studied by time-resolved fluorescence imaging microscopy—a stereochemical model for tyrosine kinase receptor activation, *J. Cell Biol.* 129, 1543–1558 (1995).
39. X. F. Wang, A. Periasamy, G. W. Gordon, P. Wodnicki, and B. Herman, Fluorescence lifetime imaging microscopy (FLIM) and its applications, in: *Time-Resolved Laser Spectroscopy in Biochemistry IV* (J. R. Lackowicz, ed.), pp. 64–76, Proc. SPIE 2137 (1994).
40. S. Nie, D. T. Chiu, and R. N. Zare, Probing individual molecules with confocal fluorescence microscopy, *Science* 266, 1018–1021 (1994).
41. Q. Xue and E. S. Yeung, Difference in the chemical reactivity of individual molecules of an enzyme, *Nature* 373, 681–683 (1995).
42. S. A. Soper, E. B. Shera, J. C. Martin, J. H. Jett, J. H. Hahn, H. L. Nutter, and R. A. Keller, Single-molecule detection of rhodamine-6G in ethanolic solutions using continuous wave laser excitation, *Anal. Chem.* 63, 432–437 (1991).
43. J. R. Lackowicz, *Principles of Fluorescence Spectroscopy*, Plenum, New York (1983).
44. C. Kittel, *Introduction to Solid State Physics*, Wiley, New York (1996).
45. A. Guinier, *X-ray Diffraction in Crystals, Imperfect Crystals and Amorphous Bodies*, W. H. Freeman, San Francisco (1963).
46. T. Wilson and C. Sheppard, *Theory and Practice of Scanning Optical Microscopy*, Academic Press, London (1984).
47. T. Wilson (ed.), *Confocal Microscopy*, Academic Press, London (1990).

48. M. Born and E. Wolf, *Principles of Optics*, 5th ed., Pergamon Press, Oxford (1985).
49. C. J. R. Sheppard and M. Gu, Image formation in two-photon fluorescence microscopy, *Optik* 86, 104 (1990).
50. O. Nakamura, Three-dimensional imaging characteristics of laser scan fluorescence microscopy: two-photon excitation vs. single-photon excitation, *Optik* 93, 39 (1993).
51. M. Gu and C. J. R. Sheppard, Effects of a finite-sized pinhole on 3D image formation in confocal two-photon fluorescence microscopy, *J. Modern Opt.* 40, 2009 (1993).
52. B. R. Frieden, Optical transfer of the three-dimensional object, *J. Opt. Soc. Am.* 57, 56 (1967).
53. J. W. Goodman, *Introduction to Fourier Optics*, McGraw-Hill, San Francisco (1968).
54. P. T. C. So, T. French, W. M. Yu, K. M. Berland, C. Y. Dong, and E. Gratton, Two-photon fluorescence microscopy: time-resolved and intensity imaging, in: *Fluorescence Imaging Spectroscopy and Microscopy* (X. F. Wang and B. Herman, eds.), Wiley, New York, pp. 351–374 (1996).
55. E. H. K. Stelzer, The intermediate optical system of laser-scanning confocal microscopes, in: *The Handbook of Biological Confocal Microscopy* (J. Pawley, ed.), pp. 139–153, Plenum, New York (1995).
56. K. M. Berland, E. Gratton, and M. J. vandeVen, A laser heterodyning detector for frequency domain ultrafast spectroscopy, in: *Time-Resolved Laser Spectroscopy in Biochemistry III* (J. R. Lakowicz, ed.), pp. 370–378, Proc. SPIE 1640 (1992).
57. J. Kusba, V. Bogdanov, I. Gryczynski, and J. R. Lakowicz, Theory of light quenching: effects on fluorescence polarization, intensity, and anisotropy decays, *Biophys. J.* 67, 2024–2040 (1994).
58. J. R. Lakowicz, I. Gryczynski, J. Kusba, and V. Bogdanov, Light quenching of fluorescence—a new method to control the excited state lifetime and orientation of fluorophores, *Photochem. Photobiol.* 60, 546–561 (1994).
59. J. R. Lakowicz, I. Gryczynski, V. Bogdanov, and J. Kusba, Light quenching and fluorescence depolarization of rhodamine-B, *J. Phys. Chem.* 98, 334–342 (1994).
60. W. Denk, J. H. Strickler, and W. W. Webb, Two-photon laser scanning fluorescence microscopy, *Science* 248, 73–76 (1990).
61. D. W. Piston, M. S. Kirby, H. Cheng, W. J. Lederer, and W. W. Webb, Two-photon excitation fluorescence imaging of three-dimensional calcium-ion-activity, *Appl. Opt.* 33, 662–669 (1994).
62. P. T. C. So, T. French, K. Berland, C. Dong, and E. Gratton, Time-resolved two-photon microscopy, *Bioimaging* 3, 49–63 (1995).
63. D. Grebner, D. V. Lap, S. Rentsch, and H. Naarmann, Spectroscopic studies of femtosecond decay processes in didecyl-sexithiophene, *Chem. Phys. Lett.* 228, 651–657 (1994).
64. M. Sander, U. Brummund, K. Luther, and J. Troe, Fast processes in UV 2- photon excitation of pure liquids, *Int. J. Phys. Chem.* 96, 1486–1490 (1992).
65. M. L. Barcellona and E. Gratton, The fluorescence properties of a DNA probe 4'-6-diamidino-2-phenylindole (DAPI), *Eur. Biophys. J.* 17, 315–323 (1990).
66. A. Penzkofer and W. Leupacher, Fluorescence behaviour of highly concentrated rhodamine-6G solutions, *J. Luminesc.* 37, 61–72 (1987).

This page intentionally left blank.

Multiphoton Excitation of Molecular Fluorophores and Nonlinear Laser Microscopy

Chris Xu and Watt W. Webb

11.1 .Introduction

Molecular two-photon excitation (2PE) was first theoretically predicted by Maria Göppert-Mayer in 1931.⁽¹⁾ Like most other nonlinear processes, two- or three-photon excitation (3PE) requires high peak intensities, typically 10^{20} to 10^{30} photons/(cm² · s) for the observation of two-photon absorption. Months after the invention in 1960 of the pulsed ruby laser, it was used by Kaiser and Garrett to excite two-photon absorption in CaF₂ Eu³⁺, manifested by fluorescent deexcitation in the blue spectral region.⁽²⁾ This was the second demonstration of nonlinear optics, closely following the demonstration of second-harmonic generation. Three-photon-excited fluorescence was observed in naphthalene crystals by Singh and Bradley in 1964, and the three-photon absorption cross section were estimated.⁽³⁾

Since the early experimental demonstrations in the 1960s, multiphoton excited fluorescence has been observed with various materials and has been used mainly in spectroscopy and chemical physics.⁽⁴⁻⁷⁾ The significance of two-photon absorption in studies of molecular electronic structures was realized at the outset. Like the complementary roles played by Raman and infrared (IR) spectroscopies in probing the vibrational levels of molecules, two-photon spectroscopy has been used to complement one-photon spectroscopy to study the electronic structure of molecules.

The application of 2PE of fluorescence in biological imaging and two-photon uncaging of biomolecules were invented by Denk, Strickler, and Webb

Chris Xu and Watt W. Webb • School of Applied Physics, Cornell University, Ithaca, New York 14853.

Topics in Fluorescence Spectroscopy; Volume 5: Nonlinear and Two-Photon-Induced Fluorescence, edited by J. Lakowicz. Plenum Press, New York, 1997.

in 1990.⁽⁸⁾ These nonlinear microscopy techniques have become a powerful new tool in cell biology and neuroscience.^(9–11) This new development of two-photon laser scanning microscopy (2PLSM) was propelled by rapid technological advances in laser scanning microscopy⁽¹²⁾ and mode-locked femtosecond lasers.^(13–14) Recently, three-photon-excited fluorescence has also been successfully applied to biological imaging.^(15–17)

This chapter is divided into three major sections. In the multiphoton spectroscopy section, we first review the multiphoton excitation (MPE) cross-sectional measurement methods and the MPE spectra of many biological fluorophores. Several key photophysics issues related to multiphoton cross-sectional measurements, such as the power dependence, pulse width dependence, and fluorescence emission spectra, are then discussed. The multiphoton microscopy section is designed to provide an overview of the applications of nonlinear excitation as a microscopic probe. Advantages of MPE are illustrated using examples of imaging and uncaging. The characterization of the spatial localization of multiphoton microscopy using the precisely defined excitation volume instead of the conventional full width at half-maximum (FWHM) is described. Two- and three-photon excitations are then compared based on this volume concept. The last section addresses several important issues in both multiphoton spectroscopy and microscopy, namely, saturation, intersystem crossing, and photobleaching, and several phenomena at high intensities, such as nonlinear scattering, dielectric breakdown, etc.

11.2. Multiphoton Spectroscopy

The basic molecular parameters in quantitative fluorescence microscopy are the fluorescence excitation cross sections. Although the one-photon absorption spectra of common biological fluorophores are well documented, little is known of their two- or three-photon absorption spectra. Furthermore, it is often difficult to predict the MPE spectra, especially the two-photon spectra, from the known one-photon absorption data because of the different selection rules involved and the effects of vibronic coupling. For many years, 2PE cross-sectional measurements were almost always carried out at 694 nm (ruby laser) and 1064 nm (Nd glass laser) on laser dyes.⁽¹⁹⁾ Less effort had been devoted to accurate quantitative studies of common fluorophores widely used in 2PLSM. In addition, it is well known that substantial disagreement (sometimes over one order of magnitude) between published values of two-photon cross sections often exists. The lack of knowledge of 2PE cross sections and spectra for common fluorophores used in biological studies has been a significant obstacle in the use of 2PLSM. Knowledge of 3PE cross section is even scarcer in the literature.

For much spectroscopic research, the primary use of two- and three-photon absorption data is to elucidate the energy states of matter. Hence, transition energies and *relative* strengths are as informative as *absolute* values. For some technological applications, however, such as nonlinear laser scanning microscopy, the absolute strengths of multiphoton transitions are required as well as the transition energies and relative strengths. Direct measurements of multiphoton absorption cross sections by recording the attenuation of the incident beam can only be achieved in highly concentrated (usually $>10\text{ mM}$) fluorophore solutions unless high-power laser systems are employed. In the case of fluorescent materials, which are most interesting in biological imaging, two- and three-photon-generated fluorescence can be measured to determine the fluorescence action cross sections and the absorption cross sections (if the fluorescence emission quantum efficiencies are known).⁽²⁰⁾ The fluorescence technique provides very high detection sensitivity, and two- or three-photon cross sections can be measured in dilute fluorophore solution (usually much less than 1.0 mM) or with low-power CW lasers (for 2PE).⁽²¹⁾

In this section, we first review methods of measuring MPE spectra and absolute cross sections using the fluorescence technique. The exact quantitative expressions are given for obtaining multiphoton cross sections from multiphoton-excited fluorescence measurements performed in two focused geometries: Gaussian-Lorentzian (GL) focus and diffraction-limited focus. Several key issues related to MPE cross-sectional measurements, such as power dependence, pulse width dependence, and fluorescence emission spectra are discussed. Detailed comparison between one-, two-, and three-photon excitation spectra are also illustrated for several fluorophores. We note that, although MPE with identical wavelength photons is discussed throughout this chapter, MPE can also be achieved using multiple-wavelength photons.⁽²²⁾

11.2.1. Estimations of Multiphoton Cross Section

The essence of the theory of multiphoton processes can be represented in perturbation theory of one form or another. The time-dependent semiclassical interaction can be used to derive the multiphoton transition amplitude because a more accurate description using quantum field theory generates completely equivalent results for virtually all processes in laser field. Details of the rigorous derivation can be found elsewhere⁽²³⁾ Here, for the purpose of an order-of-magnitude estimation, a much simplified approach will be presented to describe the MPE processes, and only the lowest-order dipole transition will be considered.

Intuitively, multiphoton processes require two or more photons to interact *simultaneously* with the molecule. For example, in a two-photon process, the

“first” photon excites the molecule to an intermediate state, and the “second” photon further excites the molecule to its final state. Because the intermediate state can be a superposition of molecular states instead of an eigenstate of the molecule, it is usually referred to as the virtual intermediate state. Although the two-photon transition strength consists of contributions from all eigenstates as possible intermediate states, the single-intermediate-state (SIS) approximation⁽⁶⁾ can be used to give an order-of-magnitude estimation. Figure 11.1. shows the schematic illustration of the SIS approximation. Therefore, by simple examination of the absorption rates, the two-photon absorption cross section (σ_2) can be obtained:

$$\sigma_2 = \sigma_{ij}\sigma_{jf}\tau_j \quad (11.1)$$

where σ_{ij} and σ_{jf} represent the appropriate one-photon absorption cross sections and τ_j is the intermediate-state lifetime that determines the time scale for photon coincidence (simultaneously arrival). We can estimate τ_j from the uncertainty principle; i.e., τ_j must be short enough in order not to violate energy conservation. Thus,

$$\tau_j \approx 1/\Delta\omega = 1/|\omega_{ij} - \omega| \quad (11.2)$$

where ω_{ij} and ω are the transition frequency and the incident photon frequency, respectively. For an electronic transition (ω_{ij}) in the visible frequency range and further assuming that the intermediate state and the final state are close in energy, we then have $\tau_j \approx 10^{-15}$ to 10^{-16} s. The one-photon absorption cross section of a molecule can be estimated by its dipole transition length (typically $\sigma_1 \approx 10^{-16}$ to 10^{-17} cm² for a transition length of 10^{-8} cm). Hence, the estimated two-photon absorption cross sections should be approximately 10^{-49} cm⁴s/photon (Eq. 11.1). The estimations for three- and four-photon excitation cross sections can be obtained by parallel analysis. They are listed in Table 11.1.

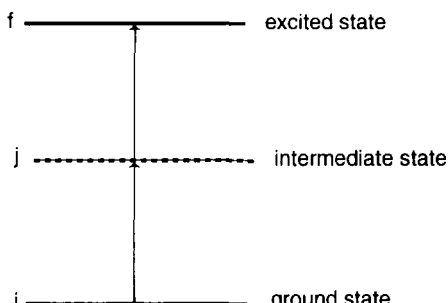


Figure 11.1. Schematic illustration of SIS approximation. i , j , and f represent the initial state, the intermediate state, and final state, respectively.

Table 11.1. Order-of-Magnitude Estimation of MPE Cross Sections^a

<i>n</i> PE	Approximate expression	Estimated cross section
2PE	$\sigma_2 = \sigma_{ij}\sigma_{if}\tau_j$	$10^{-49} \text{ cm}^2 (\text{photons/cm}^2 \text{ s})^{-1}$
3PE	$\sigma_3 = \sigma_{ij}\sigma_{jk}\sigma_{kf}\tau_j\tau_k$	$10^{-82} \text{ cm}^2 (\text{photons/cm}^2 \text{ s})^{-2}$
4PE	$\sigma_4 = \sigma_{ij}\sigma_{jk}\sigma_{kl}\sigma_{ly}\tau_j\tau_k\tau_l$	$10^{-115} \text{ cm}^2 (\text{cm}^2 (\text{photons/cm}^2 \text{ s})^{-3})$

^a *j*, *k*, *l* are the intermediate states. τ_j , τ_k , and τ_l represent the corresponding lifetimes of the intermediate states.

Note that these estimates are only valid for simultaneous MPE; i.e., virtual states with lifetimes approximately 10^{-15} s serve as the intermediate states. However, in a sequential MPE process, real states with lifetimes approximately 10^{-9} – 10^{-12} s serve as the intermediate states. Consequently, the cross section for a sequential MPE process can be orders of magnitude larger than the above estimate. Although the enhanced MPE cross sections may seem desirable for some applications, there are many limitations in such multistep MPE, which we choose not to discuss.

11.2.2. Theoretical Analysis of MPE

The crucial problem in MPE cross-sectional measurements is that the absorption rates strongly depend on the high order (≥ 2) spatial and temporal coherence of the excitation light. Knowing the relationship between the experimentally measured fluorescence power and the excitation power is essential in MPE cross-sectional measurements. In this section, we first examine the relationship in general and discuss the relevant parameters in any MPE cross-sectional measurements. Detailed analysis of several special cases will follow.

Because *n*-photon excitation is an *n*th-order process, the number of photons absorbed per molecule per unit time via *n*-photon excitation is proportional to the *n*-photon absorption cross section σ_n and to the *n*th power of the incident intensity I .⁽⁵⁾ In a particular experiment, the total number of photons absorbed per unit time N_{abs} is also a function of dye concentration C and the illuminated sample volume V :

$$N_{\text{abs}}(t) = \int_V d\mathbf{r} \sigma_n C(\mathbf{r}, t) I^n(\mathbf{r}, t) \quad (11.3)$$

In the absence of ground-state depletion and photobleaching, $C(\mathbf{r}, t)$ can be assumed a constant. Moreover, in the case where one can separate time and

space dependence of the excitation intensity, we have

$$N_{\text{abs}}(t) = C\sigma_n I_0^n(t) \int_V d\mathbf{r} S^n(\mathbf{r}) \quad (11.4)$$

where $S(\mathbf{r})$ and $I_0(t)$ describe the spatial and temporal distribution of the incident light; i.e., $I(\mathbf{r}, t) = S(\mathbf{r})I_0(t)$. We chose $S(\mathbf{r})$ to be a unitless spatial distribution function and $I_0(t)$ to be the intensity at the geometric focal point.

Assuming no stimulated emission and no self-quenching, the number of fluorescence photons collected per unit time (F) is

$$F(t) = \frac{1}{n} \phi \eta N_{\text{abs}} \quad (11.5)$$

where η and ϕ are the fluorescence quantum efficiency of the dye and fluorescence collection efficiency of the measurement system, respectively. Here the factor $1/n$ simply reflects the fact that n photons are needed for each excitation event. In practice, only the time-averaged fluorescence photon flux $\langle F(t) \rangle$ is measured:

$$\langle F(t) \rangle = \frac{1}{n} \phi \eta C \sigma_n \langle I_0^n(t) \rangle \int_V d\mathbf{r} S^n(\mathbf{r}) \quad (11.6)$$

We note that $\langle F(t) \rangle$ is proportional to $\langle I_0^n(t) \rangle$, not $\langle I_0(t) \rangle^n$. Because most detectors only give a signal that is proportional to $\langle I_0(t) \rangle$, we rewrite Eq. (11.6) in terms of the average intensity:

$$\langle F(t) \rangle = \frac{1}{n} g^{(n)} \phi \eta C \sigma_n \langle I_0(t) \rangle^n \int_V d\mathbf{r} S^n(\mathbf{r}) \quad (11.7a)$$

$$g^{(n)} = \frac{\langle I_0^n(t) \rangle}{\langle I_0(t) \rangle^n} \quad (11.7b)$$

where $g^{(n)}$ is a measure of the n th-order temporal coherence of the excitation source.

All of the relevant quantities in a MPE cross-sectional measurement are presented in Eq. (11.7). Experimental determination of σ_n usually involves the characterization of three parameters: the spatial distribution of the incident light ($\int_V S^n(\mathbf{r}) d\mathbf{r}$), the n th-order temporal coherence ($g^{(n)}$), the fluorescence collection efficiency of the system (ϕ).

11.2.2.1. Spatial Considerations

The spatial distributions of two limiting cases (i.e., the GL focus and the diffraction-limited focus) will be discussed in detail. In practice, only these two profiles have been used in quantitative measurements in order to avoid the complex nature of beam profiles that results from the partial filling of the back aperture of the focusing lens. We will only consider two- and three-photon cross-sectional measurements in the following sections. The general formula for measuring the n -photon cross section for higher n can be obtained by parallel analysis.

11.2.2.1a. Excitation with a Gaussian–Lorentzian Beam A laser that operates in TEM_{00} mode has a GL spatial profile. However, diffraction by a finite aperture distorts the wave front. A detailed theory of a GL beam propagating through such finite apertures has been developed.⁽²⁴⁾ The resulting spatial profile after the aperture is complex and depends on the ratio of the GL beam waist (w_0) and aperture size. Practically, such difficulties can be circumvented by keeping the incident beam diameter much smaller than that of the back aperture of the focusing lens. The consequences of diffraction can be neglected and, therefore, a perfect GL profile can be obtained after the lens.

The intensity distribution of a GL beam is in the following form:

$$I(\rho, z, t) = \frac{2P(t)}{\pi w^2(z)} \exp\left[-\frac{2\rho^2}{w^2(z)}\right] \quad (11.8a)$$

$$w(z) = w_0 \left[1 + \left(\frac{z}{z_R} \right)^2 \right]^{1/2} \quad (11.8b)$$

$$z_R \neq \frac{n_0 \pi w_0^2}{\lambda} \quad (11.8c)$$

where z is the distance along the optical axis, ρ is the distance away from the optical axis, λ is the wavelength of excitation light in vacuum, n_0 is the refractive index of the sample media, and $P(t)$ is the incident power. The term z_R , frequently referred to as the Rayleigh length of the beam, characterizes the focal depth of the Gaussian beam. We can easily obtain the expressions for $S(\mathbf{r})$ and $I_0(t)$ from Eq. (11.8):

$$I_0(t) = \frac{2P(t)}{\pi w_0^2} \quad (11.9a)$$

$$S(\mathbf{r}) = \frac{w_0^2 \exp[-2\rho^2/w^2(z)]}{w^2(z)} \quad (11.9b)$$

Assuming the sample thickness is much greater than the Rayleigh length, an analytical expression can be readily obtained for the integral of $(S^n(\mathbf{r}))$ (for $n \geq 2$):

$$\int_{V \rightarrow \infty} S^n(\mathbf{r}) d\mathbf{r} = \frac{(2n-5)!!}{2n(2n-4)!!} \frac{n_0 \pi^3 w_0^4}{\lambda} \quad (11.10)$$

where $!!$ denotes double factorial; i.e., $2n!! = 2 \cdot 4 \cdot 6 \cdots 2n$, $(2n-1)!! = 1 \cdot 3 \cdot 5 \cdots (2n-1)$, $(-1)!! = 1$, and $0!! = 1$.

11.2.2. 1b. A Plane Wave Focused by Diffraction-Limited Optics We first consider the three-dimensional intensity distribution at the focal spot of a diffraction-limited objective lens with uniform illumination. In practice this is achieved by expanding the incident laser beam so that the beam diameter is much larger than the back aperture of the focusing lens. Properties of the lens are then determined by its point-spread function (PSF). The dimensionless distance from the optic axis v and distance from the in-focus plane u are given by

$$v = \frac{2\pi(NA)\rho}{\lambda} \quad (11.11a)$$

$$u = \frac{2\pi(NA)^2 z}{n_0 \lambda} \quad (11.11b)$$

where $NA = n_0 \sin \theta$ and θ is the half-angle of collection for the lens. We use the paraxial form of the normalized intensity PSF ($h^2[u, v]$) for a diffraction-limited lens:⁽¹²⁾

$$I_0(t) = \frac{\pi(NA)^2}{\lambda^2} P(t) \quad (11.12a)$$

$$S(\mathbf{r}) = h^2[u, v] = 2 \left| \int_0^1 J_0(v\theta) \exp[-\frac{1}{2}iu\theta^2]\theta d\theta \right|^2 \quad (11.12b)$$

The paraxial approximation is adequate for $\sin \theta < 0.7$, or $NA < 1.0$ with an oil immersion objective.⁽²⁵⁾ After changing ρ and z to their optical units v and u by using Eq. (11.11), the integration of $S(r)$ becomes

$$\int_{V \rightarrow \infty} S^n(\mathbf{r}) d\mathbf{r} = a_n \left[\frac{n_0 \lambda^3}{8\pi^3 (NA)^4} \right] \quad (11.13)$$

where $a_n = \int_0^\infty 2\pi v dv \int_{-\infty}^\infty du [h(u, v)]^{2n}$. Here we have again assumed that the sample thickness is much greater than the focal depth of the lens. In the paraxial

approximation, the volume integrals are proportional to $(NA)^{-4}$ regardless of the order of photon processes. Because analytical expressions of a_n cannot be obtained, numerical integrations of $[(h(u, v)]^{2n}$ over the entire space have been performed for selected n values. Results are listed in Table 11.2.

11.2.2.1c. Two-Photon Excitation In the thick-sample limit, the expression for experimentally detected two-photon-excited fluorescence in a GL focus can be obtained from Eqs. (11.7) and (11.10):

$$\langle F(t) \rangle = \frac{1}{2} g^{(2)} \phi \eta C \sigma_2 n_0 \frac{\pi \langle P(t) \rangle^2}{\lambda} \quad (11.14)$$

A similar equation can also be obtained for diffraction-limited focus by using Eqs. (11.7) and (11.13):

$$\langle F(t) \rangle \approx \frac{1}{2} g^{(2)} \phi \eta C \sigma_2 n_0 \frac{8.8 \langle P(t) \rangle^2}{\pi \lambda} \quad (11.15)$$

Although the collection efficiency ϕ is dependent on the NA of the collecting lens, we note that the total fluorescence generation is independent of the NA of the focusing lens (or the beam waist size of the GL beam) in thick samples. Intuitively, one sees that the effect of the increased intensity by tighter focusing is just compensated by the shrinking excitation volume. Thus, the amount of fluorescence summed over the entire space remains unchanged for 2PE. Working with thick samples in 2PE measurements takes advantage of this interesting property: the generated fluorescence power is insensitive to the size of the focal spot, assuming no aberration. Hence, a small variation of the laser beam size (with excitation power monitored after the objective lens) or sample thickness would not affect the results of measurements.

One possible concern of using thick samples is lens aberration. Although microscope objectives are highly corrected, index mismatch between the immersion media and the sample introduces aberration that generally reduces the amount of two-photon fluorescence.⁽²⁶⁾ However, such aberration effects are negligible when low-NA lenses are used.

Table 11.2. Numerical Integrations of a_n Under Paraxial Approximation

n	2	3	4	5	6	7	8	10	12	14
a_n^a	70	28.1	18.3	13.2	10.1	8.06	6.62	4.76	3.64	2.89

^a Because numerical integrations can only be done over a limited space, the estimated uncertainty of the integral is <4% for $n = 2$ and negligible for $n > 2$. Absolute values of a_n are expected to be different in the high-NA limit where paraxial approximation is no longer valid. However, numerical calculations for $NA = 1.2$ showed that the relative values of a_n ($n = 2-6$) are approximately the same as those listed in the table.

II.2.2.1d. Three-Photon Excitation In the thick-sample limit, the expression for experimentally detected three-photon-excited fluorescence in a GL focus can be obtained from Eqs. (11.7) and (11.10):

$$\langle F(t) \rangle = \frac{1}{3} g^{(3)} \phi \eta C \sigma_3 n_0 \frac{2 \langle P(t) \rangle^3}{3 \lambda w_0^2} \quad (11.16)$$

A similar equation can also be obtained for diffraction-limited focus by using Eqs. (11.7) and (11.13):

$$\langle F(t) \rangle \approx \frac{1}{3} g^{(2)} \phi \eta C \sigma_3 n_0 \frac{3.5(NA)^2 \langle P(t) \rangle^3}{\lambda^3} \quad (11.17)$$

It is clear that the amount of three-photon-excited fluorescence depends on the size of the focal spot (i.e., NA of the lens or the beam waist size). Thus, unlike 2PE experiments with thick samples, quantitative measurements of three-photon-excited fluorescence require the characterization of the focal spot size. However, working with thick samples still provides the advantage of less sensitivity to the beam waist measurements because $\langle F(t) \rangle \propto w_0^{-6}$ or NA^6 in the thin-sample limit, in which case a small deviation of the focal spot size can cause a much larger error in the measured cross section.

11.2.2.2. Temporal Considerations

In addition to the characterization of the spatial profiles of the excitation beam, experimental determination of MPE cross sections is difficult mainly because the multiphoton absorption rates depend crucially on the temporal profiles of the excitation beam [i.e., $g^{(n)}$ as defined by Eq. (11.7b)].⁽²⁷⁾ An effective and simple experimental approach to solve this problem is to compare the generated fluorescence of the specimen to some known two- or three-photon references provided that reliable two- or three-photon standards in the wavelength range of interest exist.^(28,29) Such a reference technique also takes into account the spatial distribution if the same excitation geometry is used for both the standard and the specimen to be measured. However, several measurement methods can be used in the absence of such multiphoton standards. They will be briefly reviewed in the following sections.

11.2.2.2a. Measurements with a Single-Mode CW Laser An ideal single-mode CW laser has $g^{(n)} = 1$. Measuring MPE cross sections using such lasers only requires knowledge of the value of the average excitation intensity. However, single-mode CW excitation usually requires many orders of magnitude more average power than pulsed excitation to obtain the same rate of excitation,

because of the much smaller value of $g^{(n)}$. Using the same average power, the excitation rate achieved with a single-mode CW laser is only approximately 10^{-5} and 10^{-10} for two- and three-photon excitation, respectively, of that using a mode-locked femtosecond Ti sapphire laser with 80-MHz repetition rate and 100-fs pulse width. Nevertheless, CW excitation is feasible for dyes with relatively large cross section in 2PE. The prospect of CW 3PE is not good except for molecules with extraordinarily large three-photon cross sections (such as those reported by He *et al.*)⁽³⁰⁾ For example, with an average power of 100 mW at the specimen of 1-mM concentration and using the three-photon fluorescence action cross section ($\eta\sigma_3$) of 10^{-82} cm⁶(s/photon)², Eq. (11.17) predicts that the detected fluorescence rate is only 0.2 photon/s, assuming $NA = 1.3$, $\lambda = 1000$ nm, and a high detection efficiency of ϕ of 1 %.

It is important to stress the “true CW” nature of a single-mode CW laser. A multimode CW laser may retain enough RMS noise (such as caused by mode beating) to prevent its use as a stable CW source.

11.2.2.2b. Measurements with a Pulsed Laser Measurements performed with a pulsed laser require careful evaluation of the temporal coherence factor [$g^{(n)}$]. The focused intensity obtained from a mode-locked laser is the periodic function in time,

$$I_0(t) = I_0 \left(t + \frac{m}{f} \right), \quad m = 1, 2, 3, \dots \quad (11.18)$$

where f is the pulse repetition rate. Let $t = 0$ be at the peak of one excitation pulse. Because of the periodical nature of the pulse train, one need only calculate $g^{(n)}$ for one cycle. Defining τ as the excitation pulse width (FWHM) and $f\tau$ as the duty cycle, $g^{(n)}$ can be expressed in terms of the ratio of the dimensionless quantity $g_p^{(n)}$, which depends only on the shape of the laser pulse and the duty cycle:

$$g^{(n)} = g_n^{(n)} / (f\tau)^{n-1} \quad (11.19a)$$

$$g_p^{(n)} = \tau^{n-1} \frac{\int_{-1/2f}^{1/2f} I_0^n(t) dt}{\left[\int_{-1/2f}^{1/2f} I_0(t) dt \right]^n} \quad (11.19b)$$

For pulses with a Gaussian temporal profile one finds $g_p^{(2)} = 0.66$ and $g_p^{(3)} = 0.51$, whereas for a hyperbolic-secant-squared pulse one finds $g_p^{(2)} = 0.59$ and $g_p^{(3)} = 0.41$. Intuitively, $g^{(n)}$ represents the n-photon excitation efficiency of the excitation light at a fixed time-averaged intensity. We note that $g^{(n)} \langle I_0(t) \rangle$ is generally not the commonly referred *peak* intensity or *pulse* intensity (I_p), which should be given as $I_p = \langle I_0(t) \rangle / f\tau$.

Mode-locked lasers with their high peak intensities and broad tunability offer tremendous advantages in multiphoton fluorescence excitation. However, determination of MPE cross sections depends crucially on the estimation of the temporal coherence at zero time delay⁽³¹⁾ $g^{(n)} = \langle I_0^n \rangle / \langle I_0 \rangle^n$ of the excitation light *inside the sample*. Although the pulse width and the laser repetition rate can be routinely measured in any laser laboratory, the determination of $g_p^{(n)}$ in the femtosecond time region is difficult. In addition, external measurements of the pulse shapes do not provide reliable estimates of $g^{(n)}$ *inside the sample*, because ultrashort pulses are distorted by the optical nonlinearities and group delay dispersion (GDD) (e.g., a GDD of -2000 fs^2 at 730 nm for a Zeiss Neofluo 10X 0.3-NA lens).⁽³²⁾ To circumvent the difficulties of determining the pulse shape inside the sample while still taking full advantage of pulsed excitation, we will briefly review a new technique that we have developed in obtaining 2PE cross section.⁽³³⁾

11.2.2.2c. Autocorrelation Techniques The method described takes advantage of the fact that the fluorescence from the test chromophore itself can be used not only to measure the temporal autocorrelation⁽³⁴⁾ of the pulsed excitation light but also to gauge the amount of excitation and, by the combination of both, the absolute 2PE cross section. The sample is illuminated through focusing optics at the output of the Michelson interferometer which generates a spatial superposition of two halves of the excitation beam shifted in time by a variable delay (Figure 11.2). The setup resembles the collinear autocorrelator used routinely for pulse duration measurements, but with the sample fluorophore serving as the quadratic medium.⁽³⁴⁾ While the autocorrelation function, measured externally or *in situ*, does not determine the temporal profile of the pulse uniquely, it contains enough information for one to calculate $g^{(2)}$ without any assumptions about the pulse shape other than that all the pulse energy is contained within a finite temporal interval.

For simplicity we again consider only a single excitation pulse. In the relevant case of two beams with equal intensities that overlap perfectly in space but are temporally shifted by a delay τ_d , the fluorescence (F) recorded as a function of τ_d is simply the second-order autocorrelation function of the excitation pulse:⁽³⁵⁾

$$\begin{aligned} F(\tau_d) = & \frac{1}{2} B\sigma_2 C\eta\phi \int_{-\infty}^{\infty} dt \{ P^2(t) + P^2(t + \tau_d) + 4P(t)P(t + \tau_d) \\ & + 2P(t)P(t + \tau_d) \cos[2\omega\tau_d + \varphi(t + \tau_d) - \varphi(t)] \\ & + \sqrt{P(t)P(t + \tau_d)}[P(t) + P(t + \tau_d)] \cos[\omega\tau_d + \varphi(t + \tau_d) - \varphi(t)] \} \end{aligned} \quad (11.20)$$

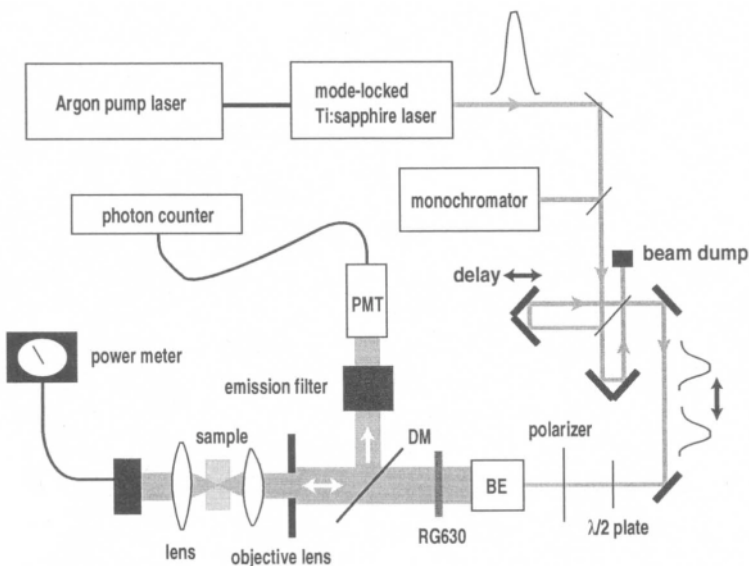


Figure 11.2. Experiment apparatus for measuring 2PE cross section using the autocorrelation technique. A long-pass filter (>630 nm) eliminates residual argon pump light and Ti sapphire fluorescence. The beam expanders (BE) expand the beam to about 25 mm in diameter ($1/e^2$), which was sufficient to overfill the back aperture (10 mm diameter) of the objective (Zeiss Neofluar 0.3NA 10X). A long-pass dichroic mirror (DM) with reflectivity $>95\%$ for $\lambda < 610$ nm separated the fluorescence from the excitation light. The incident power at the sample was measured by recollimating the transmitted beam onto a calibrated power meter. To ensure that the total generated fluorescence did not depend on the NA, a sample was used that was significantly thicker (100 μm) than the focal depth (~ 40 μm). Fluorescence was detected by a PMT (R1924; Hamamatsu) connected to a photon counter and recorded as a function of the interferometer delay.

where $\int_V S^2(\mathbf{r}) d\mathbf{r} = B$. The original and the delayed beams are represented by $P(t)$ and $P(t + \tau_d)$, respectively. Integration of Eq. (11.20) with respect to τ_d over a range $2T$ much greater than the pulse width eliminates the oscillatory terms after the integrals of t and τ_d are exchanged. Since for $P(t)P(t + \tau_d) \approx 0$ for $|\tau_d| \geq T$, the integration region can be extended from $-\infty$ to ∞ . We then obtain

$$\int_{-T}^T F(\tau_d) d\tau_d = \frac{1}{2} B\sigma_2 C\eta\phi \left\{ 4 \left[\int_{-\infty}^{\infty} P(t) dt \right]^2 + 4T \int_{-\infty}^{\infty} P^2(t) dt \right\} \quad (11.21)$$

The amount of two-photon-excited fluorescence detected at $|\tau_d| \geq T$ (F_∞) is simply twice the amount generated by a single pulse of one of the half-beams:

$$F_\infty = B\sigma_2 C\eta\phi \int_{-\infty}^{\infty} P^2(t) dt \quad (11.22)$$

Combining Eqs. (11.21) and (11.22) yields

$$\sigma_2 = \frac{\int_{-T}^T F(\tau_d) d\tau_d - 2TF_\infty}{2BC\eta\phi \left(\int_{-\infty}^{\infty} P(t) dt \right)^2} \quad (11.23)$$

Once C , η , and ϕ have been independently determined (e.g., by one-photon fluorescence calibration), the calibrated cross section (σ_2) can be obtained by recording the autocorrelation function $F(\tau_d)$ and the incident pulse energy $\int_{-\infty}^{\infty} P(t) dt$. Therefore, 2PE cross-sectional measurements by this technique do not require any prior knowledge about the temporal profile of the excitation source. Note that Eqs. (11.21) and (11.22) yield

$$g^{(2)} = 2F_\infty \left[f \int_{-T}^T F(\tau_d) d\tau_d - 2fTF_\infty \right]^{-1} \quad (11.24)$$

Although only absolute measurement of 2PE cross sections has been used to demonstrate this new method, it is relatively simple to extend the analysis for 3PE, in which case a third-order correlation trace needs to be obtained in addition to the second-order autocorrelation function. We note that such technique may be most valuable in measuring the cross sections of higher (*>second*-order) processes where absolute measurement with CW lasers becomes difficult because of the much weaker fluorescence excitation.

11.2.2.3. System Collection Efficiency (ϕ) and Fluorescence Quantum Efficiency (η)

System collection efficiency (ϕ) is a function of the collection efficiency of the collection lens, transmission of the optics, and detector quantum efficiency. The most convenient approach to determine ϕ is to use one-photon-excited fluorescence. Direct comparison with one-photon-excited fluorescence also gives the absolute values of 2PE cross section, assuming equal-emission quantum efficiencies. However, care must be taken to ensure that the collection efficiencies for one- and two-photon-excited fluorescence are the same. For example, the use of short-path-length sample cuvettes ensures uniform fluorescence collection efficiency throughout the sample, which is necessary because one-photon excitation (1PE) occurs throughout the entire sample thickness (i.e., it is not localized to the focal region as in 2PE). In general, it is assumed that one-, two-, and three-photon-excited fluorescence emission spectra are the same. As discussed later, we

observe no exceptions to this assumption for the fluorophores discussed in this chapter.

One can also determine ϕ directly based on the fluorescence emission spectrum, the measured NA of the collection lens and the transmission of the optics. The detector response can be obtained from the manufacturer's catalogue or can be independently calibrated using a known intensity source (for example, with a laser and calibrated neutral density filters). In our experiments, the collection efficiencies determined by the aforementioned two methods were quite consistent.

A measurement of the n -photon-excited fluorescence quantum efficiency η is very difficult because direct measurement of n -photon absorption (usually very small) is required. It is usually assumed that fluorescence quantum efficiencies are the same for one-, two-, and three-photon excitations and are constant over the entire spectral range. One potential method of measuring multiphoton-excited fluorescence quantum efficiency using fluorescence saturation is discussed in the appendix.

11.2.3. Two- and Three-Photon Excitation Spectra

Figure 11.3 summarizes our measurements of two-photon fluorescence excitation spectra [$\sigma_2(\lambda)$] of several fluorophores and Ca^{2+} indicators in the spectral range of 690 to 1050 nm. For comparison, the tuning ranges of several mode-locked laser sources are also plotted in Figure 11.3. Figure 11.4 shows 2PE cross-sectional measurements of another eight dyes, including fluorescein, rhodamine-B, DiI, and excitation ratiometric Ca^{2+} indicator fura-2, with their corresponding one-photon absorption spectra. These spectra show that nonlinear fluorescence microscopy based on 2PE can be expected to work well with most existing fluorophores and many available laser sources. For nonratiometric Ca^{2+} indicators, such as Ca-crimson, Ca-orange, and Ca-green-1, the 2PE spectra of the Ca^{2+} -free and Ca^{2+} -bound forms are indistinguishable. The ratios of fluorescence intensity for the Ca^{2+} -free to Ca^{2+} -bound forms of these indicators are also comparable to their reported one-photon values. Thus, the binding of Ca^{2+} does not change the shapes of the 2PE spectra for these Ca^{2+} indicators. Similar properties were observed in the case of fluorescein-dextran molecules, where the binding of fluorescein to the dextran molecule does not change its 2PE spectrum.

Green fluorescent proteins (GFPs) have attracted tremendous interest as biological reporters for gene expression.⁽³⁶⁾ Images of cultured cells using two-photon-excited GFP fluorescence have been reported recently.^(37,38) Wild-type GFP has high UV absorption at 400 nm and relatively low visible absorption at 480 nm. To facilitate the use of GFPs with visible excitation, mutant S65T (replacement of Ser65 with Thr) was engineered to enhance the visible absorption band.⁽³⁹⁾ The measured 2PE spectra of GFP wild type and the GFPS65T mutant

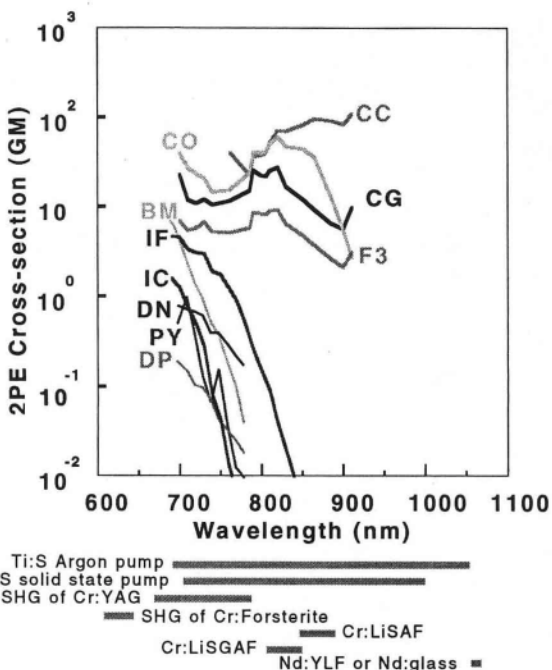


Figure 11.3. Two-photon fluorescence excitation spectra of fluorophores. For BM(bis-MSB), data represent two-photon absorption cross sections. For all the other fluorophores, data represent two-photon action cross sections, i.e., the product of the fluorescence emission quantum efficiencies and the two-photon absorption cross sections. $1 \text{ GM} = 10^{-50} \text{ cm}^4 \text{ s}/\text{photon}$. Spectra are excited with linearly polarized light using a mode-locked Ti sapphire laser. For comparison, the tuning range of conveniently available mode-locked laser sources are also plotted. The fluorophores illustrated are BM = *p*-bis(*o*-methyl-styryl) benzene; DP (DAPI not DNA bound) = 4',6-diamidino-2-phenylindole, dyhydrochloride; DN (dansyl) = 5-dimethylaminonaphthalene-1-sulfonyl hydrazine; PY = 1,2-bis(1-pyrenedecanoyl)-*sn*-glycero-3-phosphocholine; IC = Indo-1 with Ca^{2+} ; IF = Indo-1 without Ca^{2+} ; CG = calcium green-1 with Ca^{2+} ; CO = calcium orange with Ca^{2+} ; CC = calcium crimson with Ca^{2+} ; F3 = Fluo-3 with Ca^{2+} . All of the samples were purchased from Eastman Kodak or Molecular Probes. Note that the *y* axis is in logarithmic scale.

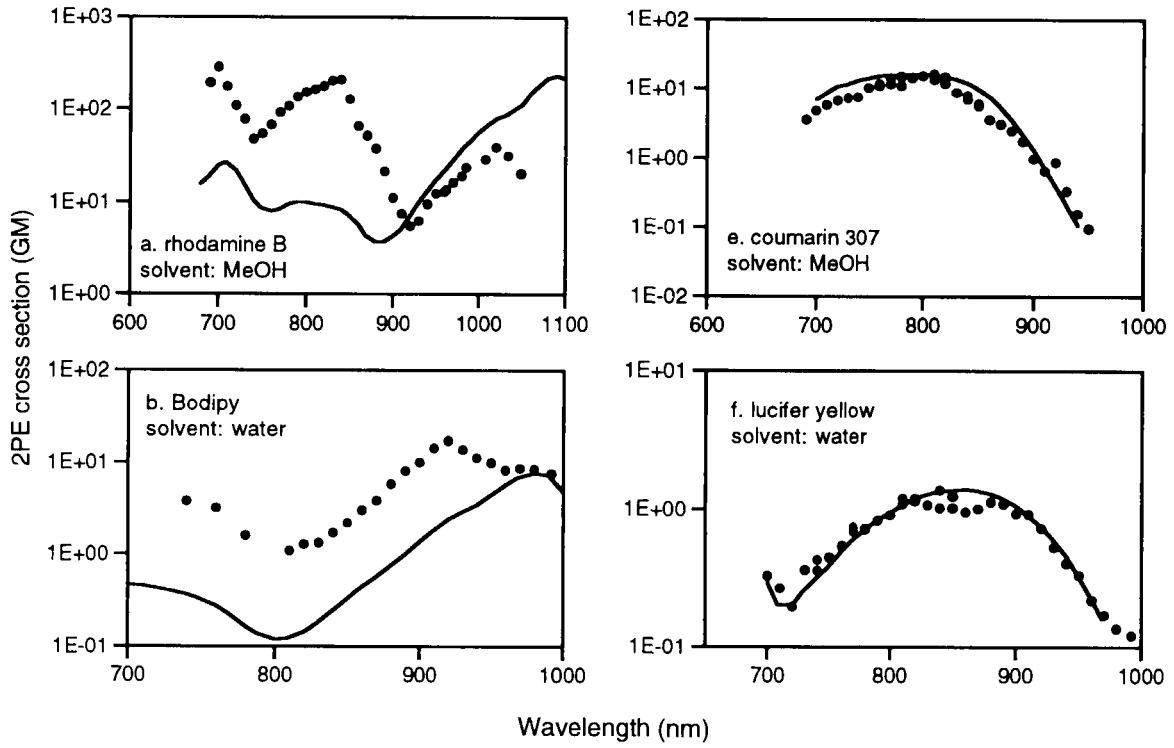
are similar to the corresponding one-photon spectra (Figure 11.5), indicating that wild-type GFP can be two-photon-excited using the same wavelength needed to excite UV and visible fluorophores (Figures 11.3 and 11.4), while only long-wavelength visible fluorophores can be simultaneously excited with the S65T mutant. The 2PE spectra of another GFP mutant, EGFP (S65T and F64L),⁽⁴⁰⁾ are similar to that of GFPS65T. However, the 2PE cross section at 960 nm is approximately 10^2 GM.

Two-photon-excited cellular autofluorescence from intrinsic chromophores such as NAD(P)H has been used to study the cellular metabolic state.⁽⁴¹⁾ Photo-damage of cells can also be detected by monitoring autofluorescence changes.⁽⁴²⁾ However, for most fluorescence imaging applications, autofluorescence background is undesirable as it limits the detection sensitivity for fluorescent probes. Thus, knowledge of the 2PE spectra of NADH and flavins should help to optimize two-photon-excited fluorescence imaging and may provide insight into the photo-damage mechanisms of living biological preparations in the near-IR.⁽⁴³⁾ Figure 11.6 shows the 2PE spectra of NADH and FMN. The 2PE spectrum of NADPH is nearly identical to NADH. The 2PE spectrum of FAD is similar to FMN, although the action cross sections of FAD are approximately nine times smaller than FMN (presumably due to quenching of fluorescence by the adenine).⁽⁴⁴⁾

One general feature conserved in all measured 2PE spectra is that the 2PE peak absorption wavelengths never appear redshifted (but are frequently blue-shifted) relative to twice the one-photon absorption peaks. For example, large blueshifts were observed for rhodamine-B, DiI, fluorescein, and several Ca^{2+} indicators (Figures 11.3 and 11.4). Although these interesting spectral features still are not understood quantitatively, there are several desirable consequences of such significant blueshifts. First, the resolution of 2PLSM using these fluorophores is considerably higher than predicted by assuming 2PE peak wavelengths at twice the one-photon absorption peak wavelengths. Second, the blueshifts allow conveniently available mode-locked laser sources to excite popular dyes as indicated in Figures 11.3 and 11.4. Finally, conventional dyes possessing different one-photon absorption spectra can be excited by 2PE at a single wavelength. This capability, combined with the large spectral separation between the excitation light and the fluorescence light, greatly simplifies experiments requiring multiple fluorophores. As an example, Figure 11.7 shows simultaneous excitation of rhodamine-123, DAPI, and pyrene using a single 705 nm illumination wavelength.

Fluorescence resonance energy transfer (FRET) is a powerful tool for measuring intermolecular distances.⁽⁴⁵⁾ The applicability of FRET depends on the overlap of fluorescence emission and excitation spectra of the donor and acceptor. As discussed later (Section 11.2.6), no significant fluorescence emission spectra differences were observed between one-and two-photon excitation for the fluorophores examined here. Knowledge of the 2PE spectra also provides new capabilities by combining FRET with 2PE. For example, the optimum excitation wavelength of 2PE FRET using fluorescein and rhodamine is ~ 920 nm (Figure 11.4). Significantly better choices of donor and acceptor in 2PE FRET would be fluorescein and DiI (or Cy-3, the 2PE spectrum of which is similar to that of DiI) when excited at ~ 790 nm, where the fluorescein 2PE cross section is approximately 200 times larger than DiI (Figure 11.4).

Very recently, unexpectedly large three-photon absorption cross sections (with $\sigma_3 \sim 10^{-75} \text{ cm}^6 \text{ s}^2$) have been reported.^(30,46) The discoveries of such



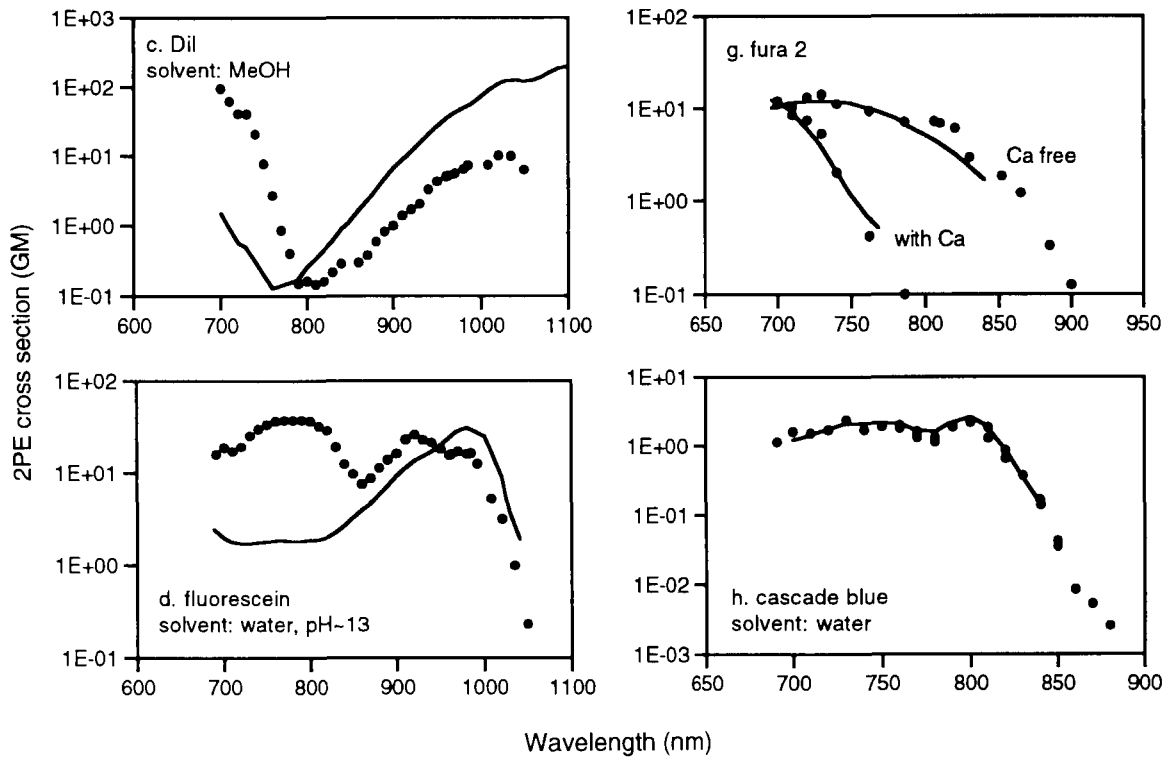


Figure 11.4. Comparison of one-photon (lines) and two-photon (solid circles) fluorescence excitation spectra. The y-axis values represent two-photon action cross sections except for rhodamine-B and fluorescein, where values of the two-photon absorption cross sections were given. For the one-photon results, the x-axis values represent twice the one-photon transition wavelengths, and the y-axis values are arbitrarily scaled: Dil (Dil \equiv 1,1-dioctadecyl-3,3',3'-tetramethyl-lindocyanine, perchlorate); cascade blue \equiv cascade blue hydrazide, trisodium salt; Lucifer yellow \equiv Lucifer yellow CH, ammonium salt; Bodipy \equiv 4,4-difluoro-1,3,5,7,8-pentamethyl-4-bora-3a,4a-diazaindacene-2,6-disulfonic acid, disodium salt. Note that the y axis is in logarithmic scale.

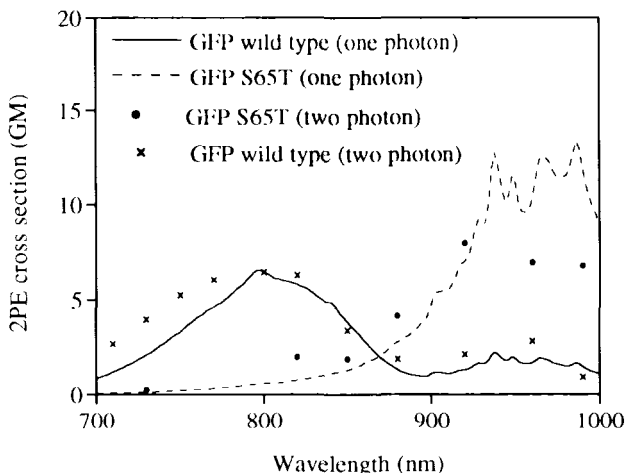


Figure 11.5. Two-photon action cross sections of GFPs. The *y*-axis values represent two-photon action cross sections for GFPs. For the one-photon results, the *x*-axis values represent twice the one-photon transition wavelengths, and the *y*-axis values are arbitrarily scaled. GFPs were provided by George Patterson and David W. Piston, Vanderbilt University.

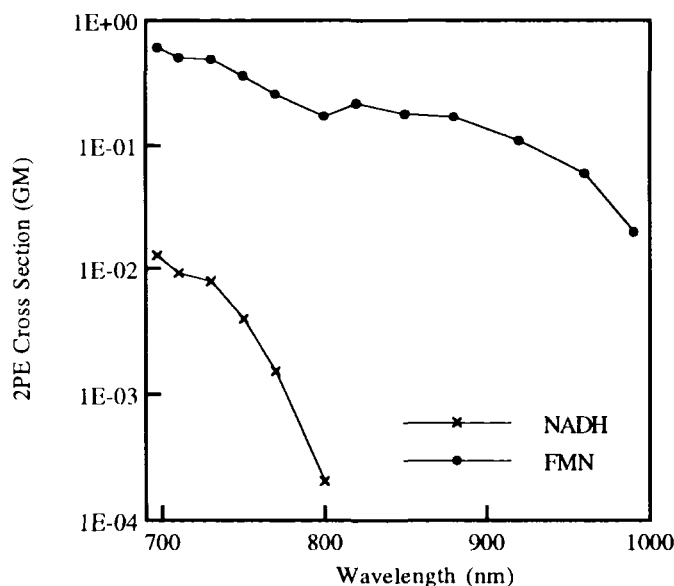


Figure 11.6. Two-photon action cross sections of the native fluorophores NADH and FMN. NADH and FMN were purchased from Sigma. Note that the *y* axis is in logarithmic scale.

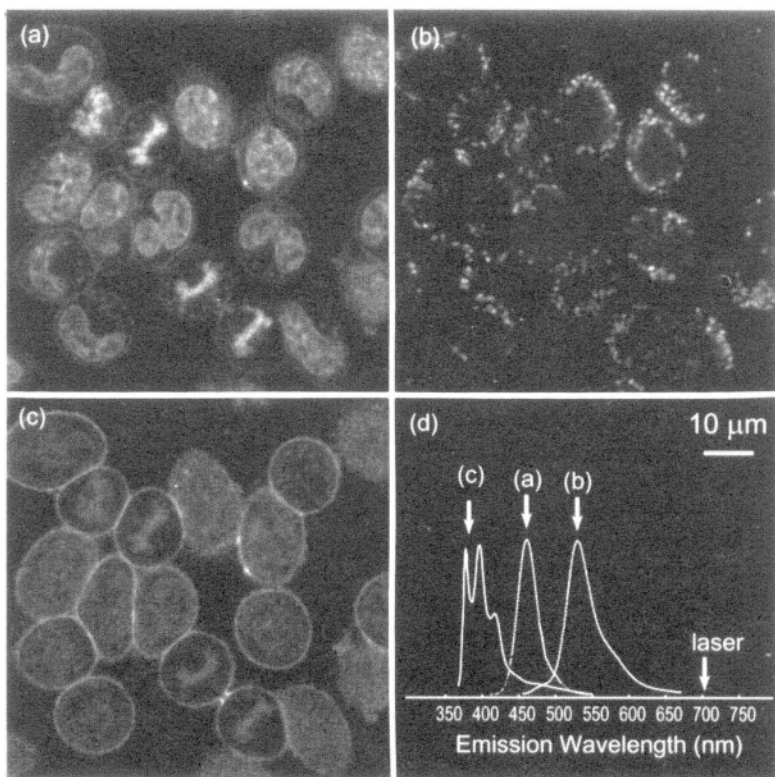


Figure 11.7. Three-color staining of plasma membrane, nuclei, and mitochondria in rat basophilic leukemia (RBL-2H3) cells visualized with two-photon illumination. The cells were incubated with three different stains: (a) nuclear stain (DAPI), (b) mitochondrial stain (rhodamine-123), and (c) plasma membrane label (pyrene lysophosphatidylcholine). The image was obtained using a modified BioRad MRC-600 confocal microscope to scan the excitation beam (705 nm, \sim 120-fs pulse width, 80-MHz repetition rate, \sim 5 mW at the sample) through a 40X/1.3 NA oil immersion objective. Epifluorescence was collected with nondescanned external detection into three channels: 400-nm, 30-nm FWHM [pyrene fluorescence (c)]; 440-nm, 50-nm FWHM [DAPI fluorescence (a)], and 530-nm, 30-nm FWHM [rhodamine-123 fluorescence (b)]. (d) Excitation laser wavelength and the approximate emission spectra of the dyes used.

large cross sections are promising. Three-photon-excited fluorescence has been reported for several fluorescent dyes.^(47,48) We have observed and measured three-photon-excited fluorescence from UV fluorophores such as Ca^{2+} indicator fura-2 and Indo-1, DNA stain DAPI, and the fluorescent reagent dansyl hydrazine by excitation at $\lambda \sim 1.0 \mu\text{m}$. These fluorophores are normally excited at approximately 330 nm to 360 nm and exhibit no linear absorption at 500 nm or $1.0 \mu\text{m}$. The three-photon energy of the $1.0\text{-}\mu\text{m}$ radiation falls into the UV

Table 11.3. One-, Two-, and Three-Photon Excitation Cross Sections (σ)^a

	σ_1 (at λ nm) 10^{-16} cm^2	$\eta \cdot \sigma_2$ (at 700 nm) $10^{-50} \text{ cm}^4 \text{ s}/\text{photon}$	$\eta \cdot \sigma_3$ (at 1.0 μm) $10^{-83} \text{ cm}^6 (\text{s}/\text{photon})^2$
DAPI ^b	1.3 (345 nm)	0.16	0.25
Dansyl	0.17 (336 nm)	1	0.3
Fura-2 with Ca^{2+}	1.2 (335 nm)	12	30
Fura-2 free	1.0 (362 nm)	11	20
Indo-1 with Ca^{2+}	1.3 (340 nm)	1.5	6
Indo-1 free	1.3 (345 nm)	3.5	2

^a Cross sections were measured in $10^{-4} M$ solution. η is the fluorescence quantum efficiency. We have assumed that two- and three-photon fluorescence quantum efficiencies are the same. The estimated uncertainties are 30% for the two-photon cross sections and about a factor of 3 for the three-photon cross sections.

^b DAPI not bound to DNA. The fluorescence quantum efficiency of DAPI is expected to go up by 20-fold upon binding to DNA. (Molecular Probes Handbook 1992 1994, R. P. Haugland, ed., p 222)

absorption band, and therefore three-photon fluorescence is expected. The approximate three-photon cross sections (σ_3) are listed in Table 11.3. For a comparison, the corresponding one- and two-photon cross sections are also given.

To investigate the photophysics of 3PE of fluorophores, we have measured several 3PE spectra [$\sigma_3(\lambda)$] from 960 to 1050 nm for comparison with 1PE spectra (Figure 11.8). The qualitative agreement shown in Figure 11.8 suggests that these 3PE spectra parallel the corresponding 1PE spectra as expected because the same initial excited states can be reached via one- or three-photon excitation without violating any selection rules.

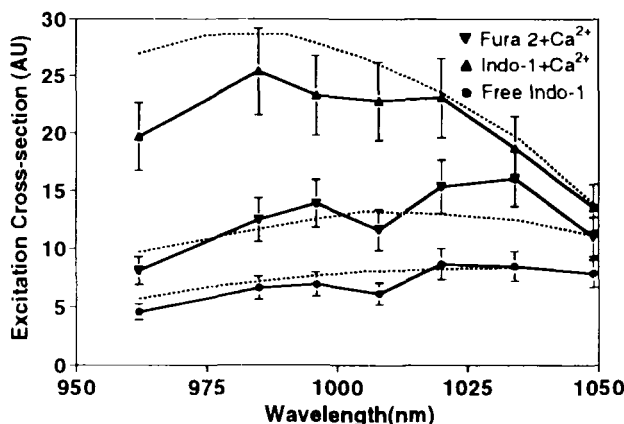


Figure 11.8. Comparison of one-photon (dashed lines) and three-photon (solid lines) fluorescence excitation of Indo-1 and fura-2. For the one-photon results, the x-axis values represent three times the one-photon transition wavelengths. The one-photon results are normalized to their corresponding three-photon data at 1050 nm.

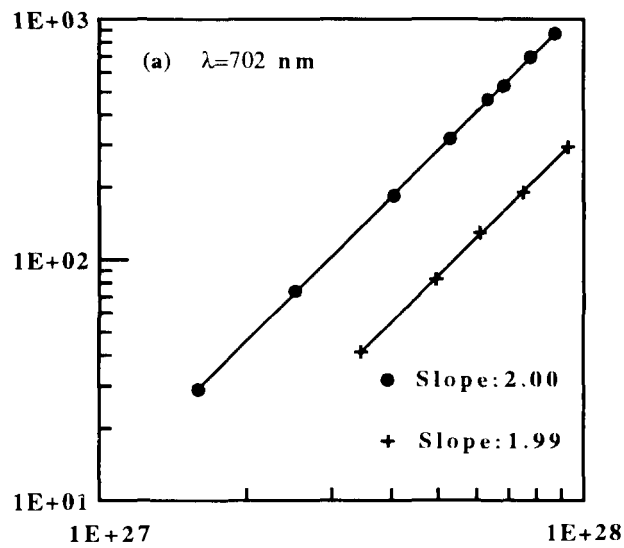
11.2.4. Power Dependence of Two- and Three-Photon-Excited Fluorescence

The power-squared dependence of two-photon-excited fluorescence for most of the dyes in this chapter was tested at one or several excitation wavelengths.⁽⁴⁹⁾ Data for rhodamine-B and fluorescein are summarized in Figure 11.9. Other results are listed in Table 11.4. In all cases nearly perfect power-squared dependence of two-photon-excited fluorescence was recorded.

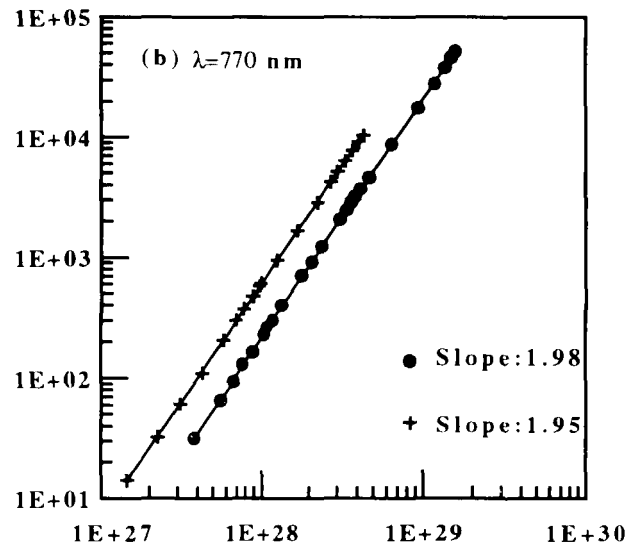
Theoretically, two-photon-excited fluorescence should obey the square-law dependence at low excitation intensity. However, because of various factors such as stimulated emission,^(50,51) excited-state absorption,⁽⁵²⁾ saturation, intensity-dependent 2PE cross section, lack of corrections for 1PE, etc., significant deviation from the square-law dependence of two-photon-excited fluorescence frequently has been observed. Hermann and Ducuing⁽⁵⁰⁾ found that rhodamine-B showed linear dependence at 694 nm at peak intensity levels above 2×10^{25} photons/(cm² s) using nanosecond pulses. The authors suggested that the deviation were caused by stimulated emission from the fluorescence state. Bradley *et al.*⁽⁵²⁾ found rhodamine-B at 1064 nm and rhodamine-6G at 694 nm had similar deviations from squared dependence at peak intensity level $\sim 10^{28}$ photons/(cm² s) using picosecond pulses. The authors suggested stimulated-emission and excited-state absorption as the cause for rhodamine-6G and excited-state absorption for rhodamine-B. Figure 11.9a shows the intensity-squared dependence for rhodamine-B when excited at 702 nm for peak intensity levels from 10^{27} – 10^{28} photons/(cm² s) using 100-fs pulses. Despite the fact that two orders of magnitude higher peak intensity than that in Hermann's experiment⁽⁵⁰⁾ were used, the fluorescence obeys an intensity-squared dependence. Assuming the deviation from square-law dependence observed by Hermann and Ducuing was indeed caused by stimulated emission alone (as the authors suggested), the discrepancy between the two experiments can be explained by the following argument. The proposed stimulated emission is a one-photon process and is proportional to the total number of photons incident on the excited fluorophore.⁽⁵¹⁾ Although a femtosecond light source provides a very high peak intensity, the average intensity is quite low. Therefore, very little stimulated emission is expected in our case. However, if pulses with much longer durations are used, as in the experiments performed by Bradley *et al.* (ps and ns) and by Hermann and Ducuing (ns), stimulated emission could occur with significant probability at high intensity levels.

Three-photon-excited fluorescence should ideally obey the power-cubed dependence. Figure 11.10 shows the power dependence for several fluorophores at relatively low intensity range. Using a high-NA water-immersion objective lens ($NA = 1.2$), no significant deviations from the cubic dependence were observed at I_p up to 6×10^{30} photons/(cm² s) for fura-2 and DAPI at 992 nm. However, dramatic decreases in the apparent power exponent were observed at photon flux

Fluorescence (A.U)



Fluorescence (A.U.)



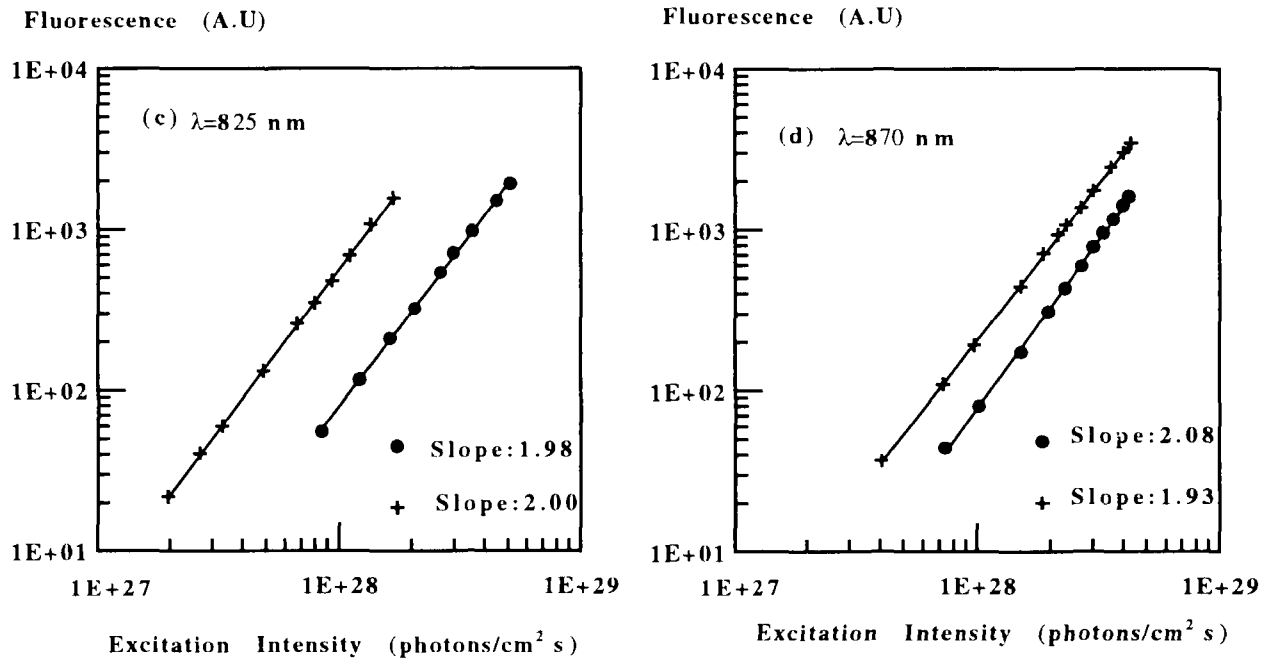


Figure 11.9. Logarithmic plots of the dependence of relative two-photon-induced fluorescence on pulse intensity for (●) $10^{-4} M$ solution of rhodamine-B in methanol and (+) $10^{-4} M$ solution of fluorescein in water. Excitation wavelength is indicated in the upper left corner of each graph. The fitted slopes are represented in the lower right corners. Excitation pulse width is about 100 fs (assuming sech² pulse shape). Ordinate scales of fluorescence are in unrelated arbitrary units. Estimated uncertainties of the fitted slopes are ± 0.03 .

Table 11.4. Dependence of Two-Photon-Excited Fluorescence on Excitation Peak Intensity

Dye	Excitation wavelength (nm)	Peak intensity (photons/cm ² s)	Slope in logarithmic plot
Dil	702	2.8×10^{27} – 1.2×10^{28}	2.01 ± 0.03
Bodipy	770	8.6×10^{27} – 2.6×10^{28}	2.02 ± 0.03
Lucifer yellow	870	4.2×10^{27} – 4.6×10^{28}	1.98 ± 0.03
Rhodamine-B	1000	4.3×10^{28} – 3.9×10^{29}	2.01 ± 0.03
Indo-1 (high Ca)	754	2.9×10^{28} – 5.5×10^{29}	2.00 ± 0.03

densities higher than 10^{31} photons/(cm² s) for both fluorophores. Although photobleaching may account for such deviation, other factors, such as field-induced changes in the electronic properties of the fluorophores, may become important at very high intensity levels.⁽⁶⁾ The instantaneous electric field (E) at the focal spot is approximately 3×10^7 V/cm at $I_p = 10^{31}$ photons/(cm² s), which is probably sufficient to modify the photophysical properties of the dye molecules.

A measurable combination of n - and $(n + 1)$ -photon-excited fluorescence is expected within certain wavelength and intensity ranges. For example, thermally assisted 1PE could become significant at low intensity levels if the wavelength of attempted 2PE overlaps the absorption band for 1PE. This causes severe departure from the square-law dependence. We have observed nearly linear power dependence with rhodamine-B at 705 nm using a single-mode CW laser at excitation intensity around 10^{24} photons/(cm² s). Significant deviation from square-law dependence is found for rhodamine-B at intensity levels approximately 10^{24}

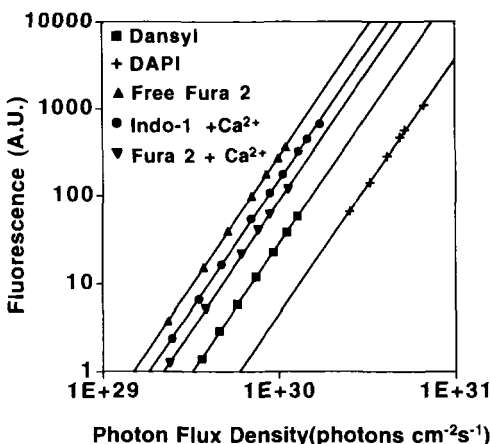


Figure 11.10. Logarithmic plots of the dependence of relative three-photon-excited fluorescence on the peak incident photon flux density at the geometric focal points in five fluorophore solutions. The concentrations are $10^{-4} M$ and the excitation wavelength is 1.0 μm . The excitation pulse width is about 110 fs (assuming sech² pulse shape). The solid lines represent the best power-law fits to the experimental data with slopes of 2.92, 2.96, 2.93, 2.94, and 2.91 for dansyl, free fura-2, Indo-1 + Ca, fura-2 + Ca, and DAPI, respectively. The estimated uncertainties in the slopes are $\pm 3\%$.

to 10^{25} photons/(cm² s) for $\lambda < 730$ nm, which were also observed by Hermann and Ducuing⁽⁵⁰⁾ at 694 nm.

Mixture of fluorescence resulting from different-order photon excitations can also be obtained in attempting 3PE. For example, as an excitation ratiometric calcium indicator, the one-photon absorption maximum of fura-2 shifts from 362 nm in the Ca-free form to 335 nm on binding to Ca,⁽⁵³⁾ and the corresponding shifts are also apparent in its two-photon fluorescence excitation spectra (Figure 11.4). This absorption change makes the ratio between three- and two-photon-excited fluorescence of the two species very different from each other. At $I_p \sim 10^{30}$ photons/(cm² s) (which is normally used in nonlinear laser microscopy⁽¹⁰⁾), it is found that for the Ca-bound species, 2PE dominates at $\lambda < 830$ nm and 3PE dominates at $\lambda > 900$ nm; for the Ca-free species two-photon dominates up to 910 nm, and three-photon dominates only at $\lambda > 960$ nm. At intermediate wavelengths, a mixture of two- and three-photon excitation was observed. Table 11.5 lists the measured power exponents for fura-2 at several wavelengths, which shows the gradual transition from two-photon to three-photon excitation. Although the three-dimensional imaging capability is preserved in this wavelength range, quantitative imaging, as is required in calcium measurements using ratiometric indicators, would be complicated by the calibration dependence on incident intensities.

Experimentally, intersystem crossing, photobleaching, and saturation cause severe deviation from the expected power-law dependence of the excited fluorescence. Photobleaching may account for the nonquadratic dependence of two-photon-excited fluorescence in some earlier reports.⁽⁵⁴⁾ Detailed discussion of these properties is given in Section 11.4.

11.2.5. Dependence of Two-Photon-Excited Fluorescence on Pulse Width

Under pulsed excitation, $g^{(2)} = g_p^{(2)}/f\tau$ is inversely proportional to the excitation pulse width. Therefore, two-photon-excited fluorescence is expected to increase linearly with $1/\tau$ under the conditions that the pulse energy and the pulse shape (i.e., $g_p^{(2)}$) are constant. Figure 11.1 la shows the fluorescence depen-

Table 11.5. Slopes in the Logarithmic Plot of Fluorescence Output Versus Incident Intensity at Selected Wavelengths^a

	838 nm	861 nm	880 nm	900 nm	922 nm	970 nm
Fura-2 + Ca	2.2	2.4	2.6	2.7	2.9	3.0
Fura-2 free	2.0	2.0	2.0	2.1	2.3	2.9

^a Slopes were measured at $I_p \sim 10^{30}$ photons/(cm² s). Slope between 2.0 and 3.0 indicates that a mixture of two- and three-photon-excited fluorescence were generated. The uncertainties in the slopes are ~6%.

dence on pulse width from 90 fs to 230 fs for Indo-1 at 770 nm with constant average excitation power. The 7% deviation from slope 1 in the logarithmic plot is probably caused by a change of pulse profile (thus of $g_p^{(2)}$) during pulse-width scanning. In Figure 11.11b, two-photon-excited fluorescence of Indo-1 and the second-harmonic generation of powder KDP particles excited using broad pulses with pulse widths approximately 500 fs to 1.2 ps were compared. These results show they have the same pulse-width dependence.

One way to distinguish simultaneous 2PE from sequential 2PE (two-step 2PE) is to study the fluorescence dependence on excitation pulse width. Two-photon-excited fluorescence is inversely proportional to τ only if τ is much longer than the intermediate-state lifetime. In simultaneous 2PE, virtual states with lifetimes around 10^{-16} s serve as the intermediate states. Hence, one expects two-

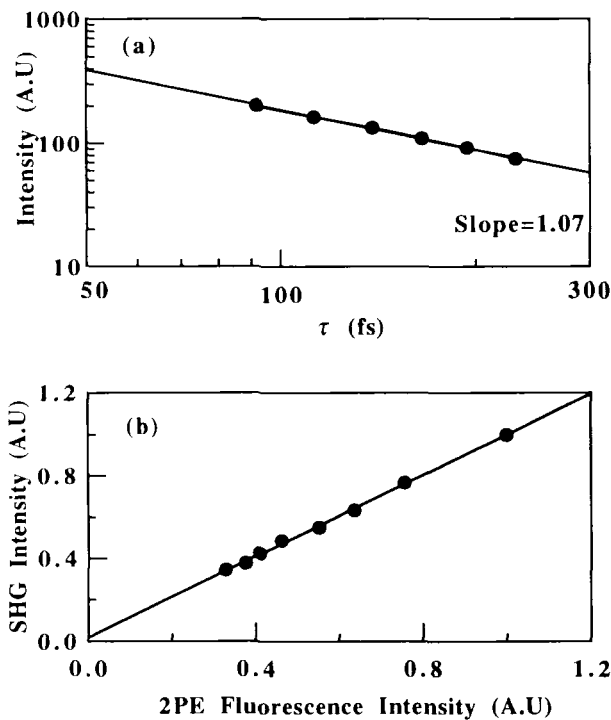


Figure 11.11. Dependence of two-photon-excited fluorescence on excitation pulse width. (a) Logarithmic plot of two-photon-excited fluorescence versus excitation pulse width in $10^{-4} M$ solution of Indo-1 (low Ca^{2+}). (b) Comparison of two-photon-excited fluorescence in $10^{-4} M$ solution of Indo-1 (low Ca^{2+}) and second-harmonic generation (SHG) in KDP powder at eight different excitation pulse widths from approximately 500 fs to 1.2 ps. Data are collected for constant average excitation power at $\lambda = 770$ nm. The size of the circle approximately represents the uncertainties of the data.

photon-excited fluorescence to be inversely proportional to τ down to the 100-fs region. However, because real states with lifetimes approximately 10^{-9} – 10^{-12} s serve as the intermediate states in sequential 2PE, two-photon-excited fluorescence should be independent of τ when τ is approximately 100 fs. Hence, the results in Figure 11.11, confirm simultaneous 2PE for Indo-1 at 770 nm. Varying the time between adjacent pulses (by using a Michelson interferometer, for example) instead of varying the pulsedwidth provides a more convenient approach for studying the intermediate-state lifetimes. Our tests showed that intermediate-state lifetimes for rhodamine-B (excited at 700 nm and 770 nm), fluorescein (excited at 700 nm and 782 nm) and coumarin 307 (excited at 770 nm) are less than 100 fs. Hence, sequential 2PE is highly unlikely for these dyes at the wavelengths tested.

11.2.6. One-, Two- and Three-Photon-Excited Fluorescence Emission Spectra Compared

In most cases reported in the literature, one- and two-photon-excited fluorescence emission spectra were the same.⁽⁵⁵⁾ However, there are cases where difference between one- and two-photon-excited fluorescence emission spectra were observed.⁽⁵⁶⁾ Figure 11.12 shows the emission spectra of fluorescein under 1PE and 2PE. For all the fluorophores described in this chapter, one- and two-photon-excited fluorescence emission spectra are identical. In general, two-photon-excited fluorescence emission spectra are independent of excitation wavelengths (Figure 11.13), supporting the assumption that the fluorescence quantum efficiency is a constant regardless of the excitation wavelength. There have been no reported difference between one- and three-photon-excited fluorescence emission spectra, suggesting that quite generally the same fluorescent states are reached regardless of the excitation mode.

11.2.7. Two-Photon Spectra Excited by CW and Femtosecond Pulsed Laser Compared

As discussed in the previous sections, determination of the second-order temporal coherence (i.e., $g^{(2)}$) is crucial for precise cross-sectional measurements. The 2PE cross sections measured with femtosecond pulses have the uncertainty of the pulse shape factor $g_p^{(2)}$. Figure 11.14 shows the 2PE spectra excited by the single-mode CW laser for cascade blue and 2PE spectra from pulsed excitation for comparison. As seen in Figure 11.14, there is good agreement. The good agreement between 2PE spectra from CW and pulsed measurements suggests that the considerable spectral spread of ultrashort pulses (5–10 nm in this experiment) does not alter the excitation spectra signif-

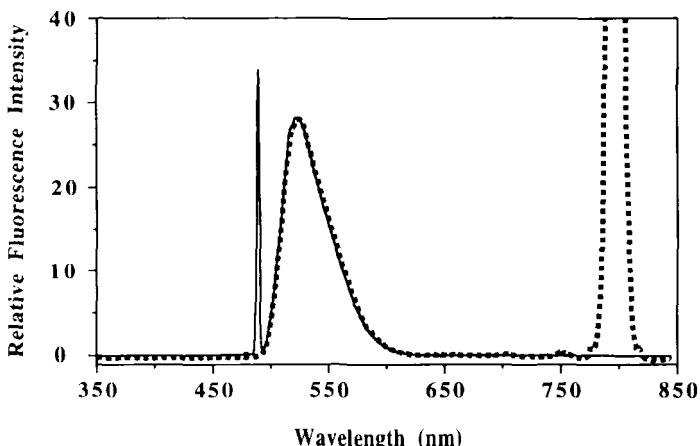


Figure 11.12. Fluorescence emission spectra of 10^{-4} M solution of fluorescein in water excited by (—) one photon (488 nm) and (---) two photons (800 nm). The peaks at 488 nm and 800 nm are residual excitation light. Instrument wavelength resolution is 1.0 nm.

icantly. Although the shapes of the 2PE spectra obtained by CW and pulsed excitation are similar, the absolute cross sections obtained by CW measurements are about 40% larger than those obtained by pulsed measurements if a sech^2 -pulse shape (i.e., $g_p^{(2)} = 0.59$) is assumed. There are several possible reasons to explain this discrepancy: (1) The excitation pulse may not have a sech^2 -pulse shape. (2) Pulse broadening caused by the group velocity dispersion

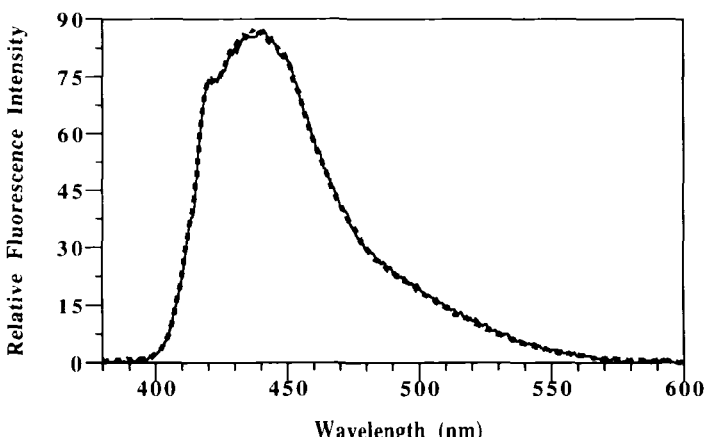


Figure 11.13. Two-photon-excited fluorescence emission spectra of 10^{-4} M solution of cascade blue in water excited at (—) 750 nm and (---) 800 nm.

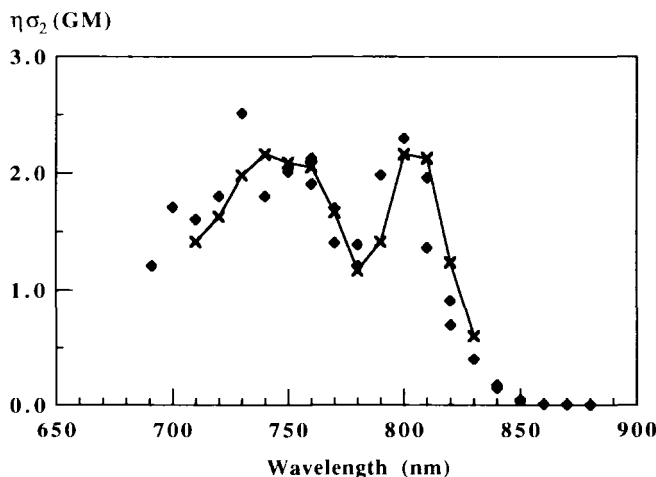


Figure 11.14. Comparison of two-photon fluorescence excitation spectra of 10^{-4} M solution of cascade blue in water obtained with (◆) a mode-locked femtosecond Ti sapphire laser and (×) a single-mode CW Ti sapphire laser.

of the excitation optics leads to a broader pulse at the sample than that indicated by external measurement. (3) An unlikely possibility is a slight deviation from the ideal quadratic power dependence. Because the peak intensities used in the pulsed excitation are approximately 1000 times that used in the CW measurement, a 1% deviation in the power exponent (i.e., a slope of 1.98) would cause a drop of fluorescence in pulsed excitation by $\sim 15\%$.

11.3. Multiphoton Microscopy

Nonlinear laser scanning microscopy gains several advantages from two- or three-photon excitation of fluorescence. Because the absorption increases quadratically or cubically with the excitation intensity, the fluorescence (and potential photobleaching and photodamage related to fluorescence excitation) are all confined to the vicinity of the focal point. This spatial localization not only provides intrinsic three-dimensional resolution in fluorescence microscopy but also provides unprecedented capabilities for three-dimensionally localized photochemistry in subfemtoliter volumes, including photolytic release of caged effector molecules.⁽⁸⁾ Because two or three photons are absorbed for each transition event, a red or near-IR laser is used to excite fluorophores that normally absorb in the UV or deep-UV region. Such a wavelength shift avoids many limitations of UV lasers and UV optics. Because wide-field detection

tion is used in nonlinear microscopy, even multiply scattered fluorescence photons contribute equally to the image formation, in contrast with confocal microscopy where the unscattered photons form the confocal image.⁽⁵⁷⁾ This efficient detection of fluorescence photons, combined with the relatively deep penetration of IR excitation light in most biological preparations,⁽⁵⁸⁾ enables nonlinear microscopy to image deep ($>200\text{ }\mu\text{m}$) into turbid biological specimens. In general, the background interference from Rayleigh and Raman scattering is negligible because multiphoton-excited fluorescence occurs at a much shorter wavelength region than the excitation light. Thus, ultrasensitive measurements are possible, including detection of single dye molecules^(59,60) and low quantities of fluorogen-labeled neurotransmitters.⁽⁶¹⁾ Finally, in addition to background interference, photodamage to living cells by deep-UV excitation has previously limited the use of imaging based on native fluorescence. Three-photon-excited fluorescence provides the unique opportunity to excite intrinsic chromophores, such as amino acids, proteins, and neurotransmitters, using relatively benign excitation wavelengths accessible with commercially available near-IR lasers.⁽⁶²⁾ The combination of two- and three-photon-excited fluorescence microscopy extends the useful range of nonlinear laser microscopy.

11.3.1. Instrument of Nonlinear Microscopy

A typical nonlinear microscope consists of four major parts: (1) excitation source(s), (2) scanning system, (3) microscope, (4) detection system, as shown schematically in Figure 11.15. The scanning system and the microscope are usually similar to those used in one-photon confocal laser scanning microscope, with the appropriate modifications to accommodate pulsed excitation source and near-IR excitation wavelength (typically 600 to 1100 nm). For example, single-stack mirror coatings must be used to minimize group velocity dispersion when ultrashort pulsed ($\sim 100\text{ fs}$) excitation is used. Details of the scanning system and the microscope can be found in many places.⁽⁶³⁾ Here we focus our discussion on the excitation source and the detection system where the unique characteristics of nonlinear microscopy reside.

11.3.1.1. Excitation Source

Nonlinear microscopy typically requires pulsed excitation sources because the high peak intensities of these sources lead to much more efficient MPE at relatively low average power (see Section 11.2.2.2). The first tunable ultrafast lasers were CW dye lasers, and the first two-photon images were recorded using a CPM dye laser.⁽⁸⁾ However, in addition to their limited tuning range, dyes have a

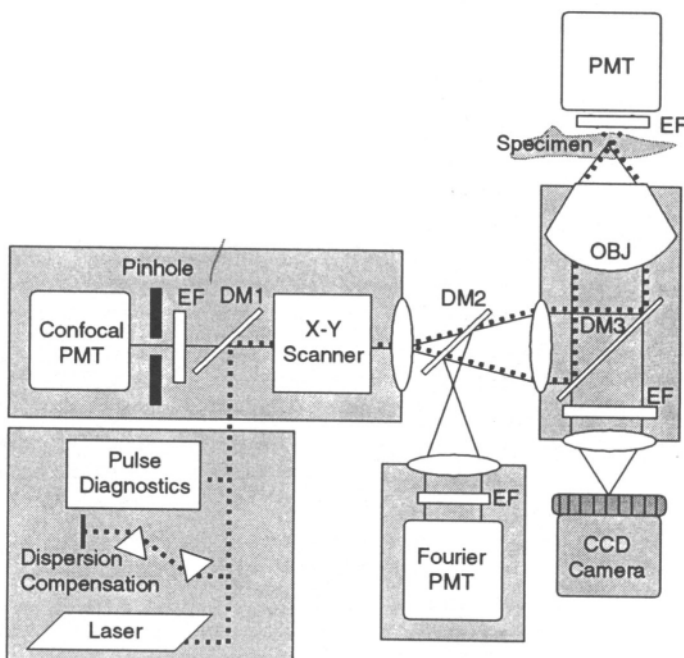


Figure 11.15. Illustration of a multiphoton laser scanning microscope with four possible detection schemes. The fluorescence path and the excitation path are separated by dichroic mirrors DM1, DM2, or DM3 for the three epifluorescence detection setups. No dichroic is necessary for the detection of fluorescence directly above the specimen. This direct detection scheme may be particularly useful for efficient collection of UV or deep-UV fluorescence in a specimen the thickness of which is approximately the working distance of the objective lens (OBJ). The EFs are emission filters.

limited lifetime and are usually toxic and difficult to handle. The stability of dye lasers is often much worse than tunable solid-state lasers. Thus, the rapidly emerging solid-state tunable lasers have been the excitation sources of choice for nonlinear microscopy and spectroscopy, with the exception of the visible spectrum where no broadly tunable solid-state lasers are available. Although CW lasers can be used to measure 2PE cross sections, their application in 2PLSM is limited⁽⁶⁴⁾ and becomes impractical in 3PE. Thus, we will limit our discussion to pulsed solid-state excitation sources.

The wavelength tunabilities of several solid-state pulsed lasers in the 600-to 1100-nm-wavelength range are illustrated in Figure 11.3. A more complete review of the developments in ultrafast lasers can be found in the review article by French.⁽⁶⁵⁾ Strong water absorption at wavelengths significantly above 1100-nm limits the usable spectral window for excitation. Although multiphoton microscopy has only been applied with excitations in the red or near-IR, nonlinear

microscopy should also be able to work with visible excitation if required. There are many factors that determine the choice of excitation wavelength in biological imaging: the fluorophore excitation spectra, the wavelength dependence of fluorophore photobleaching efficiency (i.e., the fluorophore photobleaching spectra), the cellular photodamage spectra, etc. In practice, one certainly also needs to consider the availability and the cost. Although significant amount of data has been accumulated for the 2PE spectra of common biological indicators in the last several years (see Section 11.2), the wavelength dependence of photobleaching of fluorophores and photodamage to living cells are largely unknown and may vary greatly in various applications. Thus, it is currently impossible to prescribe an optimum wavelength region for nonlinear microscopy in general. Two approaches have been used in selecting the excitation sources.

In the first approach, a broadly tunable excitation source is used to cover the most of the excitation spectra window. For example, with several different mirror sets, a mode-locked Ti sapphire laser can be continuously tuned from 690 to 1070 nm. Thus, a mode-locked Ti sapphire laser is capable of providing 2PE from 345 to 535 nm and 3PE from 230 to 357 nm, covering the excitation spectra of most biologically relevant fluorophores and intrinsic absorbers such as proteins and DNA. An even more tunable excitation source is the optical parametric oscillator (OPO). With frequency doubling, the OPO can cover part of the visible spectrum (550 to 700 nm) in addition to the near-IR. We note that the blueshifted excitation spectra of many orange- or red-excitible fluorophores, such as rhodamine-B, DiI, and Tex-red (Section 11.2), allows convenient 2PE at wavelengths significantly below 1100 nm.

A low-cost alternative to the first approach is to use an excitation source that is not tunable or with only very limited tunability, giving up some parts of the excitation spectral window. For example, a Nd YLF laser (~ 1047 nm) can be used to excite long-wavelength visible fluorophores via 2PE and some UV fluorophores via 3PE.⁽¹⁶⁾ A compromise between these two approaches is to use a set of several low-cost excitation sources that center at different wavelength ranges to increase the spectral coverage.

The requirements for the output power, pulse width, and pulse repetition rate of the excitation sources are determined by fluorophore saturation and the need to discriminate different-order photon processes. Once again, it is difficult to give universal criteria for nonlinear microscopy because optimum excitation conditions may vary greatly in different applications. Although typical 2PLSM uses several milliwatts average power (at sample) with approximately 100-fs pulses at 100-MHz repetition rate, it is not clear whether these excitation conditions are ideal. In Sections 11.4.1 and 11.4.3.2, we analyze in detail saturation of excitation and the factors that control the relative contributions from different-order photon processes, providing means of choosing the optimum excitation conditions.

11.3.1.2. Detection Systems

In addition to the excitation sources, nonlinear microscopy differs from conventional one-photon confocal laser scanning microscopy mainly in the detection system. Because the excitation is localized in all three dimensions, no confocal spatial filter is required in the detection system of nonlinear microscopy to achieve three-dimensional (3D) resolution. (We note, however, that the addition of a spatial filter in nonlinear microscopy can improve the resolution, with the expense of reduced detection efficiency.) The elimination of the spatial filter allows nondescanned detection schemes (see Figure 11.15) that cannot be applied in the one-photon system. Detailed discussion of these new detection configurations can be found in review articles by Williams *et al.*⁽¹⁰⁾ and by Denk *et al.*⁽¹¹⁾

Nondescanned detection usually offers higher overall efficiency because there are less optical elements in the detection path. However, the applicability of nondescanned detection depends on the size of the active area and the acceptance angle (defined by numerical aperture, NA_d) of the detectors or optical fibers used. Thus, there are cases, such as detection of fluorescence using a spectrometer, where descanned detection must be employed to obtain better signal detection. For simplicity, we assume a circular detector with diameter d and a circular field of view. The parameter that governs the choice of the detection mode (descanned or nondescanned) is $D \times NA$, where D is the diameter of the field of view and NA is the numerical aperture of the objective lens; D can simply be the size of the scanned field (determined by the scanning angle and the focal length of the objective) or the size of the full field of the objective if sample scattering delocalizes the fluorescence distribution. It is then straightforward to prove that large-detector, i.e., $d \times NA_d \geq D \times NA$, nondescanned detection can be employed without, in principle, any loss of signal light that is collected by the objective lens. On the other hand, when small detectors ($d \times NA_d < D \times NA$) are used in nondescanned detection mode, loss of signal light is inevitable because either the size of the detector is too small or the angle of incidence onto the detector is too large. Thus, the descanned detection mode should be used with small detectors. In practice, the maximum acceptance angle of detectors may be further limited because of the angular dependence of detector sensitivity. Although photomultiplier tubes are generally sensitive even to light incident at oblique angles, the profile of angular dependence may require close-to-normal incidence in order to achieve angle-independent detector response.

We now use the criteria to analyze one practical example: detection of multiphoton-excited fluorescence using a spectrometer. The acceptance angle of the spectrometer is determined by its *f* number. In our case, an *f*4 (corresponds to $NA_d \approx 0.12$) spectrometer (Spex 270M) is used. To achieve the highest

spectral resolution offered by the spectrometer, the entrance slit is set for $d \approx 20 \mu\text{m}$. The scanning system (BioRad600) combined with a 1.3-NA 40X objective (Zeiss) produces a scanned field of $D \approx 200 \mu\text{m}$. It is clear from the above analysis that the descanned detection mode must be used to achieve the best detection efficiency in this case. In order to use the nondescanned detection mode without significant loss of signal light, one must increase the NA of the spectrometer, widen the entrance slit to $\sim 2 \text{ mm}$ (with substantial degradation of the resolution of the spectrometer), or limit the field of view to $D \approx 2 \mu\text{m}$ by reducing the scanning angle.

11.3.2. Multiphoton Excitation Volume

An intrinsic difference between MPE and 1PE is the excitation volume. In 1PE, the excitation volume is proportional to the sample thickness (assuming attenuation of the incident light can be neglected), while in MPE the excitation volume is independent of sample thickness as long as the sample thickness is much greater than the focal depth. Thus, a sample-independent volume can be defined in MPE. As discussed previously, this localized excitation in the radial and axial directions is the main advantage in multiphoton fluorescence microscopy.

The volume integral in Eq. (11.7) provides a natural candidate for defining the MPE volume. However, such a choice does not truly reflect the size of the MPE volume without compensating for the sharpness of the intensity profile or “volume contrast.” An experimentally defined volume can be obtained by first determining the total number of molecules (N) in the excitation volume in a uniform fluorophore solution of known concentration, which can be achieved by measuring the variance of the fluctuation of multiphoton-excited fluorescence at constant excitation intensity, a technique routinely used in fluorescence correlation spectroscopy.^(66,67) Then, since $N = CV$, the subsequently defined excitation volume has the form^(5,9)

$$V_n = \gamma_n^{-1} \int_{V \rightarrow \infty} S^n(\mathbf{r}) d\mathbf{r} \quad (11.25)$$

where is $V_n = N/C$ is the n -photon excitation volume determined by the mean number of molecules in the probed volume and $\gamma_n = \int_{V \rightarrow \infty} S^{2n}(\mathbf{r}) d\mathbf{r} / \int_{V \rightarrow \infty} S^n(\mathbf{r}) d\mathbf{r}$. Intuitively, γ_n represents the “volume contrast” for an n -photon excitation volume. For an hypothetical excitation volume with infinitely sharp boundaries, $\gamma_n = 1$. For any other excitation conditions with less sharply defined boundaries, γ_n will take values that are less than unity. Values of γ_n for several illumination profiles are listed in Table 11.6.

Table 11.6. Values of γ_n for Diffraction-Limited, Gaussian–Lorentzian (GL), and Spherical Gaussian Illumination Profiles^a

γ_n	Diffraction-limited focus	GL focus	Spherical Gaussian
γ_2	0.26	3/16	$\sqrt{2}/4$
γ_3	0.36	35/128	$\sqrt{2}/4$
γ_4	0.36	77/256	$\sqrt{2}/4$

^a Note that γ_2 for diffraction-limited focus should be 0.26 instead of the previously published value of 0.5; see Mertz *et al.*⁽⁵⁹⁾

We now compare two- and three-photon excitation volumes based on the volume concept. FWHMs of the excitation profile have usually been used to represent spatial resolutions. Although such choice intuitively describes the extent of the excitation volume, it neglects the importance of the exact spatial profile. For example, a spherical Gaussian distribution and a distribution with infinitely sharp boundaries may have the same FWHM, but their three-dimensional localizations are certainly not the same. Thus, FWHM should not be used in comparing resolutions of different excitation profiles that resulted from different focusing geometry or different mode of excitation (i.e., two- or three-photon excitation, etc.). As an alternative, the MPE volume (V_n) can be used to gauge the resolutions of nonlinear microscopy under different excitation conditions. Two- and three-photon excitation volumes will be examined with GL and diffraction-limited focus.

The two- and three-photon excitation volumes in GL focus are obtained from Eqs. (11.10) and (11.25):

$$V_2 = \frac{4}{3} \frac{n_0 \pi^3 w_0^4}{\lambda} \quad (11.26)$$

$$V_3 = \frac{32}{105} \frac{n_0 \pi^3 w_0^4}{\lambda} \quad (11.27)$$

Assuming $w_0 = 0.3 \text{ } \mu\text{m}$, $\lambda = 0.5 \text{ } \mu\text{m}$, and $n_0 = 1.33$ (conditions that can be achieved with a high-power objective lens),⁽⁶⁸⁾ then $V_2 = 0.9 \text{ } \mu\text{m}^3$ and $V_3 = 0.2 \text{ } \mu\text{m}^3$ at $\lambda = 0.5 \text{ } \mu\text{m}$. Although the three-photon volume may seem much smaller than the corresponding two-photon volume, the wavelength dependence of MPE must be taken into account. In order to excite the molecule with the same energy, the excitation wavelength used in 3PE must be 1.5 times longer than that of 2PE. Because the focal waist size of a GL beam should be proportional to the incident wavelength (i.e., $w_0 \propto \lambda$), the MPE volumes should then scale as $V_n \propto \lambda^3$, a general result that can also be

obtained by simple dimensional analysis. Thus, the ratio of two- and three-photon excitation volumes becomes

$$\frac{V_2}{V_3} = \frac{4}{3} \times \frac{105}{32} \times \left(\frac{2}{3}\right)^3 = 1.3$$

Interestingly, the three-photon volume is still 30% smaller than the two-photon volume even after we take into account the excitation wavelength. This is quite contrary to the comparison based on the FWHM of the excitation profile: the FWHM in the focal plane using 2PE at wavelength λ is actually about 20% smaller than that in 3PE at wavelength 1.5λ . Intuitively, the improvement in the overall localization of 3PE, manifested by the smaller excitation volume, is due to the accentuated reduction of excitation rate in the lower-intensity region. Thus, the “volume contrast” in 3PE is much sharper than that in 2PE: $\gamma_3 = 0.27$ compared to $\gamma_2 = 0.19$, which partially compensates the wavelength effect. However, such an improvement by using higher-order photon process does not apply to many other excitation profiles. For example, in a spherical Gaussian profile, where $\gamma_n = \text{constant} = \sqrt{2}/4$, the three-photon volume (at 1.5λ) is 84% larger than the two-photon volume (at λ). The contrast parameter γ_n for a GL profile approaches that of a spherical Gaussian profile ($\sqrt{2}/4$) when n is very large.

Using Eq. (11.13) and results in Table 11.2, we obtain the two- and three-photon volumes of diffraction-limited focus:

$$\begin{aligned} V_2 &\approx \frac{33n_0\lambda^3}{\pi^3(NA)^4} \\ V_3 &\approx \frac{9.8n_0\lambda^3}{\pi^3(NA)^4} \end{aligned} \tag{11.28}$$

Assuming $NA = 1.3$, $\lambda = 0.5 \mu\text{m}$, and $n_0 = 1.33$, then $V_2 = 0.060 \mu\text{m}^3$ and $V_3 = 0.018 \mu\text{m}^3$. These volumes are less than 10% of those obtained using GL profiles. Again, we compare two- and three-photon excitation volumes by taking into account the different excitation wavelength:

$$\frac{V_2}{V_3} = \frac{33}{9.8} \times \left(\frac{2}{3}\right)^3 \approx 1$$

Thus, the excitation volumes in two- and three-photon excitation when using diffraction-limited focus are about the same. We again note that both the radial and the axial FWHMs of 3PE (at 1.5λ) are approximately 1.2 times that of 2PE (at λ).

11.3.3. Multiphoton Uncaging

Although nonlinear microscopy has become a powerful tool in imaging, it was originally devised to do three-dimensionally localized uncaging of caged biological effector molecules. Many biologically important molecules such as Ca^{2+} , ATP, neurotransmitters, etc., can be conjugated to cages and consequently become inactive.⁽⁶⁹⁾ Reactivation of such caged molecules (uncaging) can be achieved by UV illumination. Thus, uncaging provides the means to change biological parameters in well-defined spatial and temporal domains. However, the spatial resolution of conventional one-photon uncaging is at best limited to a cylindrical region that is illuminated, leading to very poor axial confinement. Multiphoton uncaging provides intrinsic three-dimensionally localized release of caged molecules with diffraction-limited spatial resolution. As discussed in Section 11.3.2, uncaging volumes as small as $0.1 \mu\text{m}^3$ can be obtained with high-NA focusing and near-IR excitation. Two-photon uncaging of neurotransmitters has been successfully used to map the distribution of ligand-gated receptors.⁽⁷⁰⁾

Figure 11.16 shows two-photon uncaging of DMNB-caged fluorescein immobilized in formvar. Although it is yet to be demonstrated, higher-order photon processes such as 3PE may also be applied to uncaging, particularly for caged compounds with strong deep-UV absorption.

Another application of multiphoton uncaging is the study of three-dimensional diffusion dynamics using caged fluorophores. Because signal is detected against a dark background, uncaging offers better signal-to-noise ratio than fluorescence photobleaching recovery (FPR) in similar studies, where small signals must be detected on top of a large background.

11.3.4. Imaging of Intrinsic Fluorophores with Multiphoton Excitation

One of the advantages of nonlinear microscopy is direct imaging of intrinsic chromophores such as NADH, tryptophan, serotonin, etc. Because these native chromophores have their one-photon absorption in the UV or deep UV, direct imaging using 1PE is severely limited by photodamage to living specimens in addition to indiscriminate background typically encountered in UV microscopy. The combination of the inherent three-dimensionally localized excitation and near-IR excitation wavelength of nonlinear microscopy circumvents these limitations. Two-photon-excited cellular autofluorescence from intrinsic chromophores such as NAD(P)H has been used to study the cellular metabolic state.⁽⁴¹⁾ As an example, Figure 11.17 shows two-photon-excited native NADH autofluorescence in living cells. Recently, 3PE has been successfully used to visualize native

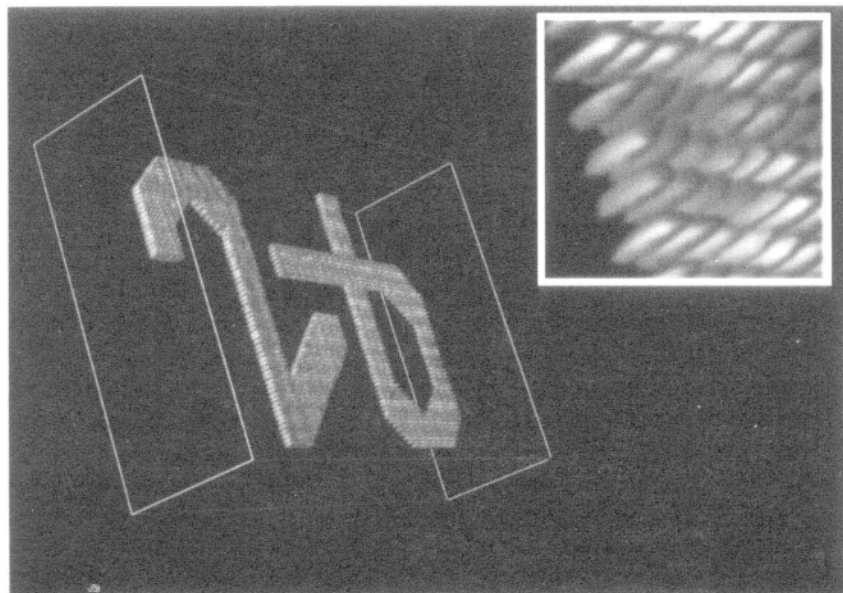


Figure 11.16. Uncaging of a fluorophore in a polymer. DMNB-caged C₁₂-fluorescein in former was point uncapped to produce a “2 gamma” (i.e., 2 photon) pattern using 5-ms bursts of Ti sapphire laser pulses (700 nm, 100-fs pulse width, 80-MHz repetition rate). Average power at sample was ~10 mW. Image is a 3D rendering of a stack of 30 optical sections taken of the polymer after the point uncaging of the pattern. The volume of the wire frame in rendering is 15 × 45 × 40 μm³. The insert shows a number of the individual uncaging volumes that make up the full pattern and demonstrates the precision obtainable with multiphoton uncaging. (Image courtesy R. M. Williams and W. R. Zipfel (DRBIO).)

serotonin and tryptophan fluorescence (see Figure 11.18),⁽¹⁸⁾ providing the opportunity to observe cellular secretion process directly.

11.3.5. Deep Imaging

Multiphoton excitation provides the unique capability to image deeply into specimens that strongly scatter the illumination light. This advantage derives from the excitation and detection characteristics of nonlinear microscopy. In conventional 1PE, the total generated fluorescence power in the specimen is proportional to the excitation power and remains unchanged with or without scattering. (We have neglected effects such as saturation and photobleaching, etc.) However, only a small portion of the total fluorescence generated by 1PE constitutes signal that originates from the focal region.⁽⁷¹⁾ The rest of the

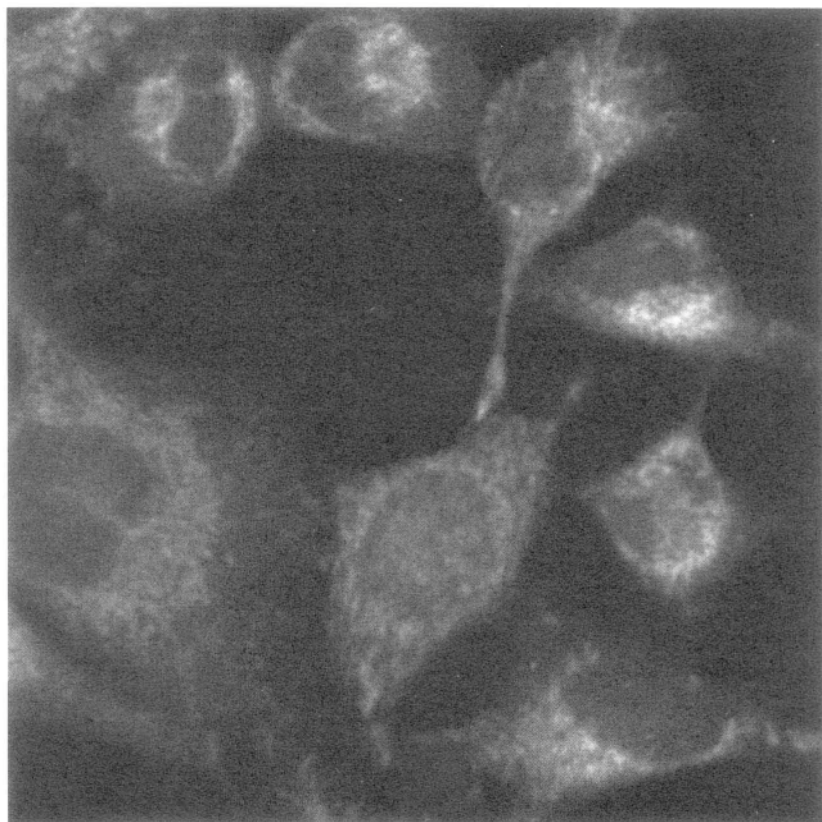


Figure 11.17. NADH autofluorescence. Intrinsic NADH autofluorescence, which usually colocalizes with standard mitochondrial stains, can be visualized in cells by using 700-nm pulsed excitation. In this image the NADH localization in HELa cells is shown. Nondescanned fluorescence was collected through a broadband blue filter (400–500 nm), power at the sample was 12 mW. (Image courtesy W. R. Zipfel (DRBIO).)

fluorescence forms the unwanted background that can typically be rejected by the spatial filter in confocal microscopy. The effect of scattering smears out the illumination profile, generating extra background at the expense of the signal fluorescence. Thus, the signal-to-background ratio is degraded. Because the fluorescence distribution is independent of excitation power (neglecting saturation, photobleaching, etc.), the degraded signal-to-background ratio cannot be compensated by increasing the excitation power.

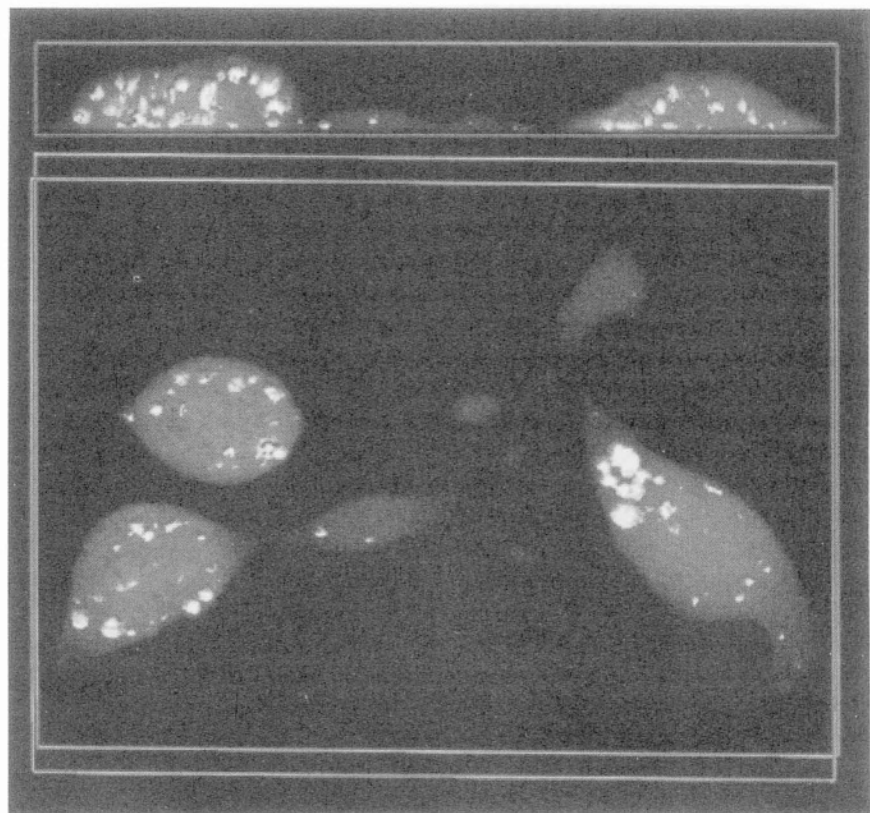


Figure 11.18. 3-D images of a set of serotonin-loaded RBL cells. The excitation wavelength is 700 nm, and the average power at the sample is ~ 25 mW. The image is rendered by reconstruction of 20 optical slices. This reconstruction draws isointensity surface (white) around regions of equal or higher brightness to demarcate the granules. The gray hue represents intensity below the granule cutoff intensity, and thus the density of gray overlapping a granule indicates the depth of the granule location. Box width = 80 μm .

We now consider MPE. As discussed in Section 11.2, multiphoton-excited fluorescence strongly depends on the spatial and temporal profiles of the excitation light (see Eq. 11.7). Excitation photons that are no longer able to reach the focal region because of scattering have very little probability of generating multiphoton-excited fluorescence. Thus, no background is generated by the scattered excitation photons. (Intuitively, the effect of scattering changes the temporal g factor (in pulsed excitation) and the spatial profile of the excitation light, reducing the probability of simultaneous multiphoton interaction with the fluorescent molecule.)

In addition to the localized excitation, multiphoton microscopy gains advantage in imaging deep into the scattering specimen because 3D resolution can be accomplished with wide-field detection. Thus, detection efficiencies can essentially be the same for scattered and unscattered fluorescence photons in nonlinear microscopy with wide-field detection. As an example, Figure 11.19

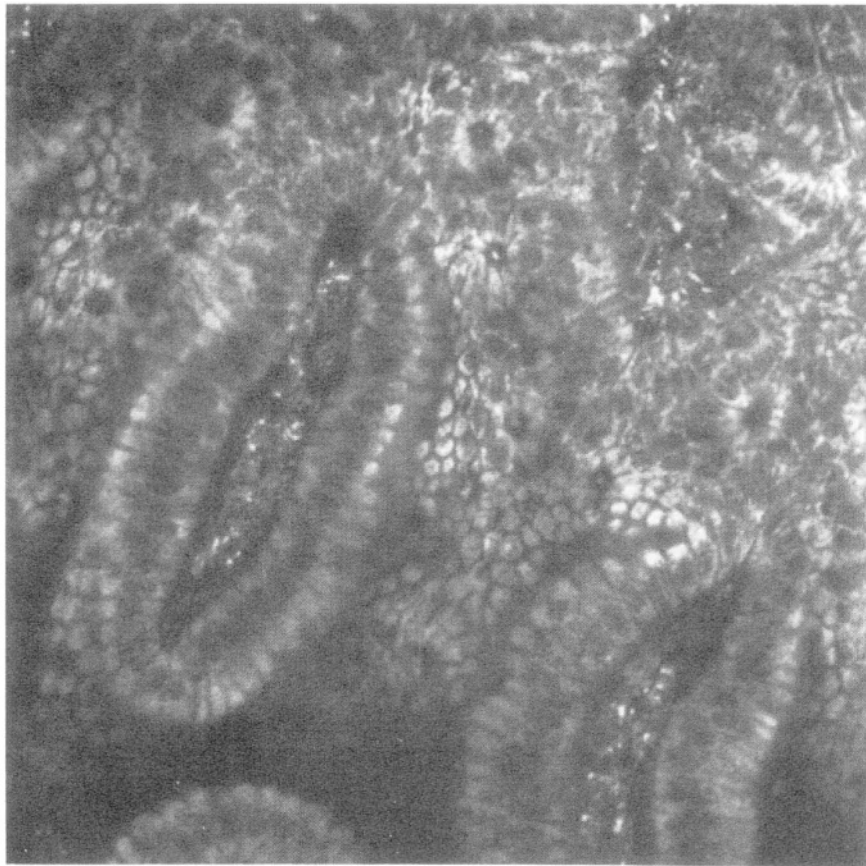


Figure 11.19. Villi in the small intestine of mouse imaged by multiphoton excited autofluorescence. The lumen side epithelial cells of an intact piece of small intestine from mouse was imaged through the basal lamina (i.e., from the outside). The base of the villi can be seen as well as the mouths of numerous crypts (small dark "holes" in the epithelial lining). The image (Kalman average of five 1-s scans) was taken 180 μm in from the basal lamina. Nondescanned fluorescence was collected through a blue glass filter; excitation was at 700 nm, 100-fs pulse width. (Image courtesy W. R. Zipfel (DRBIO), M. H. Montrose, and S. Chu (Johns Hopkins University).)

shows the autofluorescence image obtained 180 μm below the surface of a mouse small intestine specimen using 2PE and wide-field detection.

The situation is different in conventional one-photon imaging where a confocal spatial filter is required to achieve 3D resolution. Signal fluorescence photons that are scattered out of their ballistic trajectories cannot pass through the spatial filter and are not detected.⁽⁵⁷⁾ Thus, the overall detection efficiency of signal photons is reduced in one-photon confocal microscopy. Moreover, background fluorescence photons that are ordinarily blocked by the spatial filter can now possibly reach the detector because of scattering, further degrading the signal-to-background ratio. Confocal microscopy has not been successful in imaging deep into strongly scattering specimens such as represented by Figure 11.19.

Because scattered excitation photons outside the focal region cannot generate MPE, the decrease of MPE due to scattering can be compensated by increasing the excitation intensity without any adverse effects (such as photo-bleaching and photodamage) as long as one-photon absorption of the excitation light (such as heating) can be neglected. However, increasing the excitation power to compensate for the decrease of excitation and detection efficiencies in 1PE is limited by photobleaching and photodamage of the specimen because scattered excitation photons are just as capable of 1 PE (consequently photobleaching and photodamage) as unscattered photons. We note that scattering usually decreases with increasing wavelength, making it more favorable for MPE.

MPE also provides the capability of imaging deep into strongly absorbing specimens. Beer's law shows that the excitation power and, therefore, the generated fluorescence power decrease as $\exp(-\sigma_1 Cz)$, where z is the distance into the specimen. For a strongly absorbing specimen ($\sigma_1 C$ is large), fluorescence generated deep inside the specimen is very small compared to that generated on the surface. Thus, one-photon fluorescence imaging is limited only to the surface of a strongly absorbing specimen. Because MPE only occurs at the focal region of the excitation beam, attenuation of the excitation light due to multiphoton absorption can generally be neglected. For example, assuming $\sigma_2 = 100 \text{ GM}$, $C = 6 \times 10^{17} / \text{cm}^3$ (1 mM), $\tau = 100 \text{ fs}$, $\lambda = 700 \text{ nm}$, $n = 1.3$, and laser power = 10 mW ($\langle P(t) \rangle = 3.5 \times 10^{16} \text{ photons/s}$) at a repetition rate of 82 MHz, Eq. (11.15) predicts that the total power absorbed via two-photon process is approximately $4.7 \times 10^{12} \text{ photons/s}$; i.e., approximately only 1 out of 10,000 incident photons is absorbed. Thus, MPE is capable of imaging deep through high concentration of absorbing fluorophores if linear absorption of the excitation light is negligible. For example, the uptake of the drug 5-aminosalicylic (5-ASA) can be followed by recording two-photon-excited 5-ASA fluorescence deep into the specimen (Figure 11.20). Because the $1/e$ linear absorption length of 30 mM 5-ASA at its absorption peak of 360 nm is approximately 50 μm , conventional one-photon imaging is unsuitable at the desired depth.

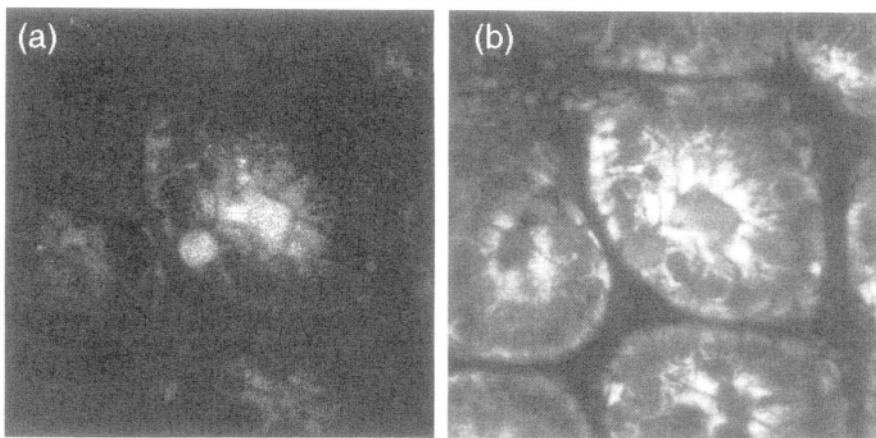


Figure 11.20. Intrinsic drug fluorescence imaging. 5-aminosalicylic acid (5-ASA), a drug used in the treatment of colitis, is UV fluorescent (1PE peak ~ 360 nm, emission peak ~ 505 nm), and its entry into the epithelial cells lining the large intestine can be followed in intact colon samples from mice perfused with therapeutic concentrations (30 mM) of the drug. The extremely high concentration of 5-ASA used in this study totally precludes the use of conventional UV confocal microscopy due to attenuation of the UV excitation by the drug. (a) Image of two-photon excited 500-nm fluorescence. The 500-nm channel shows the drug inside the crypts of the colon immediately after addition of 30 mM 5-ASA to the perfusion solution. (b) Image of two-photon-excited 440-nm fluorescence. The 440-nm channel provides a means to monitor the metabolic conversion of 5-ASA to acetyl-5-ASA (emission peak ~ 440 nm) as well as providing an autofluorescence outline of the cells that make up the crypt. The image was taken using 700-nm two-photon excitation about $30\text{ }\mu\text{m}$ into the luminal side of the colon through $100\text{ }\mu\text{m}$ of 30 mM 5-ASA in the perfusion bath. (Image courtesy W. R. Zipfel (DRBIO), M. H. Montrose, and S. Chu (Johns Hopkins University).)

One might argue that the attenuation of the excitation light by linear absorption can be made arbitrarily small by shifting the wavelength of excitation away from the absorption peak. Therefore, the specimen can always be treated as transparent. Although the method of using such alternative excitation wavelength may work in some applications, the small one-photon absorption cross section at the wavelength of excitation inevitably reduces the efficiency of fluorescence excitation. Therefore, higher than usual excitation power must be used, possibly increasing the amount of photodamage to the specimen. Moreover, drug concentration inside the specimen may be significantly lower than that in the perfusion bath. Consequently, a small fluorescence signal must be detected on top of the excessively large background in 1PE.

11.4. Considerations in MPE Spectroscopy and Microscopy

11.4.1. Fluorophore Ground-State Depletion

We have so far neglected the effects of fluorophore ground-state depletion (saturation). It is a good assumption at relatively low excitation intensity where the probability of excitation per laser pulse is much less than unity. However, effects of saturation must be taken into account in many quantitative applications of spectroscopy and microscopy. In this section, we first present a general theoretical description of multiphoton-excited fluorescence saturation under ultrashort pulsed excitation. We then analyze the resolution and signal-to-background ratio in nonlinear laser scanning microscopy in the presence of saturation.

The kinetics of saturation are quite different between CW and femtosecond-pulsed illumination. Under CW illumination, there is a steady-state population inversion between the ground state and excited state at saturation. With illumination by a train of pulses each much shorter than the fluorescence decay time ($\tau_f \sim 10^{-9}$ s) and pulse spacing ($f^{-1} \gg \tau_f$), such inversions occur only as decaying transients initiated by each pulse. Hence, two-photon saturation, when a femtosecond pulsed laser is used will not usually obey the dynamics obtained for CW illumination. Saturation depends on the pulse profile and intensity distribution within the irradiated volume. One assumption facilitates the following analysis: the laser pulse duration τ is much shorter than the fluorescent decay time τ_f . Hence, we assume no excited-state molecule decays to the ground state within the pulse duration. This assumption is generally well satisfied if pulses with duration about 100 fs are used.

We first examine the steady-state time-averaged fluorescence as a function of the laser repetition rate (f) and the probability of excitation per fluorophore per laser pulse (a). For simplicity, we assume a single-exponential decay of the fluorophore and neglect the effects of intersystem crossing, which will be discussed in the next section. The calculation to obtain the fluorescence rate is relatively straightforward. The basic idea is that the number of excitations per laser pulse should balance the number of decays between two adjacent pulses in order to achieve steady state. The final expression for the detected fluorescence rate is

$$\langle F(t) \rangle = k \frac{a}{R\tau_f} \frac{1 - e^{-R}}{1 + ae^{-R} - e^{-R}} \quad (11.29)$$

where $R = 1/f\tau_f$ and $k = n^{-1}\eta\phi\sigma_n C$ (see Eq. 11.7). In the case of very high repetition rate where $R \ll 1$ and the laser intensity so high that $a=1$, the fluorescence rate becomes independent of the pulse repetition rate and approaches its absolute maximum: $\langle F(t) \rangle = k/\tau_f$. It is easy to show that k/τ_f

is also the maximum achievable detection rate under CW illumination. On the hand, when $R \gg 1$ or $a \ll 1$, the fluorescence rate simply reduces to $\langle F(t) \rangle = fka$; i.e., excitation rate is proportional to the repetition rate. Dependence of the fluorescence rate on the pulse repetition rate are plotted for three different a values in Figure 11.21. It is clear from Eq. (11.29) and Figure 11.21 that, for $fa \leq 0.1/\tau_f$, the fluorescence rate increases nearly linearly with the repetition rate (with less than 10% deviation). Intuitively, the fluorescence rate deviates significantly from the linear dependence on the pulse repetition rate when the excitation rate constant becomes comparable to the fluorescence decay rate constant, i.e., when $fa \approx 1/\tau_f$.

In reality, the situation is complicated because the excitation intensity is, in general, not uniform. Thus, the excitation probability per fluorophore per pulse is a function of the position. To obtain the experimentally observed fluorescence rate one needs to sum over the entire illuminated volume. Thus, Eq. (11.29) should be rigorously rewritten as

$$\langle F(t) \rangle = k \int_V d\mathbf{r} \frac{a(\mathbf{r})}{R\tau_f} \frac{1 - e^{-R}}{1 + a(\mathbf{r})e^{-R} - e^{-R}} \quad (11.30)$$

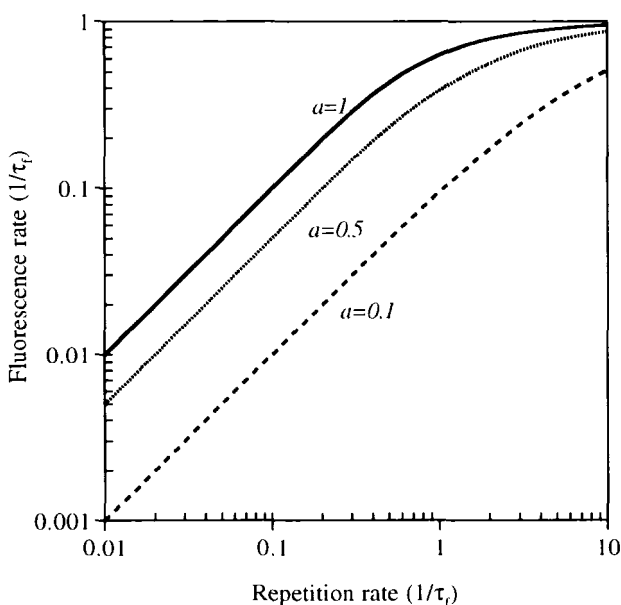


Figure 11.21. Dependence of the time-averaged steady-state fluorescence emission rate on the pulse repetition rate: a represents the probability of excitation per laser pulse per fluorophore, and τ_f is the fluorescence lifetime. Note that the maximum fluorescence emission rate is $1/\tau_f$.

The amount of fluorescence obtained per excitation pulse is therefore in the following form:

$$F_p = \frac{\langle F(t) \rangle}{f} = k \int_V d\mathbf{r} \frac{a(\mathbf{r})(1 - e^{-R})}{1 + a(\mathbf{r})e^{-R} - e^{-R}} \quad (11.31)$$

We note that Eq. (11.31) has actually provided a way to measure the fluorescence decay time by monitoring the fluorescence as a function of the laser repetition rate.

We now consider the excitation probability per fluorophore per pulse. In the steady-state condition, each individual excitation pulse will have the same initial conditions. Thus, it is only necessary to consider a *single-excitation-pulse period* provided that a mode-locked pulse train is a perfect periodical function in time. The differential equation governing the ground-state concentration $C(\mathbf{r}, t)$ in an n -photon excitation is

$$\frac{\partial C(\mathbf{r}, t)}{\partial t} = -\sigma_n I^n(\mathbf{r}, t)C(\mathbf{r}, t) \quad (11.32)$$

We have neglected fluorescence decay within the duration of the excitation pulse. The solution for Eq. (11.32) is

$$C(\mathbf{r}, t) = C(\mathbf{r}, -\infty) \exp \left[-\sigma_n \int_{-\infty}^t I^n(\mathbf{r}, t') dt' \right] \quad (11.33)$$

The excitation probability per pulse can therefore be evaluated as

$$a(\mathbf{r}) = 1 - \frac{C(\mathbf{r}, \infty)}{C(\mathbf{r}, -\infty)} = 1 - \exp \left[-\sigma_n \int_{-\infty}^{\infty} I^n(\mathbf{r}, t') dt' \right] \quad (11.34)$$

The integration boundaries should rigorously be $-1/2f$ to $1/2f$. However, because the laser pulse width is much smaller than the pulse period ($1/f$), we can extend the integration boundaries to infinity.

Following Eqs. (11.19a) and (11.19b), we can express $a(\mathbf{r})$ in terms of the average intensity:

$$a(\mathbf{r}) = 1 - \exp[-g^{(n)}\sigma_n f^{-1} \langle I_0(t) \rangle^n S^n(\mathbf{r})] \quad (11.35)$$

Equations (11.31) and (11.35) give the general relation between the detected fluorescence and the incident pulse intensity and repetition rate. Intuitively, saturation under ultrashort pulsed illumination can be caused by both high pulse intensity (saturation caused by a single excitation pulse) and high repetition

rate (saturation caused by the cumulative effects of many pulses) because the combination of them gives the appropriate excitation rate. In general, the contributions of pulse intensity and repetition rate to saturation are coupled. However, when the time between adjacent pulses is much greater than the fluorescence decay time (say $R > 3$), most (>95%) of the excited dye molecules will have decayed to their ground state before the next pulse comes in. Under such a condition, saturation is only caused by high pulse intensity. For example, commercially available mode-locked Ti sapphire or dye lasers used in two-photon microscopy typically have repetition rates ~ 80 MHz. This corresponds to a pulse separation time of ~ 12.5 ns. Although there are many fluorophores with $\tau_f > 4$ ns, a significant number of biological fluorescent markers have $\tau_f \sim 1\text{--}4$ ns.⁽⁷²⁾ In the following discussion, we consider only $R \gg 1$. Similar calculations can be performed for any R values using Eqs. (11.31) and (11.35).

It is obvious from Eq. (11.35) that the quantity which describes the degree of saturation due to pulse intensity is $g^{(n)}\sigma_n f^{-1}\langle I_0(t)\rangle^n$. We define $\alpha \equiv g^{(n)}\sigma_n f^{-1}\langle I_0(t)\rangle^n$ as a saturation parameter. (It is obvious from Eq. 11.19 and the definition of peak intensity that $\alpha = g_p^{(n)}\sigma_n I_p^n \tau$.) Under the condition $\alpha \ll 1$, α rigorously represents the excitation probability per molecule per laser pulse at the geometric focal point and the first-order approximation of Eq. (11.35) gives the expected n th-power dependence for n -photon excitation. Figure 11.22 illustrates F as a function of α for several different focusing geometries in 2PE, assuming $R \gg 1$. Significant departure from quadratic power dependence (i.e., departure from linear dependence on α) is apparent at $\alpha > 1.0$. If we require less than 3% deviation from a true quadratic dependence, then the region where quadratic dependence holds is $\alpha < 0.3$ for GL profile and $\alpha < 0.2$ for diffraction-limited focus. For example, rhodamine-B has a 2PE cross section of 210 GM at 840 nm. With a mode-locked Ti sapphire laser providing 100-fs pulses at 80-MHz repetition rate, the average power required to reach $\alpha = 1$ for rhodamine-B at 840 nm is approximately 8 mW at the specimen, assuming diffraction-limited focus with a 1.3-NA objective lens.

Note that we have neglected stimulated emission in Eq. (11.32). This is justified only if the vibrational relaxation time of the excited state is significantly shorter than the excitation pulse width. Such relaxation times, however, are unknown for most fluorophores. In general, it is estimated to be 10–1000 fs in the condensed phase. Thus, stimulated emission may become important at high levels of ground-state depletion. In the limiting case where the relaxation time is much greater than the excitation pulse width, Eq. (11.35) simply becomes

$$a(\mathbf{r}) = \frac{1}{2} \{1 - \exp[-g^{(n)}\sigma_n f^{-1}\langle I_0(t)\rangle^n S^n(\mathbf{r})]\} \quad (11.36)$$

The extra factor of 1/2 represents the fact that the maximum excitation probability is 1/2 in such a two-level system.

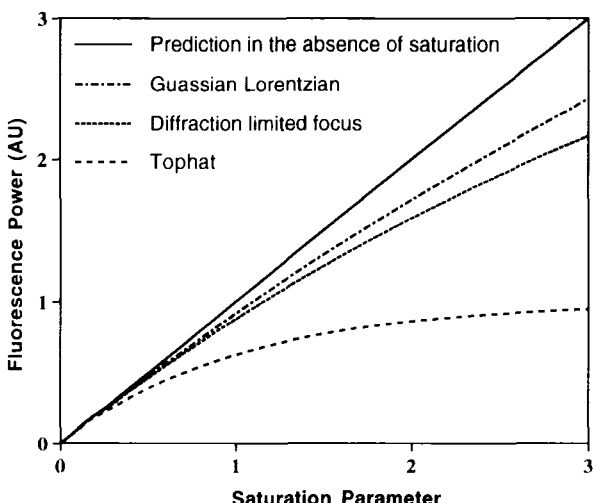


Figure 11.22. Dependence of two-photon-excited fluorescence power on the saturation parameter for several focusing geometries. For comparison, prediction of the fluorescence power in the absence of saturation is also plotted. Significant deviation from the quadratic power dependence (i.e., linear with α) are apparent for $\alpha > 1$.

11.4.1.1. Resolution in 2PLSM in the Presence of Saturation

The 3D resolution of 2PLSM results from the quadratic power dependence of the two-photon-excited fluorescence.⁽⁸⁾ However, such a quadratic relation no longer holds under saturation conditions (Figure 11.22). Thus, the spatial localization of 2PE begins to degrade when $\alpha \sim 1$ and is expected in principle to become virtually nonlocalized when $\alpha \gg 1$. To investigate the resolution and signal-to-background ratio, we name the integrand of Eq. (11.31) as

$$W(\mathbf{r}) = \frac{a(\mathbf{r})(1 - e^{-R})}{1 + a(\mathbf{r})e^{-R} - e^{-R}} \quad (11.37)$$

$W(\mathbf{r})$ describes the correct fluorescence distribution as a function of the incident intensity that determines $a(\mathbf{r})$. The spatial extent of $W(\mathbf{r})$ determines the actual resolution of two-photon fluorescence microscopy. Again under the assumption of $R \gg 1$, $W(\mathbf{r})$ simply reduces to $a(\mathbf{r})$. To demonstrate the effects of saturation for $R \gg 1$, a GL excitation profile will be used in the following calculation.

Figure 11.23 shows the 3D spatial distribution of two-photon-excited fluorescence generated by a GL excitation beam profile at several different saturation levels. Saturation effect can be practically neglected at $\alpha = 0.1$, Figure 11.23a. The excitation profiles of Figures 11.23c and 11.23d are severely distorted and

swollen because of saturation. The resulting fluorescence exhibits a flat distribution near the center of the focal volume, indicating regions that are most saturated. In order to quantitatively study the excitation profiles at various excitation intensity levels, we show in Figure 11.24 the radial and axial FWHMs of $W(\mathbf{r})$ as a function of the saturation parameter α . It is apparent that the axial resolution degrades significantly faster than the radial resolution. Intuitively, this is because the fluorescence power decreases much faster in the radial direction (exponentially) than in the axial direction (power law). In the extreme hypothetical case where the edge of the fluorescence distribution is infinitely sharp, i.e., a top-hat distribution, there should be no resolution decrease regardless of the saturation level.

To further investigate the saturation effect on the axial resolution, we examine the integrated two-photon-excited fluorescence power in each z section: $D(z) \equiv 2\pi \int_0^\infty \rho \, d\rho \, W(\mathbf{r})$. Here ρ denotes the radial distance from the optical axis. Figure 11.25 shows $D(z)$ at five saturation levels for a GL excitation beam. The z plane which has the maximum fluorescence power is no longer the focal plane (i.e., at $z = 0$) for $\alpha = 5.0, 10$, and 15 . This is because the increase in the fluorescence power at each z plane is dominated by the increase of the effective irradiated area at very saturated conditions. For an infinitesimally thin fluorescent sample, this leads to two apparent “focal planes” that give the maximum fluorescence power at equal distance away from the excitation beam waist. Similar behavior is also obtained for diffraction-limited focus.

Fluorophore saturation limits the maximum fluorescence output rate per molecule to $1/\tau_f$, or $\sim 10^8$ to 10^9 /s for most fluorophores. However, as discussed, such a limit cannot be achieved without greatly sacrificing microscope resolution. This effect is even more pronounced in nonlinear microscopy than in confocal microscopy because the 3D resolution is entirely, instead of partially, derived from the localization of excitation. (We recall that in the case of one-photon confocal microscopy a spatial pinhole has to be used to obtain 3D resolution.) The increase of fluorescence output by increasing fluorophore concentration also has its own limitation in *in vivo* biological imaging. In general, one has to compromise among imaging rate, resolution, and signal-to-noise. Equations (11.31) and (11.37) can be used to optimally choose the excitation parameters: excitation power and laser repetition rate. Thus, fast imaging can be achieved with the highest signal-to-noise ratio and minimum degradation of the resolution.

11.4.2. Intersystem Crossing and Photobleaching

Photobleaching and intersystem crossing (ISC) between excited singlet and triplet states are two important properties to consider in choosing fluorophores. In practice, fluorescent probe photobleaching limits the amount of information

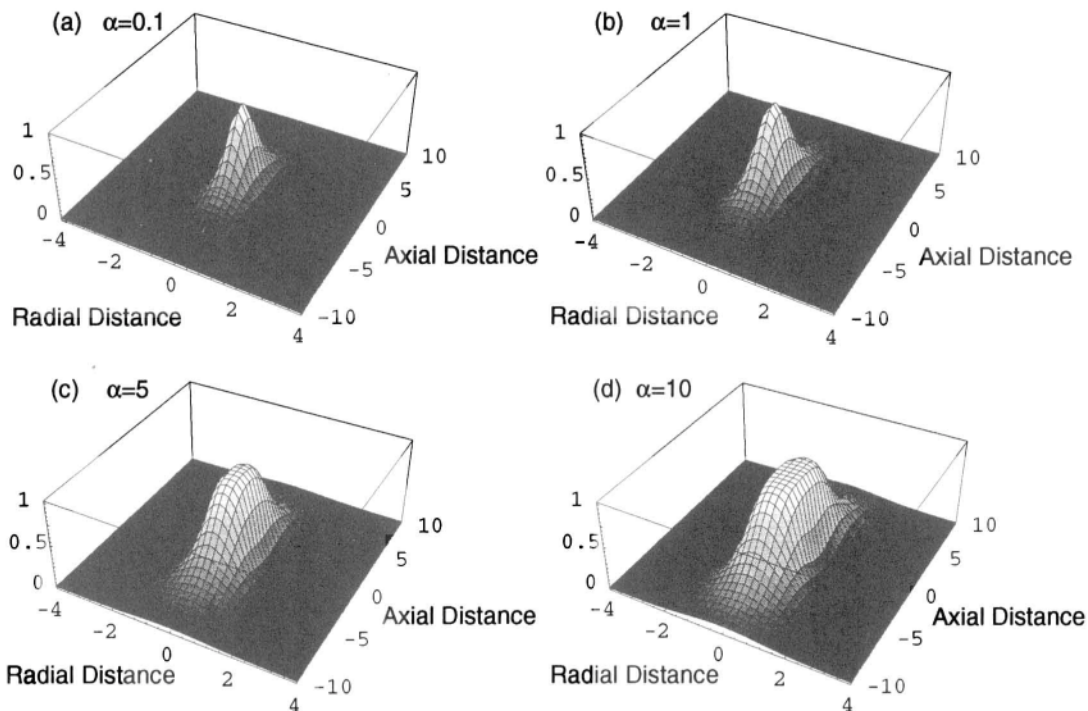


Figure 11.23. Three-dimensional plot of the two-photon-excited fluorescence distribution at four saturation levels generated by a Gaussian-Lorentzian excitation beam. The gray scales correspond to the fluorescence power, which is normalized with respect to the focal point value. The radial and axial distances are normalized to the $1/e^2$ radius of the Gaussian beam waist w_0 . The excitation wavelength (λ) is set to be $\lambda = w_0$.

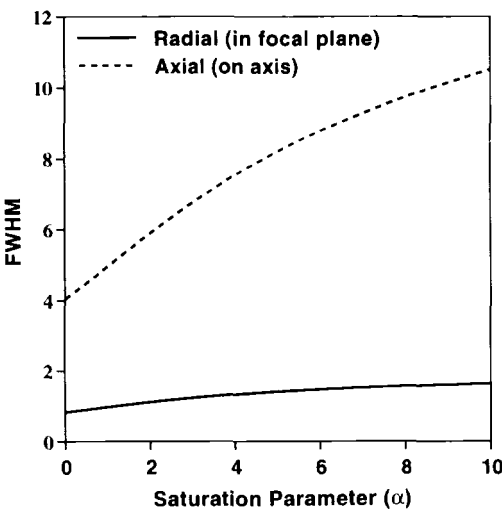


Figure 11.24. FWHM values of the two-photon-excited fluorescence distribution generated by a Gaussian-Lorentzian excitation beam as a function of the saturation parameter. FWHM values are normalized to the $1/e^2$ radius of the Gaussian beam waist w_0 . The excitation wavelength (λ) is set to be $\lambda = w_0$.

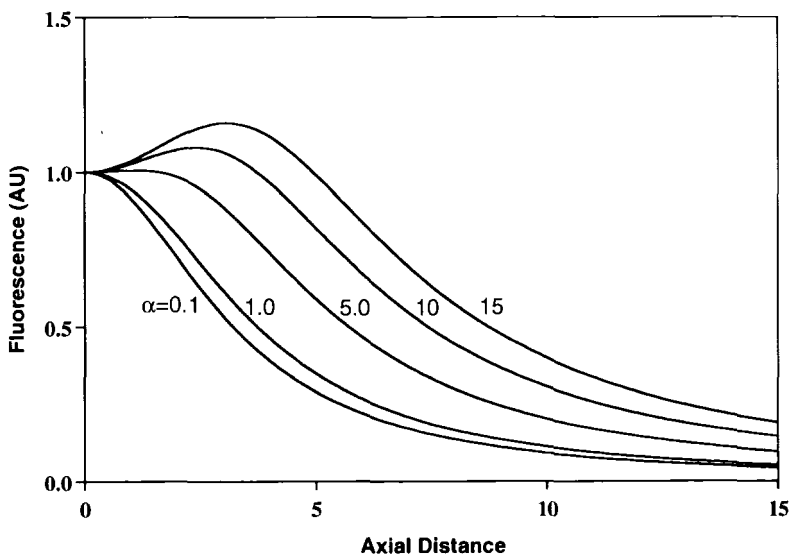


Figure 11.25. Integrated two-photon-excited fluorescence power at each axial section generated by a Gaussian-Lorentzian excitation beam. Fluorescence power is normalized to the value at the focal plane (i.e., axial distance 0). The axial distance is normalized to the $1/e^2$ radius of the Gaussian beam waist w_0 . The excitation wavelength (λ) is set to be $\lambda = w_0$.

available to the researcher (typically 10^3 to 10^5 photons/fluorophore in aqueous solution), and ISC limits the maximum fluorescence emission rate. Photo-bleaching and ISC may also be intimately related to the cellular photodamage pathway. Figure 11.26 shows a schematic molecular energy diagram with possible decay pathways. MPE has the great advantage of being able to limit photobleaching and ISC to the focal volume of the excitation beam. Because pulsed lasers are most commonly used in nonlinear spectroscopy and microscopy, we will examine ISC and photobleaching under ultrashort pulsed illumination. The following analysis can also be applied to describe uncaging, where the depletion of the caged molecules (equivalent to the depletion of the ground state) and the permanent removal of the caged molecules from the excitation cycle (equivalent to photobleaching) should always be considered in general.

11.4.2.1. ISC

Let us first consider ISC without photobleaching. For simplicity, we assume that the fluorescence decay time τ_f is significantly smaller than $1/f$. In general, the decay of the excited singlet state and the triplet state within the duration of the excitation pulse can be neglected for ultrashort pulses. Let $N_g(n)$ be the ground-state population right before the n th excitation pulse and τ_T be the triplet lifetime. The amount of excitation into the triplet by the n th pulse is then simply $N_g(n)aQ_{\text{isc}}$, where $Q_{\text{isc}} = k_{\text{isc}}\tau_f$ is the ISC efficiency. Taking into account the triplet decay during the time between the n th and the $(n+1)$ st pulses, we have

$$N_g(n+1) = N_g(0) - [N_g(n)aQ_{\text{isc}} + N_g(0) - N_g(n)]e^{-1/\tau_T f} \quad (11.38)$$

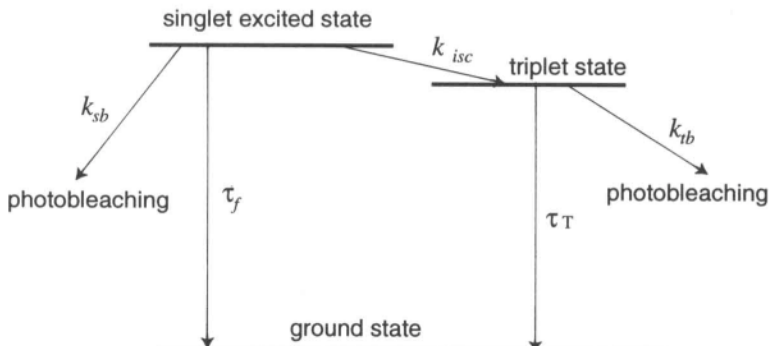


Figure 11.26. Schematic of the energy levels of a fluorophore. Two photobleaching pathways (i.e., through the excited singlet state or through the triplet state) were also illustrated. k_{isc} is the intersystem crossing rate constant, and k_{sb} and k_{tb} are the photobleaching rate constant for the singlet excited state and the triplet state, respectively.

The population in the singlet excited state can be neglected because $\tau_f \ll 1/f$. The expression for $N_g(n)$ can be obtained by simple inspection:

$$N_g(n) = N_g(0) \frac{1 - e^{-1/\tau_T f} + aQ_{\text{isc}}e^{-1/\tau_T f}(1 - aQ_{\text{isc}})^n e^{-n/\tau_T f}}{1 - e^{-1/\tau_T f} + aQ_{\text{isc}}e^{-1/\tau_T f}} \quad (11.39)$$

Figure 11.27 shows $N_g(n)$ for several chosen conditions. It is clear that a steady-state distribution between the ground state and the triplet state can be reached for large n where $(1 - aQ_{\text{isc}})^n e^{-1/\tau_T f} \ll 1$. Thus, the number of pulses needed to reach steady state is $n \approx \tau_T f$ when the excitation probability into the triplet state, aQ_{isc} , is small and becomes much less when $aQ_{\text{isc}} \sim 1$. Nevertheless, the actual time required to reach steady state (i.e., n/f) is independent of the pulse repetition rate.

In addition to the pulse intensity (i.e., a), the steady-state population of the triplet state also depends critically on the pulse repetition rate because the excitation rate under pulsed illumination is determined by pulse intensity and repetition rate. The maximum triplet population is reached at high pulse intensity ($a=1$). If the repetition rate of the excitation source is low when compared with the fluorescence lifetime (i.e., $\tau_T \gg 1/f \gg \tau_f$), the first-order approximation of Eq.

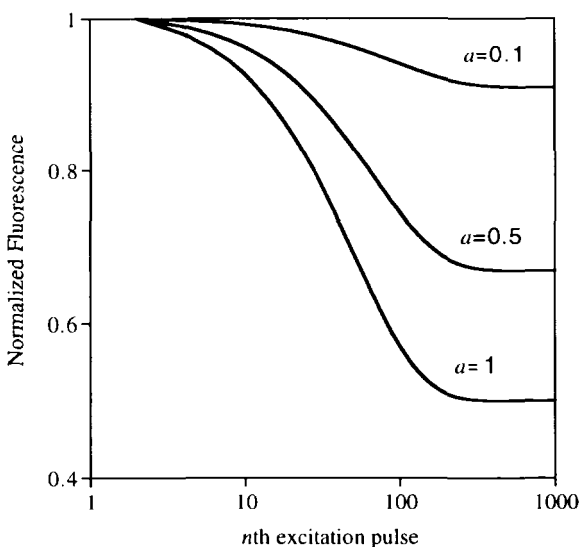


Figure 11.27. Fluorescence generation by the n th excitation pulse in the presence of ISC. Curves are plotted using Eq. (11.39) with $f\tau_T = 100$ and $Q_{\text{isc}} = 0.01$. Note that steady states are reached at approximately $n = f\tau_T = 100$.

(11.39) then gives the steady-state triplet-to-singlet population ratio of $\tau_T Q_{\text{isc}} f$. However, for high pulse repetition rate (i.e., $1/f \ll \tau_f$), the steady-state population ratio increases to $\tau_T Q_{\text{isc}} / \tau_f$, which is also the maximum limit under CW excitation. (We have assumed that $\tau_T > \tau_f$.) We note that this maximum limit is completely determined by the molecular properties of the fluorophore. Intuitively, this is understood because the highest excitation rate of fluorophores under pulsed excitation assumes the value of $1/\tau_f$ or f , whichever is lower. Let us now consider a rhodamine-6G molecule in ethanol as an example. The excited singlet- and triplet-state lifetimes are $\tau_f \approx 3.4 \times 10^{-9}$ s and $\tau_T \approx 4 \times 10^{-6}$ s, respectively, and $Q_{\text{isc}} \approx 0.2\%$.⁽⁷³⁾ Under CW illumination, the steady-state triplet population can reach 2.4 times that of the singlet state. On the other hand, under pulsed excitation with a repetition rate of 80 MHz, the same ratio can only be as high as 0.64.

Taking into account ISC, the amount of generated fluorescence for the n th excitation pulse is simply $F(n) = k a N_g(n)$. Similar to the discussions in Section 11.4.1, one again has to sum over the entire excitation volume because of the nonuniform illumination; i.e., $F(n) = k \int_V d\mathbf{r} a(\mathbf{r}) N_g(n, \mathbf{r})$. It is obvious from Eq. (11.39) that ISC can be generally neglected when $a \ll 1$. Thus, ISC and fluorophore saturation must be considered simultaneously. Equation (11.35) should be used to obtain $a(\mathbf{r})$ where the depletion of the ground state during the excitation pulse is properly taken into account.

11.4.2.2. Photobleaching

A full account of photobleaching in the presence of ISC is complicated and depends on the photobleaching pathway.⁽⁷⁴⁾ However, the effects of photobleaching and ISC can be separated if we assume small photobleaching efficiency. We recall that the time scale of establishing triplet-singlet steady state is τ_T or less, and the highest excitation rate under pulsed excitation is f or $1/\tau_f$. Thus, if the photobleaching efficiency Q_b , which is defined as the probability of photobleaching per excitation, is small when compared to $1/f\tau_T$ (for $1/f > \tau_f$) or τ_f/τ_T (for $1/f < \tau_f$), we can first neglect photobleaching during the transient of the triplet population buildup and then include photobleaching after triplet-singlet steady state has been reached. Photobleaching then appears to remove the fluorophore from the triplet and singlet manifold with the probability of Q_b per excitation. Q_b is simply the combined photobleaching probability through both the singlet state and the triplet state (Figure 11.26). It is

$$Q_b = Q_{\text{isc}} Q_{\text{tb}} + Q_{\text{sb}}$$

where $Q_{\text{sb}} = \tau_f k_{\text{sb}}$ and $Q_{\text{tb}} = \tau_T k_{\text{tb}}$ are the photobleaching efficiencies in the singlet excited state and the triplet state, respectively. The ground-state and

triplet-state populations, with both ISC and photobleaching effects, are

$$\begin{aligned} N_g(n) &= N_g(0)[(1 - A)(1 - aQ_{\text{isc}})^n e^{-n/\tau_T f} + A(1 - aAQ_b)^n] \\ N_T(n) &= N_g(0)[(A - 1)(1 - aQ_{\text{isc}})^n e^{-n/\tau_T f} + (1 - A)(1 - aAQ_b)^n] \end{aligned} \quad (11.40)$$

where A represents the weight of the ground-state population in the singlet-triplet steady state (obtained by letting $n \rightarrow \infty$ in Eq. 11.39). In the range where $aAQ_b n \ll 1$, the effects of photobleaching can be neglected. Equation (11.40) reduces to Eq. (11.39). For large n , the transient of the triplet population buildup, which is described by the first term in Eq. (11.40), can be neglected. Equation (11.40) then simply becomes

$$\left[\frac{N_g(n)}{N_T(n)} \right] \approx N_g(0) \left[\frac{A}{1 - A} \right] (1 - aAQ_b)^n \quad (11.41)$$

One observes here that $N_g(n) + N_T(n) = N_g(0)(1 - aAQ_b)^n$, indicating that aAQ_b represents the probability per excitation pulse at which a molecule is removed from the excitation cycle. We also note that the photobleaching probability, aAQ_b , is not a linear function of the excitation probability (a) so long as the ground-state population depends on a ; i.e., the degree of triplet saturation is significant. Thus, the apparent photobleaching rate does not depend linearly on the excitation rate per molecule except at low excitation probabilities where $A \approx 1$. This nonlinear behavior of the photobleaching efficiency is a direct result of ISC and remains true even if photobleaching occurs through triplet state only ($Q_{\text{sb}} = 0$) or through singlet state only ($Q_{\text{tb}} = 0$).

The small photobleaching assumption we made here should be satisfied for many fluorophores, especially for those with good photostability. Let us use fluorescein as an example. The photobleaching efficiency of fluorescein in water is around $Q_b \approx 10^{-4}$.⁽⁷⁵⁾ Using the approximate lifetimes for the triplet and singlet states, one finds $Q_b \tau_T / \tau_f \approx 0.1$. Smaller numbers are obtained for pulsed excitations with repetition rates of less than 250 MHz. Thus, the above assumption should be valid in this case. However, caution must be taken to apply the above theory to less stable molecules such as native fluorophores tryptophan, serotonin, etc.

The amount of fluorescence generated in the presence of ISC and photobleaching effects can be obtained again as $F(n) = k \int_V d\mathbf{r} a(\mathbf{r}) N_g(n, \mathbf{r})$. The spatial distribution of the illumination intensity becomes even more important with photobleaching because the contribution from the lower-intensity region is significantly enhanced due to relatively smaller photobleaching. Fluorescence generated by the n th excitation pulse is illustrated in Figure 11.28. To stress the importance of the spatial integration of the fluorescence, we point out that

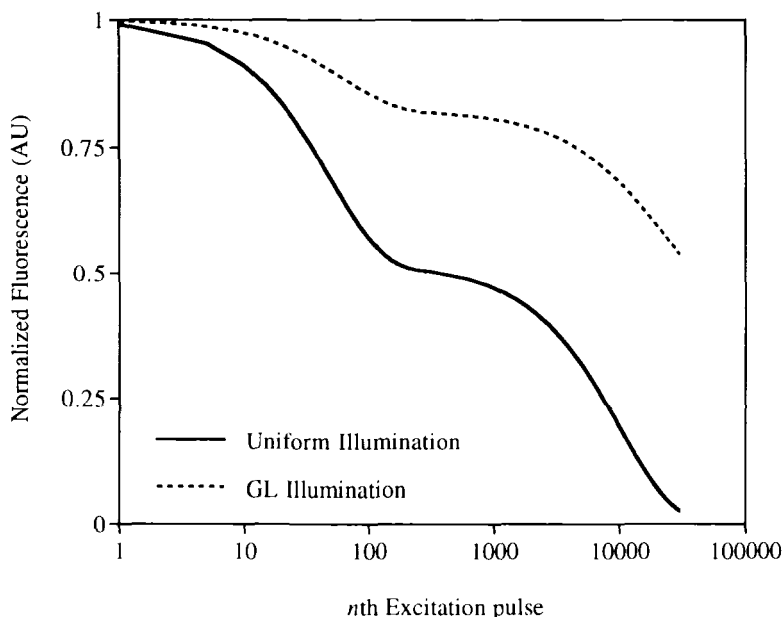


Figure 11.28. Fluorescence generation by the n th excitation pulse in the presence of ISC and photobleaching for uniform illumination profile and Gaussian–Lorentzian profile. Curves were plotted using Eqs. (11.35) and (11.40). We have assumed $f\tau_T = 100$, $Q_{isc} = 0.01$, $Q_b = 10^{-4}$, and $\alpha = 5$.

the amount of generated fluorescence is extremely different between a uniform illumination and an illumination with a GL profile.

The effects of ISC and photobleaching on microscopy resolution can be analyzed similar to Section 11.4.1.2. The degradation of resolution caused by photobleaching can be much more severe than saturation and ISC because the detected fluorescence is mostly from the lower-intensity region under conditions of deep photobleaching (Figure 11.29). Although such deep photobleaching is seldom encountered for most fluorophores, imaging of native biological molecules, an area that holds tremendous opportunities for nonlinear microscopy, may be seriously limited by photobleaching.

We close this section by pointing out that, although a considerable amount of effort has been devoted to characterize the photobleaching and ISC properties of common fluorophores under 1PE, these properties are mostly unknown under MPE. Because significant differences do exist between one- and two-photon excitation spectra of some fluorophores (see Sections 11.2), there are reasonable doubts about the validity of applying the known one-photon photobleaching efficiencies and ISC rate constants to 2PE. In addition, mechanisms

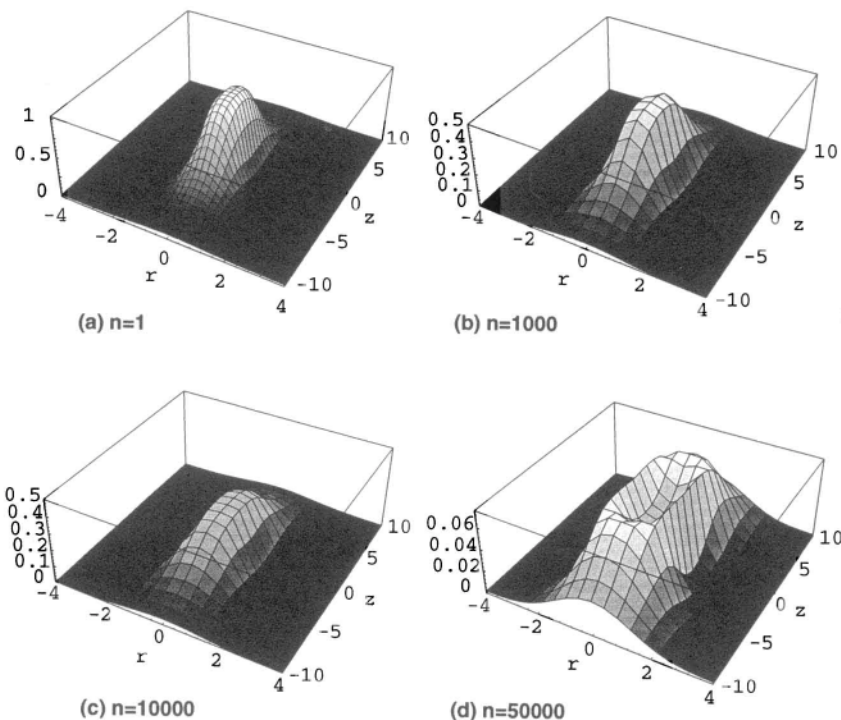


Figure 11.29. Three-dimensional plot of the two-photon-excited fluorescence distribution generated by the n th pulse of a Gaussian–Lorentzian excitation beam, taking into account saturation, ISC, and photobleaching. We have assumed $f\tau_T = 100$, $Q_{\text{isc}} = 0.01$, $Q_b = 10^{-4}$, and $\alpha = 5$. (a) At $n = 1$ only saturation effect is present. (b) At $n = 1000$ decrease of fluorescence in the middle of the focal region (from 1 to 0.5) is mainly due to ISC. (c) Photobleaching effects become significant when $n \approx 1/Q_b = 10^4$. The gray scales correspond to the fluorescence power. The radial and axial distances are normalized to the $1/e^2$ radius of the Gaussian beam waist w_0 . The excitation wavelength (λ) is set to be $\lambda = w_0$. Note that different scales were used for plot (a), (b) and (c), and (d).

of photobleaching and ISC in nonlinear excitation may differ significantly from 1PE because of the much higher excitation intensity. Thus, quantitative studies of these properties under MPE are of great practical importance in nonlinear laser scanning fluorescence microscopy.

11.4.3. Laser-Matter Interaction at High Intensity

To increase the probability of simultaneous multiphoton incidence, pulsed lasers with high peak intensity are generally used as the excitation source.

However, such high degree of temporal focus combined with the tight spatial focus (typically $<1 \mu\text{m}^2$) result in peak intensities that are many orders of magnitude higher than usual in normal 1PE. Although peak intensities at the focal point are generally less than $3 \times 10^{11} \text{ W cm}^2$ in routine 2PLSM, other applications can necessitate use of far higher intensities. Uncaging of biological effector molecules in three-dimensionally specified volumes, for example, can require as much as 10^{12} W cm^2 . Note that intensities used in 1 PE are typically less than 10^6 W cm^2 . The high peak intensities used in MPE opens a range of laser-matter interactions that have previously been neglected in 1 PE. We briefly discuss some of these phenomena.

11.4.3.1. Nonlinear Scattering

The detection of two-photon-excited fluorescence is practically free from background caused by linear scattering because two-photon-excited fluorescence occurs at a much shorter wavelength region than the excitation light. This property can be used to achieve ultrasensitive fluorescence detection. However, the intense radiation offfrequency ν can generate a spectrum of the scattered radiation that includes bands with frequency 2ν and $2\nu \pm \nu_0$, where ν_0 is the frequency associated with a transition between two energy levels of the scattering molecule. The two-photon scattering (2PS) at 2ν is referred to as *hyper-Rayleigh* scattering, that at $2\nu \pm \nu_0$ as *hyper-Raman* scattering.⁽⁷⁶⁾ Although linear scattering is not a significant component of background in two-photon-excited fluorescence measurements, the question arises as to whether 2PS background may limit the detection sensitivity of two-photon-excited fluorescence just as linear scattering does in 1PE.

Figure 11.30 shows the 2PS spectrum of liquid water obtained in a standard epifluorescence geometry with excitation at 840 nm.⁽⁷⁷⁾ For quantitative comparison, the insert of Figure 11.30 shows the two-photon-excited fluorescence emission spectrum of 5 pM fluorescein obtained in the exact same experimental setup. Integrating the areas of the corresponding signal peaks, we obtain the ratios (r_2) of 2PS cross sections of liquid water to the fluorescein 2PE cross section for the epifluorescence geometry. We find $r_2 = 6.4 \times 10^{-13}$ for the hyper-Rayleigh band and $r_2 = 5.6 \times 10^{-14}$ for the 3400-cm^{-1} hyper-Raman band. Such nonlinear scattering signals are indeed very weak. For example, with a mode-locked Ti sapphire laser of 80-MHz repetition rate and 100-fs output pulse width at 840 nm, the detection rate resulting from the hyper-Raman scattering by liquid water (3400 cm^{-1} band) is only about 10 photons/s with 10-mW excitation power and assuming a high 1% overall detection efficiency.

An issue of important practical interest is the relative values of the one- and two-photon scattering to fluorescence cross-sectional ratios (i.e., relative values of

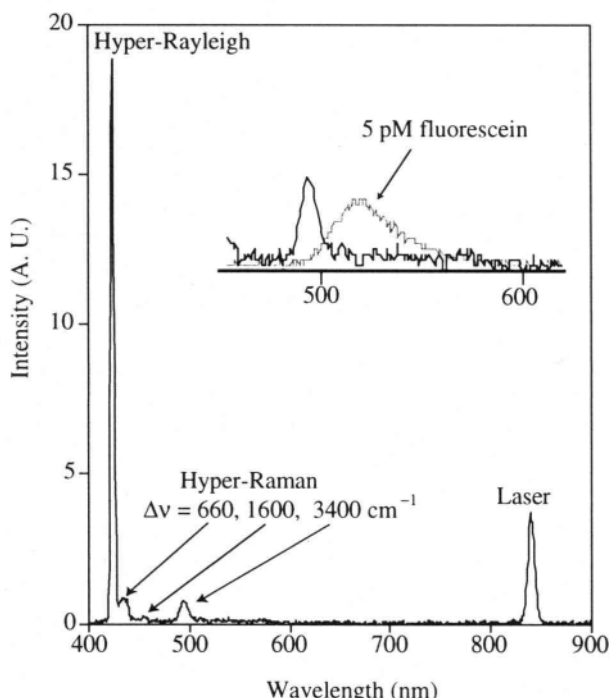


Figure 11.30. Hyper-Rayleigh and hyper-Raman spectrum of liquid water obtained with an integration time of 120 s. The insert shows the comparison between 5-pM fluorescein emission spectrum and the 3400-cm^{-1} hyper-Raman band.

r_1 and r_2). Figure 11.31 shows the 3400-cm^{-1} Raman band with 1PE at 488 nm (solid line) in the same epifluorescence setup. For comparison, the emission spectrum of rhodamine-B is also shown. Using the known one-photon cross sections and fluorescence quantum efficiencies of rhodamine-B and fluorescein, this result corresponds to $r_1 = 1.3 \times 10^{-12}$ for fluorescein. Thus, these measurements demonstrate that the hyper-Raman scattering background by water solvent relative to 2PE of fluorescein is reduced by approximately 20-fold as compared to the Raman scattering of water in 1PE in the epifluorescence geometry.

Note that, unlike the isotropic fluorescence emission for small dye molecules (such as fluorescein) in solution, the angular distributions of scattering depend on the incident polarization and symmetry of the scattering molecules and are in general not isotropic. Therefore, the ratios between scattering and fluorescence may vary in different detection geometries.

Although fluorescein is used as an example in comparing the scattering background from water solvent in one- and two-photon excitation, similar relative

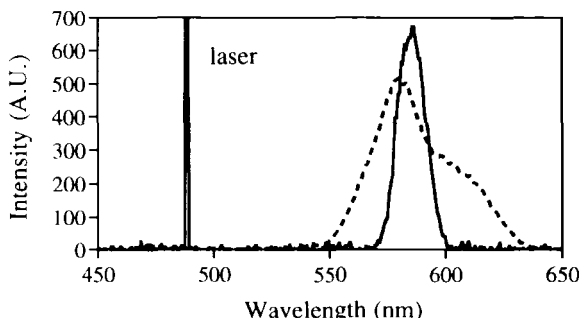


Figure 11.31. Comparison between the 3400-cm^{-1} Raman band (solid line) and the emission of 0.5-nM rhodamine-B (dashed line). The Raman spectrum is obtained with approximately 2.5-mW excitation power at the sample and an integration time of 2 s . The 1PE emission spectrum of the 0.5-nM rhodamine-B is extrapolated from the 290-nM rhodamine-B solution and scaled to the same excitation power.

reduction in scattering background using 2PE should be observed for a variety of fluorophores. As shown in Section 11.2, measurements of more than 25 2PE spectra of a wide range of molecular fluorophores revealed that σ_1/σ_2 are approximately 10^{-32} to $10^{-34}\text{ cm}^2\text{ s/photon}$. Thus, the measured hyper-Raman to Raman intensity ratio ($3 \times 10^{-35}\text{ cm}^2\text{ s/photon}$) indicated that scattering background from the strongest Raman band of liquid water is typically reduced by 10- to 100-fold in 2PE as compared to 1PE.

In general, Rayleigh scattering cross sections are approximately 10^3 times larger than the (one-photon) Raman scattering cross section.⁽⁷⁸⁾ Consequently, the background caused by hyper-Rayleigh scattering in 2PE is expected to be three to four orders of magnitude lower than Rayleigh scattering in 1PE. Moreover, the blueshifted 2PE peaks of many fluorophores (shown in Section 11.2) provide the opportunity to further reduce the background; the relatively large spectral separation between scattering and fluorescence can be adjusted by shifts of excitation wavelength to allow scattering to be readily distinguished from fluorescence using long-pass filters.

11.4.3.2. Dielectric Breakdown and Higher-Order Excitation

Let us again consider the saturation intensity for an n -photon process. For a square pulse in time, saturation occurs when $\alpha = \sigma_n I_p^n \tau \approx 1$. Therefore, the saturation peak intensity for the n -photon process (I_{ns}) is simply

$$I_{ns} \approx (\sigma_n \tau)^{-1/n} \quad (11.42)$$

Using the estimated n -photon cross sections listed in Table 11.1 and assuming $\tau \approx 100$ fs, the saturation peak intensities in units of photons/(cm² s) for two-, three-, and four-photon excitation are, respectively, 10^{31} , 5×10^{31} , and 10^{32} . In the near-IR wavelength region ($h\nu = 2$ eV), these intensities correspond to 3, 15, and 30 TW/cm², which can easily be obtained by strongly focusing the ultrashort pulses from femtosecond laser sources, such as the mode-locked Ti sapphire laser (assuming $f = 80$ MHz and $\tau = 100$ fs, an average power of 10 mW, when focused to a diffraction-limited spot by a 1.3-NA objective lens, can generate approximately 1 TW/cm² at the focal point). Thus, peak intensities around 5 TW/cm² may be used in two- and three-photon microscopy to generate the maximum excitation rate. However, the question arises as to whether it is possible to achieve such high instantaneous intensities in water or relevant biological buffer solutions without sample breakdown.

We first limit our discussion to laser-induced breakdown of water in the visible and near-IR (<1100 nm) where water is considered transparent. The 1/e absorption length of water at 1100 nm is approximately 5 cm. In general, the absorption of water is lower at shorter wavelengths in the near-IR, with the exception around 980 nm where the 1/e absorption length is only approximately 2 cm. It is well established that the relevant threshold for breakdown induced by a *highly focused laser pulse* (the relevant case in microscopy) is the threshold for dielectric breakdown,^(79,80) not the threshold for self-focusing. A previously measured peak intensity for the breakdown threshold of water is $I_B = 1.6 \times 10^{12}$ W cm⁻² for 30-ps pulses at 1.06 μm.⁽⁸¹⁾ Although I_B for transparent materials is relatively insensitive to the incident wavelength,⁽⁸²⁾ it strongly depends on the laser pulse width. Both a theoretical model and experimental data showed that $I_B \propto \tau^{-0.5}$ for bulk materials at $\tau > 10$ ps.⁽⁸³⁾ The property of the breakdown threshold with femtosecond pulsed illumination is still under intense study. Recent works from two groups showed clear deviations from the $I_B \propto \tau^{-0.5}$ behavior in the femtosecond region.^(84,85) The breakdown threshold in both studies increases significantly faster with decreasing pulse width than the $\tau^{-0.5}$ prediction for 100 fs $< \tau < 10$ ps. Thus, a lower bound of the breakdown threshold of liquid water can be obtained for $\tau = 100$ fs by using $I_B \propto \tau^{-0.5}$ and the measured threshold with 30 ps pulsed illumination. We obtain $I_B > 3 \times 10^{13}$ W cm⁻² with 100-fs pulsed illumination. Because it is also observed in general that I_B increases with decreasing laser beam spot size,⁽⁸³⁾ I_B in a tightly focused multiphoton microscopy condition may be considerably higher than our estimate. We note that peak intensities are generally less than 3×10^{11} W cm⁻² and 2×10^{12} W cm⁻² in typical two- and three-photon microscopy, respectively. Thus, the peak intensities in routine multiphoton microscopy are significantly below the dielectric breakdown threshold. In one experiment, we illuminated a pure-water sample with focal point peak intensities up to 5×10^{12} W cm⁻², using 100-fs pulses, and no significant emission was observed.

Although dielectric breakdown of pure water is not expected until peak intensities well above $I_B > 3 \times 10^{13} \text{ W cm}^{-2}$ in the 100-fs region, the photophysical responses of cellular materials and biological buffers to very intense radiation fields are yet to be explored in detail. The relative contributions of various order processes depends on the incident intensity. As the intensity increases so does the relative contribution of the higher-order processes. Thus, molecular photophysics and photochemistry can change fundamentally at high intensities. Novel processes may be encountered at a sufficiently high intensity region. For example, in addition to its characteristic UV fluorescence, we have discovered new blue-green emission from the neurotransmitter serotonin solution upon illumination by pulsed 830-nm light at peak intensities around $4 \times 10^{11} \text{ W cm}^{-2}$.⁽⁸⁶⁾ Detailed studies reveal that serotonin is photochemically transformed as a consequence of four-photon excitation to a photoproduct that then emits in the visible region via 2PE. Thus, a combined total of six photons is required to generate one visible photon.

Our preliminary studies of the behavior of buffer solutions also showed complicated photochemistry at very high incident intensities. Irradiation of HEPES and MOPS (but not phosphate) solutions with pulsed 840-nm light can generate visible emission at $I_p > 10^{12} \text{ W cm}^{-2}$. The visible emission scales approximately to the 10th power of the excitation, possibly revealing the generation of reactive photoproducts and the subsequent nonlinear excitation of the reaction products. Although relatively few experiments required $I_p > 10^{12} \text{ W cm}^{-2}$ in 2PLSM, the photochemistry and photophysics behavior of cellular materials and buffer solutions may have to be addressed in three-photon laser scanning microscopy where such high intensities are necessary.

The precise ratio of $(n+1)$ -photon-to n -photon-excited fluorescence emission can be obtained from Eqs. (11.7) and (11.19):

$$\text{Ratio} = \frac{\int_V d\mathbf{r} S^{n+1}(\mathbf{r})}{\int_V d\mathbf{r} S^n(\mathbf{r})} \frac{\sigma_{n+1}(\lambda)}{\sigma_n(\lambda)} I_p \quad (11.43)$$

Because the peak intensity of a pulsed laser scales as $I_p \propto \langle P(t) \rangle (\text{Area})^{-1} (f\tau)^{-1}$, one can increase or decrease the relative contribution of different-order excitation by manipulating the excitation pulse width, repetition rate, and focal spot size. In microscopy conditions, however, one does not have the freedom of adjusting the illuminated area since the highest possible resolution is usually demanded. Thus, the pulse width and repetition rate of the excitation source must be carefully chosen to maximize the desired excitation while reducing the unwanted excitation to a minimum. We note that fluorophore saturation and the subsequent degrada-

tion of the localized excitation must be considered at the same time in choosing such optimum pulse trains. For example, to minimize higher-order excitation processes (such as possible 3PE of amino acids and nucleic acids in 2PLSM at 700 to 800 nm) broad pulses (low pulse intensity) with high repetition rate should be used. On the other hand, to minimize the lower-order processes (such as one-photon absorption in 2PLSM) short pulses (high pulse intensity) with low repetition rate can be incorporated, with the consideration that the highest pulse intensity is limited by saturation.

The spatial integral ratios in Eq. (11.43) are in general between 0.1 to 1 for $n \geq 2$ (see Section 11.3.2). Thus, they are generally not critically important in altering the excitation mode in high-order processes ($n \geq 2$). However, because the excitation volume is proportional to the sample thickness in 1PE (assuming attenuation of the incident light can be neglected), the total amount of 1PE can be increased dramatically by increasing the sample path length. Therefore, sample thickness is an important consideration if residual 1PE exists in the wavelength region of the attempted MPE.

The ratio of the $(n + 1)$ -photon and n -photon cross sections is approximately $10^{-33} \text{ photon}^{-1} \cdot \text{cm}^2 \text{ s}$ (see Section 11.2.1). Aside from the ratio of the spatial integral, Eq. (11.43) predicts that all the different-order photon processes will be equally excitable at peak intensities around $I_p \approx 10^{33} \text{ photons} \cdot \text{cm}^{-2} \text{ s}^{-1}$. This value corresponds to approximately 300 TW/cm^2 in the near-IR-wavelength region. Thus, the photon order of the excitation becomes nondiscriminatory at extremely high intensities. This divergence of MPE is a clear indication that the description of MPE based on perturbation theory fails at such a high intensity level; i.e., the presence of the excitation light can no longer be treated as a perturbation to the molecular system. The RMS electric field (E field) at 300 TW/cm^2 is approximately $3.4 \times 10^8 \text{ V} \cdot \text{cm}^{-1}$. In this high E field, an electron moving through the distance of 1 Å would experience an energy difference of 3.4 eV, which is equivalent to the energy required for a UV transition of 370 nm. Obviously, such a large change of electron energy cannot be treated as perturbation.

Appendix: Absolute Measurement of Two-Photon Absorption Cross Sections and Two-Photon-Excited Fluorescence Emission Quantum Efficiencies Using Saturation

We describe here a potential method of direct measurement of the two-photon-excited fluorescence quantum efficiencies developed from the theory derived in Section 11.4.1.1. The exponential function in Eq. (11.35) can be

expanded in a power series:

$$e^{-g^{(2)}\sigma_2 f^{-1} \langle I_0(t) \rangle^2 S^2(\mathbf{r})} = \sum_{n=0}^{\infty} \frac{1}{n!} [-g^{(2)}\sigma_2 f^{-1} \langle I_0(t) \rangle^2 S^2(\mathbf{r})]^n \quad (11.44)$$

Assuming $R \gg 1$, substituting Eq. (11.44) into Eq. (11.35), and exchanging the summation with the integral, we obtain

$$\langle F(t) \rangle = \sum_{n=1}^{\infty} \frac{C_n}{n!} \langle I_0(t) \rangle^{2n} \quad (11.45)$$

where $C_n = -\frac{1}{2} \phi \eta C (-g^{(2)}\sigma_2 f^{-1})^n \int_V d\mathbf{r} S^{2n}(\mathbf{r})$ is the expansion coefficient. To obtain the absolute value of the two-photon absorption cross sections, we investigate the ratio of the expansion coefficients obtained in Eq. (11.45):

$$\frac{c_{n+1}}{c_n} = - \frac{\int_V d\mathbf{r} S^{2(n+1)}(\mathbf{r})}{\int_V d\mathbf{r} S^{2n}(\mathbf{r})} \sigma_2 g^{(2)} f^{-1} \quad (11.46)$$

It is clear from Eq. (11.46) that c_{n+1}/c_n is proportional to the two-photon absorption cross section σ_2 and is *independent* of the two-photon-excited fluorescence quantum efficiency (η), the system collection efficiency (ϕ), and the fluorophore concentration (C). To experimentally obtain the absolute values of σ_2 , all one need do is measure the time-averaged two-photon-excited fluorescence $\langle F(t) \rangle$ as a function of incident intensity and fit $\langle F(t) \rangle$ by using the power series of $\langle I_0(t) \rangle^{2n}$.

To obtain the absolute values of η from the same power-series fit, we consider the quantity $(c_{n+1})^n/(c_n)^{n+1}$. It is obvious that it is only a function of ϕ and η and is independent of $g^{(2)}\sigma_2 f^{-1}$. Because the fluorescence collection efficiency ϕ can be measured independently with one-photon-excited fluorescence,⁽²⁰⁾ the absolute values of two-photon-excited fluorescence emission quantum efficiency can be obtained even without any prior knowledge of $g^{(2)}$, σ_2 , or τ . It is obvious that the above analysis can be extended to n -photon excitation by raising I^2 to the appropriate order.

We note that the repetition rate of the laser can always be reduced experimentally to satisfy $R \gg 1$ regardless of the fluorescence lifetime of the test fluorophore. Because only steady-state measurements are required to measure the two-photon absorption cross sections and the two-photon-excited fluorescence quantum efficiencies, the decrease in the generated fluorescence resulting from the reduced repetition rate can always be compensated by increasing the integration time of the experiments. Such an increase in the integration time does not change the overall signal-to-background ratio because the background counts

should scale with the pulse repetition rate, unless instrument noise is the main contribution in the background. In practice, reducing the pulse repetition rate also avoids the effects of photobleaching and ISC, which may otherwise interfere with the experimental results (see Section 11.4.2).

Acknowledgments

This work was carried out in the Developmental Resource for Biophysical Imaging and Opto-electronics (DRBIO) with funding by NSF (DIR8800278), NIH (RR04224), and NIH (RR07719). The authors thank Drs. W. Zipfel and R. M. Williams for providing the figures and captions of Figures (11.16–11.20) and for help with the numerical calculation. They acknowledge fruitful discussions with Drs. J. Mertz, W. Zipfel, R. M. Williams, S. Maiti, J. B. Shear, J. B. Guild, and W. Denk.

References

1. M. Göppert-Mayer, Über Elementarakte mit zwei Quantensprüngen, *Ann. Phys.* 9, 273–295 (1995).
2. W. Kaiser and C. G. B. Garrett, Two-photon excitation in $\text{CaF}_2 \text{ Eu}^{2+}$, *Phys. Rev. Lett.* 7, 229 (1961).
3. S. Singh and L. T. Bradley, Three-photon absorption in naphthalene crystals by laser excitation, *Phys. Rev. Lett.* 12, 612–614 (1964).
4. R. Pantell, F. Pradere, J. Hanus, M. Schott, and H. Puthoff, Theoretical and experimental values for two-, three, and four-photon absorptions, *J. Chem. Phys.* 46, 3507–3511 (1966).
5. W. M. McClain and R. A. Harris, in: *Excited States* (E. C. Lim, ed.), pp. 1–56, Academic Press, New York (1977).
6. R. R. Birge, in: *Ultrasensitive Laser Spectroscopy* (D. S. Kliger, ed.), Academic Press, New York (1983), pp. 109–174.
7. A. P. Shreve and A. C. Albrecht, A three-photon fluorescence excitation study of the $S_0(\text{A}1g)$ - $S_1(\text{B}2u)$ transition in neat liquid benzene, *J. Chem. Phys.* 94, 5772–5773 (1990).
8. W. Denk, J. H. Strickler, and W. W. Webb, Two-photon laser scanning fluorescence microscopy, *Science* 248, 73–76 (1990).
9. R. Yuste and W. Denk, Dendritic spines as basic function units of neuronal integration, *Nature* 375, 682–684 (1995).
10. R. M. Williams, D. W. Piston, and W. W. Webb, Two-photon molecular excitation provides intrinsic 3-dimensional resolution for laser-based microscopy and microphotochemistry, *FASEB J.* 8, 804–813 (1994).
11. W. Denk, D. W. Piston, and W. W. Webb, in: *The Handbook of Confocal Microscopy* (J. Pawley, ed.), Plenum, New York (1995), pp. 445–458.
12. T. Wilson and C. J. R. Sheppard, *Theory and Practice of Scanning Optical Microscopy*, Academic Press, New York (1984).
13. J. A. Valdmanis and R. L. Fork, Design considerations for a femtosecond pulse laser balancing self phase modulation, group velocity dispersion, saturable absorption, and saturable gain, *IEEE J. Quantum Electron.* QE-22, 112–118 (1986).

14. D. E. Spence, P. N. Kean, and W. Sibbett, 60-fsec pulse generation from a self-mode-locked Ti sapphire laser, *Opt. Lett.* **16**, 42 (1991).
15. C. Xu, W. Zipfel, J. B. Shear, R. M. Williams, and W. W. Webb, Multiphoton fluorescence excitation: new spectral windows for biological nonlinear microscopy, *Proc. Natl. Acad. Sci. U.S.A.* **93**, 10763–10768 (1996).
16. D. L. Wokosin, V. E. Centonze, S. Crittenden, and J. G. White, Three-photon excitation of blue-emitting fluorophores by laser scanning microscopy, *Mol. Biol. Cell* **6**, 113a (1995).
17. S. W. Hell, K. Bahlmann, M. Schrader, A. Soini, H. Malak, I. Gryczynski, and J. R. Lakowicz, Three-photon excitation in fluorescence microscopy, *J. Biomed. Opt.* **1**, 71–74 (1996).
18. S. Maiti, J. B. Shear, W. Zipfel, R. M. Williams, and W. W. Webb, Measuring serotonin distribution in live cells with three-photon excitation, *Science* **275**, 530–532 (1997).
19. W. L. Smith, in: *Handbook of Laser Science and Technology* (J. Weber, ed.), pp. 229–258, CRC, Boca Raton, FL (1986).
20. J. P. Hermann and J. Ducuing, Absolute measurement of two-photon cross-sections, *Phys. Rev. A* **5**, 2557–2568 (1972).
21. I. M. Catalano and A. Cingolani, Absolute two-photo fluorescence with low-power CW lasers, *Appl. Phys. Lett.* **38**, 745–747 (1981).
22. J. R. Lakowicz, I. Gryczynski, H. Malak, and Z. Gryczynski, Two-color two-photon excitation of fluorescence, *Photochem. Photobiol.* **64**, 632–635 (1996).
23. F. H. M. Faisal, *Theory of Multiphoton Processes*, Plenum Press, New York (1987).
24. L. D. Dickson, Characteristics of a propagating gaussian beam, *Appl. Opt.* **9**, 1854–1861 (1970).
25. C. J. R. Sheppard and H. J. Matthews, Imaging in high-aperture optical systems, *J. Opt. Soc. Am. A* **4**, 1354–1360 (1987).
26. S. Hell, G. Reiner, C. Cremer, and E. H. K. Stelzer, Aberrations in confocal microscopy induced by mismatches in refractive index, *J. Microsc.* **169**, 391–405 (1993).
27. R. Swofford and W. M. McClain, The effect of spatial and temporal laser beam characteristics on two-photon absorption, *Chem. Phys. Lett.* **34**, 455–460 (1975).
28. R. D. Jones and P. R. Callis, A power-square sensor for two-photon spectroscopy and dispersion of second-order coherence, *J. Appl. Phys.* **64**, 4301–4305 (1988).
29. S. M. Kennedy and F. E. Lytle, *p*-Bis(*o*-methylstyryl)benzene as a power-square sensor for two-photon absorption measurements between 537 and 694 nm, *Anal. Chem.* **58**, 2643–2647 (1986).
30. G. S. He, J. D. Bhawalkar, and P. N. Prasad, Three-photon-absorption-induced fluorescence and optical limiting effects in an organic compound, *Opt. Lett.* **20**, 1524–1526 (1995).
31. R. Loudon, *The Quantum Theory of Light*, Clarendon Press, Oxford (1983).
32. J. Guild, C. Xu, and W. W. Webb, Measurement of group delay dispersion of high numerical aperture objectives using two-photon excited fluorescence, *Appl. Opt.* **36**, 397–401 (1997).
33. C. Xu, J. Guild, W. W. Webb, and W. Denk, Determination of absolute two-photon excitation cross-sections by *in situ* second-order autocorrelation, *Opt. Lett.* **20**, 2372–2374 (1995).
34. M. Muller, J. Squier, and G. J. Brakenhoff, Measurement of femtosecond pulses in the focal point of a high-numerical-aperture lens by two-photon absorption, *Opt. Lett.* **20**, 1038–1040 (1995).
35. J.-C. Diels, in: *Dye Laser Principles* (F. J. Duarte and L. W. Hillman, eds.), Academic Press, San Diego (1990), pp. 104–109.
36. M. Chalfie, Y. Tu, G. Euskirchen, W. W. Ward, and D. C. Prasher, Green fluorescence protein as a marker for gene expression, *Science* **263**, 802–805 (1994).
37. K. D. Niswender, S. M. Blackman, L. Rohde, M. A. Magnuson, and D. W. Piston, Quantitative imaging of green fluorescent protein in cultured cells: comparison of microscopic techniques, use in fusion proteins and detection limits, *J. Microsc.* **180**, 109–116 (1995).
38. S. M. Potter, C. M. Wang, P. A. Garrity, and S. E. Fraser, Intravital imaging of green fluorescent protein using two-photon laser-scanning microscopy, *Gene (Amsterdam)* **173**, 25–31 (1996).

39. A. B. Cubitt, R. Heim, S. R. Adams, A. E. Boyd, L. A. Gross, and R. Y. Tsien, Understanding, improving and using fluorescent proteins, *TIBS* 20, 448–455 (1995).
40. B. P. Cormack, R. H. Valdivia, and S. Falkow, FACS-optimized mutants of the green fluorescent protein (GFP), *Gene (Amsterdam)* 173, 33–38 (1996).
41. D. W. Piston, B. R. Masters, and W. W. Webb, Three dimensionally resolved NAD(P)H cellular metabolic redox imaging of the *in situ* cornea with two-photon excitation laser scanning microscopy, *J. Microsc.* 178, 20–27 (1995).
42. K. Konig, P. T. C. So, and E. Gratton, Two-photon excited lifetime imaging of autofluorescence in cells during UVA and NIR photostress, *J. Microsc.* 183, 197 (1996).
43. K. Konig, Y. Liu, G. J. Sonek, M. Bems, and B. J. Tromberg, Autofluorescence spectroscopy of optically trapped cells, *Photochem. Photobiol.* 62, 830–835 (1995).
44. J. R. Lakowicz, *Principles of Fluorescence Spectroscopy*, Plenum Press, New York (1983).
45. L. Stryer, Fluorescence energy transfer as a spectroscopic ruler, *Ann. Rev. Biochem.* 47, 819–846 (1978).
46. A. P. Davey, E. Bourdin, F. Henari, and W. Blau, Three-photon induced fluorescence from a conjugated organic polymer for infrared frequency upconversion, *Appl. Phys. Lett.* 67, 884–885 (1995).
47. I. Gryczynski, H. Szmacinski, and J. R. Lakowicz, On the possibility of calcium imaging using indo-1 with three-photon excitation, *Photochem. Photobiol.* 62, 804–808 (1995).
48. I. Gryczynski, H. Szmacinski, and J. R. Lakowicz, Three-photon induced fluorescence of 2,5-diphenyloxazole with a femtosecond Ti sapphire laser, *Chem. Phys. Lett.* 245, 30–35 (1995).
49. C. Xu and W. W. Webb, Measurement of two-photon excitation cross-sections of molecular fluorophores with data from 690 nm to 1050 nm, *J. Opt. Soc. Am. B* 13, 481–491 (1996).
50. J. P. Hermann and J. Ducuing, Dispersion of the two-photon cross-section in rhodamine dyes, *Opt. Comm.* 6, 101–105 (1972).
51. I. Gryczynski, J. Kusba, V. Bogdanov, and J. R. Lakowicz, Quenching of fluorescence by light: a new method to control the excited-state lifetime and orientations of fluorophores, *J. Fluoresc.* 4, 103–109 (1994).
52. D. J. Bradley, M. H. R. Hutchinson, T. M. Koetser, G. H. C. New, and M. S. Petty, Interaction of picosecond laser pulses with organic molecules. I: Two-photon fluorescence quenching and singlet states excitation in rhodamine dyes, *Proc. R. Soc. London A.* 328, 97–121 (1972).
53. G. Grynkiewicz, M. Poenie, and R. Y. Tsien, A new generation of Ca^{2+} indicators with greatly improved fluorescence properties, *J. Biol. Chem.* 260, 3440–3450 (1985).
54. A. Fischer, C. Cremer, and E. H. K. Stelzer, Fluorescence of coumarins and xanthenes after two-photon absorption with a pulsed titanium-sapphire laser, *Appl. Opt.* 34, 1989–2003 (1995).
55. P. F. Curley, A. I. Ferguson, J. G. White, and W. B. Amos, Application of a femtosecond self-sustaining mode-locked Ti sapphire laser to the field of laser scanning confocal microscopy, *Opt. Quantum Electron.* 24, 851–859 (1992).
56. L. Parma and N. Omenetto, Fluorescence behavior of 7-hydroxycoumarine excited by one-photon and two-photon absorption by means of a tunable dye laser, *Chem. Phys. Lett.* 54, 544–546 (1978).
57. J. M. Schmitt, A. Knuttel, and M. Yadlowsky, Confocal microscopy in turbid media, *J. Opt. Soc. Am. A* 11, 2226–2235 (1994).
58. F. A. Duck, *Physical Properties of Tissue*, Academic, London (1990).
59. J. Mertz, C. Xu, and W. W. Webb, Single molecule detection by two-photon excited fluorescence, *Opt. Lett.* 20, 2532–2534 (1995).
60. T. Plakhotnik, D. Walser, M. Pirotta, A. Renn, and U. P. Wild, Nonlinear spectroscopy on a single quantum system: two-photon absorption of a single molecule, *Science* 271, 1703 (1996).

61. J. B. Shear, E. B. Brown, and W. W. Webb, Multiphoton-excited fluorescence of fluorogen-labeled neurotransmitters, *Anal. Chem.* **68**, 1778–1783 (1996).
62. S. Maiti, J. B. Shear, and W. W. Webb, Multiphoton excitation of amino acids and neurotransmitters: a prognosis for *in situ* detection, *Biophys. J.* **70**, A210 (1996).
63. J. Pawley (Ed.), *The Handbook of Confocal Microscopy*, Plenum, New York (1995).
64. P. E. Hanninen, M. Schrader, E. Soini, and S. W. Hell, Two-photon excitation fluorescence microscopy using a semiconductor laser, *Bioimaging* **3**, 70–75 (1995).
65. P. M. W. French, The generation of ultrashort laser pulses, *Rep. Prog. Phys.* **58**, 169–267 (1995).
66. E. L. Elson and W. W. Webb, Concentration correlation spectroscopy: A new biophysical probe based on occupation number fluctuations, *Ann. Rev. Biophys. Bioeng.* **4**, 311–334 (1975).
67. N. L. Thompson, in: *Topics in Fluorescence Spectroscopy*, Vol. 1 (J. R. Lakowicz, ed.), pp. 337–378, Plenum, New York (1991).
68. M. B. Schneider and W. W. Webb, Measurement of submicron laser beam radii, *Appl. Opt.* **20**, 1382–1388 (1981).
69. J. P. Y Kao and S. R. Adams, in: *Optical Microscopy: Emerging Methods and Application* (B. Herman and J. J. Lemaster, eds.), pp. 27–85, Academic Press, London (1993).
70. W. Denk, Two-photon scanning photochemical microscopy: mapping ligand-gated ion channel distributions, *Proc. Natl. Acad. Sci. U.S.A.* **91**, 6629–6633 (1994).
71. D. R. Sandison and W. W. Webb, Background rejection and signal-to-noise optimization in confocal and alternative fluorescence microscopy, *Appl. Opt.* **33**, 603–615 (1994).
72. I. Berlman, *Handbook of Fluorescence Spectra of Aromatic Molecules*, Academic Press, New York (1971).
73. M. M. Asimov, V. N. Gavrilenko, and A. N. Rubinov, Laser photolysis of laser dyes and the influence of triplet quenchers, *J. Luminesc.* **46**, 243–249 (1990).
74. C. Xu, Cornell University, Ph.D thesis (1996).
75. T. Hirschfeld, Quantum efficiency independence of the time integrated emission from a fluorescent molecule, *Appl. Opt.* **15**, 3135–3139 (1976).
76. R. W. Terhune, P. D. Maker, and C. M. Savage, Measurements of nonlinear scattering, *Phys. Rev. Lett.* **14**, 681–684 (1965).
77. C. Xu, J. B. Shear, and W. W. Webb, Hype-Rayleigh and hyper-Raman scattering background of liquid water in two-photon excited fluorescence detection, *Anal. Chem.* **69**, 1285–1287 (1997).
78. R. M. Measures, in: *Analytical Laser Spectroscopy*, Vol. 50 (N. Omenetto, ed.), p. 321, Wiley, New York (1979).
79. Y. R. Shen, *The Principles of Nonlinear Optics*, Wiley, New York (1984).
80. E. Yablonovitch, Optical dielectric strength of Alkali-Halide crystals obtained by laser-induced breakdown, *Appl. Phys. Lett.* **19**, 495 (1971).
81. W. L. Smith, P. Liu, and N. Bloembergen, Superbroadening in H(2)O and D(2)O by self-focused picosecond pulses from a YA1G ND laser, *Phys. Rev. A* **15**, 2396–2403 (1977).
82. W. L. Smith, Laser-induced breakdown in optical materials, *Opt. Eng.* **17**, 489–503 (1978).
83. J. R. Bettis, II, R. A. House II, and A. H. Guenther, in: *Laser Induced Damage in Optical Materials*, NBS Spec. Pub., Vol. 462, U.S. GPO, Washington DC (1976) pp. 338–345.
84. D. Du, X. Liu, K. J. Squier, and G. Mourou, Laser-induced breakdown by impact ionization in SiO(2) with pulsedwidths from 7 ns to 150 fs, *Appl. Phys. Lett.* **64**, 3071–3073 (1994).
85. B. C. Stuart, M. D. Feit, A. M. Rubenchik, B. W. Shore, M. D. Perry, Laser-induced damage in dielectrics with nanosecond to subpicosecond pulses, *Phys. Rev. Lett.* **74**, 2248–2251 (1995).
86. J. B. Shear, C. Xu, and W. W. Webb, Multiphoton-excited visible emission by serotonin solutions, *Photochem. Photobiol.* **65**, 931–936 (1997).

Index

- Absorption
 - cross sections, 103
 - polyenes, 25
 - pump-probe, 453
 - two-photon, 1
- Adrenocorticotropin (ACTH)
 - light quenching, 344
- Alkanes
 - two-photon excitation, 113
- Anisotropy
 - decay, 43, 71
 - Indo-1, 129
 - multi-wave mixing, 224, 238
 - photoselection, 55
 - stimulated emission, 261
 - tryptophan, 198
 - two-photon, 11, 43, 59
 - tyrosine, 200
- Anisotropy decay
 - light quenching, 315, 334, 336
 - oxazine, 263
 - perylene, 270
- Anisotropy spectra, 92, 104
 - Hoechst 33342, 104
 - indole, 108
 - liver alcohol dehydrogenase, 201
 - ribonuclease, 202
 - tryptophan, 199
 - tyrosine, 200
- 1,2-Benzanthracene, 217
- Benzene
 - two-photon, 26
- Bifluorophores
 - multi-wave mixing, 230
- bis-MSB, 119
- Calcium probes
 - Indo-1, 126
 - two-photon excitation, 492
- Cell imaging, 462, 471; *see also* Microscopy
- Coronene, 218
- Correlation times
 - standards, 118
- Cross sections, 473
 - two-photon absorption, 103
- Cross section, 473
 - light quenching, 323
 - two-photon, 535
- DAPI, 492
- DPH, 89; *see also* Diphenylhexatriene
- Dansyl, 492
- Decay times
 - ps two-photon standard, 119
 - two-photon standards, 116
- Dichroism
 - linear, 49
- Dielectric breakdown, 532
- 4-dimethylamino-4'-cyanostibene (DCS)
 - light quenching, 330
- 4-dimethylamino- ω -diphenylphosphenyl-*trans*-styrene, 119
- 2,5-diphenyl-1,3,4-oxadiazole
 - two-color two-photon excitation, 134
- Diphenylhexatriene, 89
 - anisotropy decay, 98
 - frequency-domain, 98
 - three-photon excitation, 125
 - time-domain, 100
- 2,5-diphenyloxazole, 123
- DNA stains
 - DAPI, 492
 - Hoechst 33342, 101
- Emission spectra
 - two-photon excitation, 500
- Energy transfer
 - two-photon excitation, 487

- Evanescence wave
light quenching, 347
- Excitation spectra
multi-photon, 485
two-photon, 192
- Experimental methods
light quenching, 309, 321
total internal reflection, 349
two-photon cross sections, 535
- Fibroblasts, 462
- Fluorescence microscopy, 361, 471
erythrocytes, 462
fibroblasts, 462
scanning, 367
- Fluorescence quenching by stimulated emission, 305; *see also* Light quenching
anisotropy decay, 319, 327
experimental methods, 321
frequency-domain, 316
intensity decay, 316, 327
light quenching, 361
microscopy, 427
mixtures, 341
offset beams, 412
orientation distribution, 311
polarization, 313
scanning microscopy, 369
spectral relaxation, 339
total internal reflection, 347
wavelength selectivity, 335
- Frequency-domain
alkanes, 115
anisotropy decay, 96
diphenylhexatriene, 98
human serum albumin, 110
light quenching, 316
microscopy, 432
pump-probe, 431, 453
two-photon excitation, 97
- Fura-2, 492
- Green fluorescent protein
two-photon excitation, 490
- Ground state depletion, 387
multi-photon excitation, 516
- Hoescht 33342, 101
anisotropy spectra, 104
intensity decay, 102
- Human serum albumin
anisotropy decay, 111
intensity decay, 111
two-photon excitation, 110, 195
- Imaging
multi-photon excitation, 509
scanning microscopy, 520
skin, 510
- Indo-1, 492
three-photon excitation, 126
- INDO/S, 34
- Indole
anisotropy spectra, 108
two-photon, 31, 37, 106
- Intensity decay
light quenching, 315
pump-probe, 458
- Intersystem crossing, 521, 524
- Lifetime
light quenching, 318
- Lifetime-resolved
light quenching, 318
- Light quenching, 305; *see also* Fluorescence
quenching by stimulated emission
microscopy, 427
- Liver alcohol dehydrogenase
anisotropy, 201
two-photon excitation, 196
- Membranes, 90
anisotropy, 99, 150
DPH, 98, 125
phase transition, 99
three-photon excitation, 125
two-photon, 146
- 1-Methylperylene
vibration relaxation, 288
- 4Pi Microscopy, 392
- Microscopy, 361
3D, 418
4Pi, 394, 401
confocal, 394, 441
ground state depletion, 387
multi-photon, 501
optical transfer function, 442
pump-probe, 431
resolution, 437, 448
scanning, 503
scanning optics, 452

- Microscopy (*cont.*)
stimulated emission, 427
theta 4Pi, 414
time-resolved, 430
two-photon, 401
- Multiphoton microscopy, 87, 471
- Multi-wave mixing, 211
anisotropy, 224
bifluorophores, 230
energy transfer, 228
quantum yield, 222
- NADH
anisotropy, 204
skin, 511
two-photon, 487
two-photon excitation, 203
- N*-acetyl-L-tryptophanamide
anisotropy, 133; *see also* Tryptophan
three-photon excitation, 131
- Oriented systems, 145
anisotropy theory, 146
light quenching, 313
- Order parameters, 149
- Orientational distribution, 64
light quenching, 311
tensor, 69
- Perylene, 77
stimulated emission, 269
- Phenylalanine
two-photon excitation, 35
- Phenol
two-photon excitation, 29
- Photobleaching, 521, 526
- Photoselection
three-photon excitation, 93
- Point spread function, 364
light quenching, 377
- Point spread function engineering, 361
- Polarization, *see also* Anisotropy
circular, 14
light quenching, 313
linear, 13
photoselection, 55
two-color two-photon, 136
- Polyenes
two-photon, 25
- Prodan
light quenching, 346
- Proteins, 187
human serum albumin, 110
light quenching, 344
three-photon excitation, 131
two-photon excitation, 187
- Pump-probe, 256
absorption, 453
frequency domain, 432
light sources, 446
microscopy, 431
time-resolution, 461
- Quantum yield
multi-wave mixing, 222
- Quenching
alkanes, 114
stimulated emission, 305
- Relaxation
multi-wave mixing, 233, 242
- Ribonuclease
anisotropy spectra, 207
emission spectra, 197
two-photon excitation, 197
- Ribonuclease T₁
light quenching, 344
- Rotational diffusion, *see also* Anisotropy decay
anisotropy, 79
oxazine, 263
perylene, 77
stimulated emission, 260
- Scanning fluorescence microscopy, 367
light quenching, 369
- Scattering
non-linear, 530
- Skin
imaging, 510
- Solvent relaxation
light quenching, 320
- Spatial resolution, 477
- Spectral relaxation
light quenching, 339
- Spherical tensor
two-photon, 50, 51
- Standards
two-photon excitation, 116
- Stimulated emission, 253, 305
1-methylperylene, 274, 288
microscopy, 427
optics, 449

- Stimulated emission (*cont.*)
 perylene, 269
 time-resolution, 461
 two-photon, 457
- Tetradecane, 114; *see also* Alkanes
 quenching, 114
- Tensors
 INDO/S, 34
 orientational distribution, 69
 spherical, 50
 two-photon, 3, 12, 19
- Tetraphenylbutadiene
 light quenching, 328
- Theory
 anisotropy decays, 45
 multi-photon excitation, 475
 photoselection, 55, 93
- Three-photon excitation, 87, 123, 480, 493
 2,5-diphenyloxazole, 123
 anisotropic decays, 133
 anisotropy, 125, 129
 excitation spectra, 485
 Indo-1, 126
 proteins, 131
- T_1 relaxation
 perylene, 274
- Time-domain
 anisotropy decays, 100
 light quenching, 333
- Time-resolved anisotropy, 43
 perylene, 77
- Time-resolved fluorescence
 two-photon, 48
- Total internal reflection fluorescence
 light quenching, 347
- Transient absorption
 microscopy, 427
- Tryptophan, 190
 excitation spectra, 192
 three-photon excitation, 131
- Two-color two-photon (2C2P) excitation, 134
 2,5-diphenyl-1,3,4-oxadiazole, 134
 polarization effects, 236
- Two-photon excitation
 anisotropy, 11
 anisotropy theory, 146
 benzene, 26
- Two-photon excitation (*cont.*)
 history, 7
 multi-wave mixing, 211
 order parameters, 149
 oriented systems, 145
 perylene, 25
 polarization, 13
 tensors, 3, 12, 19
 theory, 1
 two-color, 134
- Two-photon absorption, *see also* Two-photon excitation
 nucleotides, 37
 theory, 2, 9
 transition dipoles, 10
 two-color, 134
 vibrational effects, 8
- Two-photon excitation
 4Pi, 405
 alkanes, 113
 dansyl, 492
 DNA stains, 491
 experimental methods, 205
 Fura-2, 492
 green fluorescent proteins, 490
 Indo-1, 492
 indole, 31, 37, 106
 light quenching, 326
 microscopy, 401
 NADH, 204, 487
 nucleotides, 37
 phenol, 29
 phenylalanine, 35
 photoselection, 55
 proteins, 106, 187
 skin, 420
 theta 4Pi, 414
 tryptophan, 190
- Tyrosine, 190
 excitation spectra, 192
 two-photon, 29, 36
- Vibrational relaxation
 1-methylperylene, 288
 perylene, 269
 stimulated emission, 268
- Wavelength-dependent light quenching, 337